

## CHAPTER 1: INTRODUCTION

### 1.1 Background to the Thesis

A detailed design, manufacture and testing of an extending boom was made within a teaching company scheme between Brunel and Niftylift in 1999 [1]. The closed, pentagonal steel tube was selected to provide the required strength and stiffness with internal capacity for the hydraulic piping and cables. Rees and Joyce [1, 2] selected a closed, pentagonal steel tube section to resist local buckling whilst limiting the end deflection to a value pre-determined from the weight of two men and their baggage contained within the cage at the end of a fully extended boom. Typically, from a trailer platform vehicle with stowed height of 2.2 m, the extended telescopic beam can reach a vertical height 17.1 m and provide a horizontal outreach of 8.7 m when subjected to an end load of 200 kg. The self-propelled version offers slightly improved telescoping length dimensions: vertical lift: 21 m, horizontal reach 12m, coupled with the added advantage of a moveable base [2].

A recent British Standard has recognised that strength, stiffness and stability are issues concerning safety in these elevated platforms [3]. An initial analytical model of the deflection profile under the extended outreach condition in these vehicles was developed from applying a strain energy method (i.e. to a stepped, tubular, cantilever beam [1]). Deflection experiments were conducted upon a full-scale, three-boom cantilever in which the end fixings attempted to match those arising within the knuckle-end, the pivot pin and ram fixing attachment positions for the vehicle. Additional strains were measured with gauges bonded to outer surfaces at positions along each boom where local concentrations arose from cut-outs for cabling and in areas of contact between adjacent lengths. The testing showed that whilst the analytical model provided for the global deflections with good accuracy, further work would be required to account for the effect of the local deformation behaviour upon the design. Moreover, the self-weight of steel booms added to deflection and load carrying capacity to an extent that the performance of alternative, lighter materials was deemed worthy of investigation.

The present proposal is to examine these aspects in more detail especially in context of an optimum design. It is expected that commercial software packages such as ABAQUS/CAE will be employed for this purpose. The reliance placed upon these packages demands that they be accompanied by validating analytical solutions where the latter are available. The

early work has showed that energy methods including Castigliano's theorem and the principle of virtual work may be used for checking displacements but only at specific points along the booms. More recently a continuous displacement function has been sought from applying Macaulay's method to a simplified two-boom, tubular square-section laboratory cantilever under end load [4]. The principle of successive integration from curvature to give slope and from slope to give displacement was applied to the scaled-down laboratory model. Normally, Macaulay's method works only with a uniform cross-section but here an allowance for the changing section area is required. The piecewise scheme developed here was first applied to a three section telescoping cantilever beam assembly which admits three different second moments of area: those within the two boom regions plus one overlap region, when the compatibility between rotations and displacements at their interfaces is ensured. This technique was then applied to a two section cantilever assembly, which is the candidate assembly examined throughout the course of this thesis. Surface stresses and strains may be calculated from classical mechanics, allowing for the changing section and bending moment with length.

Displacements and longitudinal surface strains were measured at various length positions with minimum and maximum overlap. This provided the displacement and strain profiles experimentally so enabling a comparison with the theory. While the deflected shape is continuous, the strain profile is interrupted at the overlap as we might expect from its strengthening influence. The theory reproduces the experimental behaviour well enough for it to be used as the validating tool described above. Where the theoretical predictions are overlaid to reveal error there may be a need for further refinements to be made as required.

Buckling is a relatively new problem that has been identified in the two-boom section cantilever. There is an urgent need to develop a theory and marry it with experimental predictions to account for these phenomena that is common amongst such sections. As opposed to the deflection and stress behaviour which are already well documented in student projects undertaken at Niftylift [2, 16, 17, 18], buckling poses a difficulty in that, considerable resources would need to be devoted in terms of the creation of a test rig and suitable apparatus to model real life working conditions. Both global and local buckling theories, especially those propagated using the energy methods are of vital importance, and these theories must be adapted to the assembly. A means of verifying the same must also be devised.

## **1.2 Statement of the Problem**

Given that telescopic sections are finding increasing applications in those instances where space is at a premium and reduction in weight and material cost is a necessity, it is vital that a design theory and subsequent methodology is generated wherein the behaviour of the telescoping assembly is accounted for, in terms of its possible application areas. Despite numerous advances over the ages in the field of mechanics, not to mention increasing use of telescoping sections all around us from simple household appliances to complex retractable stadium roofing, the lack of literature in the public domain with regards to telescoping sections is a deterrent to the further use of this simple yet highly effective structure.

This thesis aims to shed light on the uniqueness of the telescoping assembly and its detailed analysis and bring it forth into the public domain as there is an absence of material pertaining to telescoping structures in the wider engineering context as compared to the information that is available in the private sector domain.

## **1.3 Aim and Objectives**

**Aim:** To provide a design methodology to estimate stiffness related properties in telescopic cantilever beams as used for lifting devices. Stiffness refers to the load - displacement behaviour for which the related properties are to include beam geometry, material density and strength. Thus, for example, when minimising weight of the telescopic beam structure used as a lift and reach device, its stiffness and load carrying capacity are to be preserved.

**Objectives:**

1. To study known deflection, buckling and stress analyses methods and adapt them to thin-walled, telescopic tubular sections using analytical and numerical techniques. The techniques to be examined include Macaulay's flexure equation, Mohr's moment area method, energy methods including Castigliano's theorem, the principle of virtual work, the Rayleigh-Ritz method and modelling with finite elements,
2. To build a specific analytical model most suitable for the prediction of deflections stress distribution and buckling load characteristics in this structure,
3. To validate the model proposed through the conduct of experiments on scaled beam structures,
4. To apply the model to case studies including crane and elevating platform structures,

5. To disseminate predicted and experimental results through publication.

Analyses and selective laboratory experiments are to be conducted to meet the design specification. The theoretical analyses are to envelop both analytical and numerical approaches. The experiments will employ scaled models for laboratory testing to appraise each theory. Applications will then be made to commercial devices that employ the telescopic beam structure.

#### **1.4 Summary Findings**

The Literature review on Classical Mechanics identified the three major areas of investigation into the telescoping arrangement as follows.

- i. Design of the telescoping sections for their many applications often requires estimates of deflections at various length positions. The development of analytical methods for estimating deflection and stress for beams in bending were developed in the 18<sup>th</sup> century by Euler and Bernouli and are described in many textbooks [5-8]. The beam deflection is found by four common methods: (i) direct integration [5-8], (ii) Macaulay's step function [8, 9], (iii) Mohr's theorems [13-14] and (iv) strain energy [13-14]. Despite uniform section beams being well-served by the classical theory they are less often used for deflection analyses of variable section beams including tapered, stepped and telescopic designs [9, 10]. Application of classical theory and its adaptation to the telescoping arrangement is to be examined.
- ii. The nature in which buckling occurs within the telescoping cantilever assembly is to be established, as: (a) a local buckling produced within the individual rectangular hollow sections and (b) a global buckling wherein the structure in its entirety undergoes buckling. In the former, transverse shear and torsion in individual rectangular hollow section members is given special consideration because of their ability to sustain a constant shear flow irrespective of wall thickness (unlike an open section). However pure flexure is only possible when shear forces act at the shear centre of a member. A combined loading scenario is examined whereupon the telescoping arrangement is subjected to bending, torsion and shear. Considering the latter, principles of application of energy methods are scrutinised and the means by which they can be adapted to the telescoping arrangement are studied in detail. The

telescoping assembly in its entirety is examined as a cantilever-column in that one end is fixed and the other is free. In order to arrive at the critical buckling load of the assembly it was imperative to understand the concepts of bending and potential energy systems.

Based on the findings from the literature, a three-pronged methodology was developed to match the proposed theory with the results obtained from experimental work conducted as well as from Finite Element Analyses.

### **1.5 Structure of the Thesis**

Chapter 2 outlines the literature that was identified to have a vital role in achieving the summary findings presented above in §1.4.

Chapter 3 proposes the *Tip Reaction Model* as applied to the two section telescopic cantilever beam assembly and provides the detailed tip deflection analysis of the same by the four common methods namely; Direct Integration, Macaulay's Step Function, Mohr's Theorem and Strain Energy Principles. Deflection prediction techniques have been adapted to the two section telescopic cantilever beam assembly. A C-program developed using a direct integration technique, has been generated and is currently in use in industry.

Chapter 4 provides the buckling methodology wherein, by working from first principles, a better understanding of the complexity of the problem was attained. This involved a detailed understanding and application of energy methods to the case at hand. What was referred to by Timoshenko as the energy method is used as a base and applied to the cantilever column as detailed in [15]. This approach in turn is verified by validating the result obtained against the criteria for the Euler critical buckling load for a column having one end fixed and the other free as its boundary conditions. A general form for predicting the critical buckling load exactly is thus derived and is applied to suit each case individually taking into account the different cross sectional second moments and lengths.

Chapter 5 examines the phenomenon of shear, torsion and a combination of both in the individual rectangular hollow sections that comprise the overall telescoping assembly. The concept of constant shear flow in the walls of the sections as well as the importance of the shear centre is identified and applied to the structure. Importance is laid on the design

optimisation of the hollow rectangular constituent beam sections of the assembly, wherein the longer limbs of the cross section, can be adjusted to raise the stress to a predetermined design stress value, thereby saving weight, allowing for greater efficiency in load bearing and simultaneous buckling at the load limit.

Chapter 6 describes the bending and shear stress analysis of the two section telescoping assembly when it is subjected to both in-line and offset loading. Thus combined loading is examined whereupon the telescoping arrangement is subjected to bending, torsion and shear. Stresses generated are plotted graphically in which the accompanying analyses performed here originate from the second of two published papers, emanating from this work [92]. As such the results obtained are verified.

Chapter 7 provides in ample detail the FE analysis that was applied to the two section telescoping arrangement in order to obtain the tip deflections for different loadings, the stresses generated as a result of subjecting the telescoping arrangement to both inline and offset loading and finally the determination of the critical buckling load. The results thus obtained were used to verify the theoretically determined deflection, stress and buckling models.

Chapter 8 details the experimental work that was conducted on a two section telescoping cantilever beam and the results obtained for deflection and stress analysis as well as buckling load determination. The experimental section examines the variations in deflections and stresses for varying governing parameters, especially the effect the change in overlap length has on the overall strength of the structure. Also of importance is the stress analysis wherein the strain gauges readings are converted to their equivalent principal stress magnitudes and compared with their theoretically derived counterparts. The test beam itself was subjected to both in-line and offset loading in order to mimic the possible loading configurations of the telescopic assembly in its working environment. The test rig developed is the closest approximation possible to an encastre fixing.

Chapter 9 compares and discusses the results obtained from the three-pronged approach as applied to the two section telescoping cantilever beam assembly and draws conclusions, whilst also making recommendations for future work.

Appendix A details the *Tip Reaction Model* as applied to the two section telescopic cantilever beam assembly.

Appendix B outlines the C program that uses the Macaulay's theorem derived deflection equations to calculate and predict the tip deflections of the two section telescopic cantilever beam assembly, for given configurations. A similar program written and developed for the three section telescopic cantilever beam assembly is in commercial application.

Appendix C outlines the in-line loading induced stress analysis of the candidate assembly.

Appendix D analyses the offset loading induced stress analysis of the two section telescoping arrangement.

Appendix E is the first paper published as a by-product of this thesis. It is entitled '*The Telescopic Cantilever Beam Assembly: Part 1 – Deflection Analysis*'.

Appendix F represents the second paper published, entitled '*The Telescopic Cantilever Beam Assembly: Part 2 – Stress Analysis*'. Taken together, parts 1 and 2 provide an analytical theory for bending of a discontinuous beam that did not exist heretofore, thereby obviating the need for a numerical solution.

Appendix G outlines in exhaustive detail the FEA methodology and procedure for deflection, stress and buckling determination, for the given assembly.

Appendix H details the strain gauging principles, and application techniques that were used to conduct the stress analysis of the telescoping assembly.

## CHAPTER 2: LITERATURE REVIEW

### 2.1 Introduction

This thesis has its origins in Abraham's dissertation entitled "Establishing a Methodology for the Finite Element Analysis of a Complex Boom Assembly for Estimating Stress Hot Spots and Deflections", [18] which focussed entirely on the Finite Element Analysis (FEA) of the HR15N telescopic boom assembly manufactured by Niftylift, a renowned manufacturer of access platforms, both trailer-mounted and self-propelled. FEA was performed on the aforementioned telescopic boom assembly under the action of concentrated and distributed loading in order to observe, identify and interpret the results of combined loading.

At the time of undertaking of the project very little was understood about the degree of complexity and the nature of modelling the boom assembly in FEA. The software module used was ABAQUS/CAE and although Niftylift being manufacturers were adept at analysing the assembly the results generated were not entirely understood. The project started out initially as a means of verification of experimental results using FEA of the boom assembly but due to the difficulty of full-scale testing, the former was limited and eventually the project became entirely software driven.

Although the complexity of the boom assembly analysed in this project and those past [16 - 18] is much greater than the two section telescoping cantilever assembly great pains has been taken in this instance to introduce and apply well-known and age old concepts to a new structure and therein lies the novelty or the contribution to knowledge.

The theories reviewed here are by no means novel or unique but have been established through the ages. However in dealing with a 'new' structure, a starting point was needed and the sections that follow aim to follow on from this objective. At the outset, the author wishes to express that individual symbols and coordinates for each of the theories examined through the course of this chapter, have been adopted from their original sources.

## 2.2 Curvature – Bending Moment Relationship

The Curvature-Bending Moment Relationship detailed below is the basis and start of many a text on Solid Mechanics [5 – 8]. The objective of this section is to allow the reader to see behind the thought process and reasoning behind the chapters that follow.

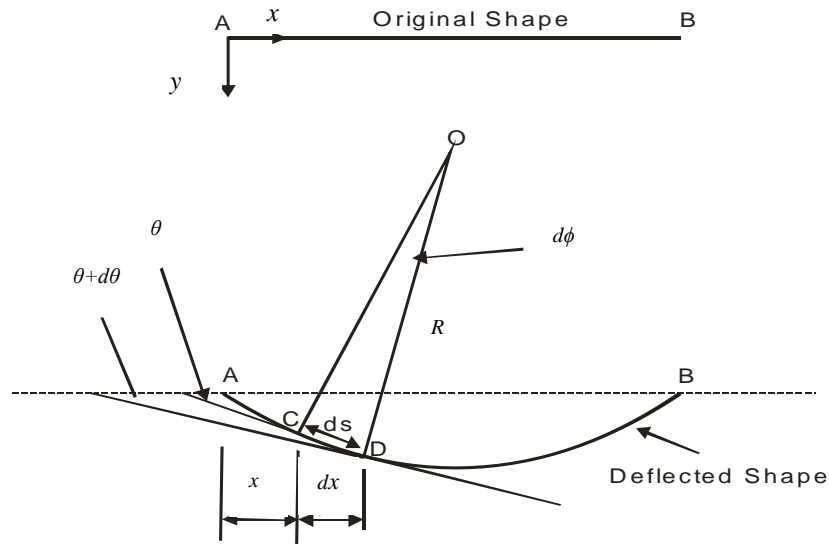


**Figure 2.1: Beam in Bending (Adapted from [20])**

The beam AB, lying along the  $x$ -axis, is loaded with positive bending moment  $M$ . The bending moment causes the beam to deform into an arc of radius  $R$ . According to the sign convention, the centre of curvature O will then be above the  $x$ -axis. A short element of beam CD of length  $ds$  subtends angle  $d\phi$  about O, where  $ds = R.d\phi$ . The change in angle at the centre of curvature, O, must equal the change in gradient of the tangent, hence  $|d\phi| = |d\theta|$ .

In moving from point C to D in the direction of positive  $x$ , and taking into account the sign convention:

$$ds = R.d\phi = -R.d\theta, \text{ or } \frac{1}{R} = -\frac{d\theta}{ds}.$$

Sagging curvature is taken to be positive and is defined by a radius of curvature  $R$  with centre at O. Since the deflection of the beam is small compared to the radius of curvature it can be approximated that  $ds \approx dx$  and hence

$$\frac{1}{R} = -\frac{d\theta}{dx}.$$

It can be assumed that for small deflections the slope  $\frac{dY}{dx} = \tan\theta \approx \theta$  such that:

$$\frac{1}{R} = -\frac{d\theta}{dx} = -\frac{d^2Y}{dx^2}$$

But  $\frac{M}{I} = \frac{\sigma}{y} = -\frac{E}{R}$  (2.1)

where  $M$  is the bending moment about the neutral axis

$R$  is the radius of curvature of the beam

$\sigma$  is the stress induced as a result of the bending moment  $M$

$y$  is the perpendicular distance to the neutral axis

$Y$  is the deflection induced

$E$  is the Young's Modulus of Elasticity of the beam material

$I$  is the second moment of area about the neutral axis

Equation (2.1) yields the relation  $\frac{1}{R} = -\frac{M}{EI}$ . Rearranging the terms yields:

$$M = -EI \frac{d^2Y}{dx^2}$$

which requires two successive integrations with constants introduced to match the boundary conditions in order to express the deflection  $Y$  in terms of the un-deflected position  $x$ .

### 2.3 Macaulay's Step Function Method

With successive integration of the flexure equation (2.2) discontinuities will arise in the moment expression when  $x$  passes points of concentrated forces, moments and abrupt changes in distributed loading. If Equation (2.2) is applied to regions in  $x$  where  $M(x)$  is continuous, the greater becomes the number of differential equations and integration constants to be solved. Fortunately the amount of work involved may be lessened when  $M(x)$  in Equation (2.2) is replaced with a step function  $M(x-a)$  as outlined in [20]

$$M[x-a] = -EI \frac{d^2Y}{dx^2} \tag{2.3}$$

in which  $a$  defines positions at which discontinuities arise. Equation (2.3) permits successive integration of a single step function as is applied to the three section telescoping cantilever beam as shown in [13]. The following rules are to be kept in mind.

- (a) Take the origin for  $x$  at the left-hand end.
- (b) Where necessary extend and counterbalance uniformly distributed loading to the right-hand end.
- (c) Let concentrated moments lie at the position  $[x-a]^0$ .
- (d) Establish the function  $M[x-a]$  in the furthest right portion of the beam. Sagging moments are positive.
- (e) Integrate such terms as  $[x-a]$  in the form  $[x-a]^2/2$ . These terms are to be ignored when, in substituting values for  $x$  the value of the bracket  $[\ ]$  becomes negative.
- (f) Apply the known slope and deflection values to find the constants of integration.

## 2.4 Mohr's Moment Area Theorems

The moment area method is convenient in case of beams acted upon by point loads in which case the bending moment area consists of triangles and rectangles. In the case of distributed load the determination of the position of the M-diagram's centroid itself involves integration and as such it no longer remains simpler than Macaulay's method. However, this method may be used in certain standard cases of distributed load where the position of the centroid of the bending moment area is known. This section shows the reader the way in which the author understood the moment area theorem. The manner in which it has been applied to the same to the two section telescoping cantilever beam assembly is detailed in §3.5.1 and §3.5.2.

Consider a beam AB as shown in Figure 2.2 (a) carrying such a load that it has a bending diagram as shown in Figure 2.2 (b). Let the beam bend into AC'D'B as shown in Figure 2.2 (c). Now consider an element of small length CD of the beam at a distance  $x$  from B as shown in Figures 2.2 (a) and 2.2 (b).

Let  $M$  = Bending moment between  $C$  and  $D$   
 $\delta x$  = Length of  $CD$   
 $R$  = Radius defined by the deflected beam

$\delta\theta$  = Angle included between the tangent at  $C'$  and  $D'$  facing the datum or the change of slope over the elementary portion  $\delta x$

$A$  = Area of bending moment diagram over the entire span

$x'$  = Horizontal distance of centre of gravity  $G$  of the entire bending moment diagram from the datum

$\theta$  = The angle in radians, included between the tangents drawn at the extremities of the beam

From the geometry of the deflected beam it can be seen that  $C'D' = R\delta\theta$  or  $\delta x = R\delta\theta$

$$\delta\theta = \frac{\delta x}{R} \tag{2.4}$$

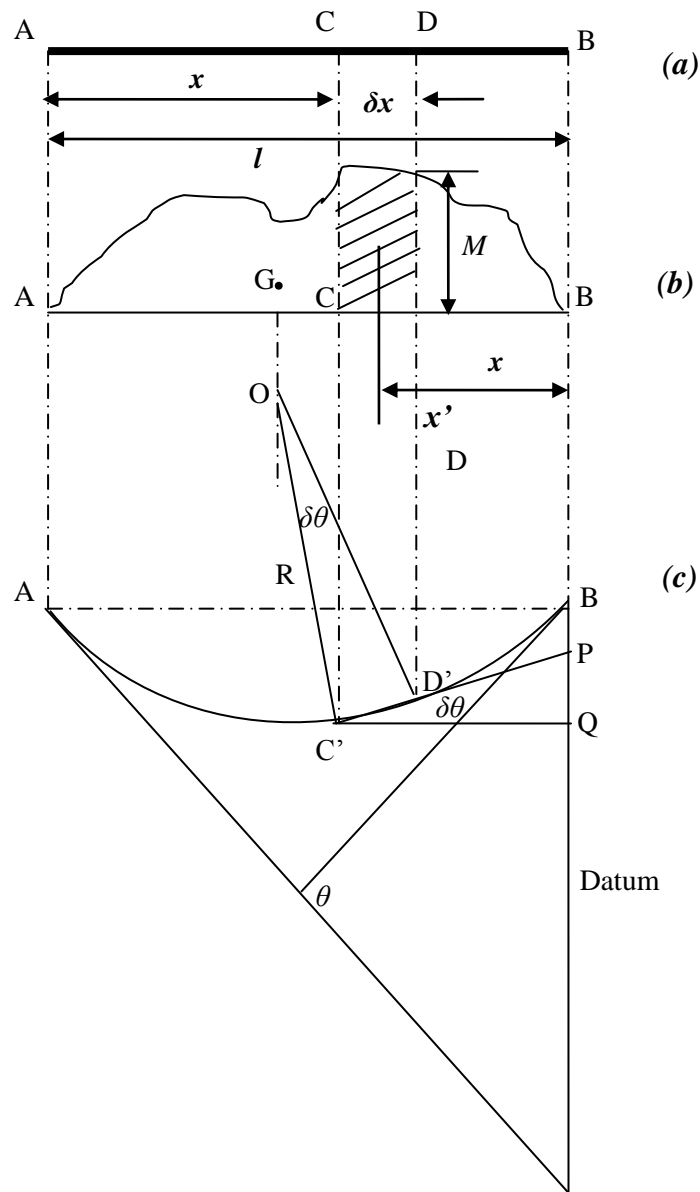


**Figure 2.2: Beam in Bending (Adapted from [19])**

But  $\frac{M}{I} = \frac{\sigma}{y} = -\frac{E}{R}$  and hence  $\frac{1}{R} = -\frac{M}{EI}$ . As opposed to Equation (2.1), the negative sign is not considered whilst dealing with areas. Substituting this value of  $R$  in Equation (2.4) reveals:

$$\delta\theta = \delta x \frac{M}{EI} \quad (2.5)$$

The total change of slope from  $A$  to  $B$  may be found out by integrating Equation (2.5) between the limits 0 to  $l$  as:

$$\theta = \int_0^l \frac{M\delta x}{EI} = \frac{1}{EI} \int_0^l M dx$$

But  $\int_0^l M dx = \text{Area of the Bending Moment Diagram}$

This leads us to the first of the two Mohr's theorems as follows:

$$\theta = \frac{A}{EI} \quad (2.6)$$

Drawing tangents at  $C'$  and  $D'$  and then making them meet at  $P$  and  $Q$  on the datum line through  $B$  as shown in Figure 2.2 (c). From the geometry of the figure it can also be seen that the tangents at  $C'$  and  $D'$  also subtend an angle of  $\delta\theta$

$$PQ = x' \delta\theta = \frac{x' M dx}{EI} = \frac{M dx \cdot x'}{EI} \quad (2.7)$$

The total intercept may be found by integrating Equation (2.7) above between the limits 0 to  $l$  as:

$$Y = \int_0^l \frac{M dx \cdot x'}{EI} = \frac{1}{EI} \int_0^l M \cdot dx \cdot x'$$

But  $M \cdot dx \cdot x' = \text{Moment of area of the Bending Moment Diagram over portion } \delta x \text{ about the datum}$

$$\int_0^L M \cdot dx \cdot x' = \text{Moment of Area of the Bending Moment Diagram over the entire span } \delta x$$

about the datum

$$= A \cdot x'$$

And finally the last of the two Mohr's theorems can be expressed as:

$$Y = \frac{Ax'}{EI} \quad (2.8)$$

A point to remember is that in Equations (2.6) and (2.8) the  $I$  value may be constant or may be variable. Equations (2.6) and (2.8) are Mohr's first and second theorems more commonly referred to as the moment-area equations. When these equations (2.6) and (2.8) are employed to find the slope and deflection at a given point in a beam respectively, their application depends upon the manner in which the beam is supported.

## 2.5 Deflection Theorems in Brief

Design of cantilever beams for their many applications often requires estimates of deflections at various length positions. The development of analytical methods for estimating deflection are described in many textbooks [5-8]. The beam deflection  $y$  is found by four common methods: (i) direct integration [5-8], (ii) Macaulay's step function [5-8, 13, 14], (iii) Mohr's theorems [5-8, 19] and (iv) strain energy [6, 13, 14]. Both (i) and (ii) are based on the flexure equation derived above

$$M = -EI \frac{d^2Y}{dx^2} \quad (2.2)$$

The product  $EI$  is the *flexural rigidity* which is constant in a uniform cross-section. Sagging and hogging moments are taken to be positive and negative, respectively. The moment function,  $M(x)$  in Equation (2.2), is the bending moment expressed in term of the length position  $x$ . The direct integration method (i) adopts successive integrations of Equation (2.2) leading to the slope  $dY/dx$  and then the displacement  $Y$ . Method (i) is restricted to relatively simple loading, including that considered here, which does not lead to discontinuous  $M(x)$  expressions. Macaulay's step-function technique (ii) is used where moment discontinuities

do arise at span positions where additional concentrated load are applied and also, for a uniform loading that does not extend to the full length. Mohr placed a geometrical interpretation upon the bending-moment diagram when integrating Equation (2.2) for slope and deflection. When A and B are separate points on the moment diagram ( $M(x)$  vs.  $x$ ), for which B is a point of zero slope and the deflection at A is required, then Mohr's two theorems (iii) state:

$$\text{Slope at A} = \frac{1}{EI} \times \text{Area of the } M\text{-diagram between A and B}$$

$$\text{Deflection of A relative to B} = \frac{1}{EI} \times \text{First moment of area the } M\text{-diagram between B and A about A.}$$

When strain energy methods (iv) are used to estimate beam deflection the energy stored through an internal stress and strain is equated to the work done by external forces and moments. Two useful interpretations of this approach, adopted for FE analyses, lie in the theorems of Castigliano and the principle of virtual work, which are dealt with in the sections that follow [6]. Despite uniform section beams being well-served by the classical theory it is less often used for deflection analyses of variable section beams including tapered, stepped and telescopic designs [9, 10]. Here, it is more likely that FE is adopted to ensure that a given deflection allowance is not exceeded. The sections that follow detail the methods of deflection determination.

## 2.6 Principle of Superposition

This principle, as stated in [20], states that the total elastic displacement at a point in a structure under a given combination of externally applied loading may be obtained by summing the displacements at that point when the loads are applied to their position independently in any sequence. This principle is amply detailed and applied to the two section telescoping cantilever beam assembly, in §3.5.3. §3.5.1 and §3.5.2. These detail the Mohr's moment area method when applied to the tip loaded and uniformly distributed loaded two section telescoping cantilever beam assembly, respectively. The principle of superposition is used to obtain the deflection of the structure when subjected to a combination of both tip and uniformly distributed loading. In §3.5.3 the principle has been applied to load versus displacement but it can also be applied to connect any one of the following: load-stress, load-strain, stress-displacement and strain-displacement. An important caveat is that

each of the afore-mentioned pairs must be linearly related as would be found for a structure obeying Hooke's law within its elastic range.

## **2.7 Energy Methods**

Chai Yoo's insightful publication was a most valuable source in the thorough grasping of the energy methods detailed in this section [28]. Energy methods provide a convenient means of formulating the governing differential equation and necessary natural boundary conditions. The solutions that are obtained by solving the governing equations are exact within the framework of the theory (for classical beam theory) computing unknown forces and displacements in elastic structures. Besides this, the energy principles are fundamental to the study of structural stability and structural dynamics. However, one of the greatest advantages of the energy methods is its usefulness in obtaining approximate solutions in situations where exact solutions are difficult or impossible to obtain [21, 22]. Undoubtedly familiarity with the energy principles will be an invaluable asset in the study of structural mechanics. Additional references for a more detailed treatment of energy methods may be found in the books of Hoff [23], Langhaar [24], Fung and Tong [25], Sokolnikoff [26] and Shames and Dym [27].

### 2.7.1 Preliminaries

Consider an infinitesimal rectangular parallelepiped at point in a stressed body and let the terms  $T_1$ ,  $T_2$  and  $T_3$  represent the traction vectors on each face perpendicular to the coordinate axes  $x_1$ ,  $x_2$  and  $x_3$  respectively as shown in Figure 2.3. The components of the stress tensor denoted by  $\sigma_{ij}$  are the projections of tractions  $T_i$  on the face whose normal is  $x_j$ .

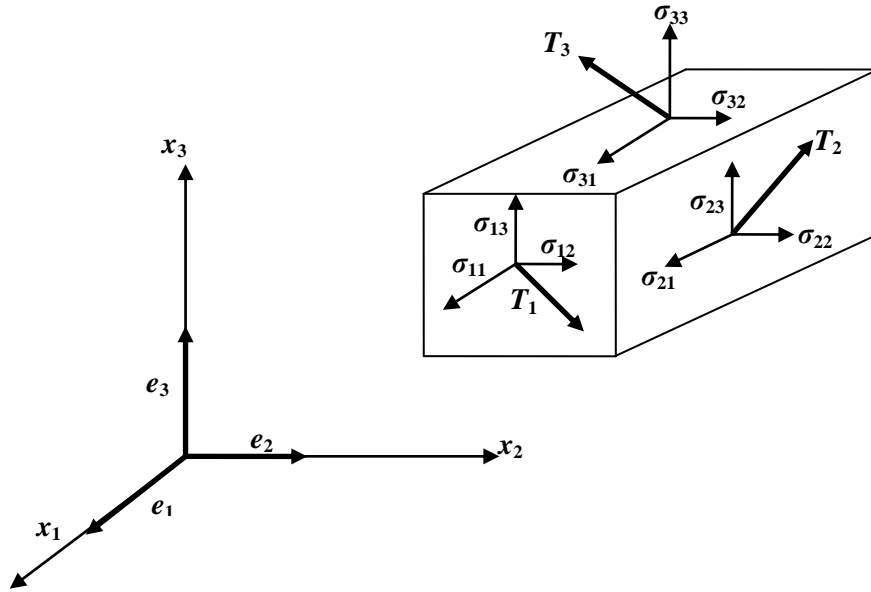


**Figure 2.3: Stress tensors and their components (Adapted from [28])**

Hence, each traction vector is written as

$$\begin{aligned} T_1 &= \sigma_{11}e_1 + \sigma_{12}e_2 + \sigma_{13}e_3 \\ T_2 &= \sigma_{21}e_1 + \sigma_{22}e_2 + \sigma_{23}e_3 \\ T_3 &= \sigma_{31}e_1 + \sigma_{32}e_2 + \sigma_{33}e_3 \end{aligned} \quad (2.9)$$

Or in compact form (index notation)

$$T_i = \sigma_{ij}e_j \quad (2.10)$$

Figure 2.4 shows the traction vector  $T$  acting on an arbitrary plane identified by  $n$  (unit normal to the plane) along with traction vectors  $T_i$  acting on the projected plane indicated by  $e_i$  and the body force per unit volume  $f$ . The force acting on the arbitrary sloping plane ABC is  $T_n dA_n$  while the force on each projected plane is  $T_i dA_i$  as each has a unit normal in the negative  $e_i$  direction.

Each projected area can be computed by

$$dA_i = dA_i \cos(\mathbf{n}, \mathbf{e}_i) = dA_i \mathbf{n} \cdot \mathbf{e}_i \quad (2.11)$$

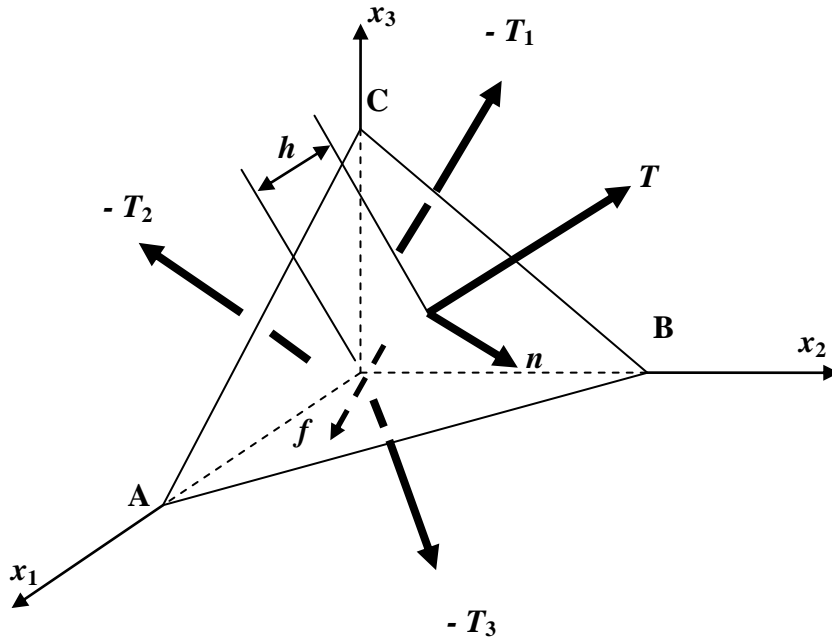


**Figure 2.4: Stresses on an infinitesimal tetrahedron (Adapted from [28])**

so that

$$dA_n = (dA_n) / (\mathbf{n} \cdot \mathbf{e}_i) = (dA_n) / (n_i \mathbf{e}_i) \quad (2.12)$$

where

$$n_i = \mathbf{n} \cdot \mathbf{e}_i = \cos(\mathbf{n}, \mathbf{e}_i) \quad (2.13)$$

Since the tetrahedron is in equilibrium the resultant of all forces acting on it must vanish.

Hence

$$\left( T_n - T_i n_i + \frac{h}{3} f \right) dA_n = 0 \quad (2.14)$$

Resolving  $T_n$  into Cartesian components ( $T_n = T_i \mathbf{e}_i$ ) and taking the limit as  $h \rightarrow 0$ , Equation (2.14) reduces to

$$T_n = T_i \mathbf{e}_i = T_i n_i \quad (2.15)$$

Substituting Equation (2.10) into Equation (2.11) yields

$$T_i e_i = T_i n_i = T_j n_j = \sigma_{ji} e_i n_j \quad (2.16)$$

from which the stress tensor components are:

$$T_i = \sigma_{ji} n_j \quad (2.17)$$

Consider a volume of material  $v$  bounded by a closed surface  $s$ . Let the body force per unit volume distributed throughout the body  $v$  be  $f$  and the stress tensors distributed over the surface  $s$  be  $T$ . If the body is in equilibrium then the sum of all forces acting on  $v$  must vanish; that is

$$\int_v f \, dv + \int_s T \, ds = 0 \quad (2.18)$$

or in component form

$$\int_v f_i \, dv + \int_s T_i \, ds = 0 \quad (2.19)$$

Equation (2.17) may be rewritten as

$$\int_s T_i \, ds = \int_s (\sigma_{ji} n_j) \, ds \quad (2.20)$$

Assuming that the components  $\sigma_{ji}$  and their first derivatives are continuous the surface integral in Equation (2.20) can be transformed into a volume integral using the divergence theorem as

$$\int_s (\sigma_{ji} n_j) \, ds = \int_v (\sigma_{ji,j}) \, dv \quad (2.21)$$

From Equations (2.19), (2.20) and (2.21) it follows immediately that

$$\int_v (f_i + \sigma_{ji,j}) \, dv = 0 \quad (2.22)$$

Equation (2.22) can only be satisfied if the integrand is equal to zero at every point in the body. Hence,

$$f_i + \sigma_{ji,j} = 0 \quad (2.23)$$

Equation (2.23) presents three equations of equilibrium written in terms of stresses and body forces.

### 2.7.2 Principle of Virtual Work

*If a structure is in equilibrium and remains in equilibrium while it is subjected to a virtual displacement the external virtual work  $\delta W_E$  done by the external forces acting on the structure remains equal to the internal virtual work  $\delta W_I$  done by the internal stresses [28].*

The external virtual work is

$$\delta W_E = \int_s (T_i \delta u_i) ds + \int_v (f_i \delta u_i) dv \quad (2.24)$$

Using Equation (2.17) and the divergence theorem the first term in Equation (2.24) can be transformed into

$$\int_s (T_i \delta u_i) ds = \int_s (\sigma_{ij} n_j \delta u_i) ds = \int_s (\sigma_{ij} \delta u_{i,j}) dv = \int_v (\sigma_{ij,j} \delta u_i + \sigma_{ij} \delta u_{i,j}) dv \quad (2.25)$$

Substituting Equation (2.25) into Equation (2.24) yields

$$\delta W_E = \int_v [(\sigma_{ij,j} \delta u_i + f_i) \delta u_i + (\sigma_{ij} \delta u_{i,j})] dv \quad (2.26)$$

Since the structure is in equilibrium  $f_i + \sigma_{ji,j} = 0$ . Hence Equation (2.26) reduces to

$$\delta W_E = \int_v (\sigma_{ij} \delta u_{i,j}) dv \quad (2.27)$$

The infinitesimal strain increment tensor is  $\delta e_{ij} = (\delta u_{i,j} + \delta u_{j,i})/2$  and  $\delta u_{i,j} = \delta u_{j,i}$  is symmetrical which leads to

$$\sigma_{ij} \delta u_{i,j} = \sigma_{ij} \delta e_{ij} \quad (2.28)$$

This transforms Equation (2.28) to

$$\int_v (\sigma_{ij} \delta e_{ij}) dv = \delta W_I = \delta U \quad (2.29)$$

Equation (2.29) describes the internal work done by the actual stresses (due to real forces) and virtual strains produced during the virtual displacement. The internal work  $W_I$  is frequently referred to as the strain energy  $U$  stored in the elastic body. From Equations (2.24), (2.28) and (2.29) one immediately obtains

$$\delta W_E = \int_s (T_i \delta u_i) ds + \int_v (f_i \delta u_i) dv = \int_v (\sigma_{ij} \delta e_{ij}) dv = \delta W_I = \delta U \quad (2.30)$$

Equation (2.30) is a mathematical statement of the principle of virtual work. The reverse of this principle is also true. That is, if  $\delta W_E = \delta W_I$  for virtual displacement then the body is in equilibrium as explained in Tauchert [22]. The principle of virtual work is valid regardless of the material stress-strain relations as shown in the derivation.

### 2.7.3 Principle of Complementary Virtual Work

Figure 2.5 shows the stress-strain diagram of a nonlinearly elastic rod. The strain energy  $U$  represents the energy stored in a deformed elastic body; however, the physical interpretation of the complementary strain energy  $U^*$  is not clear.

The strain energy  $U$  in the rod under uniaxial stress  $\sigma_{11}$  is defined by

$$U = \int_v \left( \int_0^{e_{11}} \sigma_{11} de_{11} \right) dv = v \int_0^{e_{11}} (\sigma_{11}) de_{11} \quad (2.31)$$

The strain energy density or the strain energy per unit volume is equal to the area under the material's stress-strain curve as is shown in Figure 2.5. The complementary strain energy  $U^*$  in a uniform section rod is defined by

$$U^* = \int_v \left( \int_0^{\sigma_{11}} e_{11} d\sigma_{11} \right) dv = v \int_0^{\sigma_{11}} (e_{11}) d\sigma_{11} \quad (2.32)$$

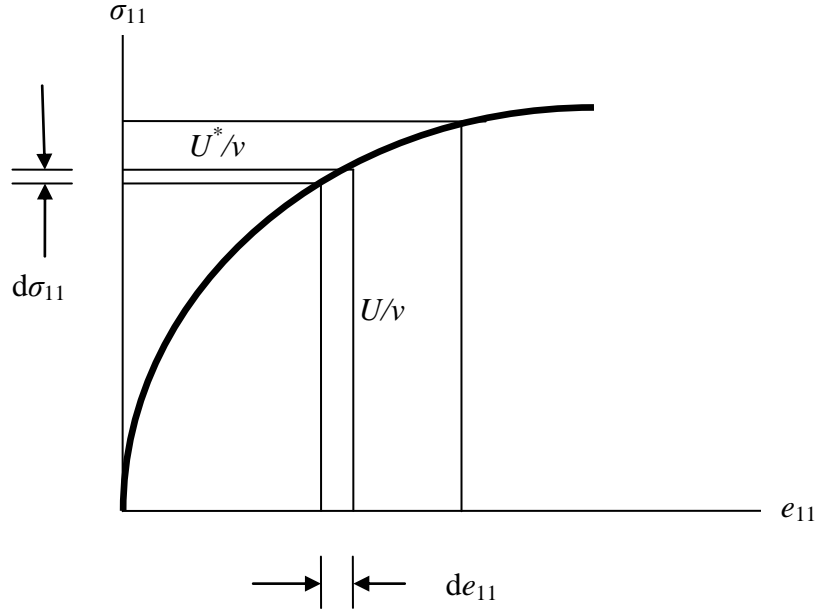


**Figure 2.5: Stress-strain curve of a non-linearly elastic rod (Adapted from [28])**

Therefore, the complementary strain energy density corresponds to the area above the stress-strain curve. For a linearly elastic material the two areas are equal and  $U^* = U$ . In order to maintain the generality the structure under consideration is assumed to have arbitrary material properties. Consider an imaginary system of surface tractions  $\delta T_i$  and body forces  $\delta f_i$  that produce a state of stress  $\delta \sigma_{ij}$  inside the structure. If these quantities are in equilibrium they must satisfy the equilibrium equations such that from Equation (2.23):

$$(\delta \sigma_{ij})_{,j} + \delta f_i = 0$$

The work done by these virtual forces during the actual displacements  $u_i$  is referred to as the complementary virtual work  $\delta W_E^*$  and is expressed as

$$\delta W_E^* = \int_S (\delta T_i u_i) dS + \int_V (\delta f_i u_i) dV \quad (2.33)$$

Proceeding in a manner similar to that used in the derivation of Equation (2.30) with the roles of the actual and virtual quantities interchanged one obtains the following

$$\int_S (\delta T_i u_i) dS + \int_V (\delta f_i u_i) dV = \int_V (\delta \sigma_{ij} e_{ij}) dV \quad (2.34)$$

The right hand side of Equation (2.34) is denoted as

$$\delta U^* = \delta W_I^* = \int_v (\delta \sigma_{ij} e_{ij}) dv \quad (2.35)$$

From Equations (2.33) and (2.35), Equation (2.34) is rewritten symbolically as

$$\delta W_E^* = \delta U^* = \delta W_I^* \quad (2.36)$$

Equation (2.35) is the principle of complementary virtual work. If a structure is in equilibrium the complementary virtual work done by the external virtual force system under the actual displacement is equal to the complementary virtual work done by the internal virtual stresses under the actual strains.

#### 2.7.4 Principle of Minimum Potential Energy

It is assumed that there exists a strain energy density  $u=U/v$ , that is a homogeneous quadratic function of strains  $u(e_{ij})$  such that

$$\sigma_{ij} = \frac{\partial u}{\partial e_{ij}} \quad (2.37)$$

It is recalled that the virtual displacement field  $\delta u_i$  was not related to the stress field  $\sigma_{ij}$  when applying the principle of virtual work. They are now related through a constitutive law expressed by Equation (2.37). Substituting Equation (2.37) into the principle of virtual work, Equation (2.30), one obtains

$$\begin{aligned} \int_s (T_i \delta u_i) ds + \int_v (f_i \delta u_i) dv &= \int_v (\sigma_{ij} \delta e_{ij}) dv = \int_v \left( \frac{\partial u}{\partial e_{ij}} \delta e_{ij} \right) dv = \int_v \delta^{(1)} u dv \\ &= \delta^{(1)} \int_v u dv = \delta^{(1)} U \end{aligned} \quad (2.38)$$

It is to be noted that the variation and integration operations are interchanged. The loss of potential energy of the applied loads  $V$  is now defined as a function of displacement field  $u_i$  and the applied loads.

$$V = - \int_s (T_i u_i) ds - \int_v (f_i u_i) dv \quad (2.39)$$

Taking the first variation of Equation (2.39) gives

$$\delta^{(1)}V = -\int_s \left( T_i \left( \frac{\partial u_i}{\partial u_j} \delta u_j \right) \right) ds - \int_v \left( f_i \left( \frac{\partial u_i}{\partial u_j} \delta u_j \right) \right) dv$$

Noting that  $\delta u_i / \delta u_j = \delta_{ij}$  and  $\delta_{ij} = 1$  for  $i = j$  and  $\delta_{ij} = 0$  for  $i \neq j$  the equation leads to

$$\delta^{(1)}V = -\int_s (T_i \delta u_j) ds - \int_v (f_i \delta u_j) dv \quad (2.40)$$

From Equations (2.38) and (2.40) it follows immediately

$$\delta^{(1)}(U + V) = 0 \quad (2.41)$$

The quantity  $(U + V)$  denoted by  $\Pi$  is the total potential energy of the body and is given as

$$\Pi = \int_v \left( \int_0^{e_{11}} \sigma_{11} de_{11} \right) dv - \int_s (T_i u_i) ds - \int_v (f_i u_i) dv \quad (2.42a)$$

$$\text{Giving } \delta^{(1)} \Pi = 0 \quad (2.42b)$$

Equation (2.42b) is known as the principle of minimum potential energy; and it can be stated that:

*An elastic structure is in equilibrium if no change occurs in the total potential energy (stationary value) of the system when its displacement is changed by a small arbitrary amount [28].*

In the early days of the original developments of the calculus of variations the developers including Bernoulli (1654-1705), Euler (1707-1783) and Lagrange (1736-1813) did not consider the stationary value of the total potential energy as indeed a minimum until Legendre (1752-1833) postulated the so-called Legendre test seeking a mathematical rigor for a minimum [29]. A proof that  $\Pi$  actually assumes a minimum value in the case of stable equilibrium is illustrated below.

From Equations (2.41) and (2.42) it follows immediately that  $\delta^{(1)} \Pi = \delta^{(1)}(U + V) = 0$ . Hence

$$\delta^{(1)} \Pi = 0 = \int_v \left( \frac{\partial u}{\partial e_{ij}} \delta e_{ij} \right) dv - \int_s (T_i \delta u_i) ds - \int_v (f_i \delta u_i) dv \quad (2.43)$$

Using the constitutive relations of Equation (2.37) and the strain-displacement relations for small displacement theory (Cauchy strain) the first integral of Equation (2.43) is expanded to

$$\int_v \left( \frac{\delta u}{\delta e_{ij}} \delta e_{ij} \right) dv = \int_v \left[ \frac{1}{2} \sigma_{ij} \delta(u_{i,j} + u_{j,i}) \right] dv = \int_v \left[ \frac{1}{2} \sigma_{ij} \delta(u_{i,j}) + \frac{1}{2} \sigma_{ij} \delta(u_{j,i}) \right] dv \quad (2.44)$$

Noting that  $\sigma_{ij} = \sigma_{ji}$  and interchanging the dummy indices  $j$  and  $i$ , the right-hand side of Equation (2.44) is expanded to

$$\begin{aligned} \int_v \left( \frac{\delta u}{\delta e_{ij}} \delta e_{ij} \right) dv &= \int_v \left[ \frac{1}{2} \sigma_{ij} \delta(u_{i,j}) + \frac{1}{2} \sigma_{ij} \delta(u_{j,i}) \right] dv = \int_v [\sigma_{ij} \delta(u_{i,j})] dv = \int_v [\sigma_{ij} \delta(u_i)_{,j}] dv \\ &= \int_v ((\sigma_{ij} \delta u_i)_{,j}) dv - \int_v (\sigma_{ij,j} \delta u_i) dv = \int_s (\sigma_{ij} \delta u_i n_j) ds - \int_v (\sigma_{ij,j} \delta u_i) dv \end{aligned}$$

where  $\delta u = \sigma_{ij} \delta e_{ij}$ ,  $\delta e_{ij} = (\delta u_{i,j} + \delta u_{j,i})/2$ ,  $\delta(u_{i,j}) = \delta u_i / \delta x_j$  and  $\delta(u_{j,i}) = \delta u_j / \delta x_i$ .

Substituting the expanded form above into Equation (2.43) yields

$$\int_s (\sigma_{ij} \delta u_i n_j) ds - \int_v (\sigma_{ij,j} \delta u_i) dv - \int_s (T_i \delta u_i) ds - \int_v (f_i \delta u_i) dv = 0$$

which can also be expressed as

$$\int_s [(\sigma_{ij} n_j - T_i) \delta u_i] ds - \int_v [(\sigma_{ij,j} + f_i) \delta u_i] dv = 0$$

This must be true for all  $\delta u_i$ . Then the equilibrium conditions follow as

$$\sigma_{ij,j} + f_i = 0$$

and

$$\begin{aligned} T_1 &= \sigma_{11} n_1 + \sigma_{12} n_2 + \sigma_{13} n_3 \\ \sigma_{ij} n_j &= T_i \text{ which when fully expanded gives; } T_2 = \sigma_{21} n_1 + \sigma_{22} n_2 + \sigma_{23} n_3 \\ T_3 &= \sigma_{31} n_1 + \sigma_{32} n_2 + \sigma_{33} n_3 \end{aligned}$$

The Euler-Lagrange equations are the equations of equilibrium and the necessary boundary conditions are embedded into the Cauchy formula as in Equation (2.17). Hence it has been proved that  $\delta^{(1)} \Pi = 0$  is a sufficient condition for equilibrium as explained in Shames and Dym [27]. If it can be shown that the total potential energy of an admissible strain field

$e_{ij} + \delta e_{ij}$  is always greater than that of the equilibrium state, then it suffices that the total potential energy  $\Pi$  is a local minimum for the equilibrium configuration.

$$\Pi_{e_{ij} + \delta e_{ij}} - \Pi_{e_{ij}} = \int_v \left[ u(e_{ij} + \delta e_{ij}) - u(e_{ij}) \right] dv - \int_s (T_i \delta u_i) ds - \int_v (f_i \delta u_i) dv \quad (2.45)$$

Expanding  $u(e_{ij} + \delta e_{ij})$  by a Taylor series

$$u(e_{ij} + \delta e_{ij}) = u(e_{ij}) + \frac{\partial u}{\partial e_{ij}} \delta e_{ij} + \frac{1}{2} \frac{\partial^2 u}{\partial e_{ij} \partial e_{kl}} \delta e_{ij} \delta e_{kl} + \dots \quad (2.46)$$

Substituting Equation (2.46) into Equation (2.45) gives

$$\begin{aligned} \Pi_{e_{ij} + \delta e_{ij}} - \Pi_{e_{ij}} &= \int_v \left( \frac{\delta u}{\delta e_{ij}} \delta e_{ij} \right) dv - \int_v (f_i \delta u_i) dv - \int_s (T_i \delta u_i) ds + \int_v \left( \frac{1}{2} \frac{\partial^2 u}{\partial e_{ij} \partial e_{kl}} \delta e_{ij} \delta e_{kl} \right) dv + \dots \\ &= \delta^{(1)} + \int_v \left( \frac{1}{2} \frac{\partial^2 u}{\partial e_{ij} \partial e_{kl}} \delta e_{ij} \delta e_{kl} \right) dv + \dots = 0 + \delta^{(2)} + \dots \end{aligned}$$

$$\delta^{(2)} \Pi = \int_v \left( \frac{1}{2} \frac{\partial^2 u}{\partial e_{ij} \partial e_{kl}} \delta e_{ij} \delta e_{kl} \right) dv \quad (2.47)$$

It will be demonstrated that the integrand of Equation (2.47) is  $u(\delta e_{ij})$  for  $e_{ij} = 0$ . Examination of Equation (2.46) in association with  $e_{ij} = 0$  reveals that the first term is a constant throughout the body and is taken to be zero, so that the strain energy vanishes in the unrestrained body. By definition  $\partial u / \partial e_{ij}$  in the second term is stress  $\sigma_{ij}$ . The stress in the unrestrained state must be equal to zero. Considering up to second order terms it gives

$$u(\delta e_{ij}) = \frac{1}{2} \left( \frac{\partial^2 u}{\partial e_{ij} \partial e_{kl}} \right)_{e_{ij}=0} \delta e_{ij} \delta e_{kl}$$

Hence Equation (2.47) can be written as

$$\delta^{(2)} \Pi = \int_v \left[ u(\delta e_{ij}) \right] dv$$

Since  $u$  is a positive definite function the second variation of the total potential energy is positive. Hence the total potential energy is a minimum for the equilibrium state  $e_{ij} = 0$  when compared to all other neighbouring admissible deformation fields. Fung and Tong [25], Love

[30], Saada [31], Shames and Dym [27] and Washizu [21] use logic similar to that shown above in the proof of the nature of the total potential energy being a minimum. It appears that Sokolnikoff [26] did not impose  $e_{ij} = 0$  to show that  $\Pi$  actually assumes a minimum value.

### 2.7.5 Principle of Minimum Complementary Potential Energy

Parallel to the concept of the strain energy density introduced in Equation (2.37) it is assumed that there exists the complementary energy density function  $u^*$  defined for elastic bodies as function of stress such that

$$e_{ij} = \frac{\delta u^*}{\delta \sigma_{ij}} \quad (2.48)$$

Substituting Equation (3.48) into Equation (2.34) gives

$$\int_s (\delta T_i u_i) ds + \int_v (\delta f_i u_i) dv = \int_v \left( \delta \sigma_{ij} \frac{\delta u^*}{\delta \sigma_{ij}} \right) dv \quad (2.49)$$

As per Equation (2.35), the right-hand side of Equation (2.49) is  $\delta U^*$ , the first variation of the complementary energy for the structure. A complementary potential energy function is defined by

$$V^* = - \int_v (u_i f_i) dv - \int_s (u_i T_i) dv$$

for which the first variation is given by

$$\delta V^* = - \int_v (u_i \delta f_i) dv - \int_s (u_i \delta T_i) dv \quad (2.50)$$

From Equations (2.49) and (2.50) it can be concluded that

$$\delta \Pi^* = \delta (U^* + V^*) = 0 \quad (2.51)$$

Equation (2.51) is the principle of total complementary energy and  $\Pi^*$  is given by

$$\Pi^* = \int_v (\sigma_{ij} e_{ij}) dv - \int_v (u_i \delta f_i) dv - \int_s (u_i \delta T_i) dv \quad (2.52)$$

It may be shown that the total complementary energy is a minimum for the proper stress field following a procedure similar to that used in the principle of minimum total potential energy.

### 2.7.6. Castigliano's Theorem, Part 1

The principle of minimum total potential energy can be used to derive the Castigliano theorem (which he presented in 1873 in his thesis for the engineer's degree at Turin Polytechnical Institute) which is extremely useful in the analysis of elastic structures. For a structure in equilibrium under a set of discrete generalized forces  $Q_i (i = 1, 2, \dots, n)$  the total potential energy is given by

$$\Pi = U(\Delta_i) - \sum_{i=1}^n Q_i \Delta_i \quad (2.53)$$

For the condition of equilibrium the first variation of  $\Pi$  found by varying  $\Delta_i$  must be equal to zero.

$$\delta \left[ U(\Delta_i) - \sum_{i=1}^n Q_i \Delta_i \right] = \sum_{i=1}^n \left( \frac{\partial U}{\partial \Delta_i} \delta \Delta_i - Q_i \delta \Delta_i \right) = \sum_{i=1}^n \left( \frac{\partial U}{\partial \Delta_i} - Q_i \right) \delta \Delta_i = 0 \quad (2.54)$$

Since the variations  $\delta \Delta_i$  are arbitrary the quantities in each parenthesis must vanish; hence,

$$\frac{\partial U}{\partial \Delta_i} = Q_i (i = 1) \quad (2.55)$$

Equation (2.55) is the Castigliano's theorem, part 1. It states that if the strain energy  $U$  stored in an elastic structure is expressed as a function of the generalized displacements  $\Delta_i$  then the first partial derivative of  $U$  with respect to any one of the generalized displacements  $\Delta_i$  is equal to the corresponding generalized force  $Q_i$ . As the stiffness influence coefficient  $k_{ij}$  is defined as the generalized force required at  $i$  for a unit displacement  $j$ , while suppressing all other generalized displacements,  $k_{ij}$  can be expressed as

$$k_{ij} = \frac{\partial Q_i}{\partial \Delta_j} \quad (2.56)$$

Using Equation (2.55) it can be rewritten as

$$k_{ij} = \frac{\partial^2 U}{\partial \Delta_i \partial \Delta_j} \quad (2.57)$$

### 2.7.7 Castigliano's Theorem, Part 2

For an elastic (not necessarily linearly elastic) structure that is in equilibrium under a system of applied generalized forces  $Q_i$  the principle of minimum complementary energy states that

$$\delta \Pi^* = \delta(U^* + V^*) = 0 \quad (2.58)$$

Assuming that the complementary strain energy  $U^*$  as shown in Figure 2.5, is expressed as a function of  $Q_i$  then Equation (2.58) may be rewritten as

$$\delta \Pi^* = \delta(U^* + V^*) = \sum_{i=1}^n \left( \frac{\partial U^*}{\partial Q_i} \delta Q_i - \Delta_i \delta Q_i \right) = \sum_{i=1}^n \left( \frac{\partial U^*}{\partial Q_i} - \Delta_i \right) \delta Q_i = 0 \quad (2.59)$$

where  $\delta V^* = \left( \frac{\partial V^*}{\partial Q_i} \right) \delta Q_i = \Delta_i \delta Q_i = 0$

Since  $\delta Q_i$  are arbitrary and non zero, Equation (2.59) requires that

$$\frac{\partial U^*}{\partial \Delta_i} = \Delta_i (i=1) \quad (2.60)$$

Equation (2.60) is known as the Engesser theorem derived by Friedrich Engesser in 1889 [25] and is valid for any elastic structure. If the structure is linearly elastic the strain energy  $U$  and the complementary strain energy  $U^*$  are equal and the Castigliano theorem, part 2 results.

$$\frac{\partial U}{\partial Q_i} = \Delta_i (i=1) \quad (2.61)$$

Equation (2.61) states that if the strain energy  $U$  in a linearly elastic structure is expressed as a function of the generalized forces  $Q_i$  then the partial derivative of  $U$  with respect to the generalized force  $Q_i$  is equal to the corresponding displacement  $\Delta_i$ . The flexibility influence coefficient of a linearly elastic structure is given by

$$f_{ij} = \frac{\partial U}{\partial Q_i \partial Q_j} \quad (2.62)$$

## **2.8 Buckling – An Introduction**

When a structure subjected usually to compression undergoes visibly large displacements transverse to the load then it is said to buckle. Buckling may be demonstrated by pressing the opposite edges of a flat sheet of cardboard towards one another. For small loads the process is elastic since buckling displacements disappear when the load is removed. Local buckling of plates or shells in turn is indicated by the growth of bulges, waves or ripples and is commonly encountered in the component plates of thin walled structural members.

Buckling proceeds in a manner which may be either (1) stable, in which case displacements increase in a controlled fashion as loads are increased i.e. the structure's ability to sustain loads is maintained or (2) unstable, whereupon deformations increase simultaneously, the load carrying capacity nose dives and the structure collapses catastrophically.

Neutral equilibrium is also a theoretical possibility during buckling; this is effectively characterised by an increase in deformation with no corresponding or equivalent change in load. From a purely linear viewpoint, buckling of struts and bending of beams are similar in that they both involve bending moments. Referring to Figure 2.6(a) in bending, these moments are substantially independent of the resulting deflections, whereas in Figure 2.6(b) for buckling, the moments and deflections are mutually interdependent – this means that the moments, deflections and stresses are not proportional to loads. If deflections resulting from buckling become too large then the structure fails – this is solely a geometric consideration and completely different from any material strength consideration. If a component or part thereof is prone to buckling then its design must satisfy both strength and buckling safety constraints, which is the why the phenomenon of buckling is examined in detail in this literature review and applied specifically to the two section telescoping cantilever section.

Buckling has become more of a problem in recent years since the advent of high strength materials requires less material for support – structures and components have become generally more slender and buckling-prone. This trend has continued through technological history as is demonstrated by the following sample case studies.

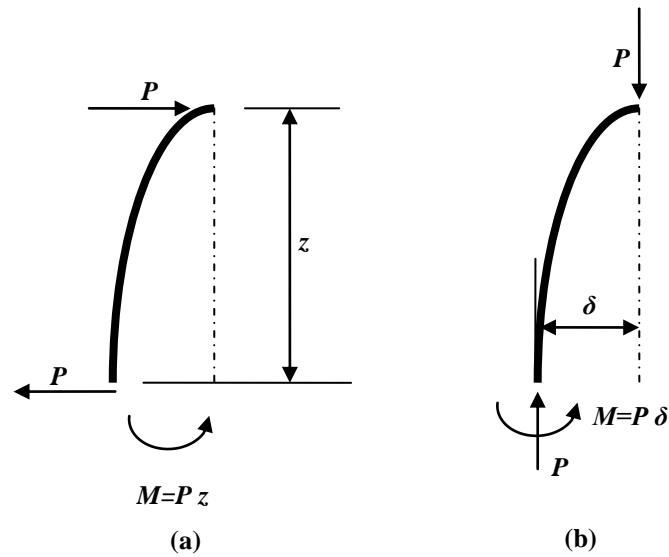


**Figure 2.6: Differences between (a) Bending and (b) Buckling (Adapted from [33])**

## 2.9 Buckling of thin walled structures

A thin walled structure is made from a material whose thickness is much less than other structural dimensions. Into this category fall plate assemblies, common hot and cold formed structural sections, tubes and cylinders and many bridge and aeroplane structures. Cold formed sections are increasingly supplanting traditional hot rolled I-beams and channels. They are particularly prone to buckling and in general must be designed against several different types of buckling. It is not difficult to visualise what can happen if a beam is made from such a cold rolled channel section. One flange is in substantial compression and may therefore buckle locally at a stress lower in magnitude than the yield stress of the channel section material. This in turn reduces the load carrying capacity of the beam as a whole. From this it can be inferred that buckling rather than strength consideration dictates the beam's performance.

The slender elastic pin-ended column is the prototype for most buckling studies. It was first examined by Euler in the 18<sup>th</sup> century. The model assumes perfection in that (1) the column is perfectly straight prior to loading and (2) the load, when applied, is perfectly coaxial with the column.

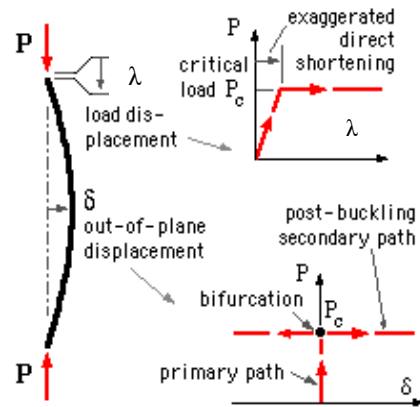


**Figure 2.7: Differentiation between the load and lateral displacements for buckling [33]**

The behaviour of the buckling system is reflected in the shape of its load-displacement curve referred to as the equilibrium path, in Figure 2.7. The lateral or ‘out-of-plane’ displacement,  $\delta$  is preferred to the load displacement,  $\lambda$ , in this context since it is more descriptive of buckling.

Nothing visibly occurs when the load on a perfect column first increases from zero- the column is stable there is no buckling and no out-of-plane displacement. The  $P$ - $\delta$  equilibrium path is thus characterised by a vertical segment-the primary path- which lasts until the increasing load reaches the critical Euler load  $P_{cr} = \frac{\pi^2 EI_{\min}}{L^2}$  a constant characteristic of the column as derived in Timoshenko’s oft cited master work [32].

When the load reaches the Euler load, the lateral deflections  $\delta$  grow instantaneously in either equally probable direction. After buckling therefore the equilibrium path bifurcates into two symmetric secondary paths illustrated in Figure 2.7. Clearly the critical Euler load limits the column’s safe load capacity.

To answer why a compression member buckles if the limiting strength of the material is not reached, Chajes [48] gives credit to Salvadori and Heller in their book [49] for clearly elucidating the phenomenon of buckling by quoting the following from *Structure in Architecture*;

*A slender column shortens when compressed by a weight applied to its top and in doing so lowers the weight's position. The tendency of all weights to lower their position is a basic law of nature. It is another basic law of nature that whenever there is a choice between different paths, a physical phenomenon will follow the easiest path. Confronted with the choice of bending out or shortening the column finds it easier to shorten for relatively small loads and to bend out for relatively large loads. In other words when the load reaches its buckling value the column finds it easier to lower the load by bending than by shortening.*

The bifurcation-type buckling is a purely conceptual one that occurs in a perfectly straight (geometry) homogeneous (material) member subjected to a compressive loading of which the resultant must pass through the centroidal axis of the member (concentric loading). The importance attached to and the considerably copious amounts of research devoted to bifurcation-type loading is justified in that the bifurcation-type buckling load or the critical buckling load gives the upper bound solution for practical columns that hardly satisfy any one of the three aforementioned conditions.

The concept of the stability of various forms of equilibrium of a compressed bar is frequently explained by considering the equilibrium of a ball (rigid-body) in various positions as shown in Figure 2.8 below [23, 32].

Although the ball is in equilibrium in each position shown, a cursory glance reveals that there are vital differences among the three scenarios. If the ball in Figure 2.8(a) is displaced slightly from its original position it will return to its initial state upon removal of the displacing or disturbing force. A body behaving thus is said to be in a state of stable equilibrium. Any slight or small displacement of the ball from its initial state of equilibrium will raise its centre of gravity and a certain amount of work is performed to bring about this displacement. On disturbing the ball in Figure 2.8(b) by an infinitesimal displacement results in it moving away from its equilibrium position and it does not return to its initial state. The equilibrium of the ball in Figure 2.8(b) can be said to be unstable. Any displacement from the position of equilibrium will lower the centre of gravity of the ball and consequently will result in a decrease in the potential energy of the ball. It can thus be inferred that in the case of stable equilibrium the energy of the system is minimum and in the case of unstable equilibrium the energy is at a maximum. In Figure 2.8(c), the ball after being displaced

slightly neither returns to its original equilibrium position nor continues in motion upon removal of the disturbance. This implies that the ball is in a state of neutral equilibrium. By virtue of its neutral equilibrium there is no change in energy during a displacement in the conservative force system.

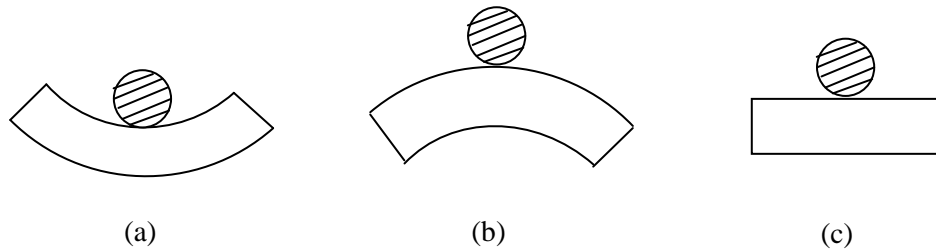


**Figure 2.8: Stability of Equilibrium [28]**

The response of the column is most similar to that of the ball in Figure 2.8. The straight configuration of the column is stable on application of small loads but unstable on application of larger loads. The state of neutral equilibrium is considered to occur in the transition from stable to unstable equilibrium in the column. This leads us to conclude that the load at which the straight configuration of the column ceases to be stable is the load at which neutral equilibrium is possible. This load is the critical load. To determine the magnitude of the critical load it is imperative to determine the load under which the member can be in equilibrium both in the straight and slight bent configuration. The magnitude of this slightly bent configuration is undetermined and is the reason why the free body of a column must be drawn to account for this slight bend in its configuration. The method whereby this slightly bent configuration for evaluating critical loads is accounted for is called the method of neutral or neighbouring or adjacent equilibrium. At critical loads the primary equilibrium path reaches a bifurcation point and branches into neutral equilibrium paths as has been shown in Figure 2.7. This type of behaviour is in essence the bifurcation-type buckling. Bifurcation-type buckling is in turn predicted by Eigenvalue analysis.

A structural member is called a beam when it is supported at one or both ends and carrying transverse loads. The same member is called a column when it is supported at one or both ends and carries a compressive axial load. The structural behaviours at both these conditions are different and the governing equations and conditions are also different. The behaviour of a crane boom when it is horizontal can be best described by a cantilever and by a column

when the boom is vertical. The members are made up of hollow sections. Literature describing the behaviour of such telescoping members is very limited and thus presents an opportunity for investigation.

## 2.10 Rayleigh-Ritz Method

Now that buckling has been explored in as brief a manner as is possible, the reader is directed to the crux of the buckling problem, as applied to the two section telescoping cantilever beam assembly. The need to determine the critical buckling load of the telescoping assembly was established from the outset, and the energy methods were explored for that purpose in §2.7 above. The energy methods introduced in §2.7 are a convenient means of computing unknown forces and displacements in elastic structures. They can be the basis of deriving the governing differential equations and required boundary conditions of the problem. They are also the starting point of many modern matrix/finite element methods. The solutions that are obtained using these methods are exact within the framework of the theory (for example, classical beam theory). Energy methods are also used to derive approximate solutions in situations where exact solutions are difficult or nearly impossible to obtain. The most widely known and used approximate procedure is the Rayleigh-Ritz method in which the structure's displacement field is approximated by functions that include a finite number of independent coefficients (or natural coordinates; one for the Rayleigh method and more than one for the Rayleigh-Ritz method). The assumed solution functions must satisfy the kinematic boundary conditions (otherwise the convergence is not guaranteed no matter how many functions are assumed) but they need not satisfy the static boundary conditions (if they satisfy the static boundary condition a fairly good solution accuracy can be expected). The unknown constants in the assumed functions are determined by invoking the principle of minimum potential energy. Suppose for example the assumed function has  $n$  independent constants  $a_i$  ( $i=1,2,\dots,n$ ). Since the approximate state of deformation of the structure is characterized (amplitude as well as shape) by these  $n$  constants the degrees of freedom of the structure have been reduced from  $\infty$  to  $n$ . Invoking the principle of minimum potential energy it follows that

$$\delta \Pi = \frac{\delta \Pi}{\delta a_1} \delta a_1 + \frac{\delta \Pi}{\delta a_2} \delta a_2 + \dots + \frac{\delta \Pi}{\delta a_n} \delta a_n = 0 \quad (2.63)$$

Since  $\delta a_i$  are arbitrary Equation (2.63) implies that

$$\frac{\delta \Pi}{\delta a_i} = 0 \quad i = 1, 2, \dots, n \quad (2.64)$$

Equation (2.64) yields a system of  $n$  simultaneous equations that can be solved for the coefficients  $a_i$  for static problems and in the case of Eigenvalue problems the determinant (characteristic determinant) for the unknown constants is set equal to zero for the  $n$  Eigenvalues [28].

A few general observations with regards to the Rayleigh-Ritz Method are now made. Although the accuracy is generally improved by increasing the number of independent functions, the computation efforts increase proportionally to the square of the number of independent functions. The type of functions to be selected for a particular problem is based on an intuitive idea of what the true deformation looks like. Trigonometric or polynomial functions are frequently used simply because of the ease of analysis involved. By virtue of using the principle of minimum potential energy all approximate solutions make the structure stiffer than what it is. Consequently the displacements predicted by the Rayleigh-Ritz method are always smaller than exact ones and Eigenvalues are greater than those predicted by exact solution methods.

Finally, if the approximate displacements are used to evaluate internal forces and stresses the latter results should be viewed with caution because the stress components depend on the derivatives of displacements. Although displacements themselves may be reasonably accurate their derivatives may not be the case. In fact the higher the derivatives the accuracy involved is further deteriorated. In a similar fashion the accuracy of Eigenvalues associated with higher mode Eigen vectors deviates much more rapidly than those associated with lower mode Eigen vectors.

## 2.11 The Rayleigh Quotient

Mikhlin [50] proposes that the approximate solution of the Eigen value problem usually reduces to the integration of a differential equation of the form

$$Lw - \lambda Mw = 0 \quad (2.65)$$

where  $w$  is the displacement that satisfies not only the differential equation (2.65), but also certain homogenous boundary conditions (which may preclude the cantilevered end-condition),  $L$  and  $M$  are certain differential operators and  $\lambda$  is an unknown numerical parameter. For the stability of a column, the governing differential equation is

$$\frac{d^2}{dx^2} \left( EI \frac{d^2 w}{dx^2} \right) = -P \frac{d^2 w}{dx^2} \quad (2.66)$$

where  $x$  is the length co-ordinate and  $w$  is the lateral displacement. For Equation (2.66)

$$L \equiv \frac{d^2}{dx^2} EI \frac{d^2}{dx^2} \quad (2.67)$$

$$M \equiv -\frac{d^2}{dx^2} \quad (2.68)$$

$$\lambda = P \quad (2.69)$$

Equations (2.67) and (2.68) are self-adjoint (symmetric), positive definite operators for the usual end supports of columns. If a linear differential operator  $L$  has the following property it is called self-adjoint or symmetric operator:

$$(Lu, v) = (u, Lv) \quad (2.70)$$

The inner product of two functions  $g$  and  $h$  over the domain  $V$  is defined as

$$(g, h) \equiv \text{inner product of } g \text{ and } h \equiv \int_V gh dv \quad (2.71)$$

An operator is said to be positive definite if the following inequality is valid for any function from its field of definition,  $u(q) \neq 0$ :

$$(Lu, u) > 0, (Lu, u) \equiv 0 \quad (2.72)$$

The reason why one is concerned whether or not a boundary-value problem has the properties of being both, a self adjoint (symmetric) and positive definite entity, is that the boundary-value problems having these properties are said to be properly posed, and there exists a unique solution to a properly posed boundary-value problem. An improperly posed boundary-value problem due to haphazardly or arbitrarily assigned boundary conditions is meaningless.

Multiplying both sides of Equation (2.66) by  $w$  and integrating over the domain yields

$$\int_0^l w \frac{d^2}{dx^2} \left( EI \frac{d^2 w}{dx^2} \right) dx = -P \int_0^l w \frac{d^2 w}{dx^2} dx \quad (2.73)$$

Integrate the left hand side of Equation (2.73) by parts twice as follows:

$$\int_0^l w \frac{d^2}{dx^2} \left( EI \frac{d^2 w}{dx^2} \right) dx = \int_0^l EI \left( \frac{d^2 w}{dx^2} \right)^2 dx + w \frac{d}{dx} \left( EI \frac{d^2 w}{dx^2} \right) \Big|_0^l - EI \frac{dw}{dx} \frac{d^2 w}{dx^2} \Big|_0^l$$

For simply supported, fixed or cantilevered end conditions, the last two quantities are zero.

Integrating the right-hand side of Equation (2.73) gives

$$-P \int_0^l w \frac{d^2 w}{dx^2} dx = P \int_0^l \left( \frac{dw}{dx} \right)^2 dx - Pw \frac{dw}{dx} \Big|_0^l$$

The last expression vanishes for fixed and simple supports (not for the cantilevered end).

Substituting the expanded integrals back into Equation (2.66) gives

$$P = \frac{EI \int_0^l \left( \frac{d^2 w}{dx^2} \right)^2 dx}{\int_0^l \left( \frac{dw}{dx} \right)^2 dx} \quad (\text{C1 method}) \quad (2.74)$$

It is noted that Equation (2.74) works for cantilevered columns despite the fact that one of the concomitants is not zero. As mentioned earlier the error involved in the approximate solution

propagates much faster in the higher order derivatives. In order to improve the critical value computed from the Rayleigh quotient,  $\frac{d^2w}{dx^2}$  in the numerator by  $\frac{M}{EI}$ . Then

$$P_{cr} = \frac{\left(\frac{1}{EI}\right) \int_0^l M^2 dx}{\int_0^l (w')^2 dx} \quad (\text{C2 method}) \quad (2.75)$$

The Rayleigh Quotient detailed here is in effect the basis of the theory outlined in §4.4, as identified by Timoshenko and applied to the cantilever-column, in order to determine its buckling load.

## 2.12 Local Buckling

Local buckling of plates or shells is indicated by the growth of bulges, waves or ripples and is commonly encountered in the component plates of thin structural members. Local buckling of an edge supported thin plate does not necessarily lead to total collapse as in the case of columns since plates can generally withstand loads greater than the critical. However the  $P$ - $\delta$  curve shown in Figure 2.9 below illustrates plates' generally reduced stiffness after buckling so plates cannot be used in the post buckling region unless the behaviour in that region is known with confidence. It should be emphasized that the knee in the  $P$ - $\lambda$  curve is unrelated to

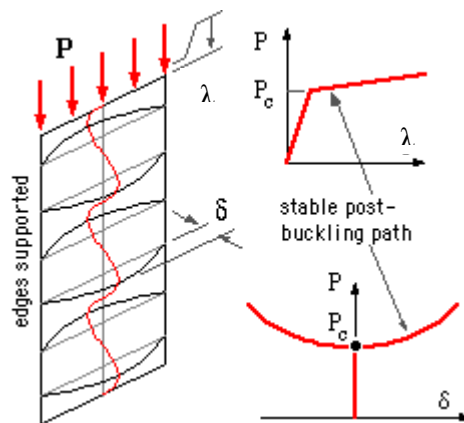


**Figure 2.9: Local buckling of edge supported thin plate with load-load induced displacement curve ( $P$ - $\lambda$ ) and the lateral displacement curve ( $P$ - $\delta$ ) [33]**

any elastic-plastic yield transition; the systems being discussed are totally elastic. The knee is an effect of overall geometric instability rather than material instability.

A fundamental difference in the buckling characteristics of framed members and plates is that for the former, buckling terminates its ability to resist any further load whereas in the case of the latter, this is not necessarily the case. A plate element may carry additional loading beyond the critical load and this reserve strength is called the postbuckling strength. The relative magnitude of the postbuckling strength to the buckling load depends on various parameters such as the dimensional properties, boundary conditions, types of loading and the ratio of buckling stress to yield stress. Plate buckling is usually referred to as local buckling [28]. Structural shapes composed of plate elements may not necessarily terminate their load-carrying capacity at the instance of local buckling of individual plate elements. Such an additional strength of structural members is attributable not only to the postbuckling strength of the plate elements but also to possible stress redistribution in the member after failure of individual plate elements [28]. The photograph in Figure 2.10 below shows the local buckling of a model box girder constructed from thin plates.

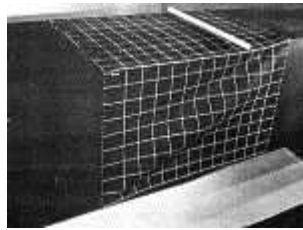


**Figure 2.10: Local buckling of model box girder [33]**

### **2.13 Torsion in Structures**

Torsion in structures is perhaps one of the least well understood subjects in structural mechanics. Purely torsional loading rarely occurs in structures except in the power transmitting shafts of automobiles or generators. However torsion does develop in structures along with bending from unintended eccentricities as can be found in spandrel beams. Generally thin-walled sections do not behave according to the law of the plane sections employed by Euler-Bernoulli-Navier [28].

A thin-walled section is referred to as rolled shape in which the thickness of an element is less than one-tenth of the width. Many stocky rolled shapes do not meet this definition;

however the general theory of thin-walled section developed by Vlasov [52], [53] in the 1930s appears to be applicable without significant consequences [28].

A thin-walled section becomes “warped” when it is subjected to end couples (torsional moment). Hence the cross section does not remain plane after deformation. Exceptions to this rule are tubular sections and thin walled open sections in which all elements meet at a point such as the cruciform, angle and tee section. Another distinct feature of the response of structural members to torsion is that an externally applied twisting moment is resisted internally by some combination of uniform or pure St. Venant torsion and non uniform or warping torsion depending on the boundary conditions that is whether a member is free to warp or whether warping is restrained. Thin walled open sections are very weak against torsion and are susceptible to lateral-torsional buckling or flexural-torsional buckling, which is affected by the torsional strength of the member even though no intentional torsional loading is applied.

Torsional buckling of columns can arise when a section under compression is very weak in torsion, and leads to the column rotating about the force axis. More commonly where the section does not possess two axes of symmetry as in the case of an angle section, this rotation is accompanied by bending and is known as flexural torsional buckling.

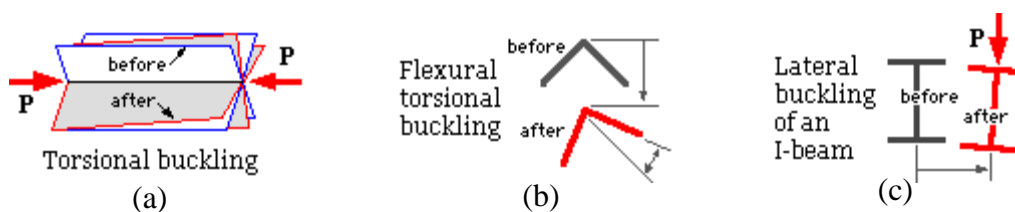


**Figure 2.11: Examples of (a) Torsional Buckling (b) Flexural-Torsional Buckling (c) Lateral Buckling [33]**

Lateral buckling of beams is possible when a beam is stiff in the bending plane but weak in the transverse plane and weak in torsion as is the *I* beam as shown in Figure 2.11.

If warping does not occur or if warping is not restrained, the applied twisting moment is entirely carried by uniform torsion. When a member is free to warp no internal normal

stresses develop despite the warping deformation. This is tantamount to the fact that a heated rod will not develop any internal stresses if it is free to expand at one or both ends despite the temperature-induced elongation of the rod. If warping is restrained the member develops additional shearing stresses as well as normal stresses. Frequently warping stresses are fairly high in magnitude and they are not to be ignored.

#### **2.14 Torsional and Flexural-Torsional Buckling**

The possibility of torsional column failure had never been recognised until open thin-walled sections were used in aircraft design in the 1930s. Experience has revealed that columns having an open section with only one or no axis of symmetry show a tendency to bend and twist simultaneously under axial compression. The ominous nature of this type of failure lies in the fact that the actual critical load of such columns may be less than that predicted by the generalised Euler formula due to their small torsional rigidities. Bleich [51] gives a thorough overview of the early development of the theory on the torsional buckling [28].

Bleich and Bleich [54], were among the early developers of the theory on torsional buckling along with Wagner and Pretschner [55], Ostenfeld [56], Kappus [57], Lundquist and Fligg [58], Goodier [59], Hoff [60] and Timoshenko [61]. All of these authors make the fundamental assumption that the plane cross sections of the column warp but that their geometry does not change during buckling [28]. Thus the theories consider primary failure (global buckling) of columns as opposed to local failure characterised by distortion of the cross sections. The dividing line between primary and local failure is not always sharp. Separate analysis of primary and local buckling based on governing differential equations without abandoning the assumption that cross sections of the column will not deform may yield only approximate solutions since there could be coupling of primary and local buckling. Modern finite element codes with refined modelling capabilities incorporating at least flat shell elements may be able to assess this combined buckling action.

## 2.15 Lateral-Torsional Buckling

A transversely or combined transversely and axially loaded member that is bent with respect to its major axis may buckle laterally if its compression flange is not sufficiently supported laterally. The reason buckling occurs in a beam at all is that the compression flange or extreme edge of the compression flange or the extreme edge of the compression side of a narrow rectangular beam becomes unstable. If the flexural rigidity of the beam with respect to the plane of bending is many times greater than the rigidity of the lateral bending the beam may buckle and collapse long before the bending stresses reach the yield point. As long as the applied loads remain below the limit value, the beam remains stable. In other words, the beam that is slightly twisted and/or bent laterally returns to its original configuration upon the removal of the disturbing force. With increasing load intensity the restoring forces become smaller and smaller until a loading is reached at which in addition to the plane bending equilibrium configuration an adjacent, deflected and twisted, equilibrium becomes equally possible. The original bending configuration is no longer stable and the lowest load at which such an alternative equilibrium configuration becomes possible is the critical load of the beam. At the critical load the compression flange tends to bend laterally exceeding the restoring force provided by remaining portion of the cross section causing the section to twist. Lateral buckling is a misnomer, for no lateral deflection is possible without concurrent twisting of the section.

Bleich [51] gives credit to Prandtl [64] and Michell [65] for producing the first theoretical studies on the lateral buckling of beams with long narrow rectangular sections. Similar credit is also extended to Timoshenko [66] for deriving the fundamental differential equation of torsion of symmetrical I-beams and investigating the lateral buckling of transversely loaded deep I-beams with the derived equation [28]. Since then, many investigators including Vlasov [52], Winter [67], Hill [68], Clark and Hill [69] and Galambos [70] have contributed on both elastic and inelastic lateral-torsional buckling of various shapes. Some of the early developments of the resisting capacities of steel structural members leading to the Load and Resistance Factor Design (LRFD) are summarised by Vincent [71].

## 2.16 Shear in Thin-Walled Closed Tube Sections

Rees in *Mechanics of Optimal Structural Design*, [14] determines from first principles the optimum dimensions for a non-uniform, thin-walled, rectangular tube having side lengths  $b$  and  $d$  with wall-thicknesses  $t_b$  and  $t_d$  when a vertical force  $F_y$  is applied at the shear centre. In § 5.2 the optimum dimensions for a uniform thin walled rectangular tube is determined, using as a basis the following theory.

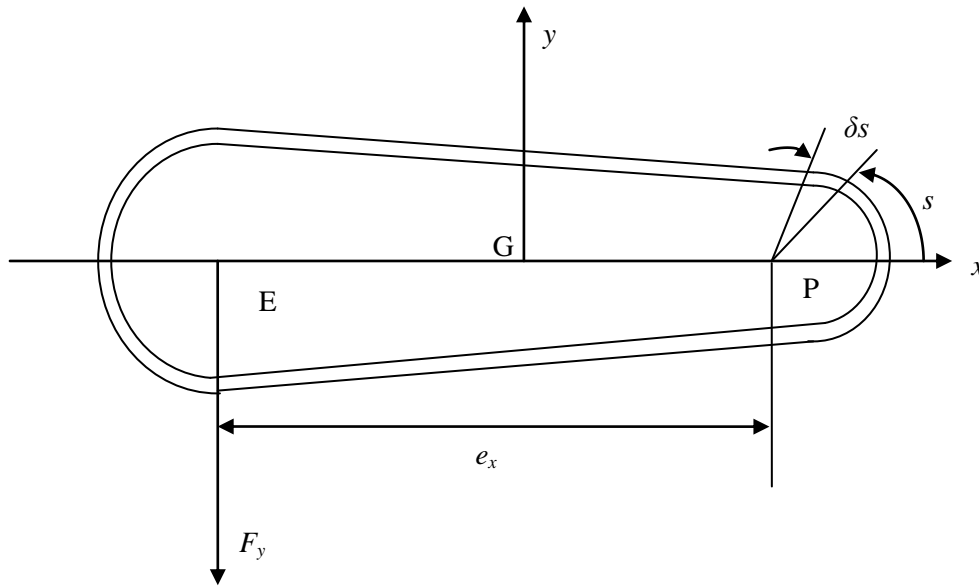


**Figure 2.12: Net Shear Flow in a closed thin walled tube**

The net shear flow in a closed, thin walled tube under a single vertical force  $F_y$  applied through the shear centre E is written as

$$q = q_b + q_E \quad (2.76)$$

Here  $q_b$  is the flexural shear flow expression used previously with open sections in [14] as

$$q_b = \frac{F_y D_{xb}}{I_x} = \frac{F_y}{I_x} \int_A y dA \quad (2.77)$$

However unlike an open section there are no free surfaces to take as an origin so for a closed tube a constant  $q_E$  must be added to  $q_b$ . Thus  $q_E$  is a constant of integration with an important

physical interpretation namely that when  $q_E$  is added to  $q_b$  it ensures the rate of twist  $\delta\theta/\delta z$  is zero at E [6]. That is

$$\oint q_b \frac{ds}{t} + q_E \oint \frac{ds}{t} = 0 \quad (2.78)$$

which allows  $q_E$  to be found. If the position of the shear centre E is not obvious it may be found by combining Equation (2.77) with the counterbalance required between the torque from the net shear flow at  $q = q_b + q_E$  and the torque with  $F_y$  applied through the shear centre, each torque being referred to any convenient reference point P. This torque balance is written as follows

$$F_y e_x = \oint q R ds = \oint q_b R ds + \oint q_E R ds \quad (2.79)$$

where  $e_x$  is the horizontal distance required between E and P. Within the first integral  $R$  is a perpendicular distance from P to the net incremental force  $q \delta s$ . Alternatively the split in this integral recognises  $q_E$  as a constant when  $\oint R ds$  becomes twice the area enclosed by the wall's mean centre-line. §5.2 demonstrates the use of Equations (2.76), (2.77), (2.78) and (2.79).

## 2.17 Torsion in Thin-Walled Closed Tube Sections

The Bredt-Batho theory provides the torque  $T = 2Aq$  in terms of the wall shear flow  $q$  and the cross-sectional area  $A$ , which refers to that area enclosed by the tube wall's mean centre line for those irregular shaped tubes of varying thickness. The shear flow  $q = \tau \times t$  is always constant in a closed tube irrespective of whether  $\tau$  or  $t$  varies as the case may be as mentioned previously. Hence in a tube with uniform thickness the torque may be expressed as

$$T = 2A \times \tau \times t \quad (2.80)$$

where  $\tau$  and  $t$  refer to a single point in the wall. An optimum design ensures that the limiting shear stress from torsion matches that required to cause shear buckling in the wall [14].

## 2.18 Combined Shear and Torsion in Thin-Walled Closed Sections

When a transverse shear force does not act through the shear centre of a given cross-section its net shear flow is a consequence of combined torsion and shear [73]. In closed sections it is more convenient to treat the effects of the St Venant's torsion and flexural shear together but if they were separated the torsional effect or the Bredt-Batho shear flow amounts to taking the difference between the net shear flow from here and that of pure flexure from § 5.2.

The shear flow in a closed tube under a single vertical force  $F_y$  applied at any position is written generally as  $q = q_b + q_0$  where  $q_b$  is the flexural shear flow [46, 73],

$$q_b = \frac{F_y D_{xb}}{I_x} = \frac{F_y}{I_x} \int_A y dA \quad (2.81)$$

Unlike an open section there is no free surface, where  $q_0 = 0$ , to take as the origin for  $s$ . In the case of the closed tube a constant  $q_0$  must be added to  $q_b$ . The sum  $q_b + q_0$  ensures static equivalence between the net shear flow and the torque that arises when  $F_y$  does not pass through the shear centre. In the case of an asymmetric tube this equivalence is written as

$$F_y p = \oint q_b R ds + q_0 \oint R ds \quad (2.82)$$

where  $p$  is the horizontal (perpendicular) distance between  $F_y$  and any convenient reference point  $P$  and  $R$  is the perpendicular distance from  $P$  to the incremental force  $q_b \delta s$  within the tube wall as shown in Figure 2.13.

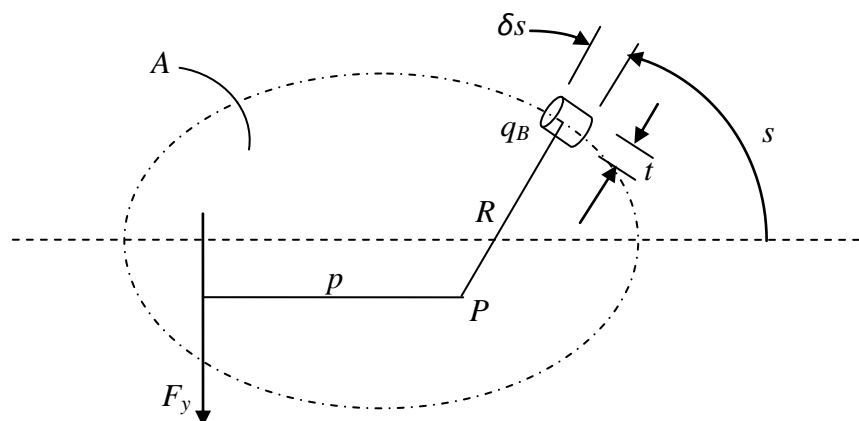


Figure 2.13: Static Equivalence between torque ( $F_y p$ ) and shear flow  $q_b$  [25]

The second path integral in Equation (2.82) is twice the area  $A$  enclosed by the mid wall. Hence the second term in Equation (2.82) becomes the contribution from the St Venant torque  $2Aq_o$ . It is convenient to consider the shear flows from transverse shear and St Venant torsion together rather than to separate them since we neither have pure flexure nor pure torsion  $F_y$ . This allows  $q_o$  to be identified with the shear flow at the origin chosen for the mid wall path  $s$ . In § 2.16 the special case where  $F_y$  passes through the shear centre was considered in which the net shear flow was written as  $q = q_b + q_E$  where the Equations (2.76), (2.77), (2.78) and (2.79) apply. The  $q_b$  shear flows found from Equation (2.77) remain unaltered in regard to the position  $F_y$ , but the net shear flow allows for its position i.e.  $q_E$  is added when  $F_y$  coincides with the shear centre,  $q_o$  is added when  $F_y$  is applied elsewhere. Again it would be convenient to treat the two effects together but if need be they can be separated with the torsional effect amounting to subtracting the shear flows given in § 5.2 from the net shear flows obtained here. In other words

$$(q_b + q_o) - (q_b + q_E) = q_o - q_E \quad (2.83)$$

showing that the torsional shear flow arising from a transverse force displaced from the shear centre is the difference between the ‘initial’ shear flows for each case.

## **2.19 Applications of the Telescoping Cantilever Beam Assembly**

The aim of the sections that follow is to introduce to the reader the present applications of the telescoping beam assembly in the different work environments.

### **2.19.1 Mobile Elevating Work Platforms**

According to EN 280 [3] – the relevant European design standard – the definition of a mobile elevating work platform, or “MEWP”, is “a machine which consists as a minimum of a work platform, an extending structure and a chassis. The work platform is a fenced platform or cage that can be moved under load to the required position and from which repair or similar work can be carried out. The extending structure is connected to the chassis and supports the work platform. It allows movement of the platform to its required position. The chassis is the base of the MEWP and may be pulled, pushed, self-propelled etc. MEWP’s are known by a variety of names including hydraulic work platform, access platform and aerial work platform. For the purposes of this thesis the term ‘access platform’ is used.

#### **(a) Related Terminology**

The access platform industry, like any other, has its own terminology. In any discussion of access platform design it is necessary to make use of various industry specific terms. For this purpose the terminology is outlined below. Figure 2.14 should be referred to, for clarification of the various measures.

##### **(i) Platform Floor Height**

The maximum height that the floor of the platform can reach with the extending structure fully unfolded. This measure takes on a particular significance in the USA where it is the accepted measure of an access platform’s height.

##### **(ii) Working Height**

In Europe it is the accepted norm to quote working height of an access platform. This is the platform floor height plus an allowance for the vertical reach of the operator(s). General practise is to add two metres to account for this reach.

**(iii) Working Outreach**

This is the horizontal distance from the slew centre of the machine to an imaginary line 600mm beyond the outside edge of the platform with the machine set to its maximum horizontal extension. Again, the extra 600mm is to account for the reach of the operator.

**(iv) Safe Working Load**

This refers to the maximum load that can be safely carried in the cage. The manufacturer specifies the “SWL”. As would be expected the manufacturer is obliged to test to 125% of the working load when evaluating a new platform design. The accepted SWL for the majority of access platforms is 225kg. This allows, according to EN280 standard, for two operators at 80kg each and 65kg of tools and equipment. It also satisfies the USA requirement of 500lb cage capacity.

**(v) Height Stowed**

This is the maximum height of the machine when it is in its fully folded position. The stowed height is particularly important when designing a machine that is extended for use indoors as well as outdoors, for obvious reasons. The usual target for machine designers is to stay below the 2-meter limit imposed by the height of a standard doorway.

**(vi) Length Stowed**

The corresponding figure for length is of considerable importance for trailer machines due to the requirements of road traffic approvals and legislation. It is equally relevant when considering how machines are to be delivered, since there are limits to the size of shipping containers and so forth.

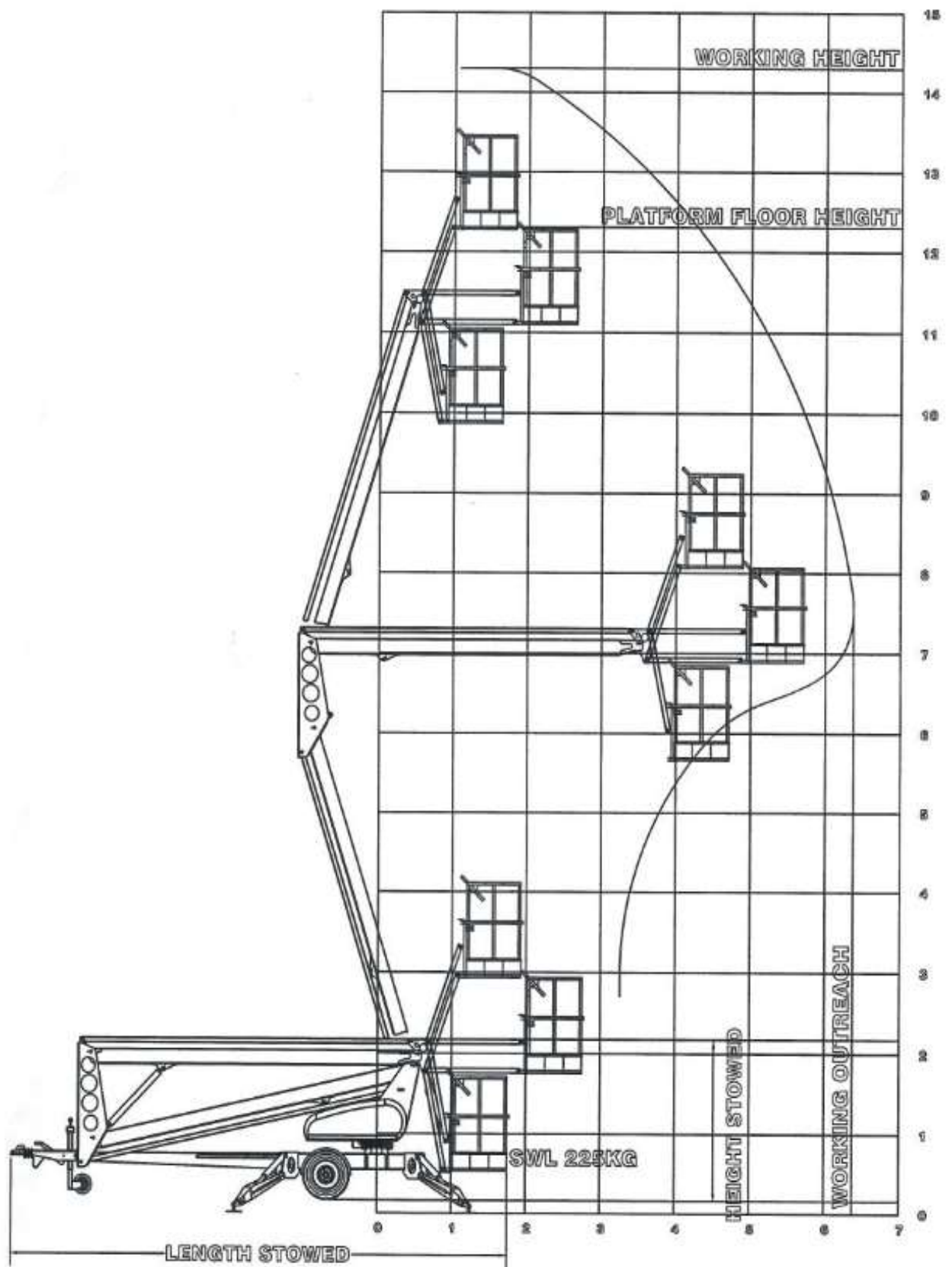


Figure 2.14: Terminology associated with the Mobile Elevating Access Platform (Taken from [2])

## **(b) Access Platform Types**

Access platforms in general can be divided into a number of groups and in the first instance the type of extending structure they employ usually classifies machines. Stick booms, articulating booms and scissors account for the majority of machines. However the stick and articulating boom types are subdivided according to the chassis, which can be trailer mounted, vehicle mounted or self-propelled.

Straight or “stick boom” machines (see Figure 2.15) elevate the operators to a given working height by means of a single straight boom. A hydraulic cylinder controls the angle of the boom. The boom can be of fixed length but more usually has an extending or “telescoping” function. Typically this telescoping function will be achieved by means of a multi stage cylinder and a series of chains. The stick boom machine is ideal for accessing areas such as the underside of bridges but lacks the ability to extend up and over an obstruction.

As the name suggests, scissors lifts (Figure 2.16) make use of a pantograph type linkage to achieve a given working height. In contrast to other machine types they provide minimal “outreach”- the maximum horizontal distance which can be reached by the operator – but platform areas can be large and the smaller types are ideal for use in confined spaces indoors.

An articulating boom machine as shown in Figure (2.17) has a number of booms that are linked by “knuckles”. Again hydraulic cylinders control the angles of the booms. One or, in some cases, several of the booms may have a telescoping capability. This type of machine is less suited to the under bridge type of work mentioned earlier. However independent operation of the booms allows the user to manoeuvre the machine up and over an obstacle.

As explained earlier the various machine types can be sub-divided into trailer mounted, self propelled and vehicle mounted machines. In trailer mounts as shown in Figure (2.18) the chassis or base of the machine forms a road-towable trailer. The trailer is fitted with outriggers or stabilisers that are extended once the machine forms a road-towable trailer. The trailer with outriggers extended forms a solid base for the machine. Outriggers can be manual or hydraulic. A common feature is a retractable axle that allows the machine width to be reduced to fit through a standard size doorway.



**Figure 2.15: Straight or “stick boom” access platform [74]**



**Figure 2.16: Scissor Lift [75]**

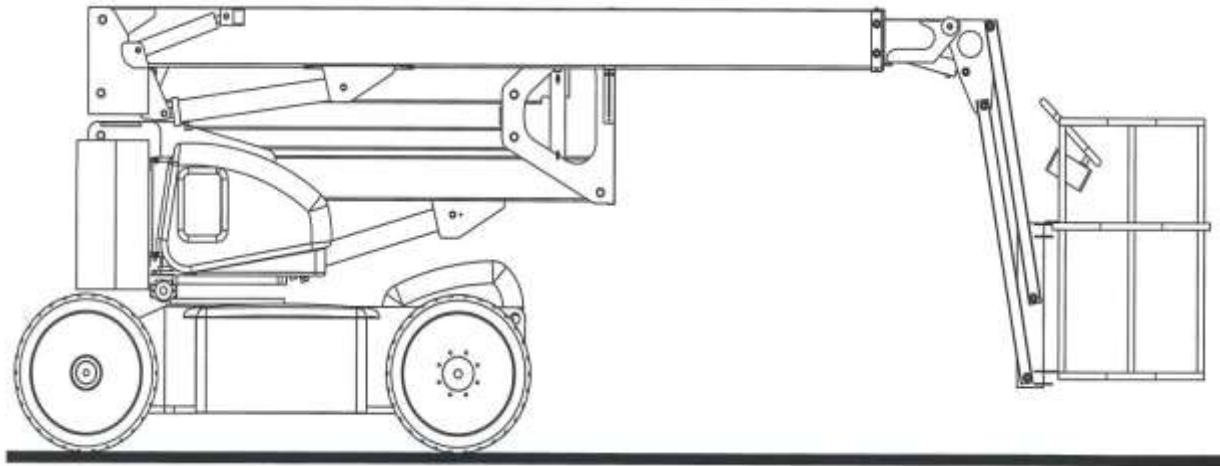


**Figure 2.17: Articulating Boom Machine (Taken from [2])**

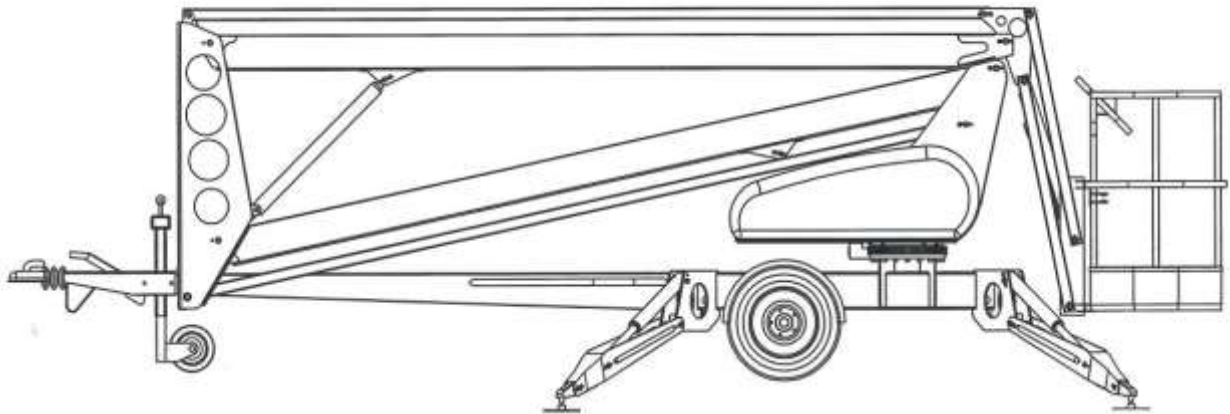


**Figure 2.18: Trailer Mounted Machine (Taken from [2])**

Self-propelled machines can be driven under their own power whilst on site. Stick booms, articulating booms and scissors can all be self-propelled. The drive facility is generally available with the booms extended or folded although drive with the booms extended is only permitted at a reduced speed. Self-propelled machines greatly reduce the amount of time needed to set up since there are no stabilisers to contend with. There have been many variations on the theme of the self-propelled machine. Rough terrain outdoor machines with petrol, diesel or liquid propane gas power sources are available as are dedicated “indoor” all electric machines. In addition, machines that make use of multiple power sources are available. The ability to switch from one power source to another instantly enables the same

machine to work indoors and outdoors. This added flexibility is a major selling point especially in the hire industry.

The term vehicle mount is self-explanatory. In general vehicle mounted machines utilise the type of articulating boom structure found on a trailer mounted or self propelled machine. Indeed in some cases a company offering a vehicle mount will simply adapt the entire extending structure from an existing trailer or self propelled machine as shown in Figure (2.19). The extending structure is built onto an existing vehicle. Typically the vehicle use would be a large box van or flat-bed truck. The extending structure can be directly attached to the chassis of the vehicle or alternatively a purpose built base is attached to the chassis and the booms are built onto the base. The increased base mass provided by a large flat-bed lorry obviously allows extremely large working height and outreach figures to be achieved if required.



**Figure 2.19: Vehicle Mounted Access Platform [76]**

### **2.19.2 Telescopic Retractable Roofing Systems**

L.I.TRA. USA [77] is one of a number of establishments engaged in the design, manufacture, installation and maintenance of retractable roofing and sliding roof systems. These offer ideal solutions for covering wide spaces such as terraces or patios of restaurants, hotels, private houses, resorts or swimming pools as is amply demonstrated in Figures 2.20 and 2.21. The

telescopic coverings offer protection from the elements as a result of thermal and acoustic isolation.



(a)

(b)

**Figure 2.20: A retractable roof enclosure (a) before deployment and (b) after deployment [77]**



(a)

(b)

**Figure 2.21: A retractable commercial garden roof canopy (a) before deployment and (b) after deployment [77]**

Figure 2.22 shows a retractable pool enclosure manufactured by the same firm [78]. Naturally, covering the swimming pool offers many advantages more important of which is the increase in commercial value and prolonged usage period, free from relying upon the effects of the elements. In winter, the retractable roofing system protects an enclosed pool from dampness, thereby lowering maintenance costs and when enclosed with lateral panels, provides thermal isolation and conversely in the summer, it offers protection from the sun and shelter from the wind.



**Figure 2.22: A retractable pool enclosure [77]**

Figure 2.23 shows a retractable awning used in a commercial setting. It has all of the advantages as mentioned earlier, for all other retractable type roofing systems.



**Figure 2.23: A retractable awning [77]**

L.I.TRA. USA [77] also manufactures retractable roofing systems for professional sports stadiums, which can be opened and closed at will, as the need demands. The retractable roof system is available in two options from the company. The first installed at the Fenway Park Stadium in the USA, as shown in Figure 2.24 consists of two parts (one fixed and the

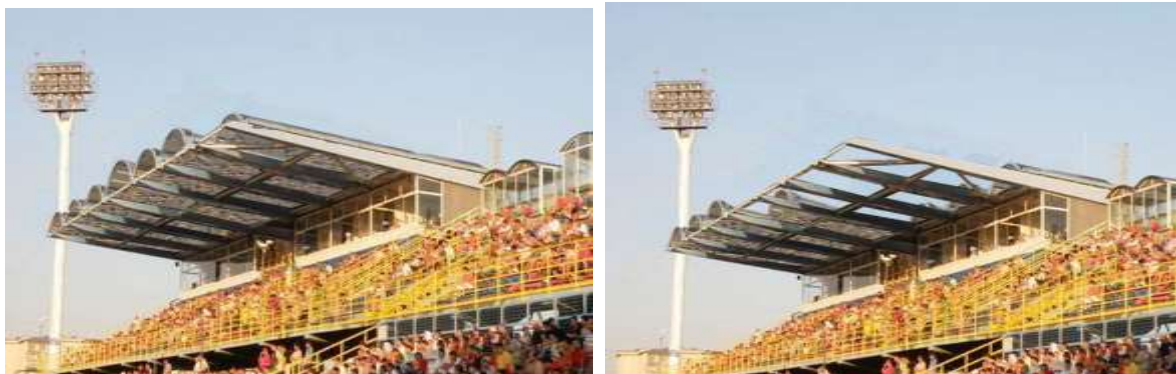
other retractable) which allows for the roof to open at half its full size. The second is a system, made of three parts of which one is fixed and the other two are movable as is shown installed at the Churchill Downs in Louisville, Kentucky, USA, in Figure 2.25. This can be opened at up to two-thirds of its full size.



(a)

(b)

**Figure 2.24: Fenway Park retractable stadium roof system consisting of two parts (a) before deployment and (b) after deployment [77]**



(a)

(b)

**Figure 2.25: Churchill Downs Enclosure with a retractable stadium roof system consisting of three parts (a) before deployment and (b) half way through full deployment [77]**

### 2.19.3 Telescoping Marine Assemblies

Nautical Structures USA are specialists in maritime structures and a wide range of manufacturing for related use. Of the many complex structures that they manufacture, the following two structures are of relevance to the topic at hand. The first is the Sliding type Overhead Beam Crane which is a compact multi-stage telescoping crane. It is designed to work independently as an aft tender garage crane or to work in synchronised matched pairs to launch large tenders from a tender garage. The primary material of construction is aluminium in order to reduce the potential for corrosion and system weight. The capacities of these cranes range from 500-10,000 kg. These compact designs permit the crane structure to nest into the vessel's overhead and live within the confines of the tender garage.



**Figure 2.26: The SL-DEX Type hydraulic overhead beam crane manufactured by Nautical Structures USA [78]**

The single, double and triple telescoping type of passerelles or gangplanks are unique designs that increase the stowed efficiency of the plank as shown in Figures 2.28 (a), (b) and (c) respectively. By virtue of their design, these telescoping gangplanks allow the ratio of stowed length to deployed length to be increased, thereby also enabling the pocketing hydraulic passerelle to stow in shorter spaces within a yacht. The gangplank may be deployed with the telescoping sections extended or retracted. The pocketing hydraulic passerelle can thus be

used in a variety of boarding conditions. As per Nautical Structures [78] the telescoping gangplanks luffs +/- twenty degrees and slews a total of ninety degrees.

As a result of the hydraulic self-centring, slew-lock and float functions incorporated as standard design features into the telescoping gangplank, the need for electric limit or proximity switches is eliminated. This results in long term reliable performance in a wet marine environment with reduced maintenance demands.



(a)



(b)



(c)

**Figure 2.27: Applications of the SL-DEX Type hydraulic overhead beam crane [78]**



(a)



(b)



(c)

**Figure 2.28 (a) Single telescoping gangplank (b) Double telescoping gangplank and (c) Triple telescoping gangplank [78]**

#### **2.19.4 Telescoping Adjustable Columns**

Telescoping adjustable columns are also known as “tele posts”, “sectional columns”, “double-sectioned columns”, “jack posts”, or “jacks”. They come in two or more hollow steel tube sections that are assembled on site. A smaller diameter tube is fitted into a larger diameter tub and the sections are held in place with steel supporting pins which pass through the pre-drilled holes of both tubes. Telescoping adjustable columns are regularly used in construction to adjust or level a structure before installing a permanent column. They also find use as temporary supports during the course of building repair. These columns also have a large screw on one end that allows the height of the column to be adjusted in site.



**Figure 2.29: Telescoping adjustable column [79]**

#### **2.19.5 Telescoping Adjustable Wheelchair Ramps**

The versatile telescoping adjustable wheelchair ramps are the perfect solution for use over different rises and obstacles. The ramp shown in Figure 2.30 can be adjusted from a minimum of six feet to a maximum of ten feet. Another advantage of these dual track ramps is their ability to accommodate any wheelchair width. These ramps come in two tracks for each set of wheels on a wheelchair or power chair and have a non-skid traction surface to prevent wheels from spinning. Also each track ramp has a handle on it so it can be easily transported and when fully closed they have a locking tab to prevent them from accidentally opening up during storage or transport. Another advantage is the extremely light weight of the ramps for their size due to an aluminium body which also means that they will not rust or corrode and will hence last the test of time. The 64mm long attaching lip has a rubber pad to

prevent slipping of the track ramp and will fit on almost any flat surface including steps, porches, side doors on a minivan, sidewalks and more.



**Figure 2.30: Telescoping adjustable wheelchair ramps [80]**

### **2.19.6 Telescoping Poles and Adjustable Masts**

Numerous firms are engaged in the manufacture and sale of telescopic poles and adjustable masts. Of the many the one of particular importance and relevance, known as the “Wonder Pole<sup>®</sup>” [80] is detailed here. According to its manufacturers [80] “it is a composite material using a minimum fibre glass content of 70 % which is then circular would with additional fibre glass strands, using a method that adds tremendous strength in excess of 520 MPa, which in turn also prevents linear splitting commonly associated with other fibre glass poles. UV inhibitors are added to prevent degradation of the pole when exposed to the elements. Each section of the pole is wrapped with two layers of the highest quality Nexus<sup>®</sup> veil which prevents fibre bloom and preserves the integrity of the outer and inner surface of the pole. The Pole has nesting sections that fit inside of each other and draw out to any desired height. Each section has exclusive “stop markers” to prevent the pole from too great an extension. The sections are secured into place by turning the “Sure Lock” grips that are factory moulded onto the pole. The Pole is non conductive and does not have any of the electrical hazards commonly associated with metal poles. Any part of the pole can be replaced or added at any time. In addition to these factors are the low weight, superior strength, available accessories,

styles, models and colours.” The construction of this “Wonder Pole®” is shown in Figure 2.31.

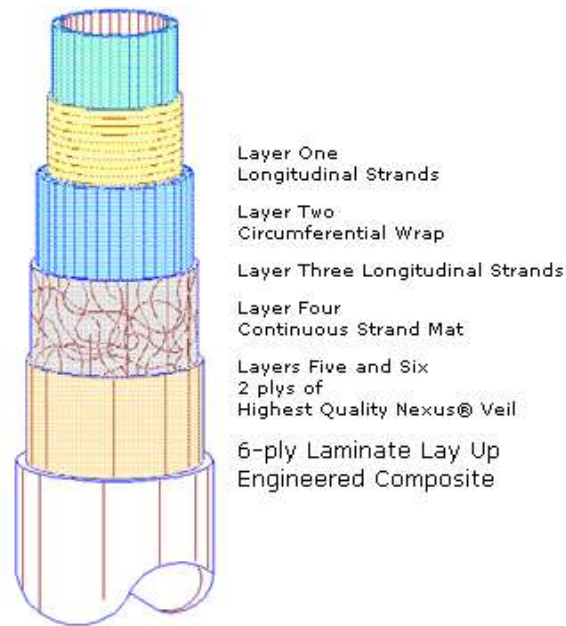


**Figure 2.31: Construction of the “Wonder Pole®” [81]**



**Figure 2.32: A telescoping “Wonder Pole®” in use [81]**

### 2.19.7 Steel Telescoping Towers

US Tower Corporation [82] has been engineering and manufacturing tower systems for close to twenty years. Their product line has since expanded to include telescoping tubular towers with a variety of options such standard, self supporting and rotating.



(a)



(b)



(c)



(d)

**Figure 2.33: Examples of trailer mounted US Tower manufactured telescoping towers [82]**



**Figure 2.34: A self contained US Tower manufactured Command, Control, Communications and Tactical Shelter or C3T Trailer [82]**

Figures 2.33(a)-(d) shows some of the many examples of US Tower manufactured telescoping towers which are trailer mounted. According to the manufacturer, US Towers [83] they are designed for rapid deployment with minimal setup time with no earth penetration required for stabilization and can be easily mounted and retracted on harsh terrain and unforgiving weather conditions. Figure 2.33 (d) shows one of these towers in a storage position whereupon it can be transported with ease on board both military and suitably modified civilian aircraft. Also highlighted in Figure 2.34 is a self-contained command, control and communications and tactical shelter also known as a C3T Trailer, which are another of their groundbreaking innovations. By combining the strength and versatility of their steel telescoping towers with the freedom and portability proffered by a trailer, the company has made it possible to access mobile communications capabilities in the most extreme conditions. As per the manufacturers [83] these telescoping towers currently find use in conflict zones around the world and also in expeditions across all manner of inhospitable climes, to maintain round the clock communications uplinks as well as surveillance and monitoring.



(a)



(b)



(c)



(d)

**Figure 2.35: Examples of vehicle mounted US Tower manufactured telescoping towers [82]**

Figure 2.35(a)-(d) exhibits some of the vehicle mounted US Tower manufactured telescoping tower systems. Figures 2.35 (a) and (b) show two vehicle mounted systems utilised for onsite demonstrations that accentuate the capabilities of different technologies used in surveillance systems. With the versatility of a high end surveillance camera mounted on an extendable telescoping tower and powered by a self contained solar system, the manufacturers [83] claim to be able to manage the most stringent security needs. Figures 2.35 (c) and (d) show vehicle mounted telescopic masts in action. The manufacturers [83] claim that these particular series of masts are operational at any intermediate height, can be mounted onto vehicles, shelters and trailers, and are automatically operated with spindle drive for full extension or retraction within 4-10 minutes.

### 2.19.8 Telescoping Storage Racks

A *SpaceSaver* Rack as manufactured by Steel Storage Systems Inc, of Denver, Colorado, USA [83] is a series of double sided vertically stacked receptacles in levels up to eighteen feet high. The receptacles roll out like drawers so they can be easily accessed for loading or retrieving the contents with an overhead crane. The racks can be structured to accommodate bars, tubing or other steel tube products up to six metres in length thereby offering practical means to store steel products as long except flat on the floor. The basic building block of the *SpaceSaver* Rack is a telescoping tube that creates a storage drawer for steel bars, tubes and other shapes. The telescoping design allows the drawer to be cranked out for convenient loading or retrieval of material. The primary customers as identified by the company are steel distributors, heavy equipment manufacturers and steel fabricators who have large inventories of steel products and the necessary overhead crane equipment, who desire effective space utilization and accessibility.



**Figure 2.36: Aerial view of a large installation of SpaceSaver Racks in a steel service center [83]**



**Figure 2.37: SpaceSaver Racks installed outdoors [83]**



**Figure 2.38: '8 Tall SpaceSaver Rack' installed with optional electric lift cage. For maximum density '8Tall' models nearly six metres high are available [83]**



**Figure 2.39: ‘5 Tall SpaceSaver Rack’ storing 50-60 cm tubing at Marmon/Keystone. A rolling platform ladder is used to access the upper levels [84]**

Figure 2.39 shows how Marmon/Keystone, an international distributor of piping and tubing, makes use of the SpaceSaver Racks for storing carbon, stainless and aluminium tubing inventory in their Denver, Colorado branch. This instalment shown in Figure 2.39 adds to the already commissioned and existing SpaceSaver racks to complete the transition from a pigeon hole rack system. The material ranges from 25-200 mm in diameter in lengths from 6-7 metres. The racks significantly reduced order filling time due to the selectivity provided by the telescoping roll-out drawers. They also improved safety by eliminating the procedure of manipulating heavy tubes in and out of pigeon holes. The ‘5 Tall SpaceSaver Rack’ model maximised the available height in the plant and complimented their existing overhead cranes. Marmon/Keystone’s choice of this model having a width of 900 mm and 400 mm high drawers, as per the manufacturer’s case study profile [84] allowed “the dual purpose of storing bulky loads of tubing and to subdivide the drawers with receptacle dividers to further increase storage density for smaller quantity items”. Each of these roll-out drawers has a 4000 kg capacity and a top level capable of 18000 kgs.

## CHAPTER 3: DEFLECTION ANALYSIS

### 3.1 Introduction – Deflection Analyses

Design of cantilever beams for their many applications often requires estimates of deflections at various length positions. The development of analytical methods for estimating deflection and stress for beams in bending were developed in the 18<sup>th</sup> century by Euler and Bernouli and are described in many textbooks [5-8]. The beam deflection  $y$  is found by four common methods: (i) direct integration [5-8], (ii) Macaulay's step function [8, 9], (iii) Mohr's theorems [5-8] and (iv) strain energy [13, 14]. Both (i) and (ii) are based on the flexure equation:

$$M = -EI \frac{d^2 y}{dx^2} \quad (3.1)$$

Unless otherwise mentioned, the term  $y$  used throughout the course of this chapter indicates the overall tip deflection. Deflection theorems have been examined in brief in § 2.3 followed by a brief yet substantial examination of the four common methods of deflection analysis. This chapter has in its origins the '*Tip Reaction Model*' proposed in order to perform deflection analysis of the three section telescopic cantilever beam assembly, as detailed in [13]. The analysis in [13] adopts the use of Macaulay's step function method to predict the deflection at major points within the beam assembly particularly at the points of discontinuity. The points of discontinuity are of course those regions wherein the sectional properties change with change in the sections themselves, for example when moving along the beam assembly from the outer beam AB to beam CD, with the emphasis being on the overlap region CB as shown in Figure 3.1 (b), for the case of the two section telescoping cantilever beam assembly. The details of the deflection analysis of the three section telescoping cantilever beam assembly were first propagated in an interim internal report [13] and then published [91]. (See also Appendix E). It was deemed necessary to understand if other established deflection prediction techniques could also be applied to the two section telescoping arrangement and herein lies the basis of the sections § 3.5, § 3.6 and § 3.7 that follow. A number of factors were taken into consideration such as the possibility of varying individual beam lengths and variations in overlap lengths. To this end a number of ratios were used to express the sectional properties of the beams constituting the two section assembly. Parameterisation was used to great effect in [14], in order to allow for ease of comparison between deflection prediction techniques.

### 3.2 Telescopic Beam Theory

In a telescopic cantilever beam one or more beams are stacked inside an outer beam which is fixed at one end to support the entire beam assembly. The inner pieces move out when the application needs the full span. Generally, the assembly will have three types of beams: (a) one with end fixed, (b) one with end free and (c) and an overlapping section between (a) and (b). It follows that a beam of two lengths, which includes (a), (b) and (c) and corresponds to the sections marked 1, 3 and 2, respectively, as shown in Figure 3.1(a), is sufficiently general for the present analysis. Thus, Figure 3.1(b) shows, schematically, a telescoping cantilever with an overlapping length  $a_1$  between beams with lengths  $L_1$  and  $L_2$ . The loading shown is a combination of the beams' self-weights  $w_1$  and  $w_2$  and a concentrated, applied end-load  $P$ .

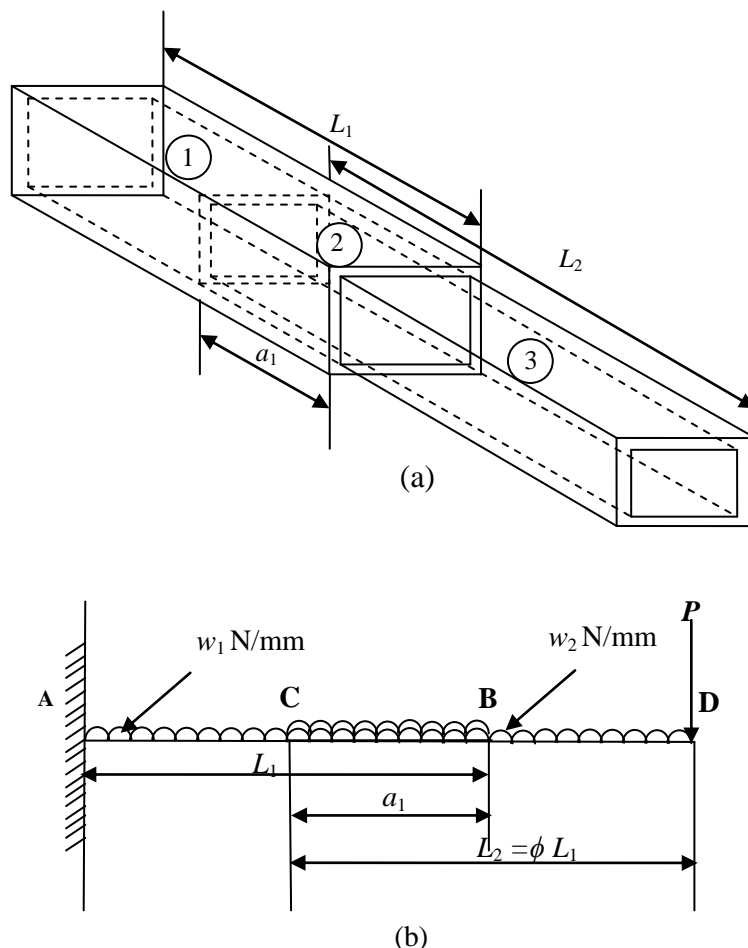


**Figure 3.1: Two-section, telescopic cantilever**

### 3.3 Tip Reactions

The tip reaction model assumes that in a telescopic cantilever beam the overlapping ends have concentrated reactions that transmit the effects of the loads applied to the top surface of the cantilever assembly. Consider the two-section beam assembly shown in Figure 3.1(a). The fixed-beam AB has an overlap of length CB with beam CD. Tip reactions exist at the contact points C and B between beams AC and BD. In addition, Figures A.2 and A.3 in Appendix A, shows the external loading applied to the assembly which is a combination of self-weight and a concentrated end-load. Thus, each of the two-sections bears the loading shown in Figures A.2 and A.3.

That the tip reactions must remain in equilibrium with the applied loading enables these reactions to be found as detailed in Appendix § A.2. In Figures A.2 and A.3 each beam section is shown separately as a free-body diagram. Within each diagram the tip reactions are the forces applied to the each section from its neighbour Thus, the free-end section CD, exerts upon the fixed-end section AB, a downward force at B and an upward force at C (see Figure A.2). The fixed-end section AB, on the other hand exerts equal forces upon the free end-section CD, at B and C but in opposition to these (see Figure A.3). Using the tip reactions detailed in Appendix § A.2, a ‘C’ program was generated using the principle outlined in §3.4, wherein the deflected shape of each portion of the beam is provided by successive integration of Equation (3.1). The analyses were carried out on a telescopic cantilever assembly consisting of two hollow sections as detailed in §3.4.

### 3.4 Macaulay’s Method for Deflection Analysis

The deflected shape of each portion of the beam is provided by successive integration of Equation (3.1). The first integration gives the slope  $dy/dx$  and the second integration provides the deflection expression  $y = y(x)$ . Constants of integration are introduced to ensure compatibility within the overlapping lengths as a similar integration process is applied to each separately and in sequence. The integration shows that the deflected shape of AC (not including the overlap BC) may be expressed as a polynomial:

$$y_1 = t_{14}x^4 + t_{13}x^3 + t_{12}x^2 + t_{11}x + t_{10} \quad (3.2)$$

in which the coefficients  $t_{10} \dots t_{14}$  are required to match the boundary conditions. Here, as both the slope and deflection are zero at the fixing, where  $x = 0$ , then  $t_{10}$  and  $t_{11}$  are both zero. The remaining coefficients are seen to depend upon the length, the loading, and the flexural rigidity  $EI$ . A further polynomial describes the deflection for the portion of this beam which extends into the overlap CB

$$y_2 = t_{24}x^4 + t_{23}x^3 + t_{22}x^2 + t_{21}x + t_{20} \quad (3.3)$$

Equation (3.3) must match the slope and deflection imposed by the adjacent beam before it (AC). This requirement also applies to a further polynomial that describes the deflection in the same overlap CB from within the second beam

$$y_3 = t_{34}x^4 + t_{33}x^3 + t_{32}x^2 + t_{31}x + t_{30} \quad (3.4)$$

The tip reactions identified in § A.2 facilitate the load transfer between the two beams. The appended sections A.3, A.4, A.5 and A.6 show how such compatibility is ensured between the  $t$ -coefficients in Equations (3.2) – (3.4) for these two portions of the length ACB. The complete analysis requires additional equation sets given in Appendix A for the remaining beam sections, which leads to the respective Equation sets (A.1)-(A.5) which contribute to the eventual determination of the overall tip deflection, represented by Equation (A.6). The sample set of Equations (3.2)-(3.4) given here are sufficient to show how they are programmed to admit a specific geometry and material. The program is then applied to predict the end-deflection of a model telescopic cantilever.

Referring to [93], we now make use of two standard sections with the specifications listed in Table 3.1 below in order to plot the Equation set (A.6) from A.6 against varying values of the parameter  $\alpha$ .

**Table 3.1: Nominal dimensions and sectional properties of rectangular hollow sections –  
Extract from ISO/FDIS 2633-2:2011 (E), [93]**

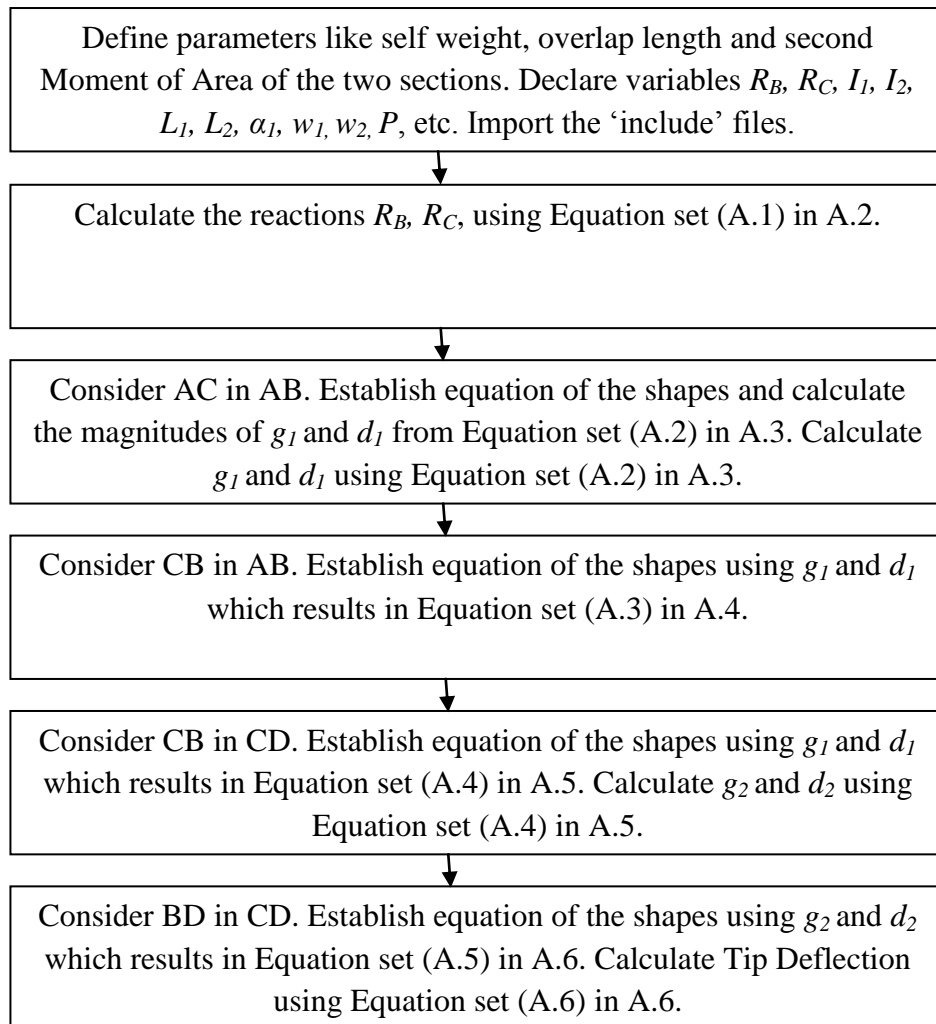
Section	Size		Thickness ( <i>T</i> mm)	Weight per unit length (N/mm)	Second Moments of Area (mm <sup>4</sup> )
	<i>H</i> mm	<i>B</i> mm			
<b>Section 1 (Fixed- End)</b>	60	40	5	0.0685	38.1x10 <sup>4</sup>
<b>Section 3 (Free-End)</b>	50	30	5	0.0528	18.7x10 <sup>4</sup>

Assuming lengths of the fixed and free sections to be 1200 mm and 1000 mm respectively, and utilising the details provided from Table 3.1, it can be determined that the values of  $\phi$ ,  $\beta$  and  $\gamma$  are 0.833, 0.49 and 0.642 respectively. The values of tip deflection were plotted (as shown in Figure 3.2) using the parameters required in Table 3.2 which were in turn entered using the ‘C’ program.

### 3.4.1 The ‘C’ Program

The ‘C’ program detailed in Appendix B, for the two section telescopic cantilever beam assembly, marries each polynomial description of deflection within the two beam sections. Table 3.2 shows the steps leading to the overall tip deflection. The program is able to calculate tip deflection under various applied loadings with different combinations of overlaps. To do this it requires the geometric parameters of the telescopic beam assembly entered interactively to find specific solutions defined by the five sets of equations given in Appendix A. Specifically it applies the acquired parameters to Equation set (A.1) to obtain the tip reactions. The shape of AC is provided by Equation set (A.2) from which it calculates boundary conditions to define the shape of overlap CB between beams AB and CD. This recursive process continues until the deflected shape of every portion is defined as was demonstrated for the three section cantilever in [13] and [91]. Finally, the shape of BD is used to estimate the value for the tip deflection.

**Table 3.2: Flow Chart of the ‘C’ program to calculate tip deflection**



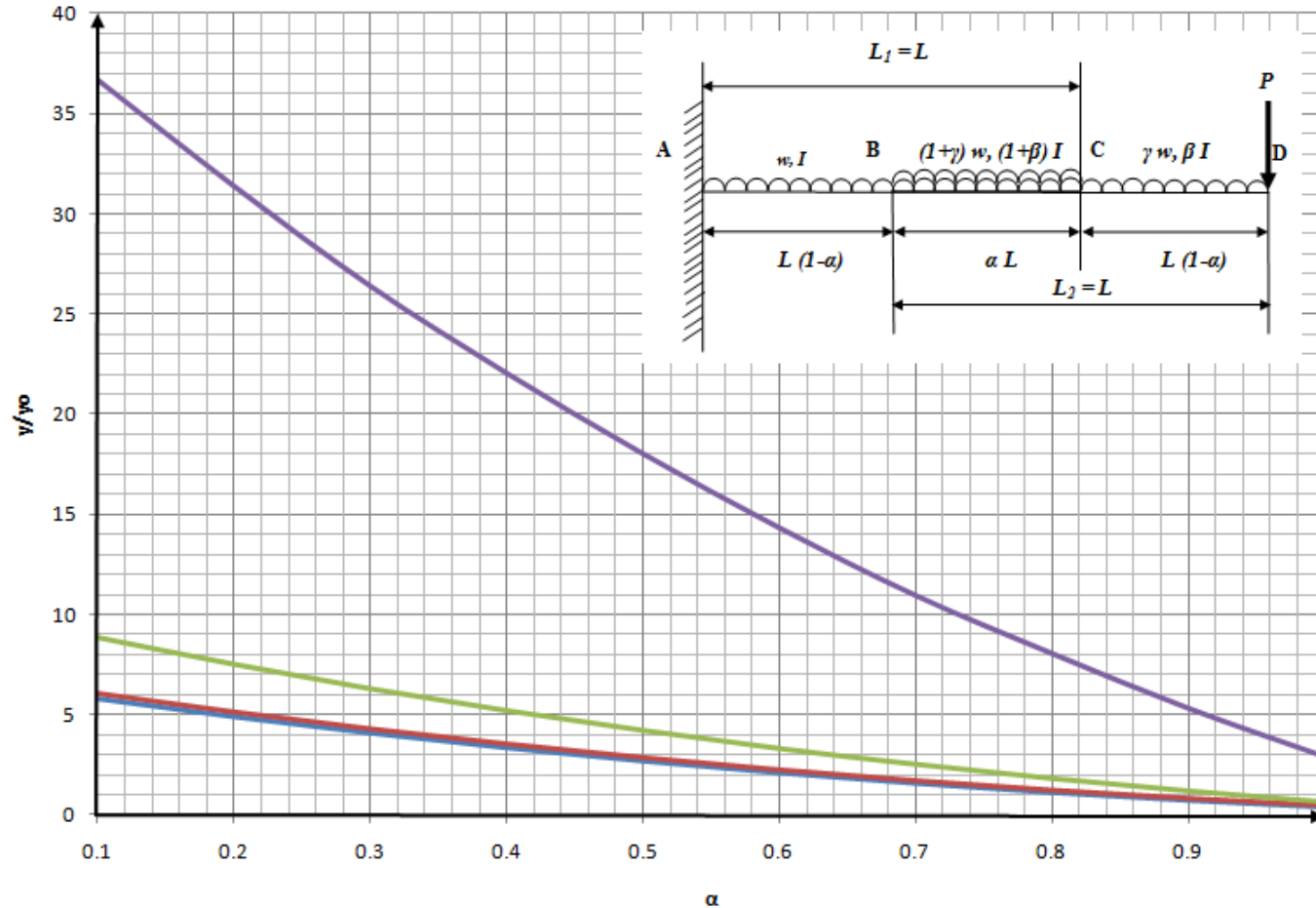


Figure 3.2: End Deflection Plot obtained from Macaulay's Theorem vs. Parameter  $\alpha$ , for the two section telescopic cantilever beam assembly having individual part dimensions outlined in Table 3.1, and fixed and free-end lengths of 1200mm and 1000mm respectively.  $y/y_0$  represents the ratio of the tip deflection for a given value of  $wL/P$ , which in turn varies from 0.01 to 10, in multiples of 10, to the tip deflection of a single fixed end section cantilever having length  $L$  and uniform second moment of area  $I$ , such that  $y_0$  equals  $(PL^3/3EI)$ .

(Key: —  $wL/P=10$ ; —  $wL/P=1$ ; —  $wL/P=0.1$ ; —  $wL/P=0.01$ )

The graph in Figure 3.2 forms the basis for the deflection plots that have been plotted in Figures 3.7, 3.10 and 3.12. Each of the methods used to plot deflection for the two section telescoping assembly make use of normalised parameters in order to obtain well defined plots over a range of varying tip loads whilst varying the overlap ratios from a minimum of 0.1 to a maximum of 1, in increments of 0.1. Non dimensionalization is in essence the partial or full removal of units from an equation involving physical quantities by a suitable substitution of variables. In the deflection analyses carried out in this chapter, non dimensionalization is used to further simplify and parameterise the complex equations that are obtained and to allow for comparison between the deflection methods utilised. To illustrate this point better, refer to Figure 3.2, where the normalised parameters used are  $\frac{y}{y_0}$  and  $\frac{wL}{P}$ . The quantity

$\frac{wL}{P}$  represents the ratio of the product of the self weight over the single fixed end section cantilever and the length over which it acts to the tip load acting on the same single fixed end cantilever section.

$\frac{y}{y_0}$  represents the ratio of the tip deflection for a given value of  $\frac{wL}{P}$  which in turn varies from 0.01 to 10, in multiples of 10, to the tip deflection of a single fixed end section cantilever having length  $L$  and uniform second moment of area  $I$ . In other words  $y_0$  equals

$$\frac{PL^3}{3EI}.$$

### 3.5 Mohr's Moment Area Method

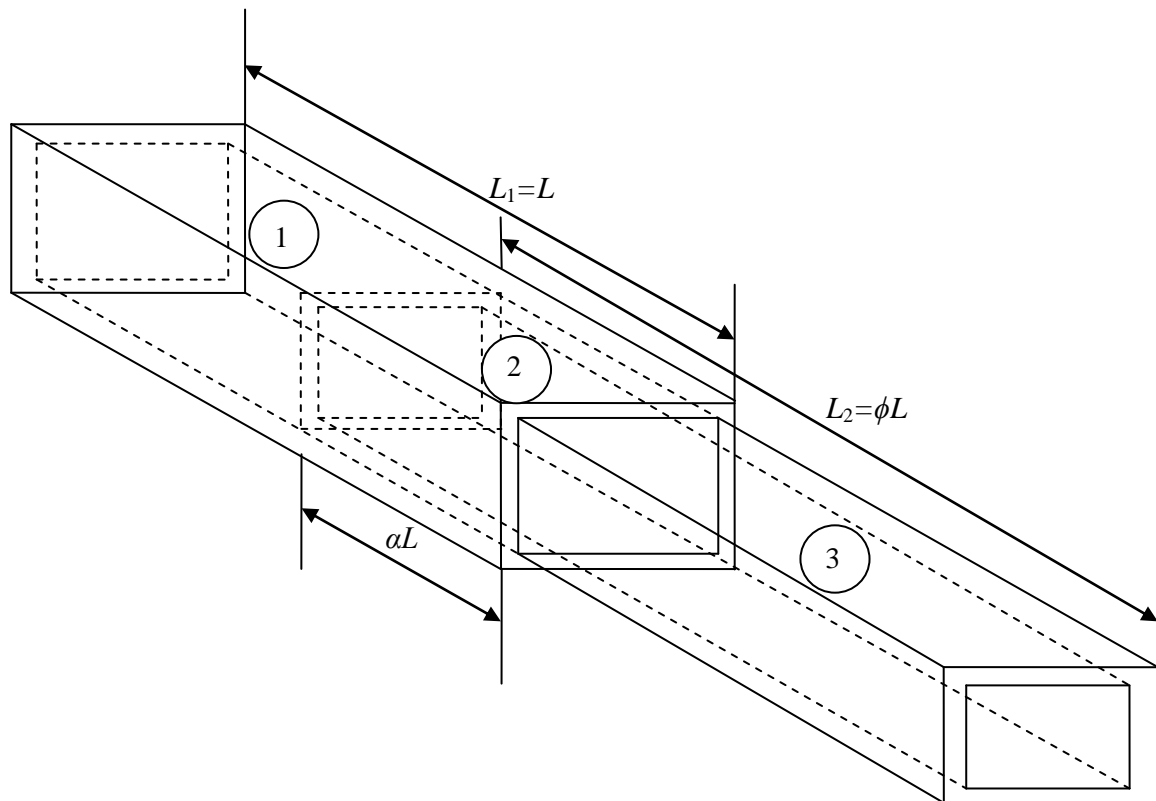


**Figure 3.3: Two section telescopic cantilever**

The thickness of the thin-walled sections that constitute the two section telescopic cantilever shown in Figure 3.3 is assumed to be constant along the beam. Of course, for the free-end section to slide within the fixed-end section the former will have dimensions smaller than that of the latter so individual dimensions of breadth, height and thickness are to be taken into account.

The Mohr's moment area method outlined here as well as the deflection analyses that follow, are applied to the telescopic beam assembly that consists of two sections each of differing length. For the purpose of this deflection analysis the sections are numbered from the fixed-end towards the free-end as shown in Figure 3.3. As can be seen from Figure 3.3 and Figure 3.4 the overlap is considered to be a separate section in order to account for changes in second moment of area and the change in self weight.

**Table 3.3: Individual Rectangular Section Properties**

Section	Length(mm)	Self Weight (N/mm)	Second Moments of Area (mm <sup>4</sup> )
<b>Section 1 (Fixed End)</b>	$L_1=L$	$w_1= w$	$I_1=I$
<b>Section 2 (Overlap)</b>	$\alpha L$	$w_2=(1+\gamma)w$	$I_2=(1+\beta)I$
<b>Section 3 (Free End)</b>	$L_2=\phi L_1= \phi L$	$w_3=\gamma w$	$I_3= \beta I$

The lengths of the sections have been broken down individually in order to facilitate ease of calculations. The lengths, second moments of area and self weights are all expressed in terms of ratio and each of these in turn relate to the fixed-end section. The ratios  $\alpha$ ,  $\beta$  and  $\gamma$  are assumed to be less than 1 which means that the fixed-end section has the larger dimensions of length, second moment of area and self weight respectively.

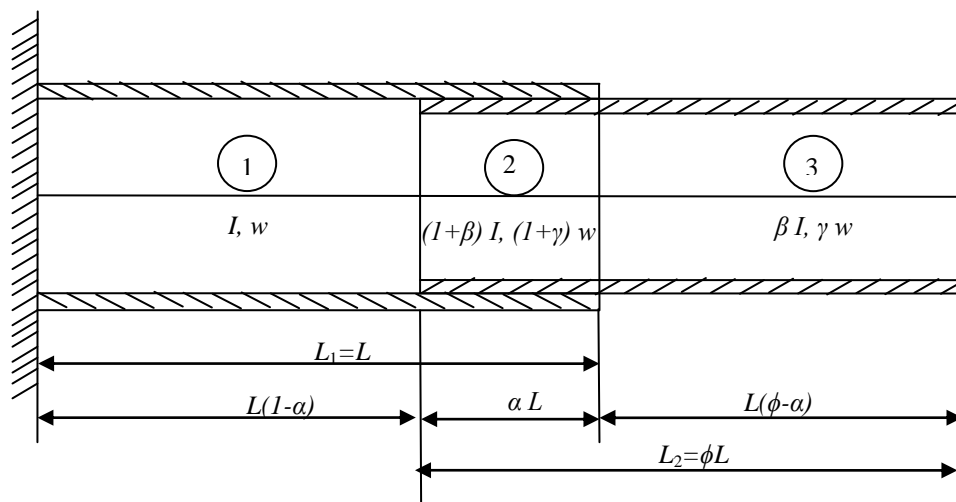


**Figure 3.4: Cross sectional view of the two section telescopic cantilever**

The moment area method developed by Mohr is a powerful tool for finding the deflections of structures primarily subjected to bending. Its ease of finding deflections of determinate structures makes it ideal for solving indeterminate structures using compatibility of

displacement. For example in a propped cantilever the method is adapted to provide the displacement at the prop.

### 3.5.1 Mohr's Moment Area Method applied to the two section tip loaded cantilever

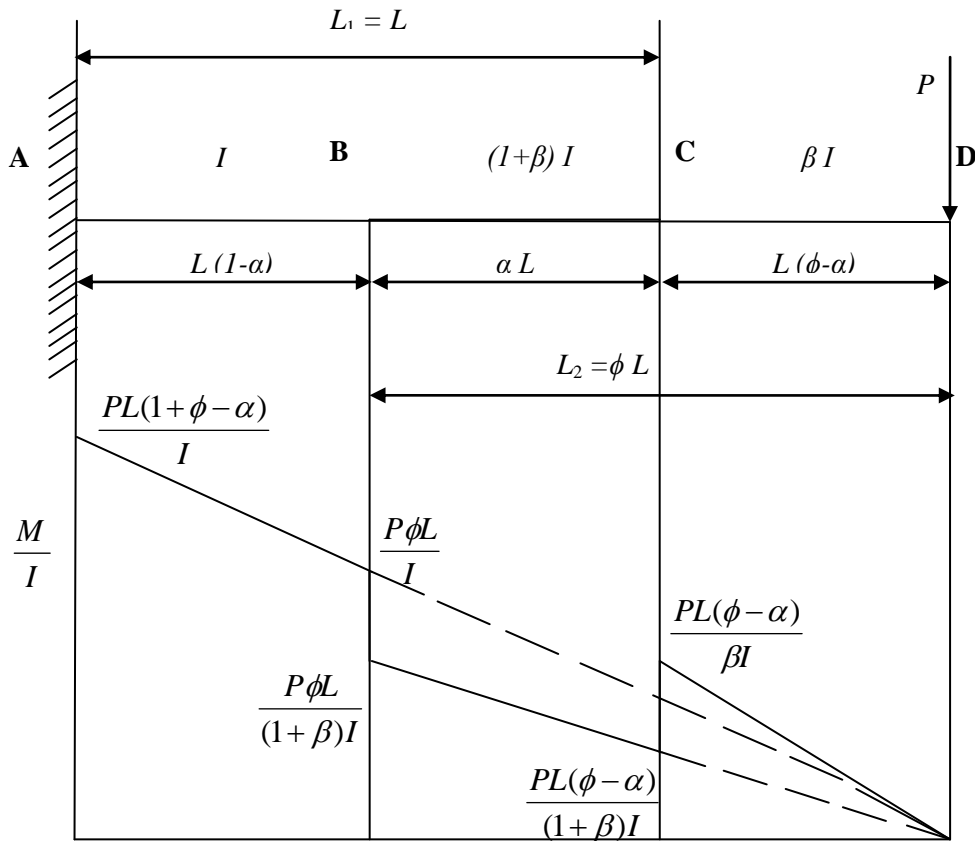


Figure 3.5: Mohr's Moment Area Method applied to the two section tip loaded cantilever beam

#### (a) Derivation of Slope for the two section tip loaded cantilever beam

Figure 3.5 shows the two section telescoping arrangement subject to a tip load having magnitude  $P$ . Taking into consideration the different variables detailed in Table 3.3 and shown in Figure 3.5, the slope of the telescopic assembly is derived as follows.

$$E\theta = \text{Area of the } \frac{M}{I} \text{ diagram from A-D}$$

$$\begin{aligned}
E\theta &= \left( \frac{PL(\phi - \alpha)}{\beta I} \times \frac{L(\phi - \alpha)}{2} \right) + \\
&\left( \frac{P\phi L}{(1 + \beta)I} \times \frac{\phi L}{2} - \frac{PL(\phi - \alpha)}{(1 + \beta)I} \times \frac{L(\phi - \alpha)}{2} \right) + \left( \frac{PL(1 + \phi - \alpha)}{I} \times \frac{L(1 + \phi - \alpha)}{2} - \frac{P\phi L}{I} \times \frac{\phi L}{2} \right) \\
E\theta &= \frac{PL^2(\phi - \alpha)^2}{2\beta I} + \frac{P\phi^2 L^2}{2(1 + \beta)I} - \frac{PL^2(\phi - \alpha)^2}{2(1 + \beta)I} + \frac{PL^2(1 + \phi - \alpha)^2}{2I} - \frac{P\phi^2 L^2}{2I} \\
\theta &= \frac{PL^2}{2EI} \left[ \left( \frac{(\phi - \alpha)^2}{\beta} \right) + \left( \frac{\phi^2}{1 + \beta} \right) - \frac{(\phi - \alpha)^2}{1 + \beta} + (1 + \phi - \alpha)^2 - \phi^2 \right] \quad (3.5)
\end{aligned}$$

Substituting  $\alpha = 0, \beta = \phi = 1$  in Equation (3.5) we get the slope of an equivalent single section cantilever having length  $2L$  and uniform second moment of area  $I$  as

$$\theta = \frac{P(2L)^2}{2EI}$$

Again substituting  $\alpha = \phi = 1$  in Equation (3.5) we get the slope of an equivalent single section cantilever having length  $L$  and uniform second moment of area  $(1 + \beta)I$  as

$$\theta = \frac{PL^2}{2E(1 + \beta)I}$$

### (b) Derivation of Deflection for the two section tip loaded cantilever beam

Having derived the slope of the two section telescopic cantilever beam assembly as shown in Equation (3.5), the deflection of the telescopic assembly is derived using the relation shown below.

$Ey =$  Moment of Area of the  $\frac{M}{I}$  diagram from A-D, about D

$$\begin{aligned}
Ey &= \left( \frac{PL^2(\phi - \alpha)^2}{2\beta I} \times \frac{2L(\phi - \alpha)}{3} \right) + \\
&\left( \frac{P\phi^2 L^2}{2(1 + \beta)I} \times \frac{2\phi L}{3} - \frac{PL^2(\phi - \alpha)^2}{2(1 + \beta)I} \times \frac{2L(\phi - \alpha)}{3} \right) \\
&+ \left( \frac{PL^2(1 + \phi - \alpha)^2}{2I} \times \frac{2L(1 + \phi - \alpha)}{3} - \frac{P\phi^2 L^2}{2I} \times \frac{2\phi L}{3} \right) \\
Ey &= \frac{PL^3(\phi - \alpha)^3}{3\beta I} + \frac{P\phi^3 L^3}{3(1 + \beta)I} - \frac{PL^3(\phi - \alpha)^3}{3(1 + \beta)I} + \frac{PL^3(1 + \phi - \alpha)^3}{3I} - \frac{P\phi^3 L^3}{3I}
\end{aligned}$$

$$y = \frac{PL^3}{3EI} \left[ \left( \frac{(\phi - \alpha)^3}{\beta} \right) + \left( \frac{\phi^3}{1 + \beta} \right) - \frac{(\phi - \alpha)^3}{1 + \beta} + (1 + \phi - \alpha)^3 - \phi^3 \right] \quad (3.6)$$

Substituting  $\alpha = 0, \beta = \phi = 1$  in Equation (3.6) we get the standard deflection expression for an equivalent single section cantilever having length  $2L$  and uniform second moment of area  $I$  as

$$y = \frac{P(2L)^3}{3EI}$$

Substituting  $\alpha = \phi = 1$  in Equation (3.6) we get the deflection for an equivalent single section cantilever having length  $L$  and uniform second moment of area  $(1 + \beta)I$  as

$$y = \frac{PL^3}{3E(1 + \beta)I}$$

**3.5.2 Mohr's Moment Area Method applied to the two section cantilever subjected to uniformly distributed loading**

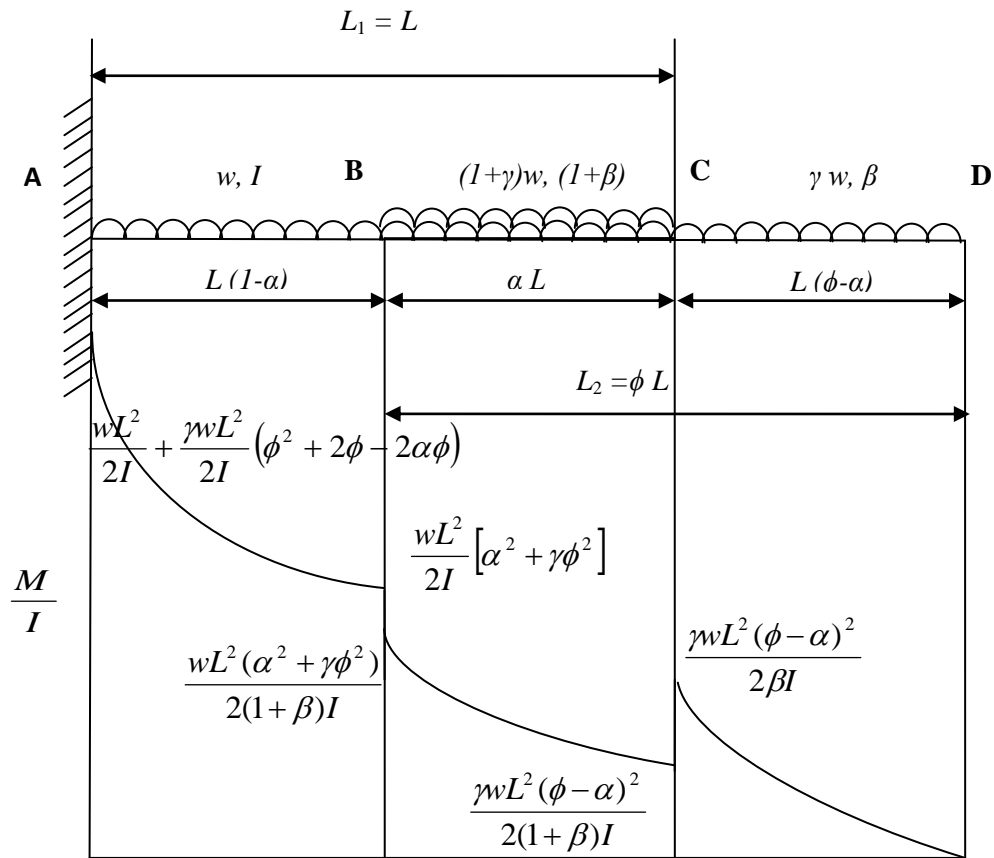


**Figure 3.6: Mohr's Moment Area Method applied to the two section cantilever beam subjected to uniformly distributed loading**

**(a) Derivation of Slope for the two section cantilever beam subjected to uniformly distributed loading**

Figure 3.6 shows the two section telescoping arrangement subject to a uniformly distributed load or under the action of the individual self weights of the constituent beam sections. Taking into consideration the different variables detailed in Table 3.3, the slope of the telescopic assembly under the action of its self weight is derived, by summing the areas of the three individual  $\frac{M}{I}$  diagrams as shown in Figure 3.6.

$$\begin{aligned}
E\theta &= \left( \frac{\gamma w L^2 (\phi - \alpha)^2}{2\beta I} \times \frac{L(\phi - \alpha)}{3} \right) + \\
&\left( \frac{w L^2 (\alpha^2 + \gamma \phi^2)}{2(1 + \beta)I} \times \frac{\phi L}{3} - \frac{\gamma w L^2 (\phi - \alpha)^2}{2(1 + \beta)I} \times \frac{L(\phi - \alpha)}{3} \right) + \\
&\left( \frac{w L^2}{2I} (1 + \gamma \phi^2 + 2\gamma\phi - 2\alpha\gamma\phi) \times \frac{L(1 + \phi - \alpha)}{3} - \frac{w L^2}{2I} (\alpha^2 + \gamma \phi^2) \times \frac{\phi L}{3} \right) \\
\theta &= \frac{w L^3}{6EI} \left[ \frac{\gamma(\phi - \alpha)^3}{\beta} + \left( \frac{\alpha^2 \phi + \gamma \phi^3}{1 + \beta} \right) - \frac{\gamma(\phi - \alpha)^3}{1 + \beta} \right] \\
&+ \frac{w L^3}{6EI} \left[ (1 + \gamma \phi^2 + 2\gamma\phi - 2\alpha\gamma\phi)(1 + \phi - \alpha) - (\alpha^2 \phi + \gamma \phi^3) \right]
\end{aligned} \tag{3.7}$$

Substituting  $\alpha = 0, \beta = \phi = 1$  in Equation (3.7) we get the slope of an equivalent single section cantilever having length  $2L$  and uniform second moment of area  $I$  as

$$\theta = \frac{w(2L)^3}{6EI}$$

Substituting  $\alpha = \phi = 1$  in Equation (3.7) we get the slope of an equivalent single section cantilever having length  $L$  and uniform second moment of area  $(1 + \beta)I$  as

$$\theta = \left( \frac{1 + \gamma}{1 + \beta} \right) \frac{w L^3}{6EI}$$

**(b) Derivation of Deflection for the two section cantilever beam subjected to uniformly distributed loading**

Having derived the slope of the two section telescopic cantilever beam assembly as shown in Equation (3.7), the deflection of the telescopic assembly is derived by summing the moments of the three individual areas of the  $\frac{M}{I}$  from A to D, about the point D as shown in Figure 3.6 as outlined below.

$$\begin{aligned}
Ey &= \left( \frac{\gamma w L^3 (\phi - \alpha)^3}{6\beta I} \times \frac{3L(\phi - \alpha)}{4} \right) + \\
&\left( \frac{w L^3 (\alpha^2 \phi + \gamma \phi^3)}{6(1 + \beta)I} \times \frac{3\phi L}{4} - \frac{\gamma w L^3 (\phi - \alpha)^3}{6(1 + \beta)I} \times \frac{3L(\phi - \alpha)}{4} \right) + \\
&\left( \frac{w L^3}{6I} (1 + \gamma \phi^2 + 2\gamma \phi - 2\alpha \gamma \phi)(1 + \phi - \alpha) \times \frac{3L(1 + \phi - \alpha)}{4} - \frac{w L^3}{6I} (\alpha^2 \phi + \gamma \phi^3) \times \frac{3\phi L}{4} \right) \\
y &= \frac{w L^4}{8EI} \left[ \frac{\gamma(\phi - \alpha)^4}{\beta} + \left( \frac{\alpha^2 \phi^2 + \gamma \phi^4}{1 + \beta} \right) - \frac{\gamma(\phi - \alpha)^4}{1 + \beta} \right] + \\
&\frac{w L^4}{8EI} \left[ (1 + \gamma \phi^2 + 2\gamma \phi - 2\alpha \gamma \phi)(1 + \phi - \alpha)^2 - (\alpha^2 \phi^2 + \gamma \phi^4) \right]
\end{aligned} \tag{3.8}$$

Substituting  $\alpha = 0, \beta = \gamma = \phi = 1$  in Equation (3.8) we get the deflection for an equivalent single section cantilever having length  $2L$  and uniform second moment of area  $I$  as

$$y = \frac{w(2L)^4}{8EI}$$

Substituting  $\alpha = \phi = 1$  in Equation (3.8) we get the deflection for an equivalent single section cantilever having length  $L$  and uniform second moment of area  $(1 + \beta)I$  as

$$y = \left( \frac{1 + \gamma}{1 + \beta} \right) \frac{w L^4}{8EI}$$

### 3.5.3 Derivation of Deflection for the two section cantilever beam subjected to uniformly distributed and tip loading

Knowing the deflections of the two-section cantilever under the action of a tip load and under the action of a distributed load (in effect the self-weight) as can be seen from Equations (3.6) and (3.8), it is imperative to find the combined total deflection of the two-section cantilever under their combined action. This is found by utilising the principle of superposition. Superposition is used to solve for beam and structure deflections of combined loads when the effects are linear, in other words each load does not affect the results or actions of other loads and the effect of each load does not alter the geometry of the structural system significantly.

Applying the principle of superposition we get the total deflection for the combined loading as the summation of equations (3.6) and (3.8)

$$\begin{aligned}
y &= \frac{PL^3}{3EI} \left[ \left( \frac{(\phi - \alpha)^3}{\beta} \right) + \left( \frac{\phi^3}{1 + \beta} \right) - \frac{(\phi - \alpha)^3}{1 + \beta} + (1 + \phi - \alpha)^3 - \phi^3 \right] + \\
&\frac{wL^4}{8EI} \left[ \frac{\gamma(\phi - \alpha)^4}{\beta} + \left( \frac{\alpha^2\phi^2 + \gamma\phi^4}{1 + \beta} \right) - \frac{\gamma(\phi - \alpha)^4}{1 + \beta} \right] + \\
&\frac{wL^4}{8EI} \left[ (1 + \gamma\phi^2 + 2\gamma\phi - 2\alpha\gamma\phi)(1 + \phi - \alpha)^2 - (\alpha^2\phi^2 + \gamma\phi^4) \right]
\end{aligned} \tag{3.9}$$

Substituting  $\alpha = 0, \beta = \gamma = \phi = 1$  in Equation (3.9) we get the deflection for an equivalent single-section cantilever having length  $2L$  and uniform second moment of area  $I$  under the action of a combined distributed loading and tip load as

$$y = \frac{P(2L)^3}{3EI} + \frac{w(2L)^4}{8EI}$$

Substituting  $\alpha = \phi = 1$  in Equation (3.9) we get the deflection for an equivalent single section cantilever having length  $L$  and uniform second moment of area  $(1 + \beta)I$  as

$$y = \left( \frac{1}{1 + \beta} \right) \frac{PL^3}{3EI} + \left( \frac{1 + \gamma}{1 + \beta} \right) \frac{wL^4}{8EI} = \left( \frac{1}{1 + \beta} \right) \left[ \frac{PL^3}{3EI} + \frac{(1 + \gamma)wL^4}{8EI} \right]$$

Equation (3.9) can be re written as

$$\begin{aligned}
y &= \frac{PL^3}{3EI} \left[ \left( \frac{(\phi - \alpha)^3}{\beta} \right) + \left( \frac{\phi^3}{1 + \beta} \right) - \frac{(\phi - \alpha)^3}{1 + \beta} + (1 + \phi - \alpha)^3 - \phi^3 \right] + \\
&\left( \frac{wL^4}{8EI} \times \frac{3EI}{PL^3} \right) \times \left\{ \left[ \frac{\gamma(\phi - \alpha)^4}{\beta} + \left( \frac{\alpha^2\phi^2 + \gamma\phi^4}{1 + \beta} \right) - \frac{\gamma(\phi - \alpha)^4}{1 + \beta} \right] \right. \\
&\left. + \left[ (1 + \gamma\phi^2 + 2\gamma\phi - 2\alpha\gamma\phi)(1 + \phi - \alpha)^2 - (\alpha^2\phi^2 + \gamma\phi^4) \right] \right\} \\
y &= \frac{PL^3}{3EI} \left[ \left( \frac{(\phi - \alpha)^3}{\beta} \right) + \left( \frac{\phi^3}{1 + \beta} \right) - \frac{(\phi - \alpha)^3}{1 + \beta} + (1 + \phi - \alpha)^3 - \phi^3 \right] + \\
&\left( \frac{3}{8} \times \frac{wL}{P} \right) \times \left\{ \left[ \frac{\gamma(\phi - \alpha)^4}{\beta} + \left( \frac{\alpha^2\phi^2 + \gamma\phi^4}{1 + \beta} \right) - \frac{\gamma(\phi - \alpha)^4}{1 + \beta} \right] \right. \\
&\left. + \left[ (1 + \gamma\phi^2 + 2\gamma\phi - 2\alpha\gamma\phi)(1 + \phi - \alpha)^2 - (\alpha^2\phi^2 + \gamma\phi^4) \right] \right\}
\end{aligned} \tag{3.10}$$

The term  $\frac{PL^3}{3EI}$  represents the end-deflection of a cantilever of length  $L$  and flexural rigidity

$EI$ , subjected to a tip load  $P$  Newton. This term is represented by the variable

$y_0$  where  $y_0 = \frac{PL^3}{3EI}$ . Equation (3.10) now becomes

$$\begin{aligned} \frac{y}{y_0} = & \left[ \left( \frac{(\phi - \alpha)^3}{\beta} \right) + \left( \frac{\phi^3}{1 + \beta} \right) - \frac{(\phi - \alpha)^3}{1 + \beta} + (1 + \phi - \alpha)^3 - \phi^3 \right] + \\ & \left( \frac{3}{8} \times \frac{wL}{P} \right) \times \left\{ \left[ \frac{\gamma(\phi - \alpha)^4}{\beta} + \left( \frac{\alpha^2\phi^2 + \gamma\phi^4}{1 + \beta} \right) - \frac{\gamma(\phi - \alpha)^4}{1 + \beta} \right] \right. \\ & \left. + \left[ (1 + \gamma\phi^2 + 2\gamma\phi - 2\alpha\gamma\phi)(1 + \phi - \alpha)^2 - (\alpha^2\phi^2 + \gamma\phi^4) \right] \right\} \end{aligned} \quad (3.11)$$

The curves in Figure 3.7 represent the plots of the non dimensional parameter  $\frac{y}{y_0}$  against the

overlap ratio parameter  $\alpha$ , for  $\frac{wL}{P}$  ratios 0.01, 0.1, 1 and 10. The non dimensional ratio  $\frac{y}{y_0}$  is

obtained from Equation (3.11) by substituting the values of  $\phi$ ,  $\beta$  and  $\gamma$  as 0.833, 0.49 and 0.642 respectively. Table 3.3 outlines how the ratios  $\phi$ ,  $\beta$  and  $\gamma$  can be derived using the specifications listed in Table 3.1. Whilst keeping the aforementioned ratios a constant, the overlap ratio parameter  $\alpha$  is varied in increments of 0.1, from 0 to 1.

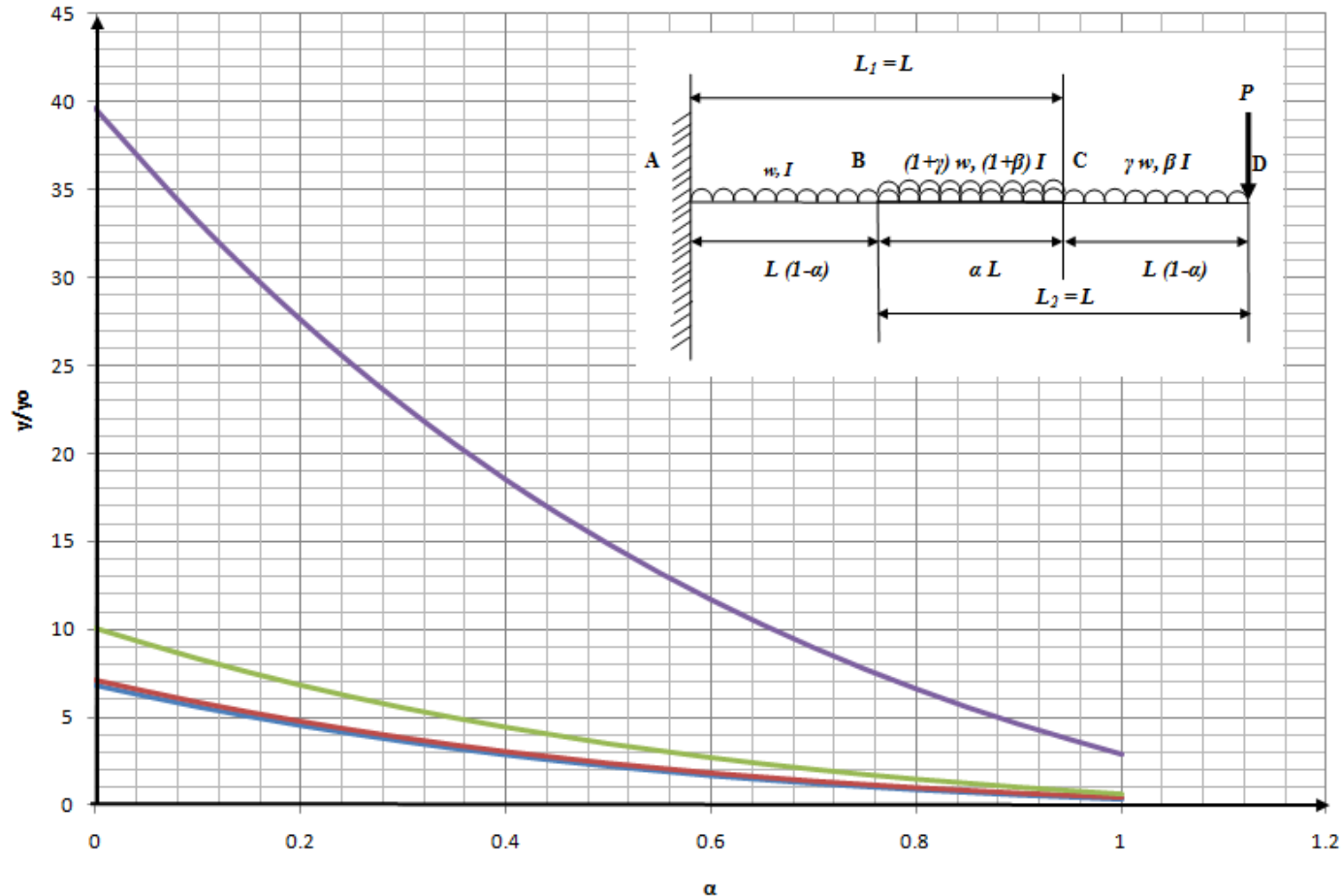
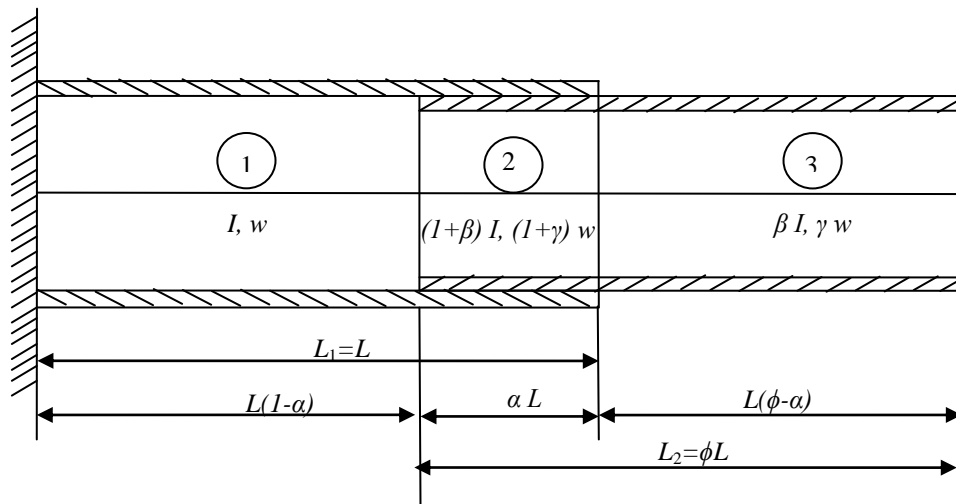


Figure 3.7: End Deflection Plot of Equation (3.11) obtained from Mohr's Moment Area Theorem vs. Parameter  $\alpha$ , for the two section telescopic cantilever beam assembly having individual part dimensions outlined in Table 3.1, and fixed and free-end lengths of 1200mm and 1000mm respectively.  $y/y_0$  represents the ratio of the tip deflection for a given value of  $wL/P$  which in turn varies from 0.01 to 10, in multiples of 10, to the tip deflection of a single fixed end section cantilever having length  $L$  and uniform second moment of area  $I$ , such that  $y_0$  equals  $(PL^3/3EI)$ .

(Key: —  $wL/P=10$ ; —  $wL/P=1$ ; —  $wL/P=0.1$ ; —  $wL/P=0.01$ )

### 3.6 Castigliano's Theorem

Castigliano's method is used for determining the displacements of a linear elastic system based on the partial derivatives of strain energy. The first of Castigliano's theorem determines the forces in a elastic structure whereas the second theorem determines the displacements in a form that is applied here. As is detailed in § 2.7.7, if the structure is linearly elastic, then the partial derivative of the strain energy of that system with respect to the applied force system is equal to the corresponding displacements produced.



**Figure 3.8: Cross sectional view of the two section telescopic cantilever**

Referring to Figures 3.8 and 3.9, Castigliano's theorem, part 2, can be applied to each of the three sections that make up the composite telescopic cantilever beam assembly in order to give the total displacement  $y$  as follows

$$y = \frac{\delta U}{\delta P} = \int_0^{L(\phi-\alpha)} \frac{M_1}{EI_1} \cdot \frac{\delta M_1}{\delta P} \cdot dz + \int_{L(\phi-\alpha)}^{\phi L} \frac{M_2}{EI_2} \cdot \frac{\delta M_2}{\delta P} \cdot dz + \int_{\phi L}^{(1+\phi-\alpha)L} \frac{M_3}{EI_3} \cdot \frac{\delta M_3}{\delta P} \cdot dz \quad (3.12)$$

Figure 3.9 makes reference to the symbol  $z'$ , where  $z' = \frac{z}{L}$ , this in turn is the basis for the Equation (3.12). The subscripts 1, 2 and 3 represent the free end, overlap area and the fixed end respectively. Prior to evaluating the integral in Equation (3.12) the bending moments  $M_1$ ,  $M_2$  and  $M_3$  at each of the three sections starting with the free end to the fixed end are

evaluated and their respective derivatives with respect to the tip load  $P$  are found as shown in Equation sets (3.13)-(3.15) and then substituted in Equation (3.12) as outlined below.

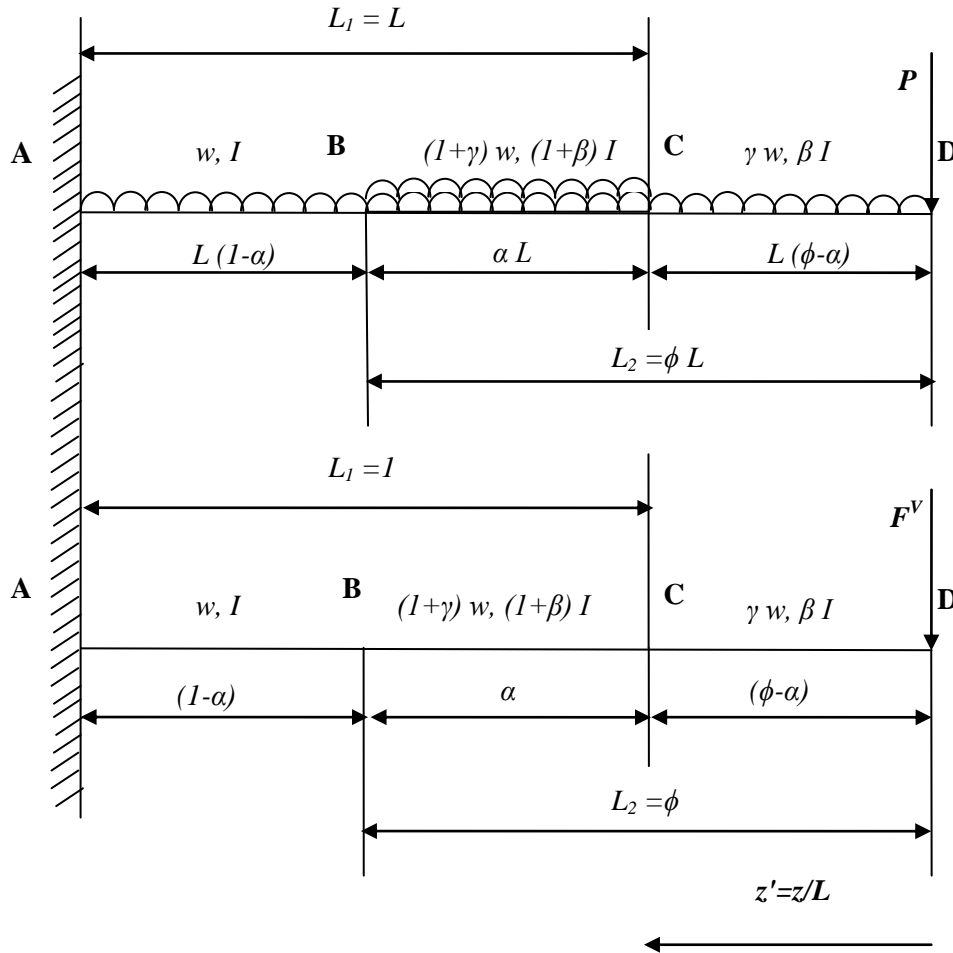


**Figure 3.9: Castigliano's Theorem applied to the two section cantilever beam**

The following moment equations are as mentioned above expressed in terms of  $z'$  where  $z' = \frac{z}{L}$ .

$$\begin{aligned}
 & \text{Bending moment for the section } 0 \leq z' \leq (1-\alpha) \\
 & M_1 = \left[ Pz + \gamma w \cdot \frac{z^2}{2} \right] = \left[ P \times L \times \left( \frac{z}{L} \right) + \gamma w \times \left( \frac{L^2}{2} \right) \times \left( \frac{z}{L} \right)^2 \right] \\
 & = \left[ PL(z') + \gamma w \left( \frac{L^2}{2} \right) \times (z')^2 \right] \quad \left. \vphantom{M_1} \right\} \quad (3.13) \\
 & \text{Derivative of } M_1 \text{ with respect to } P \text{ is } \frac{\delta M_1}{\delta P} = Lz'
 \end{aligned}$$

**Bending moment for the section  $(1-\alpha) \leq z' \leq \phi$**

$$\begin{aligned}
 M_2 &= \left[ Pz + \gamma\phi w \cdot \frac{z^2}{2} + \frac{w}{2} \times [z - (\phi - \alpha)L]^2 \right] \\
 &= \left[ P \times L \times \left( \frac{z}{L} \right) + \gamma\phi w \times \left( \frac{L^2}{2} \right) \times \left( \frac{z}{L} \right)^2 + \frac{w}{2} \times L^2 \times \left[ \left( \frac{z}{L} \right) - (\phi - \alpha) \right]^2 \right] \\
 &= \left[ PLz' + \frac{\gamma\phi w L^2}{2} (z')^2 + \frac{wL^2}{2} [z' - (\phi - \alpha)]^2 \right] \\
 \\ 
 M_2 &= \left[ PLz' + \frac{wL^2}{2} (\gamma\phi(z')^2 + [z' - (\phi - \alpha)]^2) \right] \\
 \text{Derivative of } M_2 \text{ with respect to } P &\text{ is } \frac{\delta M_2}{\delta P} = Lz'
 \end{aligned} \tag{3.14}$$

**Bending moment for the section  $\phi \leq z' \leq (1 + \phi - \alpha)$**

$$\begin{aligned}
 M_3 &= \left[ Pz + \gamma w \phi L \times \left( z - \frac{\phi L}{2} \right) + \frac{w}{2} \times [z - (\phi - \alpha)L]^2 \right] \\
 &= \left[ P \times L \times \left( \frac{z}{L} \right) + \gamma\phi w \times \left( \frac{L^2}{2} \right) \times \left( 2 \frac{z}{L} - \phi \right) + \frac{w}{2} \times L^2 \times \left[ \left( \frac{z}{L} \right) - (\phi - \alpha) \right]^2 \right] \\
 M_3 &= \left[ PLz' + \frac{wL^2}{2} (\gamma\phi \times (2z' - \phi) + [z' - (\phi - \alpha)]^2) \right] \\
 \text{Derivative of } M_3 \text{ with respect to } P &\text{ is } \frac{\delta M_3}{\delta P} = Lz'
 \end{aligned} \tag{3.15}$$

Substituting Equation sets (3.13), (3.14), (3.15) and  $dz = L \times dz'$  in the Equation (3.12) for y gives:

$$\begin{aligned}
 y &= \frac{1}{EI} \left[ \frac{1}{\beta} \int_0^{\phi-\alpha} \left( PL(z') + \gamma w \left( \frac{L^2}{2} \right) \times (z')^2 \right) \times (L \cdot z') \times L \times dz' + \right. \\
 &\frac{1}{(1+\beta)} \int_{\phi-\alpha}^{\phi} \left( PLz' + \frac{wL^2}{2} (\gamma\phi(z')^2 + [z' - (\phi - \alpha)]^2) \right) \times (L \cdot z') \times L \times dz' + \\
 &\left. \int_{\phi}^{1+\phi-\alpha} \left( PLz' + \frac{wL^2}{2} (\gamma\phi \times (2z' - \phi) + [z' - (\phi - \alpha)]^2) \right) \times (L \cdot z') \times L \times dz' \right]
 \end{aligned}$$

$$y = \frac{1}{EI} \left[ \frac{1}{\beta} \int_0^{(\phi-\alpha)} \left[ PL^3 z'^2 + \gamma w \left( \frac{L^4}{2} \right) \times (z')^3 \right] dz' + \right. \\ \left. \frac{1}{(1+\beta)} \int_{\phi-\alpha}^{\phi} \left( PL^3 z'^3 + \frac{wL^4}{2} (\gamma\phi(z')^3 + z' \times [z' - (\phi - \alpha)]^2) \right) dz' + \right. \\ \left. \int_{\phi}^{1+\phi-\alpha} \left( PL^3 z'^3 + \frac{wL^4}{2} (\gamma\phi z' \times (2z' - \phi) + z' \times [z' - (\phi - \alpha)]^2) \right) dz' \right]$$

Let  $X = \phi - \alpha$  then integrating the terms gives

$$y = \frac{1}{EI} \left[ \frac{1}{\beta} \left( PL^3 \left| \frac{z'^3}{3} \right|_0^X + \gamma w \left( \frac{L^4}{2} \right) \times \left| \frac{z'^4}{4} \right|_0^X \right) + \right. \\ \left. \frac{1}{(1+\beta)} \left( PL^3 \left| \frac{z'^3}{3} \right|_X^{\phi} + \left( \frac{wL^4}{2} \right) \times \left| (1+\gamma\phi) \frac{z'^4}{4} - \frac{2Xz'^3}{3} + \frac{X^2 z'^2}{2} \right|_X^{\phi} \right) + \right. \\ \left. \left( PL^3 \left| \frac{z'^3}{3} \right|_{\phi}^{1+X} + \left( \frac{wL^4}{2} \right) \times \left| \frac{z'^4}{4} + 2 \times (\gamma\phi - X) \times \frac{z'^3}{3} + (X^2 - \gamma\phi^2) \times \frac{z'^2}{2} \right|_{\phi}^{1+X} \right) \right]$$

Applying the limits now yields

$$y = \frac{1}{EI} \frac{1}{\beta} \left( PL^3 \times \frac{X^3}{3} + \gamma w \left( \frac{L^4}{2} \right) \times \frac{X^4}{4} \right) + \\ \frac{1}{EI} \frac{1}{(1+\beta)} \left\{ PL^3 \times \left( \frac{\phi^3}{3} - \frac{X^3}{3} \right) + \right. \\ \left. \left( \frac{wL^4}{2} \right) \times \left[ \left( (1+\gamma\phi) \frac{\phi^4}{4} - \frac{2X\phi^3}{3} + \frac{X^2\phi^2}{2} \right) - \left( (1+\gamma\phi) \frac{X^4}{4} - \frac{2X^4}{3} + \frac{X^4}{2} \right) \right] \right\} + \\ \frac{1}{EI} PL^3 \times \left\{ \left( \frac{(1+X)^3}{3} - \frac{\phi^3}{3} \right) + \right. \\ \left. \left( \frac{wL^4}{2} \right) \times \left( \frac{(1+X)^4}{4} + 2 \times (\gamma\phi - X) \times \frac{(1+X)^3}{3} + (X^2 - \gamma\phi^2) \times \frac{(1+X)^2}{2} \right) - \right. \\ \left. \left( \frac{\phi^4}{4} + 2 \times (\gamma\phi - X) \times \frac{\phi^3}{3} + (X^2 - \gamma\phi^2) \times \frac{\phi^2}{2} \right) \right\}$$

$$\begin{aligned}
y = & \frac{PL^3}{3EI} \left[ \left( \frac{X^3}{\beta} + \left( \frac{\phi^3 - X^3}{1+\beta} \right) + (1+X)^3 - \phi^3 \right) \right] + \\
& \frac{wL^4}{8EI} \left\{ \frac{\gamma}{\beta} X^4 + \left( \frac{1}{1+\beta} \right) \times \left[ \left( (1+\gamma\phi)\phi^4 - \frac{8X\phi^3}{3} + 2X^2\phi^2 \right) - \left( (1+\gamma\phi)X^4 - \frac{8X^4}{3} + 2X^4 \right) \right] \right\} + \\
& \left( \left( (1+X)^4 + \frac{8 \times (\gamma\phi - X) \times (1+X)^3}{3} + 2 \times (X^2 - \gamma\phi^2) \times (1+X)^2 \right) - \right. \\
& \left. \left( \phi^4 + \frac{8 \times (\gamma\phi - X) \times \phi^3}{3} + 2 \times (X^2 - \gamma\phi^2) \times \phi^2 \right) \right) \left. \right\}
\end{aligned}$$

The final equation can be written as

$$\begin{aligned}
y = & \frac{PL^3}{3EI} \left[ \left( \frac{X^3}{\beta} + \left( \frac{\phi^3 - X^3}{1+\beta} \right) + (1+X)^3 - \phi^3 \right) \right] + \\
& \frac{wL^4}{8EI} \left\{ \frac{\gamma}{\beta} X^4 + \left( \frac{1}{1+\beta} \right) \times \left[ \left( (1+\gamma\phi)\phi^4 - \frac{8X\phi^3}{3} + 2X^2\phi^2 \right) - \left( (1+\gamma\phi)X^4 - \frac{2X^4}{3} \right) \right] \right\} + \\
& (1+X)^2 \times \left[ \left( (1+X)^2 + \frac{8 \times (\gamma\phi - X) \times (1+X)}{3} + 2 \times (X^2 - \gamma\phi^2) \right) \right] - \\
& \left( \phi^4 + \frac{8 \times (\gamma\phi - X) \times \phi^3}{3} + 2 \times (X^2 - \gamma\phi^2) \times \phi^2 \right) \left. \right\}
\end{aligned} \tag{3.16}$$

where  $X = \phi - \alpha$

Substituting  $\alpha = 0, \beta = \gamma = \phi = 1$  in Equation (3.16) we get the deflection for an equivalent single section cantilever having length  $2L$  and uniform second moment of area  $I$  under the action of a combined distributed loading and tip load as

$$y = \frac{P(2L)^3}{3EI} + \frac{w(2L)^4}{8EI}$$

Substituting  $\alpha = \phi = 1$  in Equation (3.16) we get the deflection for an equivalent single section cantilever having length  $L$  and uniform second moment of inertia  $(1+\beta)I$  as

$$y = \left( \frac{1}{1+\beta} \right) \frac{PL^3}{3EI} + \left( \frac{1+\gamma}{1+\beta} \right) \frac{wL^4}{8EI} = \left( \frac{1}{1+\beta} \right) \left[ \frac{PL^3}{3EI} + \frac{(1+\gamma)wL^4}{8EI} \right]$$

Equation (3.16) can be re written as

$$\begin{aligned}
y = & \frac{PL^3}{3EI} \left\{ \left[ \left( \frac{X^3}{\beta} + \left( \frac{\phi^3 - X^3}{1 + \beta} \right) + (1 + X)^3 - \phi^3 \right) \right] + \right. \\
& \left( \frac{wL^4}{8EI} \times \frac{3EI}{PL^3} \right) \times \left\{ \frac{\gamma}{\beta} X^4 + \left( \frac{1}{1 + \beta} \right) \times \left[ \left( (1 + \gamma\phi)\phi^4 - \frac{8X\phi^3}{3} + 2X^2\phi^2 \right) - \left( (1 + \gamma\phi)X^4 - \frac{2X^4}{3} \right) \right] + \right. \\
& (1 + X)^2 \times \left[ \left( (1 + X)^2 + \frac{8 \times (\gamma\phi - X) \times (1 + X)}{3} + 2 \times (X^2 - \gamma\phi^2) \right) \right] - \\
& \left. \left. \left( \phi^4 + \frac{8 \times (\gamma\phi - X) \times \phi^3}{3} + 2 \times (X^2 - \gamma\phi^2) \times \phi^2 \right) \right\} \right\} \\
y = & \frac{PL^3}{3EI} \left\{ \left[ \left( \frac{X^3}{\beta} + \left( \frac{\phi^3 - X^3}{1 + \beta} \right) + (1 + X)^3 - \phi^3 \right) \right] + \right. \\
& \left( \frac{3}{8} \times \frac{wL}{P} \right) \times \left\{ \frac{\gamma}{\beta} X^4 + \left( \frac{1}{1 + \beta} \right) \times \left[ \left( (1 + \gamma\phi)\phi^4 - \frac{8X\phi^3}{3} + 2X^2\phi^2 \right) - \left( (1 + \gamma\phi)X^4 - \frac{2X^4}{3} \right) \right] + \right. \\
& (1 + X)^2 \times \left[ \left( (1 + X)^2 + \frac{8 \times (\gamma\phi - X) \times (1 + X)}{3} + 2 \times (X^2 - \gamma\phi^2) \right) \right] - \\
& \left. \left. \left( \phi^4 + \frac{8 \times (\gamma\phi - X) \times \phi^3}{3} + 2 \times (X^2 - \gamma\phi^2) \times \phi^2 \right) \right\} \right\} \tag{3.17}
\end{aligned}$$

The term  $\frac{PL^3}{3EI}$  is represented by the variable  $y_0$  such that  $y_0 = \frac{PL^3}{3EI}$  for similar reasons as mentioned in §3.5.3. Equation (3.17) is written in its entirety as

$$\begin{aligned} \frac{y}{y_0} = & \left[ \left( \frac{(\phi - \alpha)^3}{\beta} + \left( \frac{\phi^3 - (\phi - \alpha)^3}{1 + \beta} \right) + (1 + (\phi - \alpha))^3 - \phi^3 \right) \right] + \\ & \left( \frac{3}{8} \times \frac{wL}{P} \right) \times \left\{ \frac{\gamma}{\beta} (\phi - \alpha)^4 + \left( \frac{1}{1 + \beta} \right) \times \left[ \left( (1 + \gamma\phi)\phi^4 - \frac{8(\phi - \alpha)\phi^3}{3} + 2(\phi - \alpha)^2\phi^2 \right) - \right. \right. \quad (3.18) \\ & \left. \left. \left( (1 + \gamma\phi)(\phi - \alpha)^4 - \frac{2(\phi - \alpha)^4}{3} \right) \right] + \right. \\ & \left. (1 + (\phi - \alpha))^2 \times \left[ (1 + (\phi - \alpha))^2 + \frac{8 \times (\gamma\phi - (\phi - \alpha)) \times (1 + (\phi - \alpha))}{3} + \right. \right. \\ & \left. \left. 2 \times ((\phi - \alpha)^2 - \gamma\phi^2) \right] - \left( \phi^4 + \frac{8 \times (\gamma\phi - (\phi - \alpha)) \times \phi^3}{3} + 2 \times ((\phi - \alpha)^2 - \gamma\phi^2) \times \phi^2 \right) \right\} \end{aligned}$$

The curves in Figure 3.10 represent the plots of the non dimensional parameter  $\frac{y}{y_0}$  against the overlap ratio parameter  $\alpha$ , for  $\frac{wL}{P}$  ratios 0.01, 0.1, 1 and 10, calculated using Castigliano's theorem, Part 2. As was the case for Macaulay's theorem the values of the constant parameters  $\phi$ ,  $\beta$  and  $\gamma$  are taken as 0.833, 0.49 and 0.642, respectively and substituted into Equation (3.18), while varying the overlap ratio  $\alpha$  from 0 to 1 in increments of 0.1.

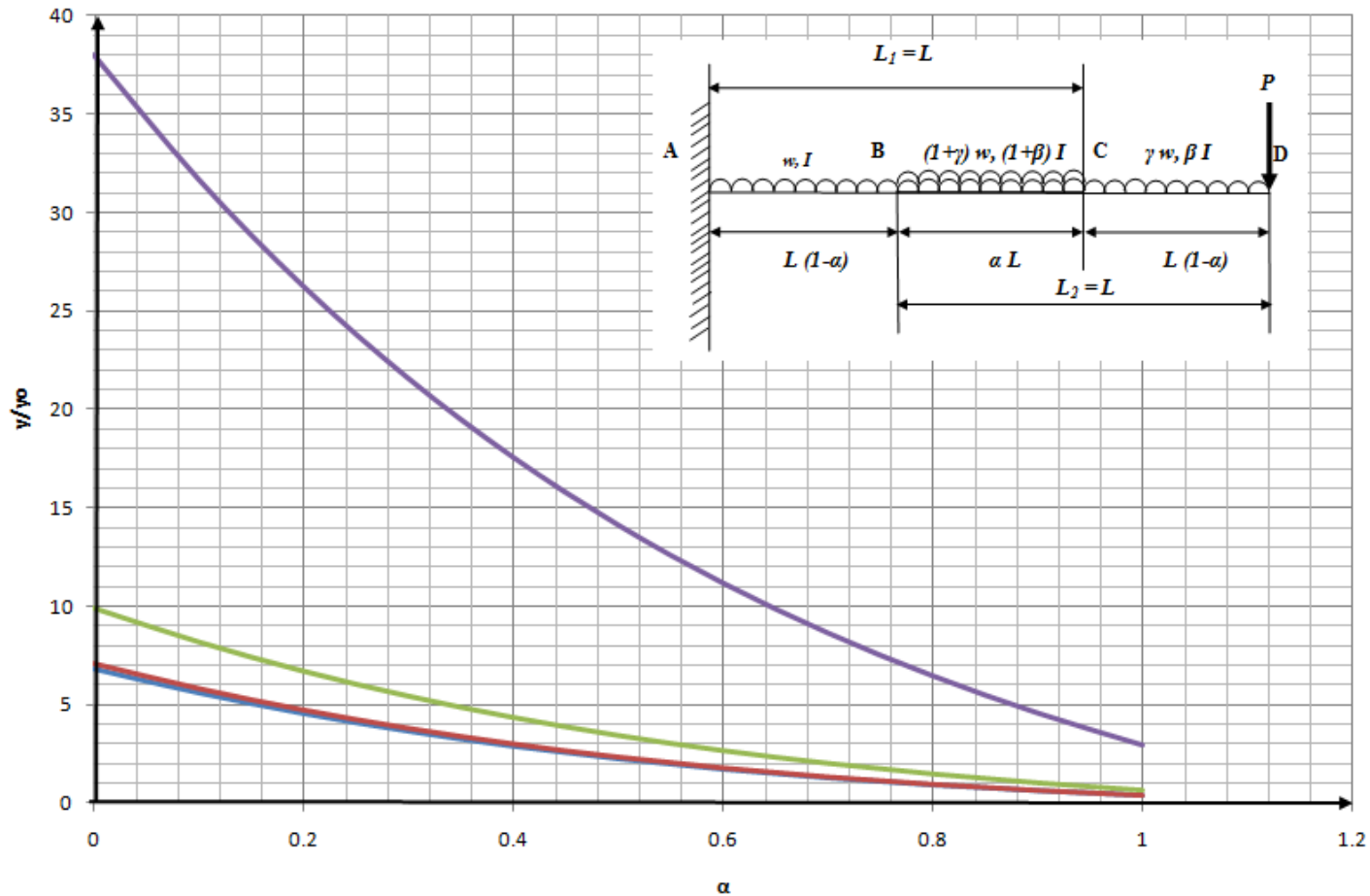


**Figure 3.10: Deflection Plot of Equation (3.18) obtained from Castigliano's Theorem vs. Parameter  $\alpha$ , for the two section telescopic cantilever beam assembly having individual part dimensions outlined in Table 3.1, and fixed and free-end lengths of 1200mm and 1000mm respectively.  $y/y_0$  represents the ratio of the tip deflection for a given value of  $wL/P$ , which in turn varies from 0.01 to 10, in multiples of 10, to the tip deflection of a single fixed end section cantilever having length  $L$  and uniform second moment of area  $I$ , such that  $y_0$  equals  $(PL^3/3EI)$ .**

**(Key: —  $wL/P=10$ ; —  $wL/P=1$ ; —  $wL/P=0.1$ ; —  $wL/P=0.01$ )**

### 3.7 Virtual Work Principle

The principle of virtual work states that for any compatible virtual displacement field imposed on the body in its state of equilibrium the total internal virtual work is equal to the total external virtual work [6]. The displacement field imposed on the body is called virtual because they need not be obtained by a displacement that actually occurs in the system. The total virtual work is in effect the work done by the virtual displacement field which can be arbitrary provided they are consistent with the constraints of the system.

In the case of the two section telescopic cantilever the total virtual work done is expressed in terms of the parameter  $F^V$  which is a virtual force as shown in Figure 3.11 below. This parameter along with the virtual moment  $M^V$  allows for the subsequent determination of the actual overall displacement of the two section cantilever assembly under the combined action of a tip load and self weight.

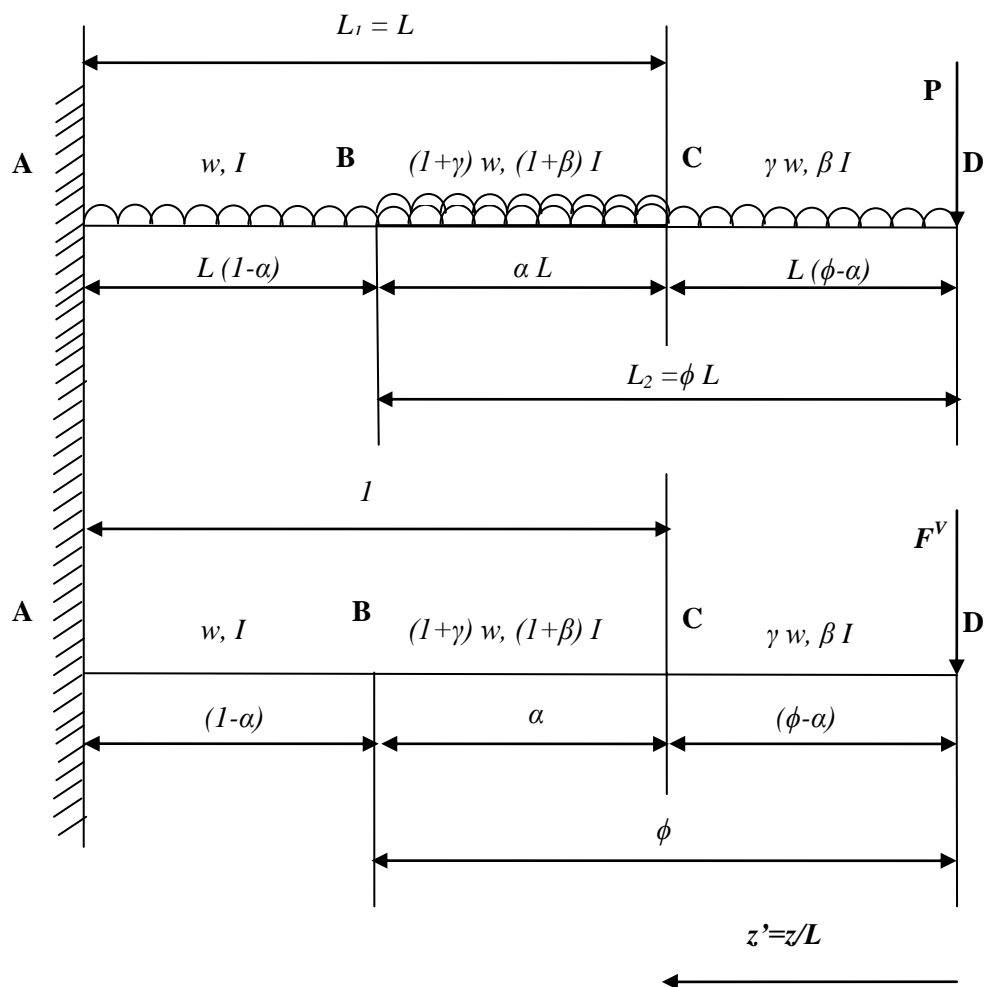


Figure 3.11: Principle of Virtual Work applied to the two section cantilever beam

As detailed in § 2.7.2, when considering the cantilever beam assembly to be in equilibrium and on subjecting it to a virtual displacement field, the internal virtual work induced or the strain energy stored within the assembly must equal the external virtual work. Referring to Figure 3.11, the principle of virtual work can be applied to each of the three sections that make up the composite telescopic cantilever beam assembly in order to give the total virtual work expressed in terms of the product of the virtual force parameter  $F^V$  and the displacement  $y$  as

$$yF^V = \sum \int_z \frac{MM^V}{EI} dz = \int_0^{L(\phi-\alpha)} \frac{M_1 M_1^V}{EI_1} dz + \int_{L(\phi-\alpha)}^{\phi L} \frac{M_2 M_2^V}{EI_2} dz + \int_{\phi L}^{(1+\phi-\alpha)L} \frac{M_3 M_3^V}{EI_3} dz \quad (3.19)$$

Figure 3.11 makes reference to the symbol  $z'$ , where  $z' = \frac{z}{L}$ , this in turn is the basis for the Equation (3.19). The subscripts 1, 2 and 3 represent the free-end, overlap area and the fixed-end respectively. As was the case in Castigliano's theorem, prior to evaluating the integral in Equation (3.19) the bending moments at each of the three sections starting with the free-end to the fixed-end are evaluated and their respective derivatives with respect to the tip load  $P$  are found as shown in Equation sets (3.20)-(3.23) and then substituted in Equation (3.19) as outlined below. Also the virtual moments are evaluated and found to be equal to the product of the virtual force parameter  $F^V$  and the distance  $z$  from the free end.

**Bending Moment for the section  $0 \leq z' \leq (1-\alpha)$**

$$M_1 = \left[ Pz + \gamma w \frac{z^2}{2} \right] = \left[ P \times L \times \left( \frac{z}{L} \right) + \gamma w \times \left( \frac{L^2}{2} \right) \times \left( \frac{z}{L} \right)^2 \right] = \left[ PL(z') + \gamma w \left( \frac{L^2}{2} \right) \times (z')^2 \right] \quad (3.20)$$

**Bending Moment for the section  $(1-\alpha) \leq z' \leq \phi$**

$$\begin{aligned} M_2 &= \left[ Pz + \gamma \phi w \frac{z^2}{2} + \frac{w}{2} \times [z - (\phi - \alpha)L]^2 \right] \\ &= \left[ P \times L \times \left( \frac{z}{L} \right) + \gamma \phi w \times \left( \frac{L^2}{2} \right) \times \left( \frac{z}{L} \right)^2 + \frac{w}{2} \times L^2 \times \left[ \left( \frac{z}{L} \right) - (\phi - \alpha) \right]^2 \right] \\ &= \left[ PLz' + \frac{\gamma \phi w L^2}{2} (z')^2 + \frac{wL^2}{2} [z' - (\phi - \alpha)]^2 \right] \\ M_2 &= \left[ PLz' + \frac{wL^2}{2} (\gamma \phi (z')^2 + [z' - (\phi - \alpha)]^2) \right] \end{aligned} \quad (3.21)$$

**Bending Moment for the section  $\phi \leq z' \leq (1 + \phi - \alpha)$**

$$\begin{aligned}
M_3 &= \left[ Pz + \gamma w \phi L \times \left( z - \frac{\phi L}{2} \right) + \frac{w}{2} \times [z - (\phi - \alpha)L]^2 \right] \\
&= \left[ P \times L \times \left( \frac{z}{L} \right) + \gamma \phi w \times \left( \frac{L^2}{2} \right) \times \left( 2 \frac{z}{L} - \phi \right) + \frac{w}{2} \times L^2 \times \left[ \left( \frac{z}{L} \right) - (\phi - \alpha) \right]^2 \right] \\
&= \left[ PLz' + \gamma \phi w \times \left( \frac{L^2}{2} \right) \times (2z' - \phi) + \frac{w}{2} \times L^2 \times [z' - (\phi - \alpha)]^2 \right] \\
&= \left[ PLz' + \frac{\gamma \phi w L^2}{2} \times (2z' - \phi) + \frac{w L^2}{2} \times [z' - (\phi - \alpha)]^2 \right] \\
M_3 &= \left[ PLz' + \frac{w L^2}{2} (\gamma \phi \times (2z' - \phi) + [z' - (\phi - \alpha)]^2) \right] \tag{3.22}
\end{aligned}$$

$$M_1^V = M_2^V = M_3^V = F^V z = F^V \left( \frac{z}{L} \right) L = F^V Lz' \tag{3.23}$$

Substituting Equation sets (3.20)-(3.23) and  $dz = L \times dz'$  in the Equation (3.19) for  $yF^V$  gives:

$$\begin{aligned}
yF^V &= \frac{1}{EI} \left\{ \frac{1}{\beta} \int_0^{(\phi - \alpha)} \left( PL(z') + \gamma w \left( \frac{L^2}{2} \right) \times (z')^2 \right) \times (F^V Lz') \times Ldz' + \right. \\
&\frac{1}{(1 + \beta)} \int_{\phi - \alpha}^{\phi} \left( PLz' + \frac{w L^2}{2} (\gamma \phi (z')^2 + [z' - (\phi - \alpha)]^2) \right) \times (F^V Lz') \times Ldz' + \\
&\left. \int_{\phi}^{1 + \phi - \alpha} \left( PLz' + \frac{w L^2}{2} (\gamma \phi \times (2z' - \phi) + [z' - (\phi - \alpha)]^2) \right) \times (F^V Lz') \times Ldz' \right\} \\
yF^V &= \frac{1}{EI} \left\{ \frac{F^V}{\beta} \int_0^{(\phi - \alpha)} \left[ PL^3 z'^2 + \gamma w \left( \frac{L^4}{2} \right) \times (z')^3 \right] dz' + \right. \\
&\frac{F^V}{(1 + \beta)} \int_{\phi - \alpha}^{\phi} \left( PL^3 z'^3 + \frac{w L^4}{2} (\gamma \phi (z')^3 + z' \times [z' - (\phi - \alpha)]^2) \right) dz' + \\
&F^V \int_{\phi}^{1 + \phi - \alpha} \left( PL^3 z'^3 + \frac{w L^4}{2} (\gamma \phi z' \times (2z' - \phi) + z' \times [z' - (\phi - \alpha)]^2) \right) dz' \left. \right\}
\end{aligned}$$

Let  $X = \phi - \alpha$  then integrating the terms gives

$$yF^v = \frac{F^v}{EI} \left\{ \frac{1}{\beta} \left( PL^3 \left| \frac{z^{13}}{3} \right|_0^X + \gamma w \left( \frac{L^4}{2} \right) \times \left| \frac{z^{14}}{4} \right|_0^X \right) + \right. \\ \left. \frac{1}{(1+\beta)} \left( PL^3 \left| \frac{z^{13}}{3} \right|_x^\phi + \left( \frac{wL^4}{2} \right) \times \left| (1+\gamma\phi) \frac{z^{14}}{4} - \frac{2Xz^{13}}{3} + \frac{X^2z^{12}}{2} \right|_x^\phi \right) + \right. \\ \left. \left( PL^3 \left| \frac{z^{13}}{3} \right|_\phi^{1+X} + \left( \frac{wL^4}{2} \right) \times \left| \frac{z^{14}}{4} + 2 \times (\gamma\phi - X) \times \frac{z^{13}}{3} + (X^2 - \gamma\phi^2) \times \frac{z^{12}}{2} \right|_\phi^{1+X} \right) \right\}$$

Applying the limits now yields

$$y = \frac{1}{EI} \frac{1}{\beta} \left( PL^3 \times \frac{X^3}{3} + \gamma w \left( \frac{L^4}{2} \right) \times \frac{X^4}{4} \right) + \\ \frac{1}{EI} \frac{1}{(1+\beta)} \left\{ PL^3 \times \left( \frac{\phi^3}{3} - \frac{X^3}{3} \right) + \right. \\ \left. \left( \frac{wL^4}{2} \right) \times \left[ \left( (1+\gamma\phi) \frac{\phi^4}{4} - \frac{2X\phi^3}{3} + \frac{X^2\phi^2}{2} \right) - \left( (1+\gamma\phi) \frac{X^4}{4} - \frac{2X^4}{3} + \frac{X^4}{2} \right) \right] \right\} + \\ \frac{1}{EI} PL^3 \times \left\{ \left( \frac{(1+X)^3}{3} - \frac{\phi^3}{3} \right) + \right. \\ \left. \left( \frac{wL^4}{2} \right) \times \left( \frac{(1+X)^4}{4} + 2 \times (\gamma\phi - X) \times \frac{(1+X)^3}{3} + (X^2 - \gamma\phi^2) \times \frac{(1+X)^2}{2} \right) - \right. \\ \left. \left( \frac{\phi^4}{4} + 2 \times (\gamma\phi - X) \times \frac{\phi^3}{3} + (X^2 - \gamma\phi^2) \times \frac{\phi^2}{2} \right) \right\}$$

$$y = \frac{PL^3}{3EI} \left[ \left( \frac{X^3}{\beta} + \left( \frac{\phi^3 - X^3}{1+\beta} \right) + (1+X)^3 - \phi^3 \right) \right] + \\ \frac{wL^4}{8EI} \left\{ \frac{\gamma}{\beta} X^4 + \left( \frac{1}{1+\beta} \right) \times \left[ \left( (1+\gamma\phi)\phi^4 - \frac{8X\phi^3}{3} + 2X^2\phi^2 \right) - \left( (1+\gamma\phi)X^4 - \frac{8X^4}{3} + 2X^4 \right) \right] + \right. \\ \left. \left( (1+X)^4 + \frac{8 \times (\gamma\phi - X) \times (1+X)^3}{3} + 2 \times (X^2 - \gamma\phi^2) \times (1+X)^2 \right) - \right. \\ \left. \left( \phi^4 + \frac{8 \times (\gamma\phi - X) \times \phi^3}{3} + 2 \times (X^2 - \gamma\phi^2) \times \phi^2 \right) \right\}$$

The final equation can be written as

$$\begin{aligned}
y = & \frac{PL^3}{3EI} \left[ \left( \frac{X^3}{\beta} + \left( \frac{\phi^3 - X^3}{1+\beta} \right) + (1+X)^3 - \phi^3 \right) \right] + \\
& \frac{wL^4}{8EI} \left\{ \frac{\gamma}{\beta} X^4 + \left( \frac{1}{1+\beta} \right) \times \left[ \left( (1+\gamma\phi)\phi^4 - \frac{8X\phi^3}{3} + 2X^2\phi^2 \right) - \left( (1+\gamma\phi)X^4 - \frac{2X^4}{3} \right) \right] + \right. \\
& (1+X)^2 \times \left[ \left( (1+X)^2 + \frac{8 \times (\gamma\phi - X) \times (1+X)}{3} + 2 \times (X^2 - \gamma\phi^2) \right) \right] - \\
& \left. \left( \phi^4 + \frac{8 \times (\gamma\phi - X) \times \phi^3}{3} + 2 \times (X^2 - \gamma\phi^2) \times \phi^2 \right) \right\}
\end{aligned} \tag{3.24}$$

where  $X = \phi - \alpha$

Substituting  $\alpha = 0, \beta = \gamma = \phi = 1$  in Equation (3.24) we get the deflection for an equivalent single section cantilever having length  $2L$  and uniform second moment of area  $I$  under the action of a combined distributed loading and tip load as

$$y = \frac{P(2L)^3}{3EI} + \frac{w(2L)^4}{8EI}$$

Substituting  $\alpha = \phi = 1$  in Equation (3.24) we get the deflection for an equivalent single section cantilever having length  $L$  and uniform second moment of area  $(1+\beta)I$  as

$$y = \left( \frac{1}{1+\beta} \right) \frac{PL^3}{3EI} + \left( \frac{1+\gamma}{1+\beta} \right) \frac{wL^4}{8EI} = \left( \frac{1}{1+\beta} \right) \left[ \frac{PL^3}{3EI} + \frac{(1+\gamma)wL^4}{8EI} \right]$$

Equation (3.24) can be re written as

$$\begin{aligned}
y = & \frac{PL^3}{3EI} \left\{ \left[ \left( \frac{X^3}{\beta} + \left( \frac{\phi^3 - X^3}{1+\beta} \right) + (1+X)^3 - \phi^3 \right) \right] + \right. \\
& \left( \frac{wL^4}{8EI} \times \frac{3EI}{PL^3} \right) \times \left\{ \frac{\gamma}{\beta} X^4 + \left( \frac{1}{1+\beta} \right) \times \left[ \left( (1+\gamma\phi)\phi^4 - \frac{8X\phi^3}{3} + 2X^2\phi^2 \right) - \left( (1+\gamma\phi)X^4 - \frac{2X^4}{3} \right) \right] + \right. \\
& (1+X)^2 \times \left[ \left( (1+X)^2 + \frac{8 \times (\gamma\phi - X) \times (1+X)}{3} + 2 \times (X^2 - \gamma\phi^2) \right) \right] - \\
& \left. \left. \left( \phi^4 + \frac{8 \times (\gamma\phi - X) \times \phi^3}{3} + 2 \times (X^2 - \gamma\phi^2) \times \phi^2 \right) \right] \right\} \\
y = & \frac{PL^3}{3EI} \left\{ \left[ \left( \frac{X^3}{\beta} + \left( \frac{\phi^3 - X^3}{1+\beta} \right) + (1+X)^3 - \phi^3 \right) \right] + \right. \\
& \left( \frac{3}{8} \times \frac{wL}{P} \right) \times \left\{ \frac{\gamma}{\beta} X^4 + \left( \frac{1}{1+\beta} \right) \times \left[ \left( (1+\gamma\phi)\phi^4 - \frac{8X\phi^3}{3} + 2X^2\phi^2 \right) - \left( (1+\gamma\phi)X^4 - \frac{2X^4}{3} \right) \right] + \right. \\
& (1+X)^2 \times \left[ \left( (1+X)^2 + \frac{8 \times (\gamma\phi - X) \times (1+X)}{3} + 2 \times (X^2 - \gamma\phi^2) \right) \right] - \\
& \left. \left. \left( \phi^4 + \frac{8 \times (\gamma\phi - X) \times \phi^3}{3} + 2 \times (X^2 - \gamma\phi^2) \times \phi^2 \right) \right] \right\}
\end{aligned} \tag{3.25}$$

Again the term  $y_0 = \frac{PL^3}{3EI}$  for reasons as mentioned in §3.5.3. Equation (3.25) is written in its

entirety as

$$\begin{aligned} \frac{y}{y_0} = & \left[ \left( \frac{(\phi - \alpha)^3}{\beta} + \left( \frac{\phi^3 - (\phi - \alpha)^3}{1 + \beta} \right) + (1 + (\phi - \alpha))^3 - \phi^3 \right) \right] + \\ & \left( \frac{3}{8} \times \frac{wL}{P} \right) \times \left\{ \frac{\gamma}{\beta} (\phi - \alpha)^4 + \left( \frac{1}{1 + \beta} \right) \times \left[ \left( (1 + \gamma\phi)\phi^4 - \frac{8(\phi - \alpha)\phi^3}{3} + 2(\phi - \alpha)^2\phi^2 \right) - \right. \right. \\ & \left. \left( (1 + \gamma\phi)(\phi - \alpha)^4 - \frac{2(\phi - \alpha)^4}{3} \right) \right] + (1 + (\phi - \alpha))^2 \times \left[ (1 + (\phi - \alpha))^2 + \frac{8 \times (\gamma\phi - (\phi - \alpha)) \times (1 + (\phi - \alpha))}{3} + \right. \\ & \left. \left. 2 \times ((\phi - \alpha)^2 - \gamma\phi^2) \right] - \left( \phi^4 + \frac{8 \times (\gamma\phi - (\phi - \alpha)) \times \phi^3}{3} + 2 \times ((\phi - \alpha)^2 - \gamma\phi^2) \times \phi^2 \right) \right\} \end{aligned} \quad (3.26)$$

Once again the curves in Figure 3.12 represent the plots of the non dimensional parameter

$\frac{y}{y_0}$  against the overlap ratio parameter  $\alpha$ , for  $\frac{wL}{P}$  ratios 0.01, 0.1, 1 and 10, calculated using

the Virtual Work Method. As before, the values of the constant parameters  $\phi$ ,  $\beta$  and  $\gamma$  are taken as 0.833, 0.49 and 0.642, respectively and substituted into Equation (3.18), while varying the overlap ratio  $\alpha$  from 0 to 1 in increments of 0.1.

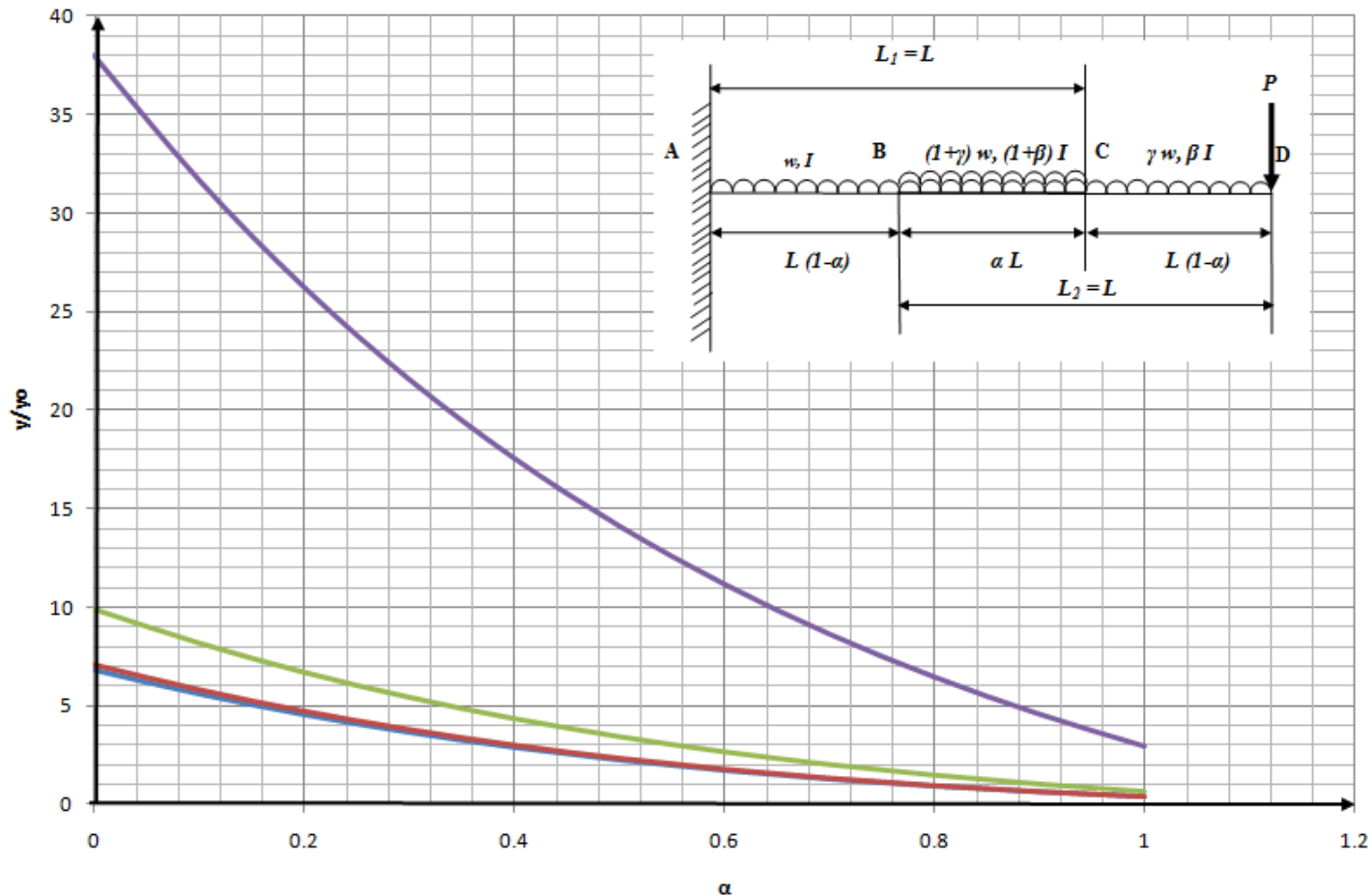


Figure 3.12: Deflection Plot of Equation (3.26) obtained from Virtual Work Theorem vs. Parameter  $\alpha$ , for the two section telescopic cantilever beam assembly having individual part dimensions outlined in Table 3.1, and fixed and free-end lengths of 1200mm and 1000mm respectively.  $y/y_0$  represents the ratio of the tip deflection for a given value of  $wL/P$ , which in turn varies from 0.01 to 10, in multiples of 10, to the tip deflection of a single fixed end section cantilever having length  $L$  and uniform second moment of area  $I$ , such that  $y_0$  equals  $(PL^3/3EI)$ .

(Key: —  $wL/P=10$ ; —  $wL/P=1$ ; —  $wL/P=0.1$ ; —  $wL/P=0.01$ )

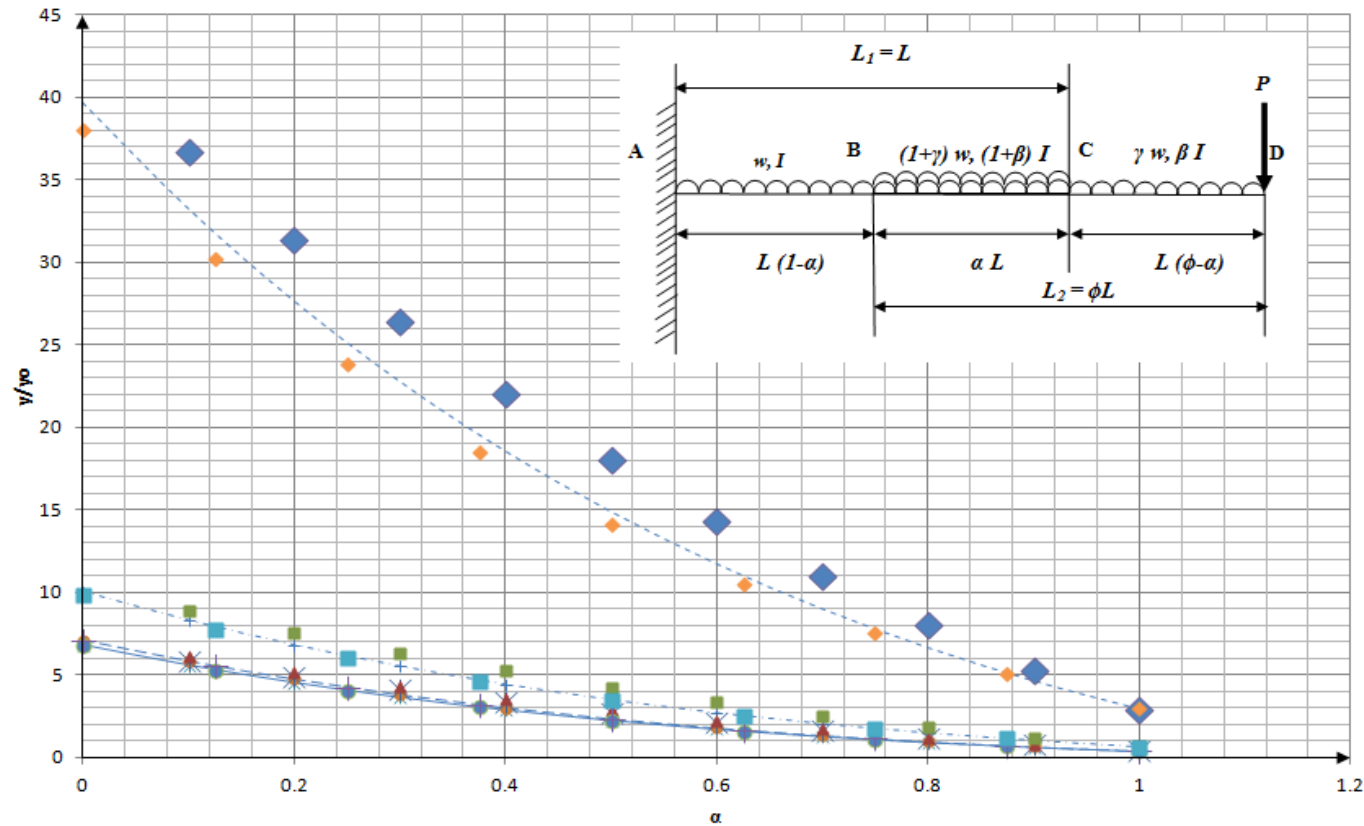
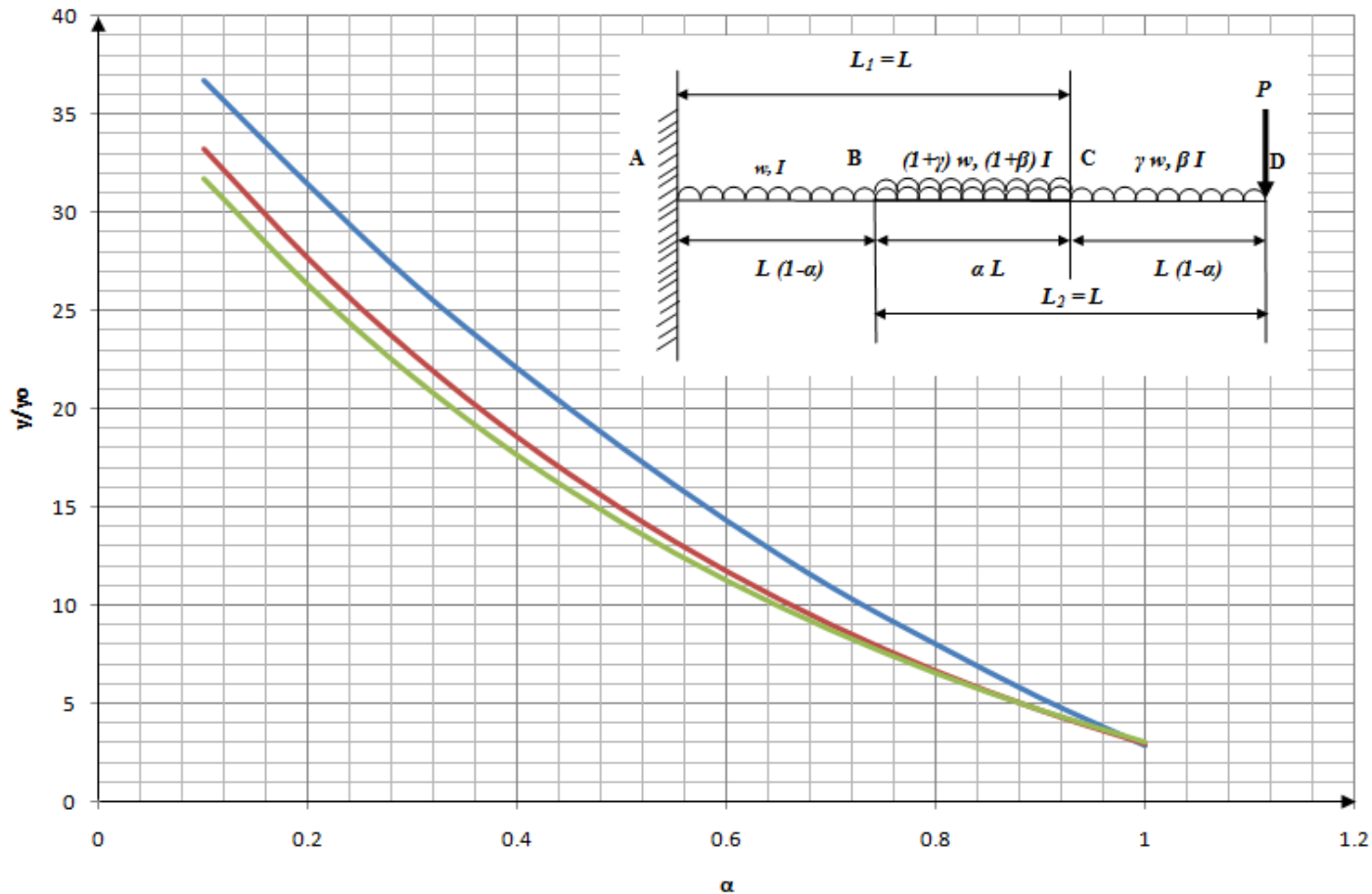


Figure 3.13: Theoretical End Deflection Plots vs. Parameter  $\alpha$ , for the two section telescopic cantilever beam assembly having individual part dimensions outlined in Table 3.1, and fixed and free-end lengths of 1200mm and 1000mm respectively.  $v/y_0$  represents the ratio of the tip deflection for a given value of  $wL/P$ , which in turn varies from 0.01 to 10, in multiples of 10, to the tip deflection of a single fixed end section cantilever having length  $L$  and uniform second moment of area  $I$ , such that  $y_0$  equals  $(PL^3/3EI)$ .

$(wL/P=10$ : ◆ Macaulay's Theorem; ..... Mohr's Method; ◆ Castigliano's Theorem and Virtual Work Method  
 $wL/P=1$ : ■ Macaulay's Theorem; -.-.- Mohr's Method; ■ Castigliano's Theorem and Virtual Work Method  
 $wL/P=0.1$ : ▲ Macaulay's Theorem; - - - Mohr's Method; + Castigliano's Theorem and Virtual Work Method  
 $wL/P=0.01$ : \* Macaulay's Theorem; — Mohr's Method; ● Castigliano's Theorem and Virtual Work Method)



**Figure 3.13 (a): Theoretical End Deflection Plots vs. Parameter  $\alpha$ , for the two section telescopic cantilever beam assembly having individual part dimensions outlined in Table 3.1, and fixed and free-end lengths of 1200mm and 1000mm respectively for a  $wL/P$  ratio of 10.  $y/y_0$  represents the ratio of the tip deflection for a  $wL/P$  ratio of 10, to the tip deflection of a single fixed end section cantilever having length  $L$  and uniform second moment of area  $I$ , such that  $y_0$  equals  $(PL^3/3EI)$ .**

**(Key:  $wL/P=10$ : — Macaulay's Theorem; — Mohr's Method; — Castigliano's Theorem and Virtual Work Method)**

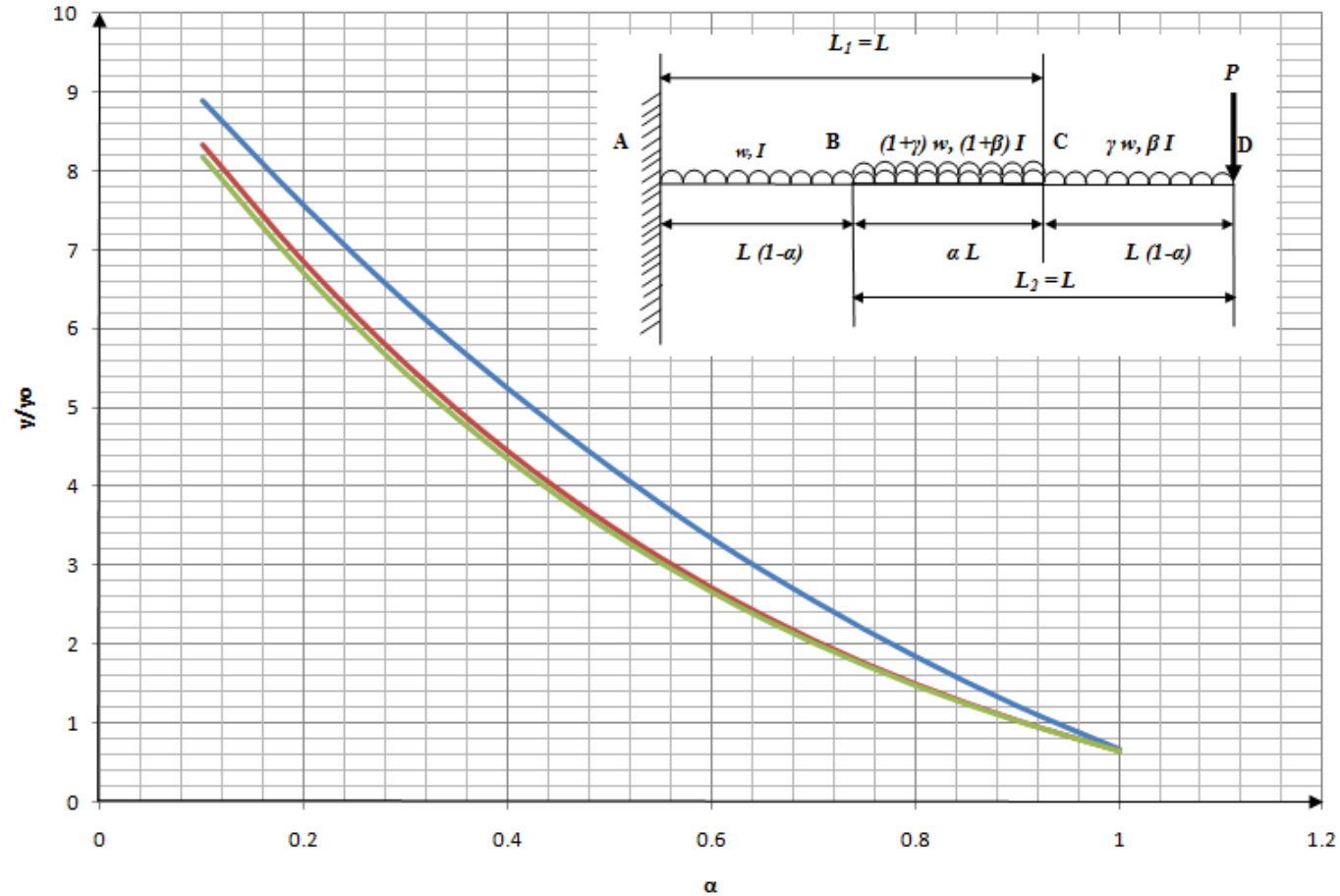


**Figure 3.13 (b): Theoretical End Deflection Plots vs. Parameter  $\alpha$ , for the two section telescopic cantilever beam assembly having individual part dimensions outlined in Table 3.1, and fixed and free-end lengths of 1200mm and 1000mm respectively for a  $wL/P$  ratio of 1.  $y/y_0$  represents the ratio of the tip deflection for a  $wL/P$  ratio of 1, to the tip deflection of a single fixed end section cantilever having length  $L$  and uniform second moment of area  $I$ , such that  $y_0$  equals  $(PL^3/3EI)$ .**

**(Key:  $wL/P=1$ : — Macaulay's Theorem; — Mohr's Method; — Castigliano's Theorem and Virtual Work Method)**

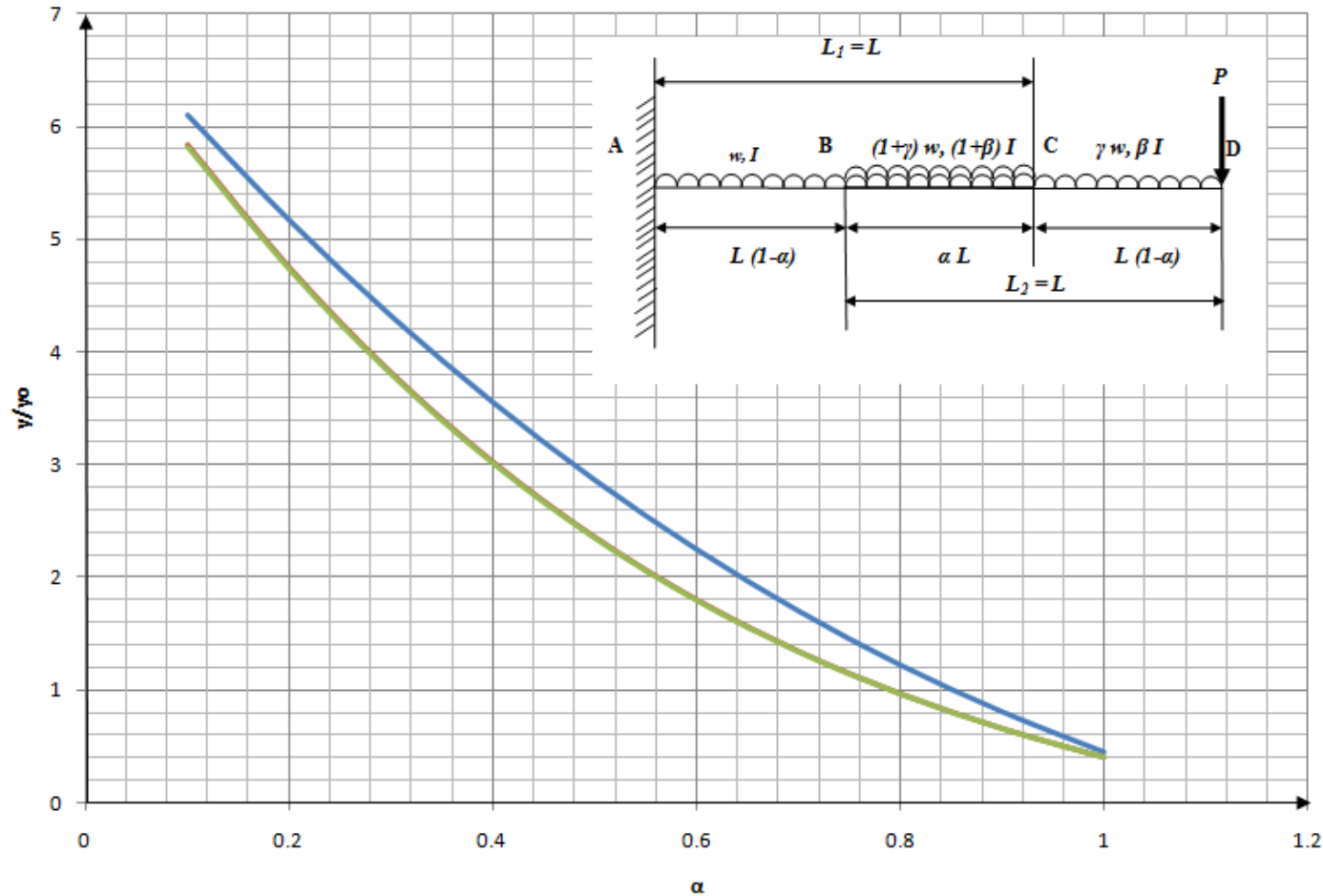
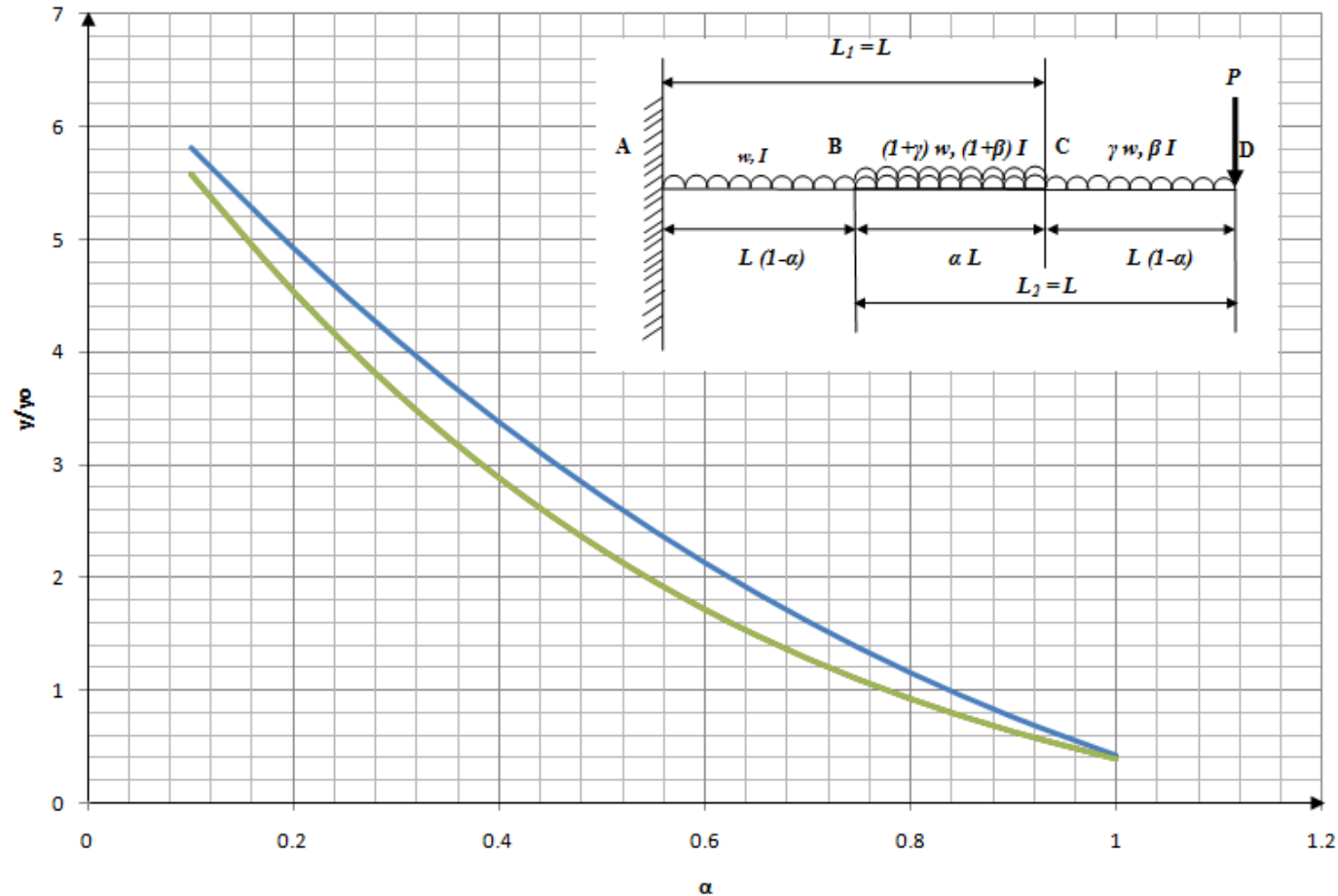


Figure 3.13 (c): Theoretical End Deflection Plots vs. Parameter  $\alpha$ , for the two section telescopic cantilever beam assembly having individual part dimensions outlined in Table 3.1, and fixed and free-end lengths of 1200mm and 1000mm respectively for a  $wL/P$  ratio of 0.1.  $y/y_0$  represents the ratio of the tip deflection for a  $wL/P$  ratio of 0.1, to the tip deflection of a single fixed end section cantilever having length  $L$  and uniform second moment of area  $I$ , such that  $y_0$  equals  $(PL^3/3EI)$ .

(Key:  $wL/P=0.1$ : — Macaulay's Theorem; — Mohr's Method; — Castigliano's Theorem and Virtual Work Method)



**Figure 3.13 (d): Theoretical End Deflection Plots vs. Parameter  $\alpha$ , for the two section telescopic cantilever beam assembly having individual part dimensions outlined in Table 3.1, and fixed and free-end lengths of 1200mm and 1000mm respectively for a  $wL/P$  ratio of 0.01.  $y/y_0$  represents the ratio of the tip deflection for a  $wL/P$  ratio of 0.01, to the tip deflection of a single fixed end section cantilever having length  $L$  and uniform second moment of area  $I$ , such that  $y_0$  equals  $(PL^3/3EI)$ .**

**(Key:  $wL/P=0.01$ : — Macaulay's Theorem; — Mohr's Method; — Castigliano's Theorem and Virtual Work Method)**

### 3.8 Summary

The two section telescopic cantilever beam assembly has been subjected to deflection analyses using the four common deflection prediction techniques which have each been tailored to suit the unique nature of the structure. This has been done using a combination of ratios as outlined in Table 3.1. The curves displayed in Figures 3.2, 3.7, 3.10 and 3.12 represent the deflection curves, produced as a result of subjecting the two section telescopic cantilever beam assembly, to a combination of both tip loading and the action of its own weight, using Macaulay's theorem, Mohr's Moment Area Method, Castigliano's Theorem and the Virtual Work Principle, respectively. It can be seen that the curves generated using Castigliano's Theorem and the Virtual Work Principle are exactly the same. It must be remembered that the four deflection prediction techniques have been applied to the candidate telescopic assembly having dimensions specified in Table 3.1, for fixed and free-end lengths of 1200 mm and 1000 mm respectively. The reason for this was simply to see how and what effect varying lengths of the individual sections would have on the overall deflection curves thus generated by the analyses. The deflection curves produced for the candidate assembly, using the four methods, are compared in Figure 3.13. The following are some of the observations that can be made from Figure 3.13:

1. The curves generated using Castigliano's theorem and the Virtual Work method are one and the same.
2. For lower  $\frac{wL}{P}$  ratios, the curves generated by Mohr's, Castigliano's and the Virtual Work methods, are inseparable as can be evidenced from Figures 3.13 (b) – (d), with the exception of the curves obtained from the Macaulay's theorem analyses. However for a  $\frac{wL}{P}$  ratio of 10, the deflection curves are spread apart, revealing a clear difference as shown in Figure 3.13 (a). The Macaulay's theorem generated curve has a greater magnitude as compared to the other deflection prediction curves, followed by Mohr's theorem and finally both, Castigliano's and the Virtual Work method.
3. The deflection curve generated from Macaulay's theorem, starts not at  $\alpha=0$ , unlike the other curves, but at  $\alpha=0.1$ . This is a consequence of the numerical implementation

scheme adopted i.e. the tip reaction model which was adapted into an equivalent ‘C’ program.

4. Irrespective of which method was used to plot a given curve, for any  $\frac{wL}{P}$  ratio, all the curves meet at the same point, which coincides to the condition  $\alpha=1$ .
5. The difference between Macaulay’s theorem and the three other methods could be explained as being due to the reliance of the former on the tip reactions calculated for the varying overlap lengths, of which the latter three in turn are independent. Of greater interest arguably, is the difference between the deflection curves obtained from Mohr’s method and those generated from both Castigliano’s and the Virtual Work Method. The deflection magnitudes derived using Castigliano’s method and the Virtual Work method are the same. This is because the equations used to generate the respective curves are the same as is evident from Equations (3.18) and (3.26). Comparing either of these equations mentioned with Equation (3.11) derived using Mohr’s method reveals a significant difference in the second term which accounts for the uniformly distributed loading or self weight of the two section telescoping assembly. This difference in the case of the Mohr’s method analysis is in part due to the changing moments of areas that are taken into consideration when computing the deflection as elaborated in §3.5.2 and shown diagrammatically in Figure 3.6.

The curves generated in Figures 3.13 and separately in Figures 3.13(a)-(d) are explained in more detail in §9.1.1. The final objective of this chapter was to derive from first principles, deflection equations that would predict the in-line deflection induced in the two section telescopic cantilever beam assembly effectively, for any applied load. Not only do these equations predict the deflections, they also take into account all the possible variable factors of the structure. Also desired was a means of displaying the deflection curves, such that a particular configuration of the two section telescoping assembly can be selected, to serve a given function, provided the required data is available. Last but certainly not least, the equations used to generate the deflection curves, are applied to the actual test rig, whose dimensions are outlined in Table 8.1, and then compared, with the experimental and FEA extracted data, for the same.

## CHAPTER 4: BUCKLING ANALYSIS

### 4.1 Introduction

In the two section telescoping cantilever buckling occurs in two parts (a) local buckling produced within the individual rectangular hollow sections and (b) global buckling wherein the structure in its entirety undergoes buckling. To establish a sense of order in this thesis, global buckling phenomena of the telescoping assembly is first scrutinised here, followed by local buckling in the individual rectangular hollow sections in the following chapter. The critical buckling load is a function of the section dimensions, namely: (a) the effective length of the column structure; whether it is the length of the individual sections, or, that of the assembly and (b) the boundary conditions. In both cases the member(s) are examined as cantilever-columns, in that one end is fixed and the other is free. This is due to the fact that the applications of the telescoping assembly relate to this boundary condition. Another point of importance is the overlap where the free end or male section fits snugly within the fixed end or female member. This overlap region is of great importance, as the theory developed in this chapter, has to account for this discontinuity. It was determined that to account for this overlap region, it should be treated as a separate section to the free-end and fixed-end sections. In order to do so, it is vital to take into consideration the ‘beefing up’ or bolstering of the second area moments in this region as being a summation of the moments of the female and male members of the telescoping assembly. In order to arrive at the critical buckling load for the assembly it was imperative to understand the concepts of bending strain energy and total potential energy systems. It was deemed appropriate to start at the simplest approximation to a single rectangular hollow section by firstly considering tapering sections.

By working from first principles a better understanding of the complexity of the problem was attained. This involved a detailed understanding and application of energy methods to the case at hand. The principles used are outlined in § 2.7. In particular, the Rayleigh quotient derived in § 2.11, and referred to by Timoshenko as the energy method [15], was used as a basis and applied in the analysis of the cantilever column in § 4.4 and in subsequent critical buckling load determinations for the sections thereafter. This approach in turn was verified by validating the result obtained against the criteria for the Euler critical buckling load for a column having one end fixed and the other free as the boundary conditions. A general form for predicting the critical buckling load exactly is thus derived and is applied to suit each case individually taking into account the different cross sectional second moments and lengths.

## 4.2 Determining the section parameters of the tapered column

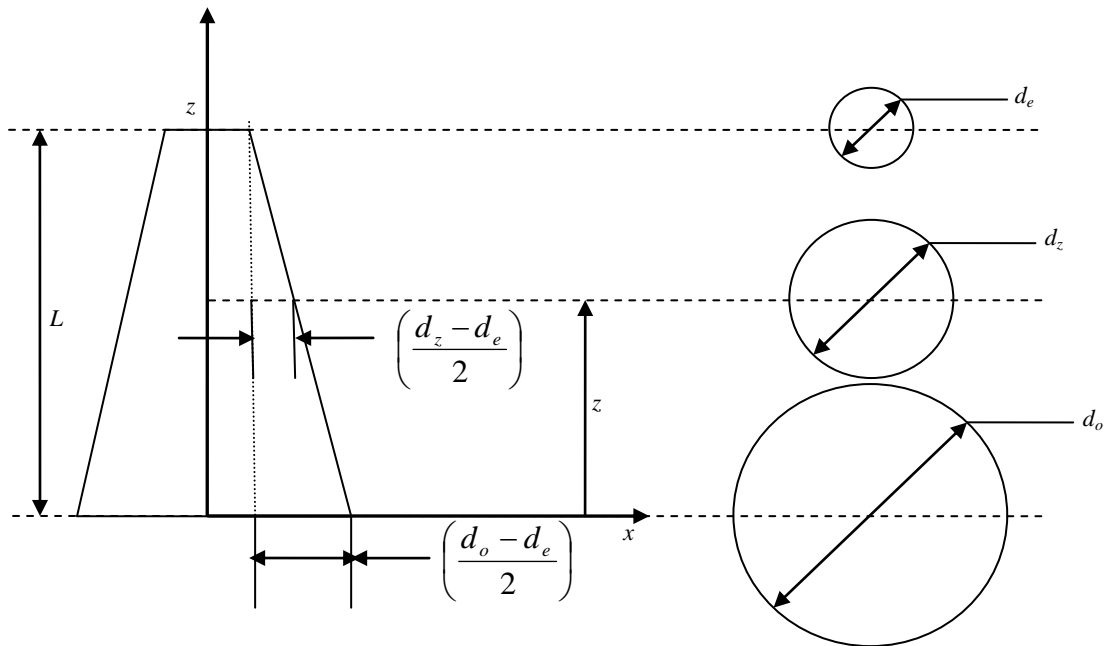


**Figure 4.1: Geometry of the tapered circular cantilever column**

Referring to Figure 4.1, the diameter ' $d_z$ ' at the arbitrarily chosen depth of ' $z$ ' from the free end can be expressed as follows using the principles of similar right angled triangles

$$\frac{d_z - d_e}{2(L - z)} = \frac{d_o - d_e}{2L}$$

$$d_z = d_e + \left(1 - \frac{z}{L}\right)(d_o - d_e)$$

$$d_z = d_o \left[ \frac{d_e}{d_o} + \left(1 - \frac{z}{L}\right) \left(1 - \frac{d_e}{d_o}\right) \right] \quad (4.1)$$

Knowing the expression for diameter at the depth ' $z$ ' from Equation (4.1) and once again referring to Figure 4.1, the second moment area at a length of  $z$ , along the length of the tapered circular cantilever column can be expressed as follows

$$I_z = \frac{\pi d_z^4}{64} = \frac{\pi}{64} \left[ d_e + \left(1 - \frac{z}{L}\right) (d_o - d_e) \right]^4 = \frac{\pi d_e^4}{64} \left[ 1 + \left[1 - \frac{z}{L}\right] \left[ \left(\frac{d_o}{d_e}\right) - 1 \right] \right]^4$$

$$I_z = I_e \times \left[ 1 + \left[1 - \frac{z}{L}\right] \left[ \left(\frac{d_o}{d_e}\right) - 1 \right] \right]^4 \quad (4.2)$$

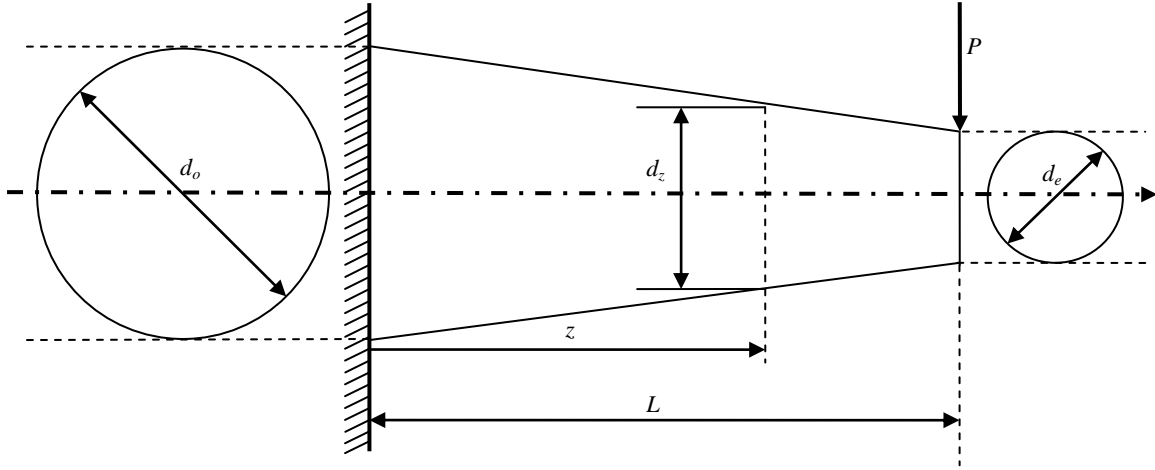


**Figure 4.2: Geometry of the tapered circular cantilever column**

$$\sigma = \frac{My}{I} = \frac{[P(L-z)] \frac{d_z}{2}}{\frac{\pi d_z^4}{64}} = \frac{32P(L-z)}{\pi d_z^3} \quad (4.3)$$

Substituting Equation (4.1) in Equation (4.3) we get

$$\sigma = \frac{32P(L-z)}{\pi \left[ d_o \left[ \frac{d_e}{d_o} + \left(1 - \frac{z}{L}\right) \left(1 - \frac{d_e}{d_o}\right) \right] \right]^3} = \frac{32P(L-z)}{\pi d_o^3 \left[ \frac{d_e}{d_o} + \left(1 - \frac{z}{L}\right) \left(1 - \frac{d_e}{d_o}\right) \right]^3} \quad (4.4)$$

Equation (4.4) can also be written as

$$\sigma = \frac{32P \times L \times \left(1 - \frac{z}{L}\right)}{\pi d_o^3 \left[ \frac{d_e}{d_o} + \left(1 - \frac{z}{L}\right) \left(1 - \frac{d_e}{d_o}\right) \right]^3} \quad (4.5)$$

Equation (4.5) has a maximum value which is determined later within in this section.

Comparing Equation (4.3) and Equation (4.5) we see that  $\sigma_o = \frac{32PL}{\pi d_o^3}$ . Let  $z' = \frac{z}{L}$ , then

differentiating Equation (4.5) with respect to  $z'$  gives

$$\sigma = \frac{\sigma_o(1-z')}{\left[\frac{d_e}{d_o} + (1-z')\left(1 - \frac{d_e}{d_o}\right)\right]^3}$$

$$\frac{d\sigma}{dz'} = \frac{-\left[\frac{d_e}{d_o} + (1-z')\left(1 - \frac{d_e}{d_o}\right)\right]^3 \times \sigma_o + \sigma_o(1-z') \times 3\left[\frac{d_e}{d_o} + (1-z')\left(1 - \frac{d_e}{d_o}\right)\right]^2 \times \left(1 - \frac{d_e}{d_o}\right)}{\left[\frac{d_e}{d_o} + (1-z')\left(1 - \frac{d_e}{d_o}\right)\right]^3}$$

Equating the differentiated quantity to zero gives

$$-\left[\frac{d_e}{d_o} + (1-z')\left(1 - \frac{d_e}{d_o}\right)\right]^3 \times \sigma_o + \sigma_o(1-z') \times 3\left[\frac{d_e}{d_o} + (1-z')\left(1 - \frac{d_e}{d_o}\right)\right]^2 \times \left(1 - \frac{d_e}{d_o}\right) = 0$$

$$\left[\frac{d_e}{d_o} + (1-z')\left(1 - \frac{d_e}{d_o}\right)\right]^2 \times \left\{-\sigma_o \times \left[\frac{d_e}{d_o} + (1-z')\left(1 - \frac{d_e}{d_o}\right)\right] + 3\sigma_o(1-z') \times \left(1 - \frac{d_e}{d_o}\right)\right\} = 0 \quad (4.6)$$

Equation (4.6) gives two quantities that can be equated to zero:

Either  $\left[\frac{d_e}{d_o} + (1-z')\left(1 - \frac{d_e}{d_o}\right)\right]^2 = 0$  which gives a negative  $z'$  and is of no consequence to the

analysis at hand

$$\text{Or } \left\{-\sigma_o \times \left[\frac{d_e}{d_o} + (1-z')\left(1 - \frac{d_e}{d_o}\right)\right] + 3\sigma_o(1-z') \times \left(1 - \frac{d_e}{d_o}\right)\right\} = 0$$

Solving the above expression gives

$$-\left[\frac{d_e}{d_o} + (1-z')\left(1 - \frac{d_e}{d_o}\right)\right] + 3(1-z')\left(1 - \frac{d_e}{d_o}\right) = 0$$

$$z' = \frac{3 \frac{d_e}{d_o} - 1}{2 \left( \frac{d_e}{d_o} - 1 \right)} \quad (4.7)$$

Figure 4.3 graphically expresses the relationship between  $\frac{d_e}{d_o}$  and  $z'$ , in Equation (4.7). The curve represents the relationship between  $\frac{d_e}{d_o}$  and  $z'$ , when  $d_e < d_o$ , for values of  $\frac{d_e}{d_o}$  varying from 0.1 to 0.6 in increments of 0.1.

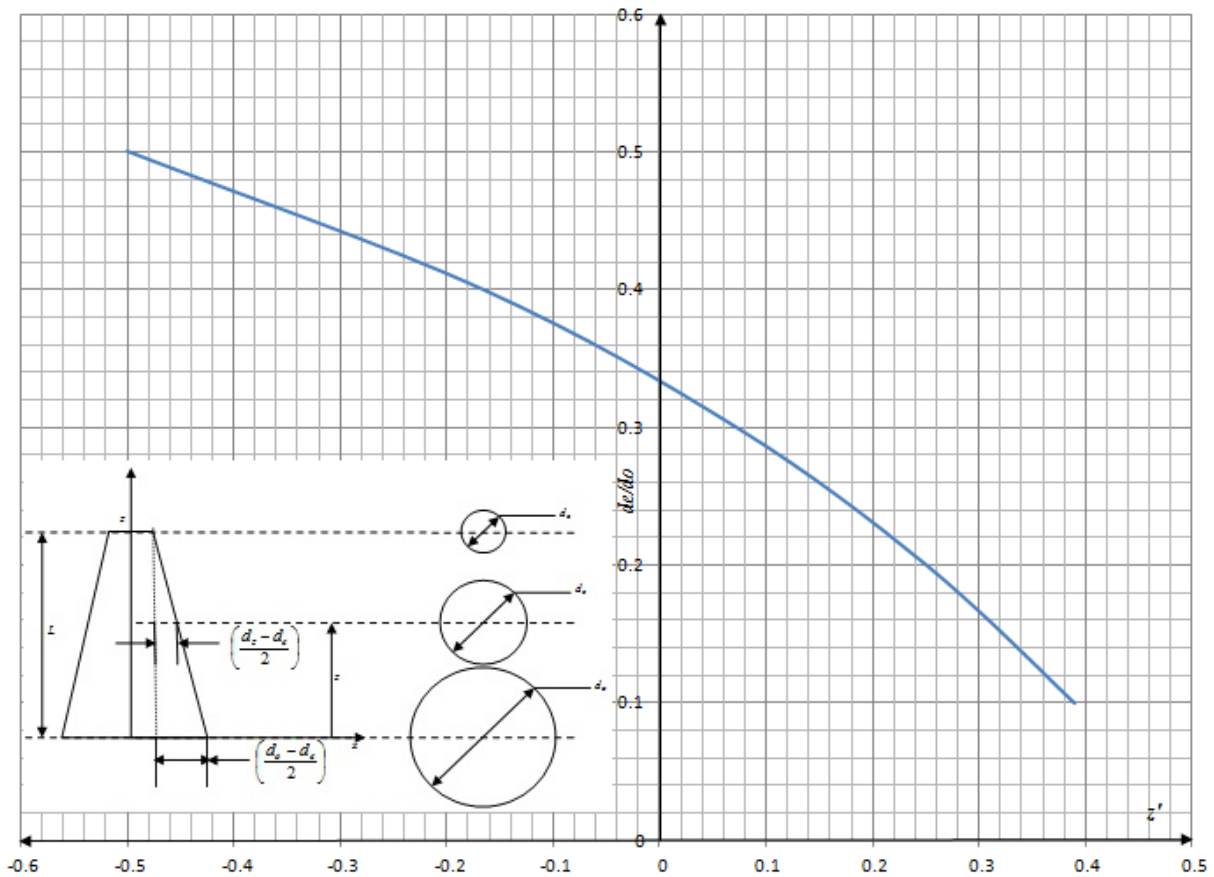


**Figure 4.3: Plot of  $\frac{d_e}{d_o}$  against  $z'$  from Equation (4.7), for the tapered circular cantilever column**

The maximum bending stress in the tapered circular column can be found by substituting Equation (4.7) in Equation (4.5) as follows

$$\sigma = \frac{32P \times L \times \left[ 1 - \frac{3 \frac{d_e}{d_o} - 1}{2 \left( \frac{d_e}{d_o} - 1 \right)} \right] \sigma_o \times \left[ 1 - \frac{3 \frac{d_e}{d_o} - 1}{2 \left( \frac{d_e}{d_o} - 1 \right)} \right]}{\pi d_o^3 \left[ \frac{d_e}{d_o} + \left[ 1 - \frac{3 \frac{d_e}{d_o} - 1}{2 \left( \frac{d_e}{d_o} - 1 \right)} \right] \times \left( 1 - \frac{d_e}{d_o} \right) \right]^3} = \frac{\sigma_o \times \left[ 1 - \frac{3 \frac{d_e}{d_o} - 1}{2 \left( \frac{d_e}{d_o} - 1 \right)} \right]}{\left[ \frac{d_e}{d_o} + \left[ 1 - \frac{3 \frac{d_e}{d_o} - 1}{2 \left( \frac{d_e}{d_o} - 1 \right)} \right] \times \left( 1 - \frac{d_e}{d_o} \right) \right]^3} \quad (4.8)$$

Figure (4.4) represents the relationship between  $\frac{\sigma}{\sigma_o}$  against  $z'$ , with the curve plotting the relationship for the condition  $d_e < d_o$  for values of  $\frac{d_e}{d_o}$  varying from 0.1 to 0.6 in increments of 0.1.

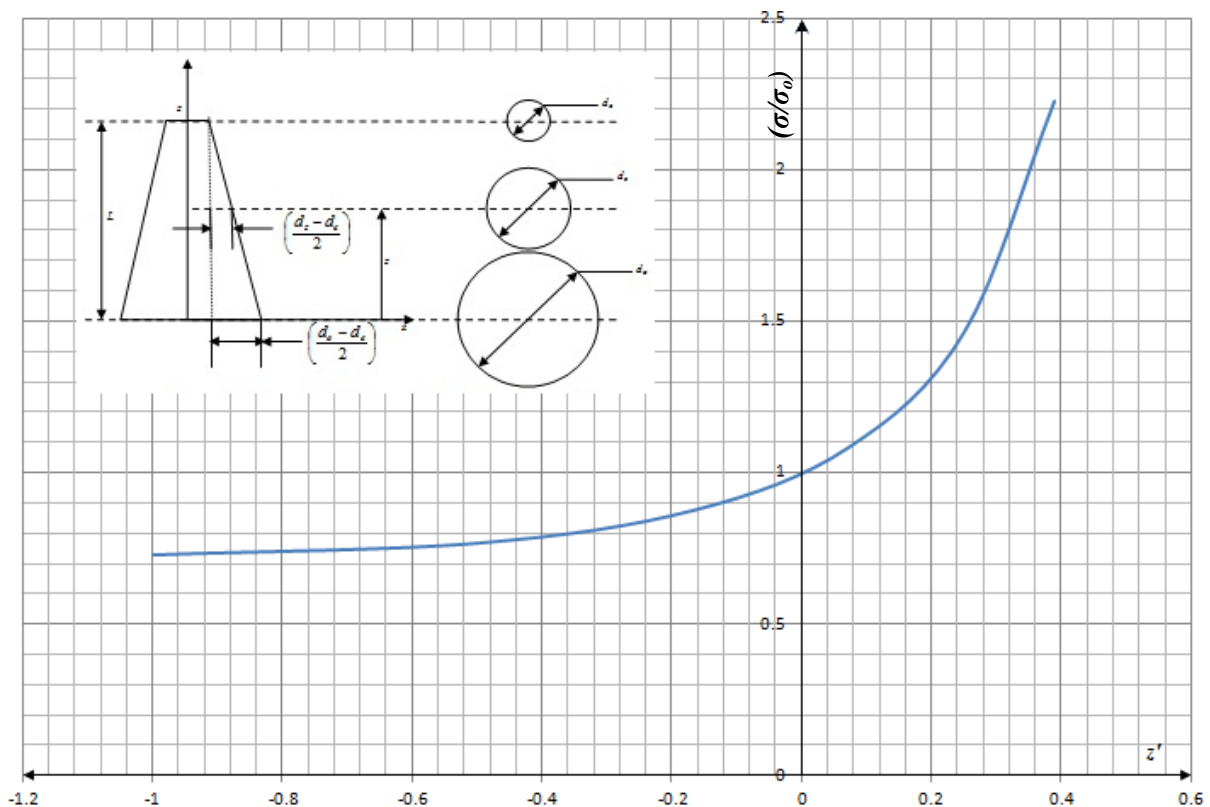


**Figure 4.4: Plot of  $\frac{\sigma}{\sigma_o}$  against  $z'$  from Equation (4.8), for the tapered circular cantilever column**

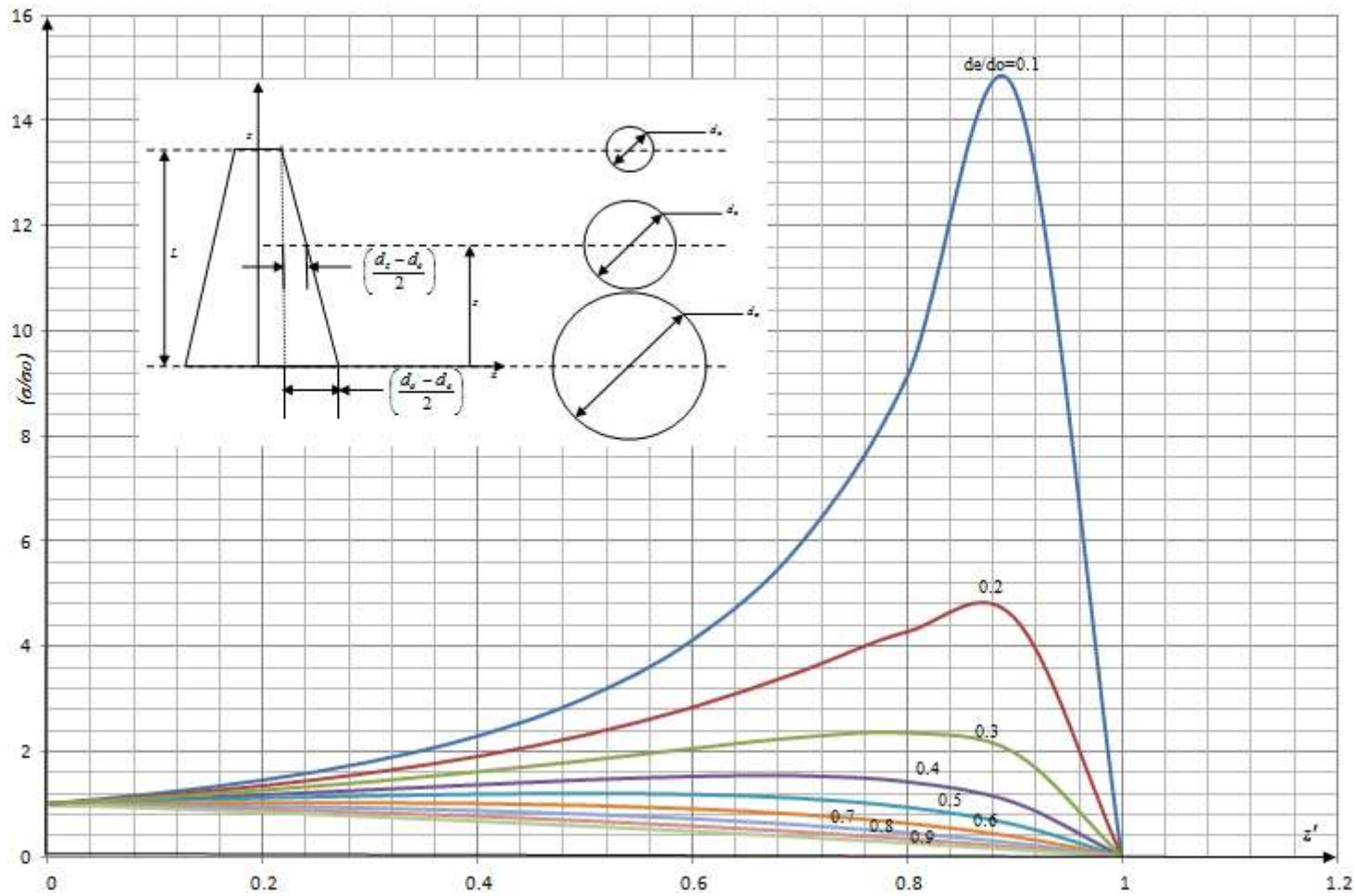
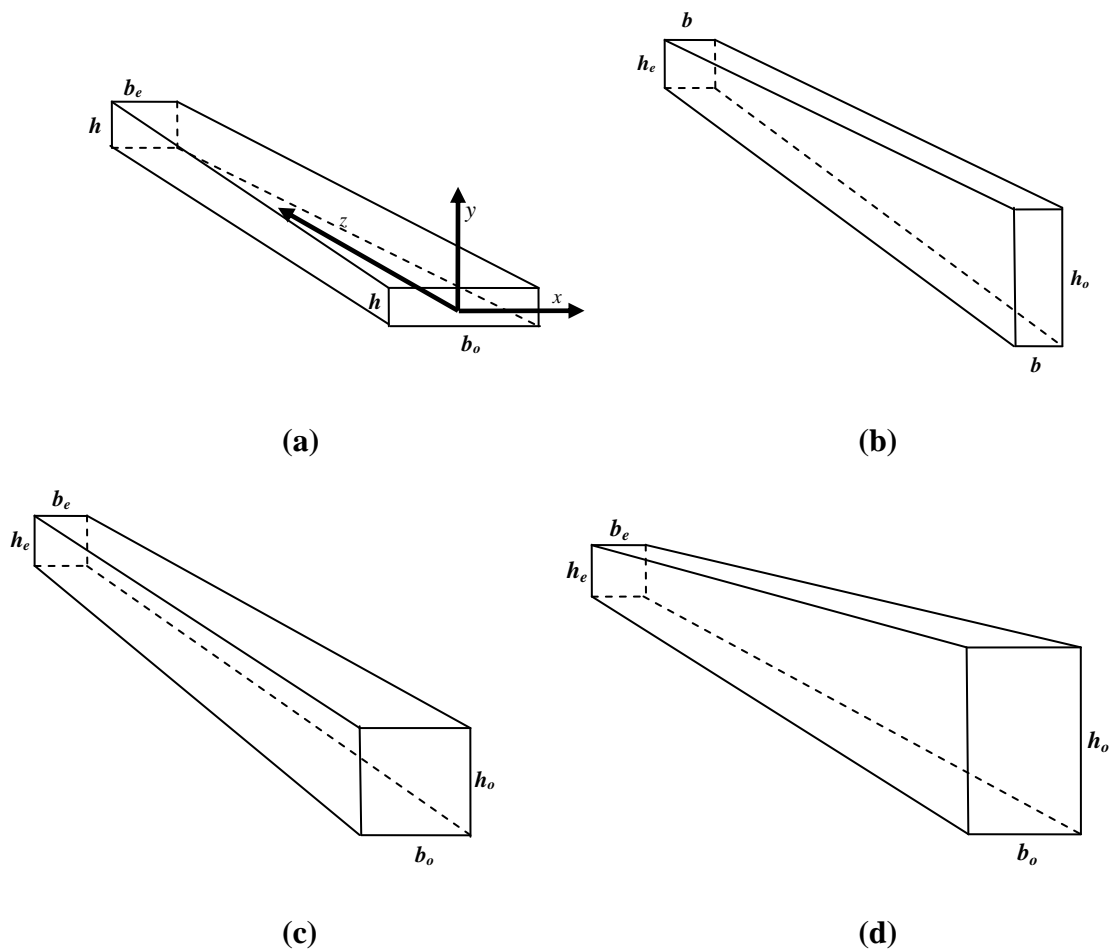


Figure 4.5: Plot of  $\frac{\sigma}{\sigma_0}$  (obtained from Equation (4.5)) against  $z'$ , where  $z'$  varies from 0 to 1, in increments of 0.1, for the tapered circular cantilever column. The curves in turn represent the values of  $\frac{d_e}{d_o}$  varying from 0.1 to 0.9, once again in increments of 0.1.

### 4.3 Section Properties of Tapered Beams

It is assumed that the sections at the two ends of a beam are the same in the shape and different in size. The size of the section changes linearly with respect to the beam centre of geometry line. Figure 4.6 shows four tapering types for a linearly tapered beam: (a) the width (horizontal dimension) changes only; (b) the height (vertical dimension) changes only; (c) both dimensions change at the same rate; (d) the two dimensions change at different rates. The different tapering types can be categorised based on the characteristics of the algebra of the changing section properties.



**Figure 4.6: Section Properties of Tapered Beams (a) Section changing breadth; (b) Section changing depth; (c) Section changing bi-dimensionally at the same rate; (4) Section changing bi-dimensionally at different rates (Adapted from [93])**

It should be noted that the tapering type does not necessarily correspond to the tapering category, since a tapering type may result in different property changes for different section

shapes. The sections are assumed to be axisymmetric. The shape functions are derived in two dimensions. It can also easily be expanded into three dimensions.

### 4.3.1 Section changing breadth

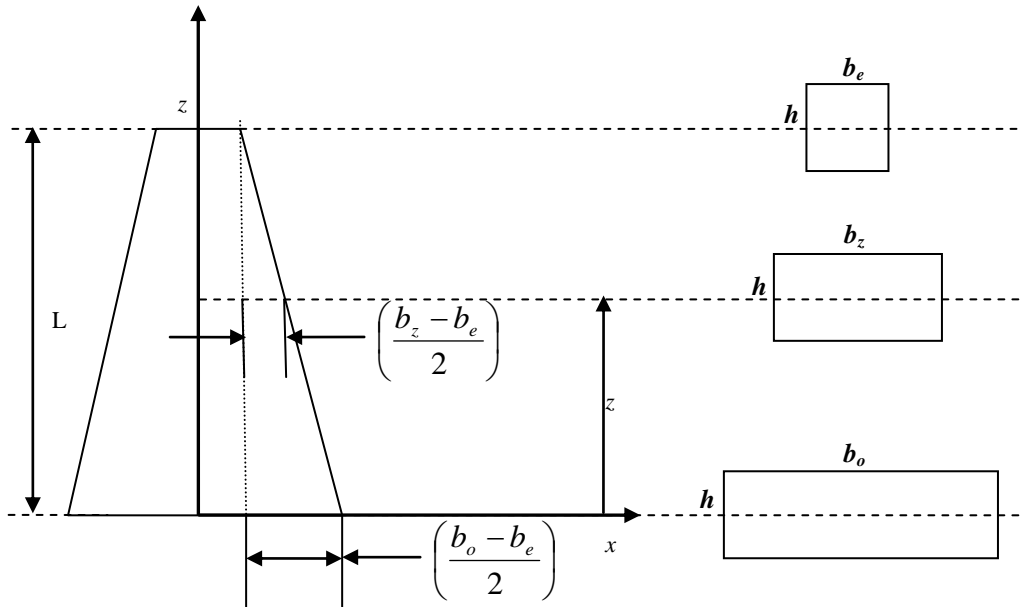


**Figure 4.7: Geometry of the tapered rectangular cantilever column whose cross section changes in breadth**

Referring to Figure 4.7, the breadth/width (horizontal dimension) ‘ $b_z$ ’, at an arbitrarily chosen depth of ‘ $z$ ’ from the free end can be expressed as follows using the principle of similar right angled triangles

$$\frac{b_z - b_e}{2(L - z)} = \frac{b_o - b_e}{2L}$$

$$b_z = b_e + \left(1 - \frac{z}{L}\right)(b_o - b_e) \quad (4.9)$$

Knowing the expression for the breadth/width (horizontal dimension) at an arbitrarily chosen depth of ‘ $z$ ’ from the free end as obtained from Equation (4.9) and once again referring to

Figure 4.8, the second moment area at a length of  $z$ , along the length of the tapered rectangular cantilever column from the free end can be expressed as follows

$$I_z = \frac{b_z h^3}{12} = \frac{h^3}{12} \left[ b_e + \left(1 - \frac{z}{L}\right)(b_o - b_e) \right] = \frac{b_e h^3}{12} \left[ 1 + \left[1 - \frac{z}{L}\right] \left[ \left(\frac{b_o}{b_e}\right) - 1 \right] \right] = I_e \left[ 1 + \left[1 - \frac{z}{L}\right] \left[ \left(\frac{b_o}{b_e}\right) - 1 \right] \right] \quad (4.10)$$

### 4.3.2 Section changing depth

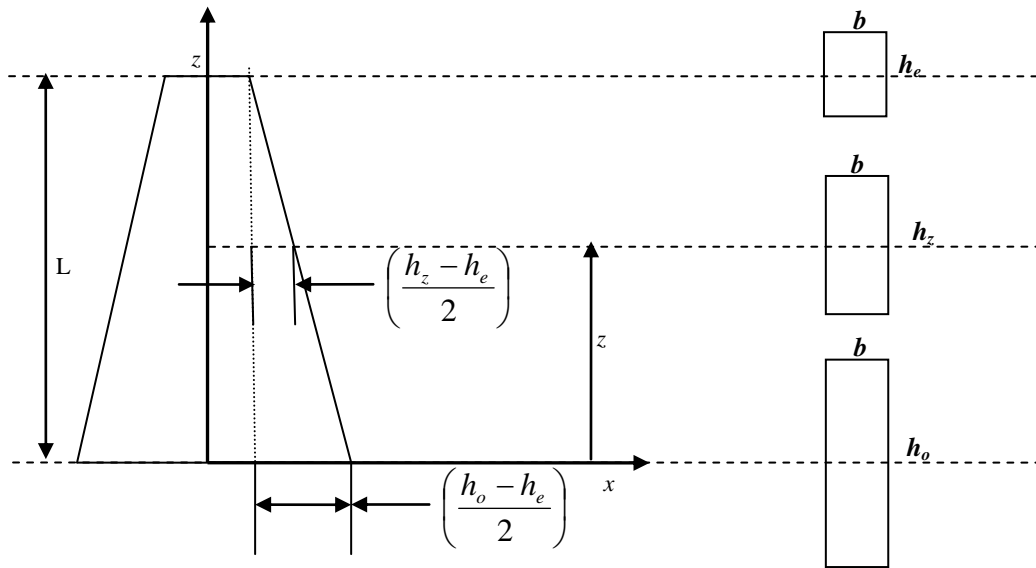


**Figure 4.8: Geometry of the tapered rectangular cantilever column whose cross section changes in depth**

Referring to Figure 4.8, the height/depth (vertical dimension) ' $h_z$ ' an arbitrarily chosen depth of ' $z$ ' from the free end can be expressed as follows using the principle of similar right angled triangles

$$\frac{h_z - h_e}{2(L - z)} = \frac{h_o - h_e}{2L}$$

$$h_z = h_e + \left(1 - \frac{z}{L}\right)(h_o - h_e) \quad (4.11)$$

Knowing the expression for the height/depth (vertical dimension) at an arbitrarily chosen depth of ' $z$ ' from the free end as obtained from Equation (4.11) and once again referring to Figure

4.8, the second moment area at a length of  $z$ , along the length of the tapered rectangular cantilever column from the free end can be expressed as follows

$$I_z = \frac{bh_z^3}{12} = \frac{b}{12} \left[ h_e + \left(1 - \frac{z}{L}\right)(h_o - h_e) \right]^3 = \frac{bh_e^3}{12} \left[ 1 + \left[1 - \frac{z}{L}\right] \left[ \left(\frac{h_o}{h_e}\right) - 1 \right] \right]^3 = I_e \left[ 1 + \left[1 - \frac{z}{L}\right] \left[ \left(\frac{h_o}{h_e}\right) - 1 \right] \right]^3 \quad (4.12)$$

### 4.3.3 Section changing bi-dimensionally at the same and at different rates

From Equations (4.9) and (4.11) the variation in width and depth can be shown to be

$$b_z = b_e + \left(1 - \frac{z}{L}\right)(b_o - b_e)$$

$$h_z = h_e + \left(1 - \frac{z}{L}\right)(h_o - h_e)$$

Referring to § 4.3.1 and 4.3.2 as well as Figures 4.6(c) and 4.6(d) it is not difficult to ascertain that the second moment area can be expressed as

$$I_z = \frac{b_z h_z^3}{12} = \frac{1}{12} \times \left[ b_e + \left(1 - \frac{z}{L}\right)(b_o - b_e) \right] \times \left[ h_e + \left(1 - \frac{z}{L}\right)(h_o - h_e) \right]^3$$

$$I_z = \frac{b_e h_e^3}{12} \times \left[ 1 + \left[1 - \frac{z}{L}\right] \left[ \left(\frac{b_o}{b_e}\right) - 1 \right] \right] \times \left[ 1 + \left[1 - \frac{z}{L}\right] \left[ \left(\frac{h_o}{h_e}\right) - 1 \right] \right]^3$$

$$I_z = I_e \times \left[ 1 + \left[1 - \frac{z}{L}\right] \left[ \left(\frac{b_o}{b_e}\right) - 1 \right] \right] \times \left[ 1 + \left[1 - \frac{z}{L}\right] \left[ \left(\frac{h_o}{h_e}\right) - 1 \right] \right]^3 \quad (4.13)$$

#### 4.4 The Cantilever Column

The following section makes use of what was referred to by Timoshenko as the energy method, which provides a shortcut to obtaining approximate values for the critical load [15]. It avoids solving differential equations and becomes very useful when applied to systems with non uniform stiffness, a case where the solution to the usual Eigen-boundary-value problem is extremely difficult and in some cases impossible.

Consider the cantilever shown in Figure 4.9 below under a constant directional thrust  $P$  applied quasistatically. As the load is increased from zero, the work done by the force  $P$  is stored into the system as stretching strain energy. On allowing a small bending formation  $Y(z)$ , that does not alter the aforementioned stretching strain energy, the change in the total potential energy  $\Delta U_T$  is given by

$$\Delta U_T = \Delta U_B + \Delta U_P \quad (4.14)$$

where  $\Delta U_B$  is the bending strain energy and  $\Delta U_P$  is the change in the potential of the external force or the work done by the load  $P$  on the cantilever column.

$$\Delta U_B = \frac{1}{2} \int_0^L EI (Y')^2 dx \quad (4.15)$$

$$\Delta U_P = -P\lambda = -\frac{1}{2} P \int_0^L (Y')^2 dx \quad (4.16)$$

According to Timoshenko's argument, the configuration is in stable equilibrium when  $\Delta U_T = 0$ . In addition it is required to assume a form for the admissible bending deformation,  $Y(z)$ . Let

$$Y(z) = \delta \left( 1 - \cos \frac{\pi z}{2L} \right) \quad (4.17)$$

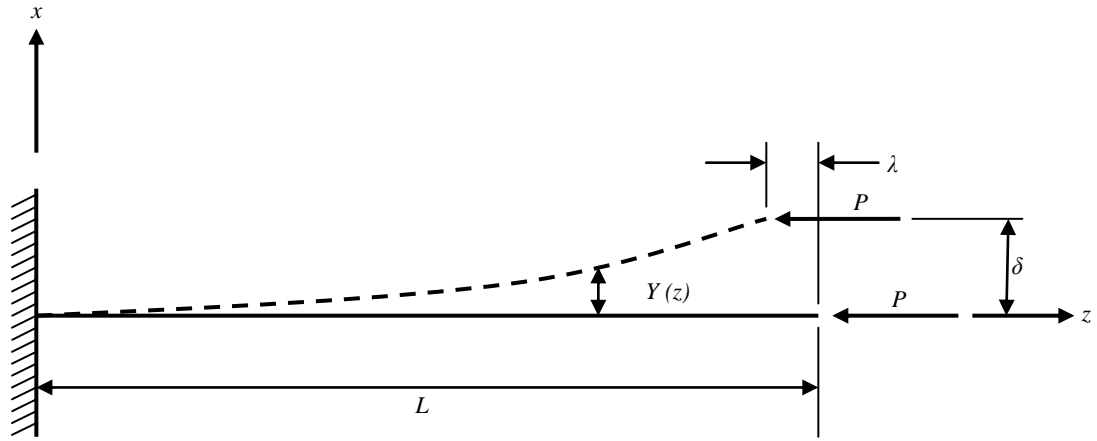


**Figure 4.9: Geometry of the cantilever column (Adapted from [15])**

where the right hand side term  $\left(1 - \cos \frac{\pi z}{2L}\right)$  satisfies the kinematic boundary conditions at  $x=0$ .

Solving Equations (4.15) and (4.16), for the bending strain energy and the work done on the column by the load, respectively, we get

$$\Delta U_B = \frac{\pi^4 EI \delta^2}{64L^3} \quad (4.18)$$

$$\Delta U_P = -P \frac{\pi^2 \delta^2}{16L} \quad (4.19)$$

Equating Equations (4.18) and (4.19) we obtain the expression for critical buckling load as

$$P_{cr} = \frac{\pi^2 EI}{4L^2}$$

which is the exact solution because the deformation function happens to be the exact Eigen function.

#### 4.5 Determination of the Buckling Load for an Axially Symmetric Truncated Cone

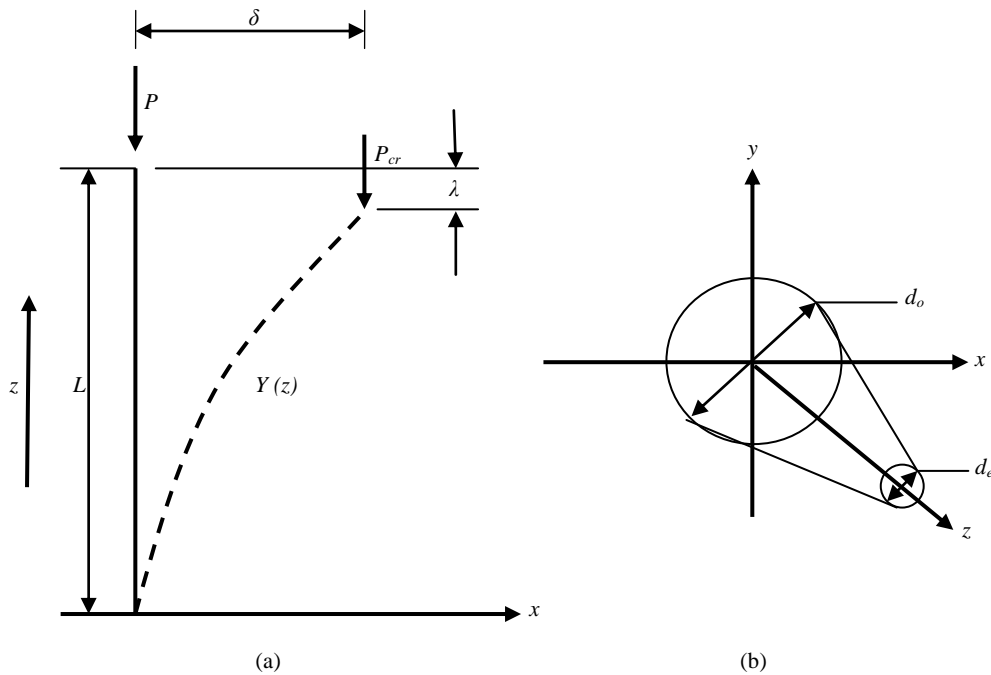


**Figure 4.10: (a) A fixed-free column subjected to a tip load (b) Cross sections of an axially symmetric truncated cone (Adapted from [94])**

The analyses that follow make use of the derivations outlined in the previous section. The variables used have been altered. Referring to Figure 4.10(a), a fixed-free column is subjected to a tip load having cross section as shown in Figure 4.10(b).  $\Delta U_B$  is the bending strain energy and  $\Delta U_P$  is the change in the potential of the external force or the work done by the load  $P$  on the tapered cantilever column.

Once again the change in the total potential energy  $\Delta U_T$  is given by

$$\Delta U_T = \Delta U_B + \Delta U_P$$

Taking  $\Delta U_T = 0$  as per the argument made in § 4.4 we get

$$\Delta U_B = -\Delta U_P \tag{4.20}$$

where  $\Delta U_B$  is the bending strain energy and this time  $\Delta U_P$  is the work done by the load  $P$  on the truncated cone. It is important to note that the displacement function  $Y(z)$  used here is an approximation and does not represent the exact displacement configuration. Hence the solution obtained as a result is approximate.

$$\Delta U_B = \int_0^L \frac{(M(z))^2}{2EI_z} dz \quad (4.21)$$

$$\Delta U_P = -P\lambda = -\frac{1}{2}P \int_0^L \left[ \frac{dY(z)}{dz} \right]^2 dz \quad (4.22)$$

The vertical movement of the load  $P$  during buckling is found from [32].

$$\lambda = \frac{1}{2} \int_0^L \left[ \frac{dY(z)}{dz} \right]^2 dz$$

Once again as in § 4.4 we make use of an assumed deflected shape that accounts for first mode buckling and satisfies the boundary conditions for a fixed-free column, such that

$$Y(z) = \delta \left( 1 - \cos \frac{\pi z}{2L} \right) \quad (4.23)$$

where  $Y=0$  at  $z=0$  and  $y=\delta$  at  $z=L$ .

Predicting the load which will cause the column to buckle is done either by numerical or finite element techniques. An exact method is to solve the differential equation

$$EI_z \times \frac{d^2Y(z)}{dz^2} + M(z) = 0, \quad (4.24)$$

with appropriate boundary conditions for the ends. Now substituting

$$M(z) = -EI_z \times \frac{d^2Y(z)}{dz^2} \quad (4.25)$$

in Equation (4.21) and using Equation (4.22) yields

$$\Delta U_B = \frac{\delta^2 E \pi^4}{32L^4} \int_0^L I_z \cos^2\left(\frac{\pi z}{2L}\right) dz \quad (4.26)$$

The critical buckling condition occurs when Equation (4.20) is satisfied and this yields the general formula for the critical buckling load as

$$P_{cr} = \frac{\pi^2 E}{2L^3} \int_0^L I_z \cos^2\left(\frac{\pi z}{2L}\right) dz \quad (4.27)$$

Using Equation (4.2) and substituting in Equation (4.27) gives

$$P_{cr} = \frac{\pi^2 E}{2L^3} \int_0^L \left\{ (I_e) \times \left[ 1 + \left[ 1 - \frac{z}{L} \right] \left[ \left( \frac{d_o}{d_e} \right) - 1 \right] \right]^4 \right\} \cos^2\left(\frac{\pi z}{2L}\right) dz \quad (4.28)$$

$$P_{cr} = \frac{\pi^2 EI_e}{2L^3} \int_0^L \left\{ \left[ 1 + \left[ 1 - \frac{z}{L} \right] \left[ \left( \frac{d_o}{d_e} \right) - 1 \right] \right]^4 \right\} \cos^2\left(\frac{\pi z}{2L}\right) dz \quad (4.29)$$

To evaluate the integral in Equation (4.29) above it is assumed that  $z' = \frac{z}{L}$  and  $\mu = \left[ \left( \frac{d_o}{d_e} \right) - 1 \right]$ .

Substituting these parameters gives

$$P_{cr} = \frac{\pi^2 EI_e}{2L^3} \times L \times \int_0^1 [1 + \mu(1 - z')]^4 \times \cos^2\left(\frac{\pi z'}{2}\right) dz'$$

$$P_{cr} = \frac{\pi^2 EI_e}{2L^2} \times \int_0^1 [1 + \mu(1 - z')]^4 \times \left[ \frac{1}{2} + \frac{1}{2} \cos(\pi z') \right] dz'$$

$$P_{cr} = \frac{\pi^2 EI_e}{4L^2} \times \int_0^1 [1 + \mu(1 - z')]^4 \times [1 + \cos(\pi z')] dz' \quad (4.30)$$

In Equation (4.30) above it can be seen that the term  $\frac{\pi^2 EI_e}{4L^2}$  represents the Euler Critical Buckling Load for a fixed-free column and so is represented as  $P_{Eu}$ . The quantity  $\frac{P_{cr}}{P_{Eu}}$  thus obtained is a non dimensional parameter that allows for ease of plotting in terms of the variable quantity  $\left(\frac{d_o}{d_e}\right)$ .

$$\frac{P_{cr}}{P_{Eu}} = \int_0^1 [1 + \mu(1 - z')]^4 \times [1 + \cos(\pi z')] dz'$$

Now integrating we get the solution as

$$\frac{P_{cr}}{P_{Eu}} = \frac{\mu^4(\pi^4 + 20\pi^2 - 120) + 5\mu^3(\pi^4 + 12\pi^2 - 48) + 10\pi^2\mu^2(\pi^2 + 6) + 10\pi^2\mu(\pi^2 + 4) + 5\pi^4}{5\pi^4} \quad (4.31)$$

where  $\mu = \left[ \left( \frac{d_o}{d_e} \right) - 1 \right]$ .

If  $d_o = d_z = d_e$  then the ratio  $\left(\frac{d_o}{d_e}\right) = 1$ , which corresponds to a uniform non-tapering section then

Equation (4.31) would give  $P_{cr} = P_{Eu} = \frac{\pi^2 EI_e}{4L^2}$  where  $\frac{\pi^2 EI_e}{4L^2}$  is the Critical Euler Buckling load for a column with one end fixed and one end free.

Figure 4.11 represents the plot of  $\frac{P_{cr}}{P_{Eu}}$  derived in Equation (4.31), for an axially symmetric

truncated cone against the non dimensional parameter  $\left(\frac{d_o}{d_e}\right)$  which varies from 1 to 5 in increments of 0.25. The objective of plotting such a curve is to present a means to ascertain the critical buckling load of an axially symmetric, truncated cone by making use of its dimensions  $d_o$  and  $d_e$  as well as the magnitude of the load applied  $P$  at its end. The dimensions  $d_o$  and  $d_e$  indicate the diameters of the base and end of the truncated cone respectively, as shown in Figure 4.10 (b). The curve reveals that the greater the value of  $d_o$  as compared to  $d_e$ , the greater

is the critical buckling load that the structure can withstand. Note that  $P_{Eu}$  is the critical buckling load for a uniform section of diameter  $d_e$  having one end fixed and the other end free.

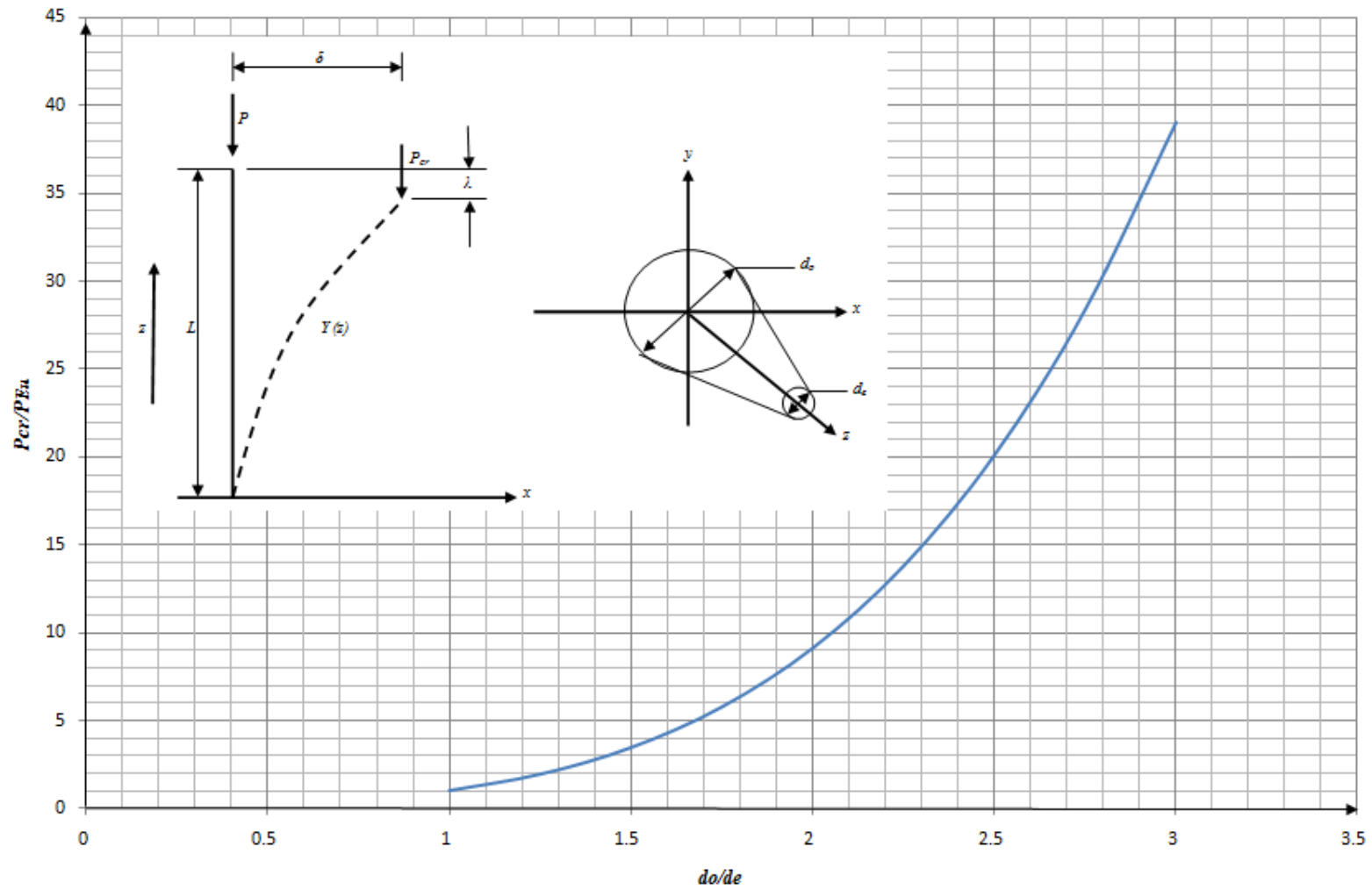
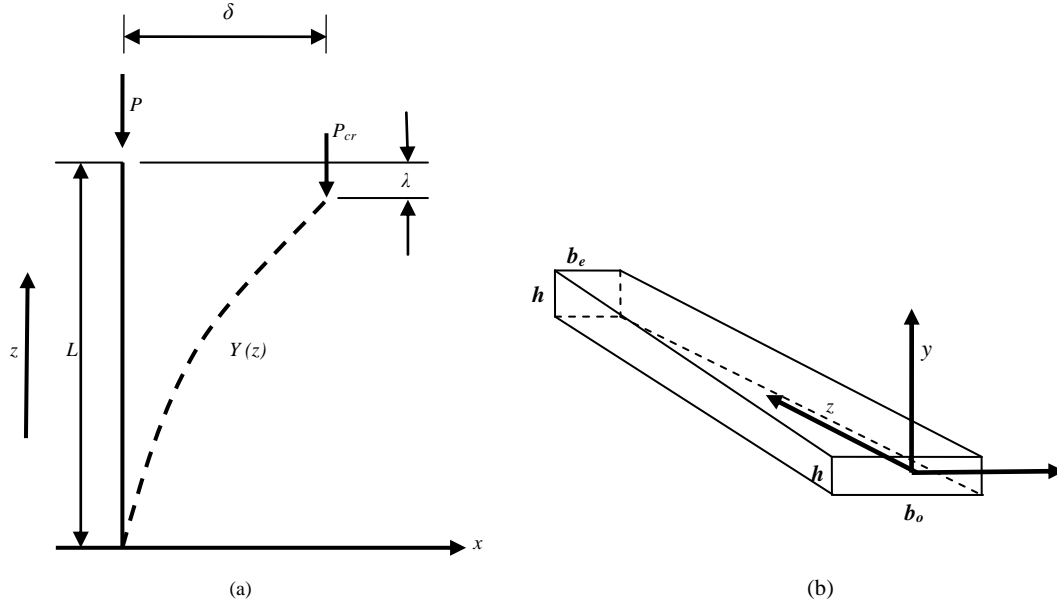


Figure 4.11: Plot of Equation (4.31) vs.  $\left(\frac{d_o}{d_e}\right)$ , for the axially symmetric, truncated cone

## 4.6 Determination of the Buckling Load for the Pyramid

### 4.6.1 Buckling Load for the Rectangular Pyramid whose sections' breadth changes



**Figure 4.12: (a) A fixed-free column subjected to a tip load (b) Cross sections of columns for a rectangular pyramid whose sections' breadth changes**

Referring to Figure 4.12(a), a fixed-free column is subjected to a tip load having cross section changing as shown in Figure 4.12(b).

Knowing that the critical buckling condition occurs when Equation (4.20) is satisfied, this yields the general formula for the critical buckling load as

$$P_{cr} = \frac{\pi^2 E}{2L^3} \int_0^L I_z \cos^2\left(\frac{\pi z}{2L}\right) dz \quad (4.32)$$

Using Equation (4.10) and substituting in Equation (4.32) gives

$$\begin{aligned} P_{cr} &= \frac{\pi^2 E}{2L^3} \int_0^L \left\{ \frac{b_e h^3}{12} \left[ 1 + \left[ 1 - \frac{z}{L} \right] \left[ \left( \frac{b_o}{b_e} \right) - 1 \right] \right] \right\} \cos^2\left(\frac{\pi z}{2L}\right) dz \\ &= \left( \frac{\pi^2 E}{2L^3} \times \frac{b_e h^3}{12} \right) \times \left\{ \int_0^L \cos^2\left(\frac{\pi z}{2L}\right) dz + \int_0^L \left[ \left[ 1 - \frac{z}{L} \right] \left[ \left( \frac{b_o}{b_e} \right) - 1 \right] \right] \times \cos^2\left(\frac{\pi z}{2L}\right) dz \right\} \end{aligned} \quad (4.33)$$

Integrating the Equation (4.33) yields

$$P_{cr} = \frac{\pi^2 EI_e}{4L^2} \times \left[ 1 + \frac{1}{2} \left( \left( \frac{b_o}{b_e} \right) - 1 \right) + \left( \frac{2}{\pi^2} \right) \left( \left( \frac{b_o}{b_e} \right) - 1 \right) \right] \quad (4.34)$$

In Equation (4.34) above it can be seen that the term  $\frac{\pi^2 EI_e}{4L^2}$  represents the Euler Critical

Buckling Load for a fixed-free column and so is represented as  $P_{Eu}$ . The quantity  $\frac{P_{cr}}{P_{Eu}}$  thus

obtained is a non dimensional parameter that allows for ease of plotting in terms of the variable

quantity  $\left( \frac{b_o}{b_e} \right)$ . If  $b_o = b_z = b_e$  then the ratio  $\left( \frac{b_o}{b_e} \right) = 1$ , which corresponds to a uniform non-tapering

section then Equation (4.34) would give  $P_{cr} = P_{Eu} = \frac{\pi^2 EI_e}{4L^2}$  where  $\frac{\pi^2 EI_e}{4L^2}$  is the Critical Euler

Buckling load for a column with one end fixed and one end free. Figure 4.13 graphically

represents the plot of  $\frac{P_{cr}}{P_{Eu}}$  derived in Equation (4.34), for the square pyramid whose breadth

changes while its depth remains constant, against the non dimensional parameter  $\left( \frac{b_o}{b_e} \right)$  which

varies from 1 to 10 in increments of 1. The objective of plotting such a curve is to enable a

designer a way to determine the critical buckling load of this structure by making use of its

dimensions  $b_o$  and  $b_e$  as well as the magnitude of the load applied  $P$  at its end. The dimensions

$b_o$  and  $b_e$  indicate the breadth dimensions of the base and end of the pyramid, as shown in

Figure 4.12 (b).

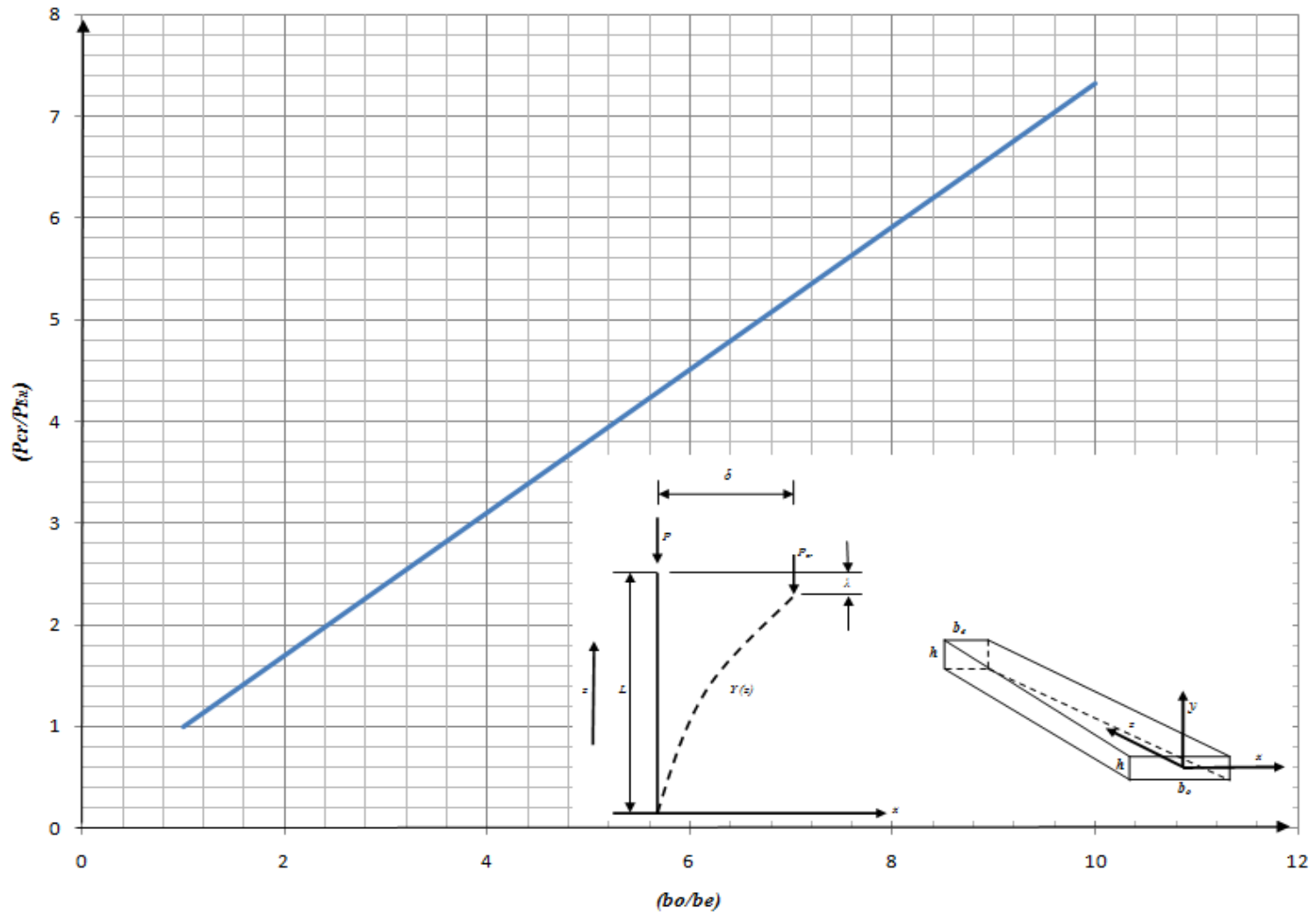
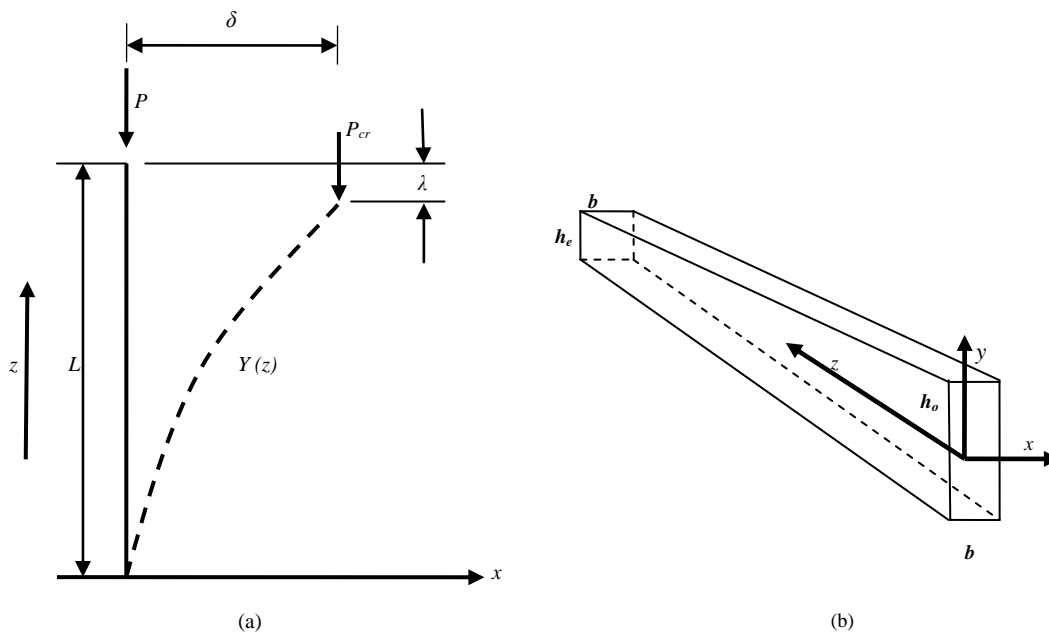


Figure 4.13: Plot of Equation (4.35) vs  $\left(\frac{b_o}{b_e}\right)$ , for the truncated, rectangular pyramid, whose breadth changes

#### 4.6.2 Buckling Load for the Rectangular Pyramid whose sections' depth changes



**Figure 4.14: (a) A fixed-free column subjected to a tip load (b) Cross sections of columns for a rectangular pyramid whose section changes depth**

Referring to Figure 4.14(a), a fixed-free column is subjected to a tip load having cross section changing as shown in Figure 4.14(b). The general formula for the critical buckling load is expressed as

$$P_{cr} = \frac{\pi^2 E}{2L^3} \int_0^L I_z \cos^2\left(\frac{\pi z}{2L}\right) dz \quad (4.35)$$

Using Equation (4.12) and substituting in Equation (4.35) gives

$$P_{cr} = \frac{\pi^2 E}{2L^3} \int_0^L \frac{b_z h_e^3}{12} \left[ 1 + \left[ 1 - \frac{z}{L} \right] \left[ \left( \frac{h_o}{h_e} \right) - 1 \right] \right]^3 \times \cos^2\left(\frac{\pi z}{2L}\right) dz \quad (4.36)$$

$$P_{cr} = \frac{\pi^2 E I_e}{2L^3} \int_0^L \left[ 1 + \left[ 1 - \frac{z}{L} \right] \left[ \left( \frac{h_o}{h_e} \right) - 1 \right] \right]^3 \times \cos^2\left(\frac{\pi z}{2L}\right) dz \quad (4.37)$$

To evaluate the integral in Equation (4.37) above it is assumed once again that  $z' = \frac{z}{L}$  and

$\psi = \left[ \left( \frac{h_o}{h_e} \right) - 1 \right]$ . Substituting these parameters yields

$$\begin{aligned}
P_{cr} &= \frac{\pi^2 EI_e}{2L^3} \times L \times \int_0^1 [1 + \psi(1-z')]^3 \times \cos^2\left(\frac{\pi z'}{2}\right) dz' \\
P_{cr} &= \frac{\pi^2 EI_e}{2L^2} \times \int_0^1 [1 + \psi(1-z')]^3 \times \left[\frac{1}{2} + \frac{1}{2} \cos(\pi z')\right] dz' \\
P_{cr} &= \frac{\pi^2 EI_e}{4L^2} \times \int_0^1 [1 + \psi(1-z')]^3 \times [1 + \cos(\pi z')] dz' \tag{4.38}
\end{aligned}$$

In Equation (4.38) above it can be seen that the term  $\frac{\pi^2 EI_e}{4L^2}$  represents the Euler Critical Buckling Load for a fixed-free column and so is represented as  $P_{Eu}$ . The quantity  $\frac{P_{cr}}{P_{Eu}}$  thus obtained is a non dimensional parameter that allows for ease of plotting.

$$\frac{P_{cr}}{P_{Eu}} = \int_0^1 [1 + \psi(1-z')]^3 \times [1 + \cos(\pi z')] dz' \tag{4.39}$$

Solving this integral we get

$$\frac{P_{cr}}{P_{Eu}} = \frac{\psi^3(\pi^4 + 12\pi^2 - 48) + 4\pi^2\psi^2(\pi^2 + 6) + 6\pi^2\psi(\pi^2 + 4) + 4\pi^4}{4\pi^4} \tag{4.40}$$

$$\text{where } \psi = \left[ \left( \frac{h_o}{h_e} \right) - 1 \right].$$

If  $h_o = h_z = h_e$  then the ratio  $\left( \frac{h_o}{h_e} \right) = 1$  which corresponds to a uniform non-tapering section then

Equation (4.38) would give  $P_{cr} = P_{Eu} = \frac{\pi^2 EI_e}{4L^2}$  where  $\frac{\pi^2 EI_e}{4L^2}$  is the Critical Euler Buckling

load for a column with one end fixed and one end free. Figure 4.15 graphically represents the plot of  $\frac{P_{cr}}{P_{Eu}}$  derived in Equation (4.40), for the square pyramid whose depth changes with

constant breadth, against the non dimensional parameter  $\left( \frac{h_o}{h_e} \right)$  which varies from 1 to 5 in

increments of 0.25. The objective of plotting such a curve is to determine the critical buckling load of this structure by making use of its dimensions  $h_o$  and  $h_e$  as well as the magnitude of the load applied  $P$  at its end. The dimensions  $h_o$  and  $h_e$  indicate the depth dimensions of the base and end of the pyramid, as shown in Figure 4.14 (b).

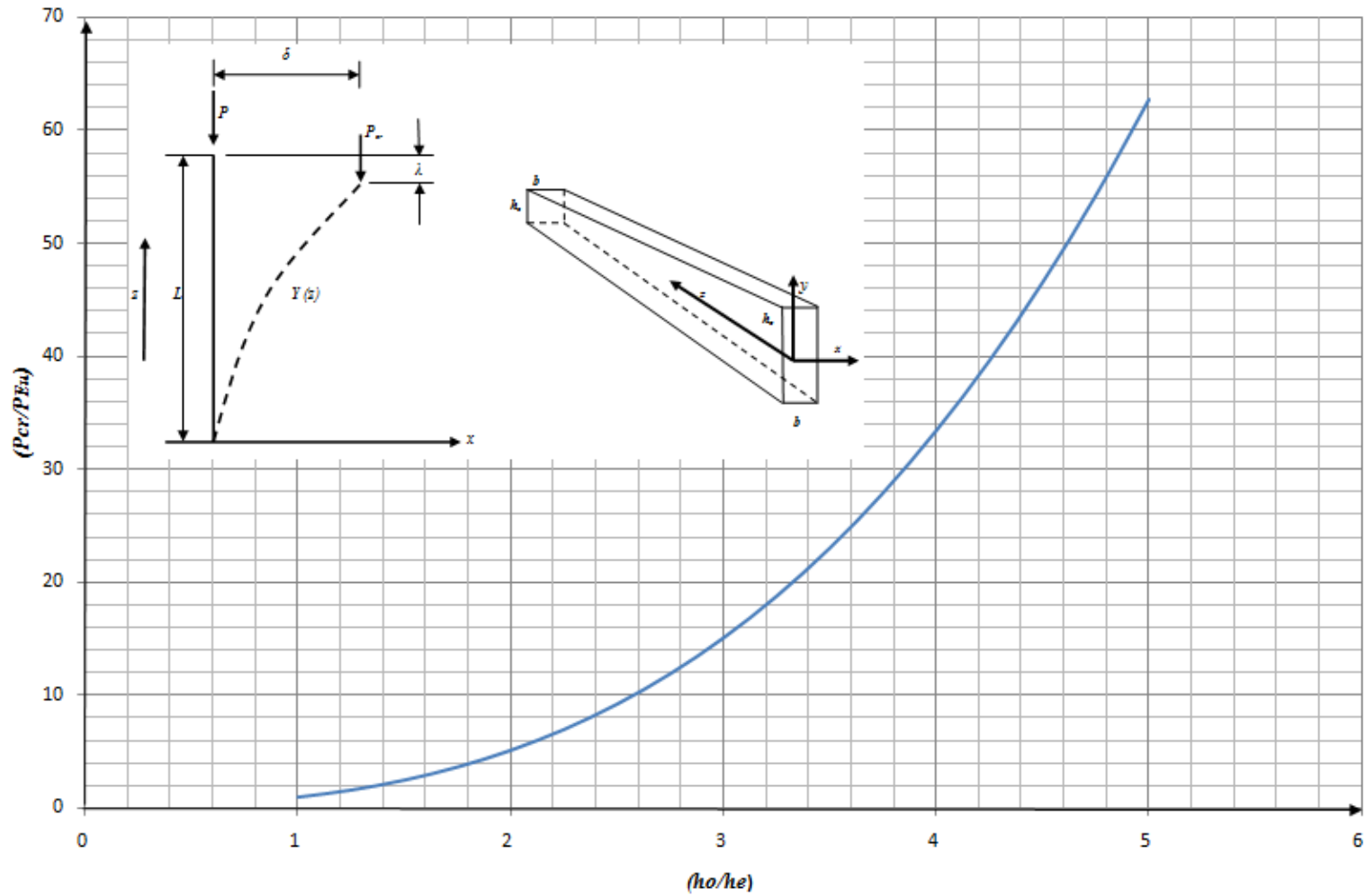


Figure 4.15: Plot of Equation (4.41) vs  $\left(\frac{h_o}{h_e}\right)$ , for the truncated rectangular pyramid, whose depth changes

Comparing Figures 4.13 and 4.15 reveals the simple fact, that a square pyramid whose section changes in depth, will have a greater critical buckling load or be able to withstand a greater load just before it buckles, as compared to that pyramid whose section changes in breadth. Figure 4.15 shows that for a square pyramid changing in depth the greater the value of  $h_o$  as compared to  $h_e$ , the greater is the critical buckling load, whereas Figure 4.13 shows that even a substantial increase in  $b_o$  as compared to  $b_e$  does not result in as a great a magnitude of critical buckling load.

### 4.6.3 Buckling Load for the Rectangular Pyramids whose sections change bi-dimensionally at the same and different rates

The general formula for the critical buckling load is expressed as

$$P_{cr} = \frac{\pi^2 E}{2L^3} \int_0^L I_z \cos^2\left(\frac{\pi z}{2L}\right) dz \quad (4.41)$$

Using Equation (4.13) and substituting in Equation (4.42) gives

$$P_{cr} = \frac{\pi^2 E}{2L^3} \int_0^L I_e \times \left[1 + \left[1 - \frac{z}{L}\right] \left[\left(\frac{b_o}{b_e}\right) - 1\right]\right] \times \left[1 + \left[1 - \frac{z}{L}\right] \left[\left(\frac{h_o}{h_e}\right) - 1\right]\right]^3 \times \cos^2\left(\frac{\pi z}{2L}\right) dz \quad (4.42)$$

$$P_{cr} = \frac{\pi^2 E}{2L^3} \times I_e \int_0^L \left[1 + \left[1 - \frac{z}{L}\right] \left[\left(\frac{b_o}{b_e}\right) - 1\right]\right] \times \left[1 + \left[1 - \frac{z}{L}\right] \left[\left(\frac{h_o}{h_e}\right) - 1\right]\right]^3 \times \left[\frac{1}{2} + \frac{1}{2} \cos\left(\frac{\pi z}{L}\right)\right] dz$$

$$P_{cr} = \frac{\pi^2 E}{2L^3} \times I_e \times \frac{1}{2} \times \int_0^L \left[1 + \left[1 - \frac{z}{L}\right] \left[\left(\frac{b_o}{b_e}\right) - 1\right]\right] \times \left[1 + \left[1 - \frac{z}{L}\right] \left[\left(\frac{h_o}{h_e}\right) - 1\right]\right]^3 \times \left[1 + \cos\left(\frac{\pi z}{L}\right)\right] dz$$

$$P_{cr} = \frac{\pi^2 E I_e}{4L^3} \times \int_0^L \left[1 + \left[1 - \frac{z}{L}\right] \left[\left(\frac{b_o}{b_e}\right) - 1\right]\right] \times \left[1 + \left[1 - \frac{z}{L}\right] \left[\left(\frac{h_o}{h_e}\right) - 1\right]\right]^3 \times \left[1 + \cos\left(\frac{\pi z}{L}\right)\right] dz \quad (4.43)$$

To evaluate the integral in Equation (4.43) above it is assumed once again that  $z' = \frac{z}{L}$

$\eta = \left[\left(\frac{b_o}{b_e}\right) - 1\right]$  and  $\psi = \left[\left(\frac{h_o}{h_e}\right) - 1\right]$ . Substituting the above parameters yields

$$P_{cr} = \frac{\pi^2 EI_e}{4L^3} \times L \times \int_0^1 [1 + \eta(1 - z')] \times [1 + \psi(1 - z')]^3 \times [1 + \cos(\pi z')] dz'$$

$$P_{cr} = \frac{\pi^2 EI_e}{4L^2} \times \int_0^1 [1 + \eta(1 - z')] \times [1 + \psi(1 - z')]^3 \times [1 + \cos(\pi z')] dz' \quad (4.44)$$

In Equation (4.45) above it can be seen that the term  $\frac{\pi^2 EI_e}{4L^2}$  represents the Euler Critical Buckling Load for a fixed-free column and so is represented as  $P_{Eu}$ . Equation (4.44) can now be written as

$$\frac{P_{cr}}{P_{Eu}} = \int_0^1 [1 + \eta(1 - z')] \times [1 + \psi(1 - z')]^3 \times [1 + \cos(\pi z')] dz'$$

Integrating by parts yields

$$\frac{P_{cr}}{P_{Eu}} = \frac{\eta[4\psi^3(\pi^4 + 20\pi^2 - 120) + 15\psi^2(\pi^4 + 12\pi^2 - 48) + 20\pi^2\psi(\pi^2 + 6) + 10\pi^2(\pi^2 + 4)]}{20\pi^4} \quad (4.45)$$

$$+ \frac{5[\psi^3(\pi^4 + 12\pi^2 - 48) + 4\pi^2\psi^2(\pi^2 + 6) + 6\pi^2\psi(\pi^2 + 4) + 4\pi^4]}{20\pi^4}$$

$$\text{where } \eta = \left[ \left( \frac{b_o}{b_e} \right) - 1 \right] \text{ and } \psi = \left[ \left( \frac{h_o}{h_e} \right) - 1 \right].$$

If both  $b_0=b_z=b_e$  and  $h_0=h_z=h_e$  then the ratios  $\left( \frac{b_o}{b_e} \right) = \left( \frac{h_o}{h_e} \right) = 1$  which corresponds to a uniform non-tapering section then Equation (4.45) would give  $P_{cr} = P_{Eu} = \frac{\pi^2 EI_e}{4L^2}$  where  $\frac{\pi^2 EI_e}{4L^2}$  is the Critical Euler Buckling load for a column with one end fixed and one end free. Figure 4.16 shows the plot of  $\frac{P_{cr}}{P_{Eu}}$  derived in Equation (4.45), for the square pyramid whose section changes bi-dimensionally, either at the same or different rates, against the non dimensional parameters  $\eta$  and  $\psi$ . In Figure 4.16, both the parameters vary at the same rate, by an increment of 0.25, between 0 and 4. The objective of plotting such a curve is to determine the

critical buckling load of such a structure by making use of the parameters  $\eta$  and  $\psi$  as well as the magnitude of the load applied at its apex,  $P$ .

Knowing that  $\eta = \left[ \left( \frac{b_o}{b_e} \right) - 1 \right]$  and  $\psi = \left[ \left( \frac{h_o}{h_e} \right) - 1 \right]$ , Table 4.1 shows that for a square pyramid,

whose  $\psi$  changes at a much greater rate than that of  $\eta$ , the critical buckling load such a structure can withstand is much greater than if a given square pyramid's  $\eta$  was greater than its  $\psi$ . Put simply that square pyramid whose depth varies at a greater rate as compared to its breadth, is capable of bearing a greater critical buckling load, than that pyramid whose breadth variation is greater than its depth variation.

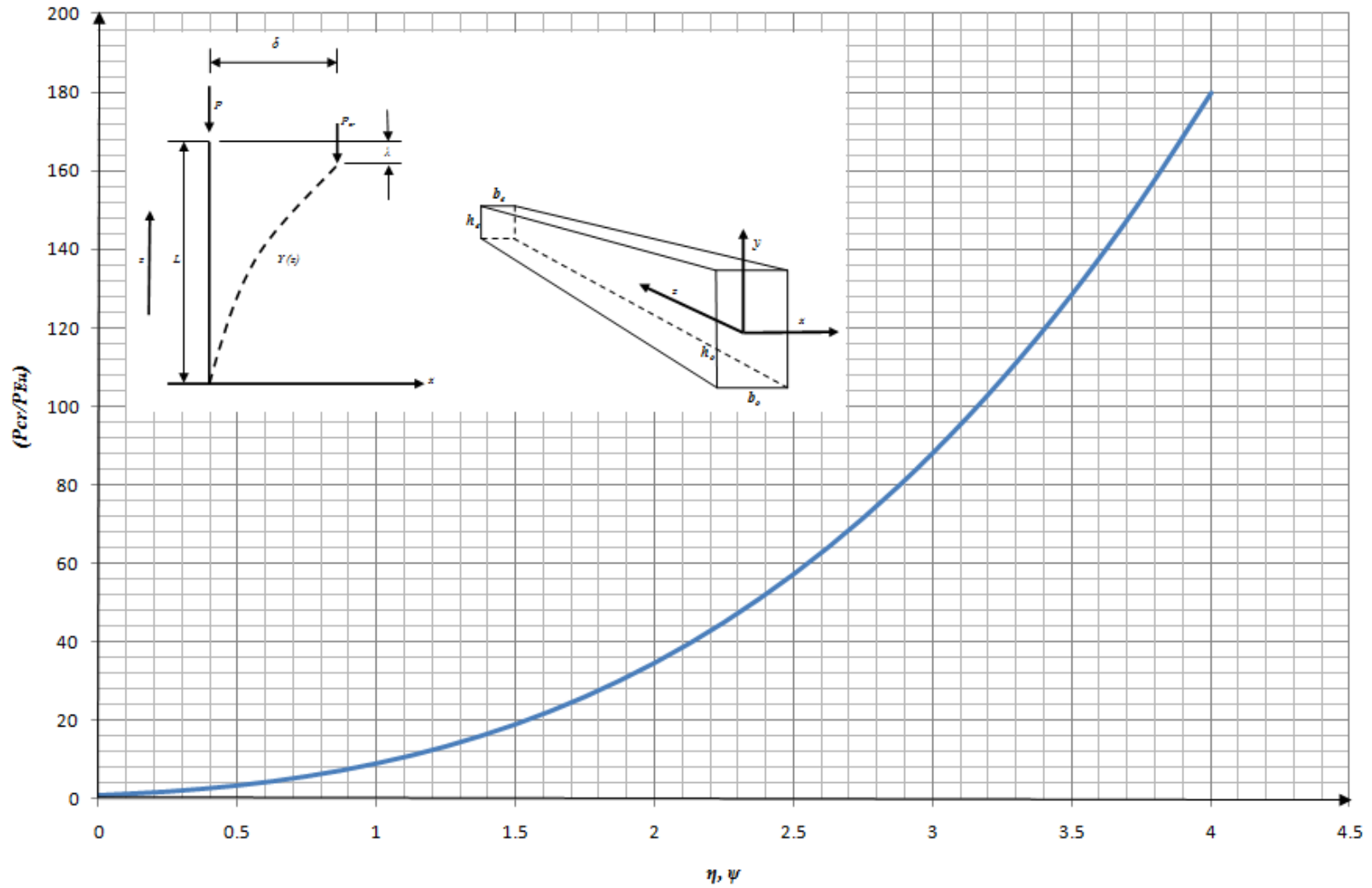
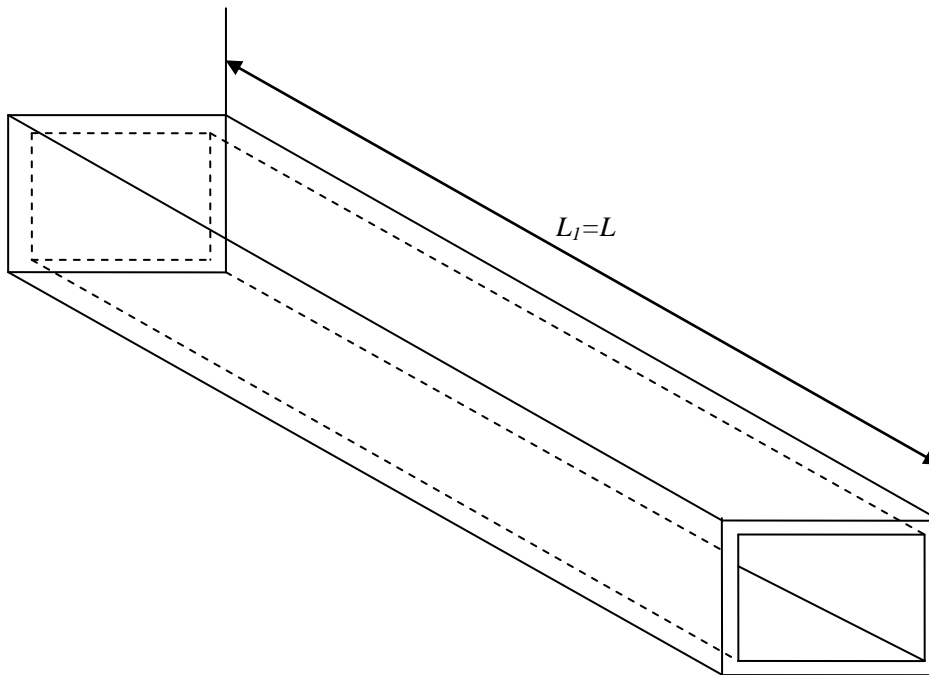


Figure 4.16: Plot of Equation (4.46) vs.  $\eta, \psi$ , for the truncated rectangular pyramid, whose section changes bi-dimensionally at the same rate

**Table 4.1: Comparison of Critical buckling loads for a rectangular pyramid, whose section changes bi-dimensionally at different rates**

Section changing bi-dimensionally such that variation of $\psi > \eta$			Section changing bi-dimensionally such that variation of $\eta > \psi$		
$\eta$	$\psi$	$P_{cr}/P_{Eu}$	$\eta$	$\psi$	$P_{cr}/P_{Eu}$
0	1	5.14	1	0	1.70
0.25	1.5	10.87	1.5	0.25	2.26
0.5	2	19.99	2	0.5	3.64
0.75	2.5	33.32	2.5	0.75	5.51
1	3	51.65	3	1	7.96
1.25	3.5	75.81	3.5	1.25	11.06
1.5	4	106.59	4	1.5	14.89
1.75	4.5	144.81	4.5	1.75	19.53
2	5	191.27	5	2	25.06
2.25	5.5	246.78	5.5	2.25	31.56
2.5	6	312.14	6	2.5	39.12
2.75	6.5	388.17	6.5	2.75	47.80
3	7	475.68	7	3	57.68
3.25	7.5	575.46	7.5	3.25	68.86
3.5	8	688.33	8	3.5	81.40
3.75	8.5	815.10	8.5	3.75	95.39
4	9	956.57	9	4	110.90

#### 4.7 Buckling Load for the single Thin walled Rectangular Section



**Figure 4.17: Geometry of a thin walled rectangular section**

A fixed-free column is subjected to a tip load having cross section as shown in Figure 4.17. The thickness of the thin-walled sections is assumed to be constant along the beam. The second moment of area of the rectangular tubular section shown in Figure 4.17 is expressed as

$$I_z = \frac{th_z^3}{6} + \frac{tb_z h_z^2}{2} \quad (4.46)$$

The first parameter in Equation (4.46) refers to the moment area of the vertical components and the second is of the horizontal components. The general formula for the critical buckling load is expressed as

$$P_{cr} = \frac{\pi^2 E}{2L^3} \int_0^L I_z \cos^2\left(\frac{\pi z}{2L}\right) dz \quad (4.47)$$

Substituting Equation (4.47) in the Equation (4.48) gives the expression

$$P_{cr} = \frac{\pi^2 E}{2L^3} \int_0^L \left\{ \frac{th_z^3}{6} + \frac{th_z^2 b_e}{2} \right\} \times \cos^2\left(\frac{\pi z}{2L}\right) dz$$

$$P_{cr} = \frac{\pi^2 EI_z}{2L^3} \int_0^L \cos^2\left(\frac{\pi z}{2L}\right) dz = \left(\frac{\pi^2 EI_z}{2L^3}\right) \times \int_0^L \left(\frac{1}{2} + \frac{1}{2} \cos\left(\frac{\pi z}{L}\right)\right) dz = \left(\frac{\pi^2 EI_z}{2L^3}\right) \times \left(\frac{L}{2}\right)$$

$$P_{cr} = \left(\frac{\pi^2 E}{4L^2}\right) \times \left(\frac{th_z^3}{6} + \frac{tb_z h_z^2}{2}\right)$$

which is the Critical Euler Buckling load for a column with one end fixed and one end free.

#### 4.8 Buckling Load for the Single Stepped Strut

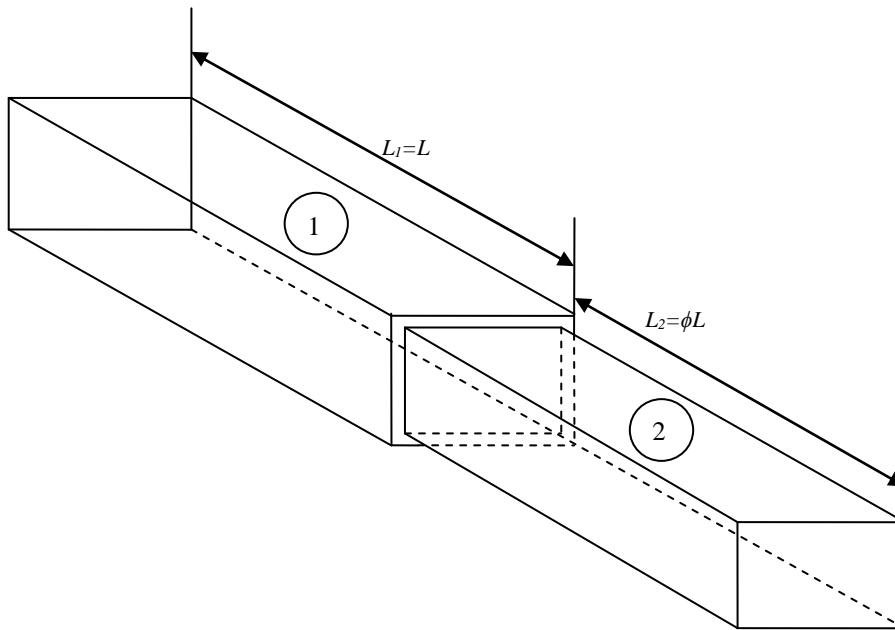


**Figure 4.18: Single stepped strut**

The single stepped composite strut shown in Figure 4.18 is the first step towards the ultimate goal of identifying the critical buckling load for the two section thin walled telescopic cantilever. For the determination of the buckling load of the single stepped cantilever shown, the problem in question needs to address the varying lengths of the sections that together make the composite assembly. To this end, the derivation of the equation for determining the buckling load (Equation (4.27)) must be adapted to account for the (a) overall length of the composite assembly, (b) individual lengths of the fixed and free end sections and finally, (c) the differing second moments of area. For ease of further calculations and also to obtain non-dimensional parameters, ratios are used to relate the defining parameters of the load-applied or

free-end section to the fixed-end section, as demonstrated in Table 4.1 and Figure 4.18. The fixed-end and free-end sections are denoted by 1 and 2 respectively in Figure 4.18.

**Table 4.2: Individual rectangular section properties**

Section	Length(mm)	Second Moments of Area (mm <sup>4</sup> )
<b>Section 1 (Fixed End)</b>	$L_1=L$	$I_1=I=\frac{b_1h_1^3}{12}$
<b>Section 2 (Free End)</b>	$L_2=\phi L_1= \phi L$	$I_2=\beta I_1=$ $\beta I= \beta \times \left(\frac{b_1h_1^3}{12}\right)$

For the purpose of this buckling analysis the sections are numbered from the fixed end towards the free end as shown in Figure 4.18, and in the section that follows.

The lengths of the sections have been considered individually in order to facilitate ease of calculations. The lengths and second moments of area are all expressed in terms of ratios and each of these in turn relate to the fixed-end section. The ratios  $\alpha$  and  $\beta$  are assumed to be less than 1 which means that the fixed end section has the larger dimensions of length, second moment of area and self weight respectively.

Consider the single stepped composite strut as being simplified as shown in Figure 4.19 below under a constant directional thrust  $P$  applied quasi statically. As the load is increased from zero, the work done by the force  $P$  is stored into the system as stretching strain energy. On allowing a small bending formation  $w(x)$ , that does not alter the afore mentioned stretching strain energy, the change in the total potential energy  $\Delta U_T$  is given by

$$\Delta U_T = \Delta U_B + \Delta U_P$$

Taking  $\Delta U_T = 0$  as per the argument made in §4.4 we get

$$\Delta U_B = -\Delta U_P \tag{4.48}$$

where  $\Delta U_B$  is the bending strain energy and this time  $\Delta U_P$  is the work done by the load  $P$  on the single stepped composite strut.

$$\Delta U_B = \int_0^L \frac{(M(z))^2}{2EI_z} dz \quad (4.49)$$

$$\Delta U_P = -P\lambda = -\frac{1}{2}P \int_0^L \left[ \frac{dY(z)}{dz} \right]^2 dz \quad (4.50)$$

Once again as in §4.4 we make use of an assumed deflected shape that accounts for first mode buckling and satisfies the boundary conditions for a fixed-free column. It must be remembered that the overall length of the composite section is  $[L(1 + \phi)]$ . Accounting for this gives

$$Y(z) = \delta \left( 1 - \cos \frac{\pi z}{2L(1 + \phi)} \right) \quad (4.51)$$

where  $Y=0$  at  $z=0$  and  $Y=\delta$  at  $z=L(1+\phi)$ .

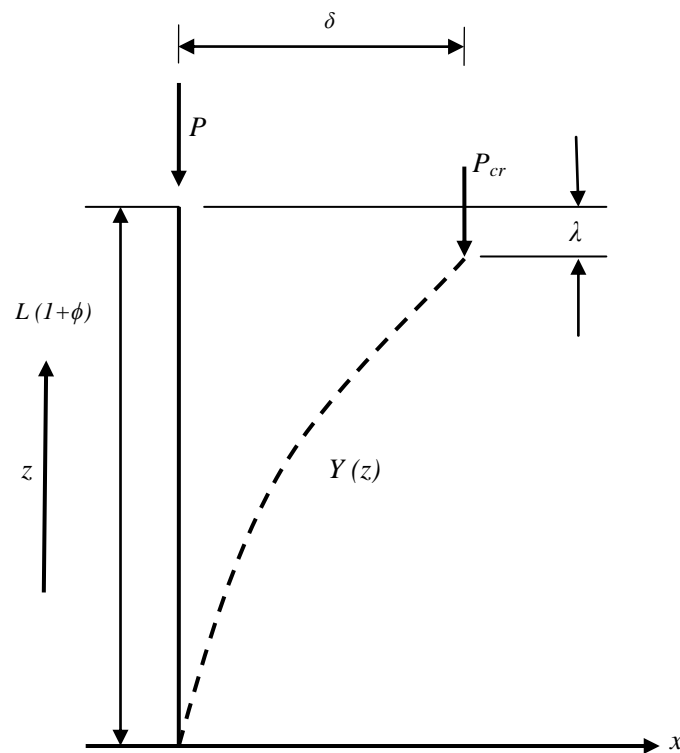


**Figure 4.19: Geometry of the cantilever column**

This means that the assumed deflection shape  $\left(1 - \cos \frac{\pi z}{2L(1+\phi)}\right)$  satisfies the kinematic boundary conditions at both  $z=0$  and  $z=L(1+\phi)$ . Predicting the load which will cause the column to buckle is traditionally done by numerical or finite element technique. An exact method is to solve the differential equation

$$EI_z \times \frac{d^2 Y(z)}{dz^2} + M(z) = 0, \quad (4.52)$$

with appropriate boundary conditions for the ends. Now substituting

$$M(z) = -EI_z \times \frac{d^2 Y(z)}{dz^2} \quad (4.53)$$

in Equation (4.49) and using Equation (4.50) yields

$$\Delta U_B = \frac{\delta^2 E \pi^4}{32[L(1+\phi)]^4} \int_0^z I_z \cos^2\left(\frac{\pi z}{2L(1+\phi)}\right) dz \quad (4.54)$$

The critical buckling condition occurs when Equation (4.48) is satisfied and this yields the general formula for the critical buckling load as

$$P_{cr} = \frac{\pi^2 E}{2[L(1+\phi)]^3} \int_0^z I_z \cos^2\left(\frac{\pi z}{2L(1+\phi)}\right) dz \quad (4.55)$$

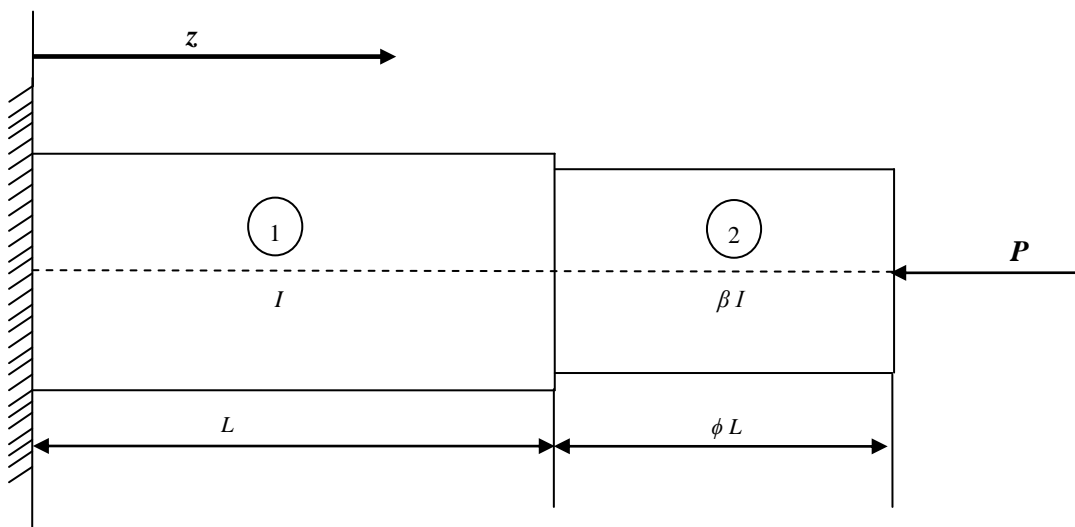


**Figure 4.20: Cross sectional view of the single stepped composite strut**

Applying the general buckling formula expressed in Equation (4.55) to the two section telescopic cantilever yields

$$P_{cr} = \frac{\pi^2 E}{2[L(1+\phi)]^3} \int_0^L I_1 \cos^2\left(\frac{\pi z}{2L(1+\phi)}\right) dz + \frac{\pi^2 E}{2[L(1+\phi)]^3} \int_L^{L(1+\phi)} I_2 \cos^2\left(\frac{\pi z}{2L(1+\phi)}\right) dz \quad (4.56)$$

where the first and second components correspond to the sections marked 1 and 2 in Figure 4.20 respectively.

$$P_{cr} = \frac{\pi^2 EI}{2[L(1+\phi)]^3} \times \left[ \frac{L}{2} + \frac{L(1+\phi)}{2\pi} \times \left[ \sin\left(\frac{\pi}{1+\phi}\right) \right] \right] + \frac{\pi^2 E\beta I}{2[L(1+\phi)]^3} \times \left[ \frac{\phi L}{2} - \frac{L(1+\phi)}{2\pi} \times \left[ \sin\left(\frac{\pi}{1+\phi}\right) \right] \right] \quad (4.57)$$

$$P_{cr} = \frac{\pi^2 EI}{2[L(1+\phi)]^3} \times \frac{L}{2} \times \left[ 1 + \frac{(1+\phi)}{\pi} \times \left[ \sin\left(\frac{\pi}{1+\phi}\right) \right] \right] + \frac{\pi^2 E\beta I}{2[L(1+\phi)]^3} \times \frac{L}{2} \times \left[ \phi - \frac{(1+\phi)}{\pi} \times \left[ \sin\left(\frac{\pi}{1+\phi}\right) \right] \right]$$

$$P_{cr} = \frac{\pi^2 EI}{4L^2(1+\phi)^2} \times \frac{1}{(1+\phi)} \times \left[ 1 + \frac{(1+\phi)}{\pi} \times \left[ \sin\left(\frac{\pi}{1+\phi}\right) \right] + \beta\phi - \frac{\beta(1+\phi)}{\pi} \times \left[ \sin\left(\frac{\pi}{1+\phi}\right) \right] \right] \quad (4.58)$$

In Equation (4.58) the term  $\frac{\pi^2 EI}{4[L(1+\phi)]^2}$  is the critical Euler buckling load which yields

$$P_{cr} = P_{Eu} \times \frac{1}{(1+\phi)} \times \left[ 1 + \frac{(1+\phi)}{\pi} \times \left[ \sin\left(\frac{\pi}{1+\phi}\right) \right] + \beta\phi - \frac{\beta(1+\phi)}{\pi} \times \left[ \sin\left(\frac{\pi}{1+\phi}\right) \right] \right]$$

$$\frac{P_{cr}}{P_{Eu}} = \frac{1}{(1+\phi)} \times \left[ 1 + \frac{(1+\phi)}{\pi} \times \left[ \sin\left(\frac{\pi}{1+\phi}\right) \right] + \beta\phi - \frac{\beta(1+\phi)}{\pi} \times \left[ \sin\left(\frac{\pi}{1+\phi}\right) \right] \right]$$

$$\frac{P_{cr}}{P_{Eu}} = \left[ \frac{1+\phi\beta}{1+\phi} + \frac{1-\beta}{\pi} \times \left[ \sin\left(\frac{\pi}{1+\phi}\right) \right] \right] \quad (4.59)$$

Referring to [97], we now make use of two standard sections with the specifications listed in Table 4.3 below in order to plot the Equation (4.59) against varying values of the parameter  $\phi$ .

**Table 4.3: Nominal dimensions and sectional properties of solid rectangular sections [95]**

Section	Size		Second Moments of Area (mm <sup>4</sup> )
	H mm	B mm	
<b>Section 1 (Fixed End)</b>	60	40	72x10 <sup>4</sup>
<b>Section 2 (Free End)</b>	50	30	31.25x10 <sup>4</sup>

Assuming the lengths of sections 1 and 2 to be 1200 mm and 1000 mm, respectively and comparing Tables 4.2 and 4.3 it can be determined that the value of  $\beta$  is 0.434. Using this value, the graph in Figure 4.22 is plotted with varying values of the overlap ratio  $\phi$ , for the non dimensionalised parameter  $\frac{P_{cr}}{P_{Eu}}$  derived in Equation (4.59).

Substituting  $\beta = \phi = 1$  and  $I_1 = I_2 = I$  in Equation (4.60) above we get the Critical Euler Buckling Load for an equivalent single section cantilever having length  $2L$  and uniform second moment of area  $I$

$$\frac{P_{cr}}{P_{Eu}} = 1 \Rightarrow P_{cr} = P_{Eu} = \frac{\pi^2 EI_e}{4[L(1+1)]^2} = \frac{\pi^2 EI}{16L^2} = \frac{\pi^2 EI}{4(2L)^2}$$

The curve in Figure 4.21 clearly indicates that for a single stepped strut, the critical buckling load that the strut can withstand is not affected to a great extent, by variations in the parameter  $\phi$ . This can be attributed to the fact that the strut, unlike the two section telescopic cantilever beam assembly, is not a thin-walled structure and as a result the  $I$  values of both sections 1 and 2 are almost the same.

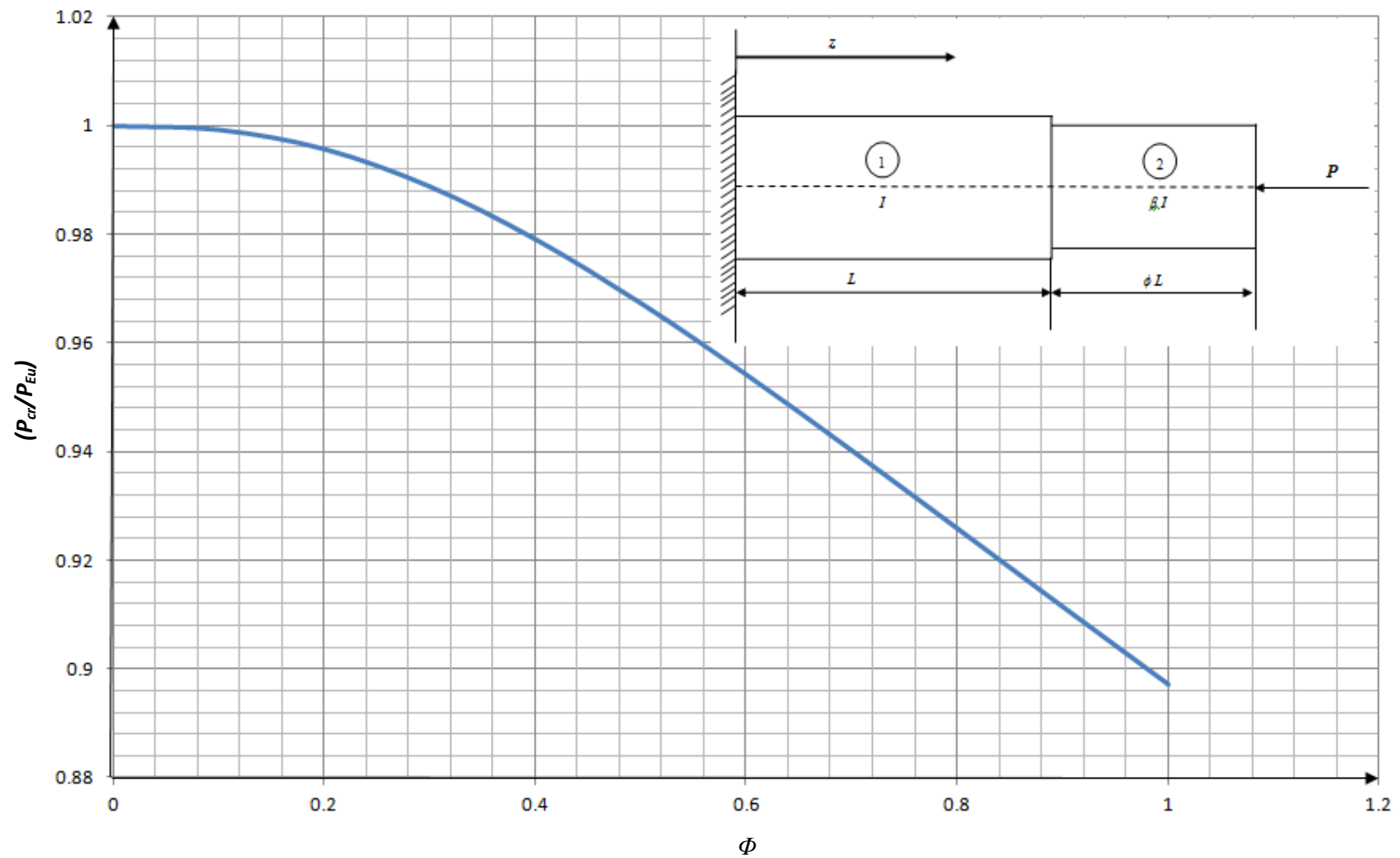


Figure 4.21: Plot of Equation (4.59) vs.  $\phi$ , for the single stepped strut, having dimensions outlined in Table 4.3 and fixed and free-end lengths of 1200 and 100mm respectively

#### 4.9 Buckling Load for the Thin walled Two Section Telescoping Cantilever Beam Assembly

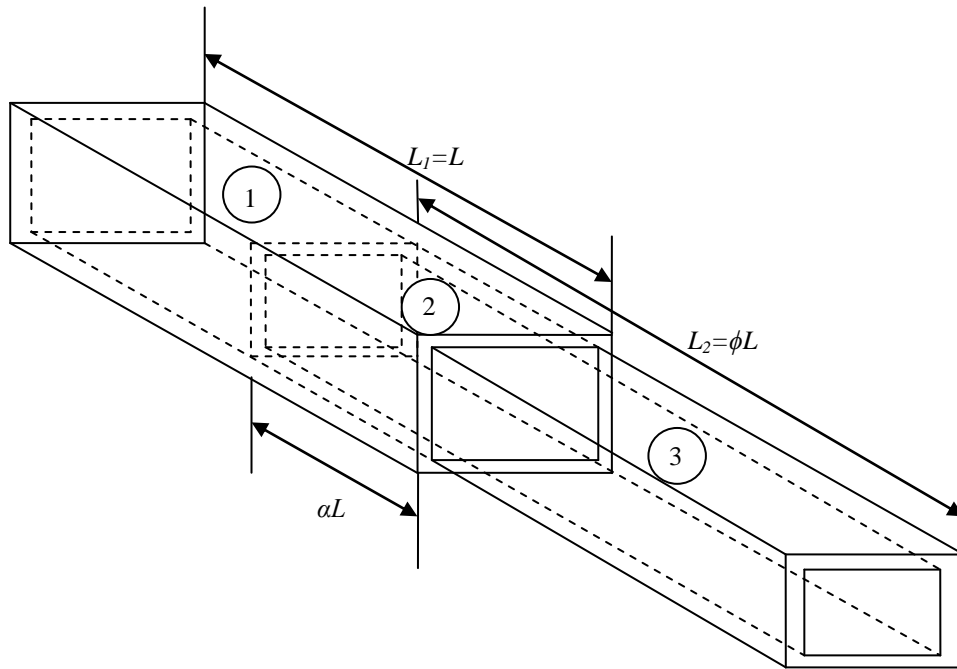


Figure 4.22: Two section telescopic cantilever

The thickness of the thin-walled sections that constitute the two section telescopic cantilever shown in Figure 4.22 is yet again assumed to be constant along the beam. The second moment of area of the rectangular tubular sections that constitute the telescopic assembly as shown in Figure 4.22 and Figure 4.23 is expressed as

$$I_z = \frac{th_z^3}{6} + \frac{tb_z h_z^2}{2} \quad (4.60)$$

Of course for the free-end section to slide within the fixed-end section, the former will have dimensions smaller than that of the latter so individual dimensions of breadth, height and thickness are to be taken into account.

The first term in Equation (4.60) refers to the second moment area of the vertical components and the second represents the horizontal components. For ease of further calculations and also to obtain non-dimensional parameters ratios are used to relate the defining characters of the free section to the fixed end section. This is demonstrated in Table 4.4 and in Figure 4.23.

**Table 4.4: Individual rectangular section properties**

Section	Length(mm)	Self Weight (N/mm)	Second Moments of Area (mm <sup>4</sup> )
<b>Section 1 (Fixed End)</b>	$L_1=L$	$W_1 =w$	$I_1=I$
<b>Section 2 (Overlap)</b>	$\alpha L$	$W_2=(1+\gamma)w$	$I_2=(1+\beta)I$
<b>Section 3 (Free End)</b>	$L_2=\phi L_1=\phi L$	$W_3=\gamma w$	$I_3=\beta I$

For the purpose of this buckling analysis the sections are numbered from the fixed end towards the free end as shown in Figure 4.24. As can be seen from Figure 4.22 and Figure 4.23 the overlap is considered to be a separate section in order to account for changes in second moment of area and the change in self weight.

The lengths of the sections have been broken down individually in order to facilitate ease of calculations. The lengths, second moments of area and self weights are all expressed in terms of ratio and each of these in turn relate to the fixed-end section. The fixed-end, overlap and free-end sections are denoted by 1, 2 and 3, respectively in Figures 4.22 and 4.33 respectively.

The ratios  $\alpha$ ,  $\beta$  and  $\gamma$  are assumed to be less than 1 which means that the fixed end section has the larger dimensions of length, second moment of area and self weight respectively. Now the general formula for the critical buckling load is expressed as

$$P_{cr} = \frac{\pi^2 E}{2[L(1+\phi-\alpha)]^3} \int_0^z I_z \cos^2\left(\frac{\pi z}{2L(1+\phi-\alpha)}\right) dz \quad (4.61)$$

For the displacement function  $Y(z) = \delta \left[ 1 - \cos\left(\frac{\pi z}{2L(1+\phi-\alpha)}\right) \right]$ .

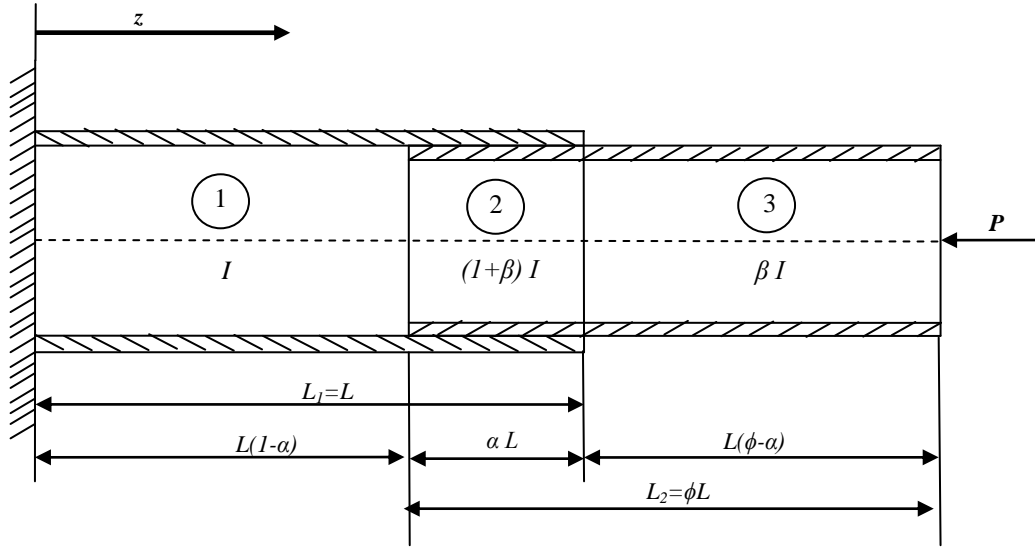


**Figure 4.23: Cross sectional view of the two section telescopic cantilever**

Applying the derived buckling formula expressed in Equation (4.61) to the two section telescopic cantilever whose cross section is shown in Figure 4.23 yields

$$\begin{aligned}
 P_{cr} &= \frac{\pi^2 E}{2[L(1+\phi-\alpha)]^3} \int_0^{L(1-\alpha)} I_1 \times \cos^2\left(\frac{\pi z}{2L(1+\phi-\alpha)}\right) dz \\
 &+ \frac{\pi^2 E}{2[L(1+\phi-\alpha)]^3} \int_{L(1-\alpha)}^L I_2 \times \cos^2\left(\frac{\pi z}{2L(1+\phi-\alpha)}\right) dz \\
 &+ \frac{\pi^2 E}{2[L(1+\phi-\alpha)]^3} \int_L^{L(1+\phi-\alpha)} I_3 \times \cos^2\left(\frac{\pi z}{2L(1+\phi-\alpha)}\right) dz
 \end{aligned} \tag{4.62}$$

where the first and second and third components correspond to the sections marked 1, 2 and 3 in Figure 4.23 respectively.

$$\begin{aligned}
 P_{cr} &= \frac{\pi^2 EI}{2[L(1+\phi-\alpha)]^3} \times \left[ \frac{L(1-\alpha)}{2} + \frac{L(1+\phi-\alpha)}{2\pi} \times \frac{1}{2} \left[ \sin\left(\frac{\pi(1-\alpha)}{1+\phi-\alpha}\right) \right] \right] \\
 &+ \frac{\pi^2 E(1+\beta)I}{2[L(1+\phi-\alpha)]^3} \times \left[ \frac{\alpha L}{2} + \frac{L(1+\phi-\alpha)}{2\pi} \times \frac{1}{2} \left[ \sin\left(\frac{\pi}{1+\phi-\alpha}\right) - \sin\left(\frac{\pi(1-\alpha)}{1+\phi-\alpha}\right) \right] \right] \\
 &+ \frac{\pi^2 E\beta I}{2[L(1+\phi-\alpha)]^3} \times \left[ \frac{L(\phi-\alpha)}{2} + \frac{L(1+\phi-\alpha)}{2\pi} \times \left[ -\sin\left(\frac{\pi}{1+\phi-\alpha}\right) \right] \right]
 \end{aligned} \tag{4.63}$$

$$\begin{aligned}
P_{cr} &= \frac{\pi^2 EI}{4[L(1+\phi-\alpha)]^2} \times \frac{1}{(1+\phi-\alpha)} \times \left[ (1-\alpha) + \frac{(1+\phi-\alpha)}{\pi} \times \left[ \sin\left(\frac{\pi(1-\alpha)}{1+\phi-\alpha}\right) \right] \right] \\
&+ \frac{\pi^2 E(1+\beta)I}{4[L(1+\phi-\alpha)]^2} \times \frac{1}{(1+\phi-\alpha)} \times \left[ \alpha + \frac{(1+\phi-\alpha)}{\pi} \times \left[ \sin\left(\frac{\pi}{1+\phi-\alpha}\right) - \sin\left(\frac{\pi(1-\alpha)}{1+\phi-\alpha}\right) \right] \right] \\
&+ \frac{\pi^2 E\beta I}{4[L(1+\phi-\alpha)]^2} \times \frac{1}{(1+\phi-\alpha)} \times \left[ (\phi-\alpha) + \frac{(1+\phi-\alpha)}{\pi} \times \left[ -\sin\left(\frac{\pi}{1+\phi-\alpha}\right) \right] \right] \\
\frac{P_{cr}}{P_{Eu}} &= \frac{1}{(1+\phi-\alpha)} \times \left[ (1-\alpha) + \frac{(1+\phi-\alpha)}{\pi} \times \left[ \sin\left(\frac{\pi(1-\alpha)}{1+\phi-\alpha}\right) \right] \right] \\
&+ \frac{(1+\beta)}{(1+\phi-\alpha)} \times \left[ \alpha + \frac{(1+\phi-\alpha)}{\pi} \times \left[ \sin\left(\frac{\pi}{1+\phi-\alpha}\right) - \sin\left(\frac{\pi(1-\alpha)}{1+\phi-\alpha}\right) \right] \right] \\
&+ \frac{1}{(1+\phi-\alpha)} \times \left[ (\phi-\alpha) + \frac{(1+\phi-\alpha)}{\pi} \times \left[ -\sin\left(\frac{\pi}{1+\phi-\alpha}\right) \right] \right] \\
\frac{P_{cr}}{P_{Eu}} &= \frac{1+\beta\phi}{1+\phi-\alpha} + \frac{1}{\pi} \times \left[ \sin\left(\frac{\pi}{1+\phi-\alpha}\right) - \beta \sin\left(\frac{\pi(1-\alpha)}{1+\phi-\alpha}\right) \right] \tag{4.64}
\end{aligned}$$

Referring to [93], we now make use of two standard sections with the specifications listed in Table 4.5 below in order to plot the Equation (4.64) against varying values of the parameter  $\alpha$ .

**Table 4.5: Nominal dimensions and sectional properties of rectangular hollow sections – Extract from ISO/FDIS 2633-2:2011 (E) [93].**

Section	Size		Thickness ( <i>T</i> mm)	Weight per unit length (N/mm)	Second Moments of Area (mm <sup>4</sup> )
	<i>H</i> mm	<i>B</i> mm			
<b>Section 1 (Fixed End)</b>	60	40	5	0.0685	38.1x10 <sup>4</sup>
<b>Section 3 (Free End)</b>	50	30	5	0.0528	18.7x10 <sup>4</sup>

Comparing Tables 4.4 and 4.5 and assuming lengths of the fixed and free sections to be 1200mm and 1000mm respectively, it can be determined that the values of  $\phi$ ,  $\beta$  and  $\gamma$  are 0.833, 0.49 and 0.642 respectively. Using these values the graph in Figure 4.24 is plotted.

Substituting  $\alpha = 0$ ,  $\beta = \phi = 1$  and  $I_1 = I_2 = I$  in the equation (4.64) above we get the Critical Euler Buckling Load for an equivalent single section cantilever having length  $2L$  and uniform second moment of area  $I$

$$\frac{P_{cr}}{P_{Eu}} = 1 \Rightarrow P_{cr} = P_{Eu} = \frac{\pi^2 EI_e}{4[L(1+1)]^2} = \frac{\pi^2 EI}{16L^2} = \frac{\pi^2 EI}{4(2L)^2}$$

The curve in Figure 4.24 plots the non dimensional parameter  $\frac{P_{cr}}{P_{Eu}}$  against the overlap ratio  $\alpha$ ,

where  $\alpha$  varies from 0 to 1, in increments of 0.1. The condition when the ratio  $\alpha=0$  arises, when there is no free-end section or no telescoping arrangement, while the condition when the ratio  $\alpha=1$ , occurs when the free-end section is fully inserted or sheathed within the fixed-end section and it is between these two maxima that the curve in Figure 4.24 is plotted. Naturally the higher value of critical buckling load will correspond to the latter rather than the former. In Equation (4.64) the parameters  $\phi$ ,  $\beta$  and  $\alpha$  can be varied depending upon the dimensions of the telescoping arrangement. For a designer, this equation could be useful in ascertaining the critical buckling load that a particular telescoping arrangement can withstand.

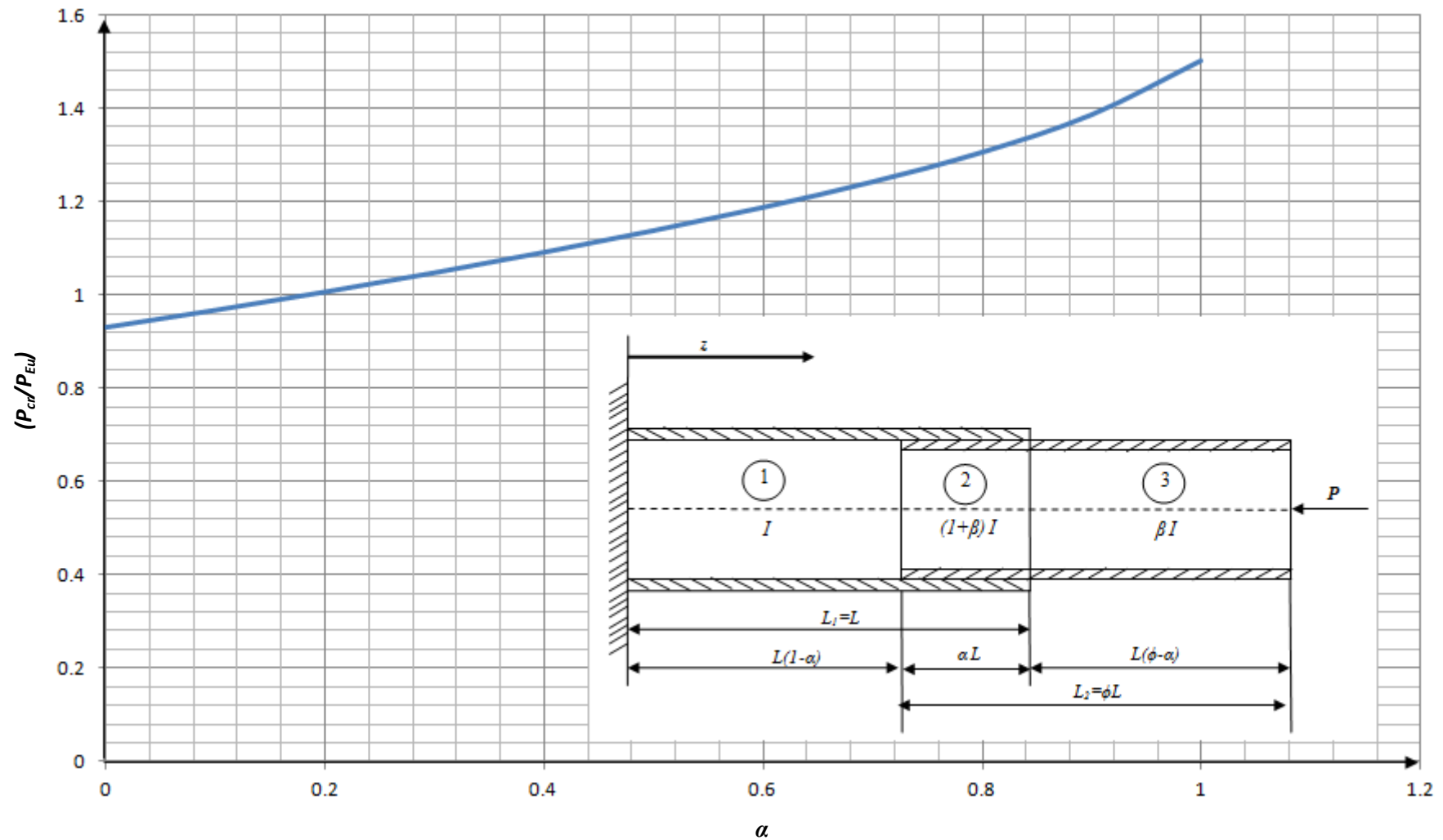


Figure 4.24: Plot of Equation (4.64) vs.  $\alpha$ , where  $\alpha$  varies from 0 to 1, in increments of 0.1, for the two section telescopic cantilever beam assembly, having dimensions outlined in Table 4.5, and fixed and free-end lengths of 1200 mm and 1000 mm respectively.

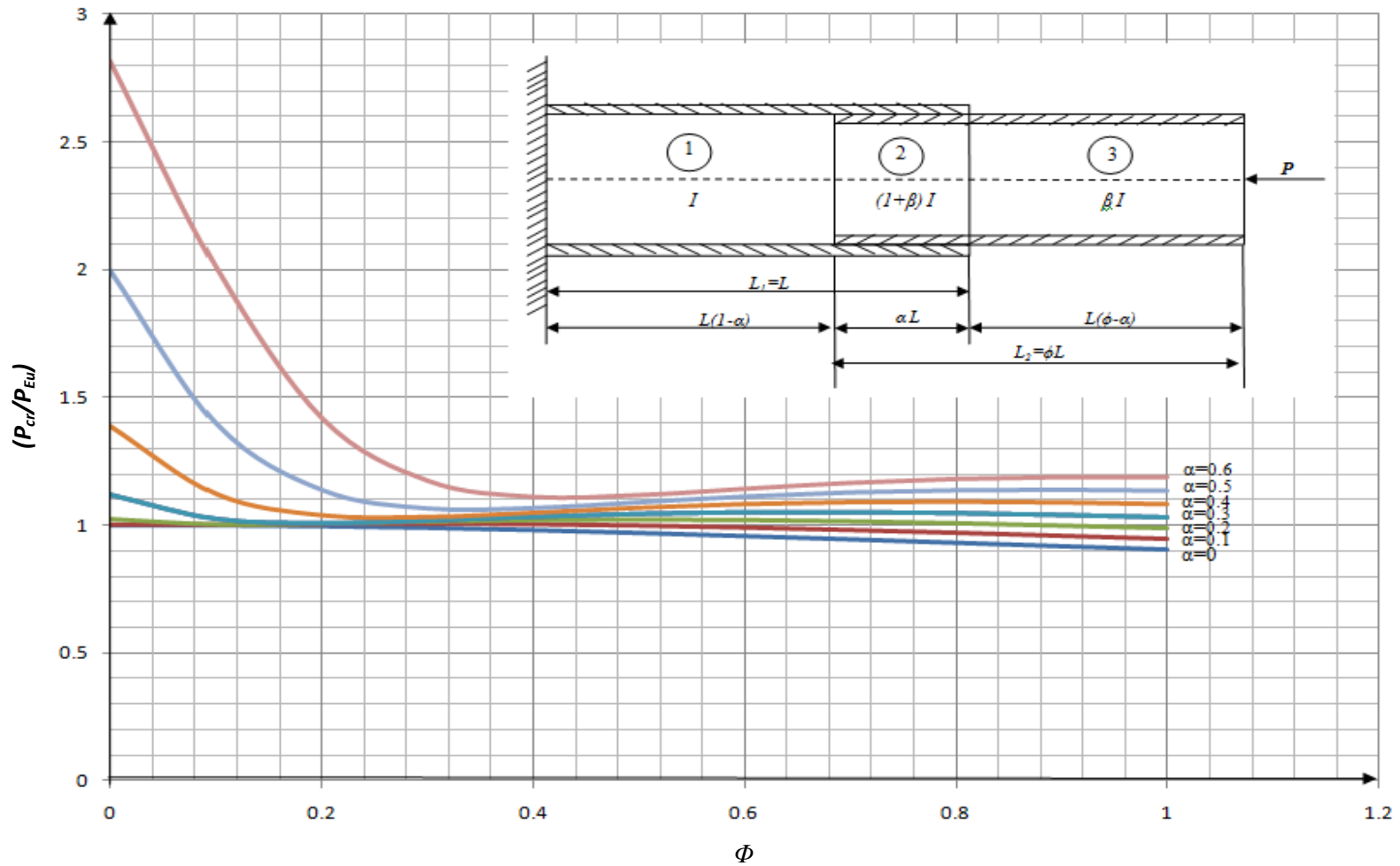


Figure 4.25: Plot of Equation (4.64) vs.  $\phi$ , where  $\phi$  varies from 0 to 1, in increments of 0.1, for overlap ratios  $\alpha$  varying from 0 to 0.6, determined for the two section telescopic cantilever beam assembly, having dimensions outlined in Table 4.5, and fixed and free-end lengths of 1200 mm and 1000 mm respectively.

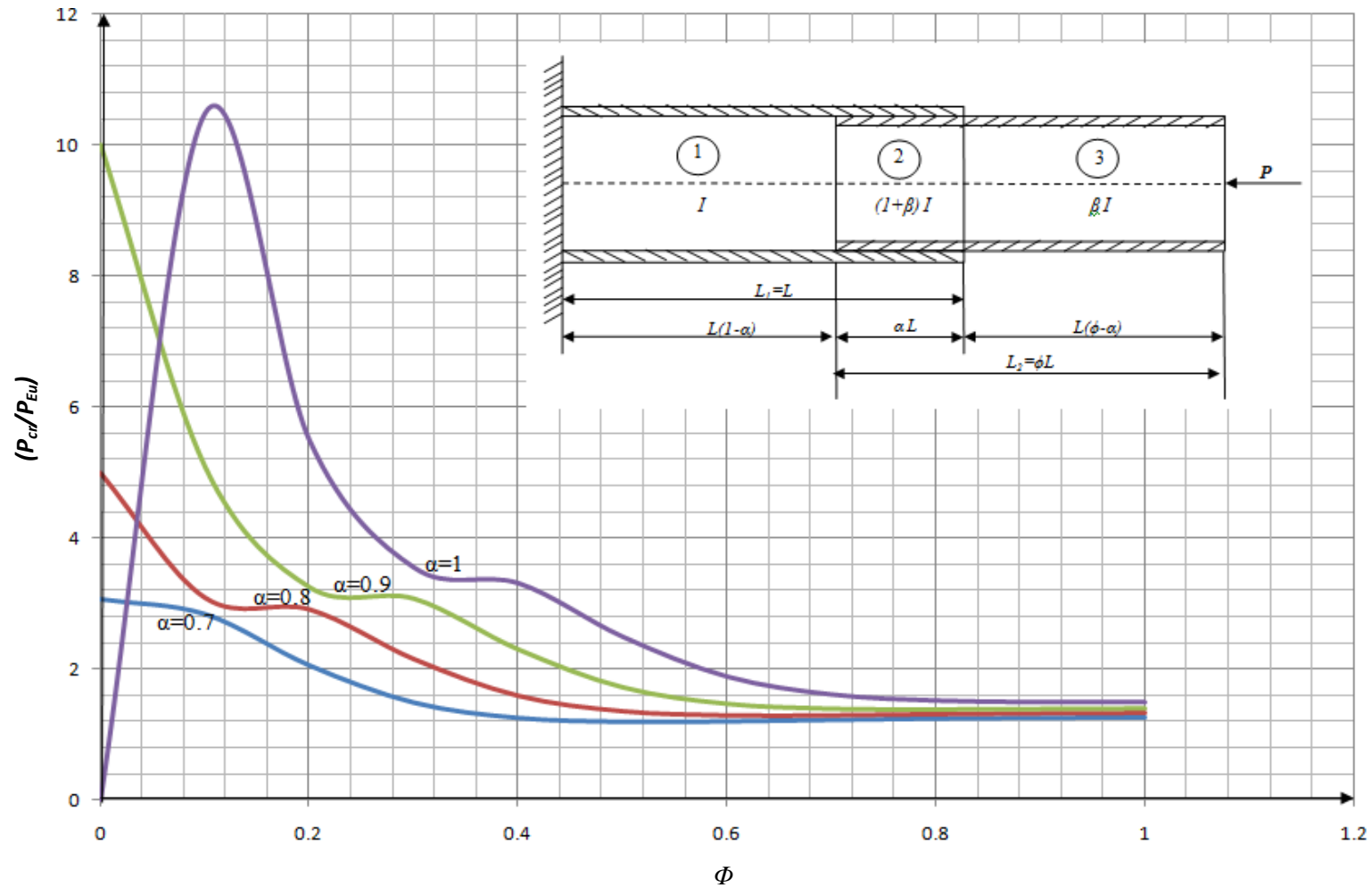


Figure 4.26: Plot of Equation (4.64) vs.  $\phi$ , where  $\phi$  varies from 0 to 1, in increments of 0.1, for overlap ratios  $\alpha$  varying from 0.7 to 1, determined for the two section telescopic cantilever beam assembly, having dimensions outlined in Table 4.5, and fixed and free-end lengths of 1200mm and 1000mm respectively.

## 4.10 Summary

The end objective of this chapter was to derive from first principles, an equation to determine the critical buckling load of the two section telescopic cantilever beam assembly. The equation thus derived had to take into consideration, all manner of variables associated with the structure and also prove adaptable to any number of telescoping sections. Another desired objective was to generate curves that would simply allow a designer to select a particular configuration of the two section telescoping arrangement, for a particular function with relative ease, provided suitable data is at hand. The equation derived is compared with the values extracted using FEA software as detailed in § 9.1.3. The following points are made in summary:

1. For an axially truncated and symmetric cone, it has been shown that larger the value of its base diameter  $d_o$  as compared to its apex diameter  $d_e$ , the greater is the critical buckling load that it can withstand.
2. A rectangular pyramid whose section changes in its depth, will have a greater critical buckling load as compared to that pyramid whose section changes in breadth. Figure 4.15 shows that for a square pyramid changing in depth the greater the value of  $h_o$  as compared to  $h_e$ , the greater is the critical buckling load, whereas Figure 4.13 shows that even a substantial increase in  $b_o$  as compared to  $b_e$  does not result in as a great a magnitude of critical buckling load. A square pyramid, whose depth varies at a greater rate as compared to its breadth, is capable of bearing a greater critical buckling load, than that pyramid whose breadth variation is greater than its depth variation, as is evidenced in Table 4.1.
3. Equation (4.64) effectively determines the critical buckling load that a particular arrangement of the two section telescopic cantilever beam arrangement, can withstand. Varying the different parameters in Equation (4.64) allows for a great deal of flexibility in the selection of a particular telescopic arrangement for a given application. The equation also allows for any number of lengths of telescoping sections to be taken into account, and does not allow itself to be restricted to just the two sections. So long as the

ratios can account for a number of telescoping sections, it is entirely possible to derive an expression to determine the critical buckling load. Once again as in Chapter 3, the candidate assembly to which Equation (4.64) was applied, has dimensions outlined in Table 4.5, with fixed and free-end lengths of 1200 mm and 1000 mm, respectively.

4. Figure 4.25 presents the plot of the non dimensionalised parameter  $\frac{P_{cr}}{P_{Eu}}$ , against the overlap ratio  $\alpha$ , which in turn varies from 0 to 1, in steps of 0.1. The curve shown was plotted assuming fixed and free section lengths of 1200 mm and 1000 mm respectively, an arrangement, for which the value of  $\phi$  is 0.833. It can be deduced from the curve that for an overlap ratio  $\alpha$  equal to 1, the given arrangement will have the greatest critical buckling load magnitude. The condition wherein the overlap ratio  $\alpha$  equals 1, corresponds to that arrangement of the assembly whereby the free-end section is entirely sheathed within the fixed-end section. This curve assumes importance in light of the fact that it can be tailored to directly suit the application for which a given configuration of the telescoping arrangement is required.
  
5. In Figures 4.26 and 4.27, for values of the overlap ratio parameter  $\alpha$  varying from 0 to 1, in increments of 0.1, the maximum critical buckling load, or the magnitude at which a structure just begins to undergo buckling, is observed to be maximum, for a length variation ratio of  $\phi$  equals 0. This naturally indicates that there is no free-end section to slide within the fixed-end section. However an ideal configuration of the telescoping assembly can be selected using the curves plotted in Figures 4.26 and 4.27, for a desired combination of ratios  $\alpha$  and  $\phi$ . Figures 4.26 and 4.27 are in essence used to demonstrate the effect differing lengths of the fixed and free sections that constitute the two section telescoping cantilever beam assembly will have upon the critical buckling load of said structure. Once again, it must be remembered that the three sets of curves in Figures 4.25 -4.27 correspond to that telescopic arrangement having dimensions outlined in Table 4.5 and fixed and free-end assumed lengths of 1200 mm and 1000 mm respectively.

## CHAPTER 5: SHEAR AND TORSION ANALYSES

### 5.1 Introduction

Equilibrium and stability conditions of one dimensional elements such as the tapered sections of varying cross sections, the composite single stepped strut and the two section telescoping cantilever assembly have been examined and dissected in the previous chapter. The analysis of these members is relatively simple as bending, the essential characteristic of buckling, can be assumed to take place in one plane only. The buckling of a plate on examination involves bending in two planes and this increases the nature of the complexity. From a mathematical point of view, the main difference between one dimensional elements and plates is that quantities such as deflections and bending moments which are functions of a single independent variable in the former become functions of two independent variables in plates. As a result the behaviour of plates is governed by partial differential equations which increase the complexity of analysis.

Another significant difference in the buckling characteristics of plates as compared to one dimensional elements is that buckling terminates the latter's ability to resist any further load, and this critical load is the failure or ultimate load. The same however, does not apply in the case of plates. A plate element may carry additional loading beyond the critical load. This ability to carry additional load above and beyond the critical load is the post-buckling strength. The magnitude of the post-buckling relative to the buckling load depends on a variety of parameters such as the dimensional properties, boundary conditions, type of loading and the ratio of buckling stress to yield stress. Plate buckling is usually referred to local buckling. Structural shapes composed of plate elements may not necessarily terminate their load-carrying capacity at the instance of local buckling of individual plate elements. This additional strength of structural members is attributable not only to the post-buckling strength of the plate elements but also to possible stress redistribution in the member after failure of individual plate elements.

This chapter has as its basis the theories put forward by Rees in *Mechanics of Optimal Structural Design*, [14] and detailed in § 2.16, § 2.17 and § 2.18 for shear, torsion and

combined shear and torsion in thin walled closed tube sections respectively. The purpose of this chapter is to analyse the concept of shear flow, the effect of torsion and a combination of both, followed by their contribution to the local buckling of closed rectangular hollow sections of uniform thickness.

## 5.2 Shear in Uniform Thin-Walled Closed Rectangular Sections

Let a vertical force  $F_y$  be applied along the vertical centre-line through the shear centre E of a rectangular tube having side lengths  $b$  and  $d$  with wall thickness  $t$  as is shown in Figure 5.1 below. The second moment of this area about the  $x$  axis is given as

$$I_x = 2 \left[ \frac{bt^3}{12} + bt \left( \frac{d}{2} \right)^2 \right] + 2 \frac{td^3}{12} \approx \frac{btd^2}{2} + \frac{td^3}{6} = \frac{td^3}{6} \left[ 1 + 3 \frac{b}{d} \right] \quad (5.1)$$

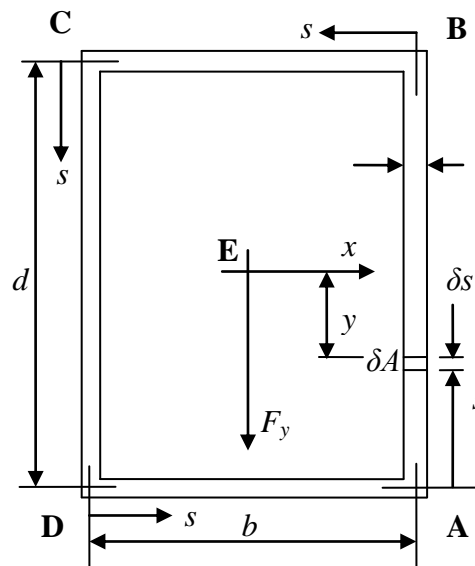


**Figure 5.1: Uniform, rectangular tube**

In thin-walled closed tubes the net shear flow  $q = q_b + q_E$ , where the basic shear flow  $q_b$  refers to any convenient origin and  $q_E$  is the shear flow existing at that origin. The  $q_b$  shear flow distribution within each side follows from Equation (2.76). For side AB with origin  $s$  at A

$$q_{AB} = \frac{F_y}{I_x} \int_A y dA = \frac{F_y t}{I_x} \int_0^s \left( s - \frac{d}{2} \right) ds = \frac{F_y t}{2I_x} (s^2 - ds) \quad (5.2)$$

Equation (5.2) gives  $q_A = q_B = 0$  for  $s=0$  and  $d$  respectively. The maximum in the parabolic distribution occurs for  $s = d/2$

$$q = -\frac{F_y t d^2}{8I_x} \quad (5.3)$$

In Equation (5.3) the negative sign implies that  $q$ -flow opposes the  $s$ -direction as is illustrated in Figure 5.2(a). For the side BC with origin  $s$  at B

$$q_{BC} = \frac{F_y}{I_x} \int_0^s \frac{d}{2} (t ds) + q_B = \frac{dF_y t s}{2I_x} \quad (5.4)$$

Equation (5.4) matches  $q_B = 0$  for  $s=0$ . Figure 5.2 (a) shows a maximum in the linear distribution for  $s = b$

$$q_C = \frac{F_y t d b}{2I_x} \quad (5.5)$$

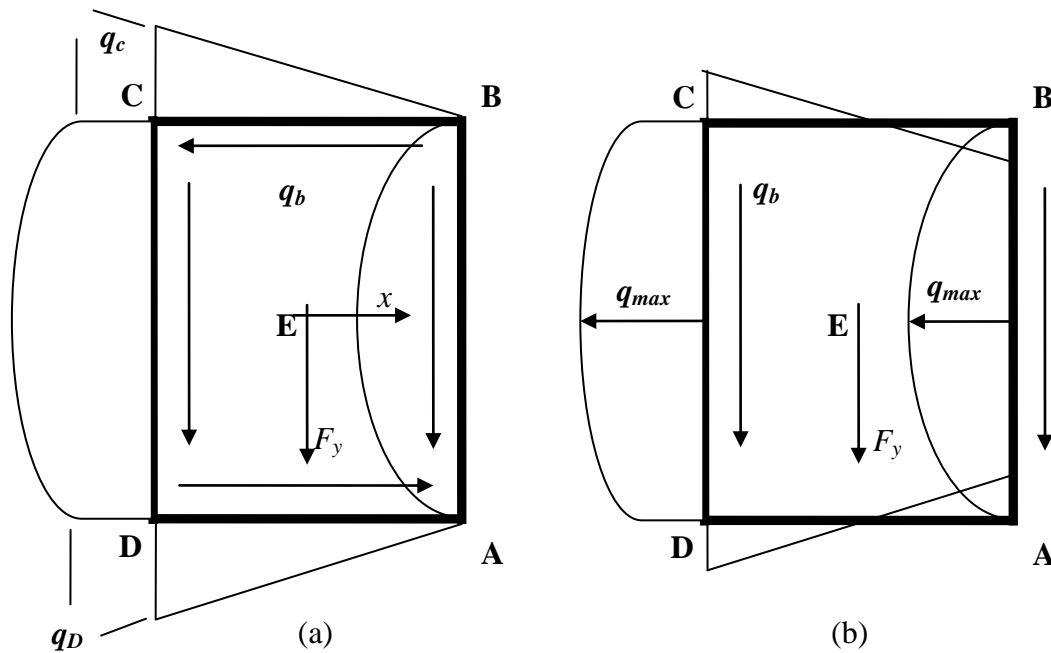


**Figure 5.2: Flexural shear flows  $q_B$  must be added to  $q_{net}$  with  $F_y$  be applied at the shear centre E**

For side CD with origin for  $s$  at C

$$q_{CD} = \frac{F_y}{I_x} \int_0^s \left( \frac{d}{2} - s \right) ds + q_C = \frac{F_y t d}{2I_x} (ds - s^2) + \frac{F_y t b d}{2I_x} \quad (5.6)$$

Equation (5.6) matches  $q_C = 0$  for  $s=0$  and gives  $q_D = q_C$  for  $s=d$ . The maximum within the parabolic shear flow distribution for CD occurs at  $s = d/2$  as is shown in Figure 5.2(a).

$$(q_{CD})_{\max} = \frac{F_y t d^2}{8I_x} + \frac{F_y t b d}{2I_x} \quad (5.7)$$

For side DA with origin for  $s$  at D

$$q_{DA} = \frac{F_y}{I_x} \int_0^s \left(-\frac{d}{2}\right) (t ds) + q_D = \frac{F_y t d}{2I_x} (-s + b) \quad (5.8)$$

Equation (5.8) gives  $q_B = 0$  for  $s=b$  and matches  $q_D$  for  $s=0$  with  $q_D$  being the maximum in the linear distribution as shown in Figure 5.2(a). Since  $F_y$  acts at the shear centre (the centroid)  $q_E$  can be found from the Equation (2.78)

$$\left[ \int_S q_{AB} \frac{ds}{t} + \int_S q_{BC} \frac{ds}{t} + \int_S q_{CD} \frac{ds}{t} + \int_S q_{DA} \frac{ds}{t} \right] + q_E \oint \frac{ds}{t} = 0 \quad (5.9)$$

Substituting the  $q_b$  distributions from Equations (5.2)-(5.8) into Equation (5.9)

$$\begin{aligned} & \frac{F_y}{2I_x} \int_0^d (s^2 - ds) ds + \frac{F_y d}{2I_x} \int_0^b s ds + \frac{F_y}{2I_x} \int_0^d (ds - s^2) ds + \frac{F_y b d}{2I_x} \int_0^d ds - \frac{F_y d}{2I_x} \int_0^b s ds + \frac{F_y b d}{2I_x} \int_0^b ds \\ & + 2q_E \left( \frac{b+d}{t} \right) = 0 \end{aligned}$$

$$\text{From which } q_E = -\frac{F_y b d t}{4I_x} \quad (5.10)$$

Equation (5.10) describes the constant shear flow in the walls of the tube that is to be added to the  $q_b$  distribution in Figure 5.2(a). This results in the net shear flow shown in Figure 5.2(b). In particular adding  $q_E$  from Equation (5.10) to Equation (5.7) leads to the equal maximum net shear flows at the centres of sides AB and CD

$$(q_{CD})_{\max} = \frac{F_y t d^2}{8I_x} \left( 1 + 2 \frac{b}{d} \right) = -(q_{AB})_{\max} \quad (5.11)$$

Similarly adding Equation (5.10) to Equation (5.5) gives the maximum shear flow at C in side BC (and at D in side DA)

$$(q_{BC})_{\max} = \frac{F_y b t d}{4I_x} = (q_{DA})_{\max} \quad (5.12)$$

Net shear flows of similar magnitude to Equation (5.12) apply to points A and B with a sign change. Substituting for  $I_x$  from Equation (5.1) into Equation (5.11) the greatest shear stress which lies at the mid-side CD is given by

$$(\tau_{CD})_{\max} = \frac{(q_{CD})_{\max}}{t} = \frac{\frac{F_y t d^2}{8} \left(1 + 2\frac{b}{d}\right)}{\frac{t^2 d^3}{6} \left(1 + 3\frac{b}{d}\right)} = \frac{3F_y \left(1 + 2\frac{b}{d}\right)}{4td \left(1 + 3\frac{b}{d}\right)} = \frac{QF_y}{td} \quad (5.13)$$

in which the geometrical coefficient  $Q$  may again reappear within the objective function. Equation (5.12) gives the lesser maximum stress at C in the side BC

$$(\tau_{BC})_{\max} = \frac{(q_{BC})_{\max}}{t} = \frac{F_y b d t}{4I_x} = \frac{F_y b d t}{4} \times \frac{6}{t^2 d^3 \left(1 + 3\frac{b}{d}\right)} = \frac{3F_y b}{2td^2 \left(1 + 3\frac{b}{d}\right)} \quad (5.14)$$

If it is required to minimise weight, the weight of the section is expressed as

$$W = 2(bt + dt)\rho L = 2td \left(1 + \frac{b}{d}\right) \rho L \quad (5.15)$$

Setting  $(\tau_{CD})_{\max} = \tau_y$  in Equation (5.13) allows the product  $td$  to be eliminated between Equations (5.13) and (5.15). This leads to the required objective function

$$\left(\frac{W}{L^3}\right)_{opt} = 2Q \left(1 + \frac{b}{d}\right) \frac{\rho}{\tau_y} \frac{F_y}{L^2} = f \left(\frac{\rho}{\tau_y}\right) \left(\frac{F_y}{L^2}\right) \quad (5.16)$$

in which the shape factor  $f$  follows from Equations (5.13) and (5.16)

$$f = 2Q \times \left(1 + \frac{b}{d}\right) = 2 \times \frac{3 \left(1 + 2\frac{b}{d}\right)}{4 \left(1 + 3\frac{b}{d}\right)} \times \left(1 + \frac{b}{d}\right) = \frac{3}{2} \times \frac{\left(1 + 2\frac{b}{d}\right) \left(1 + \frac{b}{d}\right)}{\left(1 + 3\frac{b}{d}\right)} \quad (5.17)$$

Each shear stress may be limited to  $\tau_y$  under which the limb of dimension 'a' can be arranged to buckle simultaneously, as per the general relation expressed in [14], when

$$\tau_{\max} = \tau_y = \frac{QF}{at} = K_d E_T \left( \frac{t}{a} \right)^2 \quad (5.18)$$

When sides CD and AB are allowed to buckle at a limiting plastic shear stress  $\tau_y$  then

$(\tau_{CD})_{\max} = \tau_y$  when Equation (5.18) can be expressed as follows

$$\tau_{\max} = \tau_y = \frac{QF}{dt} = K_d E_T \left( \frac{t}{d} \right)^2 \quad (5.19)$$

The optimum dimensions follow on from Equation (5.19) as

$$t_{opt} = \left( \frac{Q^2}{K_d} \right)^{1/4} \left( \frac{F_y^2}{\tau_y E_T} \right)^{1/4} \quad (5.20)$$

$$d_{opt} = \left( Q^2 K_d \right)^{1/4} \left( \frac{F_y^2 E_T}{\tau_y^3} \right)^{1/4} \quad (5.21)$$

In case of thin walled sections where the thicknesses vary all sides can be arranged to buckle from equalising their critical shear stresses. This however cannot be done in the case of a rectangular tube of uniform thickness. Here only the longer sides buckle under their optimum dimensions given in Equations (5.20) and (5.21).

### 5.3 Torsion in Uniform Thin-Walled Closed Rectangular Sections

Buckling will occur at a lower shear stress in the longer walls if this stress is to be the limiting plastic buckling stress  $\tau_y$  then the optimisation equation becomes

$$\tau_y = \frac{T}{2bdt} = K_d E_T \left( \frac{t}{d} \right)^2 \quad (5.22)$$

The buckling of the rectangular wall depends upon its depth  $d$ , length  $L$  and thickness  $t$  and the manner of its side supports. These and plasticity effects are subsumed within the buckling stress formula expressed in Equation (5.22), above [14].

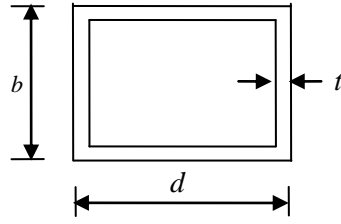


**Figure 5.3: Rectangular tube with uniform thin-walled thickness**

The optimum dimensions follow from Equation (5.22) as

$$(t)_{opt} = \left( \frac{1}{2K_d} \right)^{\frac{1}{3}} \times \left( \frac{d}{b} \right)^{\frac{1}{3}} \times \left( \frac{T}{E_T} \right)^{\frac{1}{3}} \quad (5.23)$$

$$(d)_{opt} = \left( \frac{K_d}{4} \right)^{\frac{1}{6}} \times \left( \frac{d}{b} \right)^{\frac{1}{3}} \times \left( \frac{E_T T^2}{\tau_y^3} \right)^{\frac{1}{6}} \quad (5.24)$$

The weight is expressed as

$$W = 2(bt + dt)\rho L = 2td \left( 1 + \frac{b}{d} \right) \rho L \quad (5.25)$$

Given that the shear flow  $q$  is constant in a closed tube

$$q = \tau \times t = \tau_d \times t = \tau_b \times t \quad (5.26)$$

It follows from Equations (5.22) and (5.25) that shear buckling within the section's perpendicular sides will occur simultaneously when

$$q = K_d E_d \left( \frac{t}{d} \right)^2 \times t = K_b E_b \left( \frac{t}{b} \right)^2 \times t \quad (5.27)$$

A rearrangement of Equation (5.27) gives the condition as

$$\frac{K_b}{K_d} = \left( \frac{b}{d} \right)^2 \quad (5.28)$$

Substituting Equation (5.28) into Equation (5.25) the weight becomes

$$W = 2td\left(1 + \frac{b}{d}\right)\rho L = 2\left[1 + \left(\frac{K_b}{K_d}\right)^{\frac{1}{2}}\right]\rho L \quad (5.29)$$

Substituting the optimum dimensions from Equations (5.23) and (5.24) into Equation (5.29) and dividing by  $L^3$  gives the optimum weight function

$$\begin{aligned} \left(\frac{W}{L^3}\right)_{opt} &= \left(\frac{4}{K_d}\right)^{\frac{1}{6}} \times \left[1 + \left(\frac{K_b}{K_d}\right)^{\frac{1}{2}}\right] \times \left(\frac{d}{b}\right)^{\frac{2}{3}} \times \left(\frac{\rho}{E_T^{\frac{1}{6}} \times \tau_y^{\frac{1}{2}}}\right) \times \left(\frac{T}{L^3}\right)^{\frac{2}{3}} \\ \left(\frac{W}{L^3}\right)_{opt} &= \left(\frac{4}{K_d}\right)^{\frac{1}{6}} \times \frac{\left[1 + \left(\frac{K_b}{K_d}\right)^{\frac{1}{2}}\right]}{\left(\frac{b}{d}\right)^{\frac{2}{3}}} \times \left(\frac{\rho}{E_T^{\frac{1}{6}} \times \tau_y^{\frac{1}{2}}}\right) \times \left(\frac{T}{L^3}\right)^{\frac{2}{3}} \end{aligned} \quad (5.30)$$

in which the least weight is found from minimising the shape function. That is

$$\left(\frac{4}{K_d}\right)^{\frac{1}{6}} \frac{d}{d(b/d)} \frac{\left[1 + \left(\frac{K_b}{K_d}\right)^{\frac{1}{2}}\right]}{\left(\frac{b}{d}\right)^{\frac{2}{3}}} = 0 \quad (5.31)$$

Equations (5.30) and (5.31) lead to the stationary values

$$\frac{b}{d} = 2 \quad (5.32)$$

$$f_{\min} = \left(\frac{4}{K_d}\right)^{\frac{1}{6}} \times \left[1 + \left(\frac{K_b}{K_d}\right)^{\frac{1}{2}}\right] \times \left(\frac{d}{b}\right)^{\frac{2}{3}} = \left(\frac{4}{K_d}\right)^{\frac{1}{6}} \times \left[1 + \frac{b}{d}\right] \times \left(\frac{d}{b}\right)^{\frac{2}{3}} = \frac{2.3811}{K_d^{\frac{1}{6}}} \quad (5.33)$$

Given the  $\frac{b}{d}$  ratio in Equation (5.32) the optimum dimensions in Equations (5.23) and (5.24) reduce to

$$(t)_{opt} = \left(\frac{1}{2K_d}\right)^{\frac{1}{3}} \times \left(\frac{1}{2}\right)^{\frac{1}{3}} \times \left(\frac{T}{E_T}\right)^{\frac{1}{3}} = 0.6299 \times \left(\frac{T}{K_d E_T}\right)^{\frac{1}{3}} \quad (5.34)$$

$$(d)_{opt} = \left(\frac{K_d}{4}\right)^{\frac{1}{6}} \times \left(\frac{1}{2}\right)^{\frac{1}{3}} \times \left(\frac{E_T T^2}{\tau_y^3}\right)^{\frac{1}{6}} = 0.6299 \times \left(\frac{K_d E_T T^2}{\tau_y^3}\right)^{\frac{1}{6}} \quad (5.35)$$

Hence to minimise the weight the corresponding  $\frac{b}{d}$  ratio from Equation (5.32) and then the optimum dimensions from Equations (5.34) and (5.35) are used. The procedure is assisted when one leading dimension say  $d$  is known along with the length  $L$ . Taking  $d=d_{opt}$  we can read  $K_d$  from [14] at the given  $\frac{d}{L}$  ratio and then iterate from an assumed  $\frac{b}{d}$  value until both Equations (5.24) and (5.32) are satisfied.

#### 5.4 Combined Shear and Torsion in Uniform Thin-Walled Rectangular Tube

In *Mechanics of Optimal Structural Design* [14], Rees determines from first principles the optimum dimensions for a non-uniform, thin-walled, rectangular tube having side lengths  $b$  and  $d$  with wall-thicknesses  $t_b$  and  $t_d$  when a vertical force  $F_y$  is applied to the left vertical side of a rectangular tube. Here the optimum dimensions for a uniform thin walled rectangular tube under the same conditions are determined. The analysis that follows in this section has as its basis the theory proposed within the said text and detailed in § 2.18.

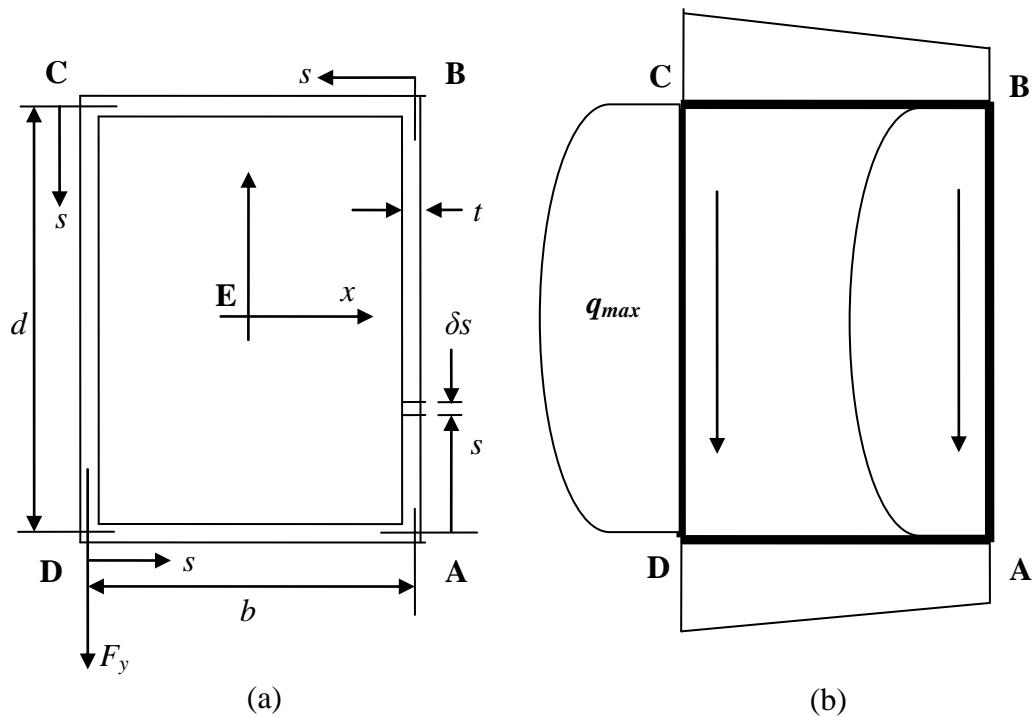


Figure 5.4: Uniform rectangular tube showing net shear flow

Let a vertical force  $F_y$  be applied to the left vertical side CD of the rectangular tube having side lengths  $b$  and  $d$  with wall thickness  $t$  as is shown in Figure 5.4 above. The  $q_b$  shear flows (see Figure 5.1) were established previously when  $F_y$  acted at the shear centre. These are from Equations (5.2) – (5.8):

$$q_{AB} = \frac{F_y t}{2I_x} (s^2 - ds) \quad (5.36)$$

$$q_{BC} = \frac{dF_y t s}{2I_x} \quad (5.37)$$

$$q_{CD} = \frac{F_y t d}{2I_x} (ds - s^2) + \frac{F_y t b d}{2I_x} \quad (5.38)$$

$$q_{DA} = \frac{F_y t d}{2I_x} (-s + b) \quad (5.39)$$

where the origin for  $s$  lies at the respective corners A,B,C and D.

It follows from Equations (5.37) and (5.38) that maxima in the linear and parabolic distributions lie along the sides BC and CD (see Figure 5.2). They are for  $s=b$  and  $s=d/2$  respectively

$$q_{BC} = \frac{F_y t d b}{2I_x} \quad (5.40)$$

$$q_{CD} = \frac{F_y t d^2}{8I_x} + \frac{F_y t b d}{2I_x} \quad (5.41)$$

where the second moment of area about the  $x$ -axis is

$$I_x = 2 \left[ \frac{bt^3}{12} + bt \left( \frac{d}{2} \right)^2 \right] + 2 \frac{td^3}{12} \approx \frac{btd^2}{2} + \frac{td^3}{6} = \frac{td^3}{6} \left[ 1 + 3 \frac{b}{d} \right] \quad (5.42)$$

The net shear flow in each side as shown in Figure 5.4(b) is found by adding  $q_0$  to  $q_b$ . Here  $q_0$  is found by applying Equation (2.82) in which moments are taken about corner A

$$F_y p = \left[ d \int_0^b q_{BC} ds + b \int_0^d q_{CD} ds \right] + 2Aq_0 \quad (5.43)$$

Substituting into Equation (5.43) the two shear flows which contribute to this moment equation from Equations (5.37) and (5.38)

$$F_y b = \frac{F_y d^2 t}{2I_x} \int_0^b s ds + \frac{F_y b t}{2I_x} \int_0^d (ds - s^2) + \frac{F_y b^2 dt}{2I_x} \int_0^d ds + 2Aq_0$$

$$F_y b = \frac{F_y d^2 t}{2I_x} \left[ \frac{s^2}{2} \right]_0^b + \frac{F_y b t}{2I_x} \left[ \frac{ds^2}{2} - \frac{s^3}{3} \right]_0^d + \frac{F_y b^2 dt}{2I_x} s \Big|_0^d + 2bdq_0 \quad (5.44)$$

Equation (5.44) leads to

$$q_0 = \frac{F_y t d^2}{24I_x} \left( 1 - 3 \frac{b}{d} \right) \quad (5.45)$$

which may be checked by taking its moments about another corner. Hence Figure 5.4 shows that the net shear flow has its greatest value ( $q_{max}$ ) at the centre of side CD. This is found by adding  $q_0$  from Equation (5.45) to Equation (5.38):

$$q_{max} = (q_{CD})_{max} = \frac{F_y t d^2}{6I_x} \left( 1 + \frac{9b}{4d} \right) \quad (5.46)$$

Substituting  $I_x$  from Equation (5.42) and with  $\tau_{max} = q_{max}/t$  the maximum shear stress in CD becomes

$$(\tau_{CD})_{max} = \frac{(q_{CD})_{max}}{t} = \frac{\frac{F_y t d^2}{6} \left( 1 + \frac{9b}{4d} \right)}{t^2 d^3 \left( 1 + 3 \frac{b}{d} \right)} = \frac{F_y \left( 1 + \frac{9b}{4d} \right)}{td \left( 1 + 3 \frac{b}{d} \right)} = \frac{QF_y}{td} \quad (5.47)$$

Limiting  $(\tau_{CD})_{max}$  to  $\tau_y$  under which buckling of side CD is to occur provides the design criterion

$$\tau_y = \frac{QF}{td} = K_d E_T \left( \frac{t}{d} \right)^2 \quad (5.48)$$

from which the optimised dimensions follow

$$t_{opt} = \left( \frac{Q^2}{K_d} \right)^{1/4} \left( \frac{F_y^2}{\tau_y E_T} \right)^{1/4} \quad (5.49)$$

$$d_{opt} = (Q^2 K_d)^{1/4} \left( \frac{F_y^2 E_T}{\tau_y^3} \right)^{1/4} \quad (5.50)$$

The optimum (minimum) weight is expressed as

$$W_{opt} = 2(bt + dt)\rho L = 2td \left( 1 + \frac{b}{d} \right) \rho L \quad (5.51)$$

and substituting for the product  $td$  from Equations (5.49) and (5.50) leads to the objective function

$$\begin{aligned} \left( \frac{W}{L^3} \right)_{opt} &= 2 \left( 1 + \frac{b}{d} \right) \frac{\rho}{L^2} \times td = 2 \left( 1 + \frac{b}{d} \right) \frac{\rho}{L^2} \times \left( \frac{Q^2}{K_d} \right)^{1/4} \left( \frac{F_y^2}{\tau_y E_T} \right)^{1/4} \times (Q^2 K_d)^{1/4} \left( \frac{F_y^2 E_T}{\tau_y^3} \right)^{1/4} \\ \left( \frac{W}{L^3} \right)_{opt} &= 2 \left( 1 + \frac{b}{d} \right) \frac{\rho}{L^2} \times Q \times \left( \frac{F_y}{\tau_y} \right) = 2Q \times \left( 1 + \frac{b}{d} \right) \times \frac{\rho}{L^2} \times \frac{F_y}{\tau_y} = f \left( \frac{\rho}{\tau_y} \right) \left( \frac{F_y}{L^2} \right) \end{aligned} \quad (5.52)$$

In Equation (5.52) the shape factor  $f$  depends upon  $Q$  given in Equation (5.47) as follows

$$f = 2Q \times \left( 1 + \frac{b}{d} \right) = \frac{2 \times \left( 1 + \frac{9b}{4d} \right) \times \left( 1 + \frac{b}{d} \right)}{\left( 1 + 3\frac{b}{d} \right)} \quad (5.53)$$

## 5.5 Summary

The concept of shear flow, torsion and the combination of the two in rectangular hollow sections of uniform thickness has been examined. In summary;

1. The net shear flow in a closed, uniform thin-walled closed rectangular section induced by a single, vertical force  $F_y$  applied through its shear centre can be expressed as a summation of the flexural shear flow  $q_B$  and a constant  $q_E$ , such that  $q = q_B + q_E$ . The shear centre in turn, is that point where a shear force can act without producing any twist in the section. The constant quantity  $q_E$  is a constant of integration with an important physical interpretation, in that when it is added to  $q_B$  it ensures that the rate of twist is zero. The net shear flow distribution in the rectangular section is shown in Figure 5.2 (b). The greatest shear stress magnitudes along the vertical and horizontal walls have been derived in Equations (5.13) and (5.14). §5.2 also details the optimum dimensions of that rectangular section, for which buckling can be arranged to occur in its longer sides first.
2. Torsion in uniform thin walled closed tube sections has been examined and an optimum design has been arrived at, to ensure that the limiting shear stress from torsion matches that required to cause shear buckling in the wall. The optimum dimensions generated for the rectangular section originate from Equation (5.22), and the dimensions are so related that shear buckling takes place within the section's perpendicular sides simultaneously. Using these optimum dimensions, the weight of the chosen rectangular section can be minimised, as outlined in §5.3.
3. The effects of combined shear and torsion in uniform thin-walled rectangular tubes has been analysed and a modified net shear flow has been derived for each side of the rectangular hollow section. The derivation for the modified net shear flow takes into account the flexural shear flow  $q_B$  and a constant  $q_o$ . The sum of these two quantities ensures static equivalence between the net shear flow and the torque that arises when  $F_y$  does not pass through the shear centre. In the case where the vertical force  $F_y$  does pass through the shear centre,  $q_o$  serves as a means of establishing the modified net shear flow, as shown in Figure 5.4 (b).

## CHAPTER 6: STRESS ANALYSIS

### 6.1 Introduction

Continuous structures balance the application of external loads with an internal resistance within their material which is commonly called stress. For a beam in particular, resisting moments arise from its internal stress to oppose the bending moments that the transverse loading produces. For example, consider the simply-supported beam with self-weight  $w/unit\ length$  subjected to four concentrated loads  $P_1 \dots P_4$  shown in Figure 6.1.

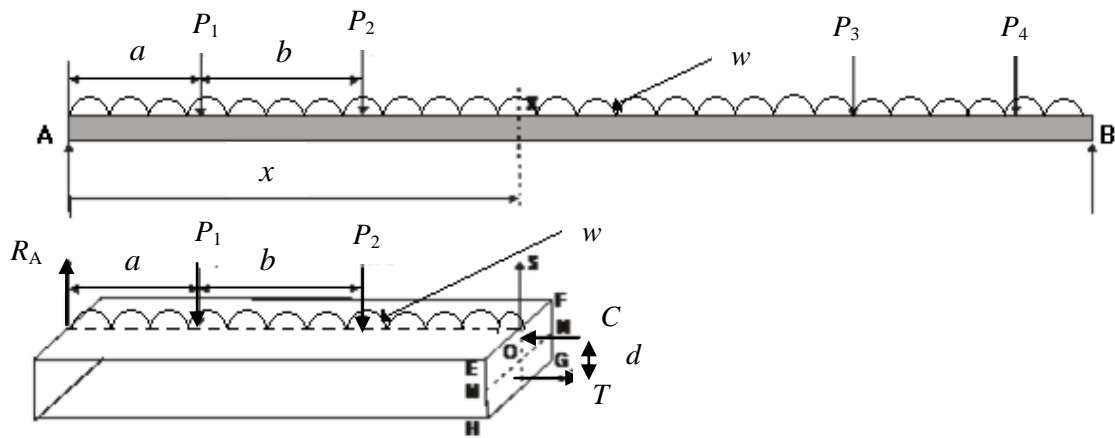


**Figure 6.1: Moment of resistance within section at  $x$ -position**

To understand how the material in the beam resists the external loads it is seen that the beam sags beneath the applied loads. Sagging creates a compressive stress within longitudinal fibres lying in the upper half of the section and tensile stress within fibres in the bottom half. A neutral (unstressed) plane MN divides each half as shown in Figure 6.1. The equivalent compressive force acting on the upper area MEFN is given by 'C'. Similarly the equivalent tensile force acting on the lower area MHGN is given by 'T'. The external loads applied and the effective shear force  $S$  acting on the plane EFGH are assumed to be concentrated on the vertical plane of symmetry, as shown. The forces that act over length AX of the beam are therefore: (a) a vertical reaction  $R_A$  at A, (b) external concentrated loads  $P_1$  and  $P_2$ , (d) uniformly distributed load  $w$  acting over the length  $x$ , (c) shear force  $S$  offered by section EFGH, (d) a compressive resistance  $C$  and (e) a tensile resistance  $T$ . The magnitudes of the

forces  $C$  and  $T$  are equal and, since they act in opposing directions, separated by a distance  $d$ , they form the section's moment of resistance:

$$M_R = Cd = Td \quad (6.1)$$

Taking moments about O gives the bending moment due to the external forces

$$M_R = R_A x - P_1(x - a) - P_2(x - a - b) - \frac{wx^2}{2} \quad (6.2)$$

In continuous beams we may equate Equations (6.1) and (6.2) when applying the principle that the moment at a given section due to externally applied loads equals the moment of resistance at that section. However, the same principle cannot be applied to telescopic beams within the discontinuous region between overlapping sections, especially where there is a sizeable gap between them. To overcome this, the authors proposed their *Tip Reaction Model* [91], the principle of which is summarised in §3.3. The stress analysis performed in [13, 92], upon the three section telescoping cantilever beam assembly forms the basis of the analysis that is detailed, within this chapter.

Consequently, the internal shear force and moment within each length may be calculated from the reactions instead of the moment of resistance used normally for a continuous beam. The shear force and bending moment variations along each length are converted to their respective stresses in the following section. The stress magnitudes are compared with those obtained from a finite element analysis. The analyses were carried out on a telescopic cantilever assembly consisting of two hollow sections, the details of which are outlined in Appendices C.1 and D.1, for both inline and offset loading scenarios, respectively.

## 6.2 Bending Stress

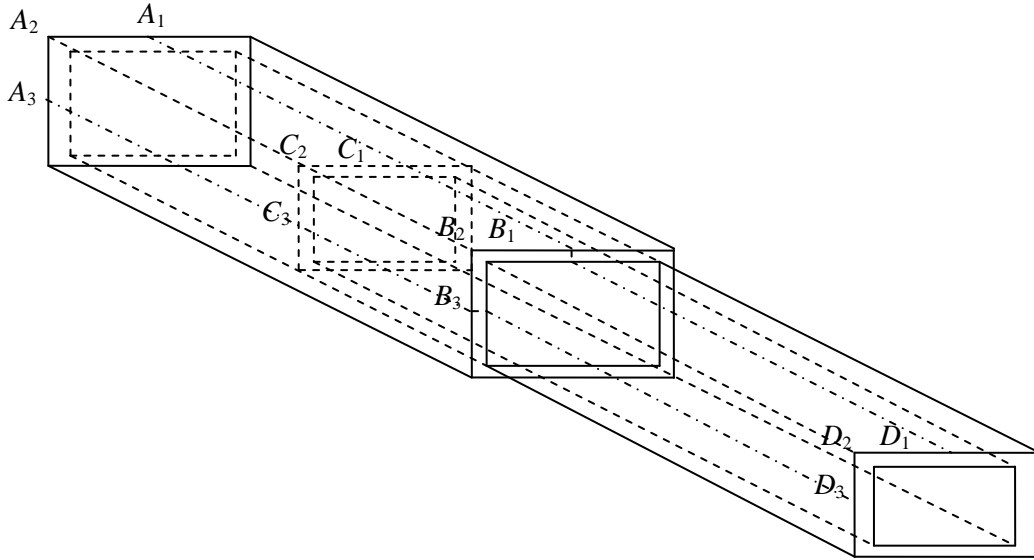


**Figure 6.2: Telescopic beam assembly with two sections**

The longitudinal bending stress in a beam is calculated from the bending moment  $M$  by a standard expression [6]:

$$\sigma = \frac{M}{I} y \quad (6.3)$$

where  $I$  is second moment of area of the beam section and  $y$  is the distance from the neutral axis at which this stress applies. Consider the beam assembly shown in Figure 6.2 and assume that it is fixed at end A and carries a tip load at  $D_1$ . Due to self-weight and the tip loading applied there will be tensile stresses in all two beam sections above the horizontal of symmetry (neutral plane) and compressive stresses below the plane of symmetry. For the each section depth  $d_1$  and  $d_2$ , the beam is represented by the vertical plane of symmetry upon which the maximum bending stress occurs at their top surfaces. These are found from Equation (6.3) as:

$$\sigma_1 = \frac{M \times d_1}{2I_1} \quad \text{and} \quad \sigma_2 = \frac{M \times d_2}{2I_2} \quad (6.4a-b)$$

The  $d$ - and  $I$ -values are referred to a chosen geometry given in Appendices C.1 and in D.1. The bending moment  $M$  in Equations 6.4a-b varies within the length in a manner provided by an  $M$ -diagram constructed from the applied loading and the tip reactions

as shown in Figure C.2 and Figure D.2. Two loading scenarios are examined in Appendices C and D respectively. Appendix C deals with an inline load applied to the telescopic assembly, whilst Appendix D examines an offset load applied to the telescopic assembly. The two load scenarios are examined in order to form a base for which the comparison of experimental, analytical and output from the software is achieved. In appended sections C.4 and D.4 the bending stresses across the entire geometry length of the telescoping assembly are attained numerically and plotted separately in Figures C.4 and D.4, for inline and offset loading of 30.55 N, respectively. This load magnitude corresponds to a  $\frac{wL}{P}$  ratio of 1. In case of the inline loading, a tip load of 30.55 N is applied at  $D_1$  as shown in Figure 6.2, whilst when subjecting the candidate assembly to offset loading, the same tip magnitude is applied, but at an offset distance of 600 mm from the same point  $D_1$ .

In similar fashion, Figures 6.5 and 6.7 presented here, within the main body of the text, graphically represent both inline and offset loading, respectively, for different  $\frac{wL}{P}$  ratios of 2, 4, 6 and 8.

### 6.3 Shear Stress

Referring to § 5.2.1 it can be seen that the shear stress distribution and shear flow in the cross section of the rectangular tube of uniform thickness is as depicted in Figure 6.3. In Figure 6.3 (b) the flexural shear flow must be added to the net shear when a vertical force  $F_y$  is applied at the shear centre.

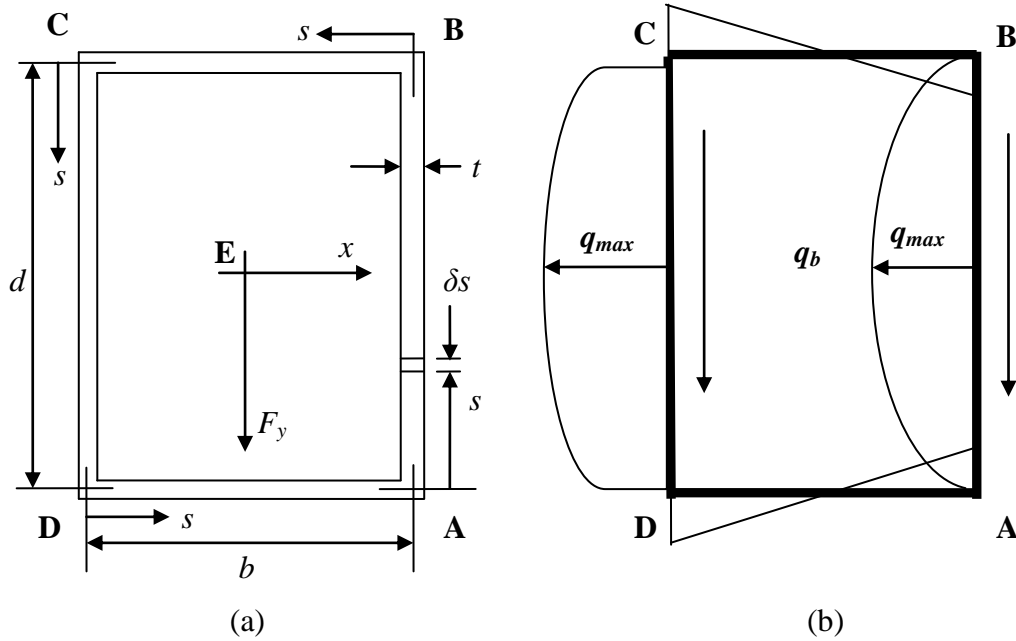


**Figure 6.3 (a) Cross section of the uniform rectangular tube (b) Net shear stress distribution in the cross section of the uniform rectangular tube**

From the detailed analysis performed in § 5.2.1 the following equations are utilised to determine the maximum magnitudes of shear stress along the vertical and horizontal walls for both the beam sections.

$$(\tau_{CD})_{\max} = \frac{(q_{CD})_{\max}}{t} = \frac{\frac{F_y t d^2}{8 I_x} \left(1 + 2 \frac{b}{d}\right)}{t} = \frac{\frac{F_y t d^2}{8} \left(1 + 2 \frac{b}{d}\right)}{t^2 d^3 \left(1 + 3 \frac{b}{d}\right)} = \frac{3 F_y \left(1 + 2 \frac{b}{d}\right)}{4 t d \left(1 + 3 \frac{b}{d}\right)} \quad (6.5)$$

$$(\tau_{BC})_{\max} = \frac{(q_{BC})_{\max}}{t} = \frac{\frac{F_y b d t}{4 I_x}}{t} = \frac{F_y b d t}{4} \times \frac{6}{t^2 d^3 \left(1 + 3 \frac{b}{d}\right)} = \frac{3 F_y b}{2 t d^2 \left(1 + 3 \frac{b}{d}\right)} \quad (6.6)$$

From Equations (6.5) and (6.6) it can be seen that the shear stress formulae can be tailored to suit each of the two beam sections that make up the composite telescoping assembly simply by substituting the required value of breadth 'b', depth 'd' and thickness 't' as is shown numerically for inline and offset loading in Appendices C.4 and D.4, respectively.

Once again in appended sections C.4 and D.4 the shear stresses across the entire geometry length of the telescoping assembly are attained numerically and plotted separately in Figures C.5 and D.5, for inline and offset loading of 30.55 N, respectively. This load is applied in the same manner for inline and offset loading as specified above in §6.2.

Figure C.5 plots both, inline loading induced, maximum shear stress distribution for the assembly on faces CD and BC of the cross section shown in Figure 6.3(a), which are plotted along the lines marked 'A<sub>3</sub>B<sub>3</sub>C<sub>3</sub>D<sub>3</sub>' and 'A<sub>2</sub>B<sub>2</sub>C<sub>2</sub>D<sub>2</sub>' along the entire length of the assembly. Figure D.5 plots both, offset loading induced, maximum shear stress distribution for the assembly on faces CD and BC of the cross section shown in Figure 6.3(a), which are plotted along the lines marked 'A<sub>3</sub>B<sub>3</sub>C<sub>3</sub>D<sub>3</sub>' and 'A<sub>2</sub>B<sub>2</sub>C<sub>2</sub>D<sub>2</sub>' along the entire length of the assembly. The values plotted in Figures C.5 and D.5, were calculated at regular intervals of 500 mm along the length of the assembly. It must be noted that these calculated values, correspond to those points where the shear stress distribution attains its maximum for the cross section at points C and at the midpoint of wall CD, respectively.

In similar fashion, Figures 6.5, 6.6, 6.8 and 6.9 are presented here in the main body of work, but for  $\frac{wL}{P}$  ratios of 2, 4, 6 and 8. Figures 6.5 and 6.6, plot the maximum shear stress distribution at face CD along the assembly length at 'A<sub>3</sub>B<sub>3</sub>C<sub>3</sub>D<sub>3</sub>' and the maximum shear stress distribution at face BC along the assembly length at 'A<sub>2</sub>B<sub>2</sub>C<sub>2</sub>D<sub>2</sub>' for inline loading corresponding to the  $\frac{wL}{P}$  ratios of 2, 4, 6 and 8, respectively. Figures 6.8 and 6.9 on the other hand, plot the maximum shear stress distribution at face CD along the assembly length at 'A<sub>3</sub>B<sub>3</sub>C<sub>3</sub>D<sub>3</sub>' and the maximum

shear stress distribution at face BC along the assembly length at 'A<sub>2</sub>B<sub>2</sub>C<sub>2</sub>D<sub>2</sub>' for offset loading corresponding to the  $\frac{wL}{P}$  ratios of 2, 4, 6 and 8, respectively.

Equations (6.3) - (6.6) may be applied to both telescopic and continuous beams when  $M$  and  $F_y$  are known. In what follows  $M$  and  $S$  are converted to their respective stress distributions from within the diagrams that show the variations in  $M$  and  $S$  over the length as in Figure C.2 and D.2. The method of constructing  $F_y$ - and  $M$ -diagrams for continuous cantilever beams, carrying combined concentrated and distributed loading, can be found in many texts [5-8, 14]. The  $F$ - and  $M$ -diagrams for a telescopic beam may be constructed separately once the tip reactions for each of Figures C.1a-c and 1a-c are known and then superimposed to find their net values within the overlaps.

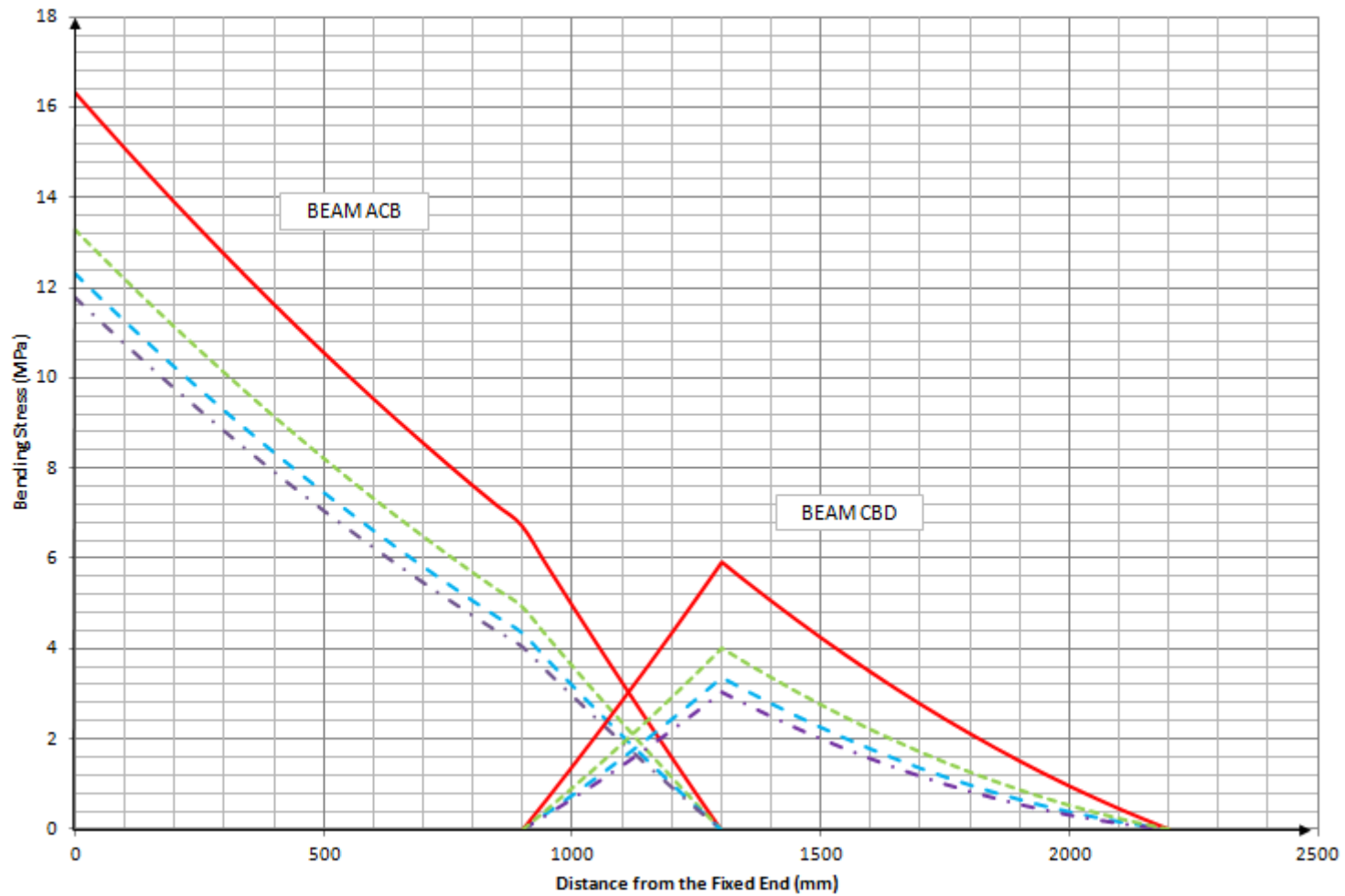


Figure 6.4: Inline loading induced bending stress (MPa) vs distance from the fixed end for 400 mm overlap along  $A_1C_1B_1D_1$  as marked in Figure 6.2, for the two section telescopic cantilever beam assembly having individual part dimensions outlined in C.1  
 (Key: —  $wL/P=2$ ; .....  $wL/P=4$ ; - - -  $wL/P=6$ ; - . -  $wL/P=8$ )

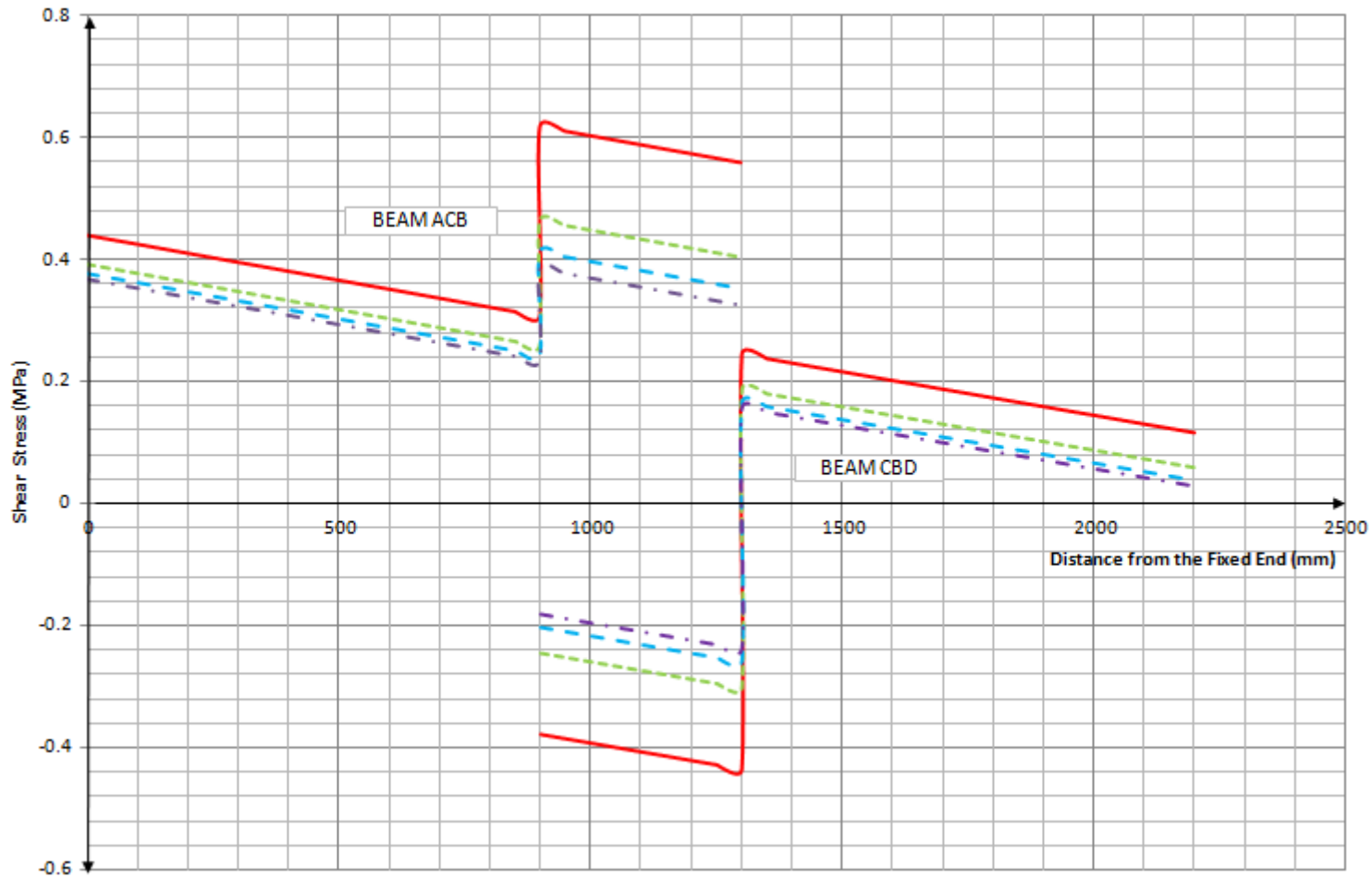


Figure 6.5: Inline loading induced shear stress (MPa) vs distance from the fixed end for 400 mm overlap along  $A_3C_3B_3D_3$  as marked in Figure 6.2, for the two section telescopic cantilever beam assembly having individual part dimensions outlined in Appendix C.1 (Key: —  $wL/P=2$ ; .....  $wL/P=4$ ; - - -  $wL/P=6$ ; - · -  $wL/P=8$ )

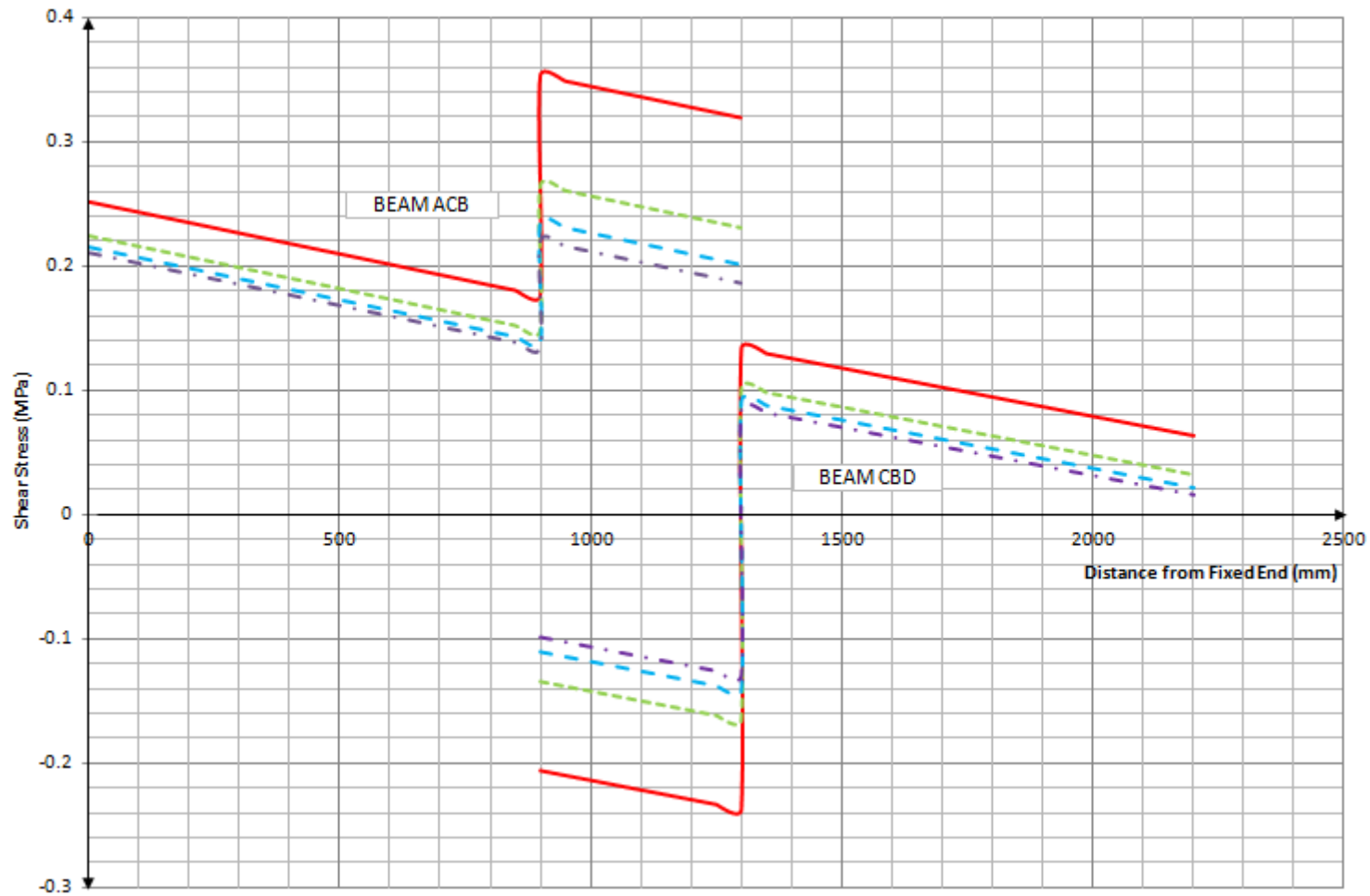


Figure 6.6: Inline loading induced Shear Stress (MPa) vs Distance from the Fixed End for 400mm overlap along  $A_2C_2B_2D_2$  as marked in Figure 6.2, for the two section telescopic cantilever beam assembly having individual part dimensions outlined in Appendix C.1  
 (Key: —  $wL/P=2$ ; .....  $wL/P=4$ ; - - -  $wL/P=6$ ; - . -  $wL/P=8$ )

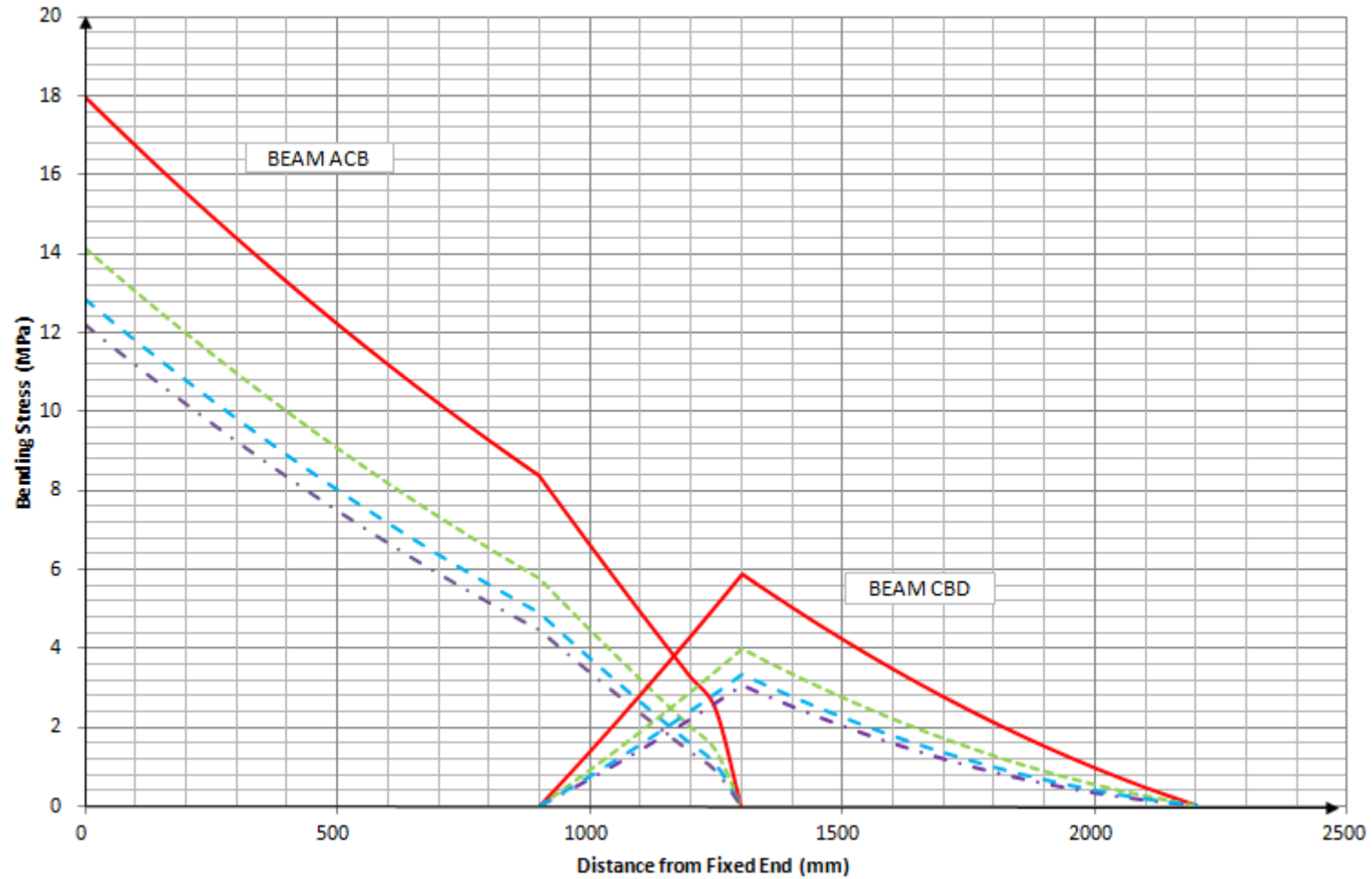


Figure 6.7: Offset loading induced bending stress (MPa) vs distance from the fixed end for 400 mm overlap along  $A_1C_1B_1D_1$  as marked in Figure 6.2, for the two section telescopic cantilever beam assembly having individual part dimensions outlined in Appendix D.1  
 (Key: —  $wL/P=2$ ; .....  $wL/P=4$ ; - - -  $wL/P=6$ ; - · -  $wL/P=8$ )

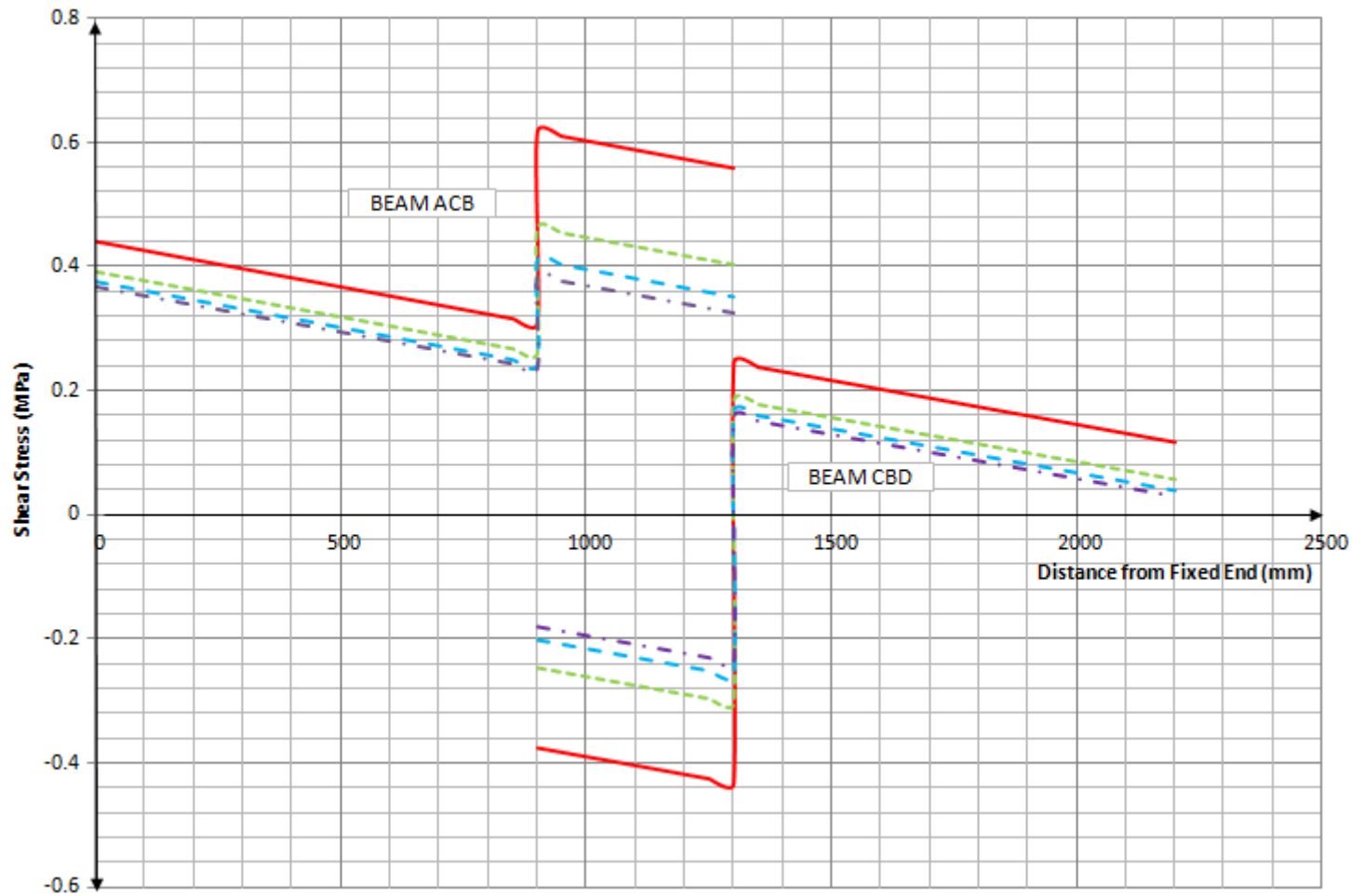


Figure 6.8: Offset loading induced shear stress (MPa) vs distance from the fixed end for 400 mm overlap along  $A_3C_3B_3D_3$  as marked in Figure 6.2, for the two section telescopic cantilever beam assembly having individual part dimensions outlined in Appendix D.1  
 (Key: —  $wL/P=2$ ; .....  $wL/P=4$ ; - - -  $wL/P=6$ ; - · -  $wL/P=8$ )

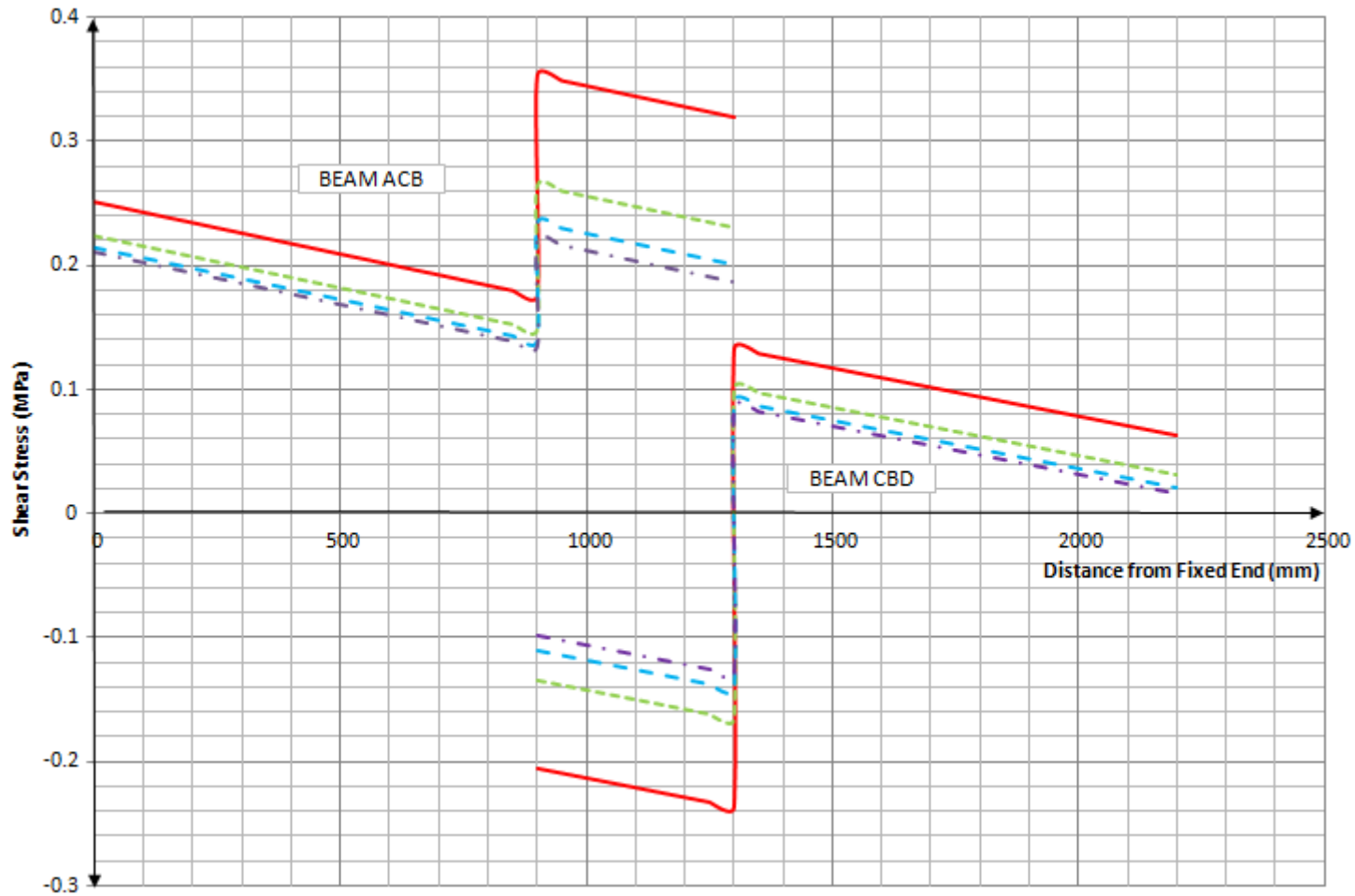


Figure 6.9: Offset loading induced shear stress (MPa) vs distance from the fixed end for 400 mm overlap along  $A_2C_2B_2D_2$  as marked in Figure 6.2, for the two section telescopic cantilever beam assembly having individual part dimensions outlined in Appendix D.1  
 (Key:  $wL/P=2$ ;  $wL/P=4$ ;  $wL/P=6$ ;  $wL/P=8$ )

## 6.4 Summary

Appendices C and D detail the bending and shear stress analysis of the two section telescopic cantilever beam assembly, for inline and offset loading, respectively. The tip load applied in both cases has a magnitude of 30.55 N. This loading corresponds to a  $\frac{wL}{P}$  ratio of 1. Corresponding to this ratio, bending moment and shear force distributions were created for both, inline and offset loading scenarios, as shown in Figures C.2 and D.2 respectively. For the offset loading induced stress analysis of the telescopic assembly, a separate torque diagram was also produced, in addition to the bending moment and shear force diagram. This was done to highlight the fact that the torque applied has a constant magnitude and that it induces a constant twisting moment upon the assembly.

The intention of the analysis performed in Appendices C and D, was to extract both bending and shear stresses induced by both types of loading and to present them in graphical form, to act as a benchmark for what has been done in this chapter. Using  $\frac{wL}{P}$  ratios of 2, 4, 6 and 8, equivalent tip loads were applied to the structure and the bending and shear stresses were plotted, in this chapter as can be seen from Figures 6.4 – 6.9. While bending stress within the assembly attains its maximum magnitude along the line marked  $A_1B_1C_1D_1$ , as shown in Figure 6.2, the shear stress distribution within the hollow rectangular section, attains its maxima, at points C and D on the horizontal walls, and at the mid-plane of side CD along the perpendicular walls, as is depicted in Figure 6.3 (b). It is at these points, at 50 mm length intervals, that the bending and shear stresses were calculated and plotted. Further conclusions are drawn from the stress analysis undertaken in this chapter, in §9.1.2. To conclude:

1. For  $\frac{wL}{P}$  ratios of 2, 4, 6 and 8, the corresponding inline loading induced bending stress distribution is plotted in Figure 6.4, against the distance from the fixed end, for a 400 mm overlap. For the same ratios, the related inline loading induced shear stresses are calculated and plotted at the locations, as mentioned above, where they attain their maximum magnitude, in Figures 6.5 and 6.6.

2. For  $\frac{wL}{P}$  ratios of 2, 4, 6 and 8, the corresponding offset loading induced bending stress distribution is plotted in Figure 6.7, against the distance from the fixed end, for a 400 mm overlap. For the same ratios, the equivalent offset loading induced shear stresses are calculated and plotted at the locations, as mentioned above, where they attain their maximum magnitude, in Figures 6.8 and 6.9.
  
3. The greatest theoretically derived bending stress magnitude of 16 MPa and 18 MPa induced by inline and offset loading in the two section telescoping assembly, respectively is in turn evident from Figures 6.4 and 6.7 for  $\frac{wL}{P}$  ratio of 2. These values show that the structure remains elastic given a yield stress for a medium carbon steel of say, 400 MPa. Similarly the greatest theoretically derived shear stress magnitudes for both inline and offset loading, determined along the horizontal and vertical walls of the assembly fall well within the yield stress magnitude. Nowhere does the shear stress magnitude become zero despite it having a relatively low magnitude compared to the accompanying bending stress.

## CHAPTER 7: FINITE ELEMENT ANALYSIS

### 7.1 Introduction

This chapter covers the extensive Finite Element Analysis that has been covered over the course of undertaking this thesis. The primary aim of this chapter involving the use of the Finite Element Analysis software package ABAQUS/CAE is to act as a means of verification and validation of theoretical results produced in addition to the experimental work performed, which is detailed in the following chapter. Figure 7.1 details the methodology that was followed to achieve the afore-mentioned objective. The three outcomes desired from the FEA are: (a) Overall Deflection of the two section telescopic assembly for both inline and offset loading (b) Bending and Shear Stress determination at regular intervals along the length of the assembly and (c) Determination of the Critical Buckling Load for the telescopic beam assembly whose individual part dimensions are detailed in Table 7.1.

Figure 7.1 shows how the overall structure was divided into two beams and wear pads, each of which was sketched and extruded. Each of the individual part instances thus generated were in turn individually assigned section and material properties followed by their assembly, to give the overall telescopic beam assembly. Individual steps were defined in order to determine the various parameters. The telescopic beam assembly now has ties defined between each of the different entities that constitute the overall assembly following which the required load and boundary conditions are applied to the model so as to simulate as closely as is possible the real working environment of the physical assembly. Meshing the entire assembly allows for the determination of the overall deflection and the bending and shear stresses at specified intervals for comparisons with theoretical and experimental results. Once meshing has been completed the telescopic beam assembly is subjected to the first of a series of analysis runs were conducted in order to determine three specific outcomes as mentioned earlier. Tables 7.1, 7.2 and 7.3 highlight the different FEA approaches that were adopted for tip deflection analysis, stress analysis and critical buckling load determination, respectively. Appendix G elaborates in exhaustive detail how ABAQUS was used to generate the outcomes as outlined in Tables 7.2, 7.3 and 7.4, for the two section telescopic cantilever beam assembly, whose individual parts dimensions are outlined in Table 7.1.

Appendices E and F provide details of the FEA that were carried on a three section telescopic cantilever beam assembly in order to obtain overall deflection and stress values respectively

[91, 92]. The same approach was used except that the assembly in this thesis deals with a two beam rather than a three beam telescopic cantilever beam assembly. In addition to these, the critical buckling load of the telescopic beam assembly was also determined.

**Table 7.1: Dimensional properties of the simulated two section telescopic cantilever beam assembly**

Section	Material	Size		Thickness (T mm)	Length (L mm)	Unit Weight (N/mm <sup>3</sup> )	Young's Modulus (N/mm <sup>2</sup> )	Poisson's Ratio
		H mm	Bmm					
<b>BEAM 1 (Fixed End)</b>	Steel	60	40	1.55	1300	7.85x10 <sup>-9</sup>	210000	0.3
<b>BEAM 2 (Free End)</b>	Steel	50	30	1.55	1300	7.85x10 <sup>-9</sup>	210000	0.3
<b>Wear Pads x 7</b>	Tufnell	2	30	2	100	1.08x10 <sup>-9</sup>	34000	0.4

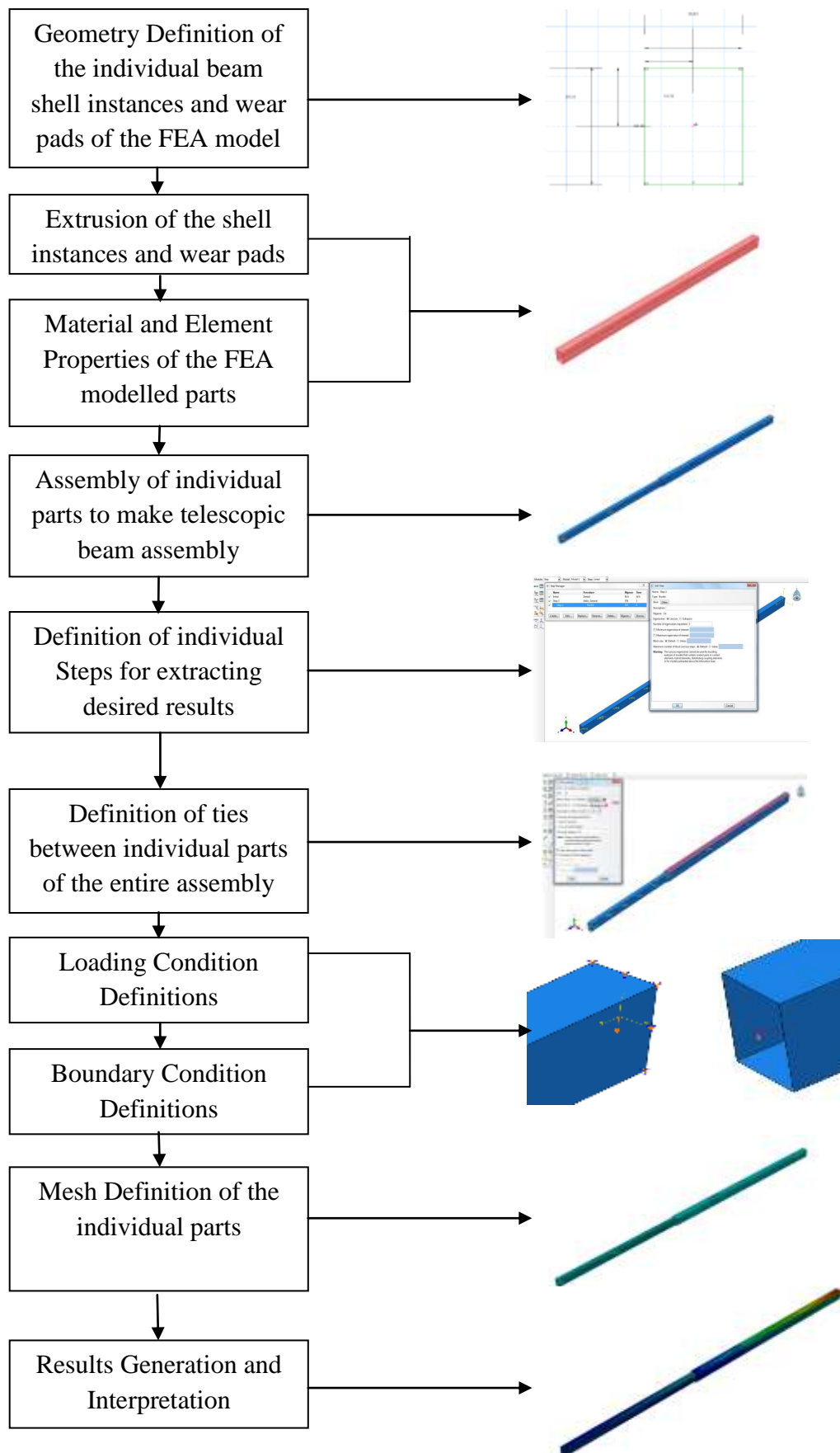


**Figure 7.1: ABAQUS/CAE Pictorial Methodology**

**Table 7.2: ABAQUS/CAE Procedure for Tip Deflection Analysis**

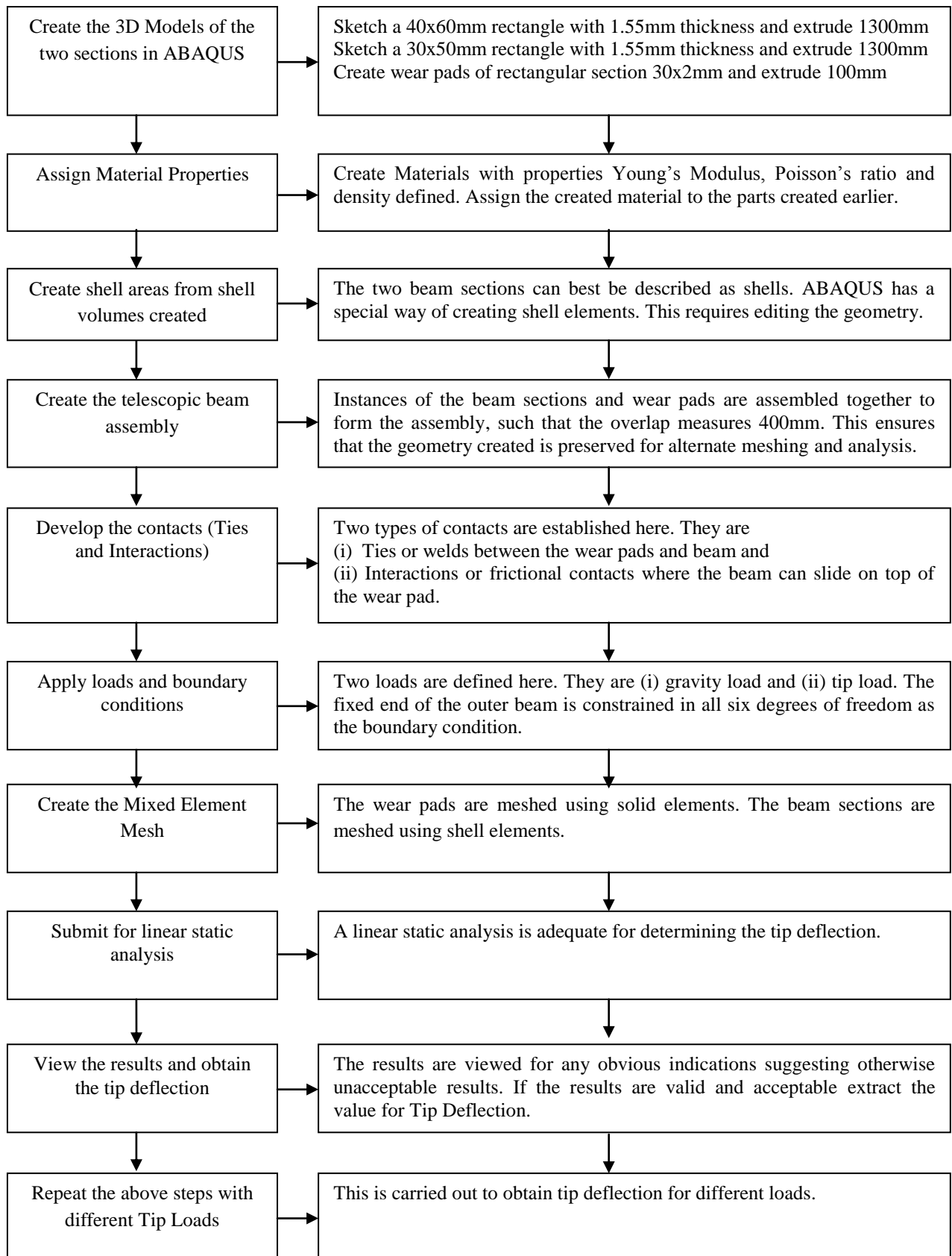


**Table 7.3: ABAQUS/CAE Procedure for Bending and Shear Stress Analysis**

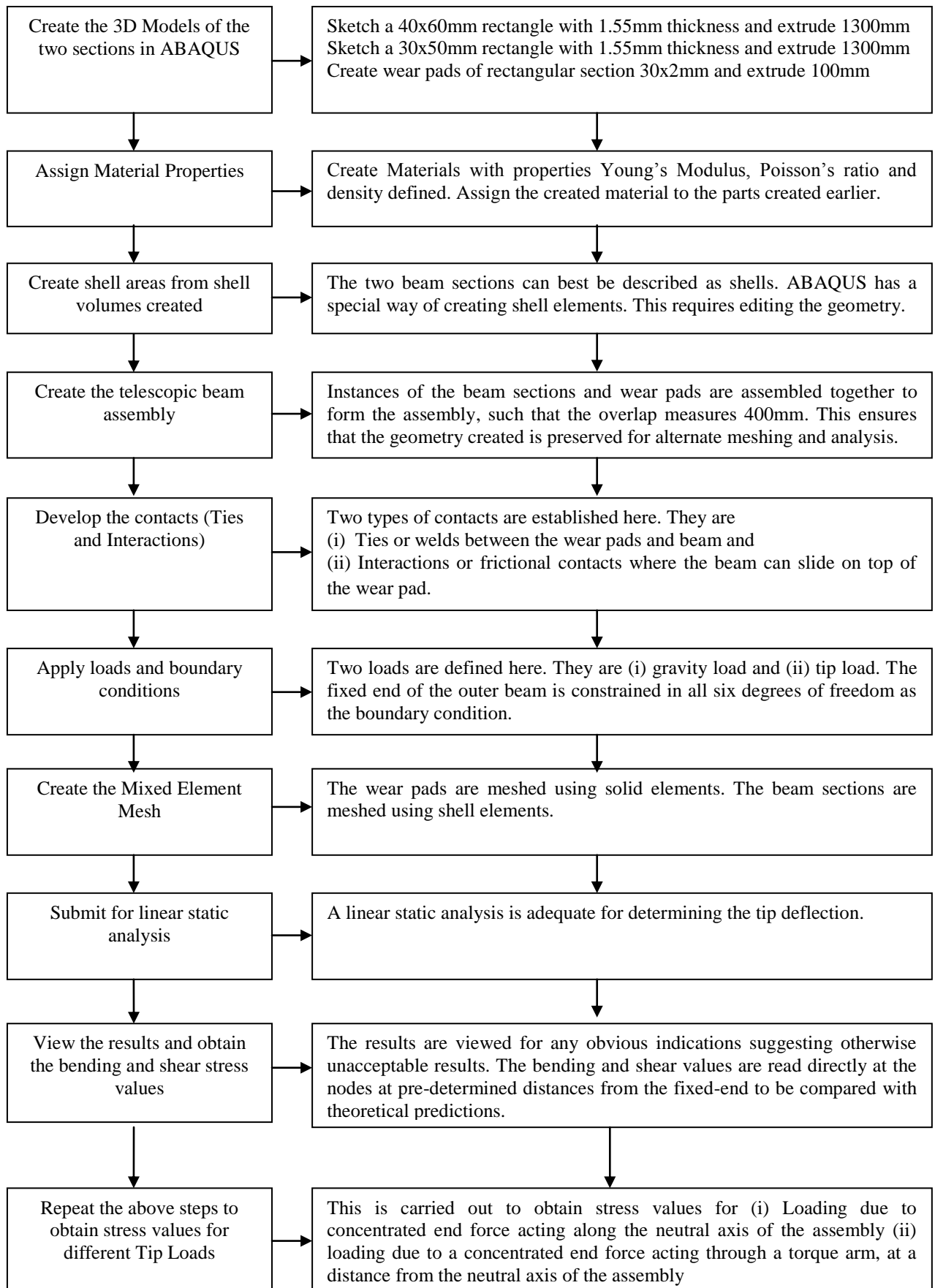
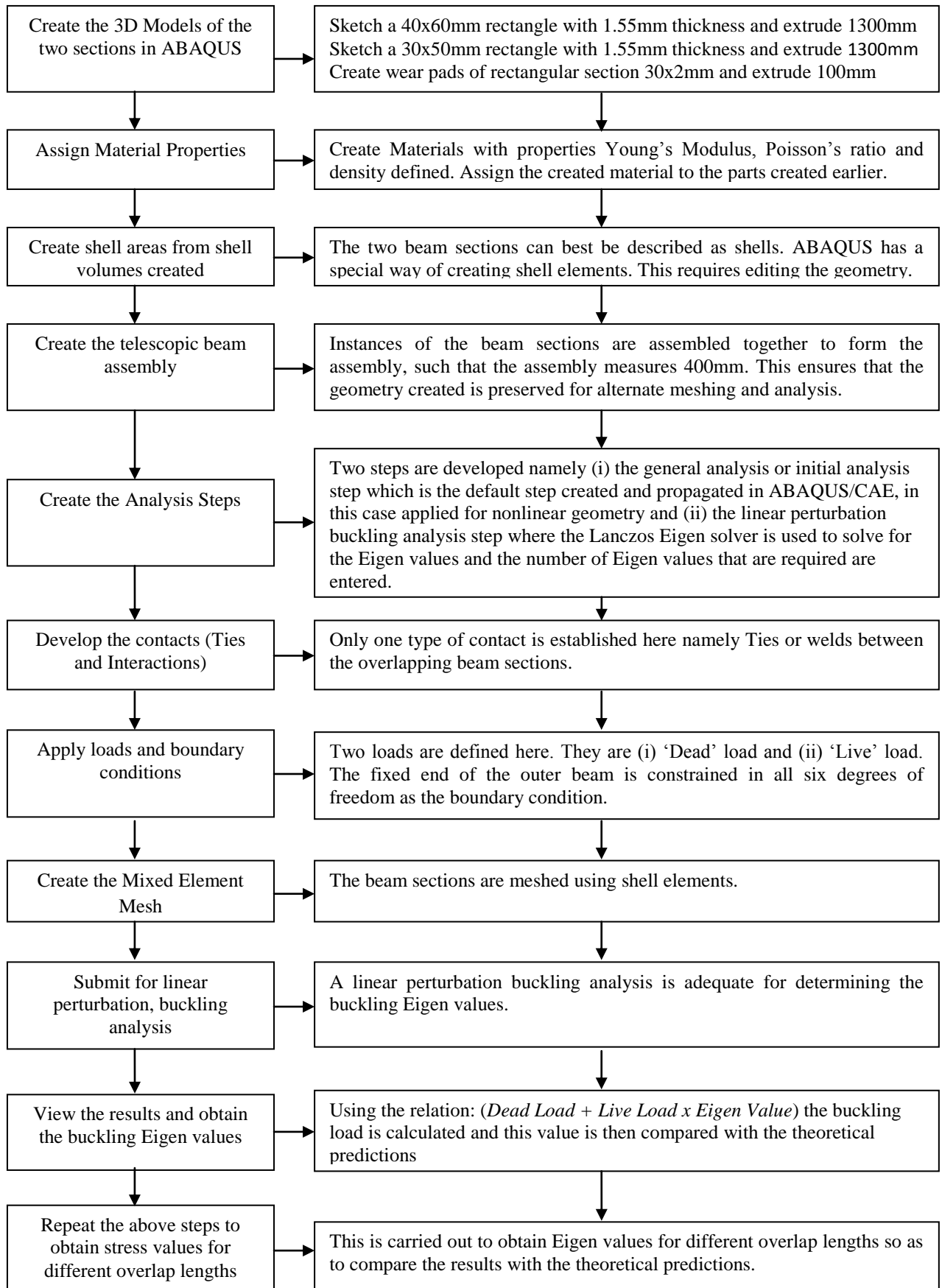


**Table 7.4: ABAQUS/CAE Procedure for determining Critical Buckling Load**



## 7.2 Deflection Analysis using ABAQUS

Tip deflections for varying inline tip loads are extracted from the FEA software and graphs of the non dimensionalised parameter  $\frac{y}{y_0}$  against the overlap ratios ' $\alpha$ ' varying from 0.2 to 0.8, in increments of 0.2 are plotted for differing  $\frac{wL}{P}$  ratios of 10, 1, 0.1 and 0.01, and shown in Figure 7.2. The methodology and reasoning behind this graphical representation are explained in detail in § 3.4.1. Following the procedure for tip deflection determination as explained in detail in Table 7.2, the end deflections for increasing load magnitudes are computed for the varying  $\frac{wL}{P}$  ratios, for differing overlap ratios ' $\alpha$ '. This involves repeated simulations using ABAQUS, and extracting the tip deflection of the assembly, for all values of the overlap ratio parameter  $\alpha$ , for the different tip loadings corresponding to their equivalent  $\frac{wL}{P}$  ratios. The procedure detailed in Table 7.2, is repeated till this objective is achieved. The results are extracted using the techniques outlined in G.9.1. In similar fashion, deflection curves were generated to match the experimentally and theoretically derived plots, as is shown in comprehensive detail in Figure 9.1.

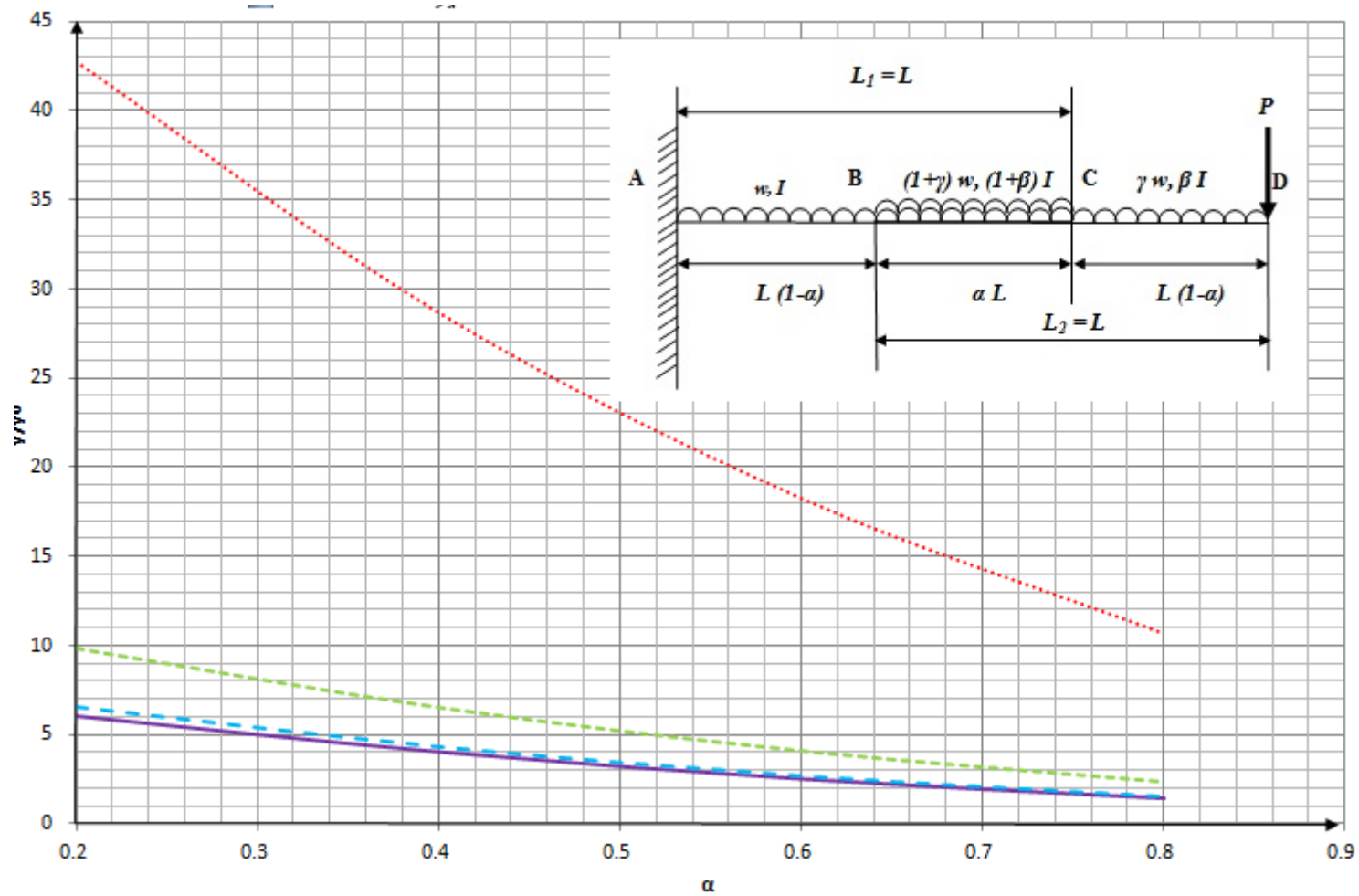


Figure 7.2: FEA generated deflection curves vs. overlap ratio  $\alpha$ , where  $\alpha$  varies from 0.2 to 0.8, in increments of 0.2, for the two section telescopic cantilever beam assembly having individual part dimensions outlined in Table 7.1.

(Key:.....  $wL/P=10$ ; .....  $wL/P=1$ ; - - -  $wL/P=0.1$ ; —  $wL/P=0.01$ )

### 7.3 Stress Analysis using ABAQUS

The bending stress values along the top line of symmetry of the assembly and the corresponding shear stress values along the top face and side walls are obtained at regular intervals of 50 mm from the fixed end. The results are displayed for both loading scenarios namely the inline and offset loading cases. The two load scenarios are examined in order to form a base for which the comparison of experimental, analytical and output from the software is achieved. The bending stresses across the entire geometry length of the telescoping assembly are attained at intervals of 50 mm and represented graphically in Figures 7.3 and 7.6 for both inline and offset loading, respectively, for different  $\frac{wL}{P}$  ratios of 2, 4, 6 and 8. The extracted shear stress values are in turn plotted in

Figures 7.4, 7.5, 7.7 and 7.8, for  $\frac{wL}{P}$  ratios of 2, 4, 6 and 8. Figure 7.4 plots the maximum value of shear stress induced by inline loading at the side walls of the telescoping assembly along the line marked as 'A<sub>3</sub>B<sub>3</sub>C<sub>3</sub>D<sub>3</sub>'. Figure 7.5 plots the maximum value of shear stress induced by inline loading along the top face of the telescoping assembly along the line marked 'A<sub>2</sub>B<sub>2</sub>C<sub>2</sub>D<sub>2</sub>'. Figures 7.7 and 7.8 were similarly plotted but for offset loading. The stress analysis results are obtained using the strategy outlined in Table 7.3 whilst the extraction of stress values is accomplished using the techniques detailed in Appendix G.9.2.

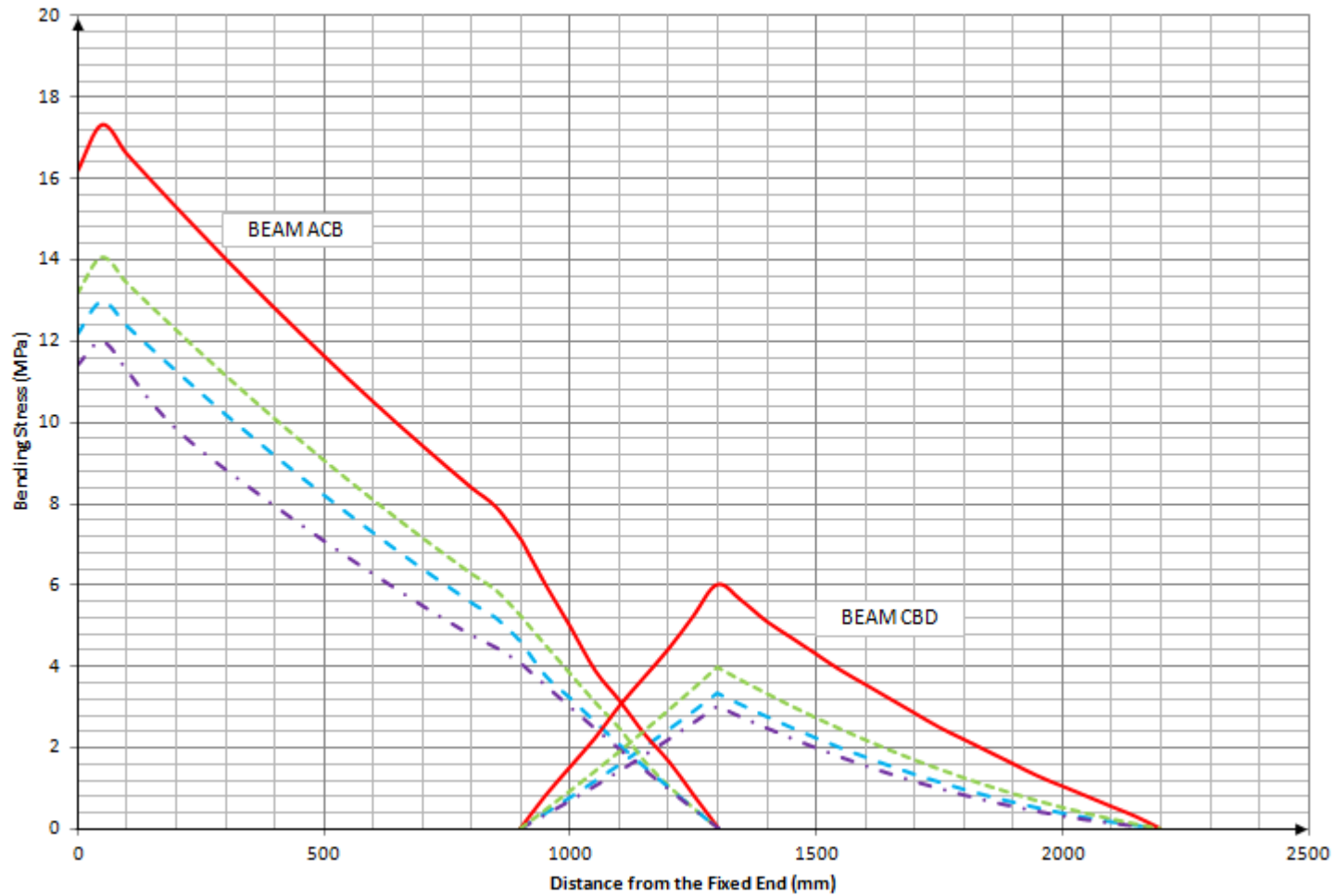


Figure 7.3: Inline loading induced bending stress (MPa) vs distance from the fixed end along  $A_1C_1B_1D_1$ , as marked in Figure 6.2, for the two section telescopic cantilever beam assembly having individual part dimensions outlined in Table 7.1, and an overlap of 400 mm  
 (Key: —  $wL/P=2$ ; .....  $wL/P=4$ ; - - -  $wL/P=6$ ; - . -  $wL/P=8$ )

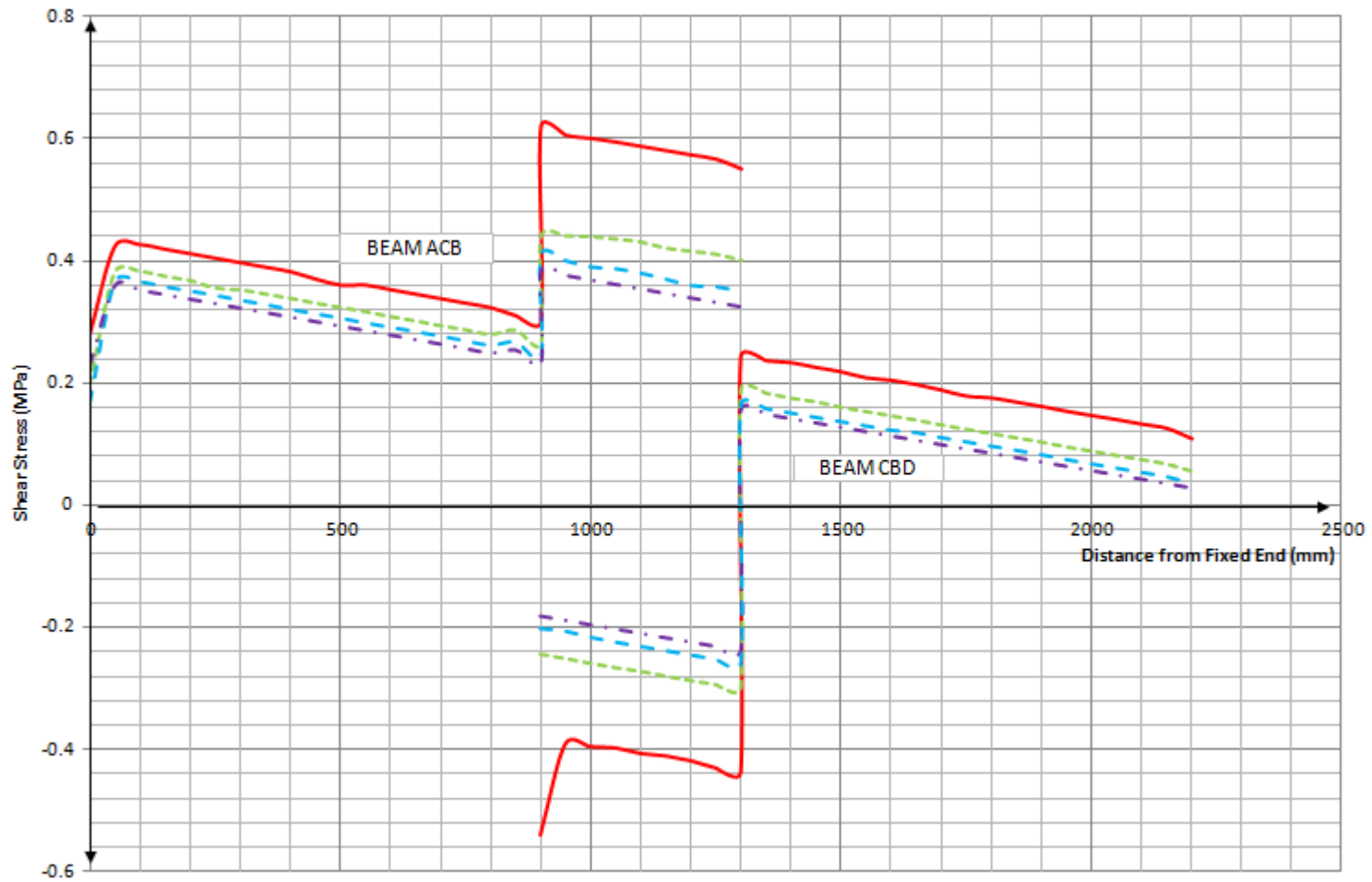
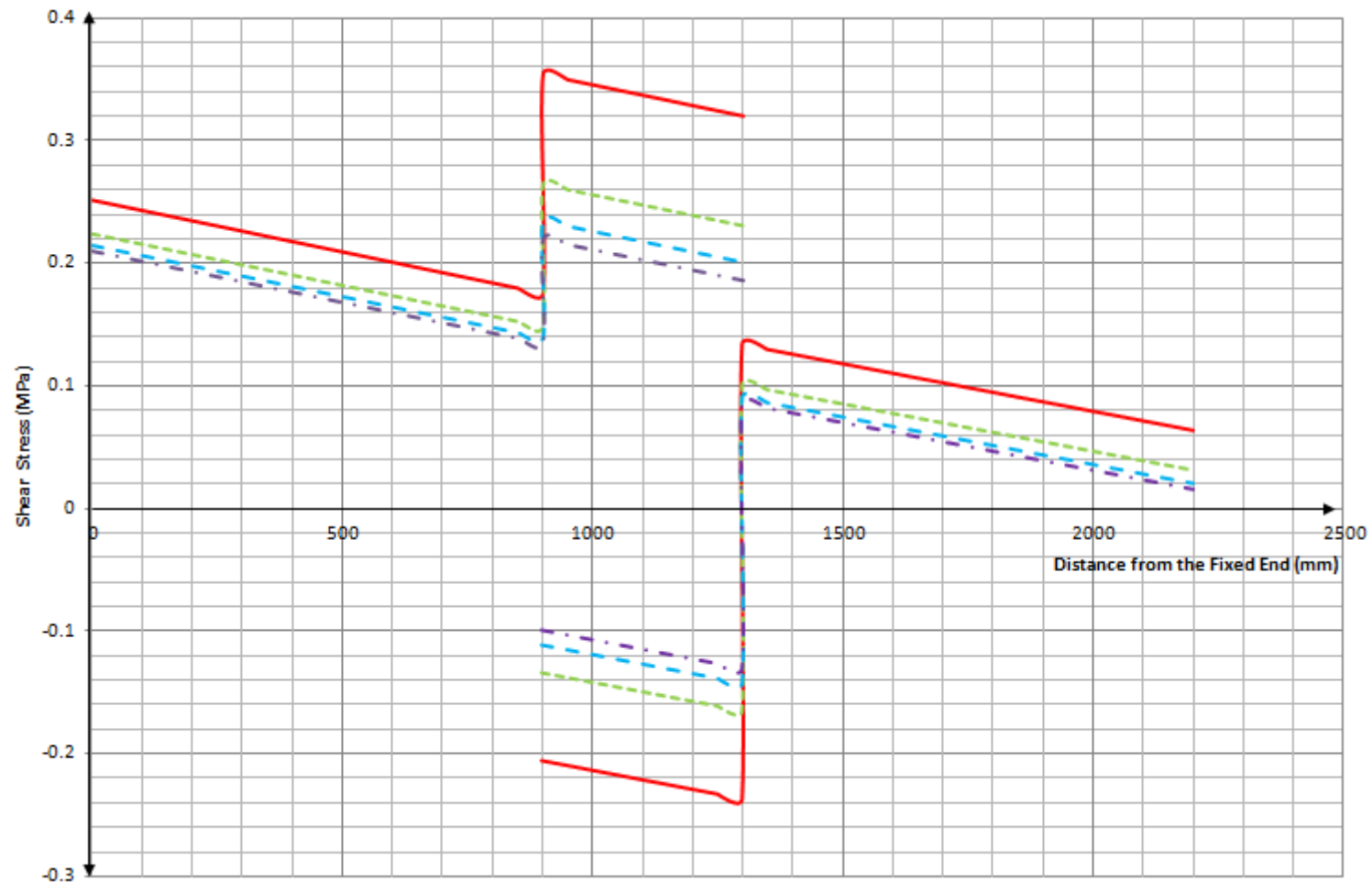


Figure 7.4: Inline loading induced shear stress (MPa) vs distance from the fixed end along  $A_3C_3B_3D_3$ , as marked in Figure 6.2, for the two section telescopic cantilever beam assembly having individual part dimensions outlined in Table 7.1, and an overlap of 400 mm (Key:  $wL/P=2$ ;  $wL/P=4$ ;  $wL/P=6$ ;  $wL/P=8$ )



**Figure 7.5: Inline loading induced shear stress (MPa) vs distance from the fixed end along  $A_2C_2B_2D_2$ , as marked in Figure 6.2, for the two section telescopic cantilever beam assembly having individual part dimensions outlined in Table 7.1, and an overlap of 400 mm (Key: —  $wL/P=2$ ; - - -  $wL/P=4$ ; - - -  $wL/P=6$ ; - . -  $wL/P=8$ )**

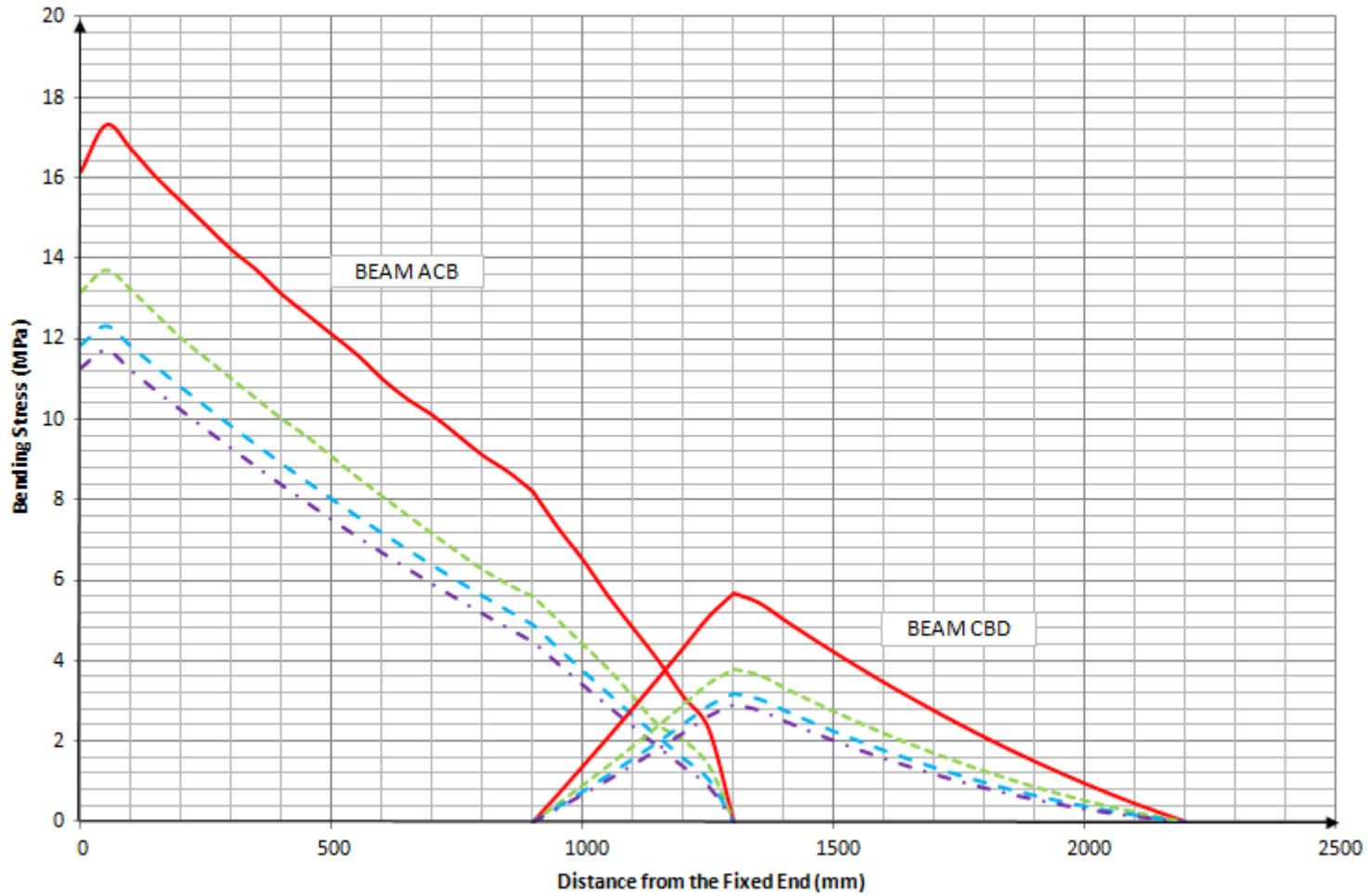


Figure 7.6: Offset loading induced bending stress (MPa) vs distance from the fixed end along  $A_1C_1B_1D_1$ , as marked in Figure 6.2, for the two section telescopic cantilever beam assembly having individual part dimensions outlined in Table 7.1, and an overlap of 400 mm (Key: —  $wL/P=2$ ; .....  $wL/P=4$ ; - - -  $wL/P=6$ ; - · -  $wL/P=8$ )

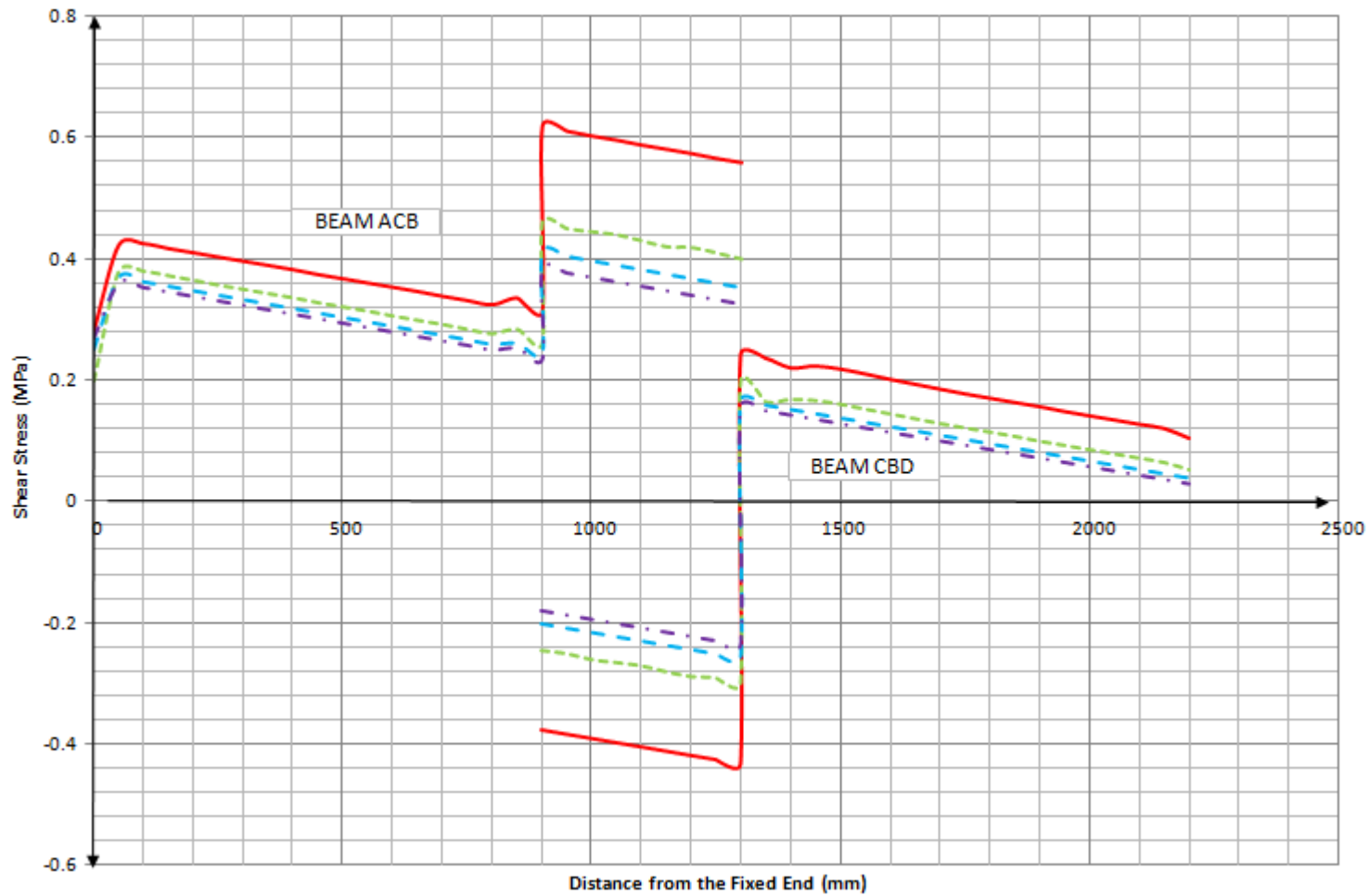
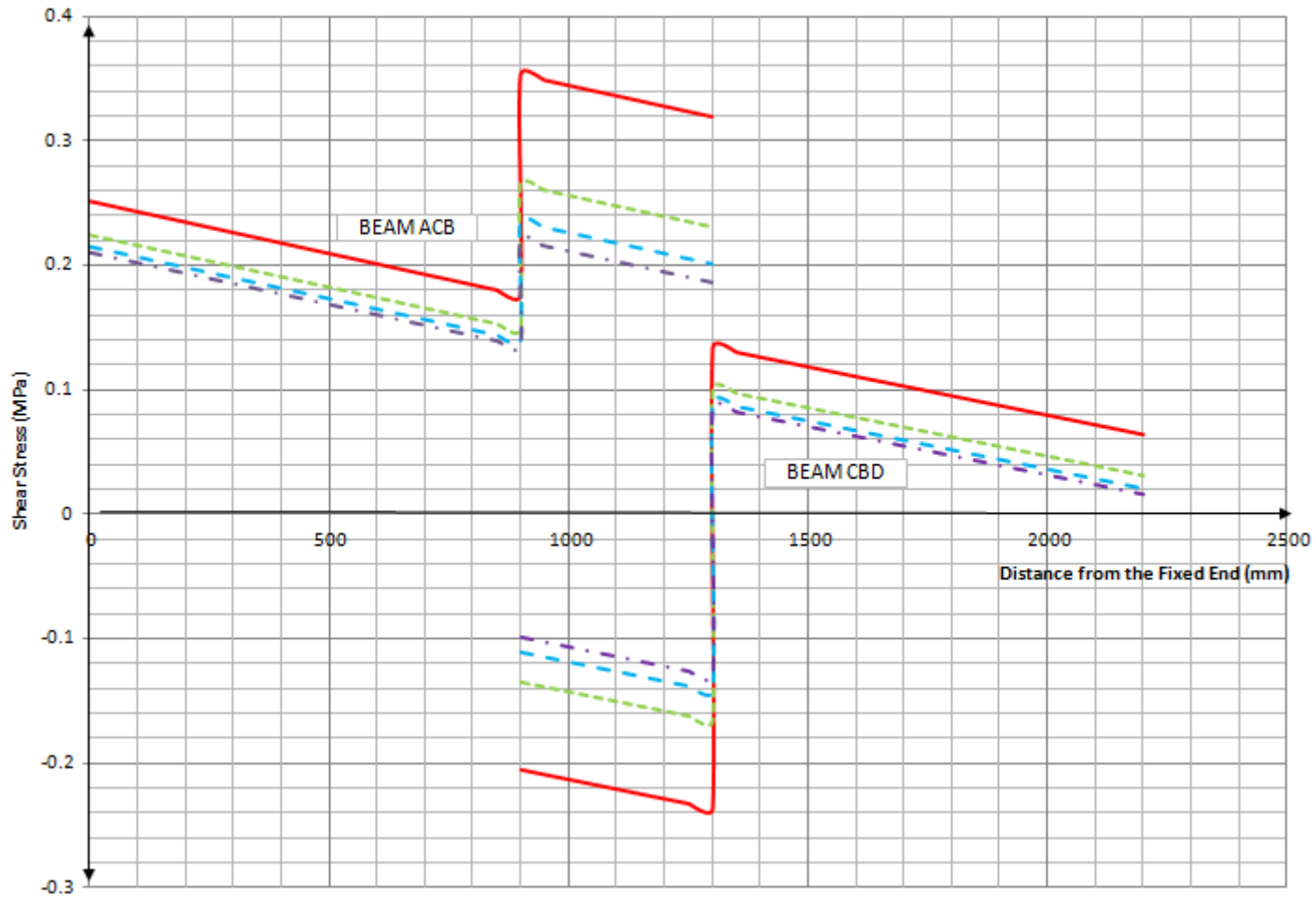


Figure 7.7: Offset loading induced shear stress (MPa) vs distance from the fixed end along  $A_3C_3B_3D_3$ , as marked in Figure 6.2, for the two section telescopic cantilever beam assembly having individual part dimensions outlined in Table 7.1, and an overlap of 400 mm (Key: —  $wL/P=2$ ; .....  $wL/P=4$ ; - - -  $wL/P=6$ ; - · -  $wL/P=8$ )



**Figure 7.8: Offset loading induced shear stress (MPa) vs distance from the fixed end along  $A_2C_2B_2D_2$ , as marked in Figure 6.2, for the two section telescopic cantilever beam assembly having individual part dimensions outlined in Table 7.1, and an overlap of 400 mm**  
**(Key: —  $wL/P=2$ ; .....  $wL/P=4$ ; - - -  $wL/P=6$ ; - . -  $wL/P=8$ )**

## 7.4 Buckling Analysis using ABAQUS

Critical Buckling loads for the two section telescoping cantilever beam assembly are determined using the strategy explained in detail in Table 7.4. The values were determined for overlap ratios from 0.2 to 0.8 in increasing intervals of 0.2 and extracted as explained in G.9.3 and plotted as shown in Figure 7.9. The graph in Figure 7.9 plots the non dimensionalised parameter  $\frac{P_{cr}}{P_{Eu}}$  against the increasing overlap ratio ' $\alpha$ '.  $P_{cr}$  is the critical

buckling load whilst  $P_{Eu}$  represents the Euler buckling load of the two section telescoping assembly as explained in § 4.9.

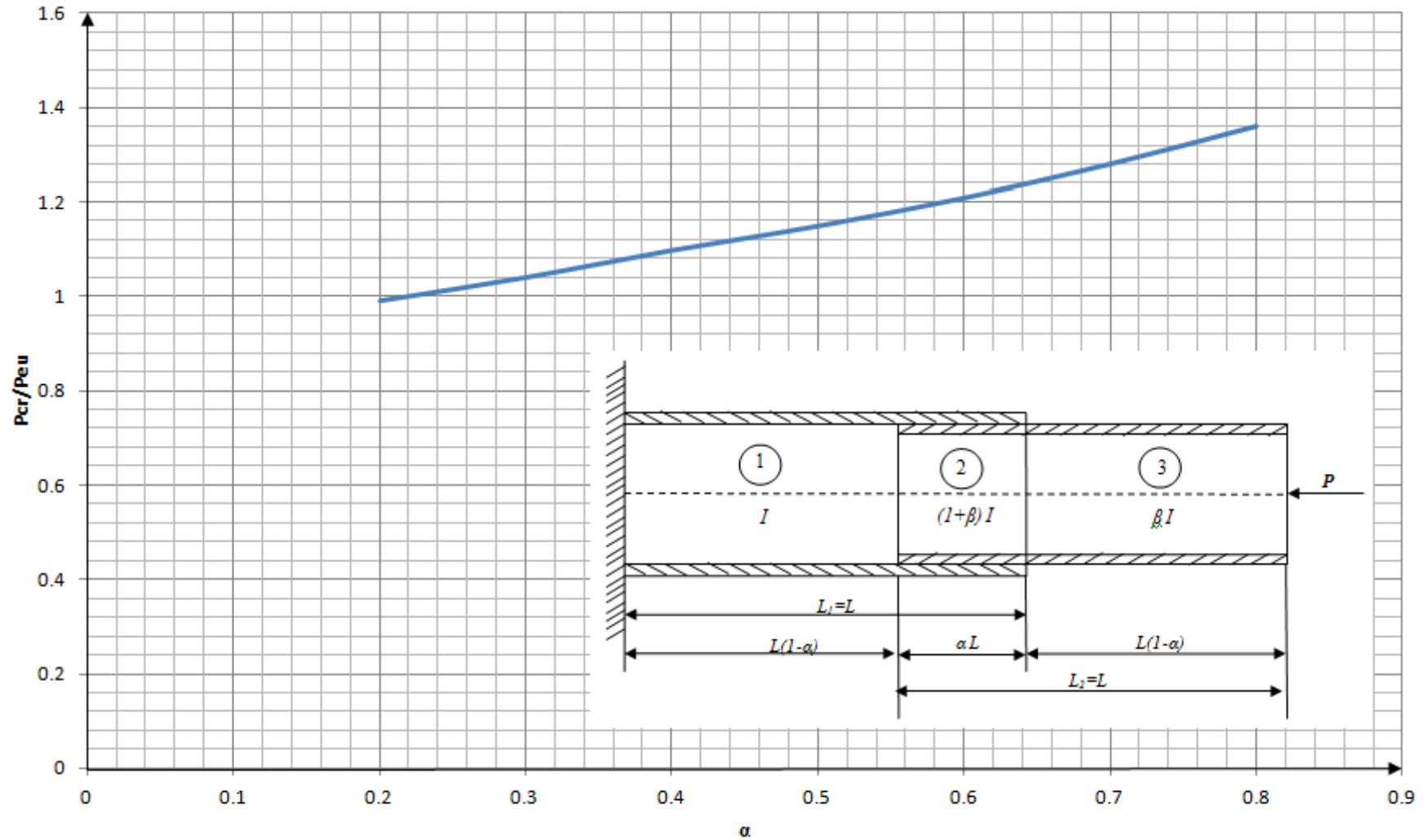


Figure 7.9: FEA extracted values of  $\frac{P_{cr}}{P_{Eu}}$  vs. Overlap ratio  $\alpha$ , where  $\alpha$  varies from 0.2 to 0.8, in increments of 0.2, for the two section telescopic cantilever beam assembly, having dimensions outlined in Table 7.1.

## 7.5 Summary

The two section telescopic cantilever beam assembly, having dimensions specified in Table 7.1 has been subjected to a rigorous and comprehensive series of analyses, using the FEA software package ABAQUS. The three outcomes desired from the FEA were identified in § 7.1 and successfully attained. The results of the FEA performed are in turn compared and contrasted with the numerical and experimentally derived results in Chapter 9. The results of the analyses performed are summarised briefly as follows:

1. The deflections induced for inline loads equivalent to their respective  $\frac{wL}{P}$  ratios, denoted by  $y$  and directly extracted from ABAQUS simulations, were divided by the tip deflection of a single fixed end section cantilever having length  $L$  and uniform second moment of area  $I$ , denoted by  $y_0$  such that  $y_0$  equals  $\frac{PL^3}{3EI}$ , to give the normalised parameter  $\frac{y}{y_0}$ . It is this parameter in turn that is plotted against the overlap ratio  $\alpha$ , varying from 0.2 to 0.8, in increments of 0.2, for  $\frac{wL}{P}$  ratios of 10, 1, 0.1 and 0.01, to give the resultant deflection predictions shown in Figure 7.2. These curves serve as a benchmark for the final objective of comparing the experimentally and theoretically extracted deflection plots as is amply detailed in §9.1.1.
2. Inline and Offset loading induced bending and shear stress distributions are plotted against the distance measured along the assembly, at 50 mm intervals, from the fixed end. These curves were in turn plotted for  $\frac{wL}{P}$  ratios of 2, 4, 6 and 8. These curves are finally compared and contrasted against the theoretical predictions for the same as outlined in § 9.1.2 and graphically presented in Figures (9.3) – (9.8).
3. The critical buckling loads of the two section telescopic cantilever beam assembly having dimensions outlined in Table 7.1, denoted by  $P_{cr}$  and extrapolated from ABAQUS as detailed in G.9.3, are divided by the Euler Critical Buckling load corresponding to a column having one end fixed and the other free, denoted

by  $P_{Eu}$  such that  $P_{Eu}$  equals  $\frac{\pi^2 EI}{4L^2}$ , to give the normalised parameter  $\frac{P_{cr}}{P_{Eu}}$ . This parameter in turn is once again plotted against the overlap ratio  $\alpha$ , varying from 0.2 to 0.8, in increments of 0.2. The curve thus generated is compared against the theoretically generated curve as shown in Figure 9.41 and detailed in §9.1.3.

## CHAPTER 8: EXPERIMENTAL ANALYSIS

### 8.1 Introduction

This chapter contains the results and analyses carried out on a two section telescopic assembly consisting of two thin walled rectangular steel sections having Tufnell wear pads at locations specified subject to a combination of bending, shear and torsion. The test rig has dimensions as specified in Table 8.1. In earlier chapters the two section telescoping cantilever beam assembly was analysed theoretically as well as modelled using Finite Element Analysis and the results extracted. This chapter aims to take the analysis that has been performed a step further and not only validate the theory and the software but in its own right highlight, if any, discrepancies that may arise in practice. The importance of experimentation in this thesis cannot be highlighted enough; it could be argued that it forms the bedrock of this body of work.

The aim of the experimental tests carried out can be outlined as follows: (i) determination of tip deflections induced by loading the assembly; and finally (ii) stress and strain analysis in the beam cross sections at two different locations along the telescopic beam assembly, which in turn leads onto; (iii) calculation of principal stresses at the four locations.

### 8.2 The Test Specimen

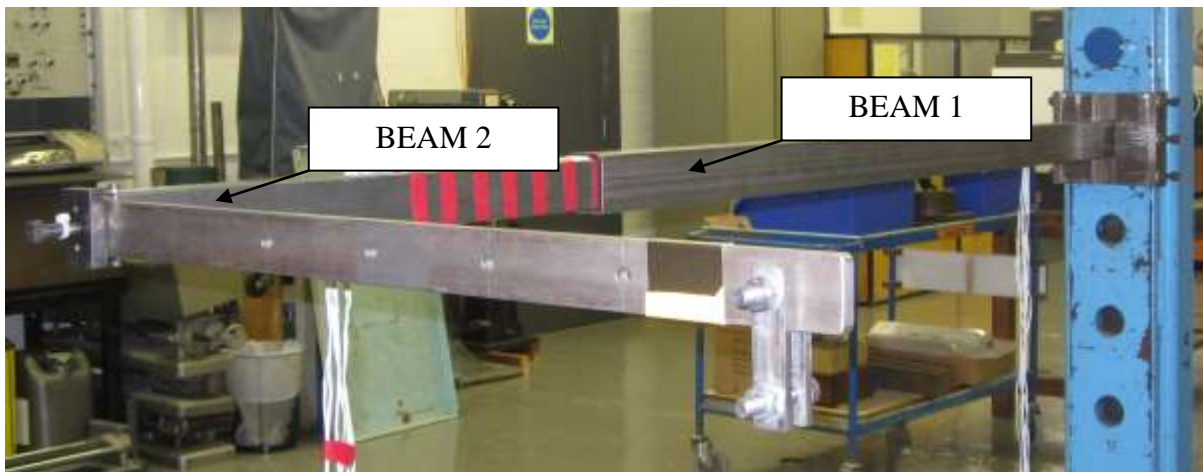


**Figure 8.1: The Experimental Test Rig**

The telescopic beam assembly model (test specimen) was assembled using two mild steel sections as shown in Figure 8.1 and the properties of which are outlined in the Table 8.1 below.

**Table 8.1: Sectional Properties of the individual beams of the test specimen**

Section	Size		Thickness (T mm)	Length (L mm)	Calculated Weight per unit length (N/mm)	Calculated Second Moments of Area (mm <sup>4</sup> )
	H mm	B mm				
<b>BEAM 1 (Fixed End)</b>	60	40	1.55	1300	0.0235	16.7x10 <sup>4</sup>
<b>BEAM 2 (Free End)</b>	50	30	1.55	1300	0.0187	9.042x10 <sup>4</sup>
<b>Wear Pads x 7</b>	2	30	2	100	-	-

The load was applied onto the test specimen by means of a loading arm shown in Figure 8.2, through which loads could be applied to simulate pure bending (inline loading) or a twisting moment (offset loading).

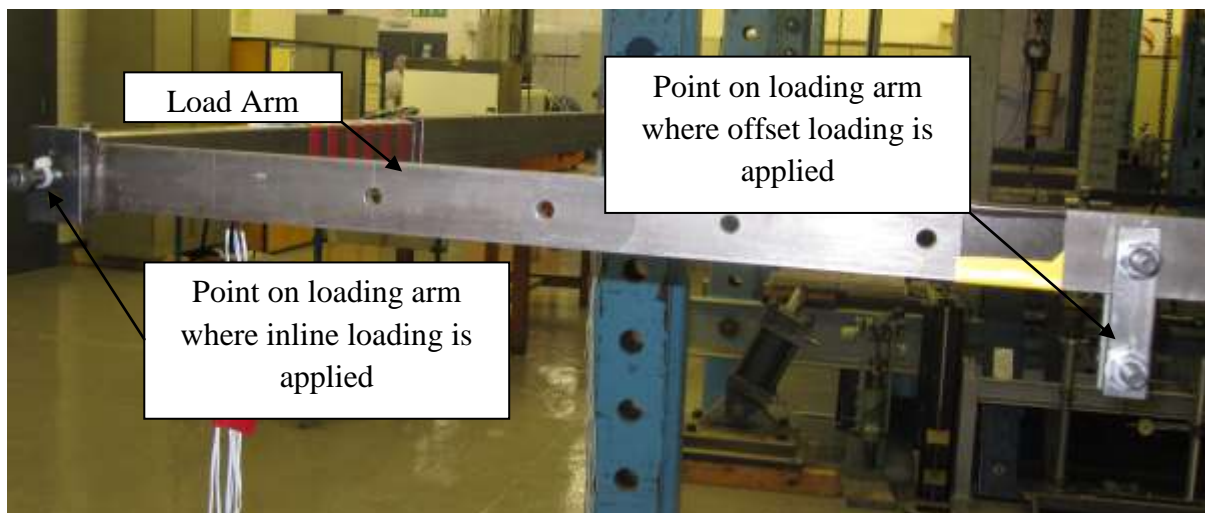


**Figure 8.2: Loading arm through which loads are applied**

Figure 8.3 (a) and (b) shows the load configurations for inline loading and offset loading.



(a)



(b)

**Figure 8.3: Loading arm configuration for (a) In-line Loading (b) Offset Loading**



**Figure 8.4: Tufnell wear pads attached to beam 2. These four wear pads are located on the four walls of beam 2, at the end opposite to that where loads are applied**

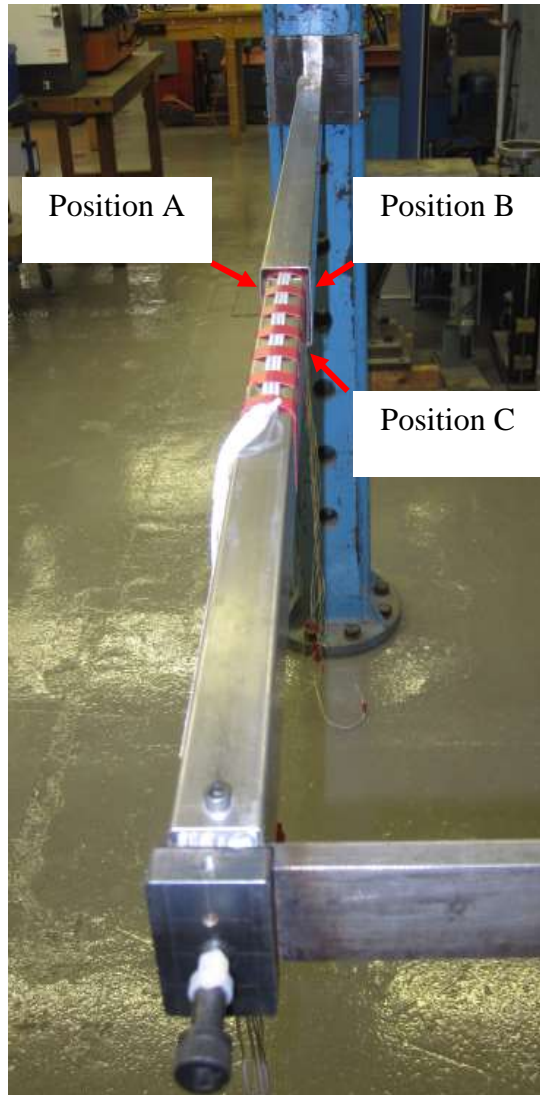


**Figure 8.5: Unattached wear pads, inserted into the gap at the three positions A, B and C, at the start of the overlap between beam 1 and beam 2**

The wear pads are placed in seven locations in the experimental test rig. Figure 8.4 shows the Tufnell wear pads that are attached to beam 2 or the free-end section of the assembly, whilst Figure 8.5 shows the locations where the unattached wear pads are inserted into the gap between the beam sections 1 and 2, when the latter is sheathed or inserted into the former. There are four attached wear pads and three unattached wear pads within the assembly. The four attached wear pads are situated at all four walls of beam 2, at the end opposite to where the loading is applied, such that they are always enclosed within the overlap region. The three unattached wear pads on the other hand are inserted into the gaps, created between both the vertical walls of Beam's 1 and 2, at positions A and B respectively and into the gap created between the horizontal walls of Beam's 1 and 2, at position C. This placement is possible only when beam 2 is sheathed within beam 1.

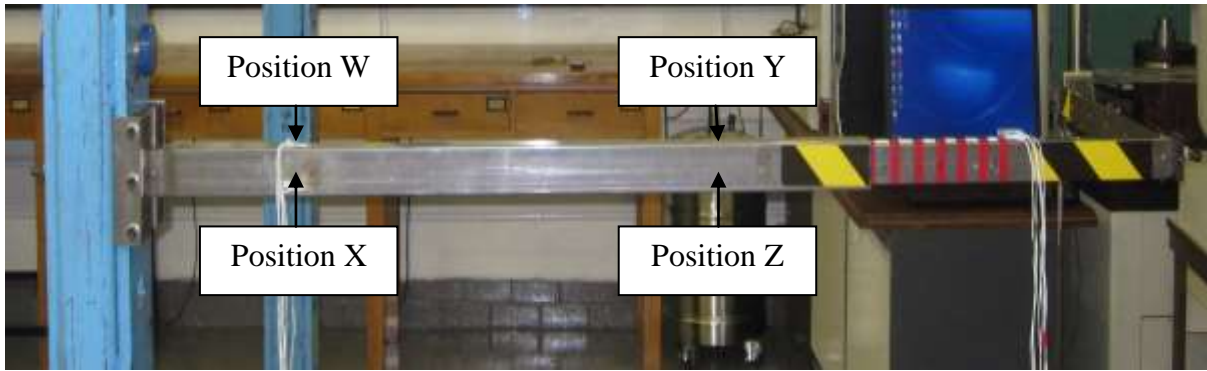


**Figure 8.6: Position where the strain gauges were bonded onto the telescopic assembly. Positions W and X are 300 mm from the fixed end of beam 1, whilst positions Y and Z are 200 mm from the inner end of beam 2**

**Table 8.2: Position of gauges along the telescopic beam assembly**

<b>Position of strain gauge along the telescopic beam assembly</b>	<b>Section to which the strain gauge is bonded</b>	<b>Distance of the gauge (mm)</b>
Position W	Beam 1	300 mm from fixed end along the top surface of the assembly
Position X	Beam 1	300 mm from fixed end along the side surface of the assembly
Position Y	Beam 2	200 mm from end encased inside the overlap along the top surface of the assembly
Position Z	Beam 2	200 mm from end encased inside the overlap along the side surface of the assembly

The strain gauge rosettes attached at positions W and X, as shown in Figure 8.7 (a) and (b) are bonded to beam 1, whilst the rosettes attached at positions Y and Z as shown in Figure 8.7(c) and (d), are bonded to beam 2.

The rosettes bonded at positions W and X are at the top and the side of beam 1 along the neutral axes, respectively. The rosettes bonded at positions Y and Z, are at the top and the side of beam 2 along the neutral axes, respectively. The gauges bonded at positions Y and Z are placed so that they are always sheathed within beam 1 in the overlap region where beam 2 slides within beam 1.

Measurements of strains of the beam sections in the tested segments at positions W, X, Y and Z were carried out using the strain gauging methods that are highlighted in detail in Appendix H. Measurements of strains were carried out using the Scorpio data acquisition system which in turn was integrated with a desktop PC.



(a)



(b)



(c)



(d)

**Figure 8.7: Strain gauge rosettes bonded at (a) position W (b) position X (c) position Y and (d) position Z, as shown in Figure 8.6.**

The overlap region is of particular significance in that the combination of the two sections (one sheathed within the other) bolsters the magnitude of its second moments of area. Also of

importance are the dimensions of the wear pads. Depending on the dimensions of the wear pad, a significant reduction in bending and shear stresses is registered as compared to away from the overlap as seen in Figure 6.4. Also of note is the fact that due to the increased moments of area within the overlap, buckling always takes place in front of the overlap in that section of smaller dimensions. Naturally this can be attributed to the susceptibility of that section to buckle first due to it having the lesser value of  $I$  or second moment of area.

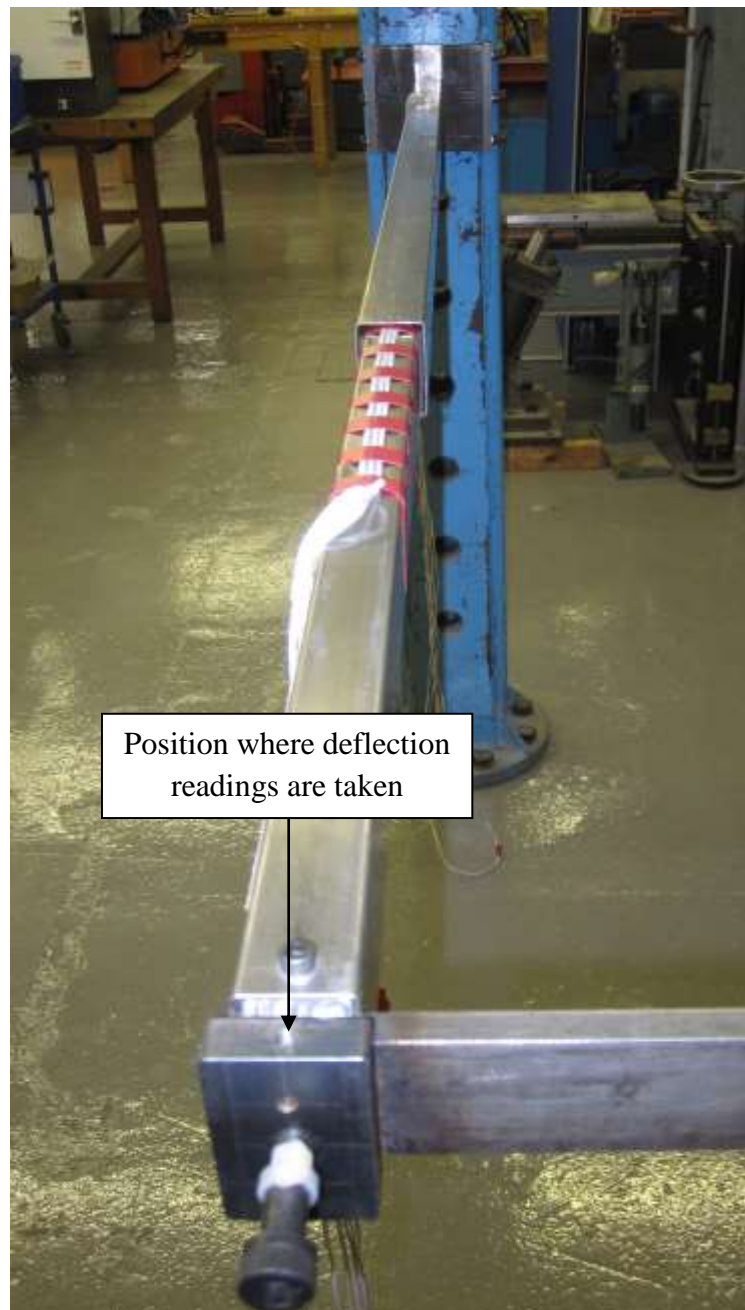


**Figure 8.8: Front view of the telescopic assembly. The arrow indicates the position where dial gauge readings of deflection for different load magnitudes were taken.**

The objectives of the stress and strain analysis is to record the strain state at the four positions on the telescoping assembly subjected to combined bending and torsion. Using the strain data collected the principal strains and their directions can be calculated. With the principal strains in turn the principal stresses can be obtained using the stress-strain transformation equations as outlined in Appendix H. It is also possible to predict the stress state of the shaft using theoretical techniques considering such factors as bending, shear stress due to torsion and the effects of shear force. This experiment will be a measure of how well the theory models reality. Apart from measurements of strains, the measurements of tip deflections was carried out at the point shown in Figure 8.8 for increasing loads using dial gauges of accuracy 0.01mm.

### 8.3 The Experimental Mounting Stand



**Figure 8.9: Frontal view of the experimental mounting jig clamped to support column.**

The experimental jig used to mount the telescopic beam assembly in order to simulate an encastre fixing or a rigidly fixed end is shown in Figure 8.9. The jig is attached to columns in the laboratory environment and is mounted onto the same using a spigot which is screwed

onto a threaded rod which in turn is screwed into the fixed beam. The spigot as well as the threaded rod and the location where it screws into beam 1 are shown in Figure 8.10.

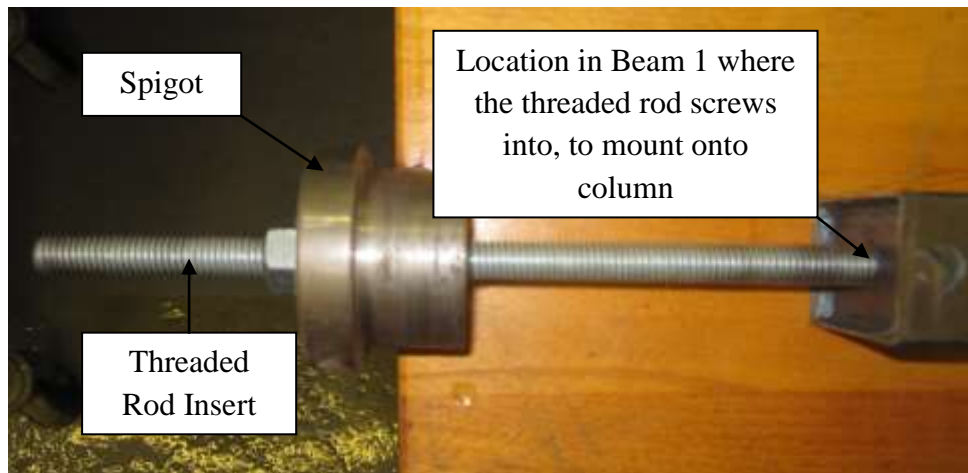
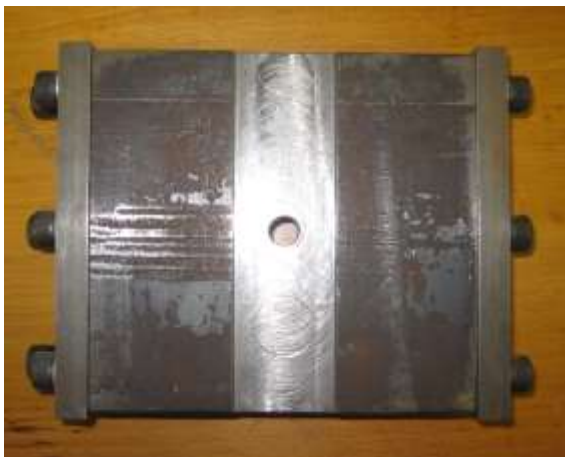
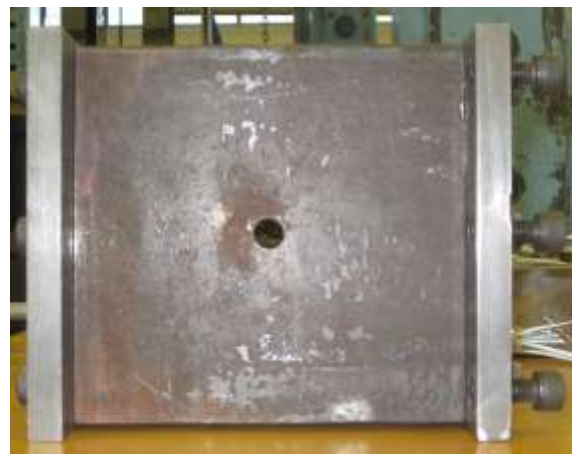


**Figure 8.10: Details of the mounting mechanism**



**(a)**



**(b)**

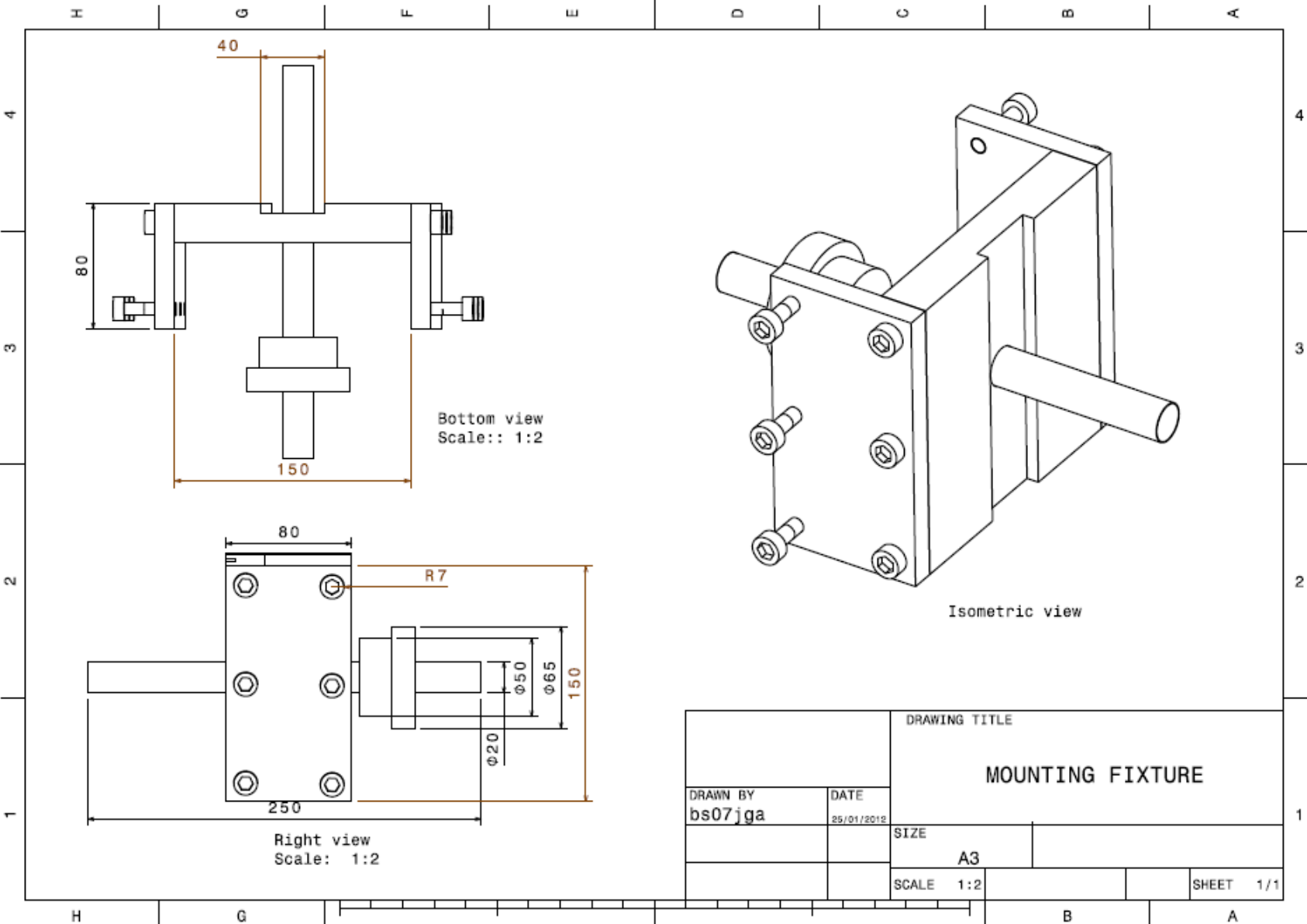
**Figure 8.11: (a) Front view of the mounting jig (b) Rear view of the mounting jig**

Figures 8.11 (a) and (b) show the different views of the mounting rig and Figure 8.12 shows the left hand view of the mounting jig. Figure 8.12 also shows the method by which the jig is clamped to the column. Once the threaded rod-insert slides into the hole in the support column, the spigot centres the insert, which in turn is what the front view of the rig slides onto, through the through-hole shown in both Figures 8.11(a) and (b).



**Figure 8.12: Left hand view of the mounting jig showing the method by which the same is clamped to the support column.**

The assembly drawing entitled 'Mounting Fixture' on the page that follows shows the detailed measurements of the mounting jig and the individual components that comprise the same.

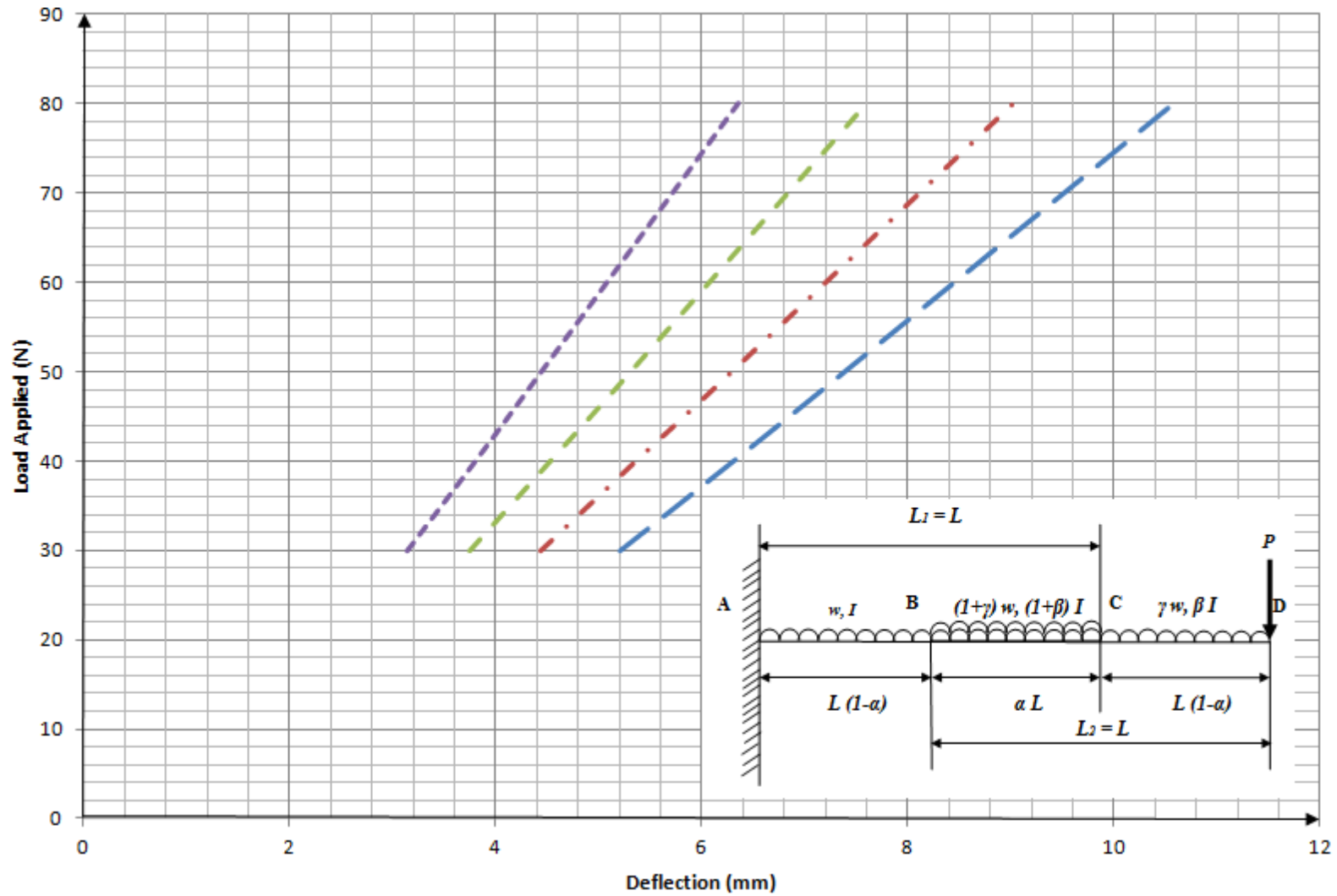


		DRAWING TITLE	
		MOUNTING FIXTURE	
DRAWN BY	DATE	SIZE	
bs07jga	25/01/2012	A3	
		SCALE	SHEET
		1:2	1/1

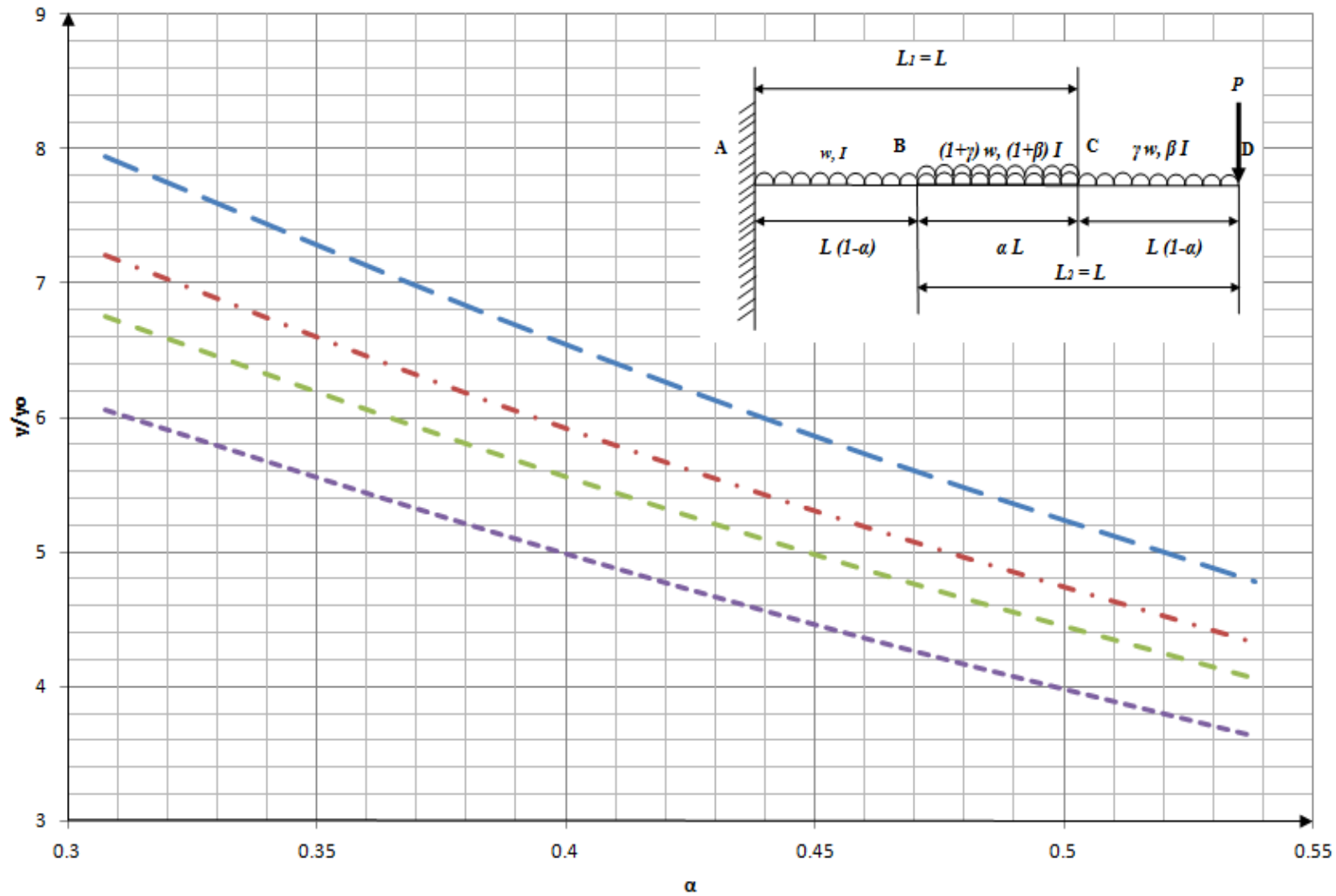
#### 8.4 Experimental Tip Deflection Analysis

Figure 8.13 represents the experimentally derived deflection curves obtained by plotting the end load applied to the corresponding tip deflection, whilst varying the overlap lengths. These curves were plotted for the experimental test rig, the dimensions of which are elaborated in Table 8.1. These curves were plotted first by initially loading the assembly in the inline loading configuration as shown in Figure 8.3 (a) with a nominal load of 10 N and setting the dial gauge to zero before commencing the deflection testing. This was done in order to reduce any errors that may creep in and remove any slack within the assembly. Tip deflections were measured for increasing magnitudes of end load, in the inline loading configuration as shown in Figure 8.3 (a). Figure 8.14, in turn represents the modified deflection curves plotted, in similar fashion to those in Figures 3.2, 3.7, 3.10 and 3.12 respectively. Knowing the tip deflection induced in the assembly by a particular end load experimentally (denoted here as ‘ $y$ ’), and the tip deflection of a single fixed end section cantilever having length  $L$  and uniform second moment of area  $I$  (here denoted by the term ‘ $y_0$ ’ such that  $y_0$  equals  $\frac{PL^3}{3EI}$ ) we obtain the normalised ordinate parameter  $\frac{y}{y_0}$ . This

ordinate parameter is in turn plotted for values of  $\frac{wL}{P}$  which can be calculated given the dimensions of the experimental rig as outlined in Table 8.1, against the overlap ratio parameter ‘ $\alpha$ ’. The intention of plotting this curve was to act as a means of comparison against the theoretical predictions and the FEA generated curves.



**Figure 8.13: Load applied in Newtons vs tip deflection in mm for the experimental test rig having dimensions outlined in Table 8.1**  
 (Key: — Overlap length 400 mm; - . - Overlap length 500 mm; - - - Overlap length 600 mm; ..... Overlap length 700 mm)



**Figure 8.14: Extrapolated deflection curves vs. overlap ratio  $\alpha$  for the experimental test rig having dimensions outlined in Table 8.1**  
 (Key: — Applied Load 30 N; - · - Applied Load 40 N; - - - Applied Load 50 N; ····· Applied Load 80 N)

## 8.5 Experimental Stress Analysis

The results of the experimental analysis performed on the experimental test rig having dimensions as detailed in Table 8.1 are presented below in Figures 8.13 – 8.44. Using the Scorpio Data Acquisition system, the principal strains are measured using the strain gauges bonded as outlined in the strain gauging techniques mentioned in H.5, H.6 and H.7. The gauges are shown in Figures 8.7 (a) – (d) and are bonded at each of the locations shown in Figure 8.6 and Table 8.2. The strains recorded are converted to their corresponding principal strain entities using the equations (H.4a) and (H.4b). Using the principal strain values calculated from equations (H.4a) and (H.4b), the equivalent principal stresses are obtained using the stress transformation equations, (H.6a) and (H.6b). Equation (H.4c) gives the principal strain directions. The values of principal stresses are plotted against the load applied, in either the inline or offset loading configurations, as shown in Figures 8.3 (a) – (b), for varying overlap lengths.

Figures 8.15 – 8.18 show the inline loading induced principal stresses at each of the four locations shown in Figure 8.6 for an overlap length of 400 mm. Figures 8.19 – 8.22 shows the offset loading induced principal stresses at each of the four locations, once again for an overlap length of 400 mm. Figures 8.23 – 8.26 show inline loading induces principal stresses for an overlap length of 500 mm whilst Figures 8.27 – 8.30 show the principal stresses induced through offset loading for the same overlap length. Inline and offset loading induced principal stresses are shown for an overlap length of 600 mm in Figures 8.31 – 8.34 and Figures 8.35 – 8.38, respectively. Finally the principal stresses plotted for inline and offset loading configurations, as induced within the assembly having an overlap length of 700 mm are presented in Figures 8.39 – 8.42 and Figures 8.43 – 8.46, in that order. These plots are compared with both theoretical and FEA obtained predictions of principal stresses, and shown in § 9.1.3.

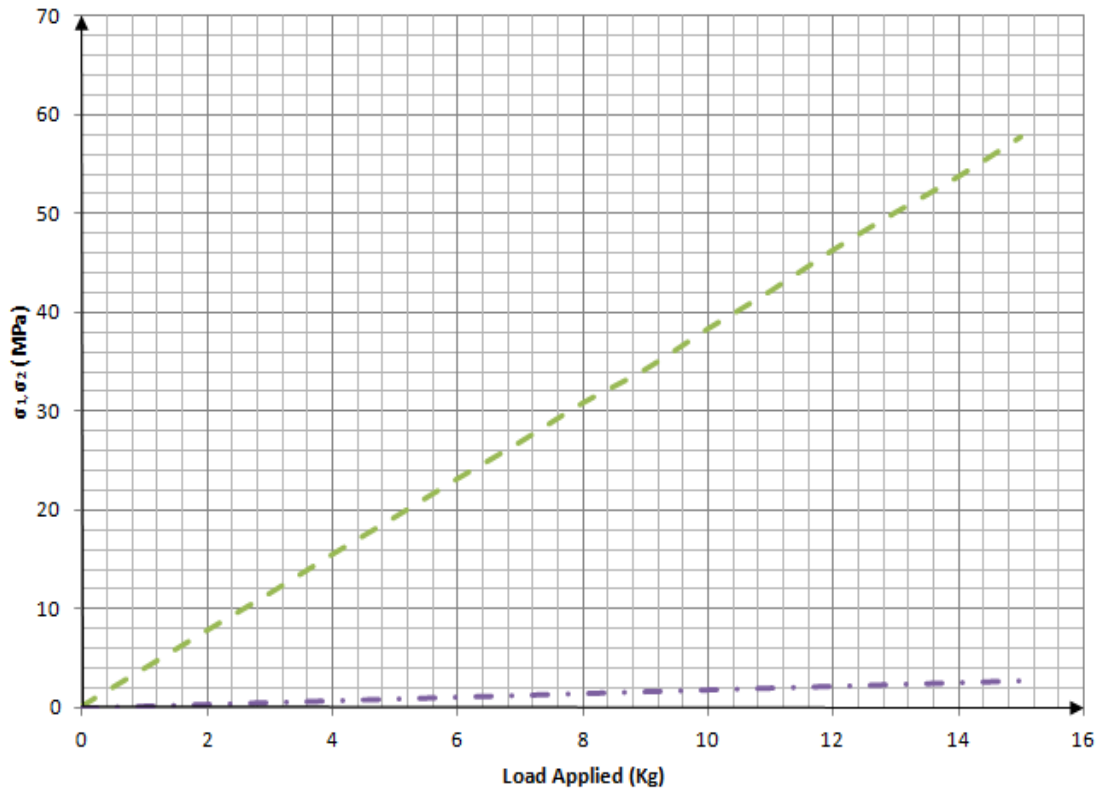


**Figure 8.15: Principal stresses ( $\sigma_1, \sigma_2$  (MPa)) at position W vs Inline load applied (kg) with 400 mm overlap**

(Key: — — — Experimental  $\sigma_1$  (MPa); — · — Experimental  $\sigma_2$  (MPa))

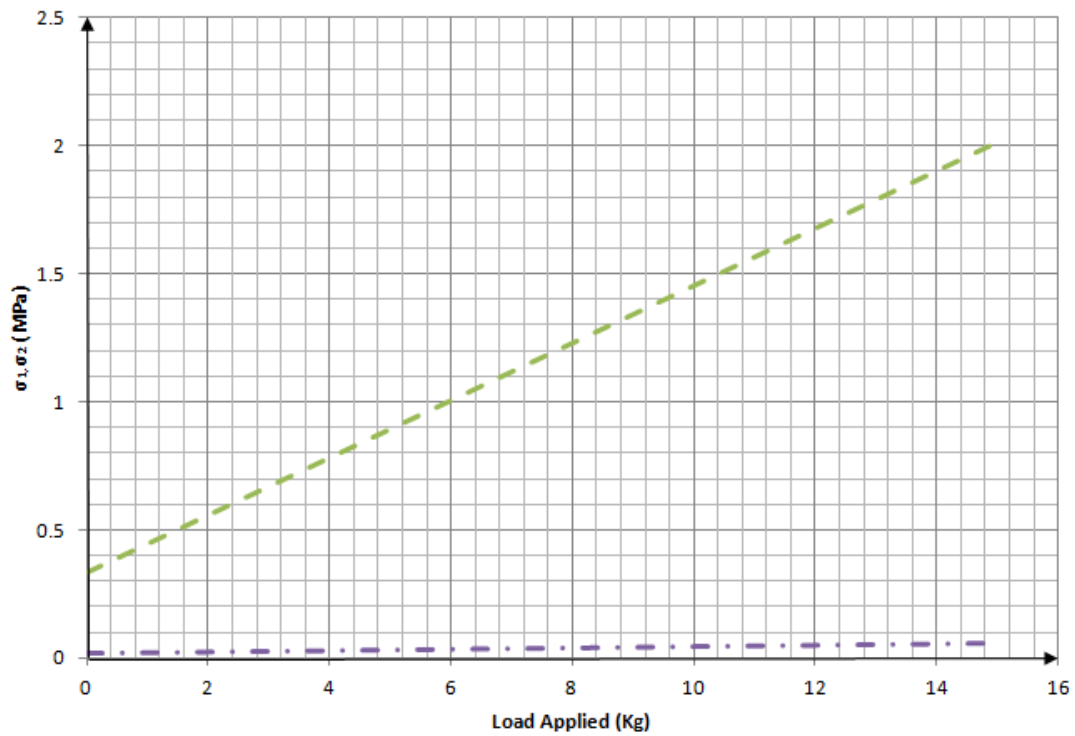


**Figure 8.16: Principal stresses ( $\sigma_1, \sigma_2$  (MPa)) at position X vs Inline load applied (kg) with 400 mm overlap**

(Key: — — — Experimental  $\sigma_1$  (MPa); — · — Experimental  $\sigma_2$  (MPa))

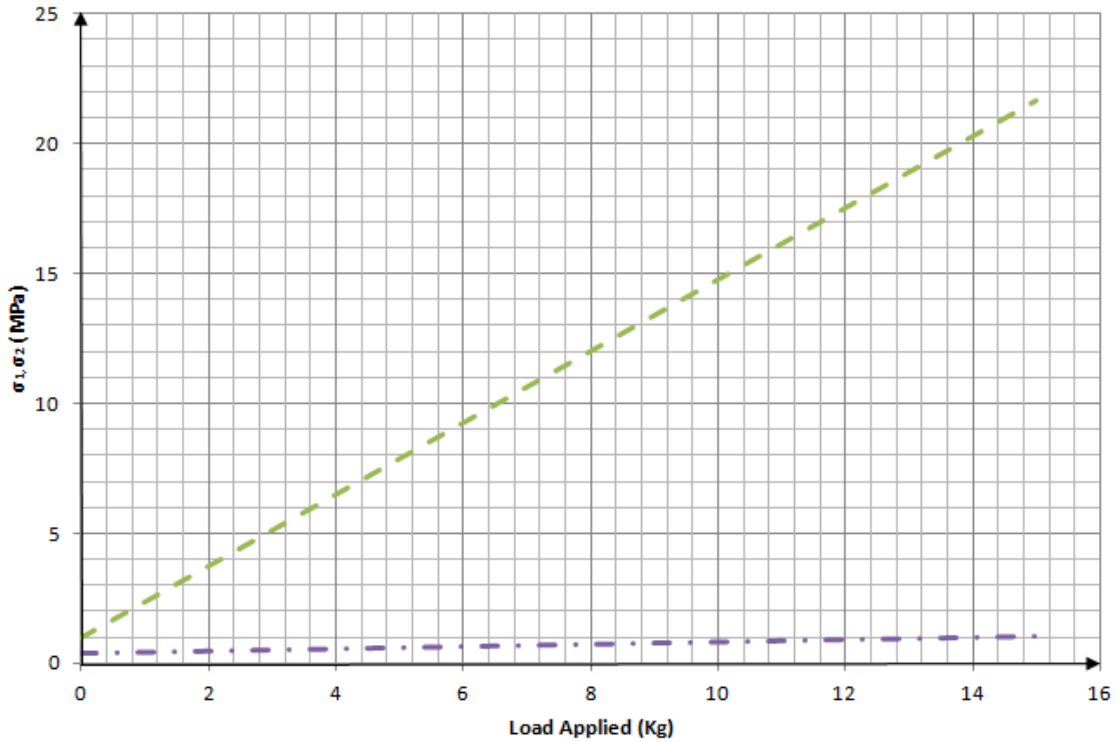


**Figure 8.17: Principal stresses ( $\sigma_1, \sigma_2$  (MPa)) at position Y vs Inline load applied (kg) with 400 mm overlap**  
 (Key: — — — Experimental  $\sigma_1$  (MPa); - · - Experimental  $\sigma_2$  (MPa))

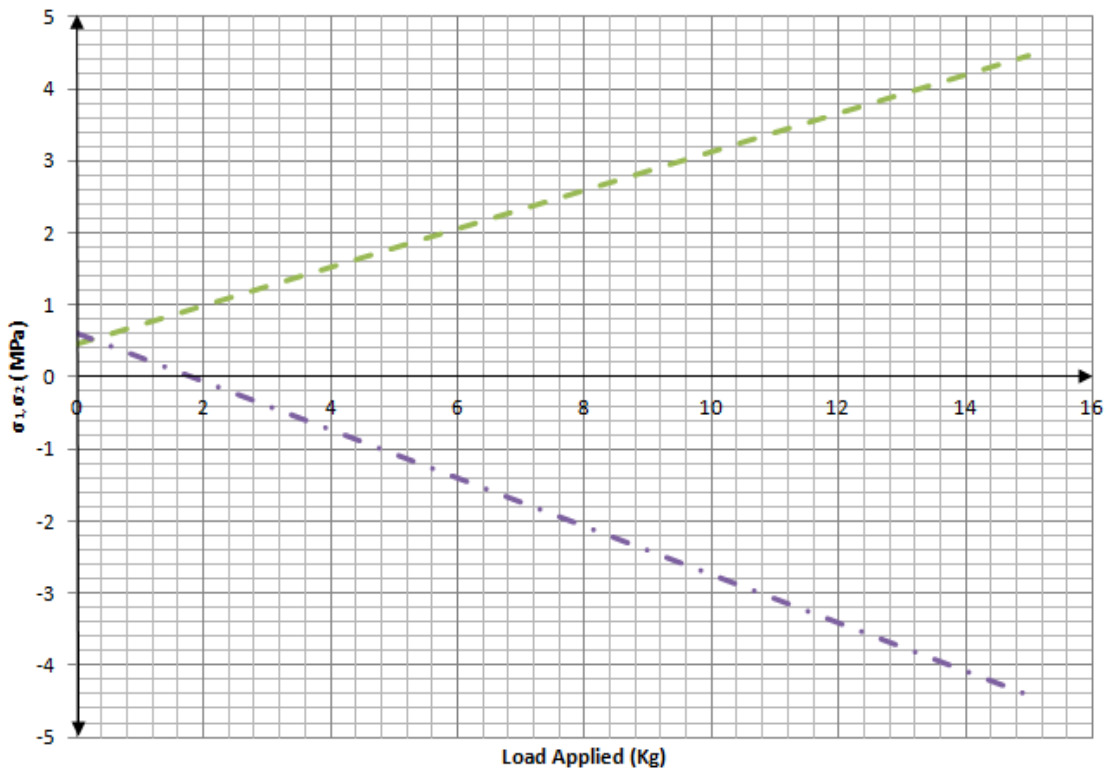


**Figure 8.18: Principal stresses ( $\sigma_1, \sigma_2$  (MPa)) at position Z vs Inline load applied (kg) with 400 mm overlap**  
 (Key: — — — Experimental  $\sigma_1$  (MPa); - · - Experimental  $\sigma_2$  (MPa))

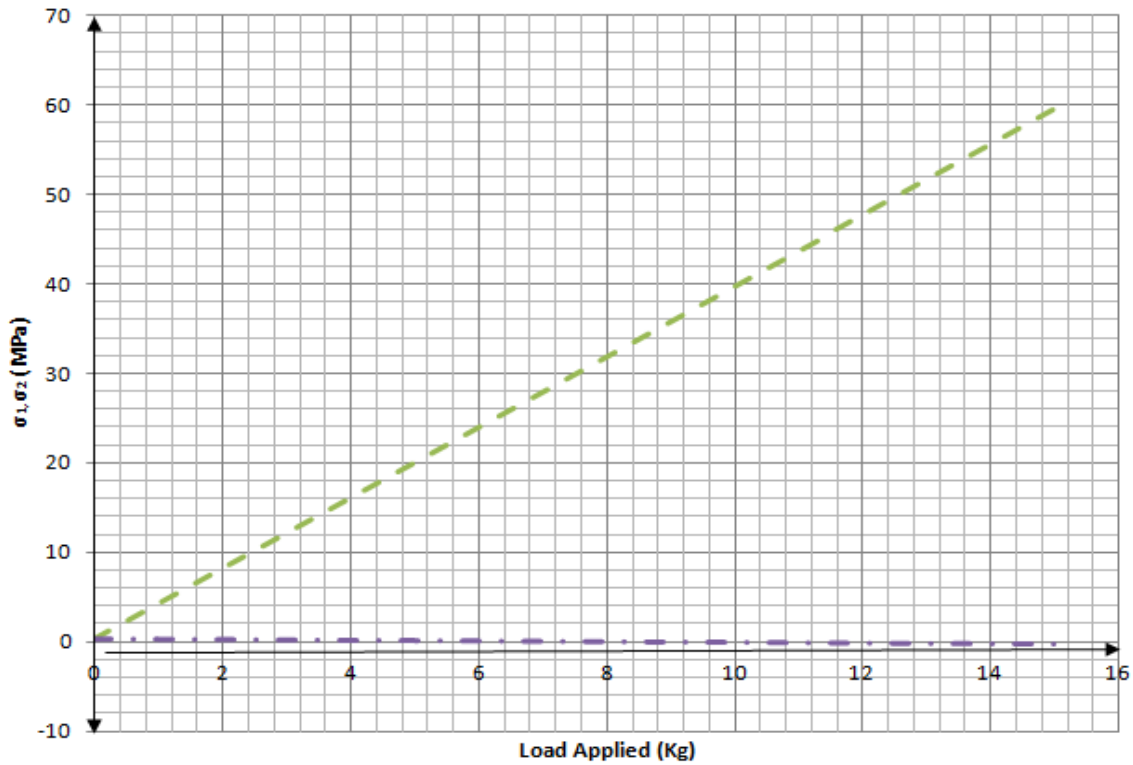


**Figure 8.19: Principal stresses ( $\sigma_1, \sigma_2$  (MPa)) at position W vs Offset load applied (kg) with 400 mm overlap**  
 (Key: — — — Experimental  $\sigma_1$  (MPa); - · - Experimental  $\sigma_2$  (MPa))

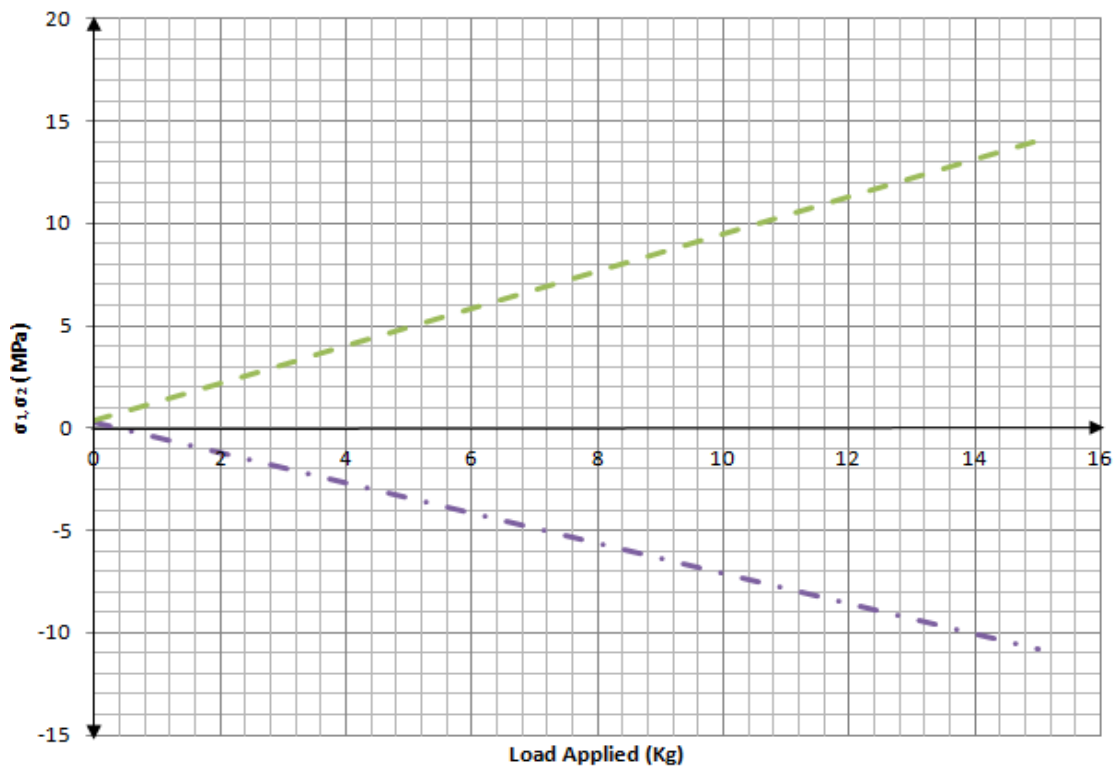


**Figure 8.20: Principal stresses ( $\sigma_1, \sigma_2$  (MPa)) at position X vs Offset load applied (kg) with 400 mm overlap**  
 (Key: — — — Experimental  $\sigma_1$  (MPa); - · - Experimental  $\sigma_2$  (MPa))

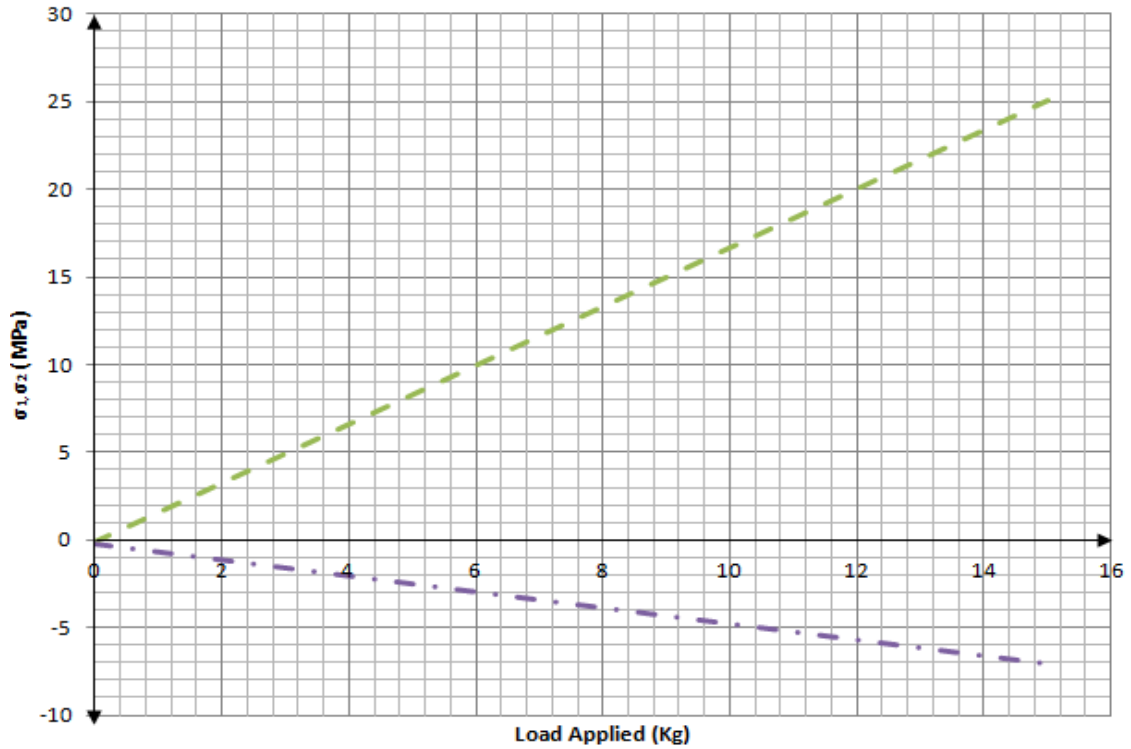


Figure 8.21 Principal stresses ( $\sigma_1, \sigma_2$  (MPa)) at position Y vs Offset load applied (kg) with 400 mm overlap

(Key: — — — Experimental  $\sigma_1$  (MPa); - . - Experimental  $\sigma_2$  (MPa))

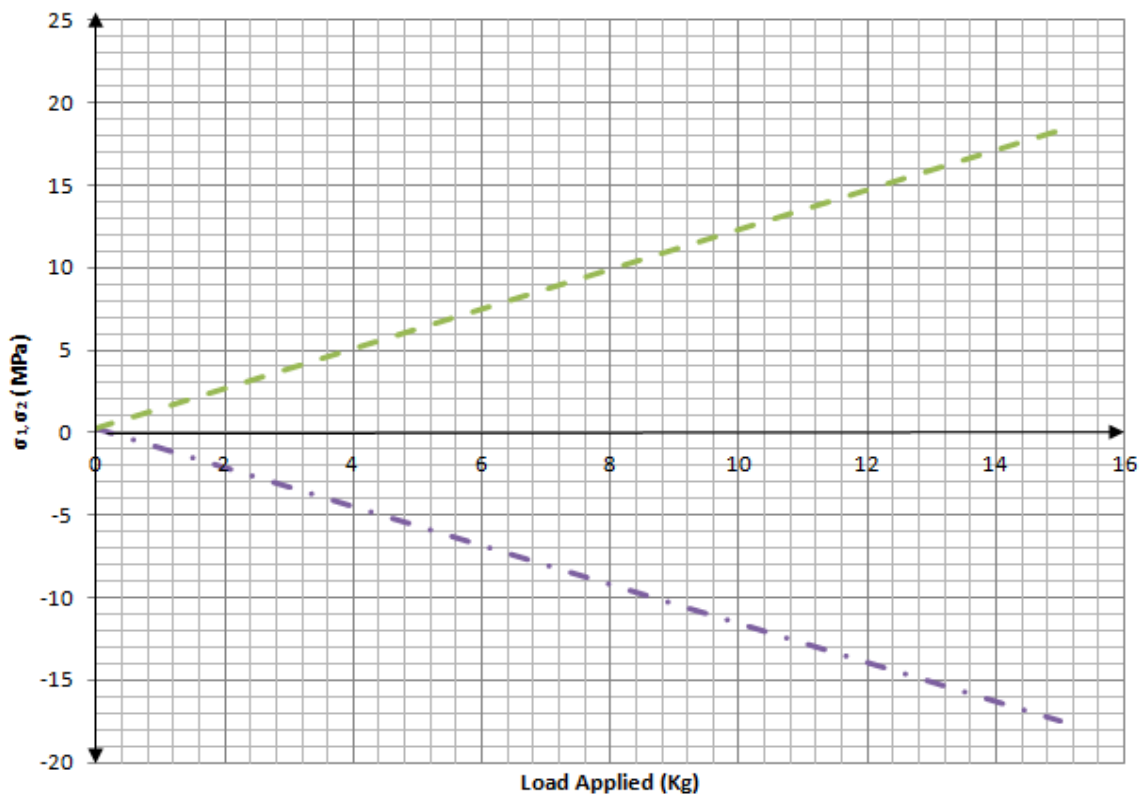
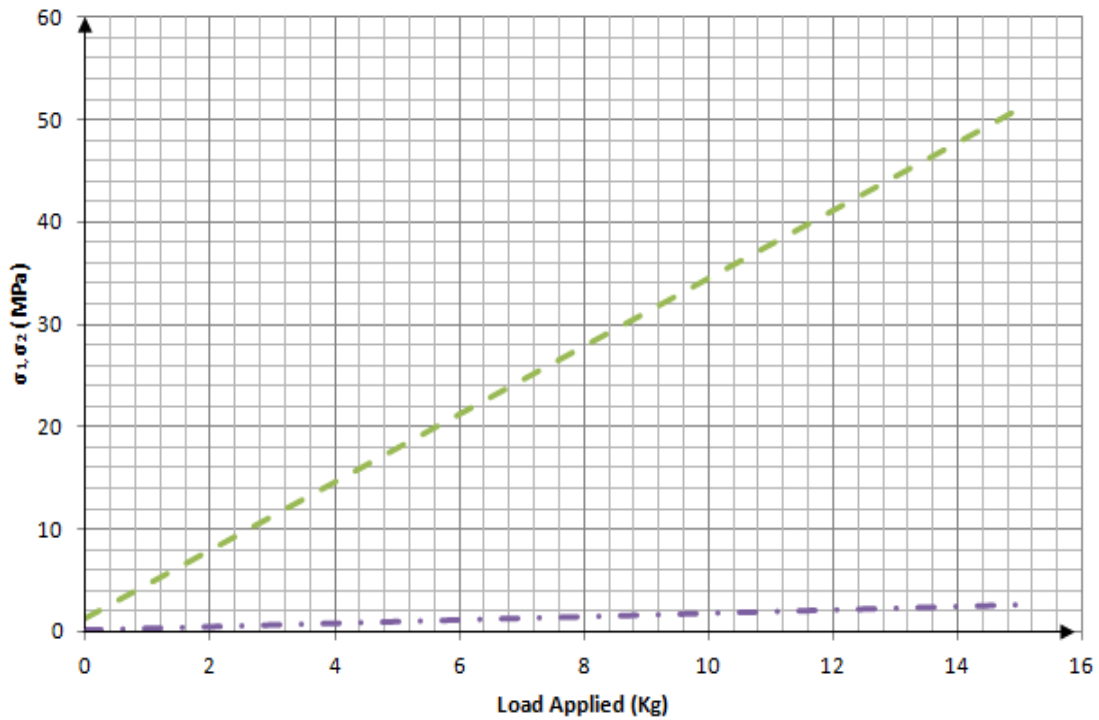
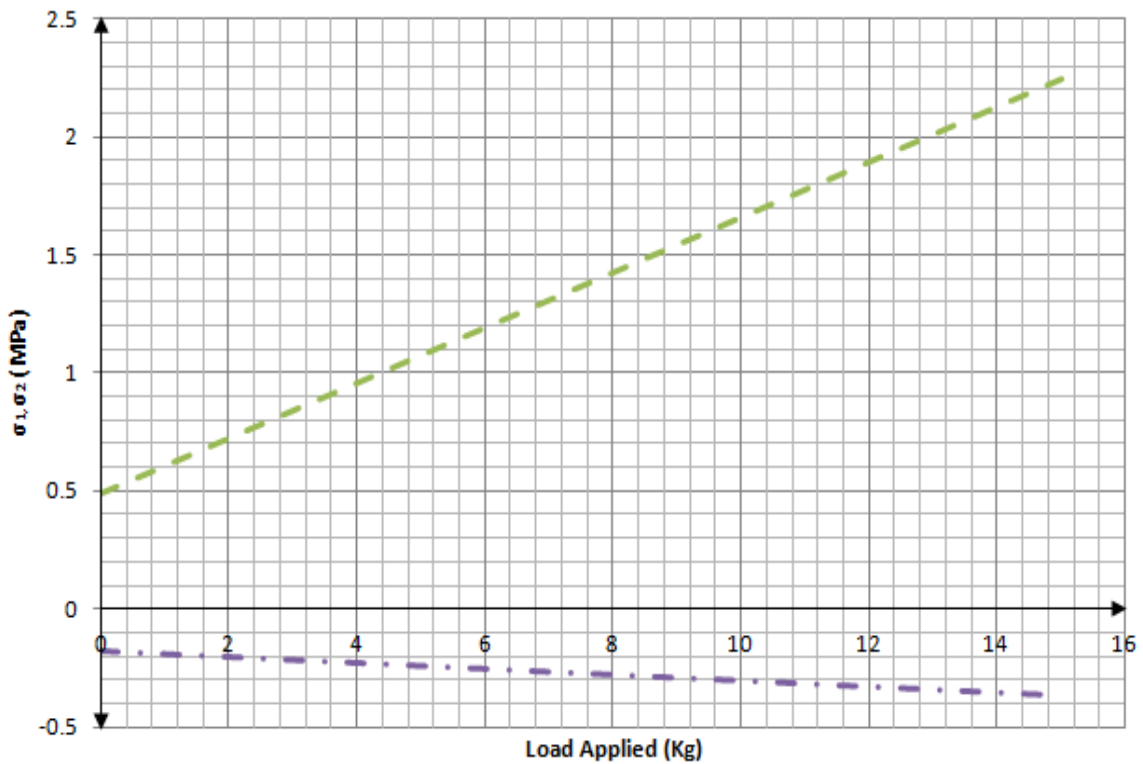


Figure 8.22 Principal stresses ( $\sigma_1, \sigma_2$  (MPa)) at position Z vs Offset load applied (kg) with 400 mm overlap

(Key: — — — Experimental  $\sigma_1$  (MPa); - . - Experimental  $\sigma_2$  (MPa))



**Figure 8.23 Principal stresses ( $\sigma_1, \sigma_2$  (MPa)) at position W vs Inline load applied (kg) with 500 mm overlap**  
 (Key: — — — Experimental  $\sigma_1$  (MPa); - . - Experimental  $\sigma_2$  (MPa))



**Figure 8.24: Principal stresses ( $\sigma_1, \sigma_2$  (MPa)) at position X vs Inline load applied (kg) with 500 mm overlap**  
 (Key: — — — Experimental  $\sigma_1$  (MPa); - . - Experimental  $\sigma_2$  (MPa))

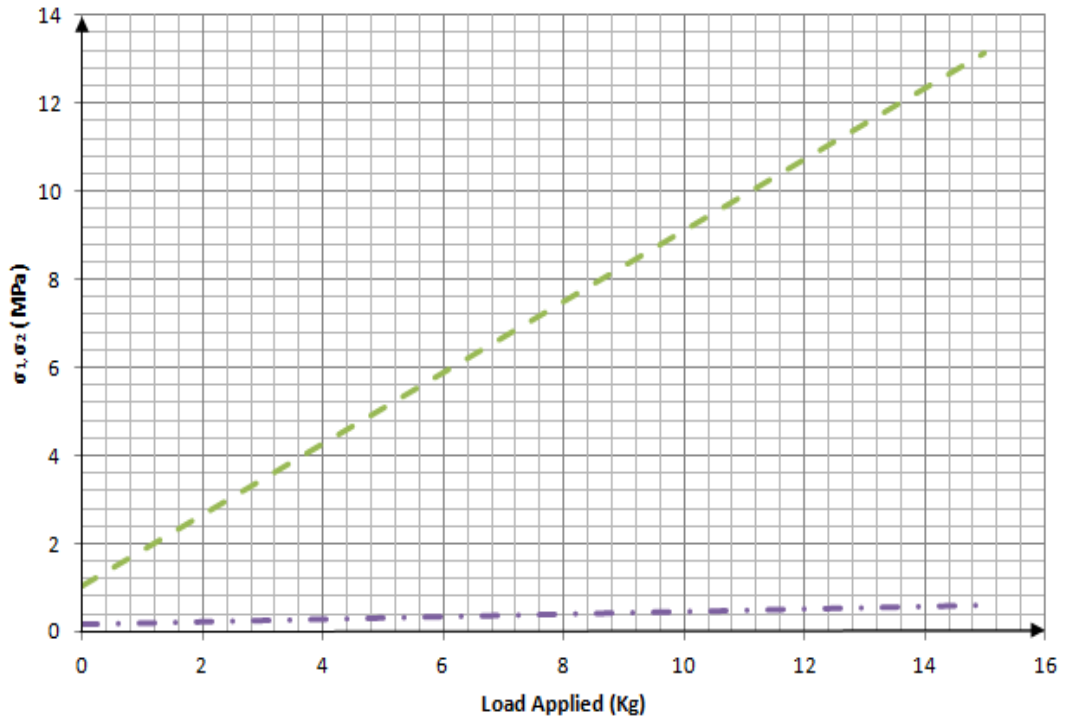


**Figure 8.25: Principal stresses ( $\sigma_1, \sigma_2$  (MPa)) at position Y vs Inline load applied (kg) with 500 mm overlap**  
 (Key: — Experimental  $\sigma_1$  (MPa); — Experimental  $\sigma_2$  (MPa))

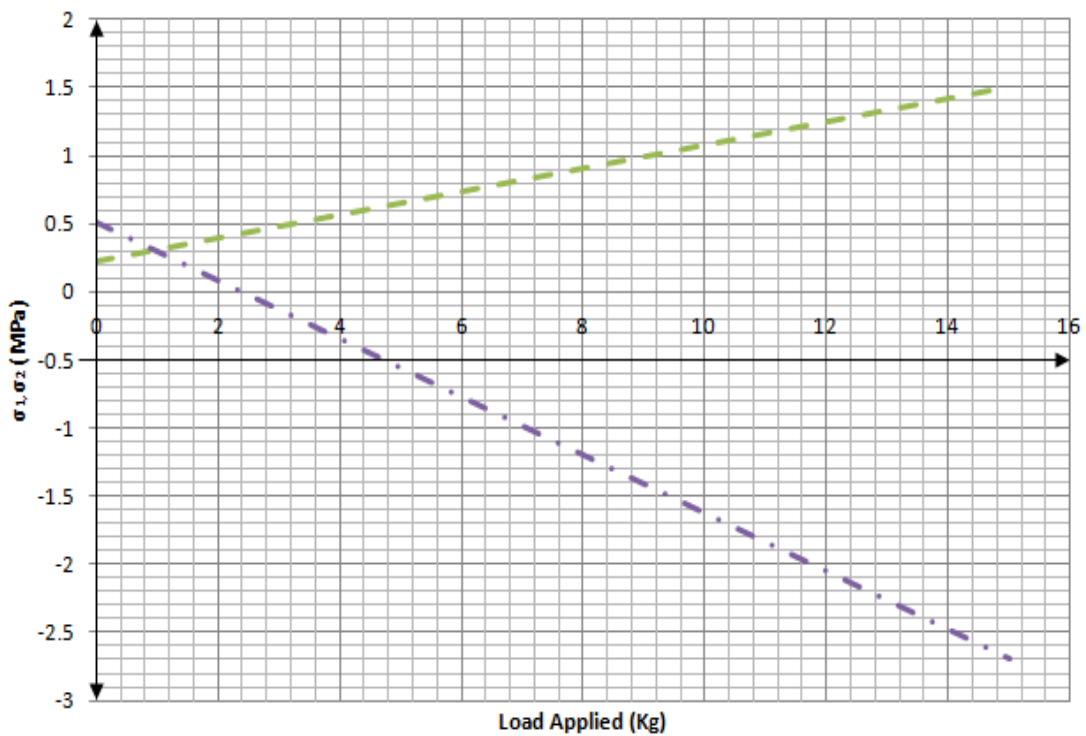


**Figure 8.26: Principal stresses ( $\sigma_1, \sigma_2$  (MPa)) at position Z vs Inline load applied (kg) with 500 mm overlap**  
 (Key: — Experimental  $\sigma_1$  (MPa); — Experimental  $\sigma_2$  (MPa))

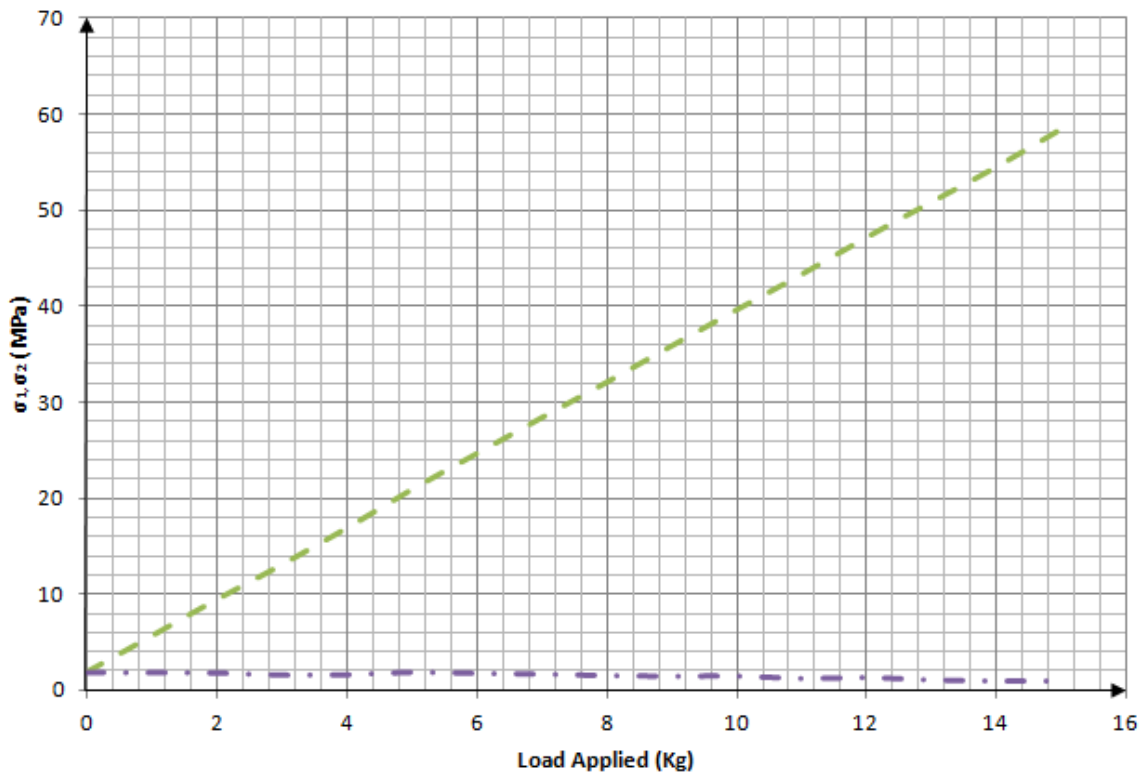


**Figure 8.27: Principal stresses ( $\sigma_1, \sigma_2$  (MPa)) at position W vs Offset load applied (kg) with 500 mm overlap**  
 (Key: — — — Experimental  $\sigma_1$  (MPa); — · — Experimental  $\sigma_2$  (MPa))

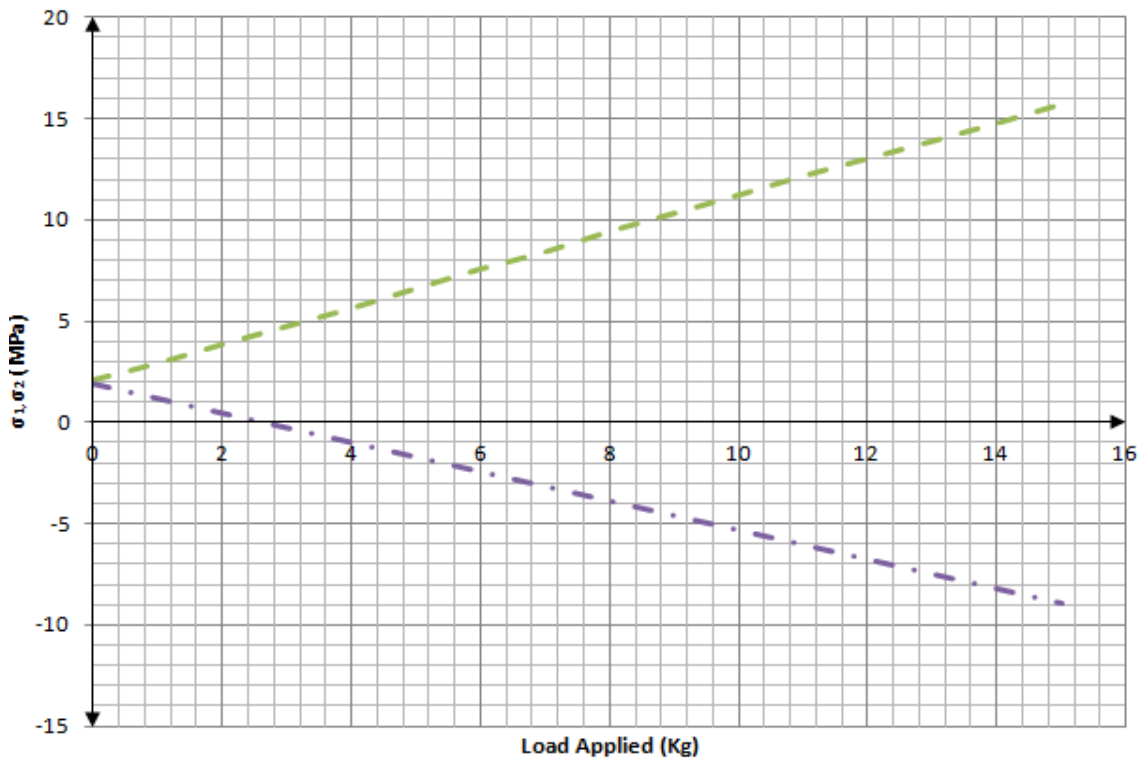


**Figure 8.28: Principal stresses ( $\sigma_1, \sigma_2$  (MPa)) at position X vs Offset load applied (kg) with 500 mm overlap**  
 (Key: — — — Experimental  $\sigma_1$  (MPa); — · — Experimental  $\sigma_2$  (MPa))

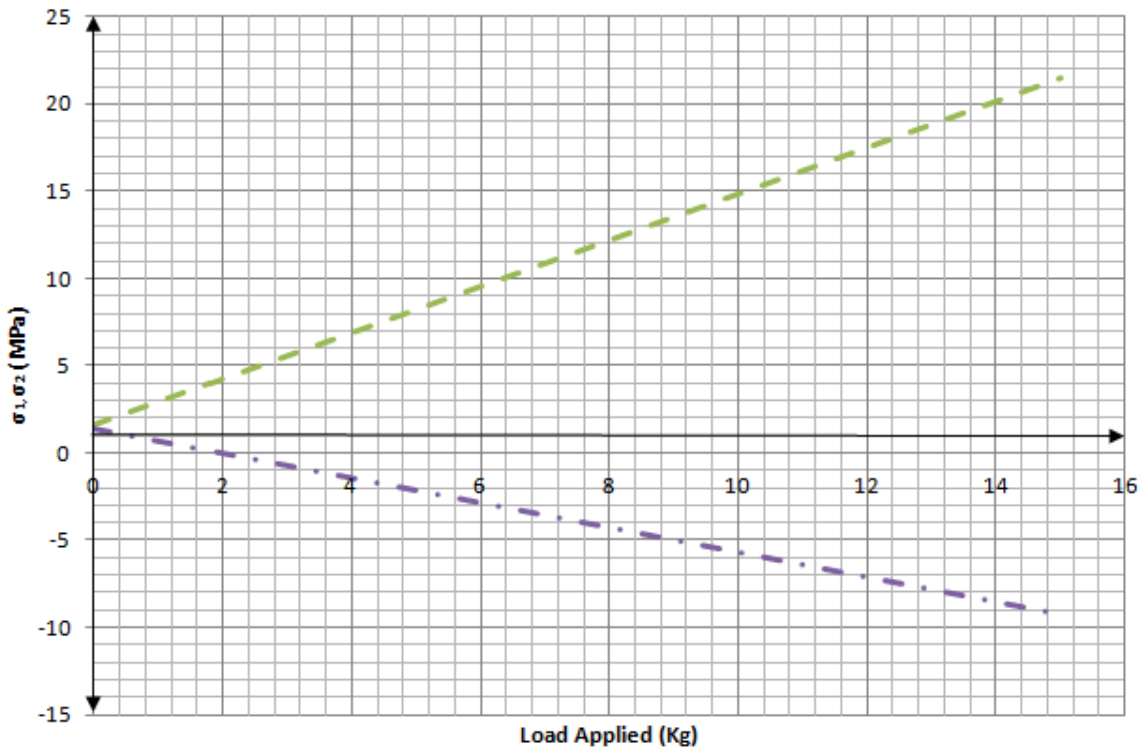


**Figure 8.29: Principal stresses ( $\sigma_1, \sigma_2$  (MPa)) at position Y vs Offset load applied (kg) with 500 mm overlap**

(Key: — — — Experimental  $\sigma_1$  (MPa); - · - Experimental  $\sigma_2$  (MPa))

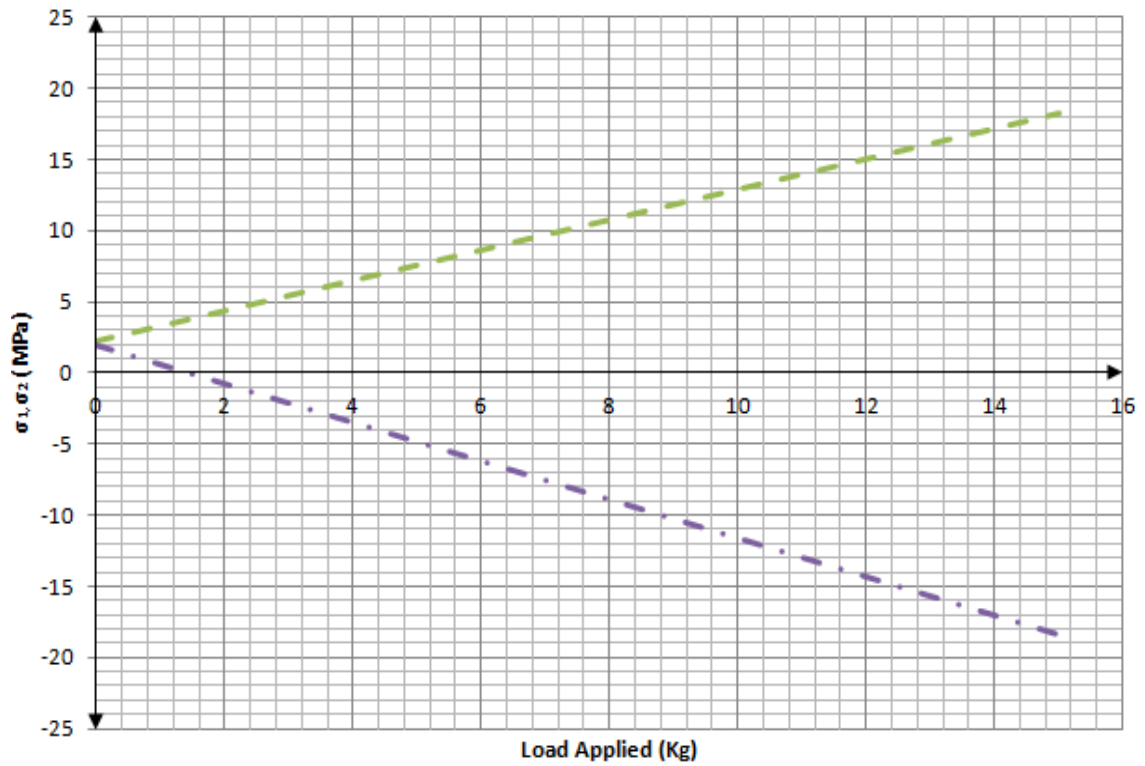


**Figure 8.30: Principal stresses ( $\sigma_1, \sigma_2$  (MPa)) at position Z vs Offset load applied (kg) with 500 mm overlap**

(Key: — — — Experimental  $\sigma_1$  (MPa); - · - Experimental  $\sigma_2$  (MPa))

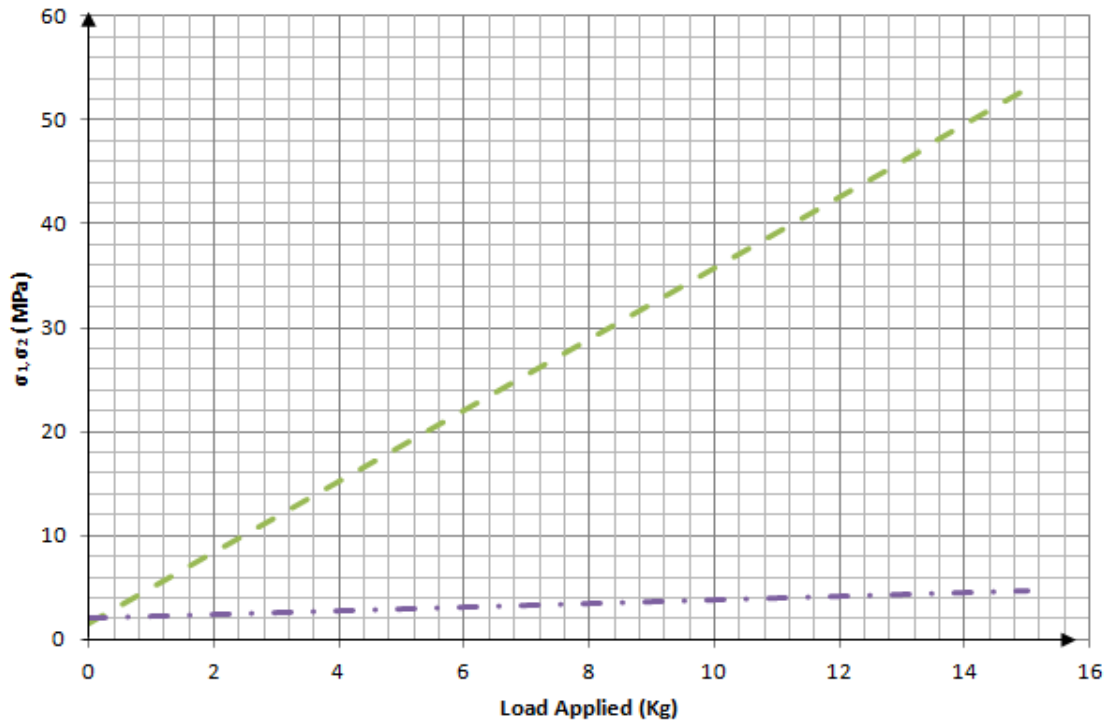


**Figure 8.31: Principal stresses ( $\sigma_1, \sigma_2$  (MPa)) at position W vs Inline load applied (kg) with 600 mm overlap**

(Key: — — — Experimental  $\sigma_1$  (MPa); — · — Experimental  $\sigma_2$  (MPa))

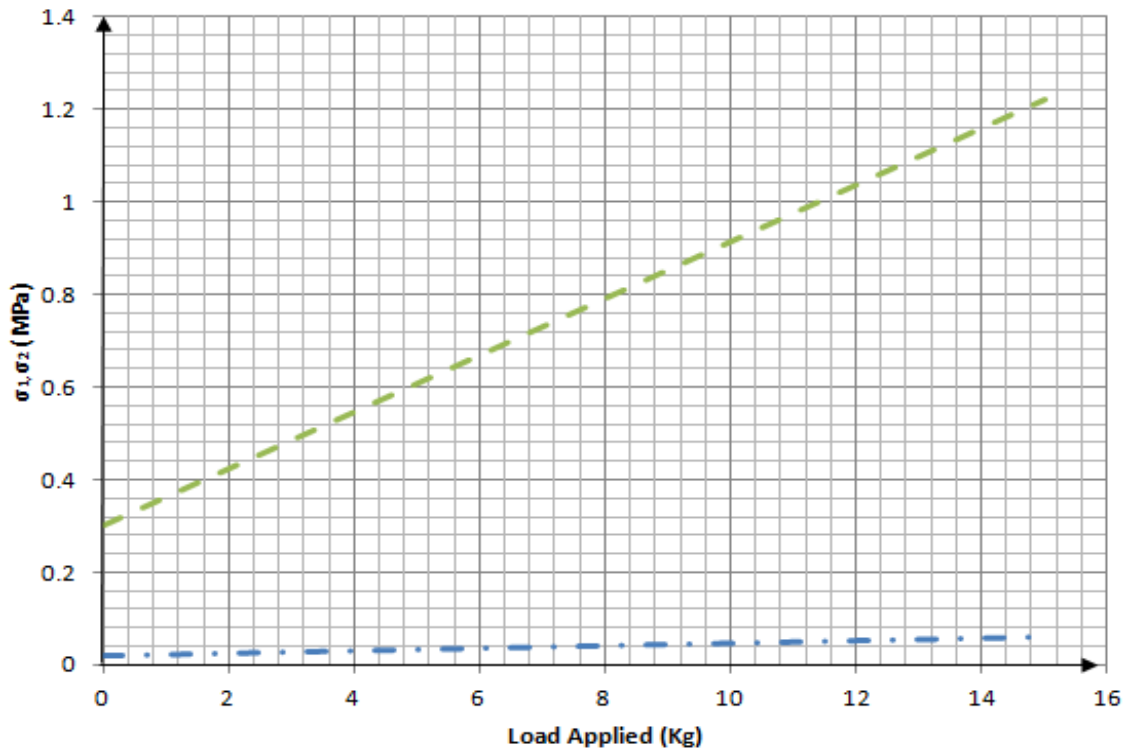


**Figure 8.32: Principal stresses ( $\sigma_1, \sigma_2$  (MPa)) at position X vs Inline load applied (kg) with 600 mm overlap**

(Key: — — — Experimental  $\sigma_1$  (MPa); — · — Experimental  $\sigma_2$  (MPa))

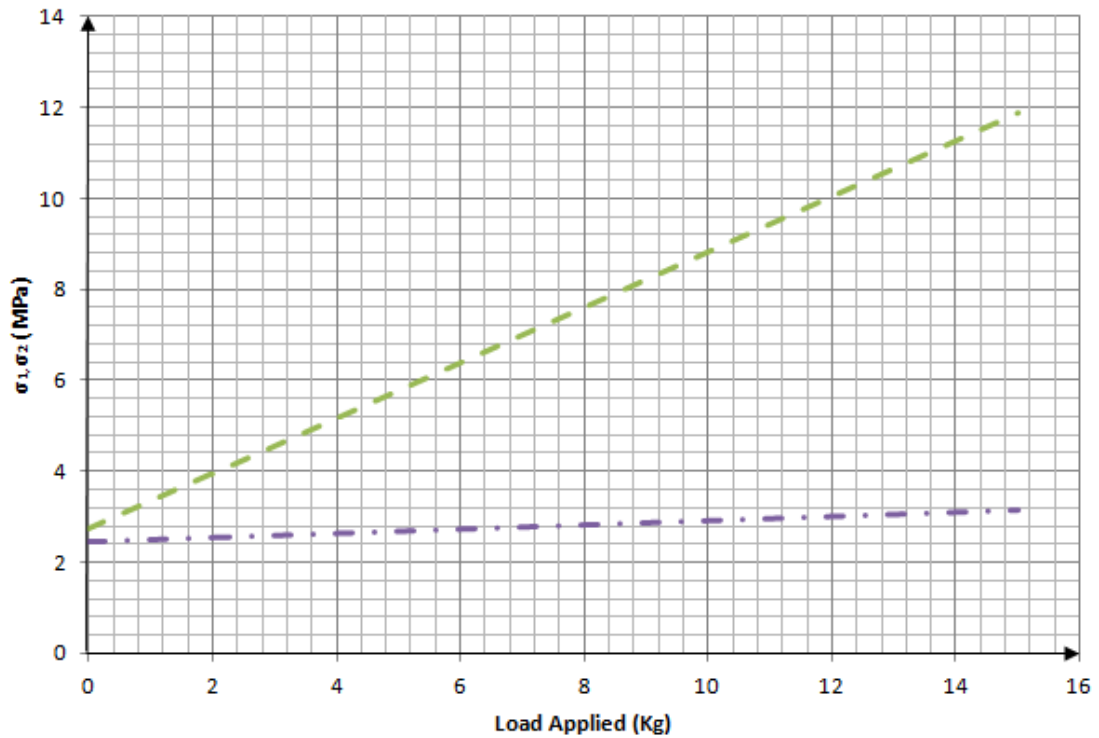


**Figure 8.33: Principal stresses ( $\sigma_1, \sigma_2$  (MPa)) at position Y vs Inline load applied (kg) with 600 mm overlap**  
 (Key: — — — Experimental  $\sigma_1$  (MPa); - · - Experimental  $\sigma_2$  (MPa))

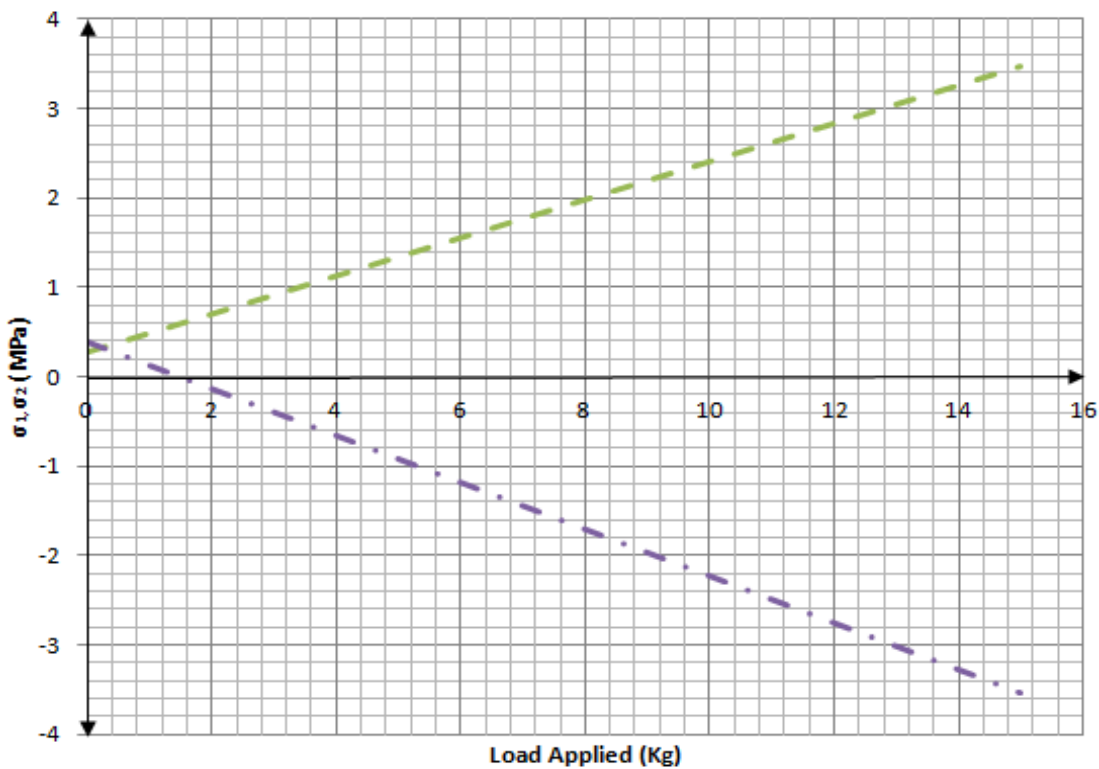


**Figure 8.34: Principal stresses ( $\sigma_1, \sigma_2$  (MPa)) at position Z vs Inline load applied (kg) with 600 mm overlap**  
 (Key: — — — Experimental  $\sigma_1$  (MPa); - · - Experimental  $\sigma_2$  (MPa))

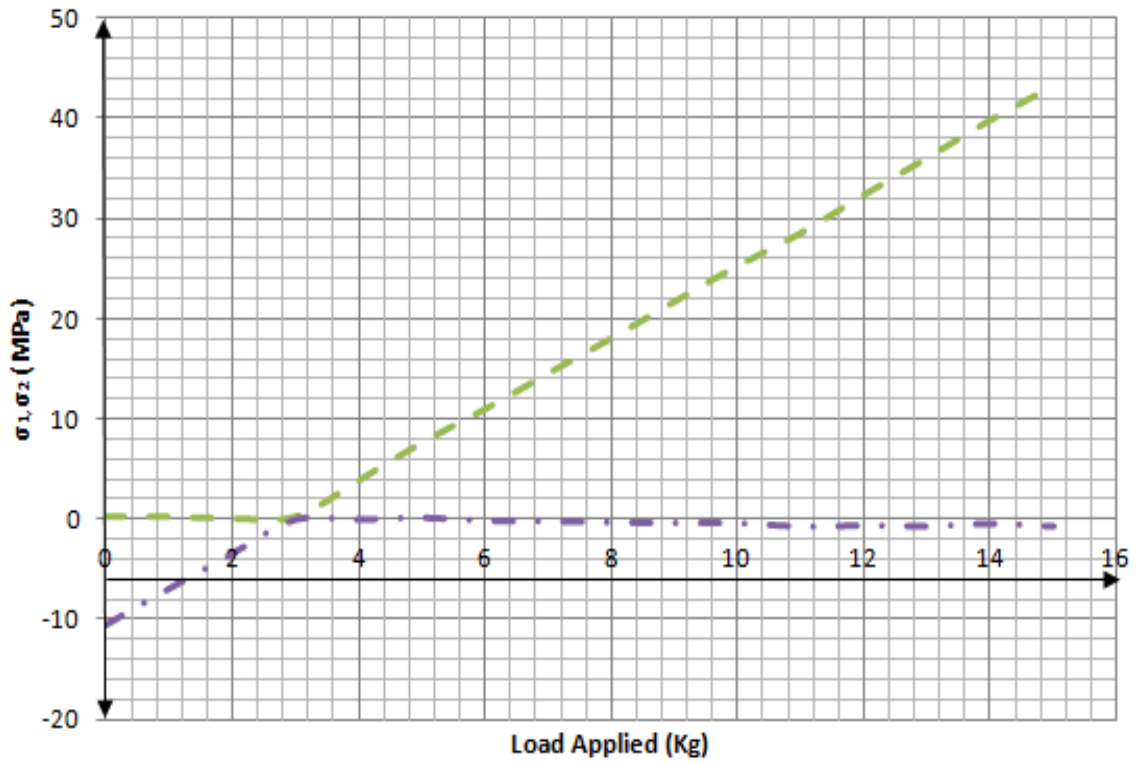


**Figure 8.35: Principal stresses ( $\sigma_1, \sigma_2$  (MPa)) at position W vs Offset load applied (kg) with 600 mm overlap**  
 (Key: — — — Experimental  $\sigma_1$  (MPa); - · - Experimental  $\sigma_2$  (MPa))

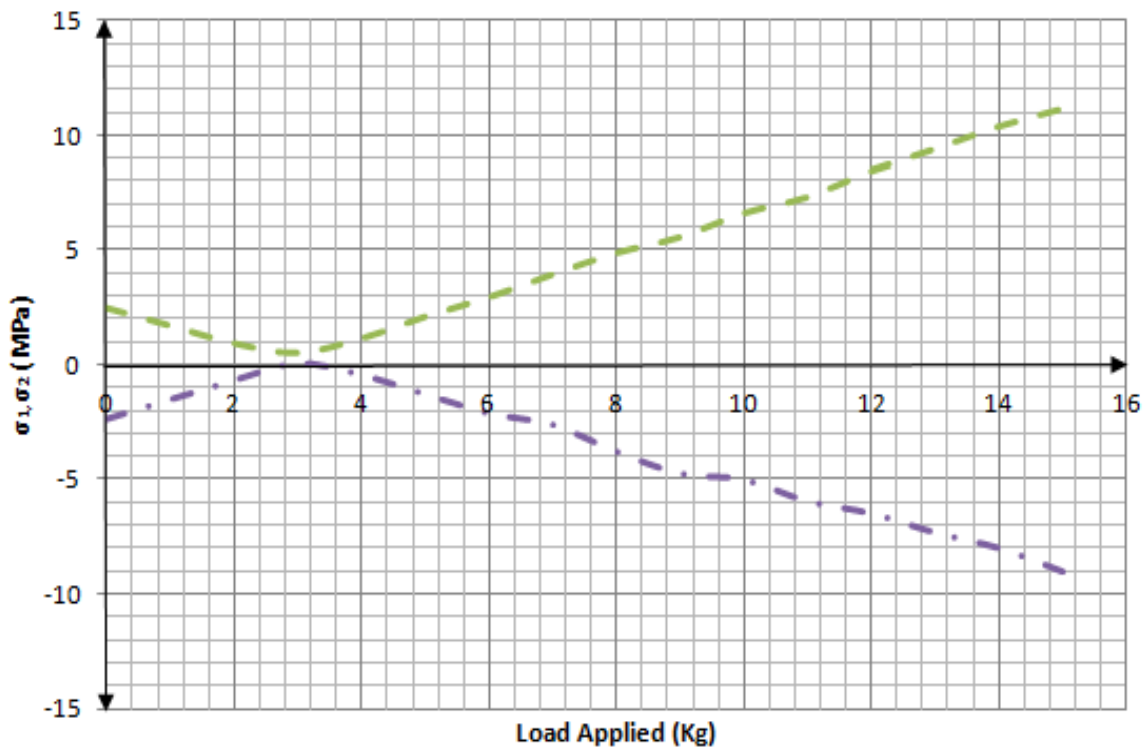


**Figure 8.36: Principal stresses ( $\sigma_1, \sigma_2$  (MPa)) at position X vs Offset load applied (kg) with 600 mm overlap**  
 (Key: — — — Experimental  $\sigma_1$  (MPa); - · - Experimental  $\sigma_2$  (MPa))

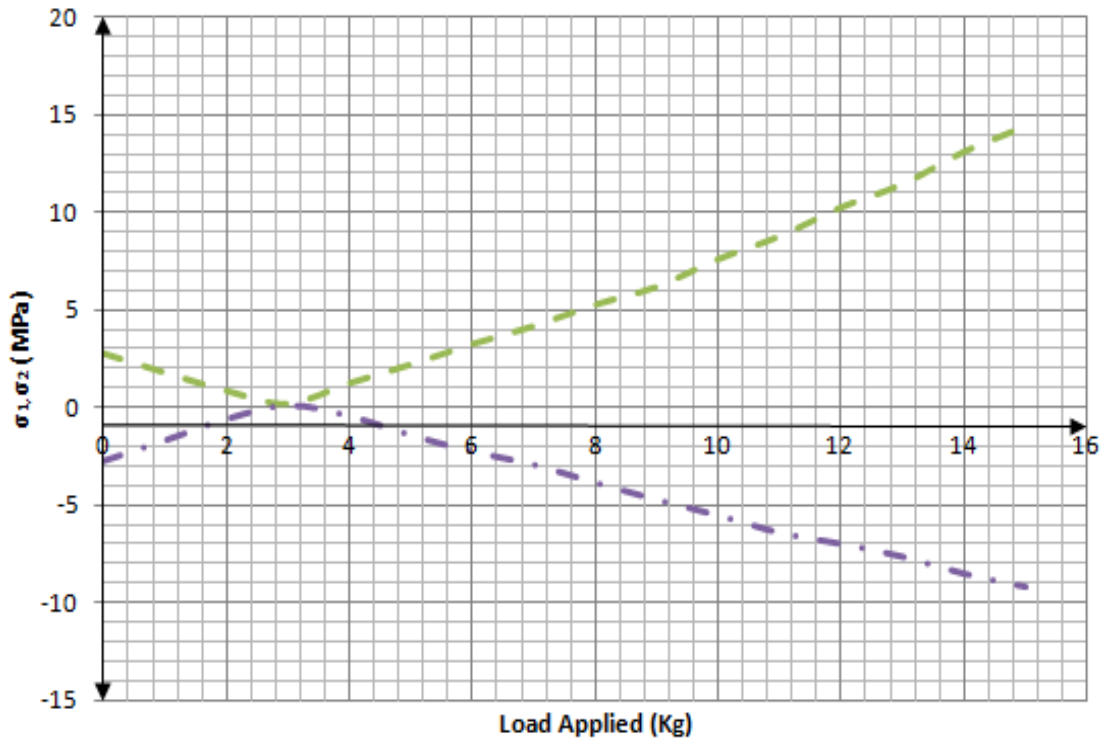


**Figure 8.37: Principal stresses ( $\sigma_1, \sigma_2$  (MPa)) at position Y vs Offset load applied (kg) with 600 mm overlap**

(Key: — — — Experimental  $\sigma_1$  (MPa); - · - Experimental  $\sigma_2$  (MPa))

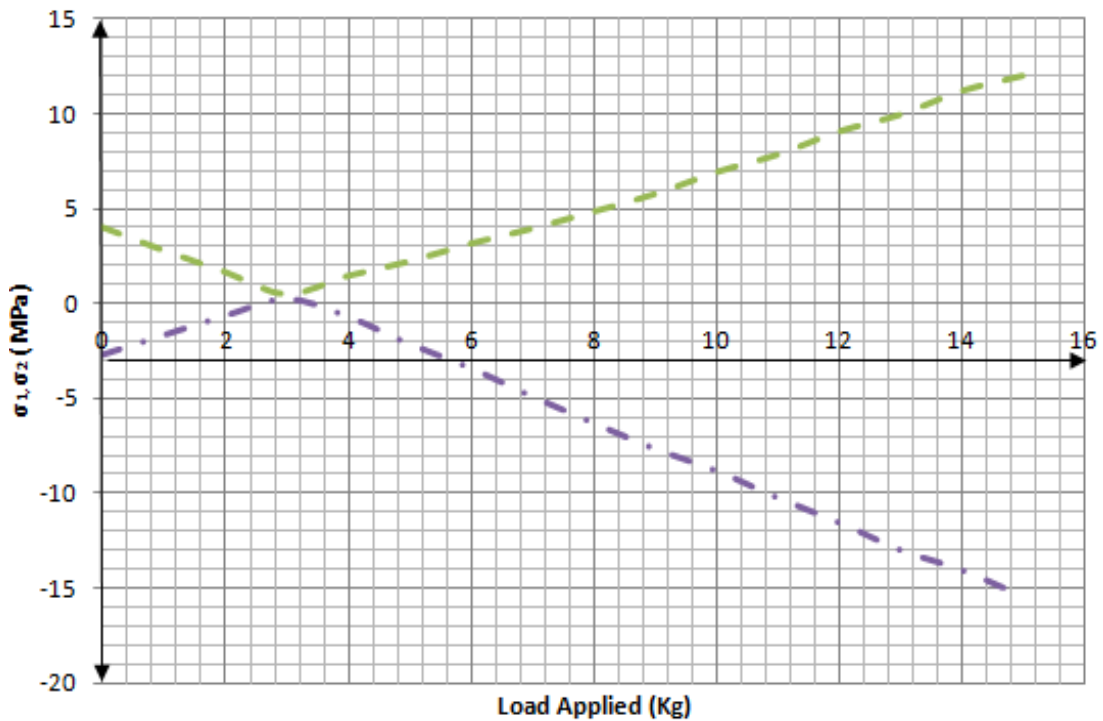


**Figure 8.38: Principal stresses ( $\sigma_1, \sigma_2$  (MPa)) at position Z vs Offset load applied (kg) with 600 mm overlap**

(Key: — — — Experimental  $\sigma_1$  (MPa); - · - Experimental  $\sigma_2$  (MPa))

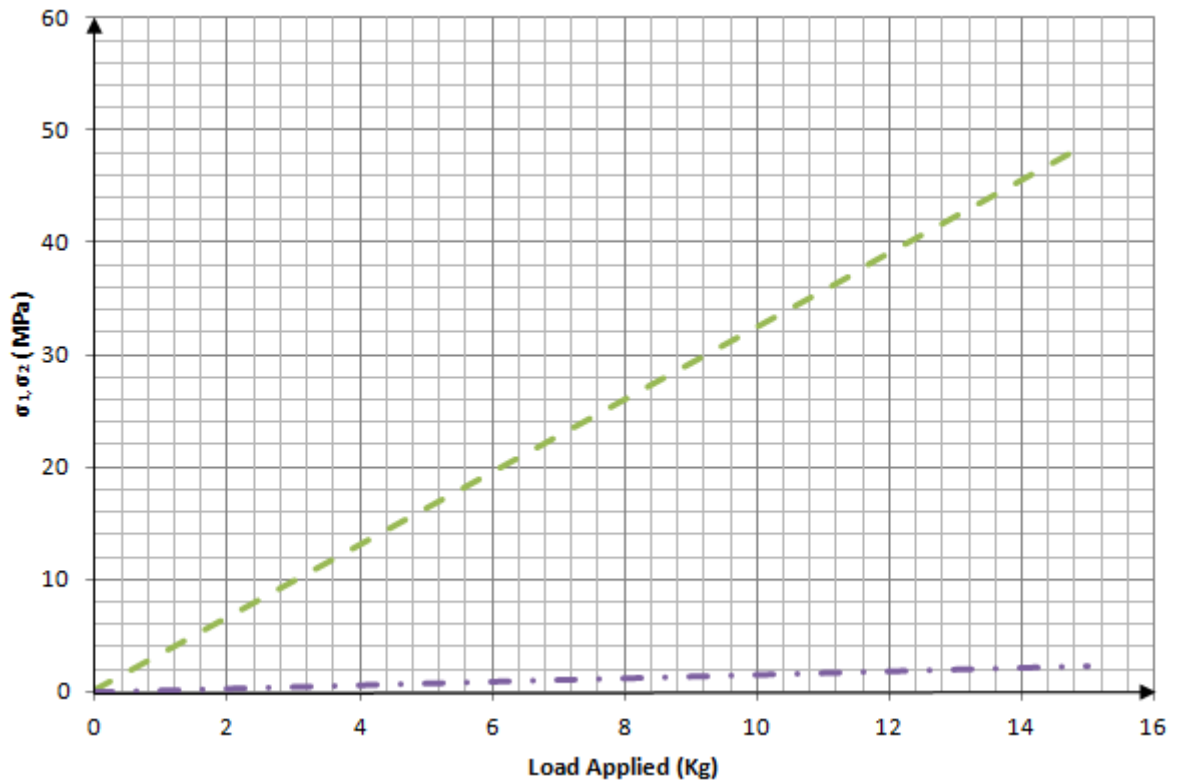


**Figure 8.39: Principal stresses ( $\sigma_1, \sigma_2$  (MPa)) at position W vs Inline load applied (kg) with 700 mm overlap**  
 (Key: — — — Experimental  $\sigma_1$  (MPa); - · - Experimental  $\sigma_2$  (MPa))

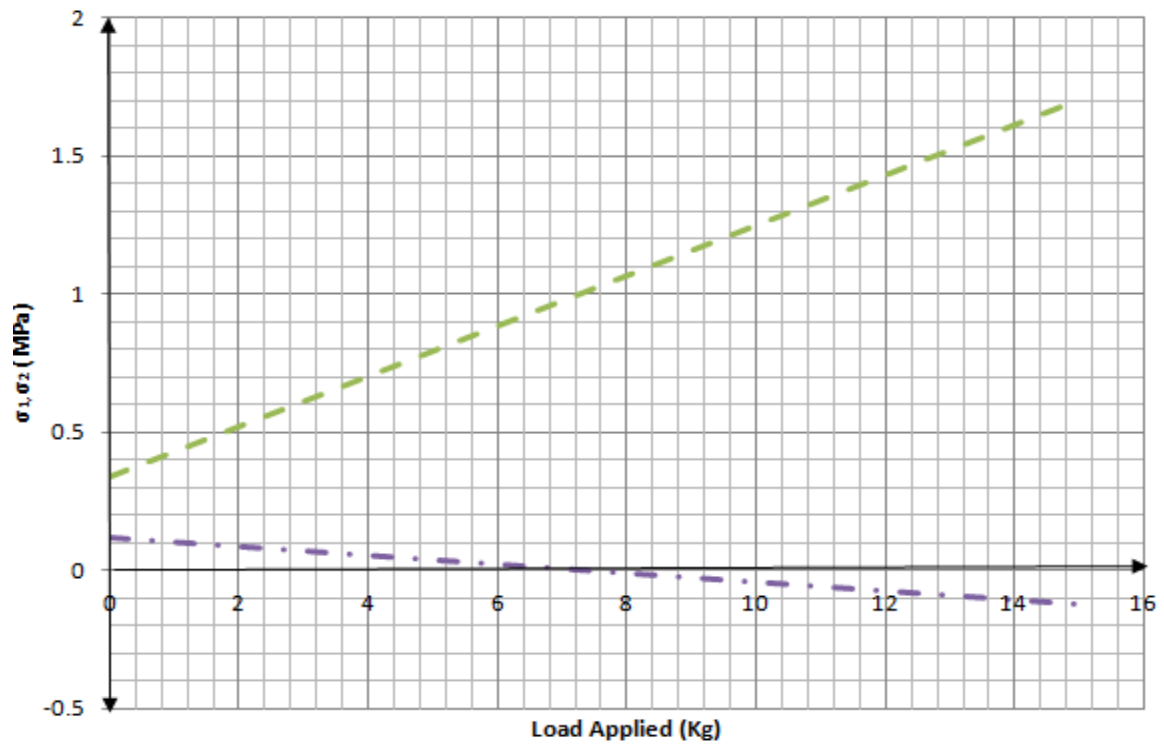


**Figure 8.40: Principal stresses ( $\sigma_1, \sigma_2$  (MPa)) at position X vs Inline load applied (kg) with 700 mm overlap**  
 (Key: — — — Experimental  $\sigma_1$  (MPa); - · - Experimental  $\sigma_2$  (MPa))

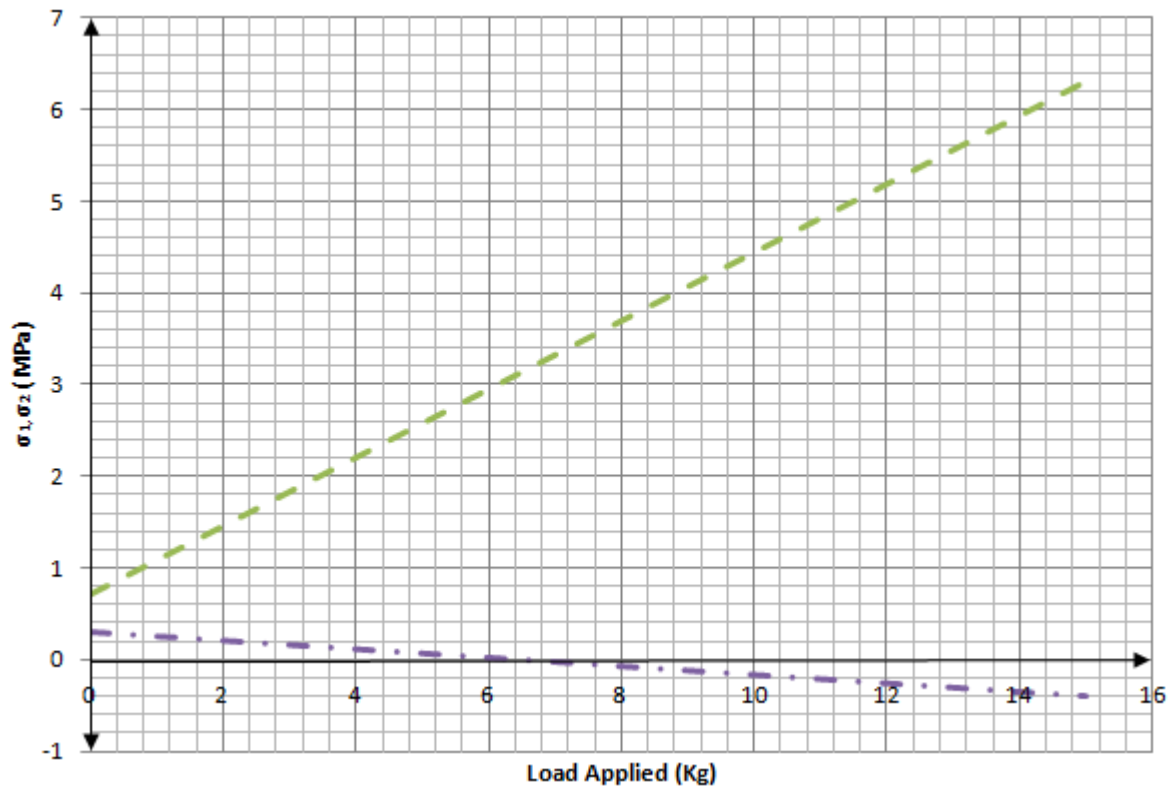


**Figure 8.41: Principal Stresses ( $\sigma_1, \sigma_2$  (MPa)) at Position Y vs Inline Load Applied (Kg) with 700 mm overlap**  
 (Key: — — — Experimental  $\sigma_1$  (MPa); - · - Experimental  $\sigma_2$  (MPa))

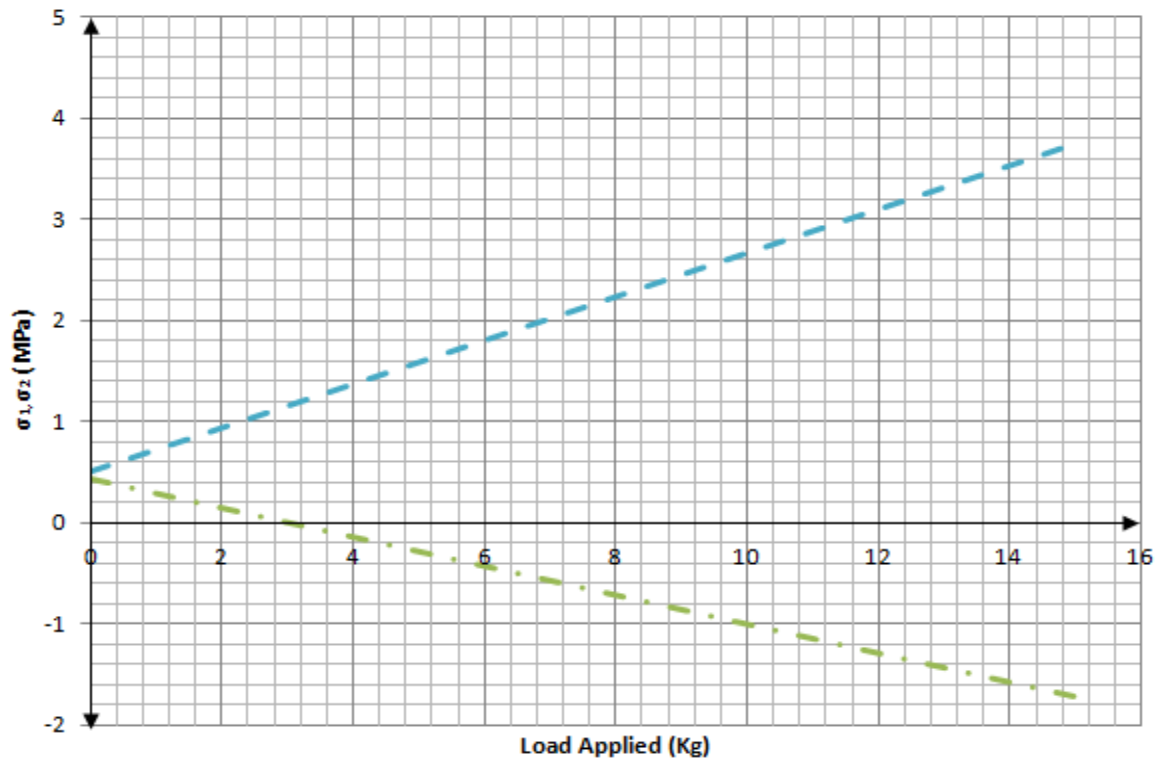


**Figure 8.42: Principal stresses ( $\sigma_1, \sigma_2$  (MPa)) at position Z vs Inline load applied (kg) with 700 mm overlap**  
 (Key: — — — Experimental  $\sigma_1$  (MPa); - · - Experimental  $\sigma_2$  (MPa))

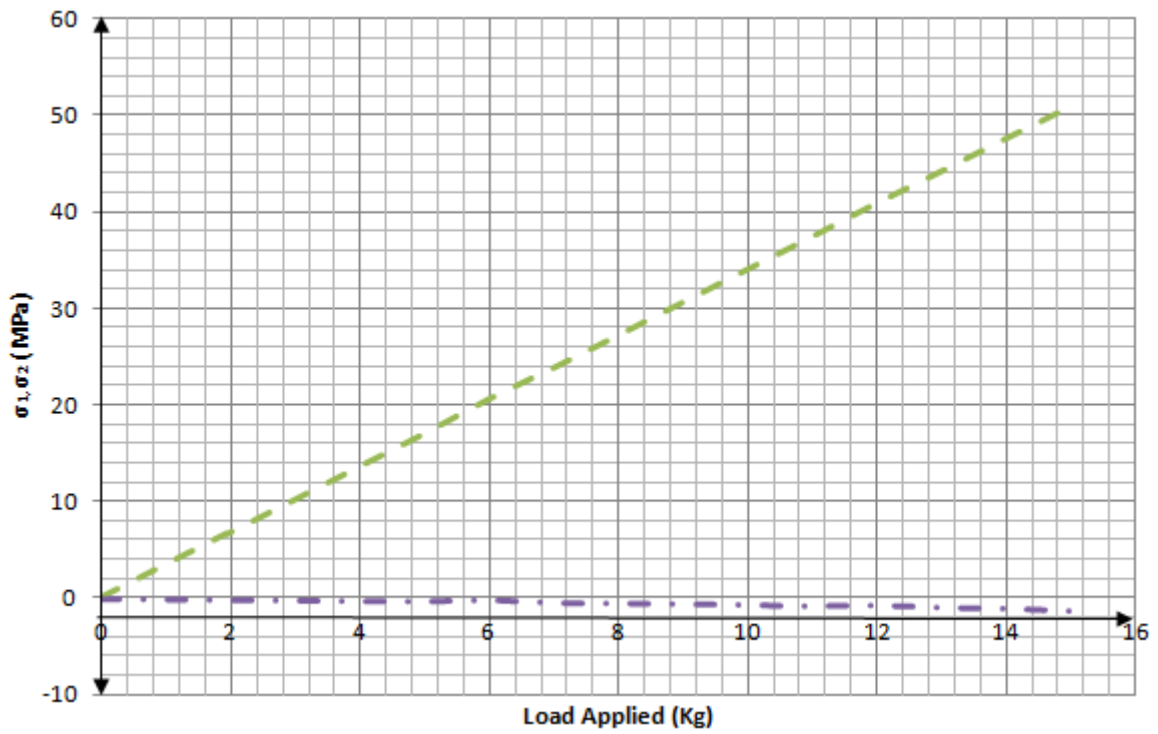


**Figure 8.43: Principal stresses ( $\sigma_1, \sigma_2$  (MPa)) at position W vs Offset load applied (kg) with 700 mm overlap**

(Key: — — — Experimental  $\sigma_1$  (MPa); - · - Experimental  $\sigma_2$  (MPa))

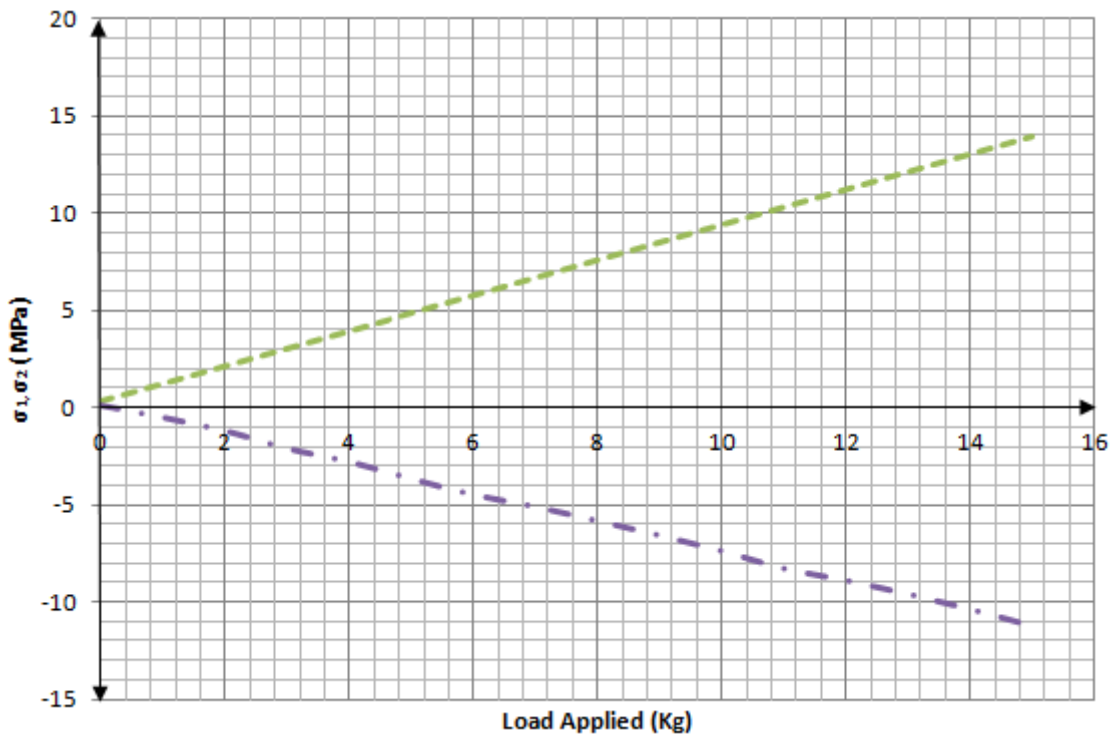


**Figure 8.44: Principal stresses ( $\sigma_1, \sigma_2$  (MPa)) at position X vs Offset load applied (kg) with 700 mm overlap**

(Key: — — — Experimental  $\sigma_1$  (MPa); - · - Experimental  $\sigma_2$  (MPa))

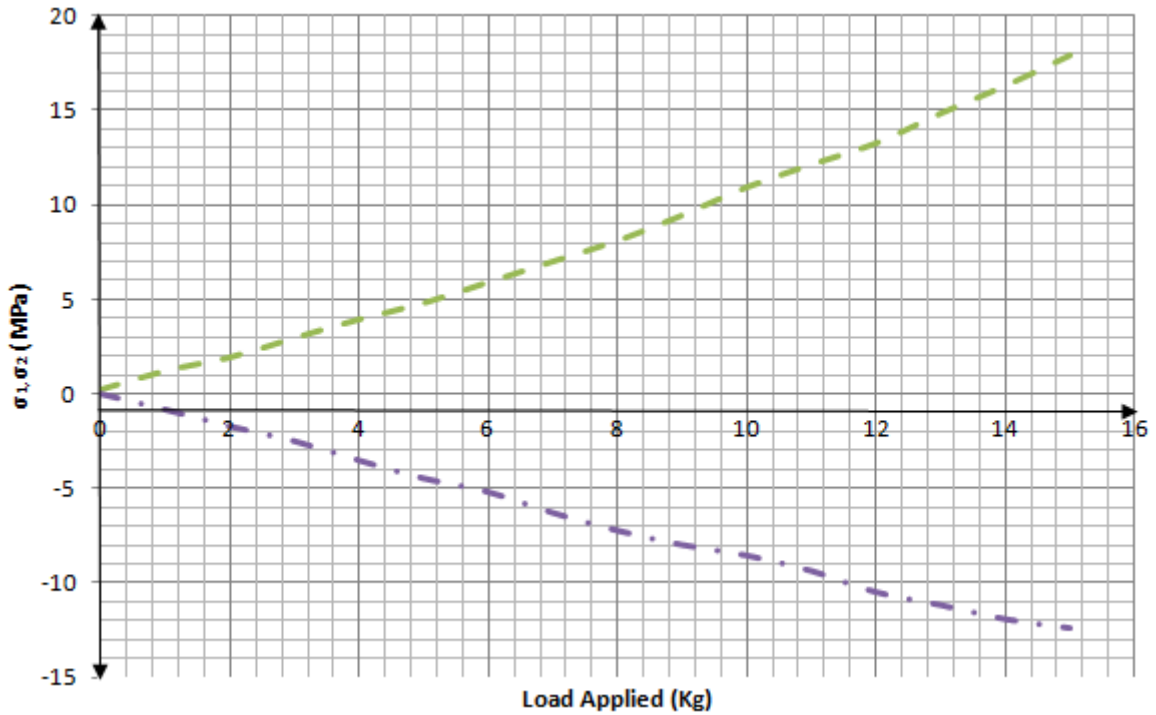


**Figure 8.45: Principal stresses ( $\sigma_1, \sigma_2$  (MPa)) at position Y vs Offset load applied (kg) with 700 mm overlap**  
 (Key: — — — Experimental  $\sigma_1$  (MPa); - . - Experimental  $\sigma_2$  (MPa))

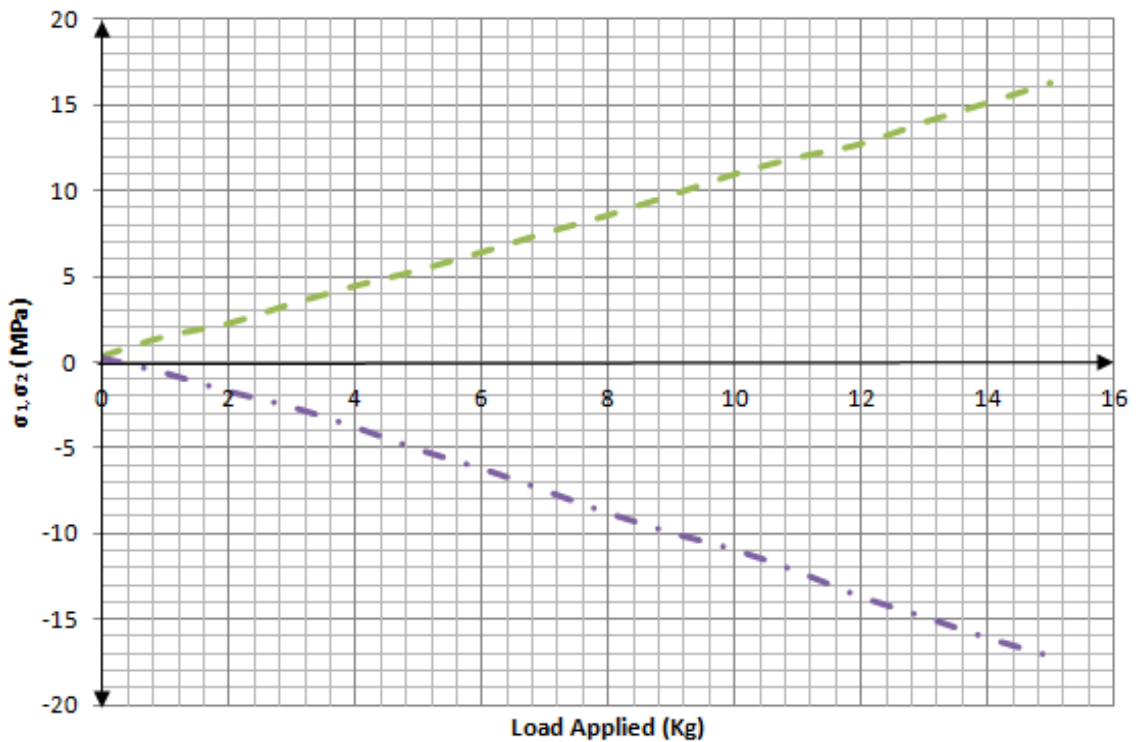


**Figure 8.46: Principal stresses ( $\sigma_1, \sigma_2$  (MPa)) at position Z vs Offset load applied (kg) with 700 mm overlap**  
 (Key: — — — Experimental  $\sigma_1$  (MPa); - . - Experimental  $\sigma_2$  (MPa))

## 8.6 Summary

The experimental analyses and results conducted on the experimental test rig having dimensions detailed in Table 8.1 are documented in this chapter. The desired outcomes of this experimental section were attained and are briefly summarised.

1. Tip deflections for varying load magnitudes were physically measured and plotted as shown in Figure 8.13, for differing overlap lengths. From experimentally determined tip deflections, the dimensionless parameter  $\frac{y}{y_0}$  is extrapolated, and plotted against the equivalent overlap ratio parameter  $\alpha$ , in turn obtained by dividing the overlap length by the length of the fixed-end section of the telescoping assembly. These curves are plotted 8.14.
2. Strain gauges were bonded at four locations along the telescopic assembly and the principal strains induced were recorded for increasing magnitudes of inline and offset loading, for varying overlap lengths of 400 mm, 500 mm, 600 mm and 700 mm. These strains were converted using relevant stress-strain transformation equations outlined in Appendix H, to their equivalent principal stresses and plotted against the load applied.

## CHAPTER 9: DISCUSSION AND CONCLUSIONS

### 9.1 Results

This chapter aims to document the results of the theoretical, experimental and Finite Element Analysis conducted thus far, upon the two section telescopic cantilever beam assembly and comparisons between them. The underlying principle of bending cantilever beams has been revisited in which the moment of resistance is identified as the mechanism for transferring the effects of external loads within continuous beams. Since this cannot be used as the mechanism for discontinuous telescopic beams an alternative '*Tip Reaction Model*' is proposed in which the external loading is reacted at the tips of the overlaps.

The two section telescoping cantilever beam assembly has been investigated and analysed in detail over the course of this body of work. Using the four common methods of tip deflection prediction as detailed in Chapter 3, unique expressions for end-load versus deflection for the two section telescoping cantilever beam assembly are derived. Each of these expressions, although unique, compares remarkably well, not only with each other, but with both experimental and Finite Element Analysis results, in the form of deflection curves plotted against increasing magnitudes of tip load, for different  $\frac{wL}{P}$  ratios. All of these results are presented in § 9.1.1.

§ 4.9 details the expression that expresses the critical buckling load, that the two section telescoping cantilever beam assembly can withstand. This expression was derived from energy methods and has been tailored to suit a number of variables within the structure such as differing sectional lengths, overlap lengths and sectional properties. In addition to the theoretical derivation of this formula, the determination of critical buckling load for the same structure using Finite Element Analysis has been achieved and then compared and used to validate the theory mentioned earlier.

§ 6.2 and § 6.3 detail the bending and shear stress formulation for the two section telescopic cantilever beam assembly for both inline and offset loading scenarios. Theoretical bending and shear stress values were determined along the relevant cross sections of the assembly and plotted for different values  $\frac{wL}{P}$  ratios. Finite Element Analysis software was also used to generate both bending and shear stress values along the cross section of the assembly, for

comparison with the afore mentioned theoretical values. Chapter 8 details the stress analysis that was performed on the two section telescoping cantilever beam assembly and graphs of principal stresses at predetermined locations along the structure are shown in Figures 8.15-8.46. The graphs plot the principal stresses at given positions against increasing magnitudes of either inline or offset applied loadings for different overlap lengths.

### 9.1.1 Deflection Results

Figure 3.2 shows the deflection plot obtained from Macaulay's theorem, plotted against increasing overlap ratios for different  $\frac{wL}{P}$  ratios. Tip deflections for differing overlap lengths and increasing tip loads are generated using a 'C' program as developed and shown in its entirety in Appendix B. Entering the variables as outlined in Table 3.2 the required tip deflections are obtained. The ordinate magnitude is obtained by dividing the ratio of tip deflection obtained from the 'C' program, for a given value of  $\frac{wL}{P}$  which in turn varies from 0.01 to 10, in multiples of 10, to the tip deflection of a single fixed end section cantilever having length  $L$  and uniform second moment of area  $I$ . In other words  $y_0$  equals  $\frac{PL^3}{3EI}$ . The quantity  $\frac{wL}{P}$  represents the ratio of the product of the self weight over the single fixed end section cantilever and the length over which it acts to the tip load acting on the same single fixed end cantilever section. The abscissa magnitude, as mentioned earlier, represents the increasing values of the overlap ratios, increasing in steps of 0.1, from 0.1 to 1. Similar deflection curves are plotted for the expressions derived using Mohr's Moment Area Theorem, Castigliano's Theorem and the Virtual Work Method as shown in Figures 3.7, 3.10 and 3.12, respectively. The only exception to the curves generated by the latter three methods and those generated in the case of Macaulay's theorem are the abscissa magnitudes varying from 0.1 to 1 in steps of 0.1. The reason for this is the fact that the 'C' program is unable to compute values for the tip reactions as detailed in Appendix A.2 for an overlap ratio of 0. On comparing the deflection curves generated for lower  $\frac{wL}{P}$  ratios of 0.01, 0.1 and 1 in Figures 3.2, 3.7, 3.10 and 3.12 it is evident that not much scope is available for comparison purely because the curves overlay upon each other. However of interest here is the fact that for a

$\frac{wL}{P}$  ratio of 10 the curves are more apart and separate from each other as is clearly evident in Figure 3.13. The difference between Macaulay's theorem and the three other methods could be explained as being due to the reliance on the former on the tip reactions calculated for the varying overlap lengths, which the latter three in turn are independent of. Of greater interest arguably, is the difference between the deflection curves obtained from Mohr's method and those generated from both Castigliano's and the Virtual Work Method. The deflection magnitudes derived using Castigliano's method and the Virtual Work method are the same. This is because the equations used to generate the respective curves are the same as is evident from Equations (3.18) and (3.26). Comparing either of these equations mentioned with Equation (3.11) derived using Mohr's method reveals a significant difference in the second term which accounts for the uniformly distributed loading or self weight of the two section telescoping assembly. This difference in the case of the Mohr's method analysis is in part due to the changing moments of areas that are taken into consideration when computing the deflection as elaborated in §3.5.2 and shown diagrammatically in Figure 3.6. An important point to be made here is that the deflection curves plotted in Chapter 3 were plotted for a candidate assembly having dimensions as specified in Table 3.1, with the fixed and free section lengths assumed to be 1200 mm and 1000 mm respectively.

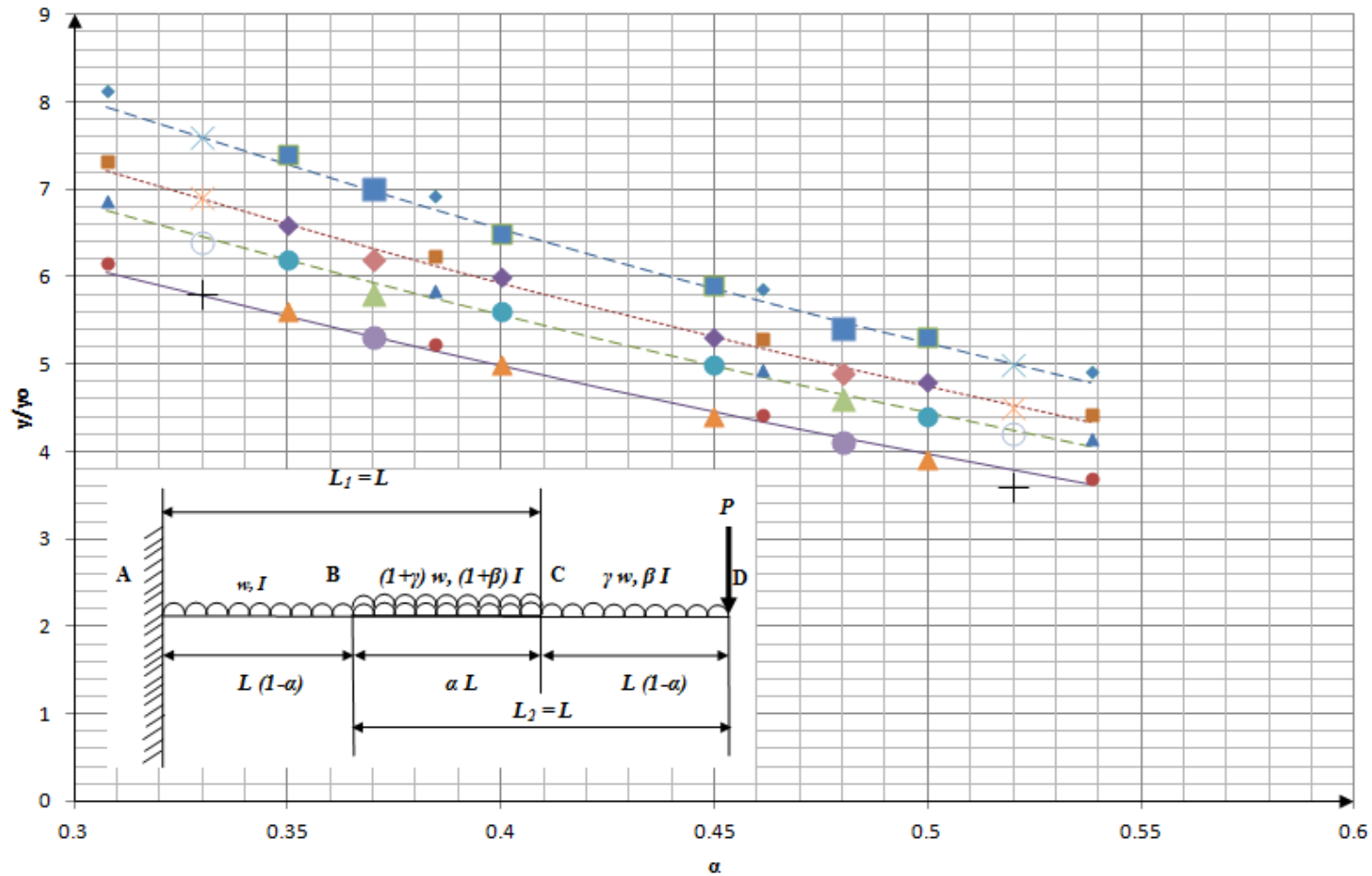
Figure 7.2 represents the deflection curves generated using Finite Element Analysis. The ordinate and abscissa magnitudes are plotted as mentioned above. It must be highlighted that the use of non dimensionalised ratios is conducive to plotting presentable values and also allows for effective comparisons. The deflection curves generated from the software use as the candidate assembly the same dimensions as that of the experimental test rig, the dimensions of which are detailed in Table 8.1, for  $\frac{wL}{P}$  ratios of 10, 1, 0.01 and 0.1. The curves thus generated and displayed in Figure 7.2, serve merely as a benchmark, for further comparison against the experimentally obtained deflection curves shown in Figure 8.13.

Figure 8.13 represents the experimentally derived deflection curves obtained by plotting the end load applied to the corresponding tip deflection produced for increasing overlap lengths as indicated by the key. Again these curves were obtained for the experimental test rig the dimensions of which are elaborated in Table 8.1. These curves were plotted first by initially loading the assembly in the inline loading configuration as shown in Figure 8.3 (a) with a

pre-load of 10 N and setting the dial gauge to zero before commencing the deflection testing. This was done in order to reduce any errors that may creep in and remove any slack within the assembly. Figure 8.14 in turn represents the deflection curves of  $\frac{y}{y_0}$  plotted against the overlap ratio  $\alpha$  for applied loads of 30, 40, 50 and 80 N. The ratio  $\frac{y}{y_0}$  was extrapolated using the data recorded in Figure 8.13.

When similar loading and experimental test rig set up conditions and are applied to generate deflection curves, using the four deflection prediction equations, they compare most favourably with the deflection curves generated from experimental results, such that there is no means of differentiation between the curves themselves for the different load magnitudes. Again this is due to the fact that the curves overlap upon each other as can be evidenced in Figure 9.1.

Another point to be considered, with regards to the experimental results is explained using Figure 9.2. The caption for Figure 8.13 details the key for each curve that has been obtained experimentally. Each of the curves meets the abscissa at certain points, each of which is a specific and unique value of tip deflection. These values correspond to the deflection of the assembly for a particular overlap length, under the action of its own weight. Also to be noted in Figure 9.3 is that all the curves irrespective of overlap lengths meet at a fixed ordinate having a magnitude of 20 N. This ordinate magnitude can be taken to be the self weight of the assembly, irrespective and independent of the overlap length or the overall length of the assembly.



**Figure 9.1: Comparison of Deflection Curves vs. Parameter  $\alpha$ , for the two section telescopic cantilever beam assembly having individual part dimensions outlined in Table 8.1**

(Applied Load 30 N:  $\blacklozenge$  Macaulay;  $\blacksquare$  Mohr;  $\blacksquare$  Castigliano and Virtual Work;  $\times$  FEA;  $-\cdot-\cdot-$  Experimental  
 Applied Load 40 N:  $\blacksquare$  Macaulay;  $\blacklozenge$  Mohr;  $\blacklozenge$  Castigliano and Virtual Work;  $\times$  FEA;  $\cdots$  Experimental  
 Applied Load 50 N:  $\blacktriangle$  Macaulay;  $\bullet$  Mohr;  $\blacktriangle$  Castigliano and Virtual Work;  $\circ$  FEA;  $-\cdot-\cdot-$  Experimental  
 Applied Load 80 N:  $\bullet$  Macaulay;  $\blacktriangle$  Mohr;  $\bullet$  Castigliano and Virtual Work;  $+$  FEA;  $-\cdot-\cdot-$  Experimental)

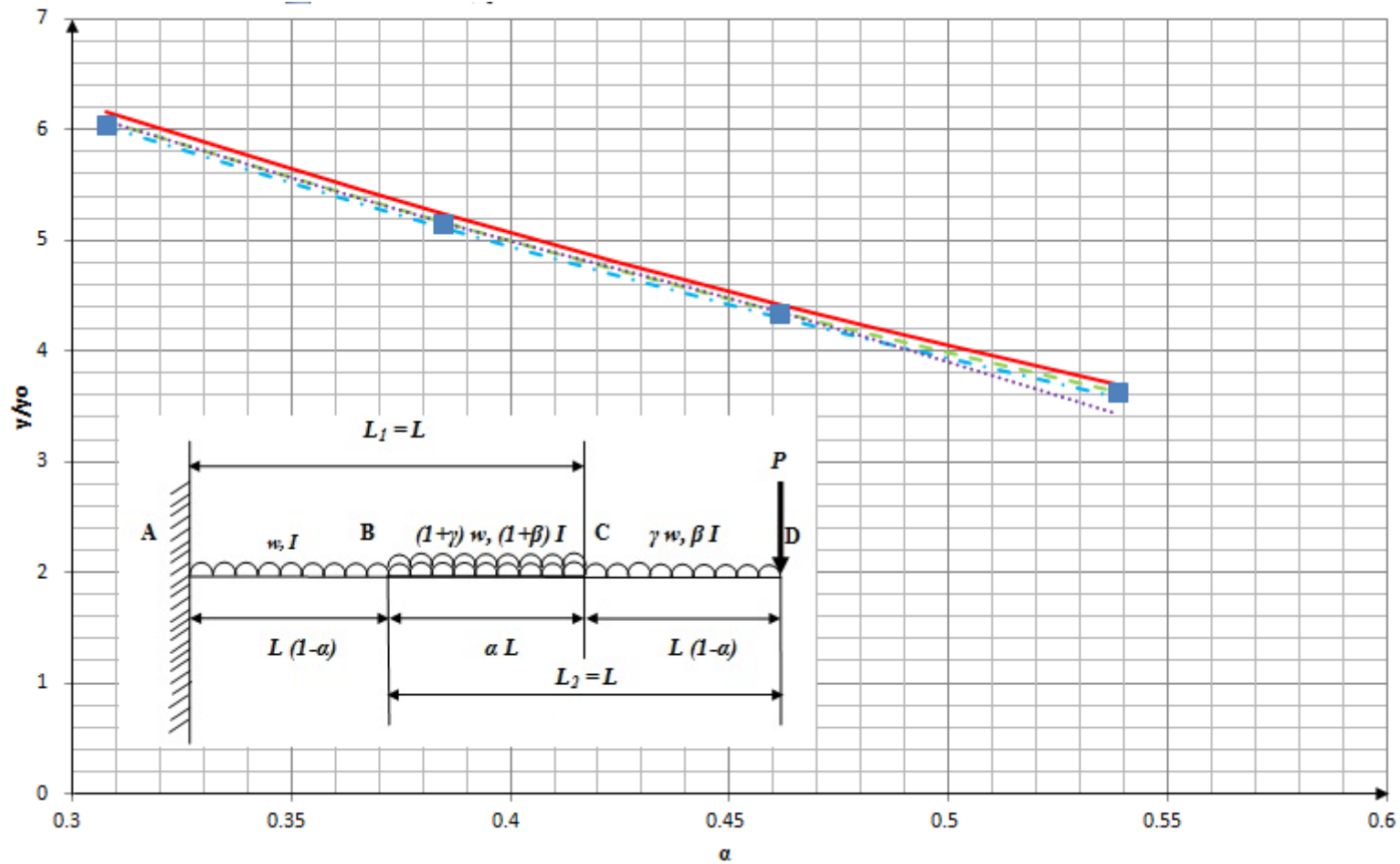


**Figure 9.1 (a): Comparison of Deflection Curves vs. Parameter  $\alpha$ , for the two section telescopic cantilever beam assembly having individual part dimensions outlined in Table 8.1, for an applied load of 80 N.**

(Applied Load 80 N: ■ Experimental; — Macaulay; - - - Mohr; - · - Castigliano and Virtual Work; ····· FEA)

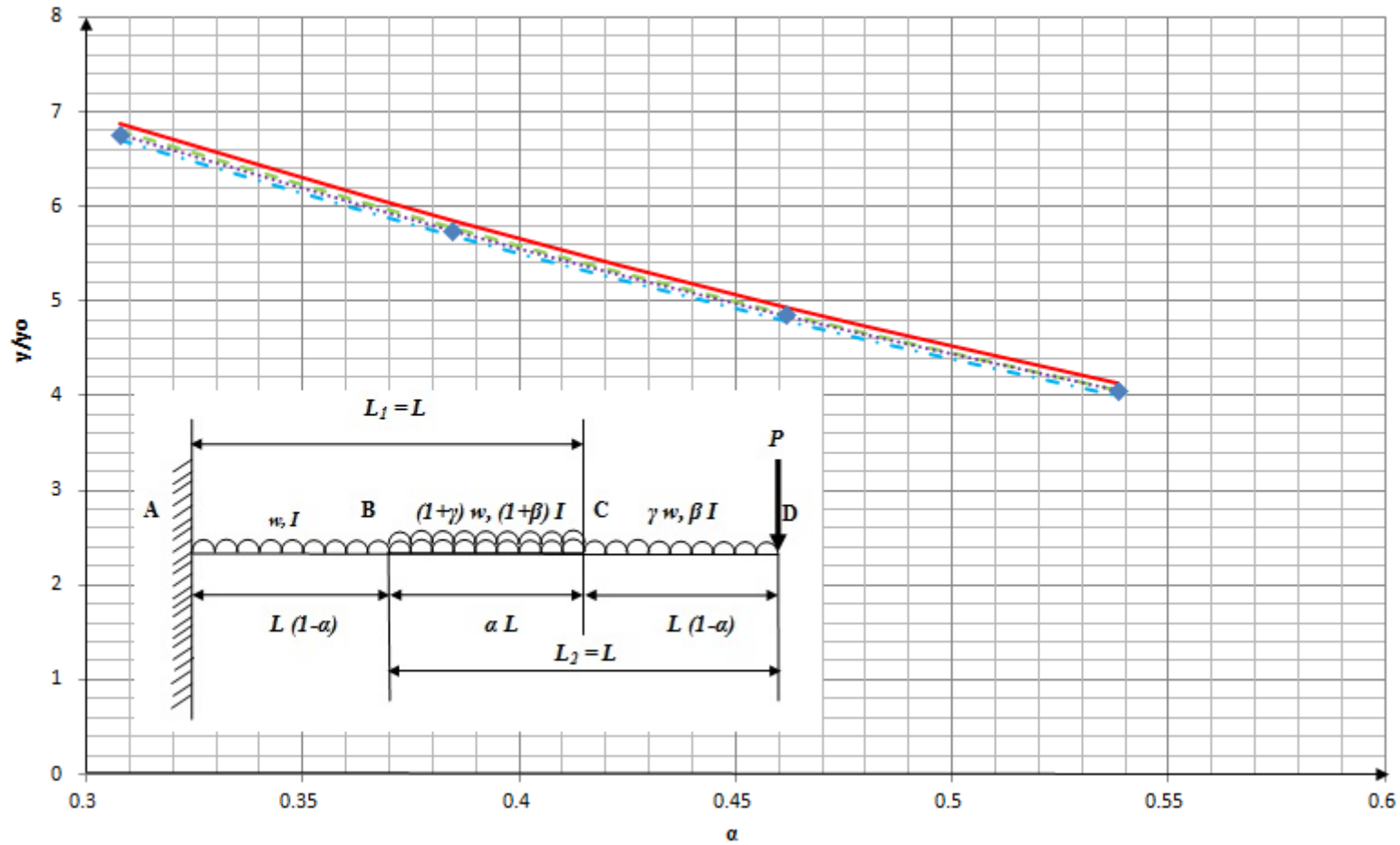


Figure 9.1 (b): Comparison of Deflection Curves vs. Parameter  $\alpha$ , for the two section telescopic cantilever beam assembly having individual part dimensions outlined in Table 8.1, for an applied load of 50 N.

(Applied Load 50 N:  $\blacklozenge$  Experimental;  $\text{---}$  Macaulay;  $\text{- - -}$  Mohr;  $\text{- \cdot -}$  Castigliano and Virtual Work;  $\text{\cdots}$  FEA)

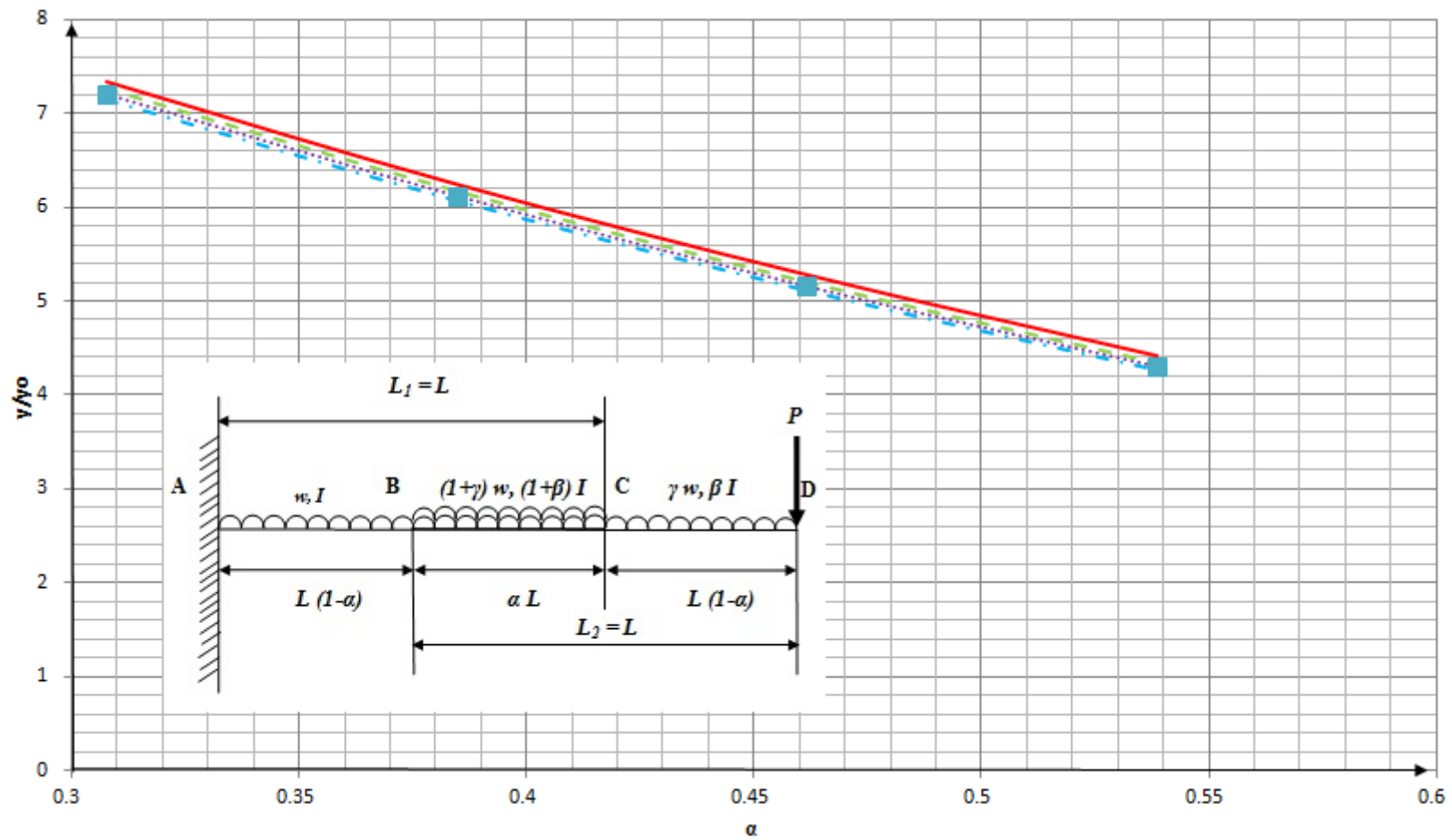


Figure 9.1 (c): Comparison of Deflection Curves vs. Parameter  $\alpha$ , for the two section telescopic cantilever beam assembly having individual part dimensions outlined in Table 8.1, for an applied load of 40 N.

(Applied Load 40 N: ■ Experimental; — Macaulay; - - - Mohr; - · - Castigliano and Virtual Work; ····· FEA)

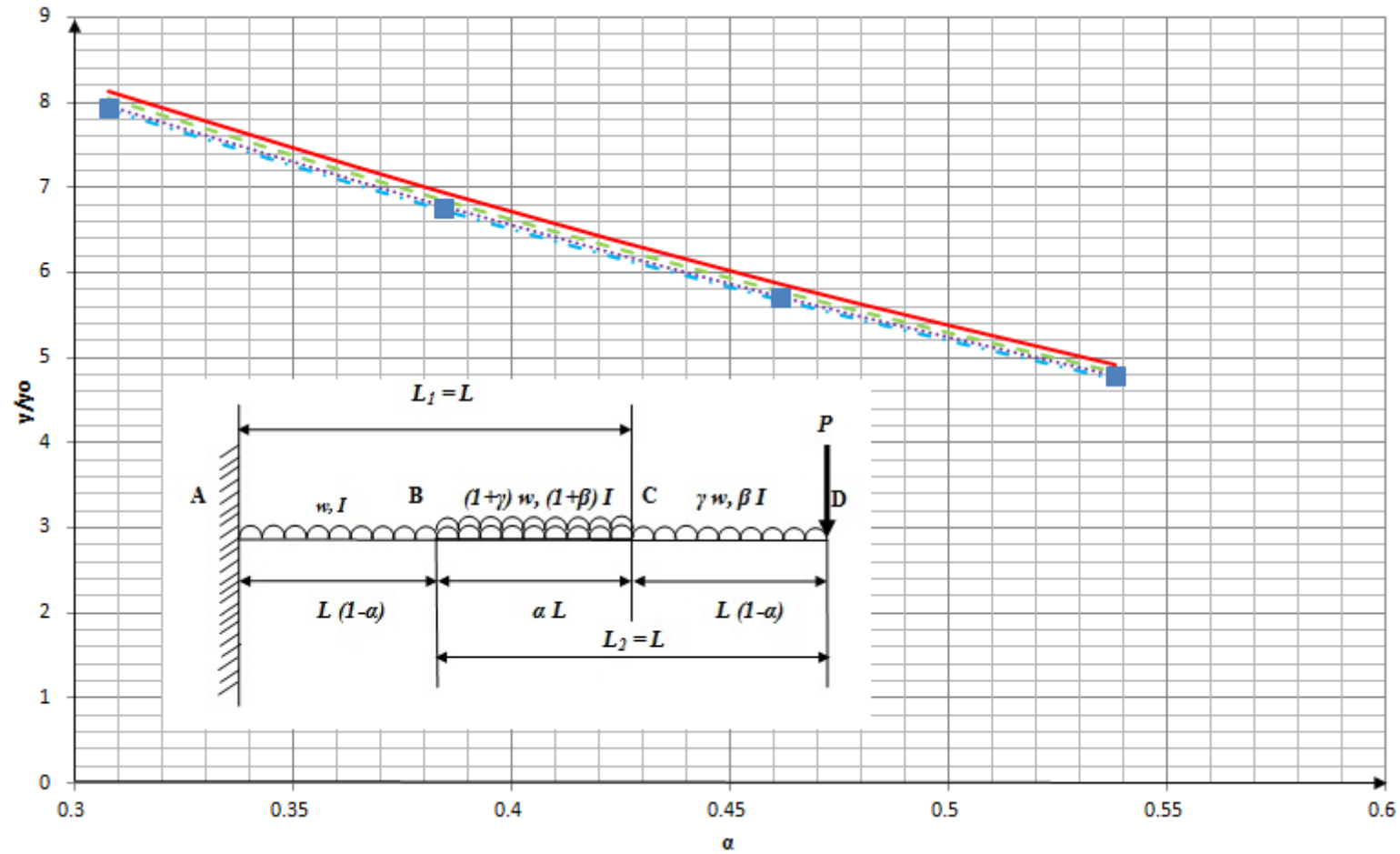


Figure 9.1 (d): Comparison of Deflection Curves vs. Parameter  $\alpha$ , for the two section telescopic cantilever beam assembly having individual part dimensions outlined in Table 8.1, for an applied load of 30 N.

(Applied Load 30 N: ■ Experimental; — Macaulay; - - - Mohr; - · - Castigliano and Virtual Work; ····· FEA)

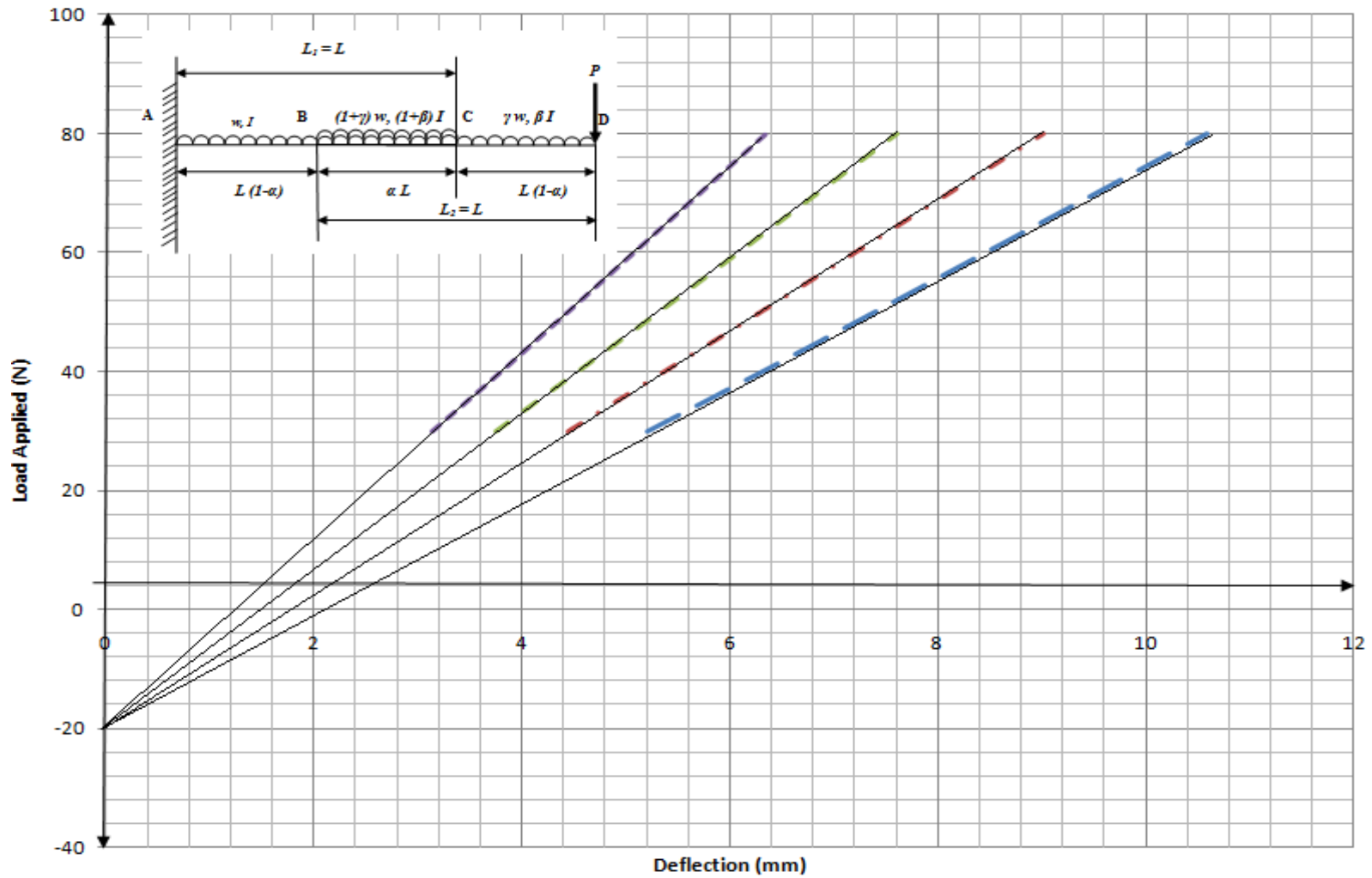


Figure 9.2: Experimental Deflection linear Plots showing Load Applied in Newton vs Tip Deflection in mm, extended such that they meet the ordinate at 20 N

(Key: — Overlap length 400 mm; - - Overlap length 500 mm; - - Overlap length 600 mm; ···· Overlap length 700 mm)  
[Refer to Figure 8.11]

### 9.1.2 Stress Analysis Results

The results of stress analysis from theoretical predictions are presented in Figures 6.4 – 6.9. Figure 6.4 represents the inline loading induced bending stress along the top surface of the beam assembly. Figure 6.5 details the inline loading induced shear stress along the side wall of the beam assembly whilst Figure 6.6 plots the inline loading induced shear stress along the top, left hand corner line of the beam assembly. Similarly Figures 6.7 – 6.9 represent the offline loading induced bending and shear stress values. The graphs are plotted for the assembly having the same dimensions as that of the experimental test rig and outlined in Table 8.1, as well as in Appendices D and E, for an overlap of 400 mm. The results of stress analysis from FEA predictions are presented in Figures 7.3 – 7.8. The order of these graphs is similar to that of those plots derived from theoretical predictions, as has been detailed above. Once again the curves have been plotted for the two section telescoping assembly having the same dimensions as that of the experimental test rig and outlined in Table 8.1, for an overlap of 400mm.

Comparisons of both the theoretically and FEA generated bending and shear stress curves, in general, was once again difficult as they overlaid upon one other to the point, where there was no means to differentiate between the generated sets of curves at all, in some instances. Figure 9.3 plots the theoretically and FEA extracted inline loading induced bending stress in MPa, along the top surface of the beam assembly against the distance from the fixed end in mm. Figure 9.4 displays the theoretically and FEA derived inline loading induced shear stress along the middle of the side wall of the beam assembly whilst Figure 9.5 depicts the inline loading induced shear stress along the top, left hand corner line of the beam assembly. In similar fashion, Figures 9.6 – 9.8 represent the offset loading induced bending and shear stress values. These comparison graphs were plotted, once again for the test rig having dimensions as specified in Table 8.1.

In case of the bending stress curves derived for both inline and offset loading scenarios, stress values were obtained at 50 mm intervals along the top of the beam sections as is detailed in Appendices C and D, respectively. FEA values were similarly obtained in a manner as outlined in Appendix G. The unreinforced beam lengths AB and CD are shown for which the stress axis refers to the maximum bending stress at their mid, outer surfaces. In [92] stress dips from FEA at lengths of 600 mm and 1500 mm were explained by the presence of wear

pads. Similarly in the candidate assembly dimensions of which are outlined in Appendices D and E, wear pads were used in the simulation in FEA, as is outlined in Appendix I. In the candidate assembly, from Figures 6.4 and 6.7, it can be seen that at a length of 900 mm there is a stress dip due in part to the set of wear pads at said length. They decrease the stress concentration in the overlap area between sections. Before and beyond each overlap the bending stress in each is seen to diminish from its greatest value at the fixed-end to zero at the free-end. Figures 6.4 and 6.7 show that there are two further ‘free-ends’ within this telescopic assembly where the bending stresses are also zero. The greatest theoretically derived bending stress magnitude of 16MPa and 18MPa induced by inline and offset loading in the two section telescoping assembly, respectively is in turn evident from Figures 6.4 and 6.7 for  $\frac{wL}{P}$  ratio of 2. Similarly, the greatest FEA extracted values of bending stresses induced by inline and offset loading, is roughly 17 MPa and 17.5 MPa, respectively. A significant difference between the curves generated by FE and theory for inline loading bending stresses can be seen in Figure 9.3 for Beam ACB. This in part, is due to the boundary conditions used while modelling the FE model in ABAQUS/CAE. The fixed end beam is constrained in six degrees of freedom, and this in turn contributes to a reduction in stress values noted up to 50 mm along its length after which there is a sharp spike in the stress values registered. This may be due to the boundary condition making its effect felt along the assembly, albeit over a small length.

In case of the shear stress curves derived for both inline and offset loading scenarios, stress values were obtained at 50 mm intervals along the top and sides of the beam sections as is detailed in Appendices C and D, respectively. FEA values were similarly obtained in a manner as outlined in Appendix G. Shear stress values were derived and obtained from both the mid wall position of the top, horizontal and nearest corner to it, on the side, vertical walls respectively as is made clear in Figures 6.5 and 6.6 for inline loading and Figures 6.8 and 6.9 for offset loading. In comparison FEA generated curves were also produced in similar fashion and are comprehensively detailed in Figures 7.4 and 7.5 for inline loading and Figures 7.7 and 7.8 for offset loading respectively. The reversal in the tip reaction between beams AB and CD is responsible for the alternation in signs of the shear stress as is shown in Figures 6.5, 6.6, 6.8, 6.9, 7.4, 7.5, 7.7 and 7.8. Nowhere does the shear stress magnitude become zero despite it having a relatively low magnitude compared to the accompanying bending stress.

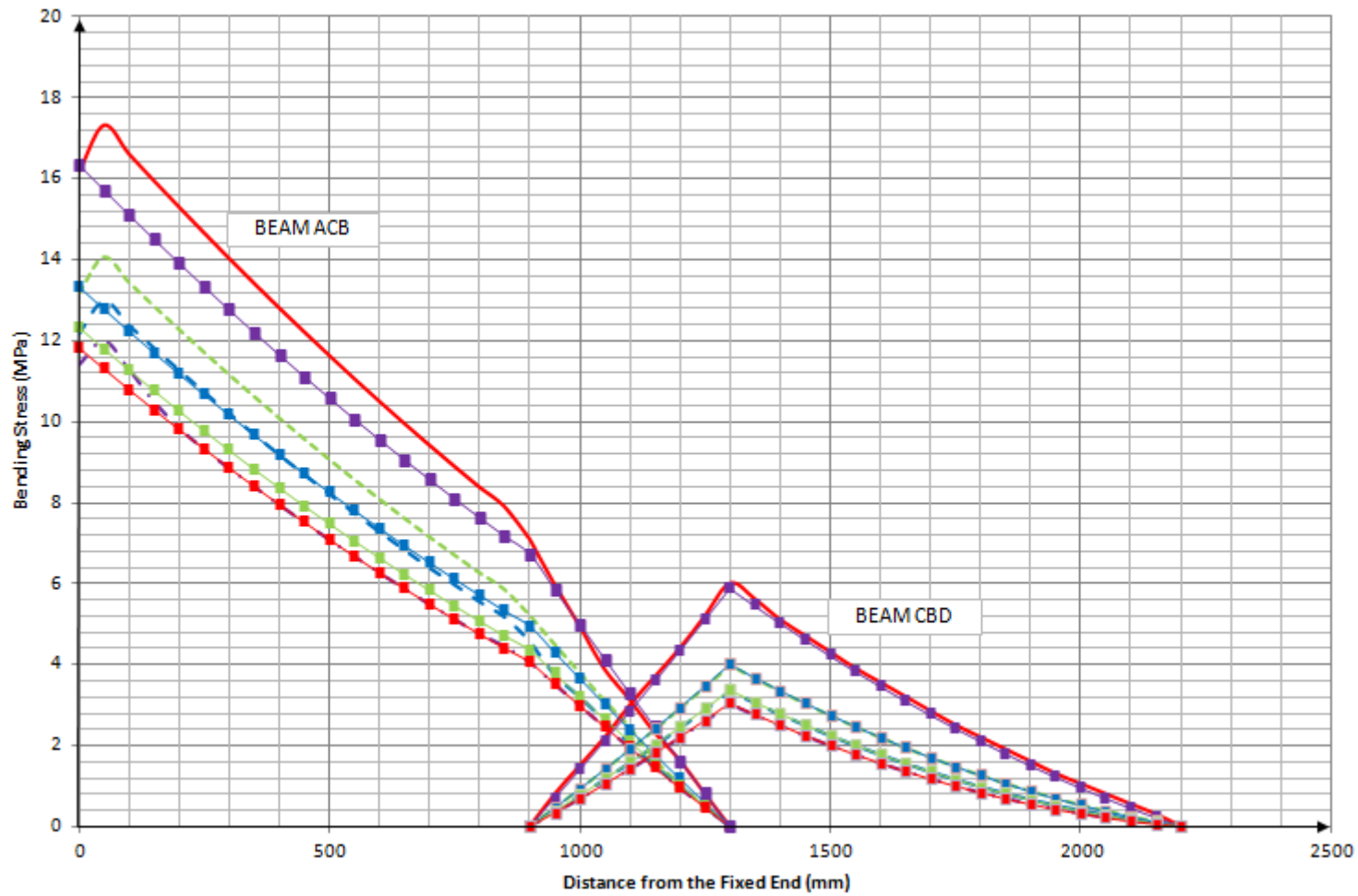
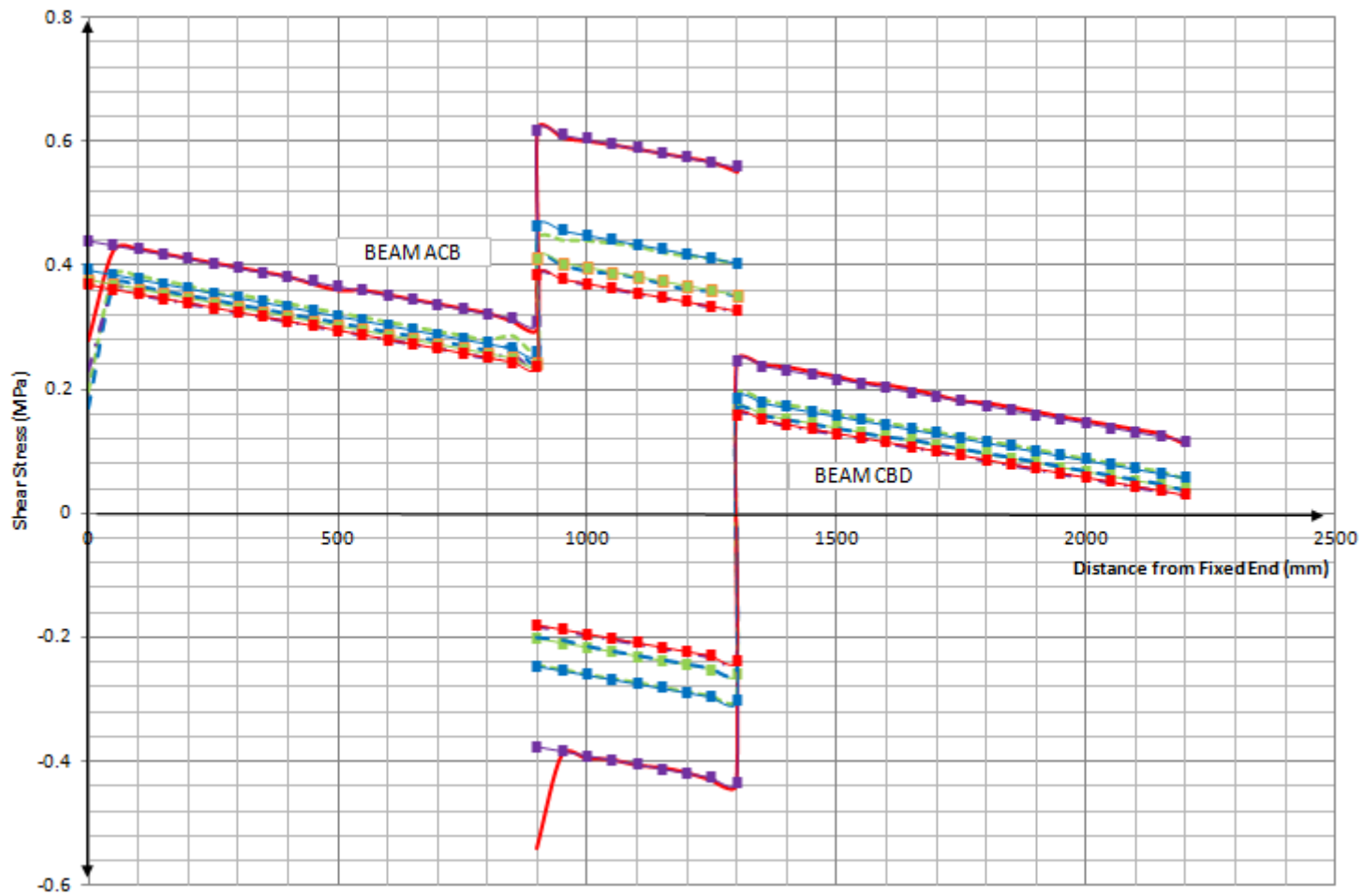
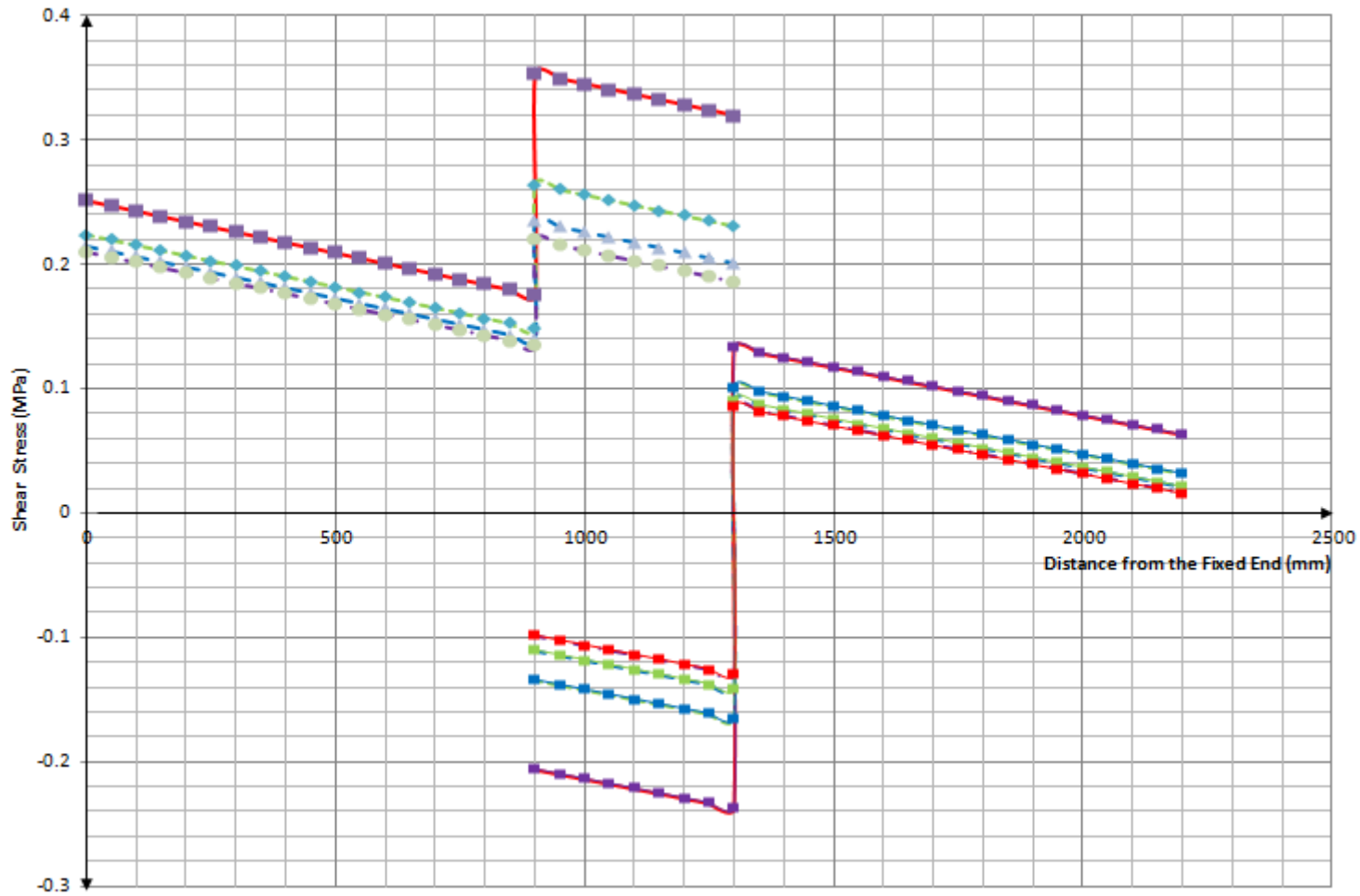


Figure 9.3: Inline loading induced bending stress (MPa) vs distance from the fixed end along  $A_1C_1B_1D_1$ , as marked in Figure 6.2, for the two section telescopic cantilever beam assembly having individual part dimensions outlined in Table 7.1, and an overlap of 400 mm  
 (Key to FEA Predictions: —  $wL/P=2$ ; .....  $wL/P=4$ ; - - -  $wL/P=6$ ; - · -  $wL/P=8$ )  
 (Key to Theoretical Predictions: -■-  $wL/P=2$ ; -■-  $wL/P=4$ ; -■-  $wL/P=6$ ; -■-  $wL/P=8$ )



**Figure 9.4: Inline loading induced shear stress (MPa) vs distance from the fixed end along  $A_3C_3B_3D_3$ , as marked in Figure 6.2, for the two section telescopic cantilever beam assembly having individual part dimensions outlined in Table 7.1, and an overlap of 400 mm**  
 (Key to FEA Predictions: —  $wL/P=2$ ; .....  $wL/P=4$ ; - - -  $wL/P=6$ ; - · -  $wL/P=8$ )  
 (Key to Theoretical Predictions: -■-  $wL/P=2$ ; -■-  $wL/P=4$ ; -■-  $wL/P=6$ ; -■-  $wL/P=8$ )



**Figure 9.5: Inline loading induced shear stress (MPa) vs distance from the fixed end along  $A_2C_2B_2D_2$ , as marked in Figure 6.2, for the two section telescopic cantilever beam assembly having individual part dimensions outlined in Table 7.1, and an overlap of 400 mm**  
 (Key to FEA Predictions: —  $wL/P=2$ ; .....  $wL/P=4$ ; - - -  $wL/P=6$ ; - · -  $wL/P=8$ )  
 (Key to Theoretical Predictions: —■—  $wL/P=2$ ; —■—  $wL/P=4$ ; —■—  $wL/P=6$ ; —■—  $wL/P=8$ )

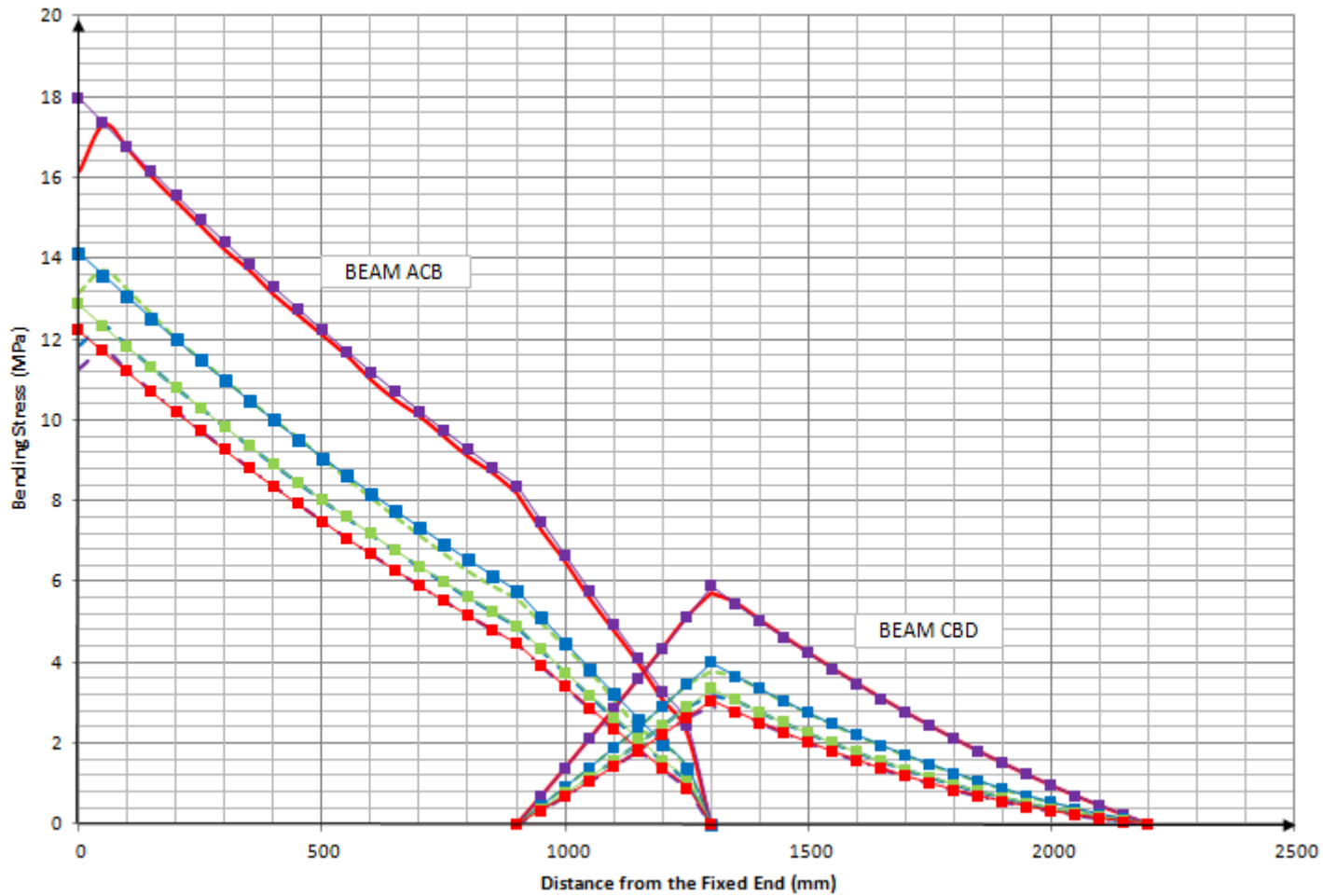


Figure 9.6: Offset loading induced bending stress (MPa) vs distance from the fixed end along  $A_1C_1B_1D_1$ , as marked in Figure 6.2, for the two section telescopic cantilever beam assembly having individual part dimensions outlined in Table 7.1, and an overlap of 400 mm  
 (Key to FEA Predictions: —  $wL/P=2$ ; .....  $wL/P=4$ ; - - -  $wL/P=6$ ; - · -  $wL/P=8$ )  
 (Key to Theoretical Predictions: - - -  $wL/P=2$ ; - - -  $wL/P=4$ ; - - -  $wL/P=6$ ; - - -  $wL/P=8$ )

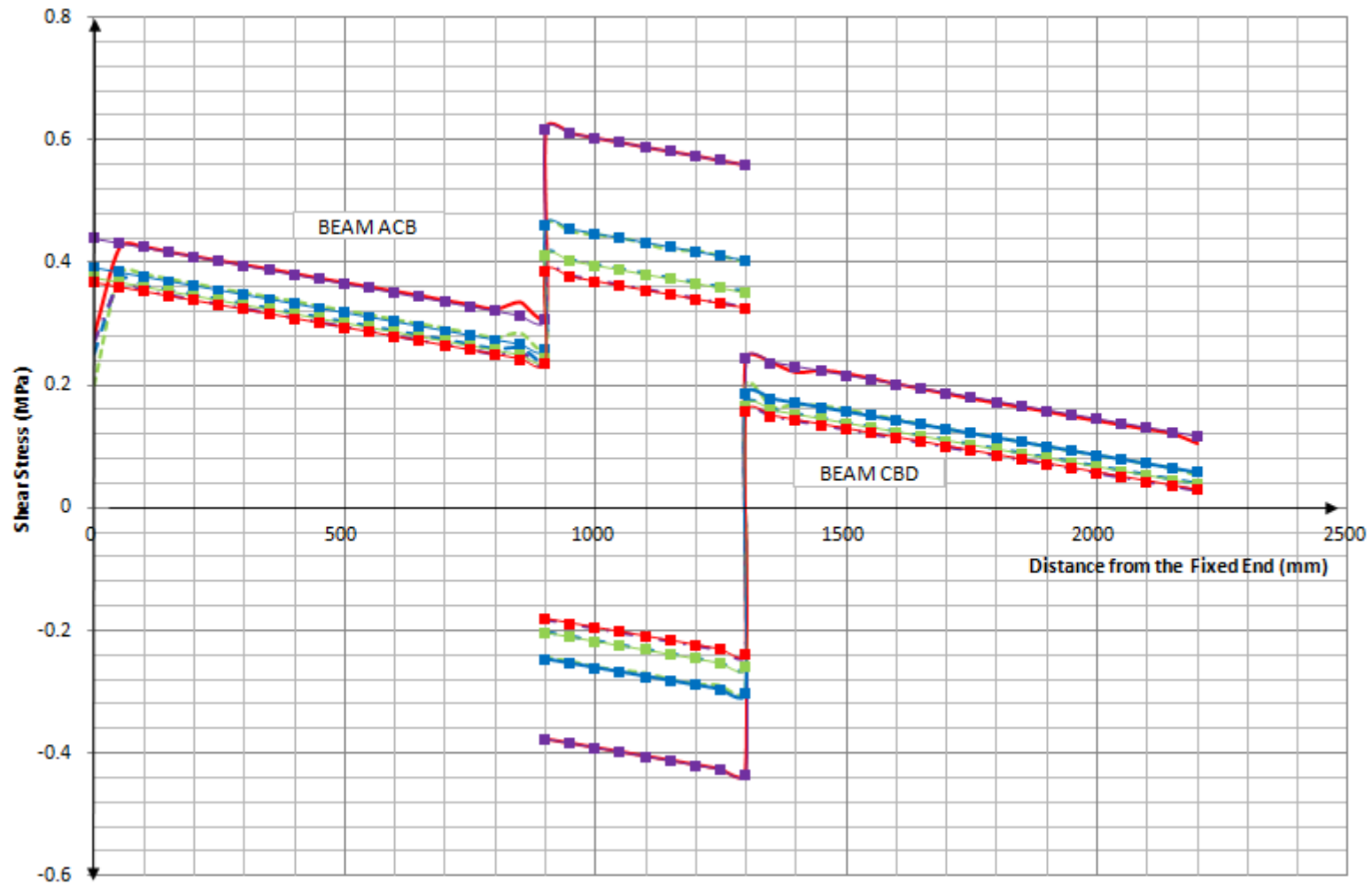
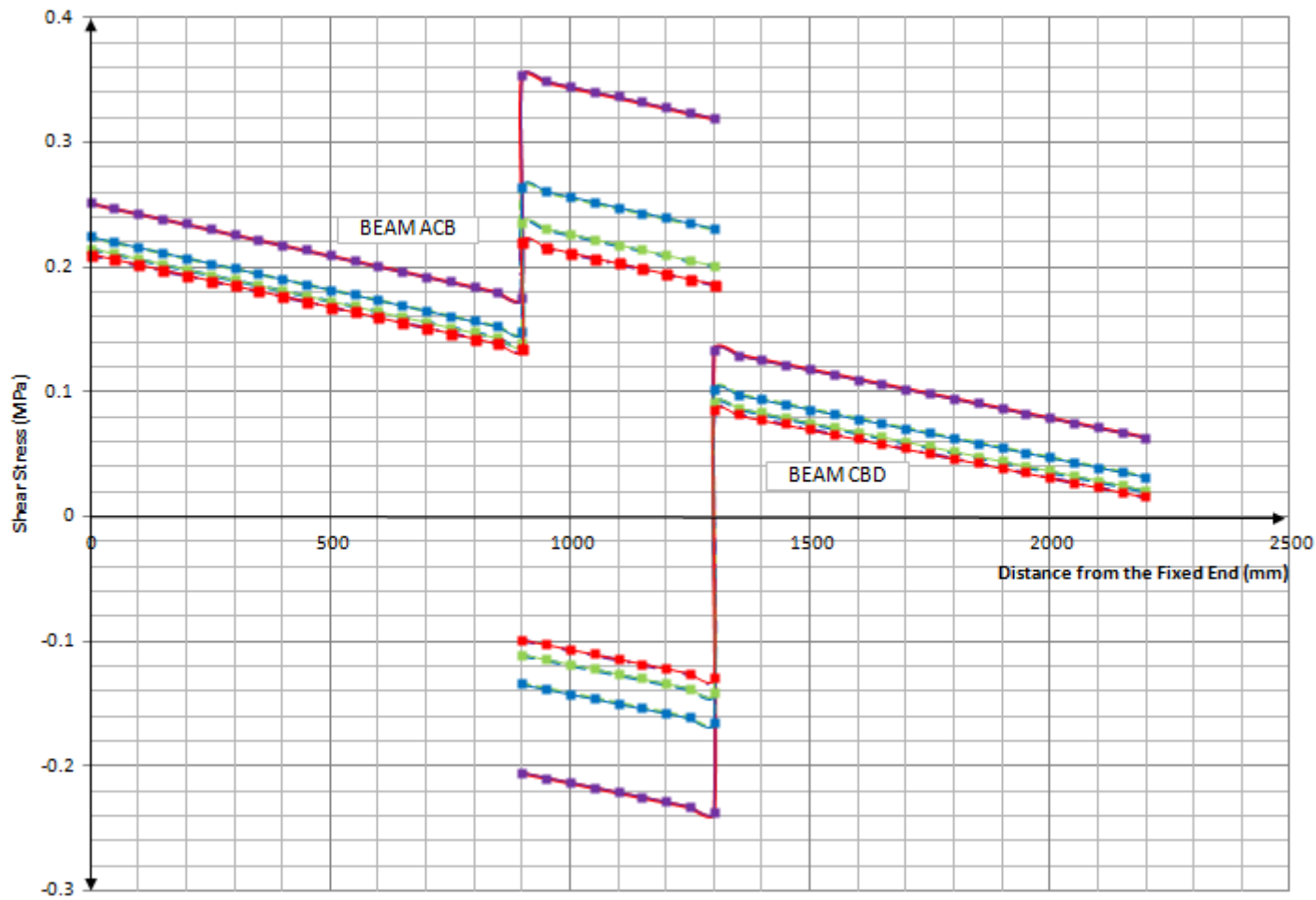


Figure 9.7: Offset loading induced shear stress (MPa) vs distance from the fixed end along  $A_3C_3B_3D_3$ , as marked in Figure 6.2, for the two section telescopic cantilever beam assembly having individual part dimensions outlined in Table 7.1, and an overlap of 400 mm  
 (Key to FEA Predictions: —  $wL/P=2$ ; .....  $wL/P=4$ ; - - -  $wL/P=6$ ; - · -  $wL/P=8$ )  
 (Key to Theoretical Predictions: - - -  $wL/P=2$ ; - - -  $wL/P=4$ ; - - -  $wL/P=6$ ; - - -  $wL/P=8$ )



**Figure 9.8: Offset loading induced Shear Stress (MPa) vs Distance from the Fixed End along  $A_2C_2B_2D_2$ , as marked in Figure 6.2, for the two section telescopic cantilever beam assembly having individual part dimensions outlined in Table 7.1, and an overlap of 400mm**  
 (Key to FEA Predictions: —  $wL/P=2$ ; - - -  $wL/P=4$ ; - - -  $wL/P=6$ ; - - -  $wL/P=8$ )  
 (Key to Theoretical Predictions: -■-  $wL/P=2$ ; -■-  $wL/P=4$ ; -■-  $wL/P=6$ ; -■-  $wL/P=8$ )

Experimentally determined values of stress are obtained using strain gauging techniques and data acquisition techniques outlined at Appendix G, at points as shown in Figure 8.6. Using data acquisition techniques the principal strain values are determined at said points and converted to their equivalent principal stresses using equations derived in Appendix G, the results of which are plotted in Figures 8.15 – 8.46. Theoretically determined principal stresses are then used as a comparison tool against the experimentally determined values of principal stress and these are compared against each other in Figures 9.9 – 9.40. The principal stress values obtained both theoretically and experimentally compare favourably with each other for both inline and offset loading scenarios.

The broad question of why indulge in experimentation in the age of highly advanced and ever increasing computer and numerical modelling is addressed and five primary motives are put forward: (i) to gain a better understanding of stress and stress induced behaviour within the telescopic structure; (ii) to discover new phenomena for the overlap region; (iii) to obtain improved input data for further computer modelling; (iv) to determine the correlation factors between analysis and test embracing material effects; and finally (v) to fine tune and build further confidence in general computer software.

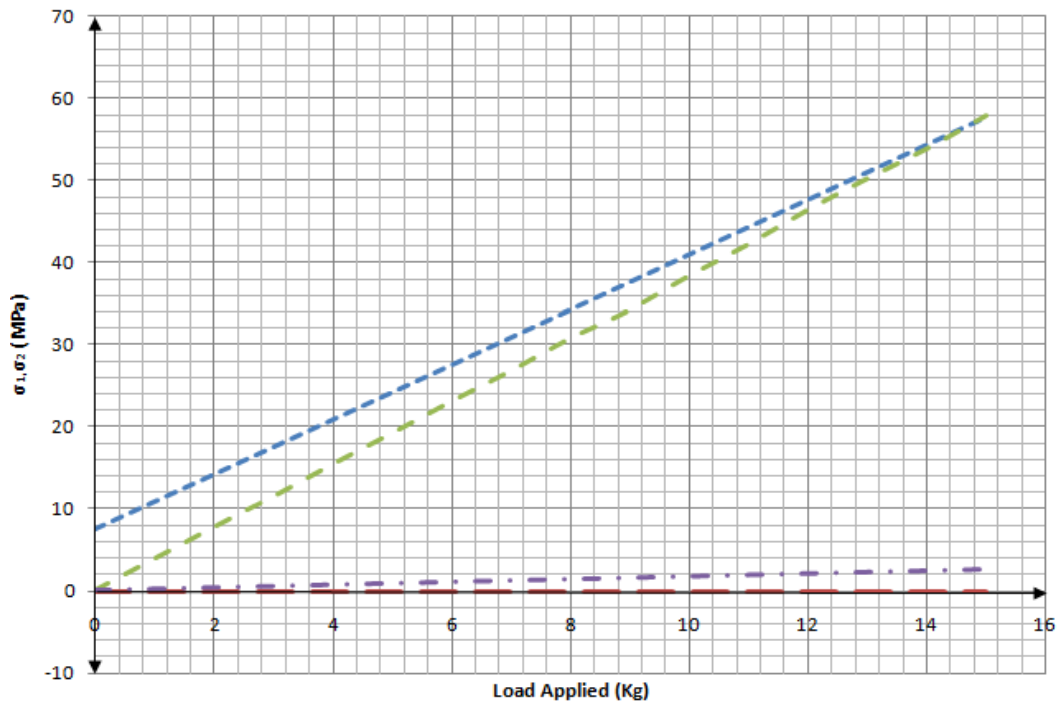


**Figure 9.9: Comparison of principal stresses ( $\sigma_1, \sigma_2$  (MPa)) at position W vs Inline load applied (kg) with 400 mm overlap**

(Key: ..... Theoretical  $\sigma_1$  (MPa); - - - Experimental  $\sigma_1$  (MPa); - . - Experimental  $\sigma_2$  (MPa); - - - Theoretical  $\sigma_2$  (MPa))

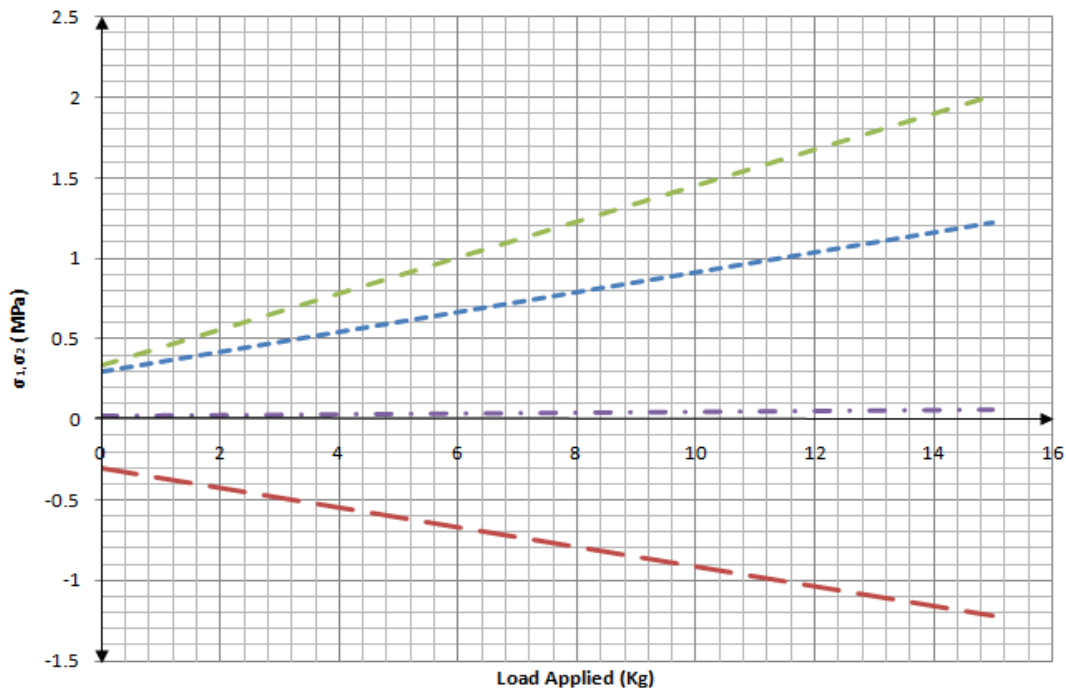


**Figure 9.10: Comparison of principal stresses ( $\sigma_1, \sigma_2$  (MPa)) at position X vs Inline load applied (kg) with 400mm overlap**

(Key: ..... Theoretical  $\sigma_1$  (MPa); - - - Experimental  $\sigma_1$  (MPa); - . - Experimental  $\sigma_2$  (MPa); - - - Theoretical  $\sigma_2$  (MPa))

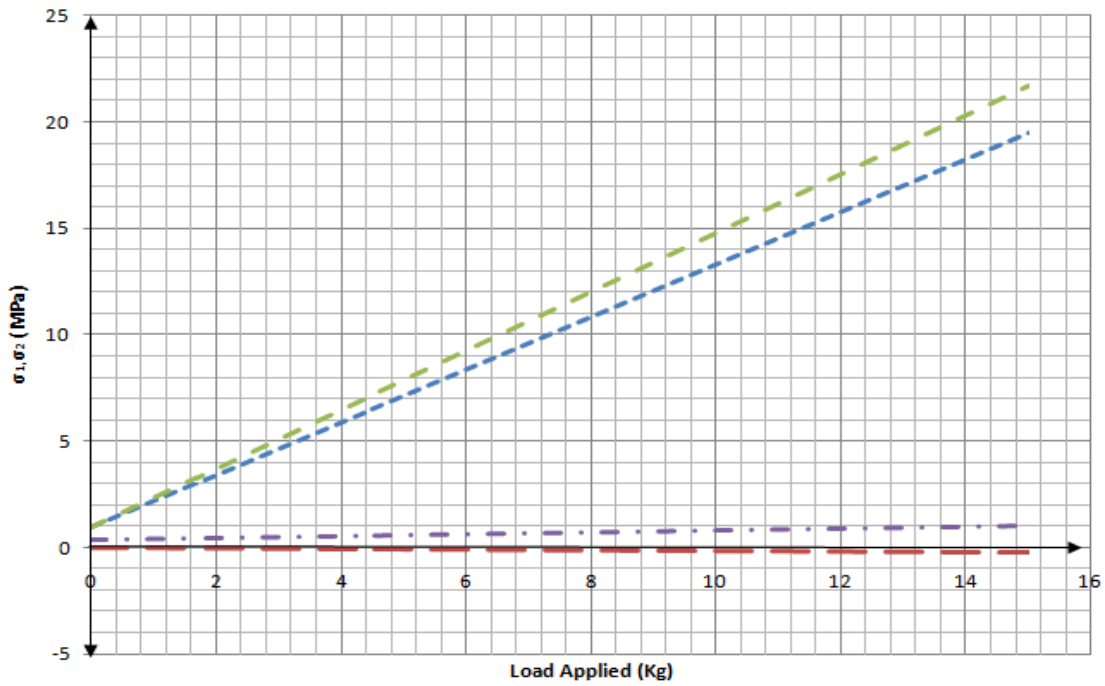


**Figure 9.11: Comparison of principal stresses ( $\sigma_1, \sigma_2$  (MPa)) at position Y vs Inline load applied (kg) with 400 mm overlap**

(Key: ..... Theoretical  $\sigma_1$  (MPa); - - - Experimental  $\sigma_1$  (MPa); - . - Experimental  $\sigma_2$  (MPa); - - - Theoretical  $\sigma_2$  (MPa))

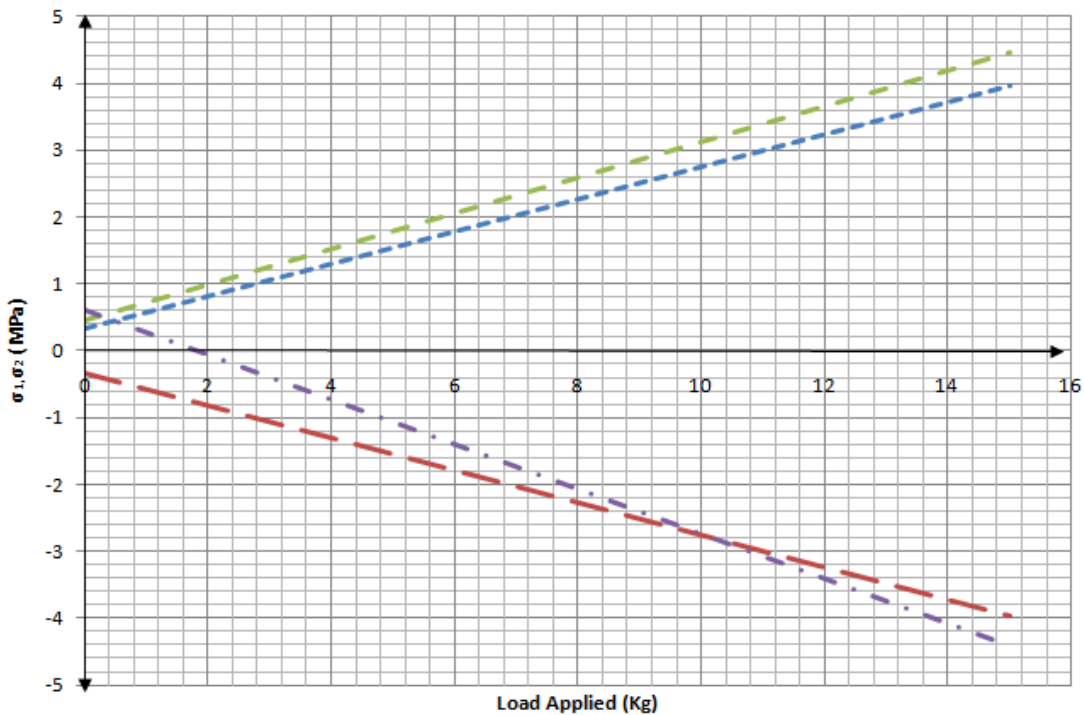


**Figure 9.12: Comparison of principal stresses ( $\sigma_1, \sigma_2$  (MPa)) at position Z vs Inline load applied (kg) with 400 mm overlap**

(Key: ..... Theoretical  $\sigma_1$  (MPa); - - - Experimental  $\sigma_1$  (MPa); - . - Experimental  $\sigma_2$  (MPa); - - - Theoretical  $\sigma_2$  (MPa))

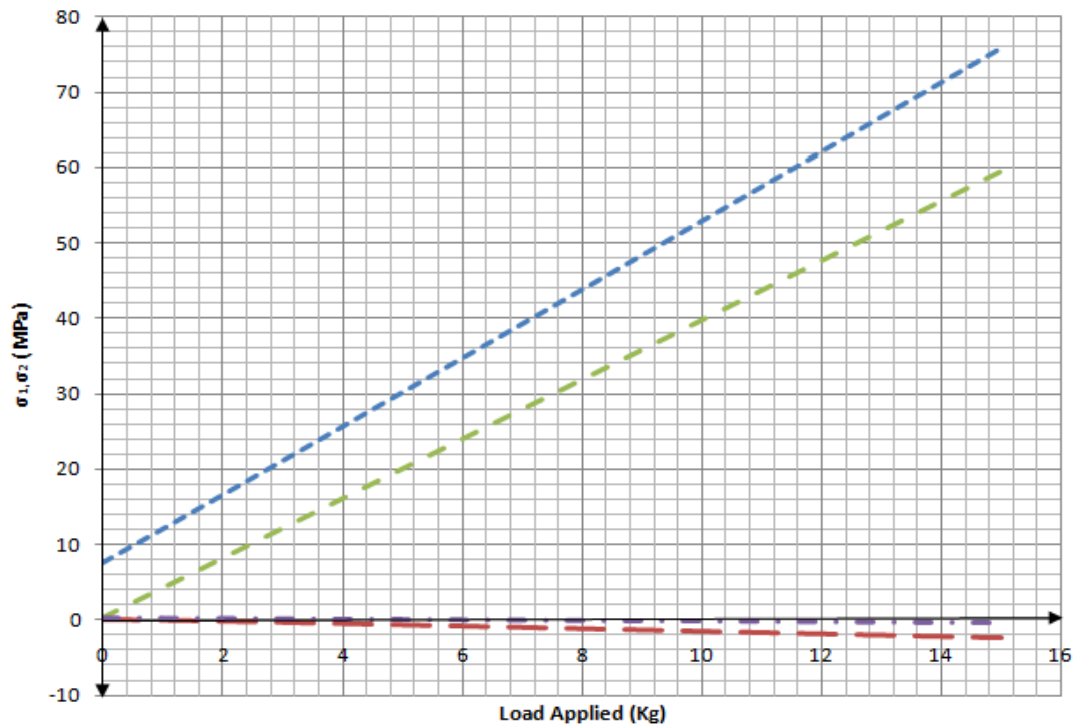


**Figure 9.13: Comparison of principal stresses ( $\sigma_1, \sigma_2$  (MPa)) at position W vs Offset load applied (kg) with 400 mm overlap**  
 (Key: ..... Theoretical  $\sigma_1$  (MPa); - - - Experimental  $\sigma_1$  (MPa); - . - Experimental  $\sigma_2$  (MPa); - - - Theoretical  $\sigma_2$  (MPa))

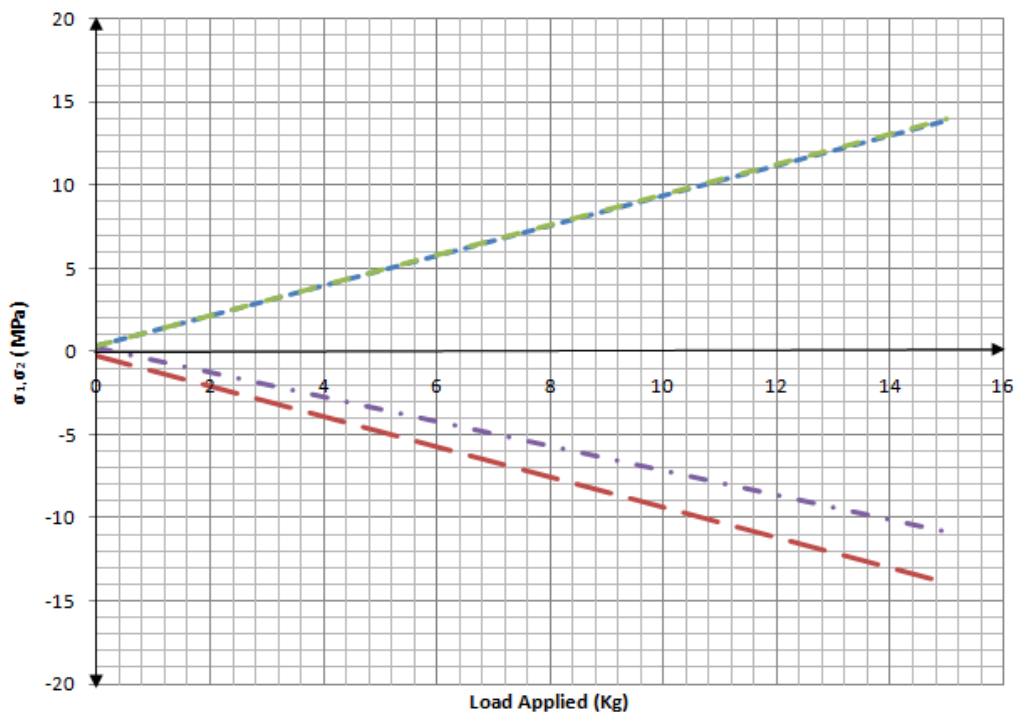


**Figure 9.14 Comparison of principal stresses ( $\sigma_1, \sigma_2$  (MPa)) at position X vs Offset load applied (kg) with 400 mm overlap**  
 (Key: ..... Theoretical  $\sigma_1$  (MPa); - - - Experimental  $\sigma_1$  (MPa); - . - Experimental  $\sigma_2$  (MPa); - - - Theoretical  $\sigma_2$  (MPa))

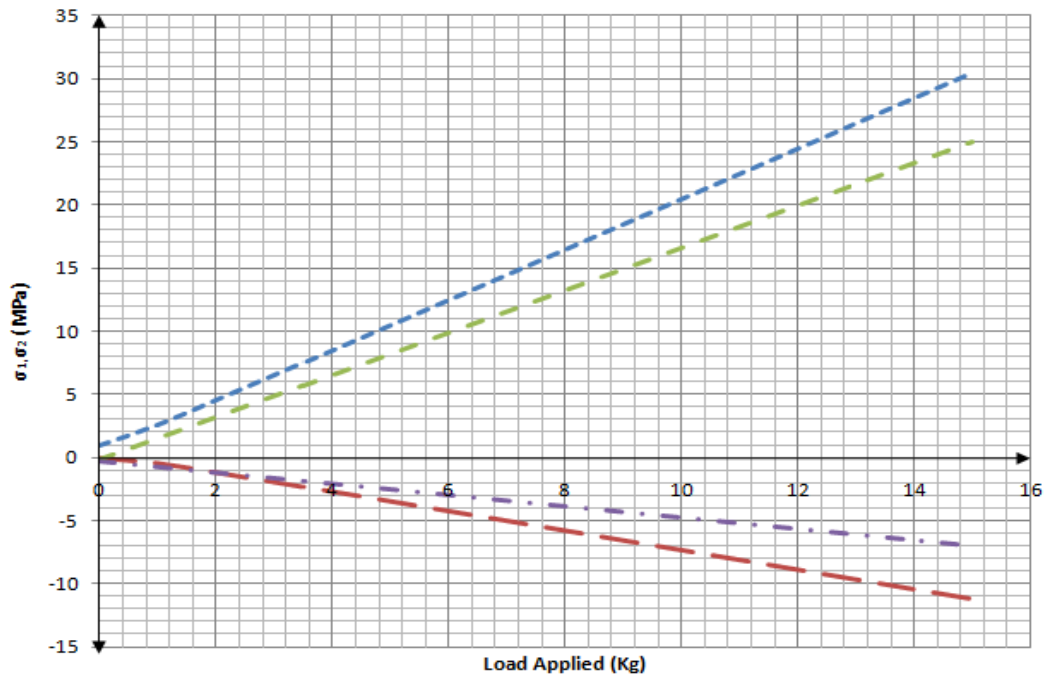


**Figure 9.15 Comparison of principal stresses ( $\sigma_1, \sigma_2$  (MPa)) at position Y vs Offset load applied (kg) with 400 mm overlap**  
 (Key: ..... Theoretical  $\sigma_1$  (MPa); - - - Experimental  $\sigma_1$  (MPa); - · - Experimental  $\sigma_2$  (MPa); - - - Theoretical  $\sigma_2$  (MPa))

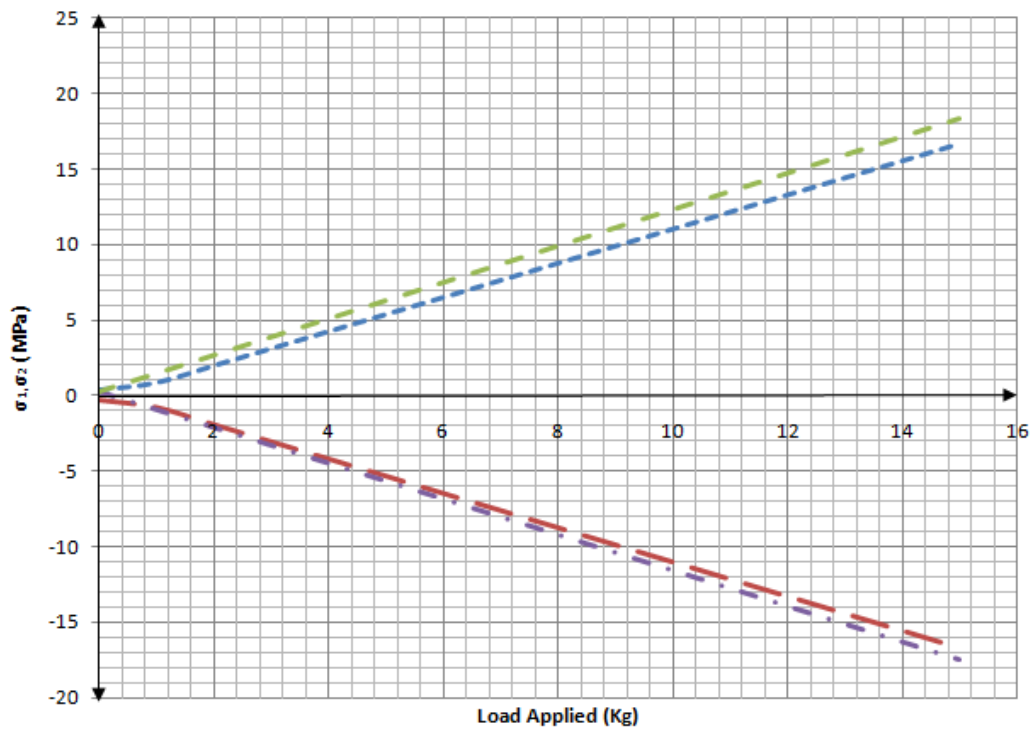


**Figure 9.16: Comparison of principal stresses ( $\sigma_1, \sigma_2$  (MPa)) at position Z vs Offset load applied (kg) with 400 mm overlap**  
 (Key: ..... Theoretical  $\sigma_1$  (MPa); - - - Experimental  $\sigma_1$  (MPa); - · - Experimental  $\sigma_2$  (MPa); - - - Theoretical  $\sigma_2$  (MPa))

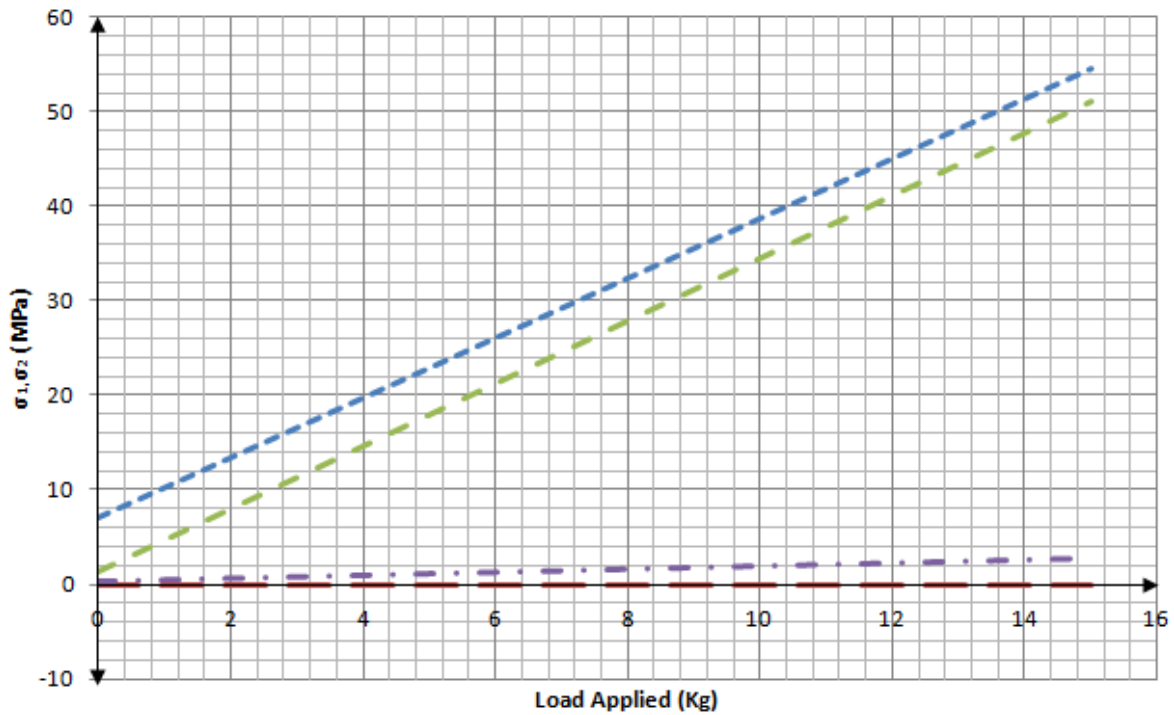


**Figure 9.17: Comparison of principal stresses ( $\sigma_1, \sigma_2$  (MPa)) at position W vs Inline load applied (kg) with 500 mm overlap**  
 (Key: ..... Theoretical  $\sigma_1$  (MPa); - - - Experimental  $\sigma_1$  (MPa); - . - Experimental  $\sigma_2$  (MPa); - - - Theoretical  $\sigma_2$  (MPa))

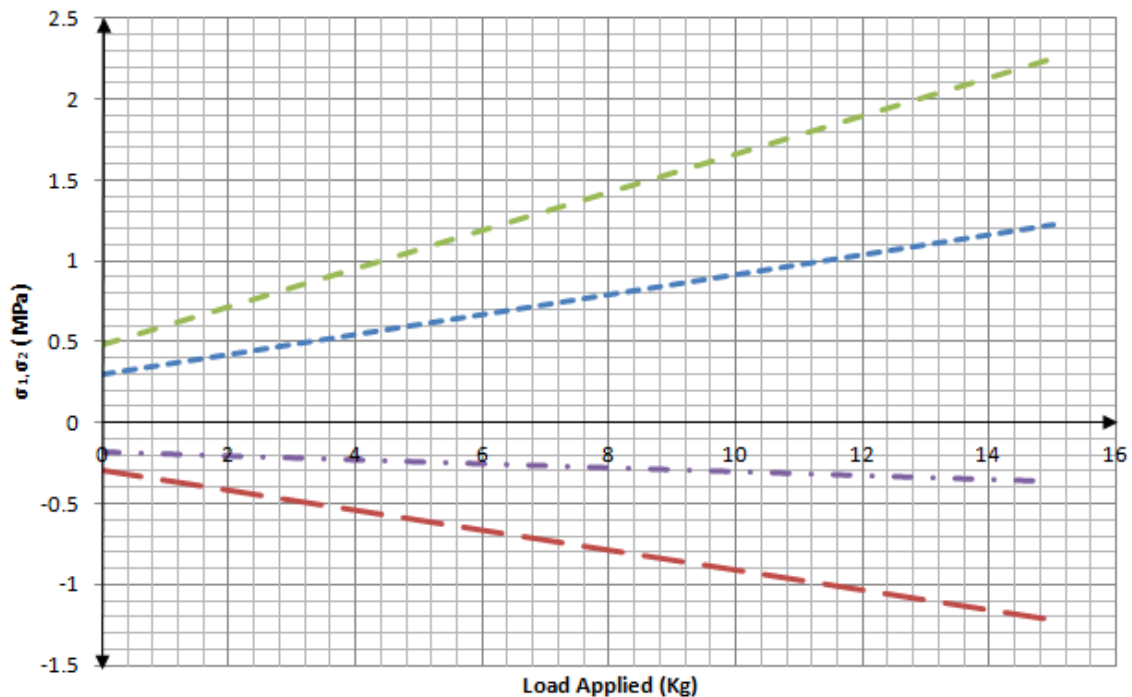


**Figure 9.18: Comparison of principal stresses ( $\sigma_1, \sigma_2$  (MPa)) at position X vs Inline load applied (kg) with 500 mm overlap**  
 (Key: ..... Theoretical  $\sigma_1$  (MPa); - - - Experimental  $\sigma_1$  (MPa); - . - Experimental  $\sigma_2$  (MPa); - - - Theoretical  $\sigma_2$  (MPa))

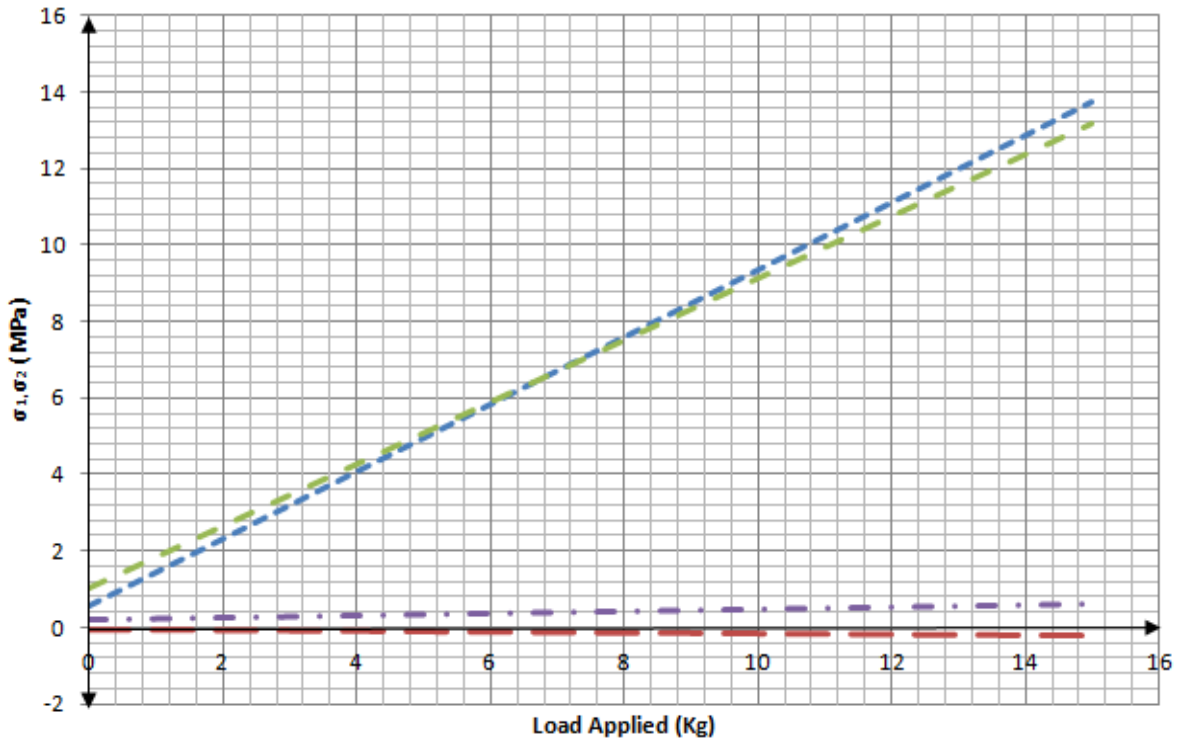


**Figure 9.19: Comparison of principal stresses ( $\sigma_1, \sigma_2$  (MPa)) at position Y vs Inline load applied (kg) with 500 mm overlap**

(Key: ..... Theoretical  $\sigma_1$  (MPa); - - - Experimental  $\sigma_1$  (MPa); - . - Experimental  $\sigma_2$  (MPa); - - - Theoretical  $\sigma_2$  (MPa))

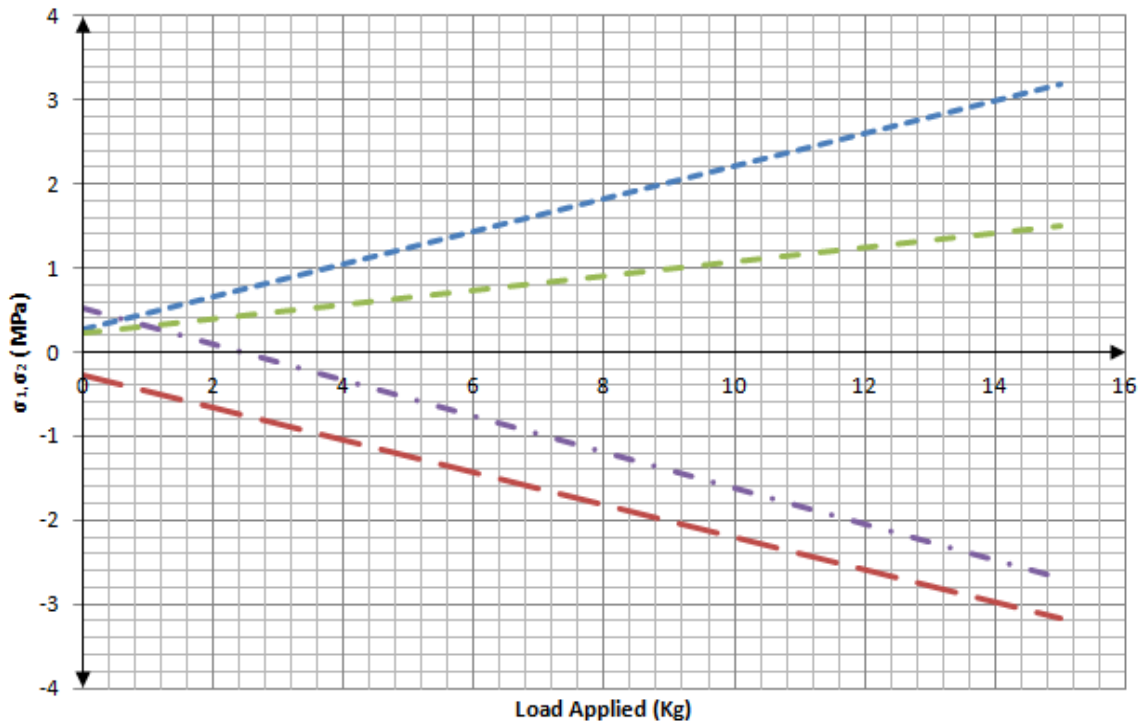


**Figure 9.20: Comparison of principal stresses ( $\sigma_1, \sigma_2$  (MPa)) at position Z vs Inline load applied (kg) with 500 mm overlap**

(Key: ..... Theoretical  $\sigma_1$  (MPa); - - - Experimental  $\sigma_1$  (MPa); - . - Experimental  $\sigma_2$  (MPa); - - - Theoretical  $\sigma_2$  (MPa))

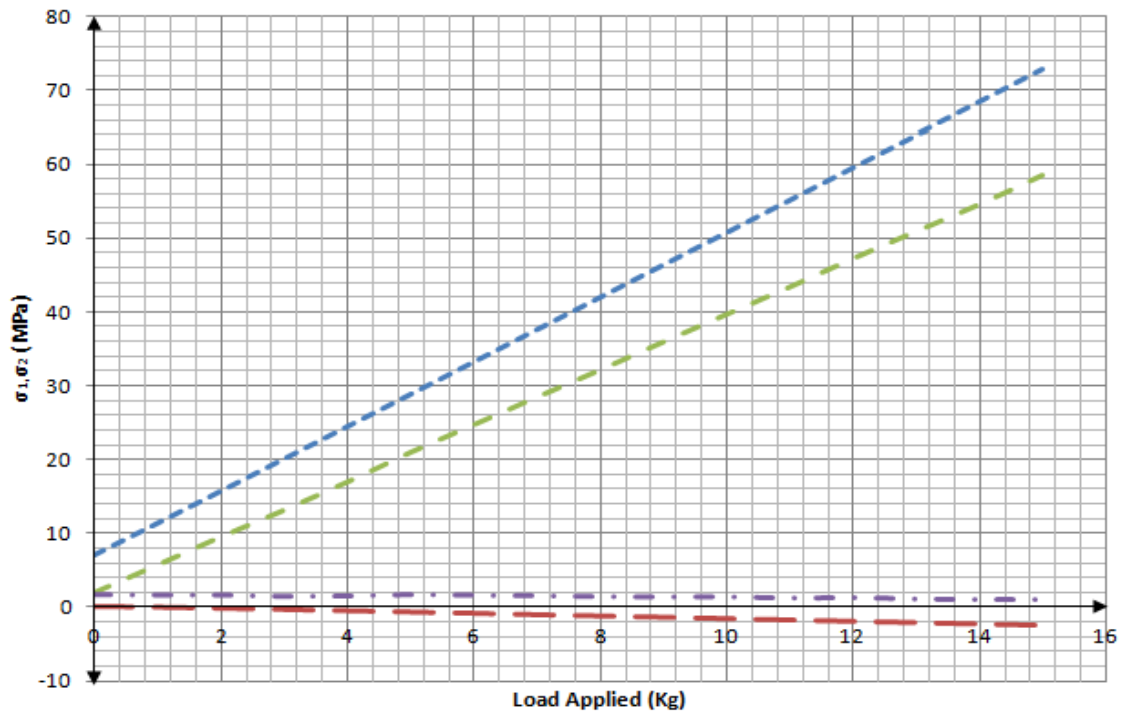


**Figure 9.21: Comparison of Principal Stresses ( $\sigma_1, \sigma_2$  (MPa)) at Position W vs Offset Load Applied (Kg) with 500 mm overlap**  
 (Key: ..... Theoretical  $\sigma_1$  (MPa); - - - Experimental  $\sigma_1$  (MPa); - · - Experimental  $\sigma_2$  (MPa); - - - Theoretical  $\sigma_2$  (MPa))

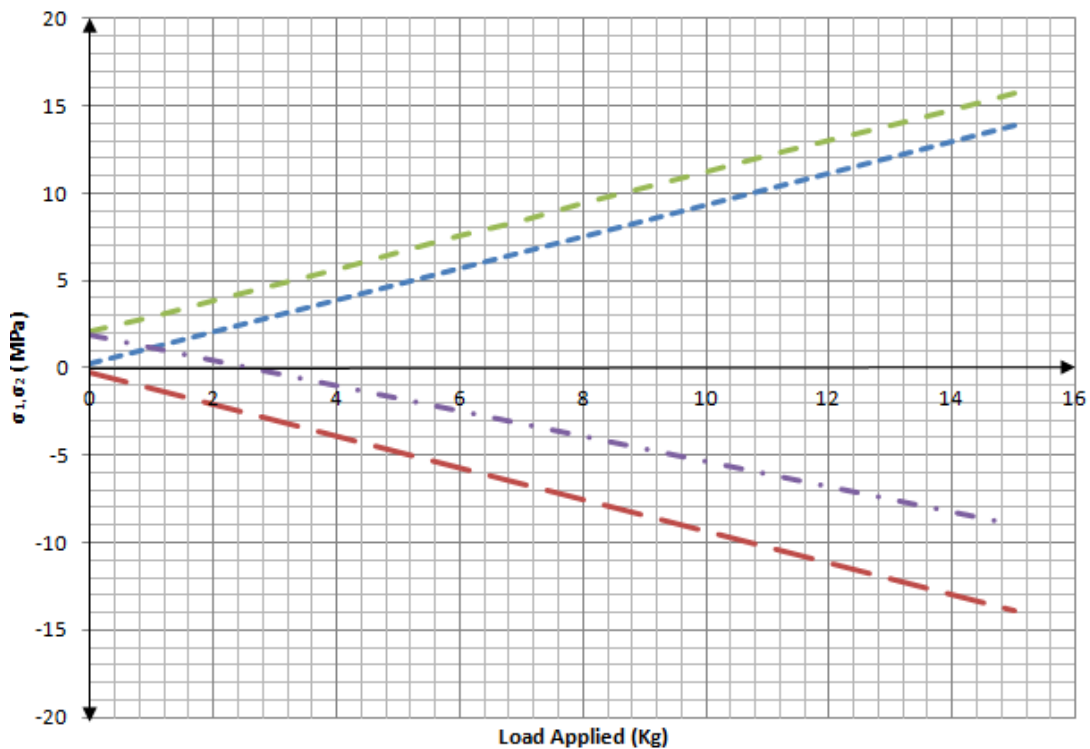


**Figure 9.22: Comparison of principal stresses ( $\sigma_1, \sigma_2$  (MPa)) at position X vs Offset load applied (kg) with 500 mm overlap**  
 (Key: ..... Theoretical  $\sigma_1$  (MPa); - - - Experimental  $\sigma_1$  (MPa); - · - Experimental  $\sigma_2$  (MPa); - - - Theoretical  $\sigma_2$  (MPa))

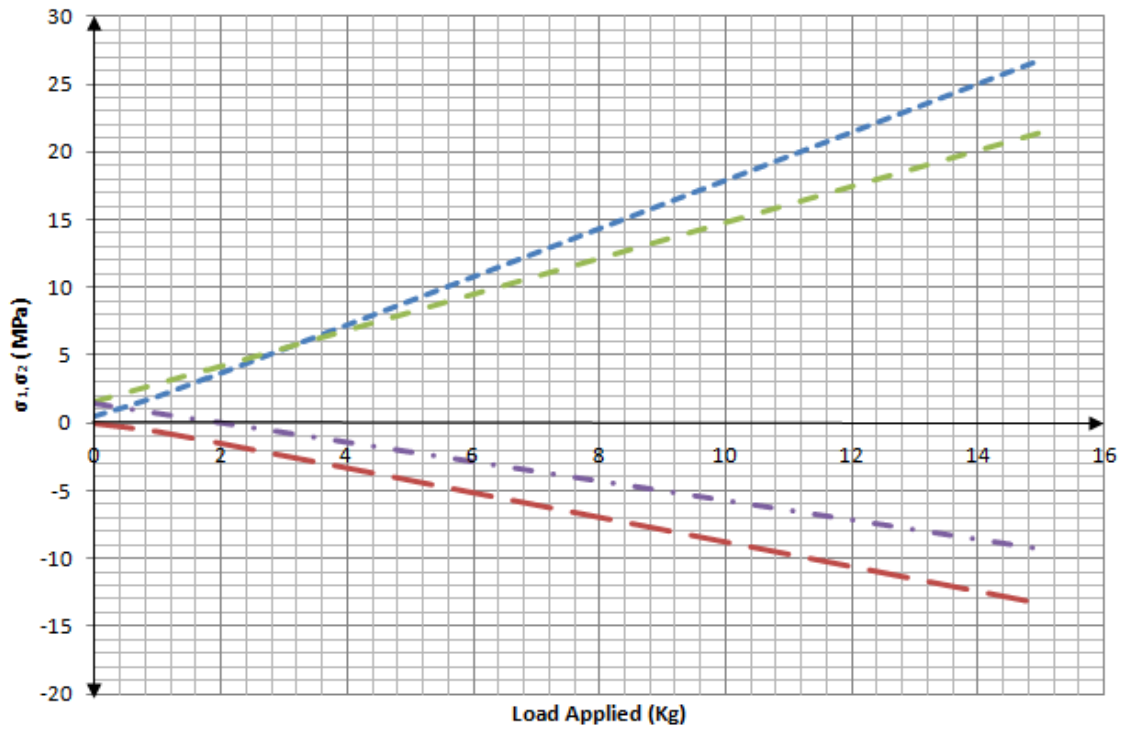


**Figure 9.23: Comparison of principal stresses ( $\sigma_1, \sigma_2$  (MPa)) at position Y vs Offset load applied (kg) with 500 mm overlap**

(Key: ..... Theoretical  $\sigma_1$  (MPa); - - - Experimental  $\sigma_1$  (MPa); - · - Experimental  $\sigma_2$  (MPa); - - - Theoretical  $\sigma_2$  (MPa))

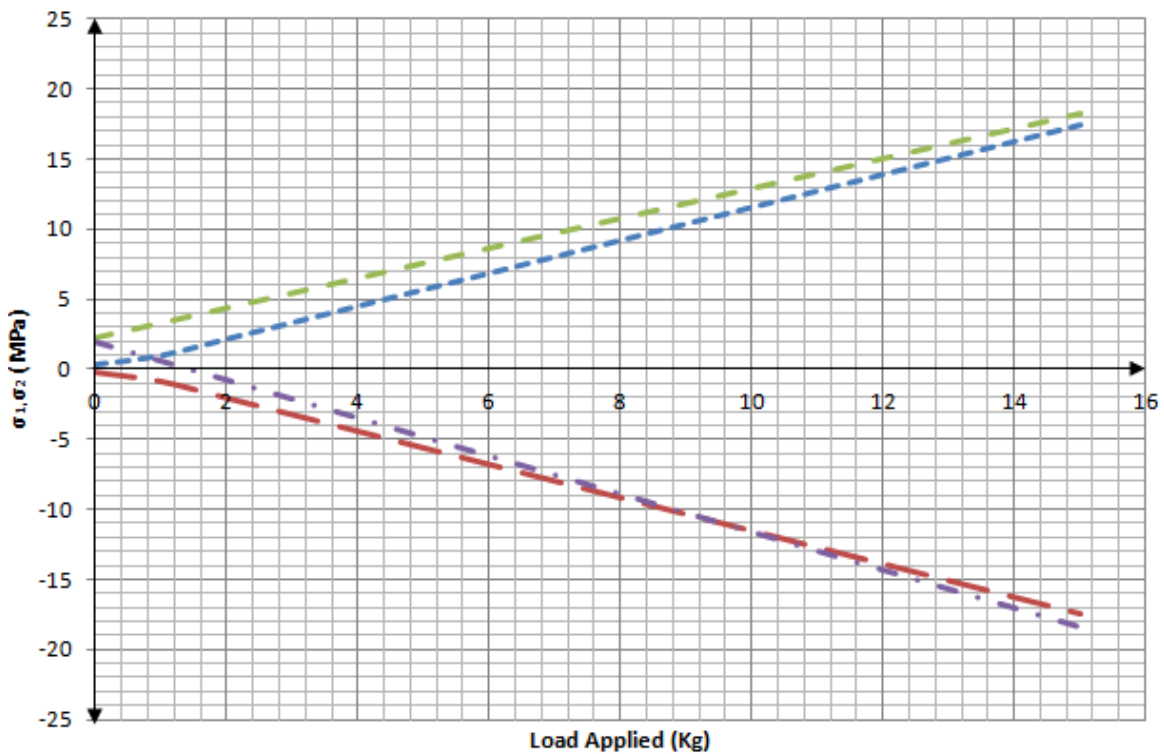


**Figure 9.24: Comparison of principal stresses ( $\sigma_1, \sigma_2$  (MPa)) at position Z vs Offset load applied (kg) with 500 mm overlap**

(Key: ..... Theoretical  $\sigma_1$  (MPa); - - - Experimental  $\sigma_1$  (MPa); - · - Experimental  $\sigma_2$  (MPa); - - - Theoretical  $\sigma_2$  (MPa))

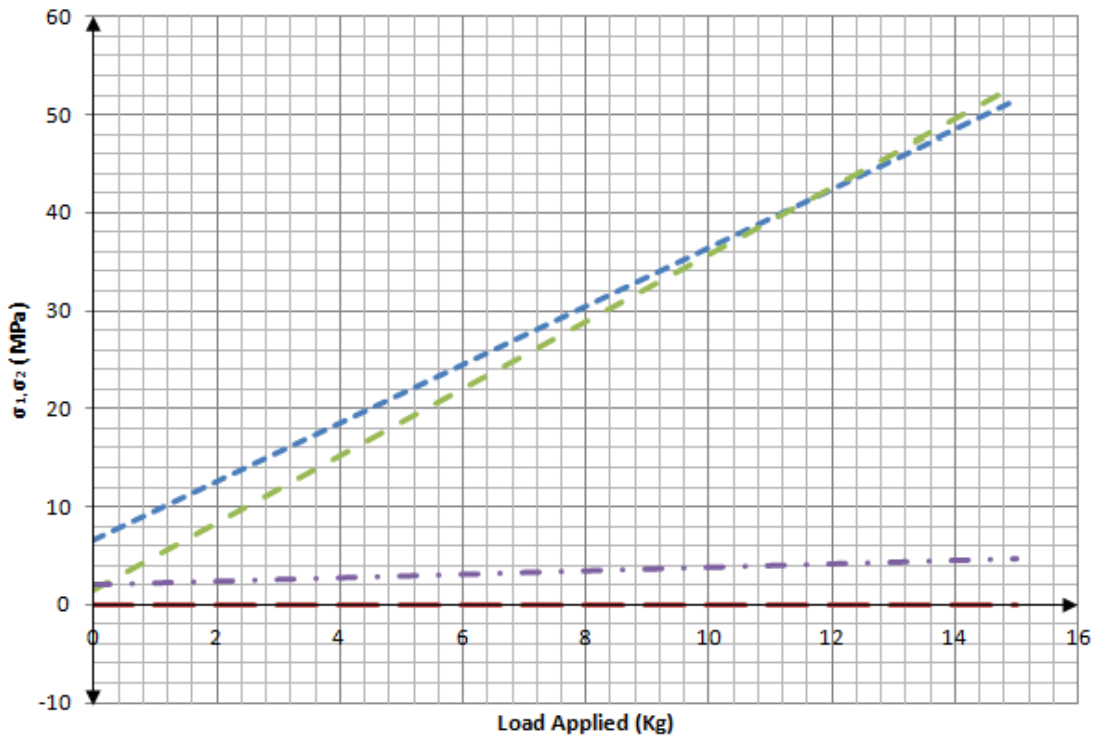


**Figure 9.25: Comparison of principal stresses ( $\sigma_1, \sigma_2$  (MPa)) at position W vs Inline load applied (kg) with 600 mm overlap**

(Key: ..... Theoretical  $\sigma_1$  (MPa); - - - Experimental  $\sigma_1$  (MPa); - . - Experimental  $\sigma_2$  (MPa); - - - Theoretical  $\sigma_2$  (MPa))

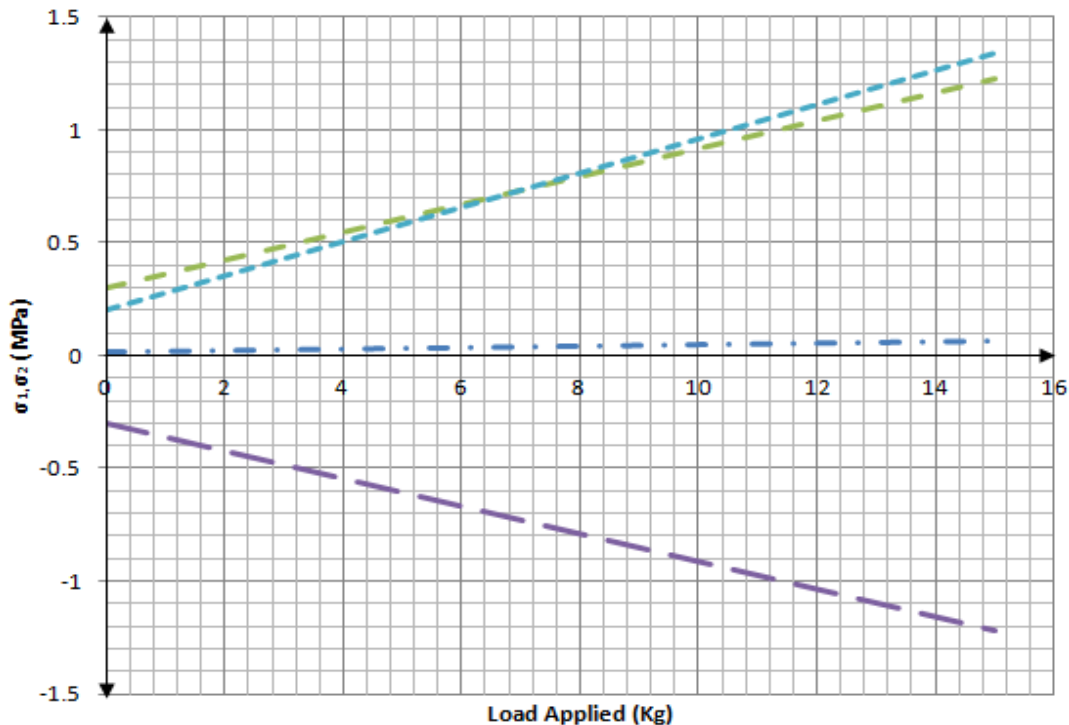


**Figure 9.26: Comparison of principal stresses ( $\sigma_1, \sigma_2$  (MPa)) at position X vs Inline load applied (kg) with 600 mm overlap**

(Key: ..... Theoretical  $\sigma_1$  (MPa); - - - Experimental  $\sigma_1$  (MPa); - . - Experimental  $\sigma_2$  (MPa); - - - Theoretical  $\sigma_2$  (MPa))

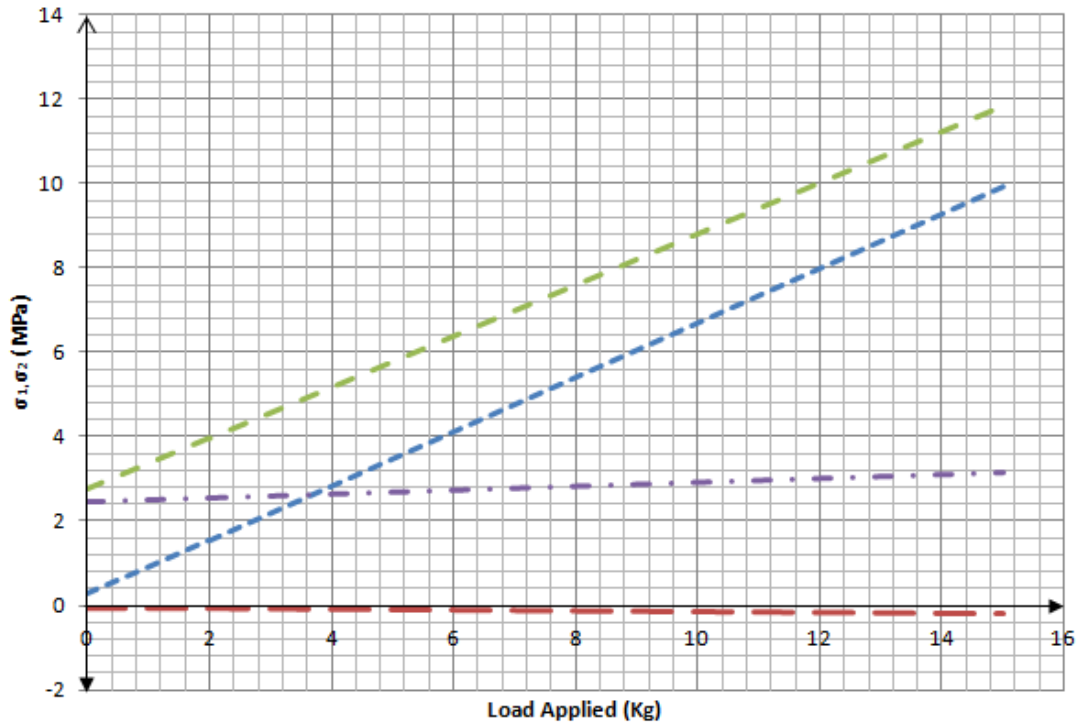


**Figure 9.27: Comparison of principal stresses ( $\sigma_1, \sigma_2$  (MPa)) at position Y vs Inline load applied (kg) with 600 mm overlap**

(Key: ..... Theoretical  $\sigma_1$  (MPa); - - - Experimental  $\sigma_1$  (MPa); - . - Experimental  $\sigma_2$  (MPa); - - - Theoretical  $\sigma_2$  (MPa))

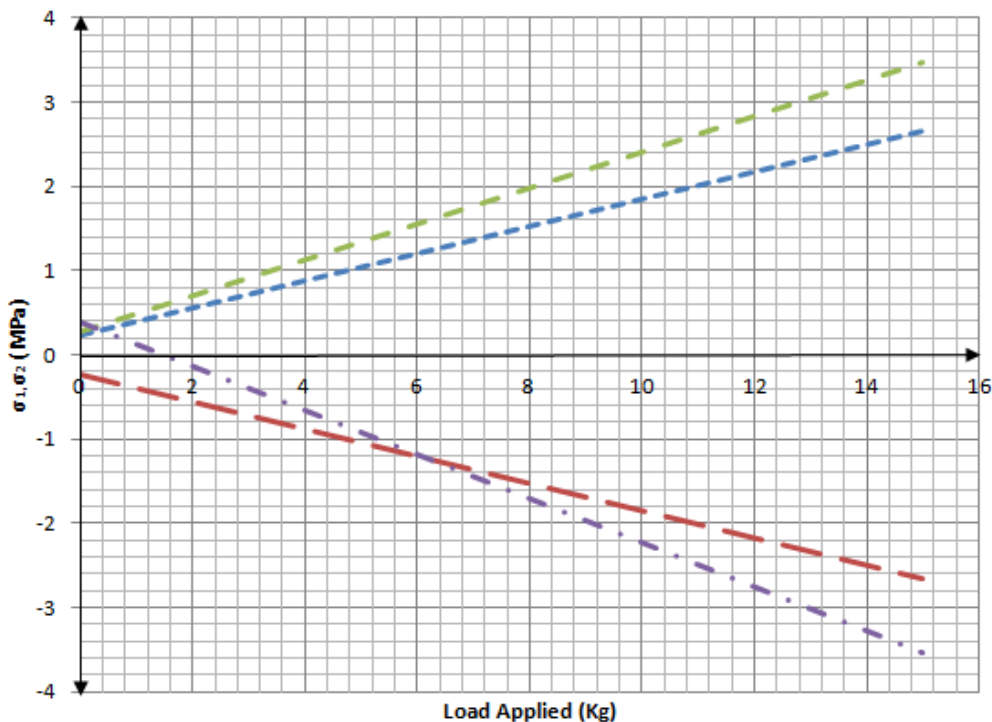


**Figure 9.28: Comparison of principal stresses ( $\sigma_1, \sigma_2$  (MPa)) at position Z vs Inline load applied (kg) with 600 mm overlap**

(Key: ..... Theoretical  $\sigma_1$  (MPa); - - - Experimental  $\sigma_1$  (MPa); - . - Experimental  $\sigma_2$  (MPa); - - - Theoretical  $\sigma_2$  (MPa))

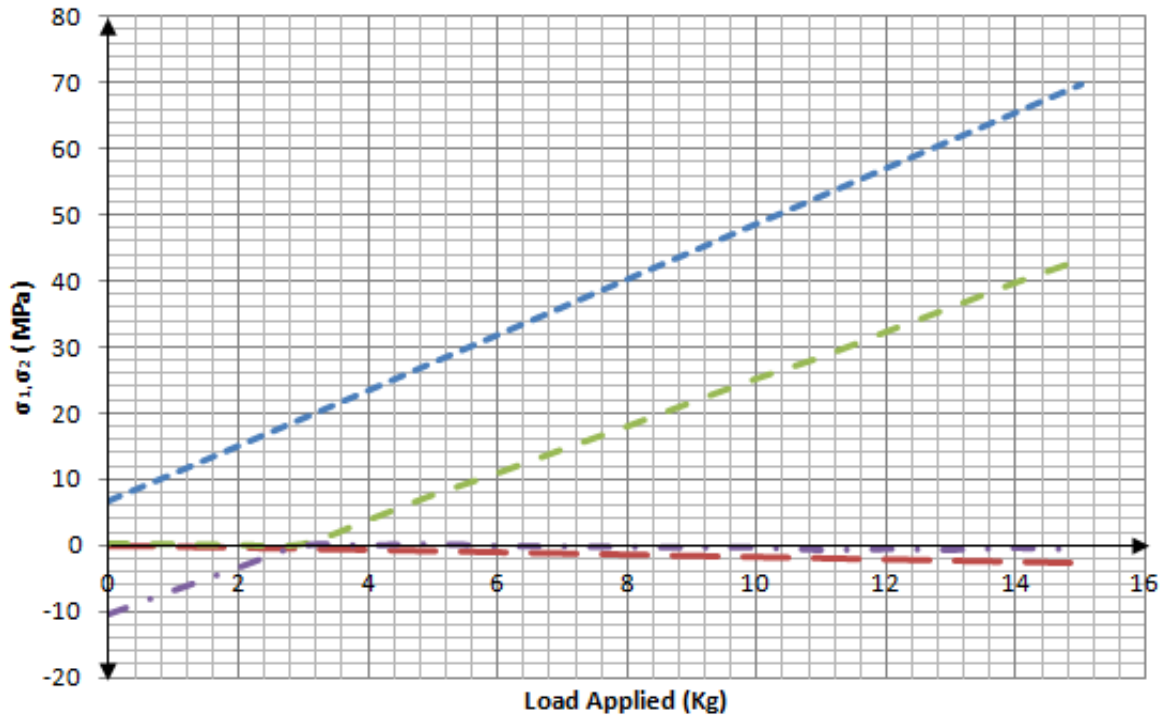


**Figure 9.29: Comparison of principal stresses ( $\sigma_1, \sigma_2$  (MPa)) at position W vs Offset load applied (kg) with 600 mm overlap**  
 (Key: ..... Theoretical  $\sigma_1$  (MPa); - - - Experimental  $\sigma_1$  (MPa); - · - Experimental  $\sigma_2$  (MPa); - - - Theoretical  $\sigma_2$  (MPa))

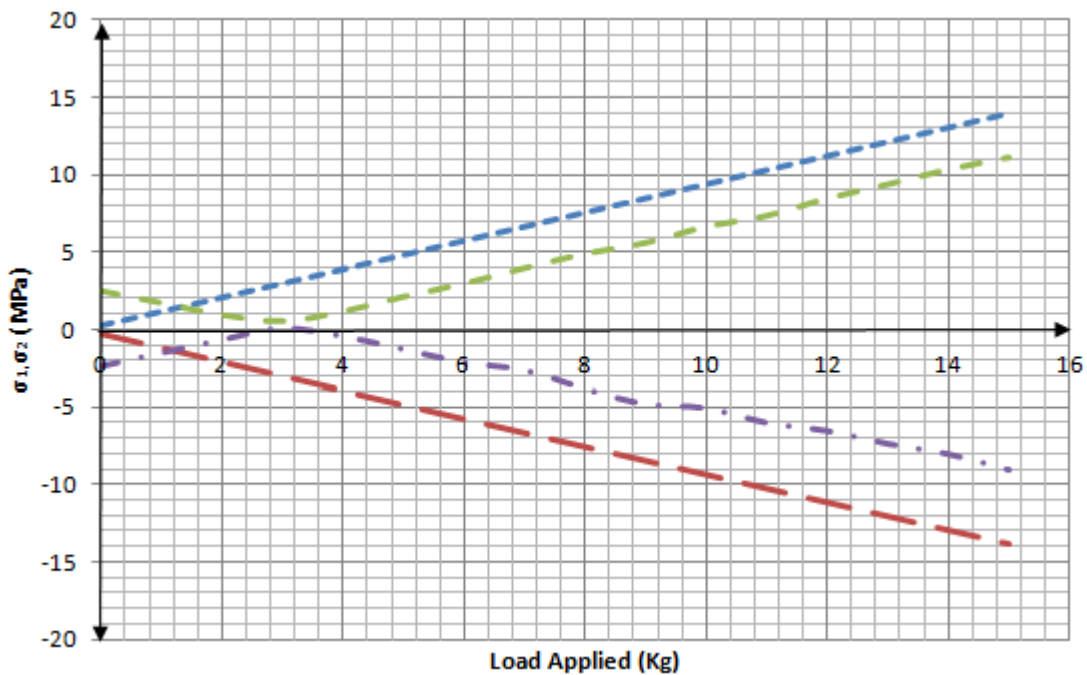


**Figure 9.30: Comparison of principal stresses ( $\sigma_1, \sigma_2$  (MPa)) at position X vs Offset load applied (kg) with 600 mm overlap**  
 (Key: ..... Theoretical  $\sigma_1$  (MPa); - - - Experimental  $\sigma_1$  (MPa); - · - Experimental  $\sigma_2$  (MPa); - - - Theoretical  $\sigma_2$  (MPa))

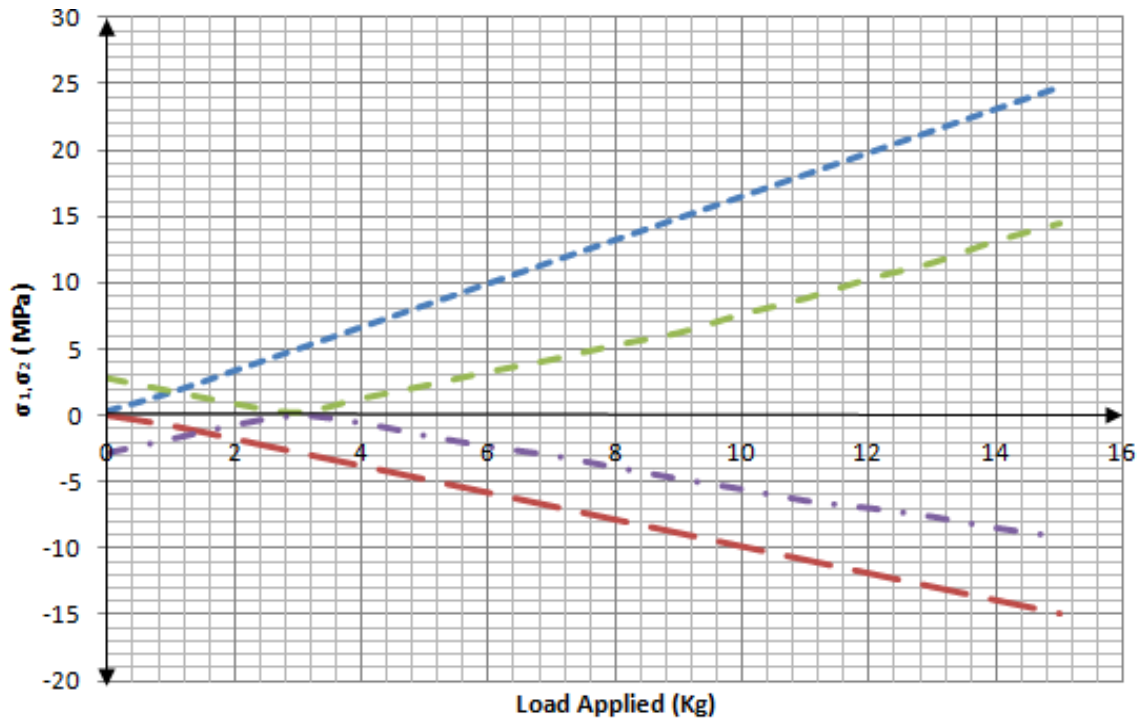


**Figure 9.31: Comparison of principal stresses ( $\sigma_1, \sigma_2$  (MPa)) at position Y vs Offset load applied (kg) with 600 mm overlap**

(Key: ..... Theoretical  $\sigma_1$  (MPa); - - - Experimental  $\sigma_1$  (MPa); - . - Experimental  $\sigma_2$  (MPa); - - - Theoretical  $\sigma_2$  (MPa))

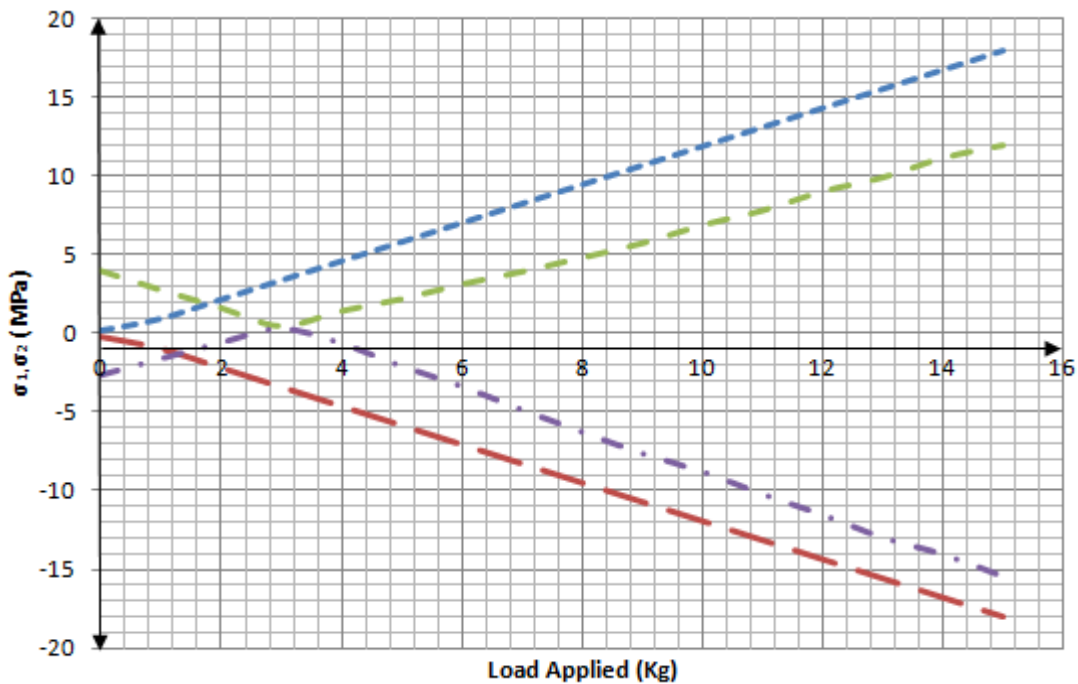


**Figure 9.32: Comparison of principal stresses ( $\sigma_1, \sigma_2$  (MPa)) at position Z vs Offset load applied (kg) with 600 mm overlap**

(Key: ..... Theoretical  $\sigma_1$  (MPa); - - - Experimental  $\sigma_1$  (MPa); - . - Experimental  $\sigma_2$  (MPa); - - - Theoretical  $\sigma_2$  (MPa))

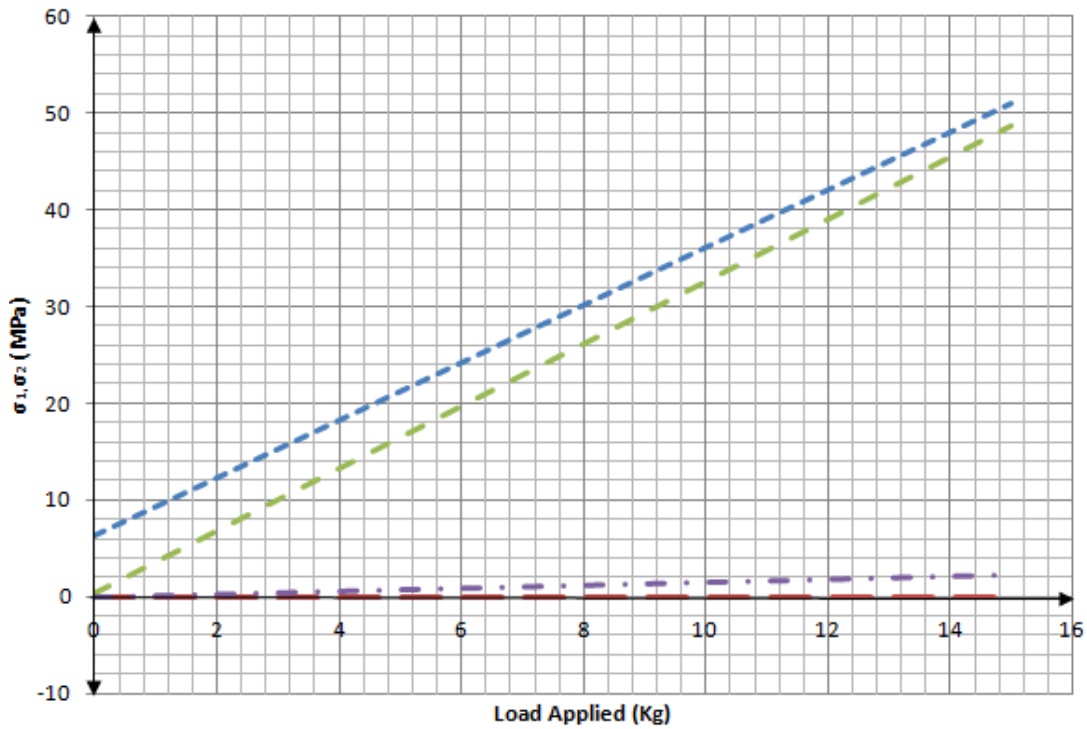


**Figure 9.33: Comparison of principal stresses ( $\sigma_1, \sigma_2$  (MPa)) at position W vs Inline load applied (kg) with 700 mm overlap**  
 (Key: ..... Theoretical  $\sigma_1$  (MPa); - - - Experimental  $\sigma_1$  (MPa); - · - Experimental  $\sigma_2$  (MPa); — Theoretical  $\sigma_2$  (MPa))

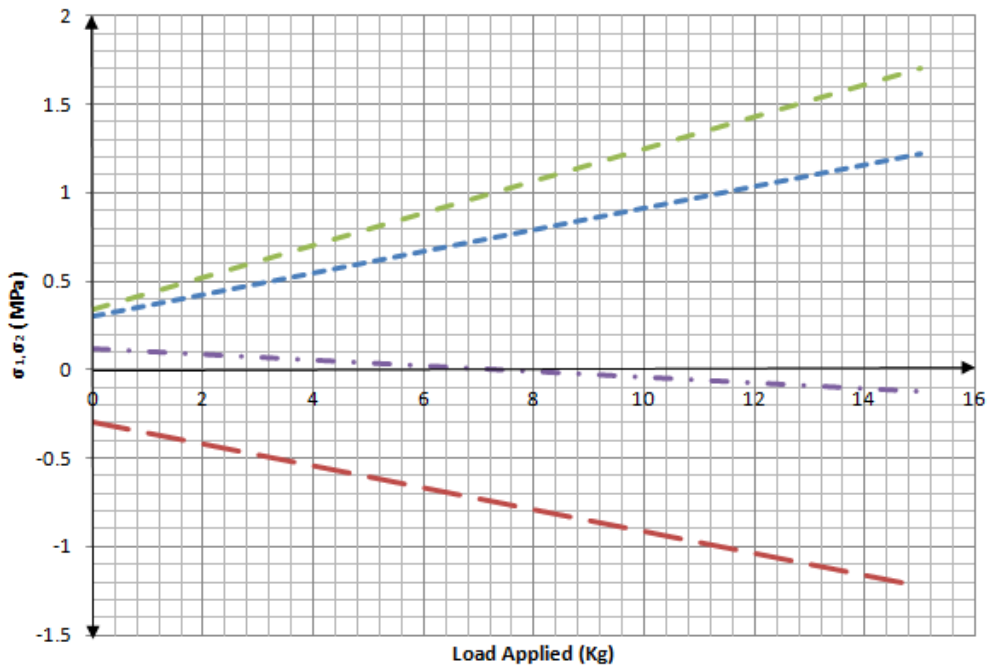


**Figure 9.34: Comparison of principal stresses ( $\sigma_1, \sigma_2$  (MPa)) at position X vs Inline load applied (kg) with 700 mm overlap**  
 (Key: ..... Theoretical  $\sigma_1$  (MPa); - - - Experimental  $\sigma_1$  (MPa); - · - Experimental  $\sigma_2$  (MPa); — Theoretical  $\sigma_2$  (MPa))

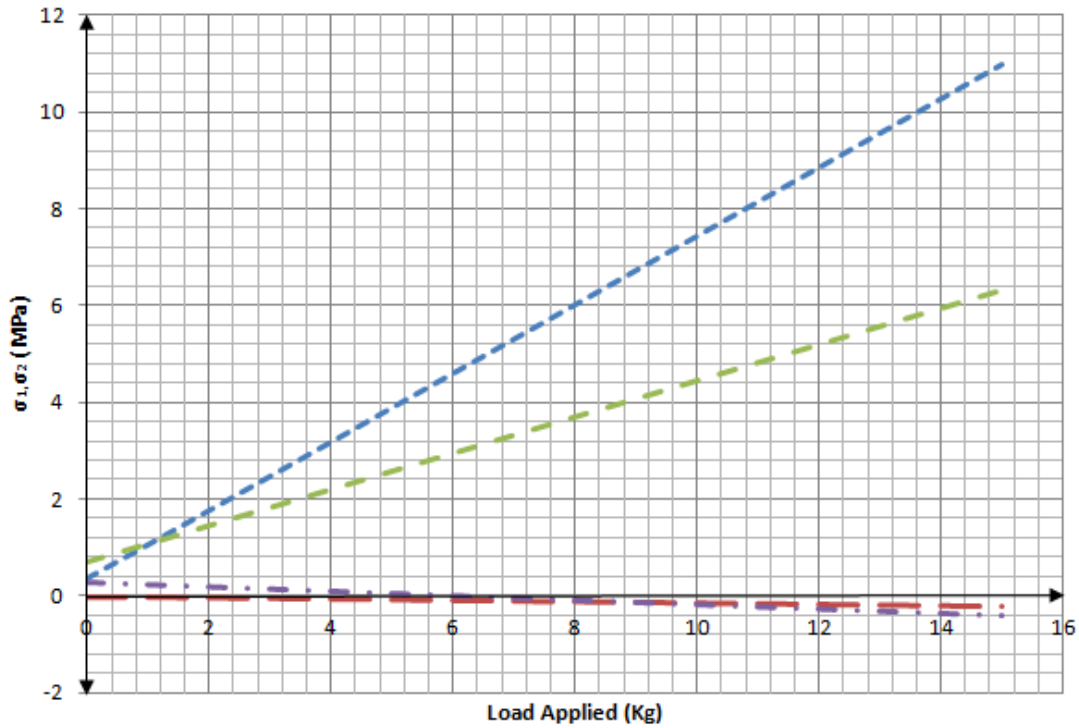


**Figure 9.35: Comparison of principal stresses ( $\sigma_1, \sigma_2$  (MPa)) at position Y vs Inline load applied (kg) with 700 mm overlap**

(Key: ..... Theoretical  $\sigma_1$  (MPa); - - - Experimental  $\sigma_1$  (MPa); - · - Experimental  $\sigma_2$  (MPa); - - - Theoretical  $\sigma_2$  (MPa))

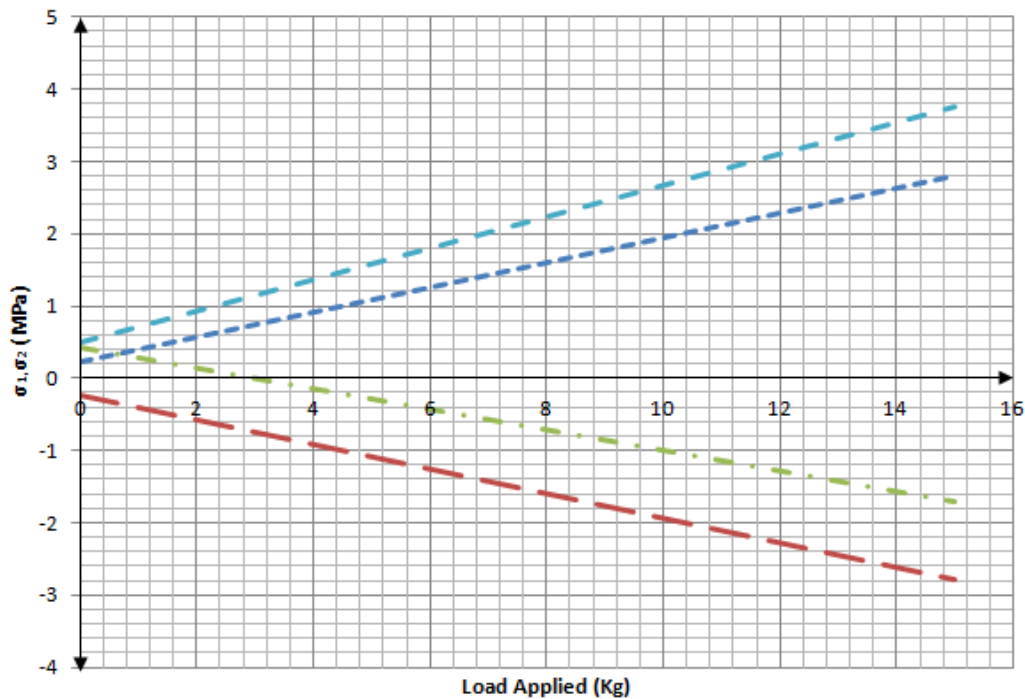


**Figure 9.36: Comparison of principal stresses ( $\sigma_1, \sigma_2$  (MPa)) at position Z vs Inline load applied (kg) with 700 mm overlap**

(Key: ..... Theoretical  $\sigma_1$  (MPa); - - - Experimental  $\sigma_1$  (MPa); - · - Experimental  $\sigma_2$  (MPa); - - - Theoretical  $\sigma_2$  (MPa))

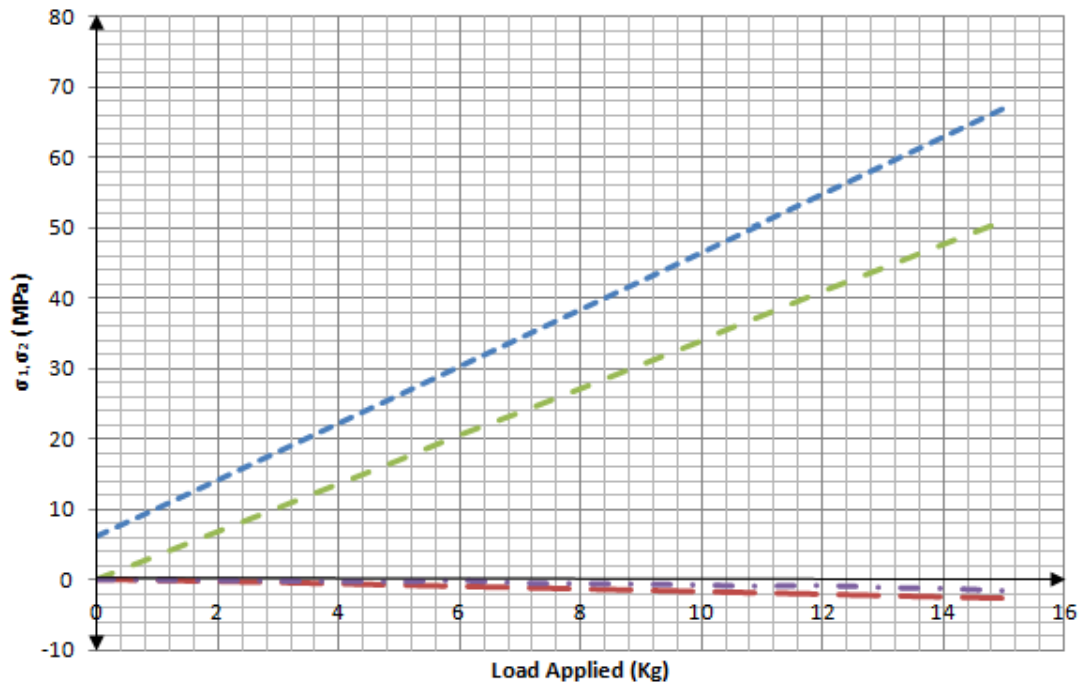


**Figure 9.37: Comparison of principal stresses ( $\sigma_1, \sigma_2$  (MPa)) at position W vs Offset load applied (kg) with 700 mm overlap**  
 (Key: ..... Theoretical  $\sigma_1$  (MPa); - - - Experimental  $\sigma_1$  (MPa); - . - Experimental  $\sigma_2$  (MPa); - - - Theoretical  $\sigma_2$  (MPa))

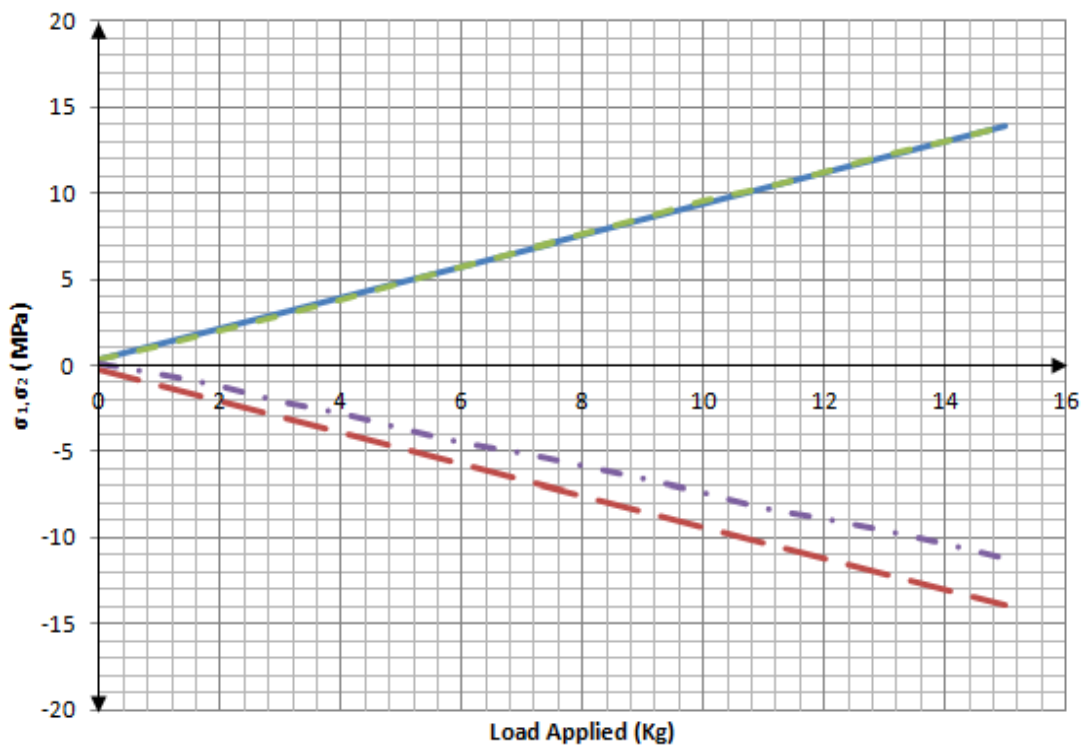


**Figure 9.38: Comparison of principal stresses ( $\sigma_1, \sigma_2$  (MPa)) at position X vs Offset load applied (kg) with 700 mm overlap**  
 (Key: ..... Theoretical  $\sigma_1$  (MPa); - - - Experimental  $\sigma_1$  (MPa); - . - Experimental  $\sigma_2$  (MPa); - - - Theoretical  $\sigma_2$  (MPa))

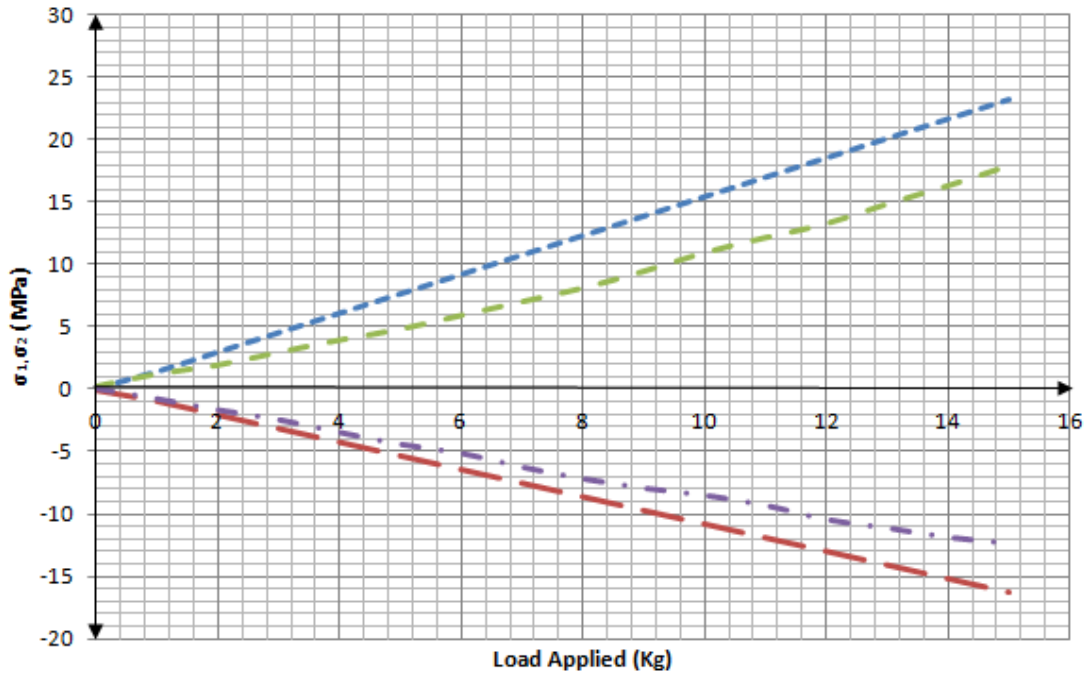


**Figure 9.39: Comparison of principal stresses ( $\sigma_1, \sigma_2$  (MPa)) at position Y vs Offset load applied (kg) with 700 mm overlap**  
 (Key: ..... Theoretical  $\sigma_1$  (MPa); - - - Experimental  $\sigma_1$  (MPa); - . - Experimental  $\sigma_2$  (MPa); - - - Theoretical  $\sigma_2$  (MPa))

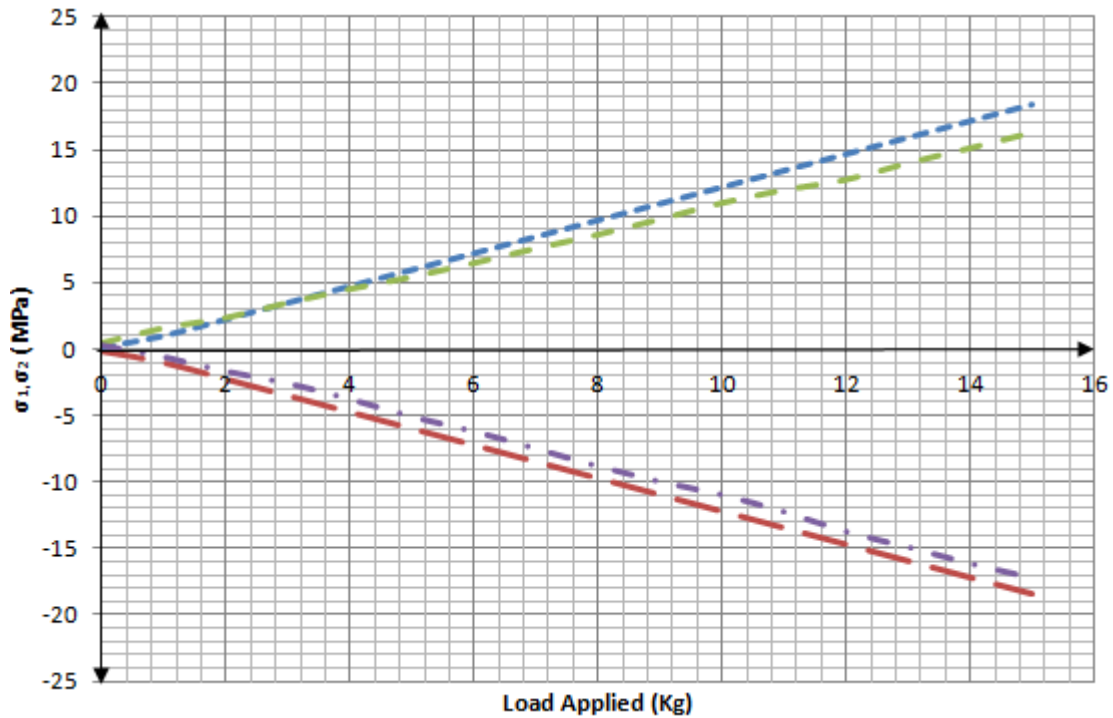


**Figure 9.40 Comparison of principal stresses ( $\sigma_1, \sigma_2$  (MPa)) at position Z vs Offset load applied (kg) with 700 mm overlap**  
 (Key: ..... Theoretical  $\sigma_1$  (MPa); - - - Experimental  $\sigma_1$  (MPa); - . - Experimental  $\sigma_2$  (MPa); - - - Theoretical  $\sigma_2$  (MPa))

### 9.1.3 Buckling Results

Of all the curves related to buckling of sections dealt with in comprehensive detail in Chapter 4, of prime importance to this body of work are those curves generated for the two section telescopic cantilever beam assembly. The curves in question are represented in Figures 4.24, 4.25 and 4.26. On examination, Equation (4.64) reveals that, the higher the value of the overlap ratio parameter  $\alpha$ , the closer the structure tends to be a single section strut, in that the free end is subsumed within the fixed end, and naturally due to the subsequent increase in the second moment area magnitude, the greater will be the critical buckling load for said structure.

Figure 4.24 presents the plot of the non dimensionalised parameter  $\frac{P_{cr}}{P_{Eu}}$ , against the overlap ratio  $\alpha$ , which in turn varies from 0 to 1, in steps of 0.1. The curve shown was plotted assuming fixed and free section lengths of 1200 mm and 1000 mm respectively, an arrangement, for which the value of  $\phi$  is 0.833. It can be deduced from the curve that for an overlap ratio  $\alpha$  equal to 1, the given arrangement will have the greatest critical buckling load magnitude. The condition wherein the overlap ratio  $\alpha$  equals 1, corresponds to that arrangement of the assembly, whereby the free-end section is entirely sheathed within the fixed-end section. This curve assumes importance in light of the fact that it can be tailored to directly suit the application for which a given configuration of the telescoping arrangement is required.

In Figures 4.25 and 4.26, for values of the overlap ratio parameter  $\alpha$  varying from 0 to 1, in increments of 0.1, the maximum critical buckling load, or the magnitude at which a structure just begins to undergo buckling, is observed to be maximum, for a length variation ratio of  $\phi$  equals 0. This indicates that there is no free-end section to slide within the fixed-end section. However an ideal configuration of the telescoping assembly can be selected using the curves plotted in Figures 4.25 and 4.26, for a desired combination of ratios  $\alpha$  and  $\phi$ . Figures 4.25 and 4.26 are in essence used to demonstrate the effect differing lengths of the fixed and free sections that constitute the two section telescoping cantilever beam assembly will have upon the critical buckling load of said structure. Once again, it must be remembered that the three sets of curves in Figures 4.24 -4.26 correspond to that telescopic arrangement having

dimensions outlined in Table 4.5 and fixed and free-end assumed lengths of 1200 mm and 1000 mm respectively.

The experimental test rig was simulated using FEA and subjected to theoretical analysis using Equation (4.64) to generate the curves shown in Figure 9.41. Both the curves compare most favourably and thus the theory generated has been validated, but these plots await experimental verification.

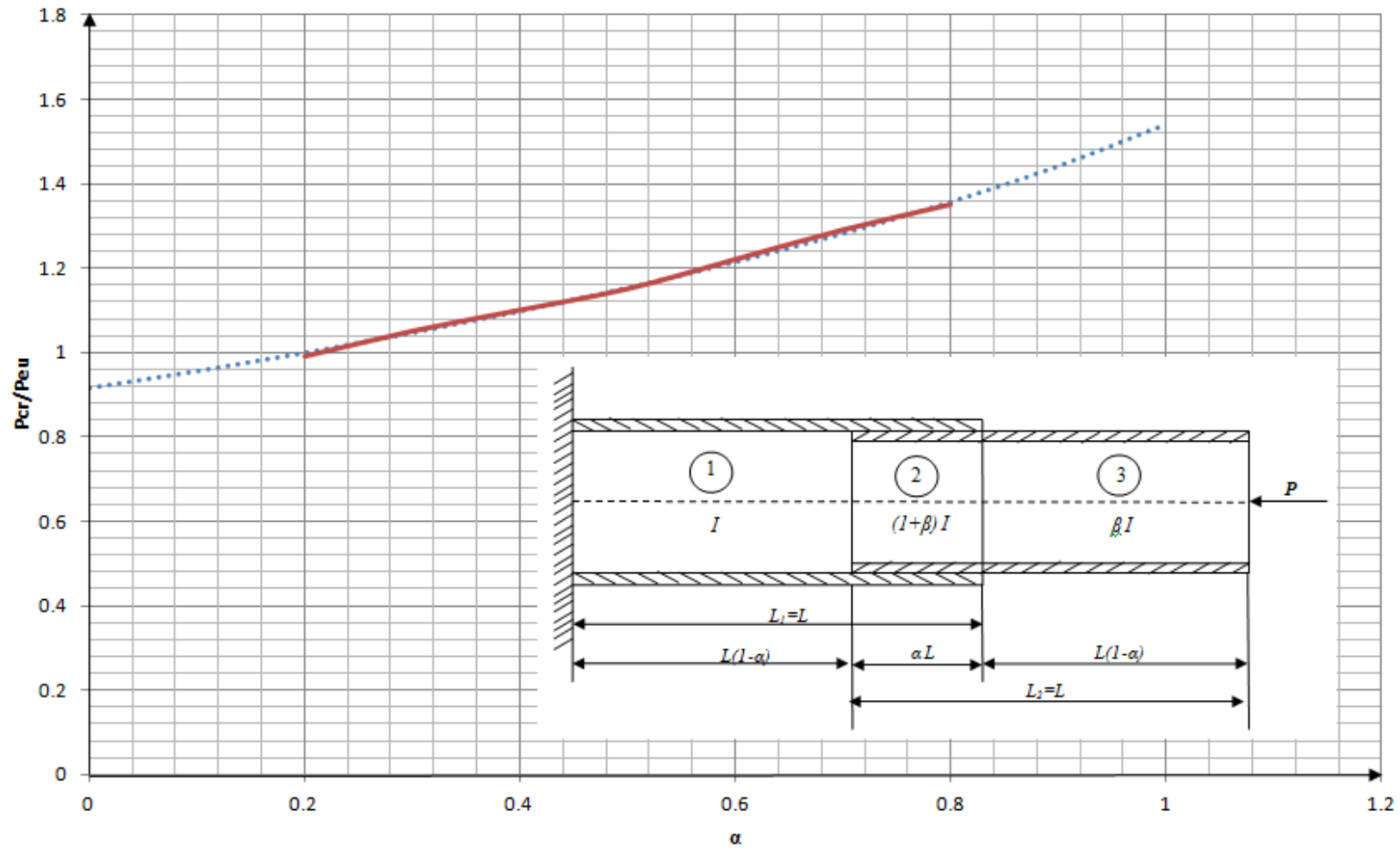


Figure 9.41: Comparison between buckling curves generated from theoretical predictions and FEA, for the telescopic assembly whose individual part dimensions are outlined in Table 7.1  
 (Key: — FEA Predictions; ..... Theoretical Predictions)

## 9.2 Contributions to Knowledge

Despite the increasing use of telescoping sections all around us from simple household appliances to complex retractable stadium roofing, as detailed in §2.19, there is an alarming lack of literature in the public domain, as compared to the data available in the private domain. This is a deterrent to the further use of this simple yet highly effective structure. This thesis has attempted to bridge this gap, in its consistent application to designing with telescoping beams and struts.

In Chapter 3, the four most common deflection prediction theorems are applied to the telescoping cantilever beam assembly and in each instance a unique deflection equation was derived. These equations not only predict the deflection that is induced within the assembly for an inline applied loading effectively, but also take into account the variables within the arrangement, such as the length of the overlap, difference in sectional lengths, changing second moments of area and finally varying self weights of the individual constituent sections. A user looking to attain a particular configuration of a telescoping assembly (providing dimensional data is available) for a task at hand would be able to plot the deflections anticipated, using a C program, based on the calculations detailed in Appendix A, which performs the deflection calculations. This program was adapted to predict deflections in a three section telescopic cantilever beam assembly [91] and is now in commercial application. Chapter 3 also alludes to the *Tip Reaction Model*, first proposed in [91] and applied in this instance to the two section cantilever beam assembly.

Chapter 4 derives from the energy principles, the critical buckling load for the two section telescoping cantilever beam assembly. Not only does this equation predict the critical buckling load, that a particular configuration of the telescopic cantilever beam assembly can withstand, but it also accounts for variables within the assembly, as stated above. The variables used in the derivation of both the tip deflections and in the determination of critical buckling load, are the same, hence lending to the continuity in the analyses of the two section telescoping arrangement. Non dimensionalisation is used throughout the analysis conducted, to simplify the complex equations that were generated as well as to allow for relative ease in determining solutions, for a particular buckling problem. The equations thus derived using these techniques also lend themselves to design curves and further comparisons with results obtained from other avenues. The equation used to determine the critical buckling load is not limited to just the two section telescoping arrangement. Provided ratios can be derived to

account for more telescoping sections within the assembly, it is entirely possible to determine the critical buckling load for an assembly having more than two telescoping sections. What was referred to by Timoshenko as the energy method is used as a base and applied to the cantilever column as detailed in [15]. This approach in turn is verified by validating the result obtained against the criteria for the Euler Critical Buckling load for a column having one end fixed and the other free as the boundary conditions. A general form for predicting the critical buckling load exactly is thus derived and is applied to suit each case individually taking into account the different cross sectional second moments of area and lengths.

Chapter 5 examines the phenomena of local buckling as applied to the individual rectangular hollow section members that comprise the overall telescoping assembly. It has been shown that the best saving in material can be attained when the force is applied directly at the shear centre of the chosen rectangular hollow section. The analysis of shear loading in the constituent, hollow rectangular sections of the telescopic assembly, is complicated by the distribution in shear stress that a section suffers under a transverse force. In that case where both torsion and flexural shear stress are considered, the combination contributes to a raising of the beam's weight, thereby offsetting the greatest weight saving that can be attained, when the force is applied directly at the shear centre. However in the case of the latter, it is not necessary to separate the two effects when determining the position and magnitude of the maximum shear stress upon which the optimum design is based. When considering either the former or the latter, it is possible to optimise the rectangular sections' dimensions, to provide minimum weight, as is shown in this chapter. This has been achieved by limiting the greatest shear stress to a pre determined design stress value, at which buckling will also take place, so as to ensure that the most highly stressed material, is used to its full load-bearing capability. This chapter details optimum design criteria wherein the longer limbs of the rectangular cross section beam, can be adjusted to raise the stress to a similar design stress value, as mentioned, thereby saving weight, allowing for greater efficiency in load bearing and simultaneous buckling at the load limit.

Chapter 6 describes the bending and shear stress analysis of the two section telescoping assembly when it is subjected to both inline and offset loading. The stress analysis performed

on the two section telescoping assembly, in this chapter, has in its basis the work [92], undertaken with respect to the three section telescopic cantilever beam assembly.

Chapter 7 provides a numerical analyses of the two section telescopic assembly using FEA software package, ABAQUS. The analysis performed here validated the deflection, stress and buckling analyses performed on the same.

Chapter 8 details the experimental work that was conducted on a two section telescoping cantilever beam and the results obtained for deflection and stress analysis. The assumptions made in the deflection theory, were validated in experimental work. Despite exhaustive documentation of the experimental stress analysis of the telescoping arrangement, a more effective understanding of the stress distributions within the overlap region, is highly desired. This is because the overlap region has been identified as being of great importance to the overall structural strength. The test rig in itself was subjected to both inline and offset loading in order to mimic the possible loading configurations of the telescopic assembly in its working environment. The mounting fixture used to simulate the fixed end, is perhaps the closest approximation available, besides physically encasing the fixed-end beam within an enclosure. The nature of the beam sections and the flexibility provided allowed the free-end section to be slid in and out of the fixed-end section at will, thereby allowing one to vary the overlap length, as desired. A wide variety of testing was thus accomplished as a result, along with the flexibility afforded by repeatability.

Chapter 9 compares and discusses the results obtained from all the analyses that have been performed on the two section telescopic cantilever beam arrangement. The deflection resulting from end loading produced experimentally, theoretically and through FEA have compared well. The bending and shear stress analysis undertaken both theoretically and through FE has been compared and the theory propagated has been validated. Comparison of the theoretical and experimentally measured principal stresses has been achieved. In terms of buckling, the results obtained from FE matches the theory propagated in Chapter 4, and hence the theory has been partially validated.

Two papers have been published [91, 92], the first of which proposes the *Tip Reaction Model* to provide the deflection of a telescopic cantilever beam. The model uses the reactions at the tips of the overlapping portions as the mechanism of transfer of the external loads between

sections. A generalised, three-section, telescopic beam is analysed in which the *direct integration method* is applied repeatedly to provide deflection. The theory is developed then adapted to a convenient 'C' program listed here. The program is applied to provide deflections under end-loading in a model beam consisting of three hollow, thin-walled sections. The accuracy in the model's end-deflection is checked from a further finite element analysis of the beam. The fact that the two deflections compare validates the tip reaction model of end-deflection arising from self-weight and external loading in a telescopic cantilever. A linear structural response between load and deflection appears consistently from both predictions. This paper is appended to the thesis, as Appendix E.

In the second paper, appended to this thesis, Appendix F, the bending and shear stresses for the three-section cantilever, are obtained both analytically and numerically. A check upon stress levels is provided from a parallel study upon an equivalent, two-stepped, continuous beam. Graphical presentations of the beam stresses, found from applying the two methods to each structure, are self-validating. That is, the continuous beam theory provides a check upon numerical stress levels from FEA and, in turn, FEA provides a check upon the analytical stresses calculated from tip reactions within a telescopic beam. The fact that comparable stress levels were found confirms that the analytical technique proposed is perfectly adequate for a telescoping beam, just as the classical theory is adequate for continuous beams. Taken together, the two papers provide an analytical theory for bending of a discontinuous beam that did not exist heretofore, thereby obviating the need for a numerical solution.

### 9.3 Limitations

1. Although the buckling analysis has been verified from the FEA models, the buckling theory has to be fully validated by conducting buckling on telescopic antenna sections. To fulfil this comparison satisfactorily it will be necessary to adapt the existing test rig to model the boundary conditions, such that one end of the telescopic antenna is fixed whilst the load applied end is to be unconstrained, or free to move. The test rig available has end conditions wherein the load applied end is equivalent to a pinned end. A displacement function would need to be conceived to account for this condition.
2. Experimentally conducted stress analyses of the test rig have been documented in detail in this thesis. Theoretically and experimentally extrapolated values of principal stresses have been plotted and compared against each other. However, these stress values have been collected at four strategic locations. Ideally, gauges would be placed all along the length of the assembly to further validate the models derived. The access particularly to the overlap region is physically constrained. The overlap region is probably a critical area of the assembly and the effect on the overall strength of the assembly has yet to be assessed. With respect to this overlap region a variable of the assembly that has not been investigated is the effect of wear pads. The stress analysis conducted used Tufnell sections, but experimentation with other composites need to be examined.

#### 9.4 Recommendations for Future Work

1. A test rig that accommodates a number of gauges at regular intervals along the length of the assembly, especially within the overlap would greatly enhance the understanding of the actual mechanics of the telescoping arrangement.
2. A long slender telescoping strut, susceptible to buckling is essential to validate the theory that has been developed. A test rig that can accommodate this specimen and also model the boundary conditions wherein one end is fixed and the load applied end is free is preferential to validate the analytical model.
3. Adapting and applying the methodology undertaken in thesis to a three section telescoping cantilever beam assembly and validating with equivalent FEA models and experimental set ups would demonstrate and expand the use of the *Tip Reaction Model*.
4. Ascertaining the critical effect of wear pads present within the assembly and the effects the associated variables can have on the structural behaviour of the assembly.
5. The effect of using beams consisting of non homogeneous anisotropic materials (i.e. composites), upon the characteristics of the assembly needs to be examined. This would be of great relevance as the engineering sector implements the use of composite material widely in structural application.

## REFERENCES

1. Joyce, N and Rees, D.W.A., Niftylift and Brunel University Teaching Company Scheme, 37/1 Doctoral Research Conference Runnymede, June 1996.
2. Joyce, N. Design of a mobile elevating work platform, M.Phil Thesis, Brunel University 1995.
3. BS EN 280 Mobile elevating work platforms: Construction, Safety, Examination and Testing, B.S.I. 2001
4. Pala, Rishi Experimental investigation into compound cantilever beams, M.Sc. Thesis, Brunel University, 2007.
5. Benham, P. P. and Crawford, R. J. *Mechanics of Engineering Materials*, English Language Book Society/ Longman Group Limited, Essex, England, 1987.
6. Rees, D. W. A. *Mechanics of Solids and Structures*, World Scientific, 2000.
7. Gere, J. M. and Timoshenko, S. P. *Mechanics of Materials*, Van Nostrand, 1984.
8. Ramamrutham, S. and Narayan, R. *Strength of Materials*, Eleventh Edition, Dhanpatrai & Sons, Dehli, 1992.
9. Gaafar, M. L. A. Large deflection analysis of a thin-walled channel section cantilever beam, *Int Jl Mech Sci*, 22(12), 1980, pp. 755-766.
10. Tatham, R. and Price, H. L. Deflection of tapered beams, *Aircraft Eng*, 17 (201), 1945, pp. 312-316.
11. ESAB Welding Products, TELBO - *The Telescopic Boom Brochure*, 322 High Holborn, London WC1V 7PB.
12. Niftylift, *Access Platform Catalogue*, 2010, Milton Keynes, MK40, UK.
13. Abraham, J. Estimating deflection and stress in a telescopic cantilever beam using the tip reaction model, Ph.D. Interim Report, School of Engineering and Design, Brunel University, November, 2010.
14. Rees, D.W.A. *Mechanics of Optimal Structural Design – Minimum Weight Structures*, Wiley 2009.
15. Simitses, G. and Hodges, D., *Fundamentals of Structural Stability*, Elsevier Inc., 2006.
16. Fatola, B. O. I., "FEA Driven product Design: Design of a Fly-Knuckle for use on the HR15/17N", A Dissertation presented to the Engineering Design Group of the Engineering and Design School of Brunel University, 2007.

17. Kumar, K., Sivaloganathan, S., Mobasser, O., Kulatunga, M., Lakshman, J.A.U, Ambegoda, C., “Stress Analysis of a Telescopic Boom Assembly”, A Project Report undertaken by Brunel University in Partnership with Niftylift Ltd, Brunel University, April 2008.
18. Abraham, J., “Establishing a Methodology for the Finite Element Analysis of a Complex Boom Assembly for Estimating Stress Hot Spots and Deflections”, A Dissertation presented to the Engineering Design Group of the Engineering and Design School of Brunel University, October 2009.
19. Rajput, R. K., *Strength of Materials*, S. Chand & Company Ltd., Ram Nagar, New Delhi – 110 055, India, 2006.
20. Rees, D. W. A. *Basic Solid Mechanics*, Macmillan, 1997.
21. Washizu, K. (1974). *Variational Methods in Elasticity and Plasticity* (2<sup>nd</sup> Edition), Oxford, UK, Pergamon Press, Ltd.
22. Tauchert, T.R. (1974). *Energy Principles in Structural Mechanics*. New York: McGraw Hill.
23. Hoff, N.J. (1956). *The Analysis of Structures*. New York: John Wiley and Sons.
24. Langhaar, H.L. (1962). *Energy Methods in Applied Mechanics*. New York: John Wiley and Sons.
25. Fung, Y.C., & Tong, P. (2001). *Classical and Computational Solid Mechanics*. Singapore: World Scientific.
26. Sokolnikoff, I.S. (1956). *Mathematical Theory of Elasticity* (2<sup>nd</sup> Ed.). New York: McGraw Hill.
27. Shames, I.H., & Dym, C.L. (1985). *Energy and Finite Element Methods in Structural Mechanics*. New York: Hemisphere.
28. Yoo, C.H., Lee, S.C., *Stability of Structures: Principles and Applications*, (March 2011), 1<sup>st</sup> Ed, Butterworth-Heineman, USA
29. Forsyth, A.R. (1960). *Calculus of Variations*. New York: Dover.
30. Love, A.E.H. (1944). *A Treatise of the Mathematical Theory of Elasticity*. New York, NY:Dover.
31. Saada, A.S. (1974). *Elasticity Theory and Applications* (2<sup>nd</sup> Ed.). Malabar, FL: Krieger Publishing Company.
32. Timoshenko, (with J.M. Gere), *Theory of Elastic Stability*, McGraw-Hill Book Co., Inc., New York, 1st Ed., 1936, 2nd Ed., 1961

33. Notes on Design and Analysis of Machine Elements, Douglas Wright, Department of Mechanical and Materials Engineering, The University of Western Australia, May 2005 [online] Available at: <<http://school.mech.uwa.edu.au/~dwright/DANotes/buckling>> [Accessed July 2011]
34. Croll, J.G.A & Walker, A.C, *Elements of Structural Stability*, Macmillan 1972
35. Dowling, P.J., *et al, eds, Steel Plated Structures*, Granada 1977
36. Elishakoff, I. *et al, eds, Buckling of Structures: Theory and Experiment*, Elsevier 1988
37. Godoy L.A., *Thin-Walled Structures with Structural Imperfections*, Pergamon 1996
38. Gorenc, B.E. & Tinyou R., *Steel Designers Handbook*, NSWUP 1981
39. Kenny, J.P. & Partners, *Buckling of Offshore Structures*, Granada 1984
40. Murray, N.W, *When it Comes to the Crunch: the Mechanics of Car Collisions*, World Scientific 1995
41. Ramm, E. *ed, Buckling of Shells*, Springer 1982
42. Rhodes, J.R. & Walker, A.C. *eds, Thin Walled Structures*, Granada 1980
43. Rhodes, J. *ed, Design of Cold Formed Steel Members*, Elsevier 1991
44. Steel, W.J.M. & Spence, J., 'On Propagating Buckles and Their Arrest in Sub-sea Pipelines', Proc IMechE, v197A, April 1983
45. Tooth, A.S. & Spence, J. *eds, Applied Solid Mechanics - 2*, Elsevier 1988
46. Trahair, N.S. & Bradford, M.A., *The Behaviour & Design of Steel Structures*, Chapman & Hall 1977
47. Young, B.W., 'Steel Column Design', Structural Engineer, v51, n9, Sept 1973
48. Chajes, A. (1974). Principles of Structural Stability Theory. Englewood Cliffs, NJ: Prentice-Hall.
49. Salvadori, M., Heller, R. (1963). Structure in Architecture. Englewood Cliffs, NJ: Prentice-Hall
50. Mikhlin, S.G. (1964). *Variational Methods in Mathematical Physics*. Macmillan Company.
51. Blicch, F. (1952). Buckling Strength of Metal Structures. New York: McGraw-Hill.
52. Vlasov, V.Z. (1940). *Tonkostennye uprugie sterzhni (Thin-walled elastic beams)*. Stroiizdat (in Russian).
53. Vlasov, V.Z. (1961). In *Tonkostennye uprugie sterzhni (Thin-walled elastic beams)*. Moscow, 1959, (2<sup>nd</sup> ed.), translated by Schechtman. Jerusalem: Israel Program for Scientific Translation.

54. Blicch, F. & Blicch, H. (1936). Bending Torsion and Buckling of Bars Composed of Thin Walls, Prelim. Pub. 2<sup>nd</sup> Cong. International Association for Bridge and Structural Engineering, English ed., p. 871, Berlin.
55. Wagner, H. & Pretschner, W. (1936). Torsion and Buckling of Open Sections, NACA Tech. mem. No. 784.
56. Ostenfeld, A. (1931). *Politeknisk Laereanstalts Laboratorium for Bygningsstatik*. Copenhagen: Meddelelse No. 5.
57. Kappus, R. (1938). Drillknicken zentrisch gedhrckter Stäbe emit offenem Profile im elastischen Bereich. *Lufthahrt-Forschung*, Vol. 14 (No. 9), 444457, English translation, Twisting Failure of Centrally Loaded Open-Sections Columns in the Elastic Range, NACA Tech. Mem. No. 851.
58. Lundquist, E.F., & Fligg, C.M. (1937). A Theory for Primary Failure of Straight Centrally Loaded Columns, NACA Tech: Report No. 582.
59. Goodier, J.N. (1941). *The Buckling of Compressed Bars by Torsion and Flexure*. Cornell University Engineering Experiment Station. Bulletin No. 27.
60. Hoff, N.J. (1944). A Strain Energy Derivation of the Torsional-Flexural Buckling Loads of Straight Columns of Thin-Walled Open Sections. *Quarterly of Applied Mathematics*, Vol. 1 (No. 4), 341-345.
61. Timoshenko, S.P. (1945). Theory of Bending, Torsion and Buckling if Thin-Walled Memebers of Open Cross Section, J. Franklin Institute (Philadelphia), Vol. 239, No. 3, p.201, No. 4, p.248, No. 5, p.343
62. Galambos, T.V. (1968). *Structural Members and Frames*. Englewood Cliffs, NJ: Prentice Hall.
63. Kolbrunner, C.F., & Basler, K. (1969). E.C.Glauser (ed.) *Torsion in Structures; An Engineering Approach*, translated from German Berlin: Springer-Verlag.
64. Prandtl, L. (1899). Kipperscheinungen, Dissertation, Munich Polytechnical Institue.
65. Michell, A. G. M. (1899). Elastic Stability of Long Beams under Transverse Forces. *Philosophic Magazine*, Vol. 48, 298.
66. Timoshenko, S. P. (1910). Einige Stabilitäts-problme der Elasticitäts-theorie. *Zeitschrift für Mathematik und Phisik*, Vol. 58, 337-385.
67. Winter, G. (1943). Lateral Stability of Unsymmetrical I-Beams and Trusses in Bending, *Proceedings*, ASCE. Vol. 67, pp. 1851-1864.

68. Hill H. N. (1954). Lateral Buckling of Channels and Z-beams. *Transactions, ASCE, Vol. 119*, pp. 829-841.
69. Clark, J. W., & Hill, H. N. (1960). Lateral Buckling of Beams. *Journal of the Structural Div., ASCE, Vol. 86* (No. ST7), 175-196.
70. Galambos, T.V. (1963). Inelastic Lateral Buckling of Beams. *Journal of the Structural Div., ASCE, Vol. 89* (No. ST5), 217-244.
71. Vincent, G. S. (1969). *Tentative Criteria for Load Factor Design of Steel Highway Bridges. AISI Report No. 15*. New York: American Iron and Steel Institute.
72. ESDU 71005, Buckling of flat plates in shear, September 1976
73. Heins, C.P. *Bending and Torsional Design in Structural Members*, Lexington, MA, 1975
74. 4starequipment Rental Product Catalogue [online] Available at: <<http://www.4starequipment.com>> [Accessed December 2011]
75. Sky Reach Access Product Catalogue [online] Available at: <<http://www.skyreachaccess.com>> [Accessed December 2011]
76. L'usine Nouvelle (The New Plant) General Products Section [online] Available at: <<http://www.usinenouvelle.com>> [Accessed December 2011]
77. L.I.T RA. USA American Covering Systems Product Catalogue [online] Available at: <<http://www.litrausa.com>> [Accessed December 2011]
78. Nautical Structures North America Product Catalogue [online] Available at: <<http://www.nautical-structures.com>> [Accessed December 2011]
79. October Home Inspections Article: 'Inspecting Adjustable Steel [online] Available at: <<http://www.octoberhome.com/articles/adjustcolumn/adjustcolumn.html>> [Accessed December 2011]
80. Discount Ramps Wheelchair Ramps Product Catalogue [online] Available at: <<http://www.discountramps.com/wheelchair-ramps.htm>> [Accessed December 2011]
81. American Flag and Banner Company WonderPole® Telescoping Products Catalogue [online] Available at: <<http://wonderpole.com/telescopingflagpole.html>> [Accessed December 2011]
82. US Tower Corporation, North America, Product Catalogue [online] Available at: <[http://www.ustower.com/uploads/pdf\\_file/product\\_catalog.pdf](http://www.ustower.com/uploads/pdf_file/product_catalog.pdf)> [Accessed December 2011]

83. Steel Storage Systems, Denver, Colorado, USA Product Photo Gallery: Racks [online]  
Available at: <<http://www.steelstorage.com/photosracks.htm>> [Accessed December 2011]
84. Steel Storage Systems, Denver, Colorado, USA Marmon/Keystone Case Study [online]  
Available at: < <http://www.steelstorage.com/marmon.htm>> [Accessed December 2011]
85. Wikipedia, the free encyclopaedia Article: ‘Pont du Gard’ [online] Available at:  
<[http://en.wikipedia.org/wiki/Pont\\_du\\_gard](http://en.wikipedia.org/wiki/Pont_du_gard)> [Accessed July 2011]
86. Wikipedia, the free encyclopaedia Article: ‘Royal Border Bridge’ [online] Available at:  
<[http://en.wikipedia.org/wiki/Royal\\_Border\\_Bridge](http://en.wikipedia.org/wiki/Royal_Border_Bridge)> [Accessed July 2011]
87. Old UK Photos, Article: ‘Old Photos of Crumlin in Monmouthshire / Sir Fynwy in South Wales, United Kingdom of Great Britain’, Photo of the Crumlin Viaduct [online]  
Available at:  
<<http://www.oldukphotos.com/graphics/Wales%20Photos/Monmouthshire,%20Crumlin%20Viaduct%20-%201280pix.jpg>> [Accessed July 2011]
88. Wikipedia, the free encyclopaedia Article: ‘Humber Bridge’ [online] Available at:  
<[http://en.wikipedia.org/wiki/Humber\\_bridge](http://en.wikipedia.org/wiki/Humber_bridge)> [Accessed July 2011]
89. Wikipedia, the free encyclopaedia article about present day twin suspension bridges: ‘Tacoma Narrows Bridge’ [online] Available at:  
<[http://en.wikipedia.org/wiki/Humber\\_bridge](http://en.wikipedia.org/wiki/Humber_bridge)> [Accessed July 2011]
90. Wikipedia, the free encyclopaedia article about the first Tacoma Narrows Bridge which collapsed in 1940: ‘Tacoma Narrows Bridge (1940)’ [online] Available at:  
<[http://en.wikipedia.org/wiki/Tacoma\\_Narrows\\_Bridge\\_\(1940\)](http://en.wikipedia.org/wiki/Tacoma_Narrows_Bridge_(1940))> [Accessed July 2011]
91. Abraham J, Sivaloganathan S, Rees D.W.A. The Telescopic Cantilever Beam: Part 1 – Deflection Analysis, *Engineering Integrity*, February 2011.
92. Abraham J, Sivaloganathan S, Rees D.W.A. The Telescopic Cantilever Beam: Part 2 – Stress Analysis, *Engineering Integrity*, September 2011
93. International Standards ISO/FDIS 12633-2 [Hot-finished structural hollow sections of non alloy and fine grain steels – Part 2: Dimensions and sectional properties].
93. Tang, Xiadong, *Shape Functions of Tapered Beam-Column Elements*, Computers and Structures, 46(5), 1993, pp. 943-953.

94. Smith, W.G., *Analytic Solutions for Tapered Column Buckling*, Computers and Structures, 28(5), 1988, pp. 677-681.
95. RoyMech, A Website Providing useful information, tables, schedules and formulae related to mechanical engineering and engineering materials, 'Rectangular Bar Sections: Table of Dimensions and Properties' [online] Available at: <[http://www.roymech.co.uk/Useful\\_Tables/Sections/Rectangular\\_sections.html](http://www.roymech.co.uk/Useful_Tables/Sections/Rectangular_sections.html)> [Accessed July 2011]
96. ProEngineer Associative Interface User's Guide, 2007
97. Kurowski, P.M., "Finite Element Analysis for Design Engineers", SEA International, 2004.
98. Krishnakumar, R., Finite Element Analysis Tutorials (CD), Indian Institute of Technology Madras
99. Mottram, J.T., & Shaw, C.T., "Using Finite Element Analysis in Mechanical Design", McGraw-Hill Book Company, 1999.
100. Szabo, B., AND Babuska, I., "Finite Element Analysis", John Wiley & Sons, Inc., New York, 1991.
101. MacNeal, R., "Finite Elements: Their Design and Performance", Marcel Dekker, Inc., New York, 1994.
102. Spyrakos, C "Finite Element Modeling in Engineering Practise", West Virginia University Printing Services, Morgantown, WV, 1994.
103. Adams, V., and Askenazi, A., "Building Better Products with Finite Element Analysis", Onword Press, Santa Fe, NM, 1998.
104. Robert D. Cook, "Concepts and Application of Finite Element Analysis", John Wileys & Sons Inc, 2002.
105. Tirupathi R. Chandrupatla, "Introduction to Finite Element in Engineering", Pearson Education Inc, 2002.
106. ABAQUS/CAE User's Manual, ABAQUS Documentation, Abaqus Inc, 2010.
107. ABAQUS Analysis User's Manual, ABAQUS Documentation, Abaqus Inc, 2010.
108. Getting Started with ABAQUS Version 6.6, Abaqus Inc, 2006.
109. Zienkiewicz, O., and Taylor, R., "The Finite Element Method", McGraw-Hill Book Company, London, 1989.
110. Corrin J. Meyer, "Finite Element Analysis for the Masses; an Introduction", FEAdomian.com, 2006.

111. Fagan M.J., "Finite Element Analysis: Theory and Practice", Longman Group UK Limited 1992.
112. Kulatunga M. *Stress Analysis of a Telescopic Boom Assembly of an MEWP using Direct Measurements*, MSc Engineering Design Dissertation submitted to the Advanced Manufacturing and Enterprise Engineering Group of the School of Engineering and Design, Brunel University (March 2008)
113. Robert Reis *Strain Gauge- Piezoelectric Gauges* Department of Agricultural and Biological Engineering February 20, 2006 pp 4-25
114. Dobie, W.B., and Isaac, P.C.G., *Electric Resistance Strain Gauges*, English Universities Press, 1948.
115. Perry, C.C., and Lissner, H.R., *The Strain Gauge Primer*, McGraw Hill, 1962.
116. Dove, R.C., and Adams, P.H., *Experimental Stress Analysis and Motion Measurement*, Merrill 1964.
117. Frocht, M.M., *Photoelasticity Vols. 1 & 2*, John Wiley and Sons, 1941.
118. Coker, E.G., and Filon, L.N.G., *A treatise on photoelasticity*, CUP, 1931, Revised 1957.
119. Hendry, A.W., *Elements of Experimental Stress Analysis*, Maxwell 1964.
120. Dally, J.W. and Riley, W.F., *Experimental Stress Analysis*, McGraw Hill 1965.
121. Durelli, A.J. and Riley, W.F., *Introduction of Photo mechanics*, Prentice-Hall 1965.
122. Holister, G.S., *Experimental Stress Analysis*, CUP, 1967.
123. Bush, A. J., *Strain Gauge Installation for Advance Environment* April 1969.
124. Doebelin, E. O., *Measurement Systems-Application and Design* 1975
125. Aes. C. S and L. H. N. Lee *Strain gauge measurements in regions of high stress gradient* vol 1 pp 199-200
126. Strain gauge technology-Product catalogue [online] Available at <<http://www.vishay.com/strain-gauges>> [Accessed February 2010]
127. ABAQUS/CAE User's Manual, *The Part Module*, ABAQUS Documentation, Abaqus Inc, 2010.
128. ABAQUS/CAE User's Manual, *The Property Module*, ABAQUS Documentation, Abaqus Inc, 2010.
129. ABAQUS/CAE User's Manual, *The Assembly Module*, ABAQUS Documentation, Abaqus Inc, 2010.

130. ABAQUS/CAE User's Manual, *The Step Module*, ABAQUS Documentation, Abaqus Inc, 2010.
131. ABAQUS/CAE User's Manual, *Mesh Tie Constraints*, ABAQUS Documentation, Abaqus Inc, 2010.
132. ABAQUS/CAE User's Manual, *Over Constraint Checks*, ABAQUS Documentation, Abaqus Inc, 2010.
133. ABAQUS/CAE User's Manual, *The Mesh Module*, ABAQUS Documentation, Abaqus Inc, 2010.
134. J. M. T. Thompson and G. W. Hunt, *A general theory of elastic stability*, Wiley, London, 1973.
135. G. W. Hunt and M. A. Wadee, *Localiation and mode interaction in sandwich structures*, *Proc. R. Soc. A*, 454 (1972): 1197-1216, 1998.
136. G. W. Hunt and M. A. Wadee, *Comparitive lagarangian formulations for localized buckling*, *Proc. R. Soc. A*, 434 (1892): 485-502, 1991.
137. D. Saito and M. A. Wadee, *Numerical studies of interactive buckling in prestressed steel styed column*, *Eng. Sruct.*, 31(2):432-443,2009.
138. J. Becque and K. J. R. Rasmusen, *Experimental investigation of the interaction of local and overall buckling of stainless steel I-columns*, *J. Struct. Eng. – ASCE*, 135(11): 1340-1348, 2009.
139. J. Becque and K. J. R. Rasmusen, *Numerical investigation of the interaction of local and overall buckling of stainless steel I-columns*, *J. Struct. Eng. – ASCE*, 135(11): 1340-1348, 2009.

## **APPENDIX A**

## APPENDIX A – THE TWO SECTION TELESCOPIC CANTILEVER BEAM ASSEMBLY

### A.1 Deflection in the two section telescoping assembly

Deflection of the assembly is considered as the combination of deflection in the three beams AB, CD and EF in a three-section, telescopic cantilever beam. The deflected shapes of the different beams however are assumed to be the same in the overlapped regions. Beam AB has two deflected portions AC' and C'B'. Similarly Beam CD has two deflected portions C'B' and B'D'. The equations of the deflected shapes of the beams can be derived by integrating the flexure equation twice. There are four different lengths having different bending moments in this assembly. They are identified within Fig. A1 as follows

- i. AC in beam AB
- ii. CB in beam AB
- iii. CB in beam CD
- iv. BD in beam CD

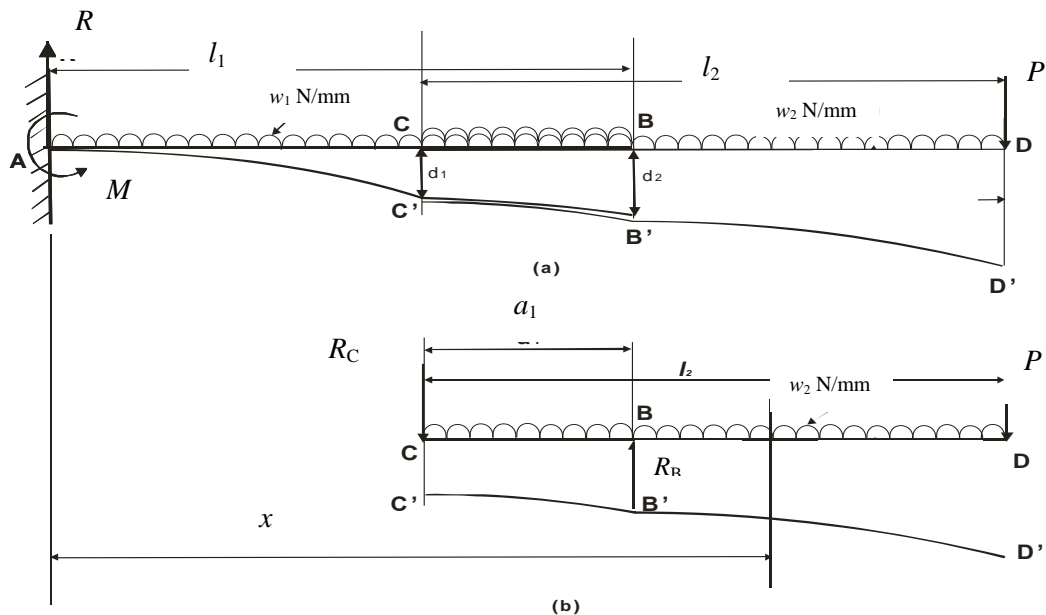
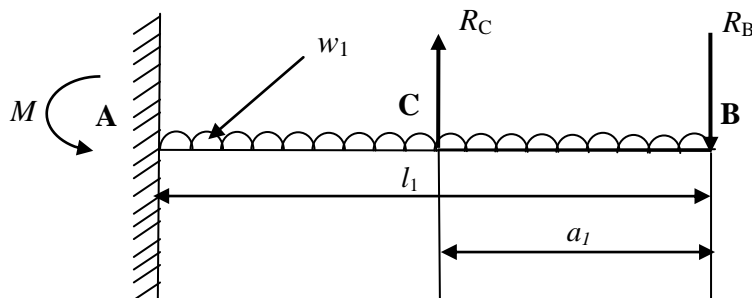


Figure A.1: Deflected shapes of the two-section telescopic cantilever beam assembly

Equations describing the bent shape equations of the four segments are derived by integrating  $EI \frac{d^2y}{dx^2} = -M$  twice, where  $M$  is the sagging bending moment. The integration starts with AC with integration constants found from the known boundary condition at A. Using the equation so derived the slope and deflection at C are calculated. These then become the boundary conditions for the overlap CB in beam AB. This process of matching the individual equations to the boundary conditions calculated from the adjoining section is continued to establish the full beam's deflection curve AC'B'D' in Figure A.1.

## A.2 Tip Reactions

The tip reactions identified here facilitate the load transfer between the two beams. To show this, consider the beam assembly shown in Figure A.2. Since a part of beam CD lies inside beam AB it will produce an upward reaction at C in beam AB and a downward reaction at B in beam AB. The applied forces and moments acting upon the fixed-end beam AB are as shown in Figure A.2.



**Figure A.2: Fixed-end beam loading**

These include: the tip forces  $R_B$  and  $R_C$ , the self-weight loading  $w_1$  and the fixing moment  $M$ . Similarly, when beam CD is considered, at C there will be a downward reaction and at B there will be an upward reaction, due to its contacts with beam AB. Thus the forces upon CD will be those shown in Figure A.3.

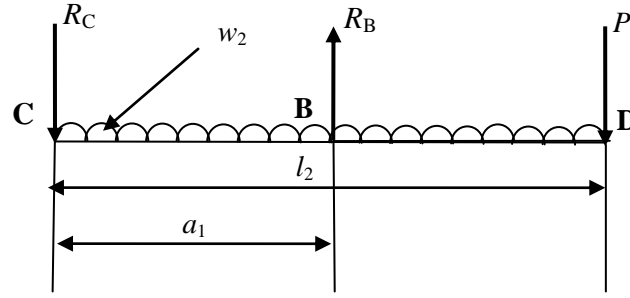


**Figure A.3: Free-end beam loading**

Consider the beam section CD as shown in Figure A.3. Taking moments about C gives

$$R_B \times a_1 = P \times l_2 + w_2 l_2 \times \frac{l_2}{2}$$

But  $a_1 = \alpha_1 l_2$

From the above equations 
$$R_B = \frac{P + \frac{w_2 l_2}{2}}{\alpha_1}$$

In a similar fashion taking moments about B gives

$$R_C \times l_2 \alpha_1 = P \times (1 - \alpha_1) l_2 + w_2 l_2 \times \left( \frac{l_2}{2} - \alpha_1 l_2 \right)$$

Hence 
$$R_C = \left[ \frac{P(1 - \alpha_1) + w_2 l_2 \frac{(1 - 2\alpha_1)}{2}}{\alpha_1} \right]$$

$$\left. \begin{aligned} R_B &= \frac{P + \frac{w_2 l_2}{2}}{\alpha_1} \\ R_C &= \left[ \frac{P(1 - \alpha_1) + w_2 l_2 \frac{(1 - 2\alpha_1)}{2}}{\alpha_1} \right] \end{aligned} \right\} \text{Equation Set (A.1)}$$

Thus, in the proposed ‘*Tip Reaction Model*’ the internal reactions are used to transmit the forces. The effects of the external loads applied to the telescopic cantilever beam can then be calculated using tip reactions instead of the bending moment or, moment of resistance, used in the continuous beam. This technique allows the equilibrium and compatibility requirements for each beam to be considered separately as the free-body diagrams given in Figure A.2 and A.3. In this way the normal tip reactions at the beginning and end of the

overlap are established. Once the reactions are known, the deflection of each beam can be calculated as shown in Appendices § A.3, A.4 and A.5.

### A.3 Derivation of the deflection curve for the section AC in beam AB

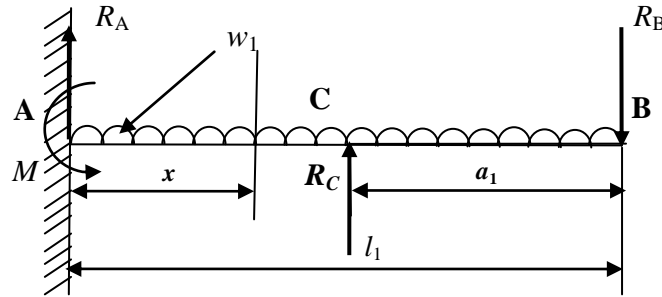


**Figure A.4: A section in AC**

Consider section AC shown in Figure A.4. The bending moment at the section at a distance  $x$  from A is

$$M = -R_B \times (l_1 - x) + R_C \times (l_1 - a_1 - x) - w_1 \times (l_1 - x) \times \frac{(l_1 - x)}{2} \quad \text{for } 0 \leq x \leq (l_1 - a_1)$$

assuming the sign convention 'Sagging is positive'.

But  $EI_1 \frac{d^2y}{dx^2} = -M$  for the beam portion taking  $I_1$  to be the second moment of area of beam

ACB. Integrating this twice will give

$$y = \iint \frac{-M}{EI_1} dx \cdot dx + C_1 x + C_2$$

To find  $C_1$  and  $C_2$  substitute the boundary conditions at A i.e. when  $x = 0$   $y = 0$  and slope

$$\frac{dy}{dx} = 0$$

$$y = \frac{1}{EI_1} \iint R_B \times (l_1 - x) - R_C \times (l_1 - a_1 - x) + w_1 \times (l_1 - x) \times \frac{(l_1 - x)}{2} dx \cdot dx$$

$$\frac{dy}{dx} = \frac{1}{EI_1} \left( R_B \times (l_1 x - \frac{x^2}{2}) - R_C \times [(l_1 - a_1)x - \frac{x^2}{2}] + \frac{w_1}{2} (l_1^2 x - l_1 x^2 + \frac{x^3}{3}) \right) + C_1$$

$C_1 = 0$  because when  $x = 0$  the slope  $\frac{dy}{dx} = 0$ . Integrating again

$$y = \frac{1}{EI_1} \left( R_B \times \left( \frac{l_1 x^2}{2} - \frac{x^3}{6} \right) - R_C \times \left[ \frac{(l_1 - a_1)x^2}{2} - \frac{x^3}{6} \right] + \frac{w_1}{2} \left( l_1^2 \frac{x^2}{2} - l_1 \frac{x^3}{3} + \frac{x^4}{12} \right) \right) + C_1 x + C_2$$

$C_2 = 0$  because when  $x = 0$   $y = 0$

Thus, if the deflection equation for the section AC in the beam AB is given by

$$y_1 = t_{14}x^4 + t_{13}x^3 + t_{12}x^2 + t_{11}x + t_{10}$$

then it follows that the coefficients  $t$  are

$$\left. \begin{aligned} t_{10} &= C_2 = 0 \\ t_{11} &= C_1 = 0 \\ t_{12} &= \frac{1}{EI_1} \left[ \frac{R_B \times l_1}{2} - \frac{R_C l_1 \left( 1 - \frac{l_2}{l_1} \alpha_1 \right)}{2} + \frac{w_1 l_1^2}{4} \right] \\ t_{13} &= \frac{1}{EI_1} \left[ \frac{-R_B}{6} + \frac{R_C}{6} - \frac{w_1 l_1}{6} \right] \\ t_{14} &= \frac{1}{EI} \left[ \frac{w_1}{24} \right] \end{aligned} \right\} \text{Equation Set (A.2)}$$

Let  $\left( \frac{dy}{dx} \right)_C^{AC} = g_1$  where  $\left( \frac{dy}{dx} \right)_C^{AC}$  means the slope of section AC at C and  $\therefore x = (l_1 - a_1)$

Also let  $y_C^{AC} = d_1$  where  $y_C^{AC}$  means the deflection of section AC at C.

$$g_1 = 4t_{14}k_1^3 + 3t_{13}k_1^2 + 2t_{12}k_1$$

$$d_1 = t_{14}k_1^4 + t_{13}k_1^3 + t_{12}k_1^2$$

#### A.4 Derivation of the deflection curve for the section CB in beam AB

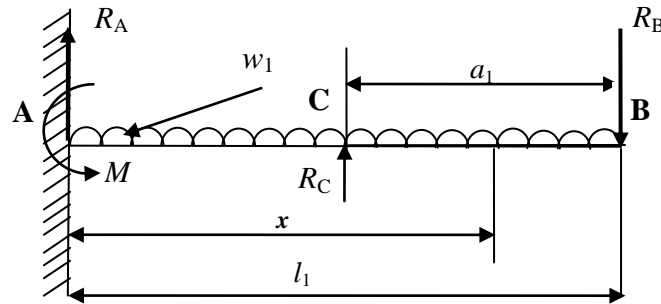


**Figure A.5: A section in CB**

Consider the section CB shown in Figure A.5. The methodology is similar to the one adopted for the portion AC but the boundary conditions applied correspond to point C ( $g_1$  and  $d_1$ ) calculated earlier in A.3.

Consider the section at a distance  $x$  from A as shown in Figure A.5.

Bending moment  $M = -R_B \times (l_1 - x) - w_1 \times (l_1 - x) \times \frac{(l_1 - x)}{2}$  for  $l_1 - a \leq x \leq l_1$

$$\text{But } EI_1 \frac{d^2 y}{dx^2} = -M$$

Integrating this twice will give

$$y = \iint \frac{-M}{EI_1} dx \cdot dx + C_3 x + C_4$$

$$\frac{dy}{dx} = \frac{1}{EI_1} \left( R_B \times \left( l_1 x - \frac{x^2}{2} \right) + \frac{w_1}{2} \left( l_1^2 x - l_1 x^2 + \frac{x^3}{3} \right) \right) + C_3$$

When  $x = l_1 - a_1 = k_1$  slope  $\frac{dy}{dx} = g_1$

$$C_3 = g_1 - \frac{1}{EI_1} \left( R_B \times \left[ l_1 k_1 - \frac{k_1^2}{2} \right] + \frac{w_1}{2} \left[ l_1^2 k_1 - l_1 k_1^2 + \frac{k_1^3}{3} \right] \right)$$

Integrating again

$$y = \frac{1}{EI_1} \left( R_B \times \left( \frac{l_1 x^2}{2} - \frac{x^3}{6} \right) + \frac{w_1}{2} \left( l_1^2 \frac{x^2}{2} - l_1 \frac{x^3}{3} + \frac{x^4}{12} \right) \right) + C_3 x + C_4$$

When  $x = (l_1 - a_1) = k_1$   $y = d_1$

$$C_4 = d_1 - \frac{1}{EI_1} \left( R_B \times \left( \frac{l_1 k_1^2}{2} - \frac{k_1^3}{6} \right) + \frac{w_1}{2} \left( \frac{l_1^2 k_1^2}{2} - \frac{l_1 k_1^3}{3} + \frac{k_1^4}{12} \right) \right) - C_3 k_1$$

Thus if the equation of the section CB in the beam AB is given by

$$y_2 = t_{24}x^4 + t_{23}x^3 + t_{22}x^2 + t_{21}x + t_{20}$$

Then the coefficients  $t$  become

$$\left. \begin{aligned} t_{20} &= C_4 \\ t_{21} &= C_3 \\ t_{22} &= \frac{1}{EI_1} \left[ \frac{R_B \times l_1}{2} + \frac{w_1 l_1^2}{4} \right] \\ t_{23} &= \frac{1}{EI_1} \left[ \frac{-R_B}{6} - \frac{w_1 l_1}{6} \right] \\ t_{24} &= \frac{1}{EI_1} \left[ \frac{w_1}{24} \right] \end{aligned} \right\} \text{Equation Set (A.3)}$$

### A.5 Derivation of the deflection curve for the section CB in beam CD

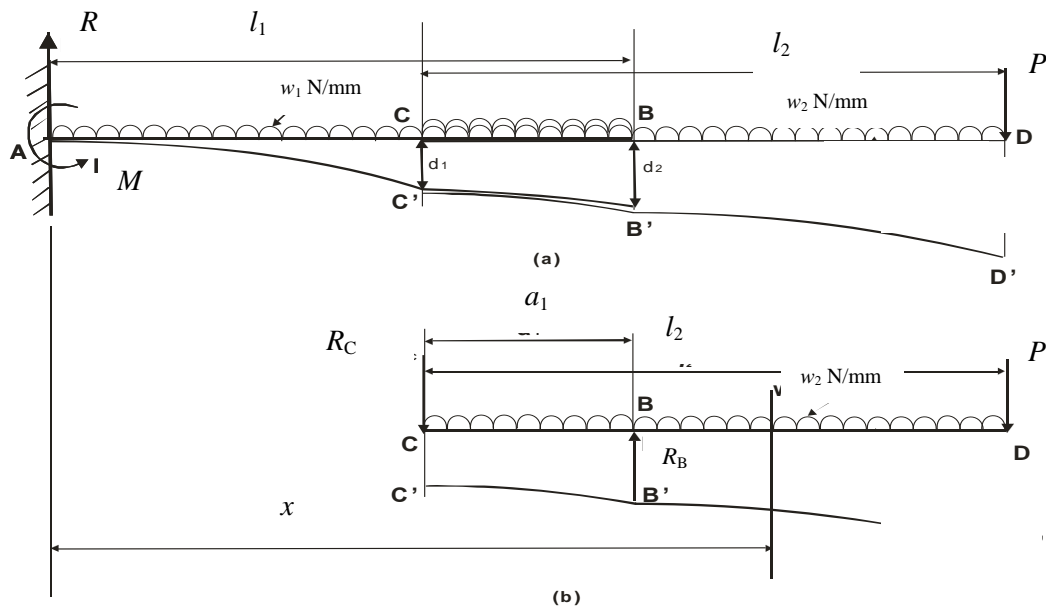


Figure A.6: Deflection of beams AB and CD

Again, the methodology is similar to the one adopted earlier and the boundary conditions applied correspond to point C ( $g_1$  and  $d_1$ ) calculated earlier in §A.4. When, instead of beam AB, the beam CD is considered, the bending moment is from Figure A.6(b):

$$M = -R_C \times (x - l_1 + a_1) - w_2 \times (x - l_1 + a_1) \times \frac{(x - l_1 + a_1)}{2} \quad \text{for } l_1 - a_1 \leq x \leq l_1$$

Substituting  $(l_1 - a_1) = k_1$  this limit becomes  $k_1 \leq x \leq l_1$

But  $EI_2 \frac{d^2 y}{dx^2} = -M$  where  $I_2$  is the second moment of area of beam CBD.

Integrating once gives the slope

$$\frac{dy}{dx} = \frac{1}{EI_2} \left( R_C \times \left[ -k_1 x + \frac{x^2}{2} \right] + \frac{w_2}{2} \left[ k_1^2 x - k_1 x^2 + \frac{x^3}{3} \right] \right) + C_5$$

Integrating again gives the equation

$$y = \frac{1}{EI_2} \left( R_C \times \left[ -\frac{k_1 x^2}{2} + \frac{x^3}{6} \right] + \frac{w_2}{2} \left[ \frac{k_1^2 x^2}{2} - \frac{k_1 x^3}{3} + \frac{x^4}{12} \right] \right) + C_5 x + C_6$$

When  $x = (l_1 - a_1) = k_1$ ,  $\frac{dy}{dx} = g_1$

$$g_1 = \frac{1}{EI_2} \left( R_C \times \left[ -\frac{k_1^2}{2} + \frac{k_1^3}{6} \right] + \frac{w_2}{2} \left[ \frac{k_1^4}{2} - \frac{k_1^4}{3} + \frac{k_1^4}{12} \right] \right) + C_5 k_1$$

$$C_5 = g_1 - \frac{1}{EI_2} \left( R_C \times \left[ -\frac{k_1^2}{2} + \frac{k_1^3}{6} \right] + \frac{w_2}{2} \left[ \frac{k_1^4}{2} - \frac{k_1^4}{3} + \frac{k_1^4}{12} \right] \right)$$

When  $x = (l_1 - a_1) = k_1$   $y = d_1$  and when  $x = l_1$   $y = d_2$  See Figure A.6(a).

$$d_1 = \frac{1}{EI_2} \left( R_C \times \left[ -\frac{k_1^3}{2} + \frac{k_1^3}{6} \right] + \frac{w_2}{2} \left[ \frac{k_1^4}{2} - \frac{k_1^4}{3} + \frac{k_1^4}{12} \right] \right) + C_5 k_1 + C_6$$

$$C_6 = d_1 - \frac{1}{EI_2} \left( R_C \times \left[ -\frac{k_1^3}{2} + \frac{k_1^3}{6} \right] + \frac{w_2}{2} \left[ \frac{k_1^4}{2} - \frac{k_1^4}{3} + \frac{k_1^4}{12} \right] \right) - C_5 k_1$$

Thus if the equation of the section CB in the beam CD

$$y = \frac{1}{EI_2} \left( R_C \times \left[ -\frac{k_1 x^2}{2} + \frac{x^3}{6} \right] + \frac{w_2}{2} \left[ \frac{k_1^2 x^2}{2} - \frac{k_1 x^3}{3} + \frac{x^4}{12} \right] \right) + C_5 x + C_6 \text{ is given by}$$

$$y_3 = t_{34} x^4 + t_{33} x^3 + t_{32} x^2 + t_{31} x + t_{30}$$

Where the coefficients  $t$  are

$$\left. \begin{aligned}
 t_{30} &= C_6 \\
 t_{31} &= C_5 \\
 t_{32} &= \frac{1}{EI_2} \left[ \frac{-R_C \times k_1}{2} + \frac{w_2 k_1^2}{4} \right] \\
 t_{33} &= \frac{1}{EI_2} \left[ \frac{R_C}{6} - \frac{w_2 k_1}{6} \right] \\
 t_{34} &= \frac{1}{EI_2} \left[ \frac{w_2}{24} \right]
 \end{aligned} \right\} \text{Equation Set (A.4)}$$

The deflection of section CB at B is  $d_2$ .

$$d_2 = t_{34}l_1^4 + t_{33}l_1^3 + t_{32}l_1^2 + t_{31}l_1 + t_{30}$$

Also at B, when  $x = l_1$ , the slope is  $\frac{dy}{dx} = g_2$

$$g_2 = 4t_{34}l_1^3 + 3t_{33}l_1^2 + 2t_{32}l_1 + t_{31}$$

### A.6 Derivation of the Deflection Curve for the Section BD in Beam CD

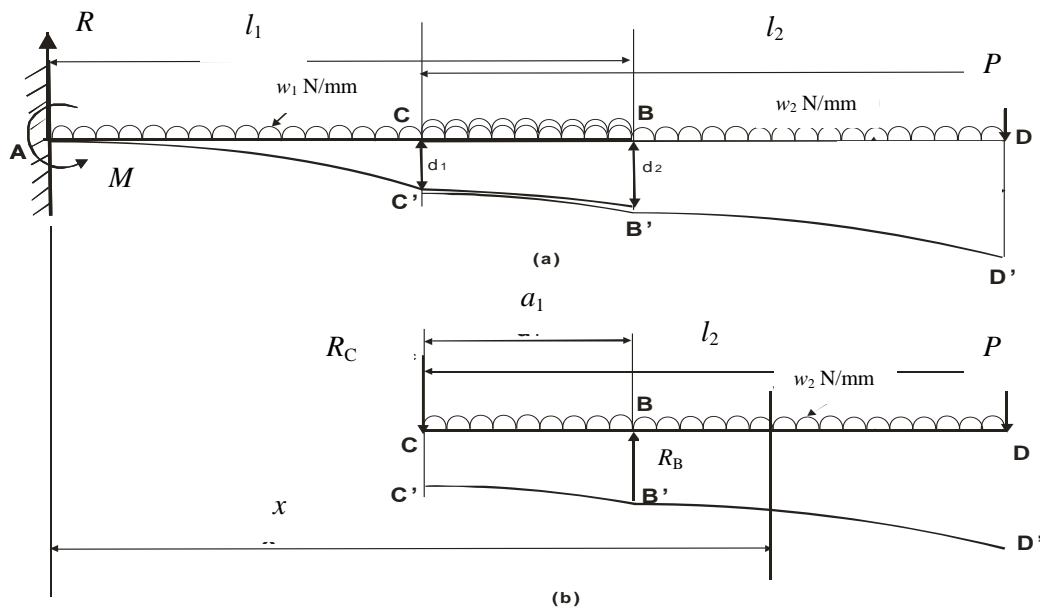


**Figure A.7: Deflection of Beam CD**

Again the methodology is similar to the one adopted earlier and the boundary conditions applied correspond to point B ( $g_2$  and  $d_2$ ) calculated earlier in A.5.

From Figure A.7(b) bending moment

$$M = -R_C \times (x - l_1 + a_1) - w_2 \times (x - l_1 + a_1) \times \frac{(x - l_1 + a_1)}{2} + R_B \times (x - l_1)$$

for  $l_1 \leq x \leq (l_1 - a_1 + l_2)$ , which is  $l_1 \leq x \leq (k_1 + l_2)$ .

But  $EI_2 \frac{d^2 y}{dx^2} = -M$  where  $I_2$  is the second moment of area of beam CBD.

$$EI_2 \frac{d^2 y}{dx^2} = \left( R_C \times [x - k_1] + \frac{w_2}{2} [x - k_1]^2 - R_B \times [x - l_1] \right)$$

Integrating once gives the slope

$$\frac{dy}{dx} = \frac{1}{EI_2} \left( R_C \times \left[ \frac{x^2}{2} - k_1 x \right] + \frac{w_2}{2} \left[ k_1^2 x - k_1 x^2 + \frac{x^3}{3} \right] - R_B \times \left[ \frac{x^2}{2} - l_1 x \right] \right) + C_7$$

Integrating again gives the equation

$$y = \frac{1}{EI_2} \left( R_C \times \left[ \frac{x^3}{6} - \frac{k_1 x^2}{2} \right] + \frac{w_2}{2} \left[ \frac{k_1^2 x^2}{2} - \frac{k_1 x^3}{3} + \frac{x^4}{12} \right] - R_B \times \left[ \frac{x^3}{6} - \frac{l_1 x^2}{2} \right] \right) + C_7 x + C_8$$

When  $x = l_1$ ,  $\frac{dy}{dx} = g_2$  and when  $x = l_1$   $y = d_2$

$$\frac{dy}{dx} = \frac{1}{EI_2} \left( R_C \times \left[ \frac{x^2}{2} - k_1 x \right] + \frac{w_2}{2} \left[ k_1^2 x - k_1 x^2 + \frac{x^3}{3} \right] - R_B \times \left[ \frac{x^2}{2} - l_1 x \right] \right) + C_7$$

$$g_2 = \frac{1}{EI_2} \left( R_C \times \left[ \frac{l_1^2}{2} - k_1 l_1 \right] + \frac{w_2}{2} \left[ k_1^2 l_1 - k_1 l_1^2 + \frac{l_1^3}{3} \right] + R_B \left[ \frac{l_1^2}{2} \right] \right) + C_7$$

$$C_7 = g_2 - \frac{1}{EI_2} \left( R_C \times \left[ \frac{l_1^2}{2} - k_1 l_1 \right] + \frac{w_2}{2} \left[ k_1^2 l_1 - k_1 l_1^2 + \frac{l_1^3}{3} \right] + R_B \left[ \frac{l_1^2}{2} \right] \right)$$

$$y = \frac{1}{EI_2} \left( R_C \times \left[ \frac{x^3}{6} - \frac{k_1 x^2}{2} \right] + \frac{w_2}{2} \left[ \frac{k_1^2 x^2}{2} - \frac{k_1 x^3}{3} + \frac{x^4}{12} \right] - R_B \times \left[ \frac{x^3}{6} - \frac{l_1 x^2}{2} \right] \right) + C_7 x + C_8$$

$$= \frac{1}{EI_2} \left( R_C \left[ \frac{l_1^3}{6} - \frac{k_1 l_1^2}{2} \right] + \frac{w_2}{2} \left[ \frac{k_1^2 l_1^2}{2} - \frac{k_1 l_1^3}{3} + \frac{l_1^4}{12} \right] + \frac{R_B l_1^3}{3} \right) + C_7 l_1 + C_8$$

$$C_8 = d_2 - \frac{1}{EI_2} \left( R_C \left[ \frac{l_1^3}{6} - \frac{k_1 l_1^2}{2} \right] + \frac{w_2}{2} \left[ \frac{k_1^2 l_1^2}{2} - \frac{k_1 l_1^3}{3} + \frac{l_1^4}{12} \right] + \frac{R_B l_1^3}{3} \right) - C_7 l_1$$

Thus if the equation of the section BE in the beam CD

$$y = \frac{1}{EI_2} \left( R_C \times \left[ \frac{x^3}{6} - \frac{k_1 x^2}{2} \right] + \frac{w_2}{2} \left[ \frac{k_1^2 x^2}{2} - \frac{k_1 x^3}{3} + \frac{x^4}{12} \right] - R_B \times \left[ \frac{x^3}{6} - \frac{l_1 x^2}{2} \right] \right) + C_7 x + C_8 \text{ is given}$$

by  $y_4 = t_{44}x^4 + t_{43}x^3 + t_{42}x^2 + t_{41}x + t_{40}$

Here the coefficients  $t$  are

$$\left. \begin{aligned} t_{40} &= C_8 \\ t_{41} &= C_7 \\ t_{42} &= \frac{1}{EI_2} \left[ \frac{-R_C \times k_1}{2} + \frac{w_2 k_1^2}{4} + \frac{R_B \times l_1}{2} \right] \\ t_{43} &= \frac{1}{EI_2} \left[ \frac{R_C}{6} - \frac{w_2 k_1}{6} - \frac{R_B}{6} \right] \\ t_{44} &= \frac{1}{EI_2} \left[ \frac{w_2}{24} \right] \end{aligned} \right\} \text{Equation Set (A.5)}$$

The full length of the beam assembly is given by:  $l_1 - a_1 + l_2 = k_1 + l_2$

The total tip deflection or the deflection at D is found by substituting

$$x = l_1 - a_1 + l_2 = k_1 + l_2$$

$$d_3 = t_{44}(k_1 + l_2)^4 + t_{43}(k_1 + l_2)^3 + t_{42}(k_1 + l_2)^2 + t_{41}(k_1 + l_2) + t_{40} \quad (\text{A.6})$$

$$g_3 = 4t_{44}(k_1 + l_2)^3 + 3t_{43}(k_1 + l_2)^2 + 2t_{42}(k_1 + l_2) + t_{41} \quad (\text{A.7})$$

## **APPENDIX B**

## APPENDIX B – THE C PROGRAM

```
#include <stdio.h>
#include <math.h>
#include <string.h>
#include <stdlib.h>

float w1, w2, P, alpha1;
float l1, l2, Rb, Rc;
float I1, I2, r1, r2, r3;
float t14n, t14, t13n, t13, t12n, t12, t11n, t11, t10n, t10, t20n, t20, t21n, t21, t22n, t22, t23n, t23, t24n, t24;
float t30, t31, t32, t33, t34, t40, t41, t42, t43, t44, g1, d1, k1, m1, g2, d2;
float k1, d1, d2, d3, g1, g2, g3;
float C1, C2, C3, C4, C5, C6, C7, C8;
float t34, t33, t32, t31, t30, t44, t43, t42, t41, t40, t50, t51, t52, t53, t54, t60, t61, t62, t63, t64, t70, t71, t72, t73, t74;
float tmp1, tmp2, d1n, d2n, d3n, d4n;
float nd1;

int main()
{
    printf("          CALCULATION OF REACTIONS\n");
    printf("          -----\n");
    printf("\n");
    printf("\n");
    printf("Enter the Self Weight in N/mm for Section 1: \n");
    scanf( "%f", &w1 );
    printf("\n");
    printf("Enter the Self Weight in N/mm for Section 2: \n");
    scanf( "%f", &w2 );
    printf("\n");
    printf("Enter the Tip Load: \n");
    scanf( "%f", &P );
    printf("\n");
    printf("Enter the overlap between beams 1 and 2 as a decimal fraction of\n\nthe length of beam 2: \n");
    scanf( "%f", &alpha1 );
    printf("\n");
    printf("Enter the length of beam 1: \n");
    scanf( "%f", &l1 );
    printf("\n");
    printf("Enter the length of beam 2: \n");
    scanf( "%f", &l2 );
    printf("\n");
    Rb=(P+((w2*l2)/2))/alpha1;
    Rc=((P*(1-alpha1))+((w2*l2*(1-2*alpha1))/2))/alpha1;
    printf("Reaction at B = %f\n", Rb);
    printf("\n");
    printf("Reaction at C = %f\n", Rc);
    printf("\n");
    printf( "CALCULATION OF REACTIONS IS COMPLETE. Press any character to\n\ncontinue\n");
    printf("\n");
    printf("\n");
    getchar();
}
```

```

printf("                OBTAINING SECOND MOMENTS OF AREA\n");
printf("                -----\n");
printf("\n");
printf("\n");
printf("Enter the Second Moment of Area of Section 1:  \n");
scanf( "%f", &I1);
printf("\n");
printf("Enter the Second Moment of Area of Section 2:  \n");
scanf( "%f", &I2);
printf("\n");
printf( "CALCULATION OF SECOND MOMENTS OF AREA IS COMPLETE. Press any
character to continue\n");
printf("\n");
printf("\n");
getchar();

printf("1.CALCULATION OF THE COEFFICIENTS OF THE 4TH ORDER EQUATION FOR AC
IN BEAM AB\n");
printf("-----
-----\n");
printf("\n");
printf("\n");

t10=0;
t11=0;
k1=l1-alpha1*I2;
r1= 200000*I1;
t12n=((Rb*I1/2)-(Rc*((l1-(alpha1*I2))/2))+((w1*pow(l1,2))/4));
t12=(t12n)/r1;
t13n=(-Rb/6+Rc/6-(w1*l1)/6);
t13=(t13n)/r1;
t14=(w1/24)/r1;
g1= 4*t14*pow(k1,3)+ 3*t13*pow(k1,2) + 2*t12*k1;
d1= t14*pow(k1,4)+t13*pow(k1,3)+t12*pow(k1,2);

printf("The equation of AC in the beam AB is y=
t14x^4+t13x^3+t12x^2+t11x+t10 :  \n");
printf( "t14 = %f\n", t14);
printf( "t13 = %f\n", t13);
printf( "t12 = %f\n", t12);
printf( "t11 = %f\n", t11);
printf( "t10 = %f\n", t10);
printf("Slope at C is      %f\n",g1);
printf("Deflection at C in Beam AB through AC is      %f\n",d1);
printf("\n");
printf("\n");
getchar();

```

```

printf("2. CALCULATION OF THE COEFFICIENTS OF THE 4TH ORDER EQUATION FOR
CB IN BEAM AB\n");
printf("-----\n");
printf("\n");
printf("\n");

C3=g1-(Rb*(l1*k1 - (pow(k1,2)/2)) + ((w1/2)*((pow(l1,2)*k1) -
(l1*pow(k1,2)) + (pow(k1,3)/3))))/(r1);
C4=d1-(C3*k1)-(Rb*((l1*pow(k1,2))/2) - (pow(k1,3)/6)) +
(w1/2)*((pow(l1,2)*(pow(k1,2))/2) - ((l1*pow(k1,3))/3) +
(pow(k1,4)/12))/(r1);

printf("C3 is    %f\n",C3);
printf("C4 is    %f\n",C4);
t20=C4;
t21=C3;
t22=((Rb*l1)/2)+((w1*pow(l1,2))/4)/r1;
t23=(-Rb/6-((w1*l1)/6))/r1;
t24=(w1/24)/r1;

printf("The equation of CB in the beam AB is y=
t24x^4+t23x^3+t22x^2+t21x+t20 : \n");
printf("t24 = %f\n", t24);
printf("t23 = %f\n", t23);
printf("t22 = %f\n", t22);
printf("t21 = %f\n", t21);
printf("t20 = %f\n", t20);
nd1=t24*pow(k1,4)+t23*pow(k1,3)+t22*pow(k1,2)+t21*(k1)+t20;
printf("Deflection at C in Beam AB through CB is    %f\n",nd1);
printf("\n");
printf("\n");
d2=t24*pow(l1,4)+t23*pow(l1,3)+t22*pow(l1,2)+t21*(l1)+t20;
printf("Deflection at B in Beam AB is    %f\n",d2);
printf("\n");
printf("\n");
getchar();

printf("3. CALCULATION OF THE COEFFICIENTS OF THE 4TH ORDER EQUATION FOR
CB IN BEAM CD\n");
printf("-----\n");
printf("\n");
printf("\n");
r2=200000*I2;
C5=g1-((Rc*(-pow(k1,2))/2) + (w2/6)*(pow(k1,3)))/(r2);
C6=d1-(C5*k1)-((Rc*(-(pow(k1,3)/3)))+(w2/8)*pow(k1,4))/(r2);
t30=C6;
t31=C5;
t32=((-Rc*k1)/2)+((w2*pow(k1,2))/4)/(r2);
t33=(Rc/6-((w2*k1)/6))/r2);
t34=(w2/24)/(r2);

printf("The equation of CB in the beam CD is y=
t34x^4+t33x^3+t32x^2+t31x+t30 : \n");
printf("t34 = %f\n", t34);
printf("t33 = %f\n", t33);
printf("t32 = %f\n", t32);
printf("t31 = %f\n", t31);

```

```

printf( "t30 = %f\n", t30);
printf("\n");
printf("\n");
nd1=t34*pow(k1,4)+t33*pow(k1,3)+t32*pow(k1,2)+t31*k1+t30;

printf("Deflection at C in the Beam CD through CB is      %f\n",nd1);
printf("\n");
printf("\n");
d2=t34*pow(l1,4)+t33*pow(l1,3)+t32*pow(l1,2)+t31*l1+t30;
g2=4*t34*pow(l1,3)+3*t33*pow(l1,2)+2*t32*l1+t31;
printf("Slope at B is      %f\n",g2);
printf("Deflection at B in the Beam CD through CB is      %f\n",d2);
getchar();

printf("4. CALCULATION OF THE COEFFICIENTS OF THE 4TH ORDER EQUATION FOR BE
      IN BEAM CD\n");
printf("-----\n");
printf("\n");
printf("\n");
C7=g2-(Rc*((pow(l1,2)/2)-(k1*l1))+((w2/2)*((pow(k1,2)*l1)-
(k1*pow(l1,2))+pow(l1,3)/3))+((Rb*pow(l1,2))/2))/(r2);
C8=d2-(C7*l1)-(Rc*((pow(l1,3))/6)-
((k1*(pow(l1,2)))/2))+((w2/2)*((pow(k1,2)*pow(l1,2))/2)-
((k1*pow(l1,3))/3)+((pow(l1,4)/12)))+Rb*((pow(l1,3)/3)))/(r2);
t40=C8;
t41=C7;
t42=(-Rc*k1)/2 + (w2*pow(k1,2))/4 + (Rb*l1)/2)/(r2);
t43=(Rc/6 - (w2*k1)/6 - (Rb/6))/(r2);
t44=(w2/24)/r2;

printf("The equation of BE in the beam CD is y=
      t44x^4+t43x^3+t42x^2+t41x+t40 :  \n");
printf( "t44 = %f\n", t44);
printf( "t43 = %f\n", t43);
printf( "t42 = %f\n", t42);
printf( "t41 = %f\n", t41);
printf( "t40 = %f\n", t40);
printf("\n");
printf("\n");

d3=t44*pow((k1+l2),4)+t43*pow((k1+l2),3)+t42*pow((k1+l2),2)+t41*(k1+l2
)+t40;
g3=4*t44*pow((k1+l2),3)+3*t43*pow((k1+l2),2)+ 2*t42*(k1+l2)+ t41;
printf("Slope at D is      %f\n",g3);
printf("The overall tip deflection at D is      %f\n",d3);
getchar();
return 0;
}

```

## APPENDIX C

**APPENDIX C – PART 1 – INLINE LOADING ANALYSIS OF INDUCED STRESS IN THE TWO SECTION TELESCOPIC ASSEMBLY**

**C.1 Calculation of tip reactions**

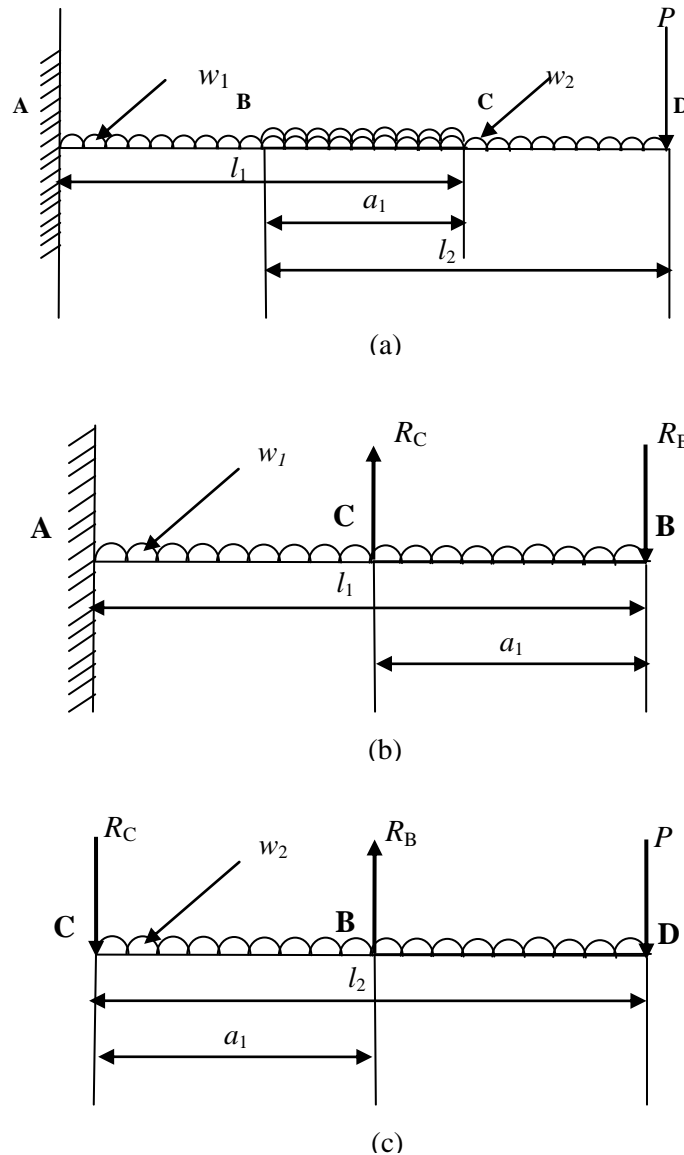


**Figure C.1: Tip Reaction Model – Beam assembly and reactions on individual beams**

The experimental telescopic cantilever beam assembly consists of two hollow rectangular steel sections, each 1.55 mm thick, with outer dimensions: 60mm x 40mm x 1300mm and 50mm x 30mm x 1300mm. In the first scenario a load of 30.55 N is applied at the end of the beam assembly. Beams CD and AB have an overlap of 400 mm. The second moment of area about the neutral axis for the cross-section of beams AB and CD are 167400 mm<sup>4</sup> and 90416.67 mm<sup>4</sup> respectively. Their linear densities (distributed self-weights) are 0.0235 N/mm

and 0.0187 N/mm respectively. Referring to Figure C.1 (a), the tip load is  $P = 30.55$  N and the distributed self-weights are once again  $w_1 = 0.0235$  N/mm and  $w_2 = 0.0187$  N/mm. Consider Figure C.1 and the Equation Set (A.1) derived in [13] for the following calculations and taking moments about C gives

$$R_B = \frac{P + \frac{w_2 l_2}{2}}{\alpha_1} = \frac{30.55 + \frac{0.0187 \times 1300}{2}}{0.3076} = 138.83 \text{ N}$$

$$R_C = \left[ \frac{P(1 - \alpha_1) + w_2 l_2 \frac{(1 - 2\alpha_1)}{2}}{\alpha_1} \right] = \left[ \frac{30.55(1 - 0.3076) + 0.0187 \times 1300 \times \left( \frac{(1 - 2 \times 0.3076)}{2} \right)}{0.3076} \right]$$

$$R_C = 83.97 \text{ N}$$

Thus when  $l_1 = 1300$ mm,  $l_2 = 1300$ mm and  $\alpha_1 = 0.3076$  the reactions are

$$R_B = 138.83 \text{ N}$$

$$R_C = 83.97 \text{ N}$$

Reaction R at A

$$R_A = 30.55 + 0.0235 \times 1300 + 0.0187 \times 1300 = 85.41 \text{ N}$$

Moment at A

$$M = 30.55 \times 2200 + 0.0187 \times 1550 \times 1300 + 0.0235 \times 1300 \times 650 = 124748 \text{ N mm}$$

## C.2 Shear force and bending moment diagram for beam ACB

$$R_B = 138.83 \text{ N} \quad w_1 = 0.0235 \text{ N/mm}$$

$$R_C = 83.97 \text{ N} \quad w_2 = 0.0187 \text{ N/mm}$$

### Length AC

Referring to Figure D.1 (b):

Shear force is  $= 85.41 - 0.0235 \times x$  where  $x$  is the distance from A.

$$\text{Bending moment} = -124748 + (85.41 \times x - 0.0235 \times x \times \frac{x}{2})$$

Therefore Shear force at  $\begin{cases} A & 85.41 \text{ N} \\ C & 64.26 \text{ N} \end{cases}$

Bending moment at  $\begin{cases} A & -124748 \text{ N mm} \\ C & -57396.5 \text{ N mm} \end{cases}$

**Length CB**

Referring to Figure D.1 (b):

Shear force is  $= 85.41 - 0.0235 \times x + 83.97$  where  $x$  is the distance from A.

Bending moment  $= -124748 + (85.41 \times x - 0.0235 \times x \times \frac{x}{2} + 83.97 \times (x - 900))$

Therefore Shear force at  $\begin{cases} C & 148.23 \text{ N} \\ B & 138.83 \text{ N} \end{cases}$

Bending moment at  $\begin{cases} C & -57396.5 \text{ N mm} \\ B & 0 \end{cases}$

**C.3 Shear force and bending moment diagram for beam CBD**

**Length CB**

Referring to Figure C.1 (c):

Shear force is  $= -83.97 - 0.0187 \times (x - 900)$  where  $x$  is the distance from A.

Bending moment  $= -83.97 \times (x - 900) - 0.0187 \times (x - 900) \times \frac{(x - 900)}{2}$

Therefore Shear force at  $\begin{cases} C & -83.97 \text{ N} \\ B & -91.45 \text{ N} \end{cases}$

Bending moment at  $\begin{cases} C & 0 \\ B & -35085.15 \text{ N mm} \end{cases}$

**Length BD**

Referring to Figure C.1 (c):

Shear force is  $= -83.97 - 0.0187 \times (x - 900) + 138.83$  where  $x$  is the distance from A.

Bending moment

$= -83.97 \times (x - 900) - 0.0187 \times (x - 900) \times \frac{(x - 900)}{2} + 138.83 \times (x - 1300)$

Therefore Shear force at  $\begin{cases} B & 47.38 \text{ N} \\ D & 30.55 \text{ N} \end{cases}$

$$\text{Bending moment at } \begin{cases} B & -35085.16 \text{ N mm} \\ D & 0 \end{cases}$$

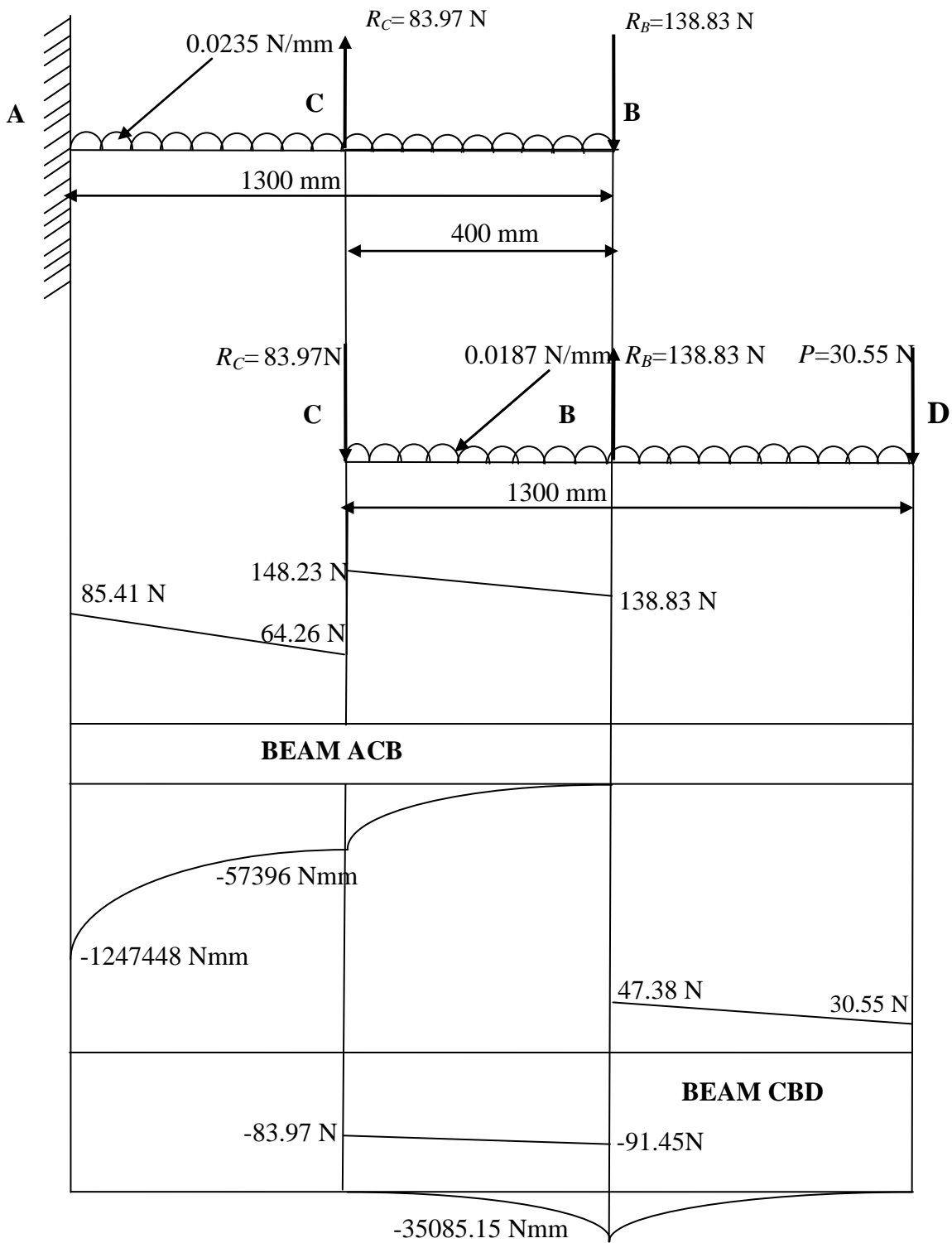
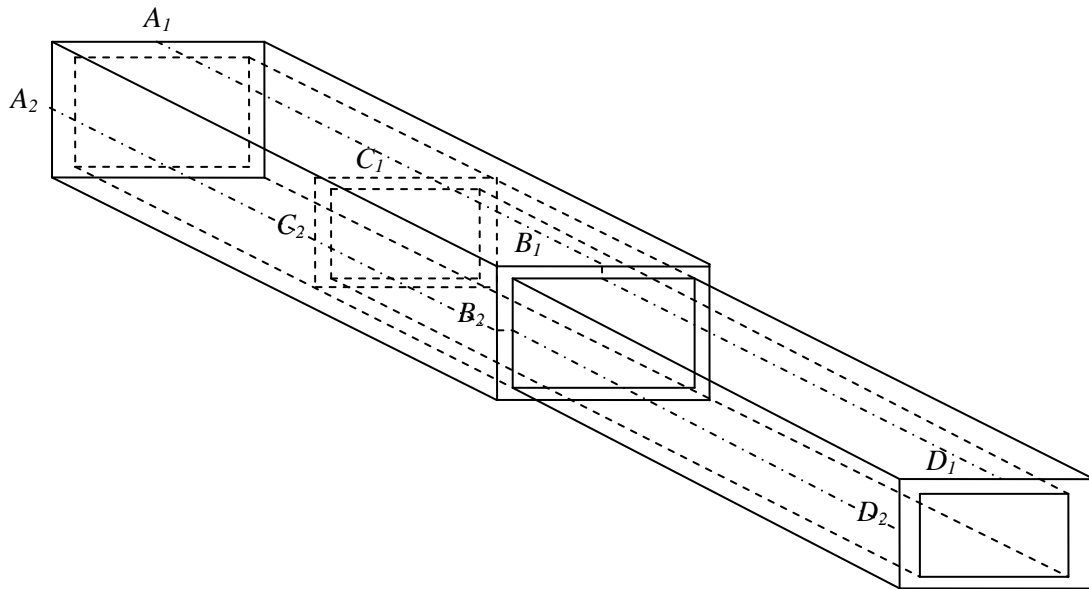


Figure C.2: Shear force and bending moment diagrams for the individual sections

### C.4 Calculation of bending and shear stresses for beam ACB

The bending stress will be maximum along the vertical plane of symmetry at the top of the beam assembly marked as shown in Figure C.3. The net shear stress distribution will vary across the cross section as detailed in § 5.2.1 and depicted in Figure 5.4 (b).



**Figure C.3: A Telescopic beam assembly with two sections and the vertical and horizontal planes of symmetry shown**

#### *Length AC*

Consider, firstly, the uniform section within the length portion AC as shown in Figure C.3. The bending moment at the section at a distance  $x$  from A

$$M = -124748 + (85.41 \times x - 0.0235 \times x \times \frac{x}{2}) \text{ N mm}$$

Taking sagging moments as positive, the maximum bending stress from Equation (6.3) as

$$\sigma_{Max} = \frac{-M \times y_{max}}{I} = \frac{-M \times 30}{167400} \text{ MPa}$$

The shear force in AC is given by

$$S = 85.41 - 0.0235 \times x \text{ N}$$

The maximum shear stress magnitude in sides CD and AB follows from Equation (6.5) as follows

$$(\tau_{CD})_{\max} = \frac{3F_y \left(1 + 2\frac{b}{d}\right)}{4td \left(1 + 3\frac{b}{d}\right)} \text{ MPa}$$

and the maximum shear stress magnitude in sides BC and DA follows from Equation (6.6) as follows

$$(\tau_{BC})_{\max} = \frac{3F_y b}{2td^2 \left(1 + 3\frac{b}{d}\right)} \text{ MPa}$$

where  $b=40$  mm,  $d=60$  mm and  $t=1.55$  mm for the section length AC within beam ACB with  $F_y=30.55$  N.

### **Length CB**

Considering the uniform section within the length portion CB as shown in Figure C.3 the bending moment at the section at a distance  $x$  from A

$$M = -124748 + (85.41 \times x - 0.0235 \times x \times \frac{x}{2} + 83.97 \times (x - 900)) \text{ N mm}$$

Taking sagging moments as positive, the maximum bending stress follows from Equation (6.3)

$$\sigma_{Max} = \frac{-M \times y_{\max}}{I} = \frac{-M \times 30}{167400} \text{ MPa}$$

The shear force in AC is given by

$$S = 85.41 - 0.0235 \times x + 83.97 \text{ N}$$

Once again the maximum shear stress magnitude in sides CD and AB follows from Equation (6.5) to give

$$(\tau_{CD})_{\max} = \frac{3F_y \left(1 + 2\frac{b}{d}\right)}{4td \left(1 + 3\frac{b}{d}\right)} \text{ MPa}$$

and the maximum shear stress magnitude in sides BC and DA follows from Equation (6.6) as

$$(\tau_{BC})_{\max} = \frac{3F_y b}{2td^2 \left(1 + 3\frac{b}{d}\right)} \text{ MPa}$$

where  $b=40$  mm,  $d=60$  mm and  $t=1.55$  mm for the section length CB within beam ACB with  $F_y=30.55$  N.

## C.5 Calculation of Bending and Shear Stresses for Beam CBD

### *Length CB*

Taking into consideration the uniform section within the length portion CB as shown in Figure C.3 the bending moment at the section at a distance  $x$  from A

$$M = -83.97 \times (x - 900) - 0.0187 \times (x - 900) \times \frac{(x - 900)}{2} \text{ N mm}$$

Taking sagging moments as positive, the maximum bending stress from Equation (6.3) as

$$\sigma_{Max} = \frac{-M \times y_{\max}}{I} = \frac{-M \times 25}{90416.67} \text{ MPa}$$

The shear force in AC is given by

$$S = -83.97 - 0.0187 \times (x - 900) \text{ N}$$

The maximum shear stress magnitude in sides CD and AB follows from Equation (6.5) as follows

$$(\tau_{CD})_{\max} = \frac{3F_y \left(1 + 2\frac{b}{d}\right)}{4td \left(1 + 3\frac{b}{d}\right)} \text{ MPa}$$

and the maximum shear stress magnitude in sides BC and DA follows from Equation (6.6) as follows

$$(\tau_{BC})_{\max} = \frac{3F_y b}{2td^2 \left(1 + 3\frac{b}{d}\right)} \text{ MPa}$$

where  $b=30$  mm,  $d=50$  mm and  $t=1.55$  mm for the section length CB within beam ACB with  $F_y=30.55$  N.

### **Length BD**

Considering the uniform section within the length portion BD as shown in Figure C.3 the bending moment at the section at a distance  $x$  from A

$$M = -83.97 \times (x - 900) - 0.0187 \times (x - 900) \times \frac{(x - 900)}{2} + 138.83 \times (x - 1300) \text{ N mm}$$

Taking sagging moments as positive, the maximum bending stress follows from Equation (6.3)

$$\sigma_{\max} = \frac{-M \times y_{\max}}{I} = \frac{-M \times 25}{90416.67} \text{ MPa}$$

The shear force in AC is given by

$$S = -83.97 - 0.0187 \times (x - 900) + 138.83 \text{ N}$$

Once again the maximum shear stress magnitude in sides CD and AB follows from Equation (6.5) to give

$$(\tau_{CD})_{\max} = \frac{3F_y \left(1 + 2\frac{b}{d}\right)}{4td \left(1 + 3\frac{b}{d}\right)} \text{ MPa}$$

and the maximum shear stress magnitude in sides BC and DA follows from Equation (6.6) as

$$(\tau_{BC})_{\max} = \frac{3F_y b}{2td^2 \left(1 + 3\frac{b}{d}\right)} \text{ MPa}$$

where  $b=30$  mm,  $d=50$  mm and  $t=1.55$  mm for the section length BD within beam ACB with  $F_y=30.55$  N.

The bending and shear stresses induced by inline loading for a tip load of 30.55 N or  $wL/P$  ratio of 1 are shown for both beams ACB and CBD in Figures C.4 and C.5 that follow.

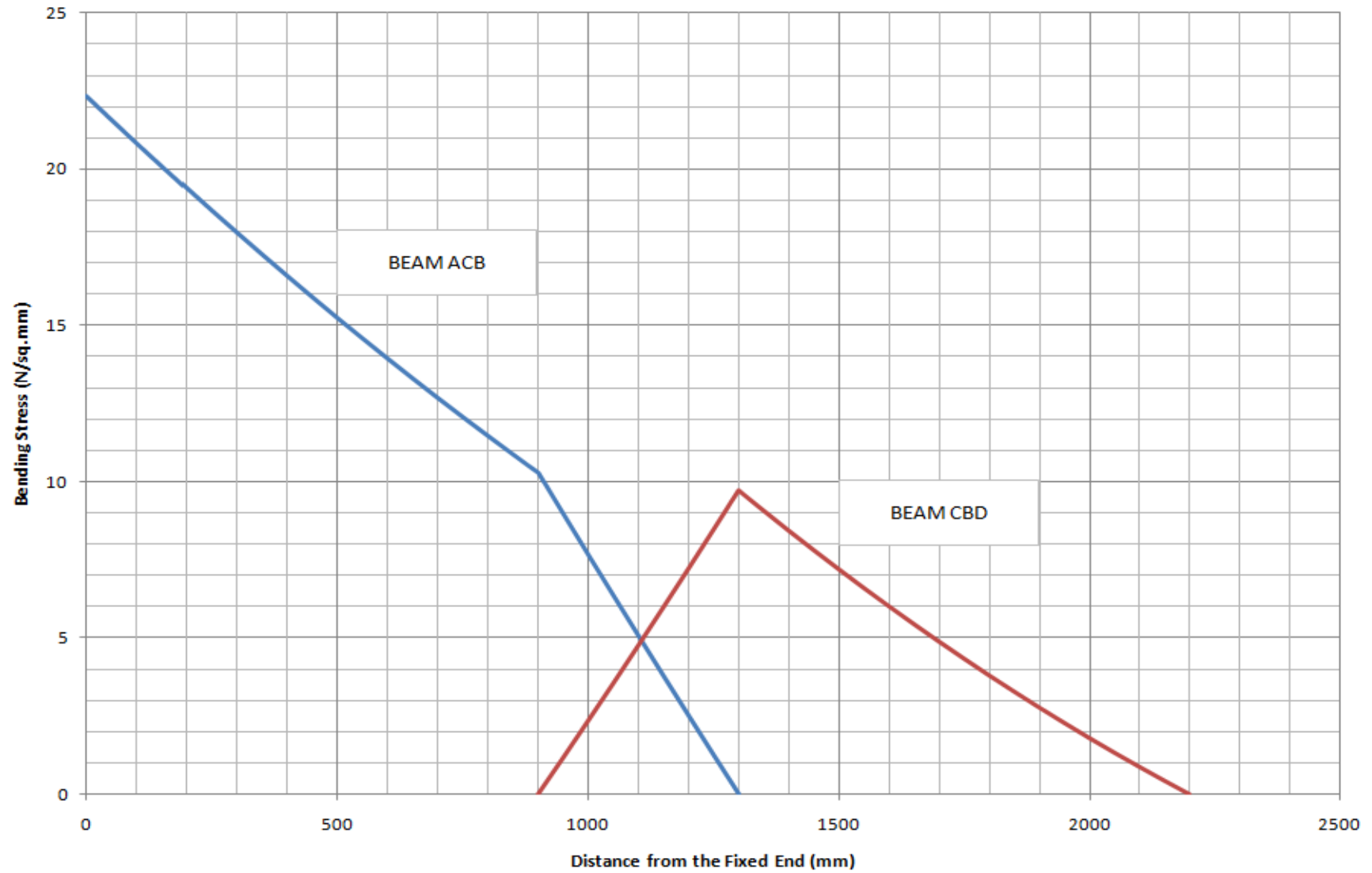


**Figure C.4: Telescopic beam bending stresses induced by inline loading, from tip reaction analysis.**

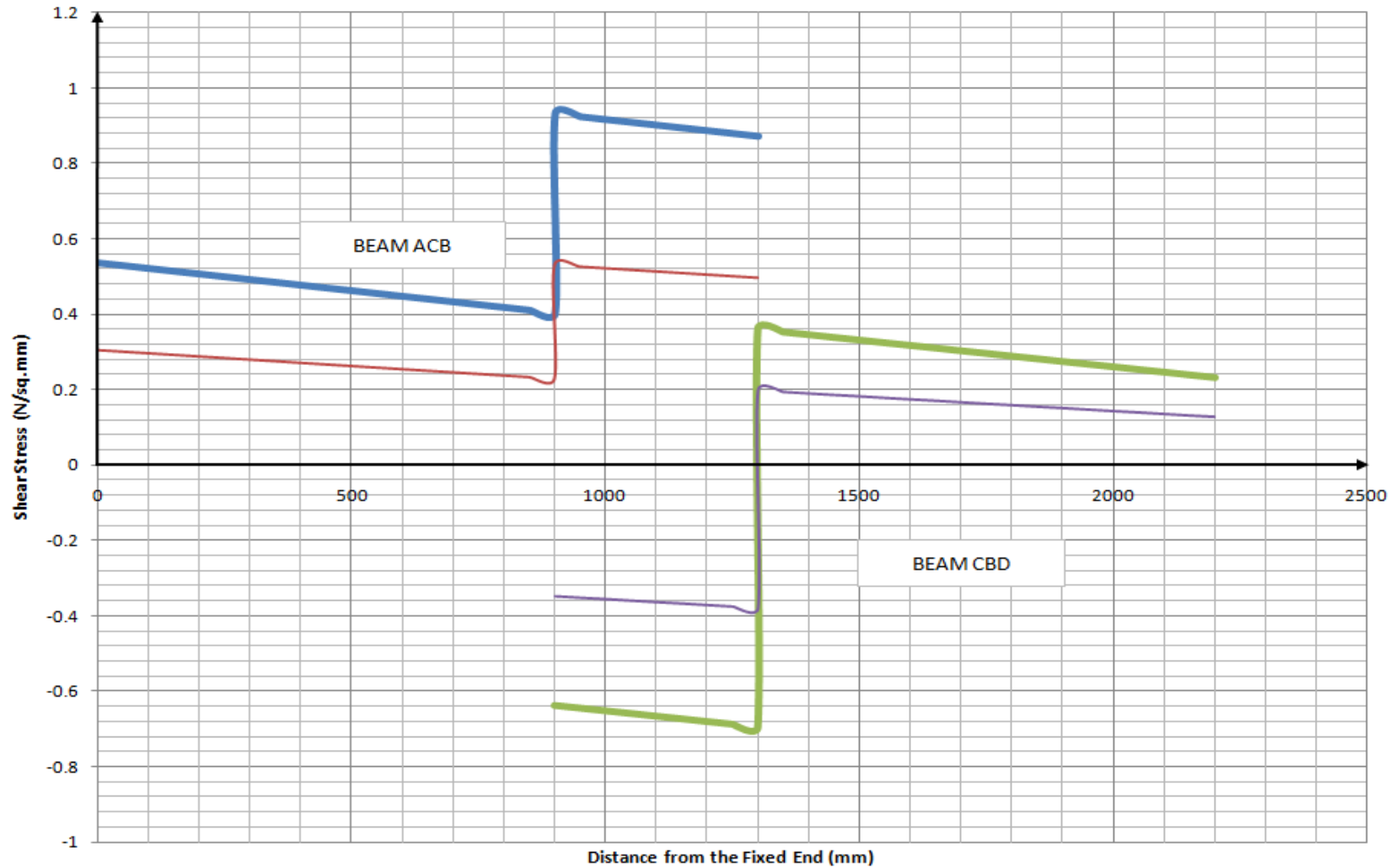


**Figure C.5: Telescopic beam shear stresses induced by inline loading, from tip reaction analysis**  
 ( Key: — Side BC/DA; — Side CD/AB; refer to Figure 6.3 (b))

## **APPENDIX D**

**APPENDIX D - PART 2 – OFFSET LOADING ANALYSIS OF INDUCED STRESS IN  
THE TWO SECTION TELESCOPIC ASSEMBLY**

**D.1 Calculation of Tip Reactions**

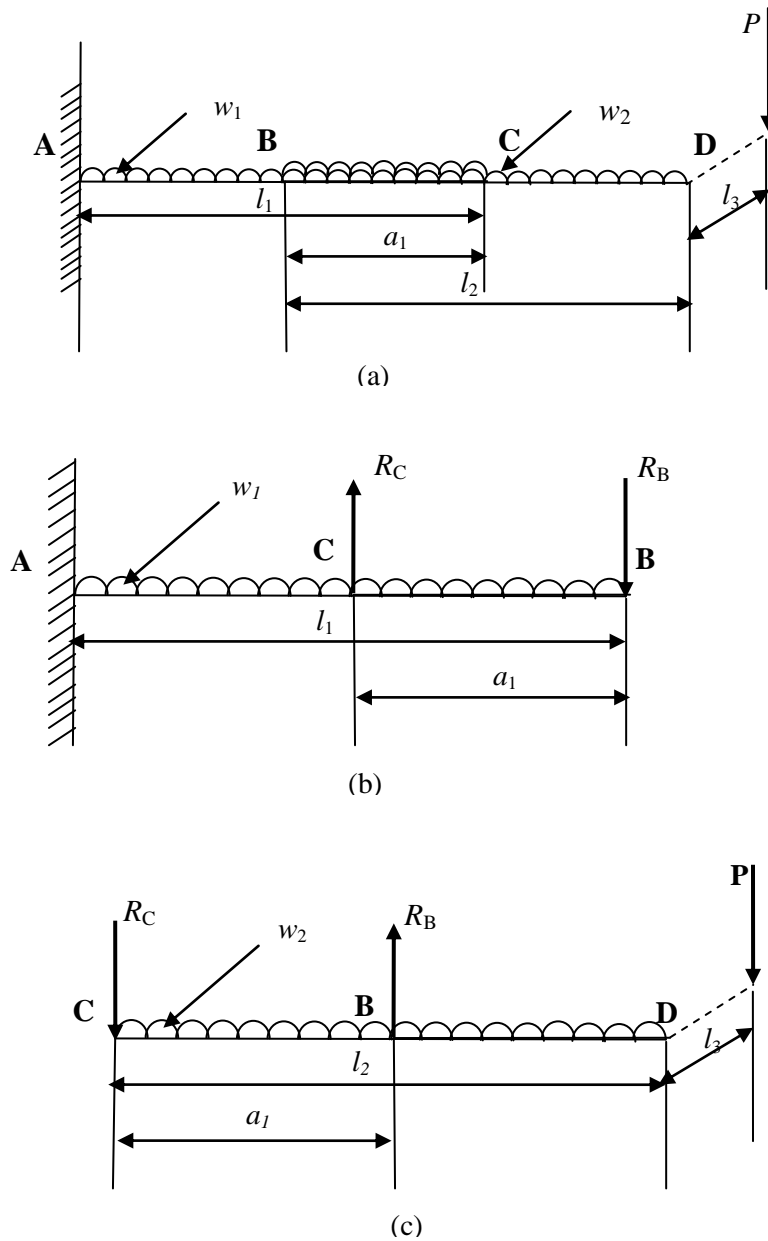


**Figure D.1: Tip Reaction Model – Beam Assembly and Reactions on Individual Beams**

The experimental telescopic cantilever beam assembly consists of two hollow rectangular steel sections, each 1.55 mm thick, with outer dimensions: 60 mm x 40 mm x 1300 mm and 50 mm x 30 mm x 1300 mm. As in Appendix D – Part 1, a load of 30.55 N is applied at the

end of the beam assembly, but offset from the neutral axis of the assembly by 600 mm. In other words the load of 30.55 N is applied as a torque through a load arm of 600 mm length. Beams CD and AB have an overlap of 400 mm. The second moment of area about the neutral axis for the cross-section of beams AB and CD are  $167400 \text{ mm}^4$  and  $90416.67 \text{ mm}^4$  respectively. Their linear densities (distributed self-weights) are 0.0235 N/mm and 0.0187 N/mm respectively.

Referring to Figure D.1 (a), the tip load is  $P = 30.55 \text{ N}$  which in turn acts through a distance of 600mm and the distributed self-weights are once again  $w_1 = 0.0235 \text{ N/mm}$  and  $w_2 = 0.0187 \text{ N/mm}$ . Consider Figure D.1 and the Equation Set (A.1) derived in A.2 for the following calculations and taking moments about C gives

$$R_B = \frac{P + \frac{w_2 l_2}{2}}{\alpha_1} = \frac{30.55 + \frac{0.0187 \times 1300}{2}}{0.3076} = 138.83 \text{ N}$$

$$R_C = \left[ \frac{P(1 - \alpha_1) + w_2 l_2 \frac{(1 - 2\alpha_1)}{2}}{\alpha_1} \right] = \left[ \frac{30.55(1 - 0.3076) + 0.0187 \times 1300 \times \left( \frac{(1 - 2 \times 0.3076)}{2} \right)}{0.3076} \right]$$

$$R_C = 83.97 \text{ N}$$

Thus when  $l_1 = 1300$ ,  $l_2 = 1300$ , and  $\alpha_1 = 0.3076$  the reactions are

$$R_B = 138.83 \text{ N}$$

$$R_C = 83.97 \text{ N}$$

Reaction R at A

$$R_A = 30.55 + 0.0235 \times 1300 + 0.0187 \times 1300 = 85.41 \text{ N}$$

Bending Moment at A

$$M = 30.55 \times 2200 + 0.0187 \times 1550 \times 1300 + 0.0235 \times 1300 \times 650 = 124748 \text{ Nmm}$$

Twisting Moment induced at A

$$M = 30.55 \times 600 = 18330 \text{ Nmm}$$

## D.2 Shear Force, Bending Moment and Torque Diagram for Beam ACB

$$R_B = 138.83 \text{ N} \quad w_1 = 0.0235 \text{ l N/mm}$$

$$R_C = 83.97 \text{ N} \quad w_2 = 0.0187 \text{ l N/mm}$$

### *Length AC*

Referring to Figure D.1 (b):

Shear force is  $= 85.41 - 0.0235 \times x$  where  $x$  is the distance from A.

$$\text{Bending moment} = -124748 + (85.41 \times x - 0.0235 \times x \times \frac{x}{2})$$

$$\text{Therefore Shear force at } \begin{cases} A & 85.41 \text{ N} \\ C & 64.26 \text{ N} \end{cases}$$

$$\text{Bending moment at } \begin{cases} A & -124748 \text{ Nmm} \\ C & -57396.5 \text{ Nmm} \end{cases}$$

$$\text{Twisting moment at } \begin{cases} A & 18330 \text{ Nmm} \\ C & 18330 \text{ Nmm} \end{cases}$$

### *Length CB*

Referring to Figure D.1 (b):

Shear force is  $= 85.41 - 0.0235 \times x + 83.97$  where  $x$  is the distance from A.

$$\text{Bending moment} = -124748 + (85.41 \times x - 0.0235 \times x \times \frac{x}{2} + 83.97 \times (x - 900))$$

$$\text{Therefore Shear force at } \begin{cases} C & 148.23 \text{ N} \\ B & 138.83 \text{ N} \end{cases}$$

$$\text{Bending moment at } \begin{cases} C & -57396.5 \text{ Nmm} \\ B & 0 \end{cases}$$

$$\text{Twisting moment at } \begin{cases} C & 18330 \text{ Nmm} \\ B & 18330 \text{ Nmm} \end{cases}$$

### D.3 Shear Force, Bending Moment and Torque Diagram for Beam CBD

#### *Length CB*

Referring to Figure D.1 (c):

Shear force is  $= -83.97 - 0.0187 \times (x - 900)$  where  $x$  is the distance from A.

$$\text{Bending moment} = -83.97 \times (x - 900) - 0.0187 \times (x - 900) \times \frac{(x - 900)}{2}$$

$$\text{Therefore Shear force at } \begin{cases} C & -83.97 \text{ N} \\ B & -91.45 \text{ N} \end{cases}$$

$$\text{Bending moment at } \begin{cases} C & 0 \\ B & -35085.15 \text{ Nmm} \end{cases}$$

$$\text{Twisting moment at } \begin{cases} C & 18330 \text{ Nmm} \\ B & 18330 \text{ Nmm} \end{cases}$$

#### *Length BD*

Referring to Figure D.1 (c):

Shear force is  $= -83.97 - 0.0187 \times (x - 900) + 138.83$  where  $x$  is the distance from A.

Bending moment

$$= -83.97 \times (x - 900) - 0.0187 \times (x - 900) \times \frac{(x - 900)}{2} + 138.83 \times (x - 1300)$$

$$\text{Therefore Shear force at } \begin{cases} B & 47.38 \text{ N} \\ D & 30.55 \text{ N} \end{cases}$$

$$\text{Bending moment at } \begin{cases} B & -35085.16 \text{ Nmm} \\ D & 0 \end{cases}$$

$$\text{Twisting moment at } \begin{cases} B & 18330 \text{ Nmm} \\ D & 18330 \text{ Nmm} \end{cases}$$

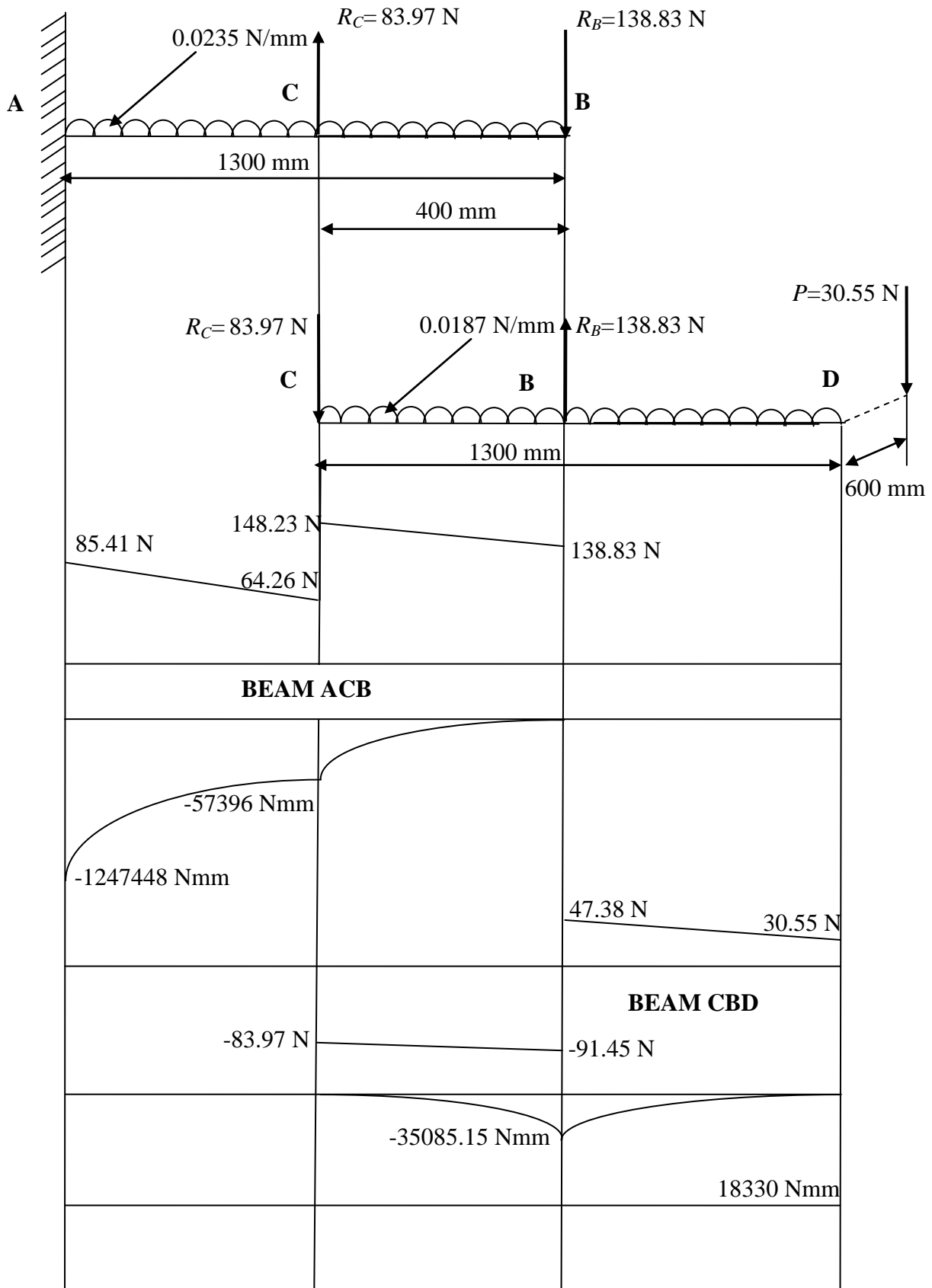
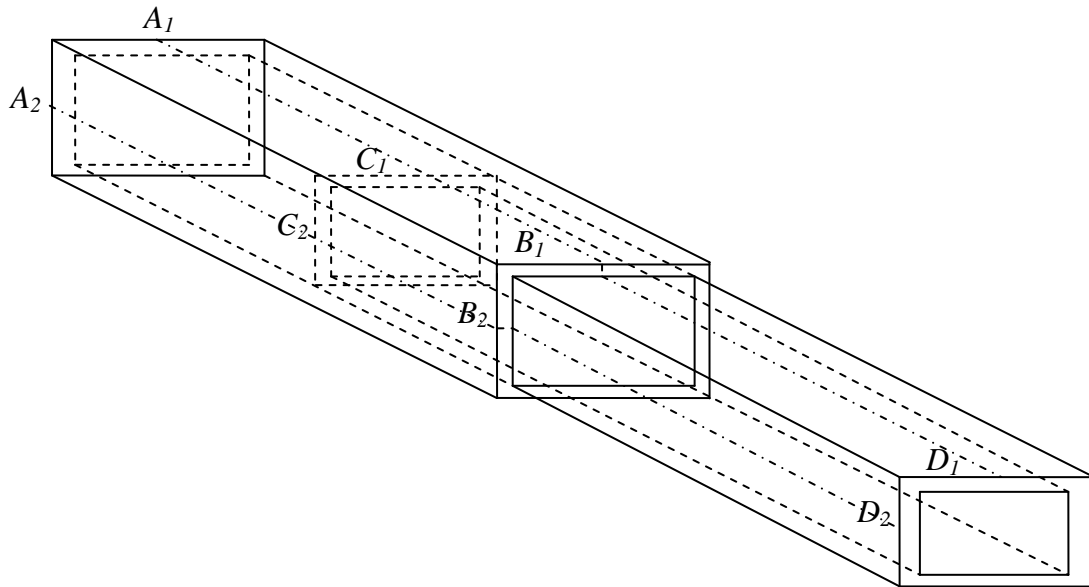


Figure D.2: Shear force, bending moment and torque diagrams for the individual sections

#### D.4 Calculation of Bending and Shear Stresses for Beam ACB

The bending stress will be maximum along the vertical plane of symmetry at the top of the beam assembly marked as shown in Figure D.3. The net shear stress distribution will vary across the cross section as detailed in § 5.2.1 and depicted in Figure 5.4 (b).



**Figure D.3: A telescopic beam assembly with two sections and the vertical and horizontal planes of symmetry shown**

##### *Length AC*

Consider, firstly, the uniform section within the length portion AC as shown in Figure D.3. The bending moment at the section at a distance  $x$  from A

$$M = -124748 + (85.41 \times x - 0.0235 \times x \times \frac{x}{2}) \text{ N/mm}$$

Taking sagging moments as positive, the maximum bending stress from Equation (6.3) is

$$\sigma_{Max} = \frac{-M \times y_{max}}{I} = \frac{-M \times 30}{167400} \text{ MPa}$$

The shear force in AC is given by

$$S = 85.41 - 0.0235 \times x \text{ N}$$

The maximum shear stress magnitude in sides CD and AB follows from Equation (6.5) as follows

$$(\tau_{CD})_{\max} = \frac{3F_y \left(1 + 2\frac{b}{d}\right)}{4td \left(1 + 3\frac{b}{d}\right)} \text{ MPa}$$

and the maximum shear stress magnitude in sides BC and DA follows from Equation (6.6) as follows

$$(\tau_{BC})_{\max} = \frac{3F_y b}{2td^2 \left(1 + 3\frac{b}{d}\right)} \text{ MPa}$$

where  $b=40$  mm,  $d=60$  mm and  $t=1.55$  mm for the section length AC within beam ACB with  $F_y=30.55$  N.

### ***Length CB***

Considering the uniform section within the length portion CB as shown in Figure D.3 the bending moment at the section at a distance  $x$  from A

$$M = -124748 + (85.41 \times x - 0.0235 \times x \times \frac{x}{2} + 83.97 \times (x - 900)) \text{ Nmm}$$

Taking sagging moments as positive, the maximum bending stress from Equation (6.3)

$$\sigma_{Max} = \frac{-M \times y_{\max}}{I} = \frac{-M \times 30}{167400} \text{ MPa}$$

The shear force in AC is given by

$$S = 85.41 - 0.0235 \times x + 83.97 \text{ N}$$

Once again the maximum shear stress magnitude in sides CD and AB follows from Equation (6.5) to give

$$(\tau_{CD})_{\max} = \frac{3F_y \left(1 + 2\frac{b}{d}\right)}{4td \left(1 + 3\frac{b}{d}\right)} \text{ MPa}$$

and the maximum shear stress magnitude in sides BC and DA follows from Equation (6.6) as

$$(\tau_{BC})_{\max} = \frac{3F_y b}{2td^2 \left(1 + 3\frac{b}{d}\right)} \text{ MPa}$$

where  $b=40$  mm,  $d=60$  mm and  $t=1.55$  mm for the section length CB within beam ACB with  $F_y=30.55$  N.

## D.5 Calculation of Bending and Shear Stresses for Beam CBD

### *Length CB*

Taking into consideration the uniform section within the length portion CB as shown in Figure D.3 the bending moment at the section at a distance  $x$  from A

$$M = -83.97 \times (x - 900) - 0.0187 \times (x - 900) \times \frac{(x - 900)}{2} \text{ Nmm}$$

Taking sagging moments as positive, the maximum bending stress follows from Equation (6.3)

$$\sigma_{\max} = \frac{-M \times y_{\max}}{I} = \frac{-M \times 25}{90416.67} \text{ MPa}$$

The shear force in AC is given by

$$S = -83.97 - 0.0187 \times (x - 900) \text{ N}$$

The maximum shear stress magnitude in sides CD and AB follows from Equation (6.5) as follows

$$(\tau_{CD})_{\max} = \frac{3F_y \left(1 + 2\frac{b}{d}\right)}{4td \left(1 + 3\frac{b}{d}\right)} \text{ MPa}$$

and the maximum shear stress magnitude in sides BC and DA follows from Equation (6.6) as follows

$$(\tau_{BC})_{\max} = \frac{3F_y b}{2td^2 \left(1 + 3\frac{b}{d}\right)} \text{ MPa}$$

where  $b=30$  mm,  $d=50$  mm and  $t=1.55$  mm for the section length CB within beam CBD with  $F_y=30.55$  N.

### **Length BD**

Considering the uniform section within the length portion BD as shown in Figure D.3 the bending moment at the section at a distance  $x$  from A

$$M = -83.97 \times (x - 900) - 0.0187 \times (x - 900) \times \frac{(x - 900)}{2} + 138.83 \times (x - 1300) \text{ Nmm}$$

Taking sagging moments as positive, the maximum bending stress follows from Equation (6.3)

$$\sigma_{Max} = \frac{-M \times y_{max}}{I} = \frac{-M \times 25}{90416.67} \text{ MPa}$$

The shear force in AC is given by

$$S = -83.97 - 0.0187 \times (x - 900) + 138.83 \text{ N}$$

Once again the maximum shear stress magnitude in sides CD and AB follows from Equation (6.5) to give

$$(\tau_{CD})_{max} = \frac{3F_y \left(1 + 2\frac{b}{d}\right)}{4td \left(1 + 3\frac{b}{d}\right)} \text{ MPa}$$

and the maximum shear stress magnitude in sides BC and DA follows from Equation (6.6) as

$$(\tau_{BC})_{max} = \frac{3F_y b}{2td^2 \left(1 + 3\frac{b}{d}\right)} \text{ MPa}$$

where  $b=30$  mm,  $d=50$  mm and  $t=1.55$  mm for the section length BD within beam CBD with  $F_y=30.55$  N.

The bending and shear stresses induced by offset loading for a tip load of 30.55 N or  $wL/P$  ratio of 1 are shown for both beams ACB and CBD in Figures D.4 and D.5 that follow.

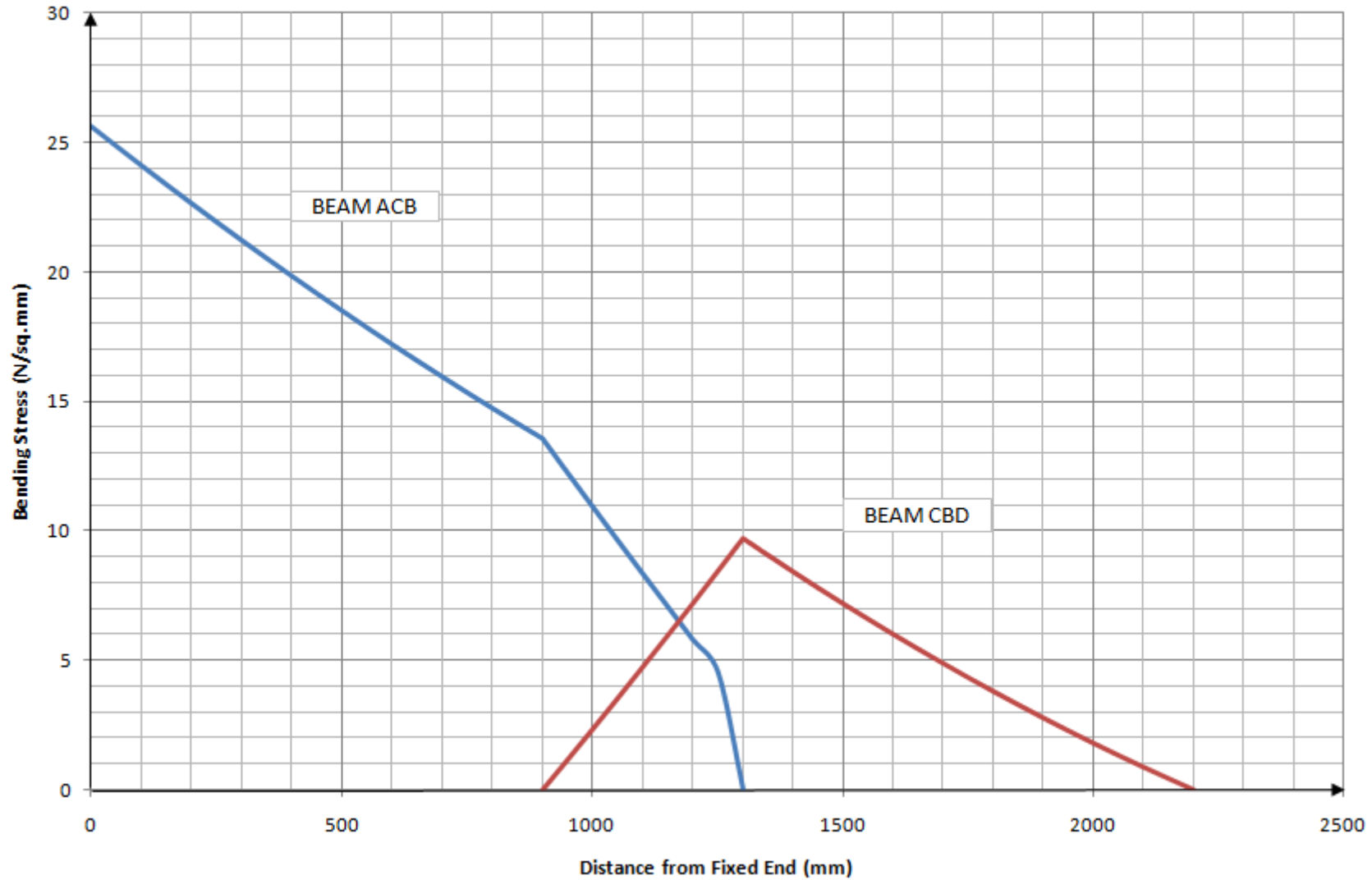


Figure D.4: Telescopic beam bending stresses induced by offset loading, from tip reaction analysis

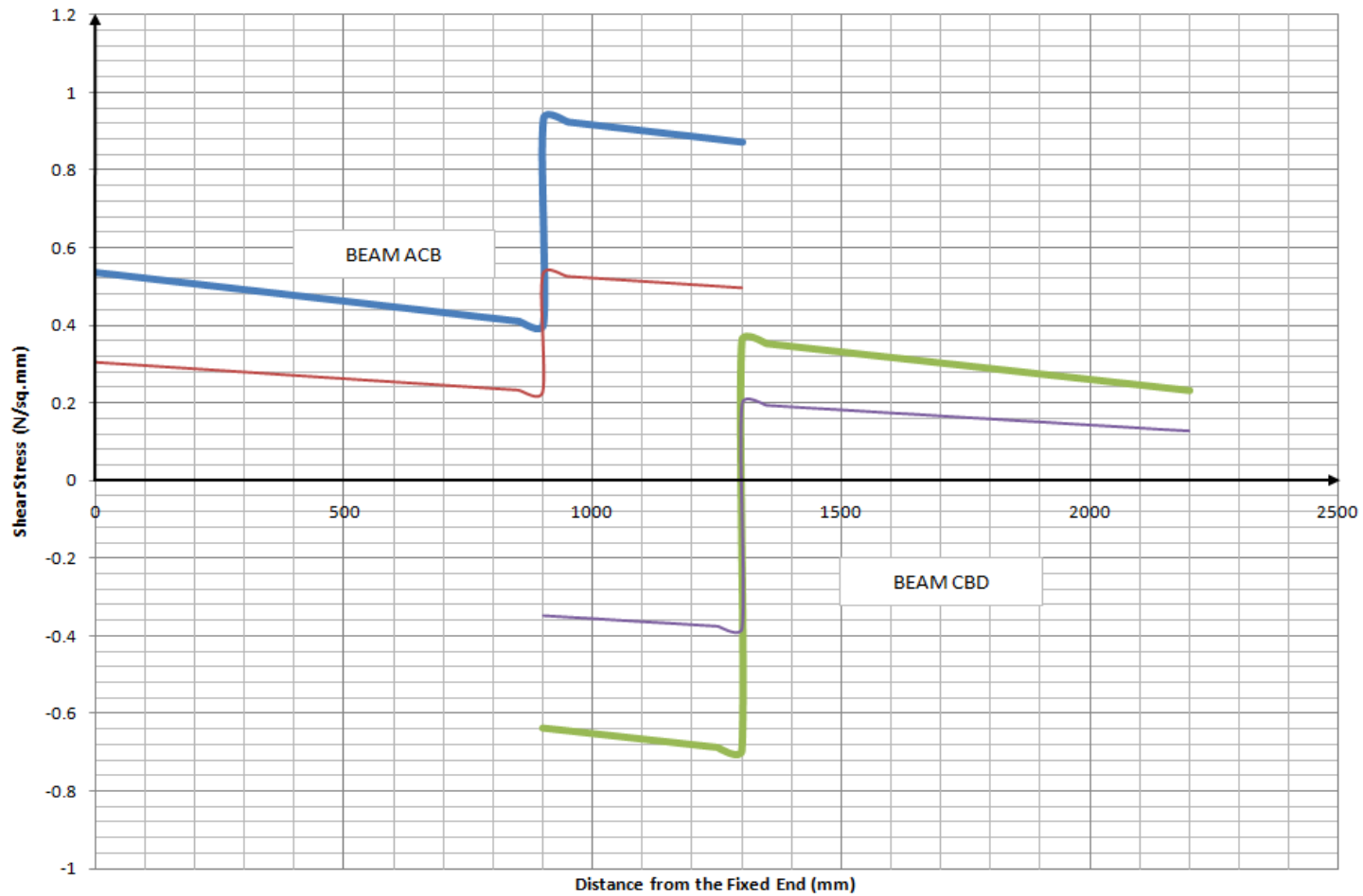


Figure D.5: Telescopic beam shear stresses, induced by offset loading from tip reaction analysis  
 ( Key: — Side BC/DA; — Side CD/AB; refer to Figure 6.3 (b))

## **APPENDIX E**

## **APPENDIX F**

**APPENDIX G**

## APPENDIX G –FINITE ELEMENT ANALYSIS PROCEDURE

### G.1 Part Module

The Part module is used to create, edit, and manage the parts in the current model. ABAQUS/CAE stores each part in the form of an ordered list of features. The parameters that define each feature such as extruded depth, diameter, sweep path, etc; combine to define the geometry of the part.

The functions of the Part module are listed as follows [127]:

1. Create deformable, discrete rigid or analytical rigid parts. The part tools also allows the editing and manipulation of the existing parts defined in the current model.
2. Create those features such as solids, shells, wires, cuts, and rounds that define the geometry of the part.
3. Use the Feature Manipulation toolset to edit, delete, suppress, resume, and regenerate a part's features.
4. Assign the reference point to a rigid part.
5. Use the Sketcher to create, edit, and manage the two-dimensional sketches that form the profile of a part's features. These profiles can be extruded, revolved, or swept to create part geometry; or they can be used directly to form a planar or axisymmetric part.
6. Use the Set toolset, the Partition toolset, and the Datum toolset. These toolsets operate on the part in the current viewport and allow the creation of sets, partitions, and datum geometry, respectively.

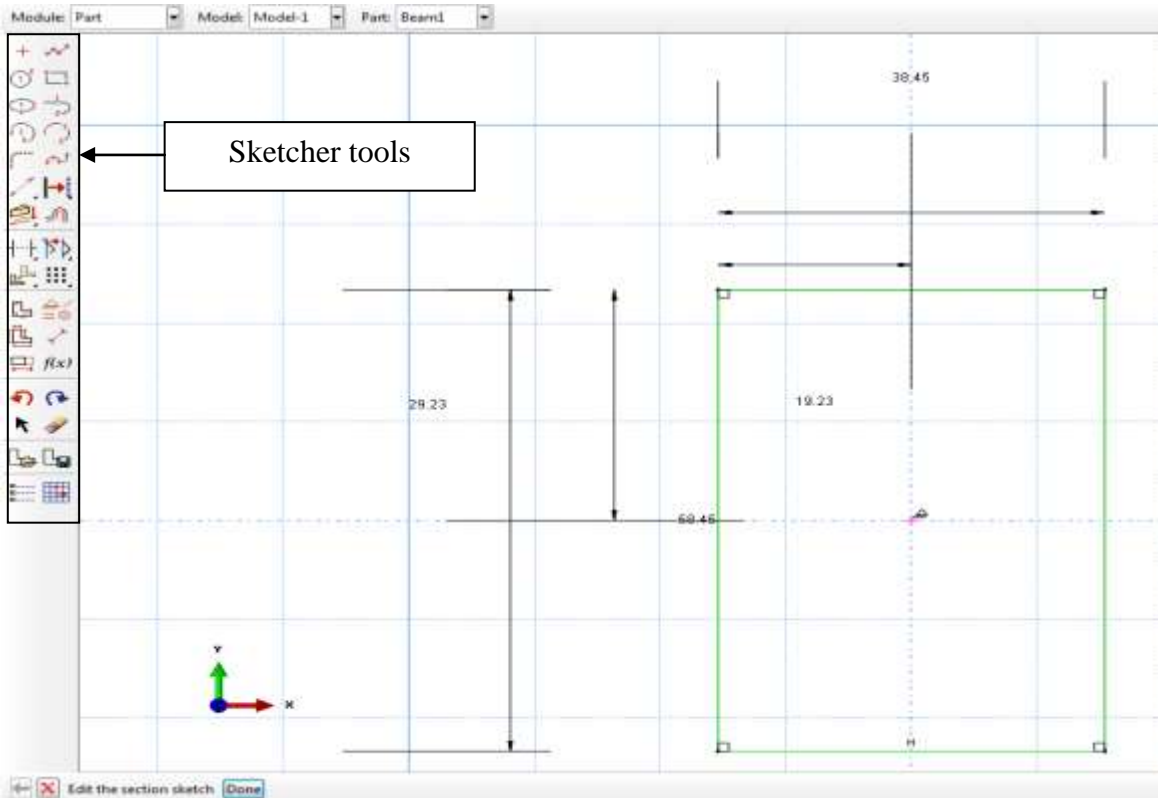


**Figure G.1: Sketcher Window in ABAQUS/CAE**

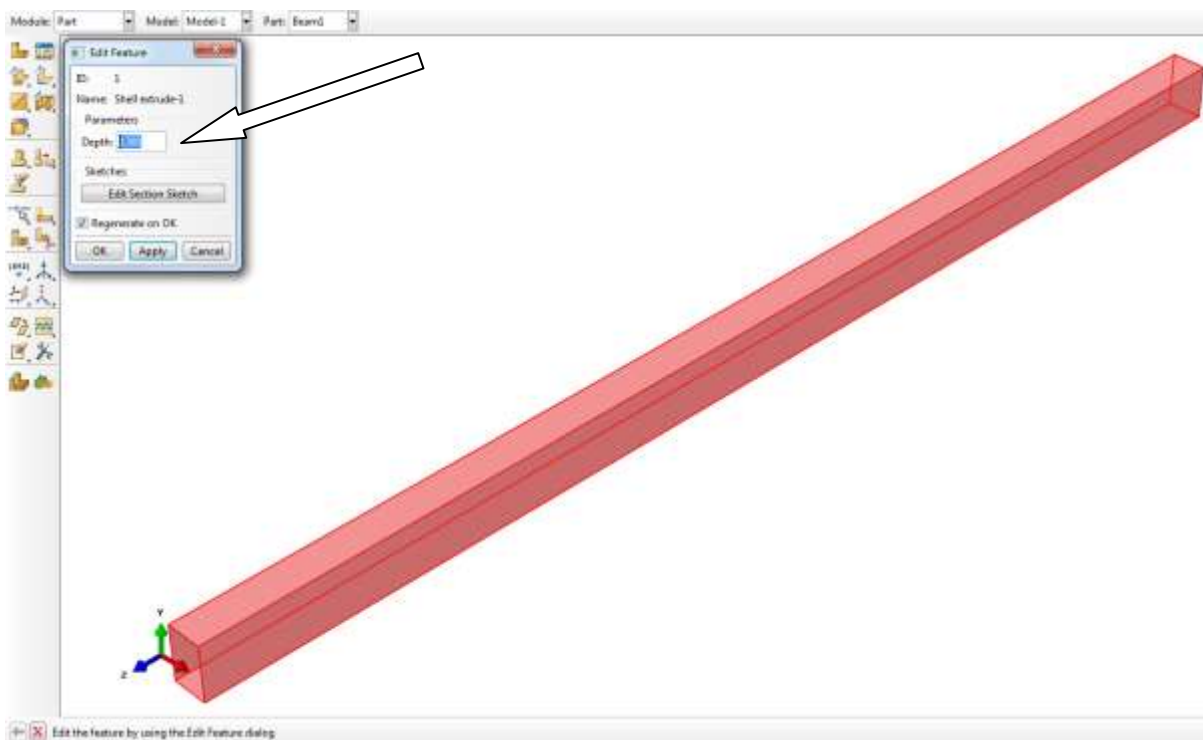


**Figure G.2: Extrusion of the Part Instance sketched in Figure I.1, the arrow indicates the depth to which the part is extruded**

Figures G.1 and G.2 detail the creation of the first or fixed beam instance of the telescopic beam assembly followed by its extrusion, respectively. The two beam instances are created as shell sections having thicknesses of 1.55mm each. This procedure is repeated for the second beam instance as detailed in Figures G.3 (a)-(b). Figures G.3 (c) and (d) illustrate the creation and extrusion of the wear pad instance. The dimensions of the sketched and extruded parts are detailed in Table 7.1.

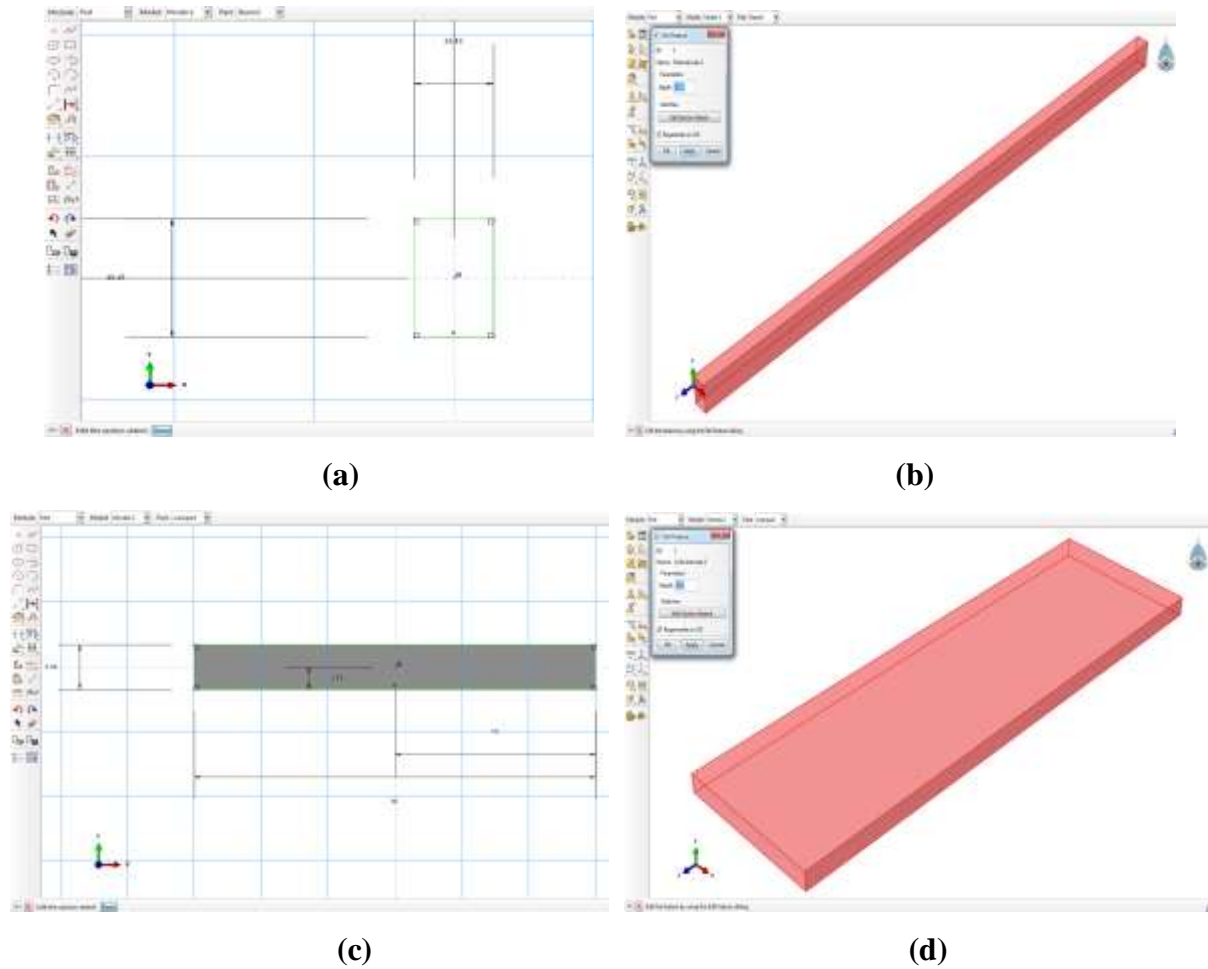


**Figure G.3 (a) Dimensioned Sketch of the second or free end beam instance, (b) Extrusion of the second beam instance (as sketched in G.3 (a)), (c) Dimensioned Sketch of the wear pad instance, (d) Extrusion of the wear pad instance (as sketched in G.3 (c))**

## G.2 Material and Element Properties Definition

In this step the material and element properties are defined and assigned to the parts individually. The two materials that are defined are steel and Tufnell; which in turn are used to represent metal structures and wear pads respectively. These materials are specified by their Density, Elastic Moduli and respective values of Poisson's ratio, which have been specified in Table 7.1.

When a part with shell regions or an axisymmetric part with wire regions is encountered, ABAQUS assigns a direction for the normals of the regions. It is possible to reverse the directions of the normals for these regions. In addition, it is also possible to reverse the directions for the normals of imported parts or selected elements of an orphan mesh. In the figure shown on the next page, the normal is assigned to the given shell component in the Property Module by selecting the following options: '*Assign>Normal*'. As shown in the Figure G.4 the thickness is added onto the inner surface of the shell, brown being the positive direction along which the thickness is added while purple represents the negative or direction in which the thickness is not added.

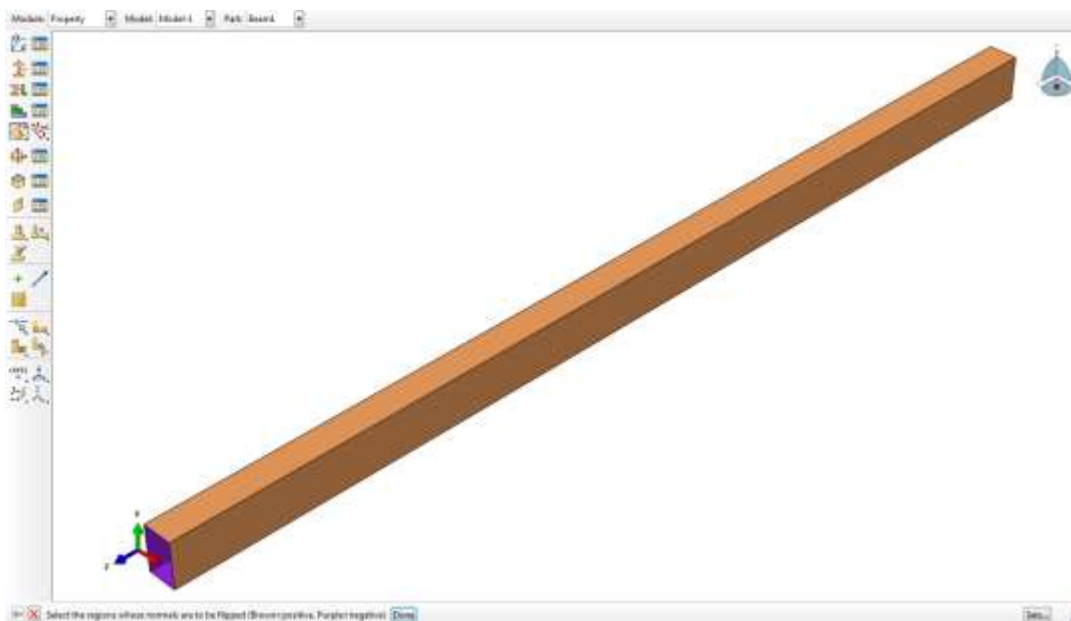


**Figure G.4: Assigning normals to the shell elements (Purple is the negative direction while Brown is the positive direction)**

Also, more importantly in this module, the materials and element section used are defined and assigned to the parts individually. Changing the Module to Property, as shown in the Figures G.5 and G.6, the relevant manager tabs will be pop up on the left hand tool bar. ‘Material Manager>Create’, allows the input of the required material properties.

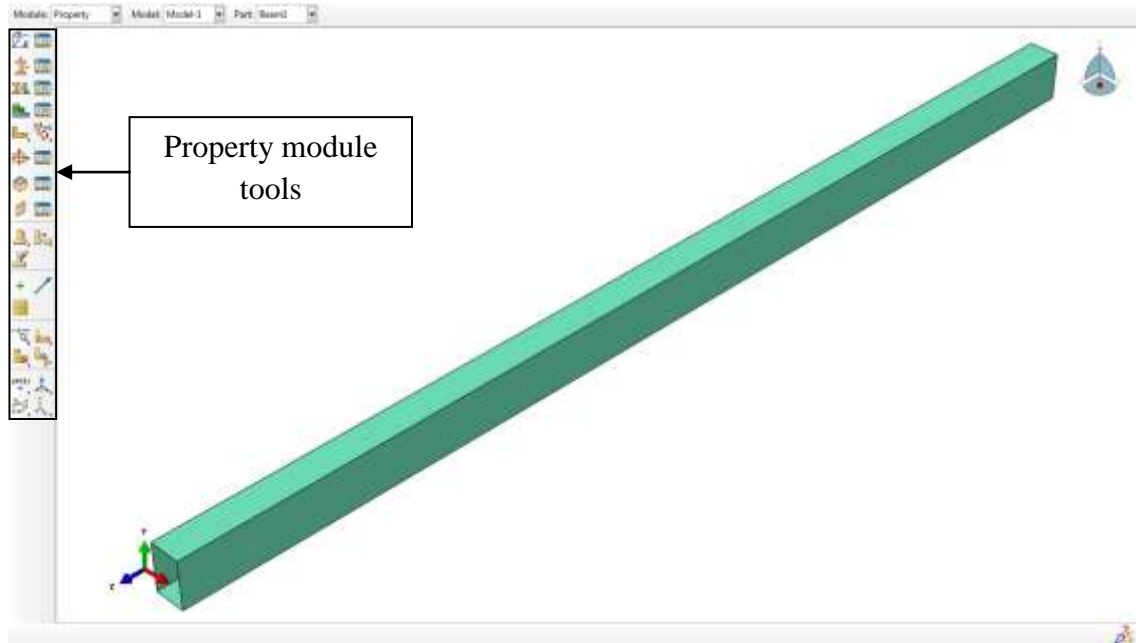


**Figure G.5: Property module tools**

Materials used in this study are Steel and Tufnell to represent the structure and wear pads respectively. Material properties consist of Modulus of elasticity and Poisson’s ratio, which are inputted by selecting the following options within the Property module: ‘Material Manager > Create > Mechanical > Elasticity > Elastic’ and applying relevant figures in the boxes as it is shown in Figures G.6, G.7 and G.8 [128].

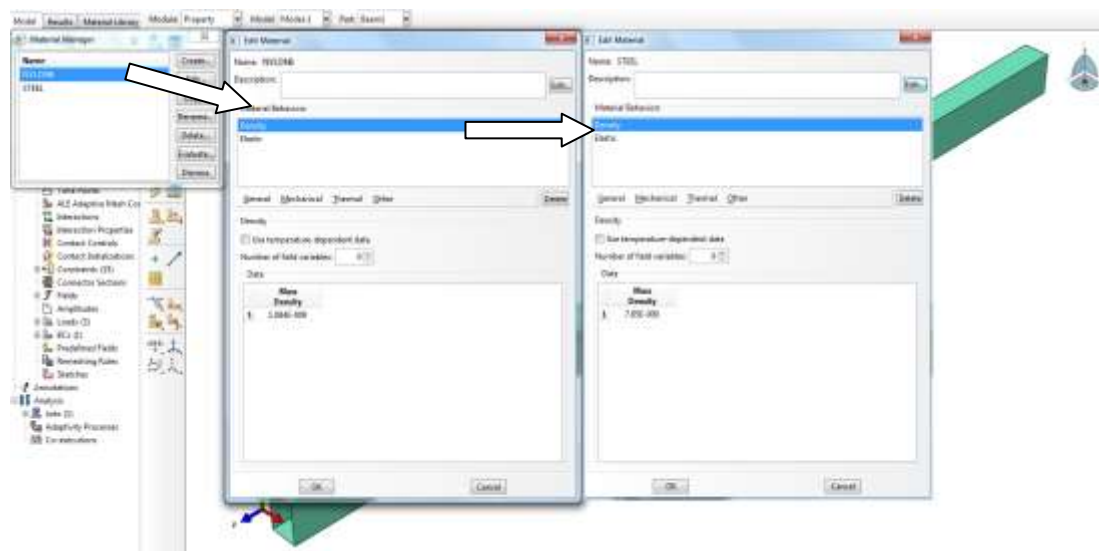


**Figure G.6: Steps to create and define material properties**

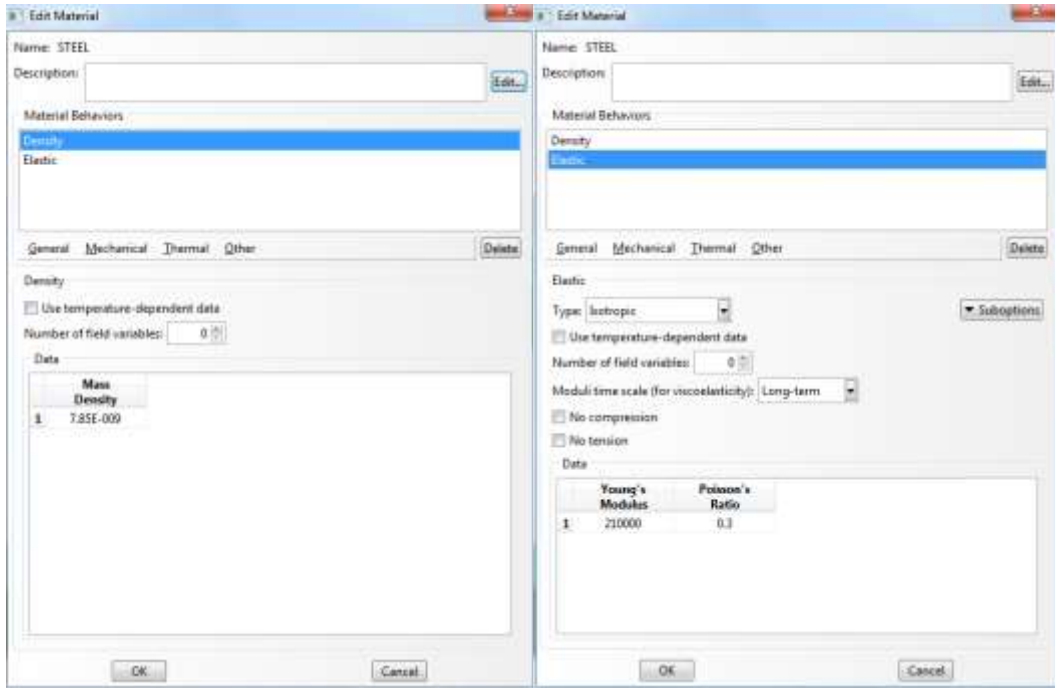


**Figure G.7: Tabs to be filled in order to create material section having properties of Steel**

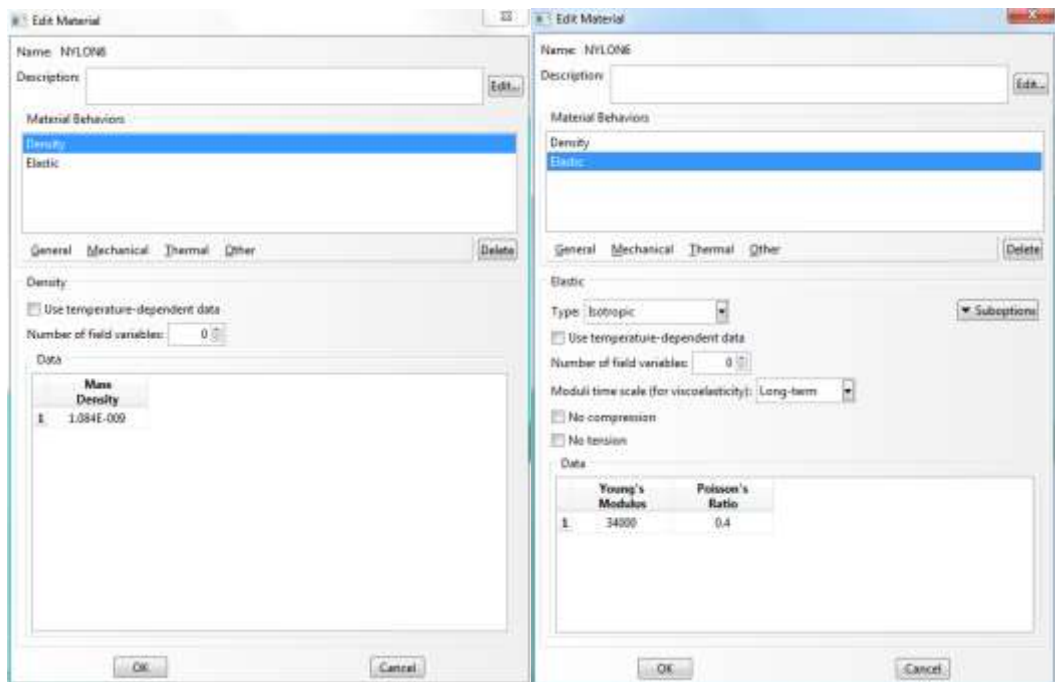


**Figure G.8: Tabs to be filled in order to create material section having properties of Tufnel**

With respect to element assignments, solid-homogeneous element is chosen for all wear pads; while shell-homogeneous element is allocated to the shell sections in the assembly. The details of the material and element sections are elaborated in the Table G.2.

**Table G.2: Materials and Elements defined in the analysis**

S.No	Name	Material	Element	Specification
1.	Tufnell	Tufnell	Solid-Homogeneous	NA
2.	Shell 1.55mm	Steel	Shell-Homogeneous	1.55mm thick

Both the shell and solid sections are defined by selecting the ‘*Section Manager*’ tab and setting the required sections as is shown in Figures G.8 and G.9.

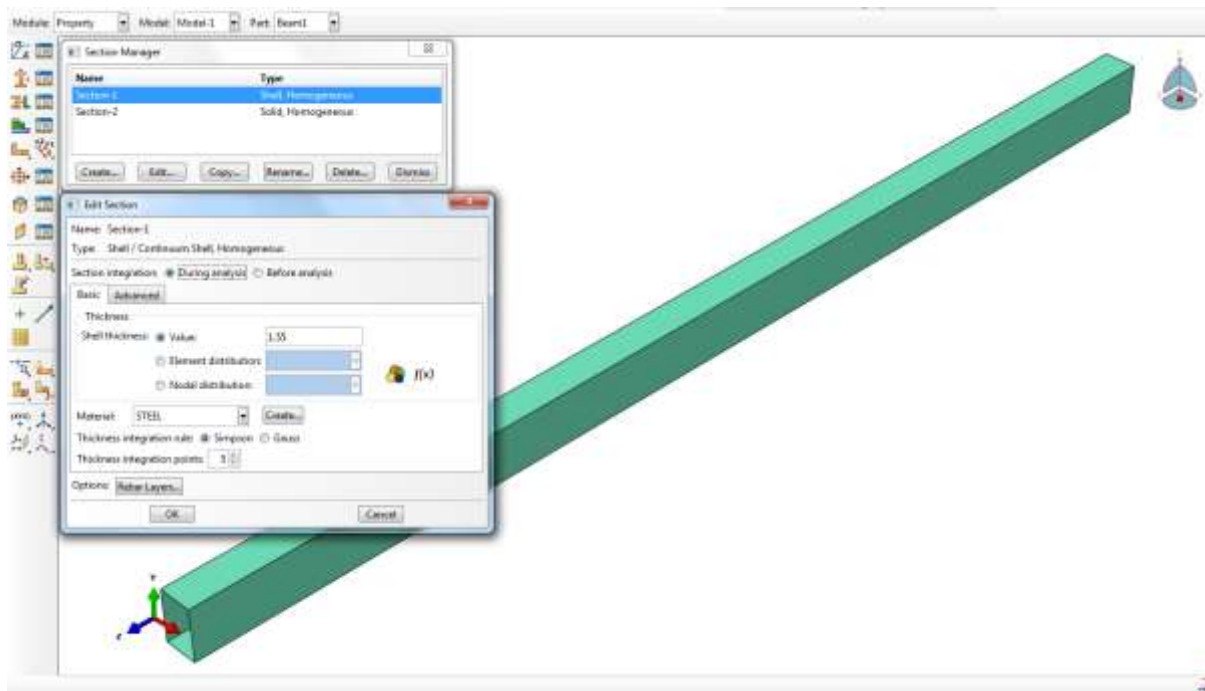


**Figure G.9: Creating a homogeneous, shell section of thickness 1.55 mm, having properties of steel**

Finally elements are assigned to each part individually through ‘*Section Assignment Manager>Create*’, and selecting the target part and assigning the relevant section to the part in the blank box as shown in Figures G.10 and G.11 for the solid Tufnell and shell steel sections respectively.

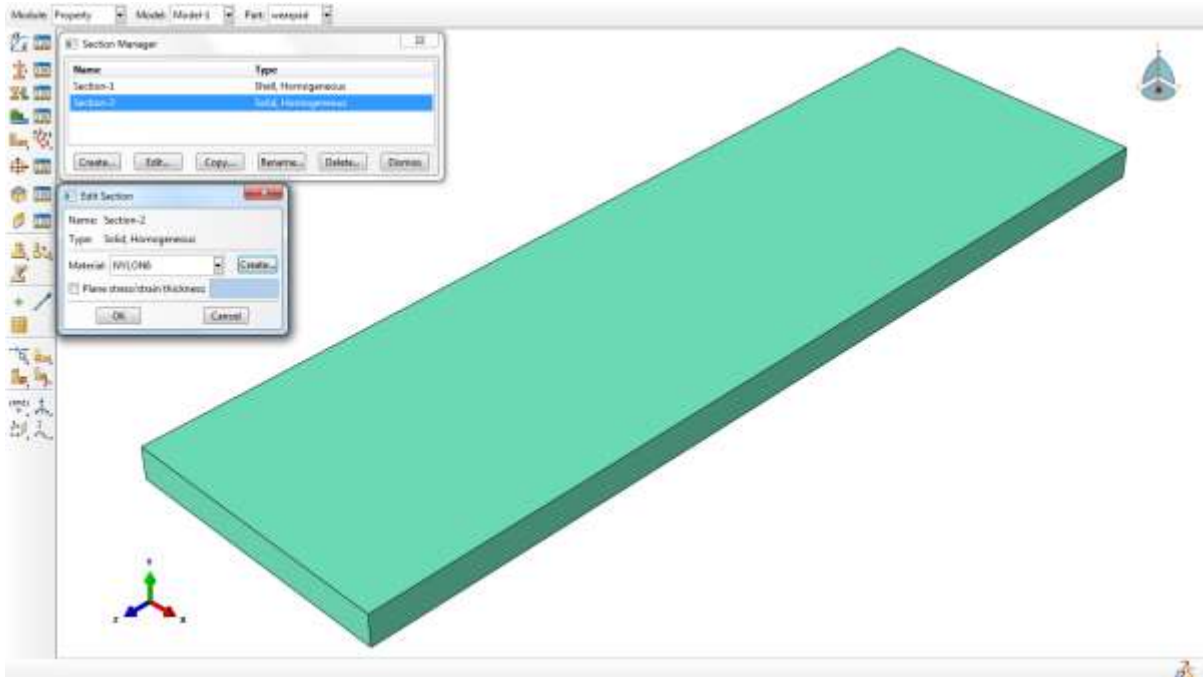


**Figure G.10: Creating a homogeneous, solid section having properties of Tufnell**

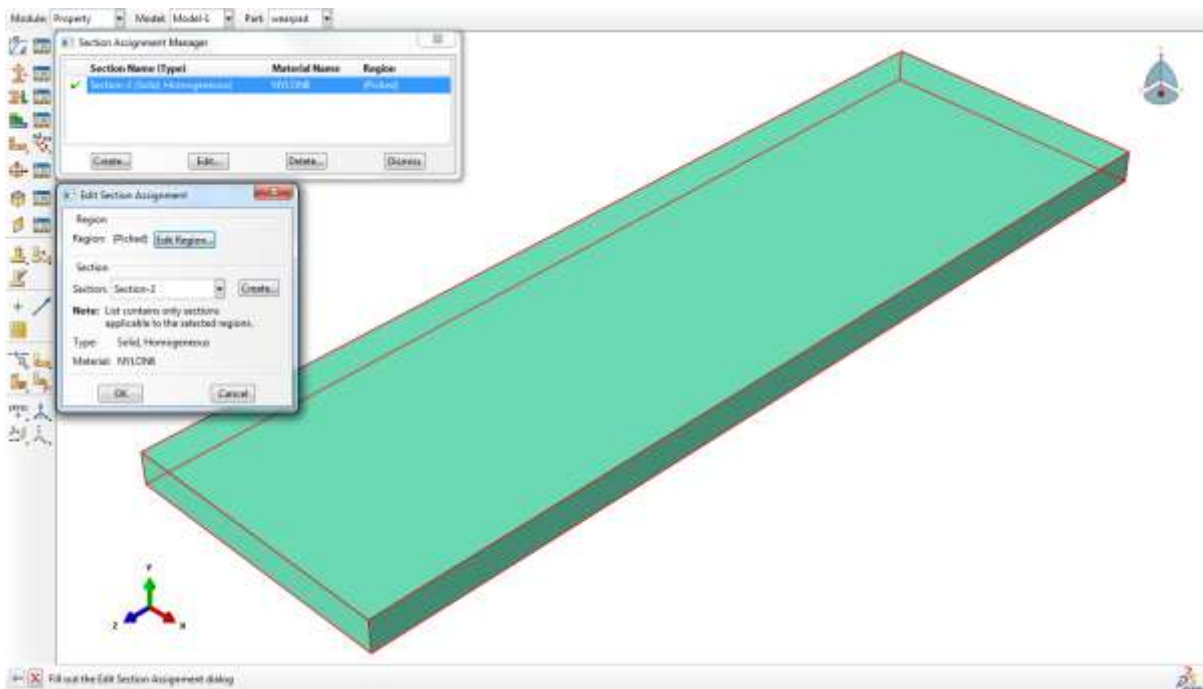


**Figure G.11: Assigning the homogeneous, solid Tufnell section to the part highlighted**

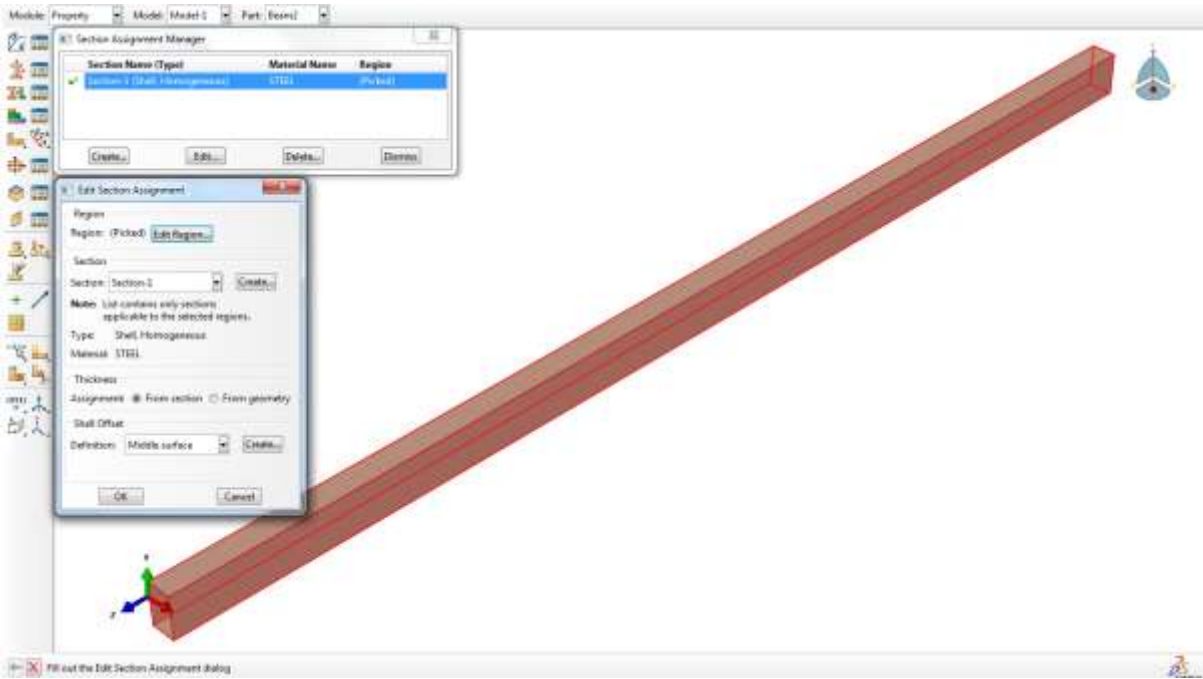


**Figure G.12: Assigning the homogeneous, shell steel section to the part highlighted**

### G.3 Assembling the Two Section Telescopic Cantilever Beam Assembly

When a part is created, it exists in its own coordinate system, independent of other parts in the model. In contrast, the Assembly module is used to create instances of the beam instances and the wear pad and to position the instances relative to each other in a global coordinate system, thus creating the assembly. The wear pad instance that has been created is repeatedly instanced seven times in order to position the individual instances in seven different predetermined locations within the assembly. The overall assembly, in turn replicates the experimental test rig. The part instances are positioned by sequentially applying position constraints that align selected faces, edges or vertices or by applying simple translations and rotations.

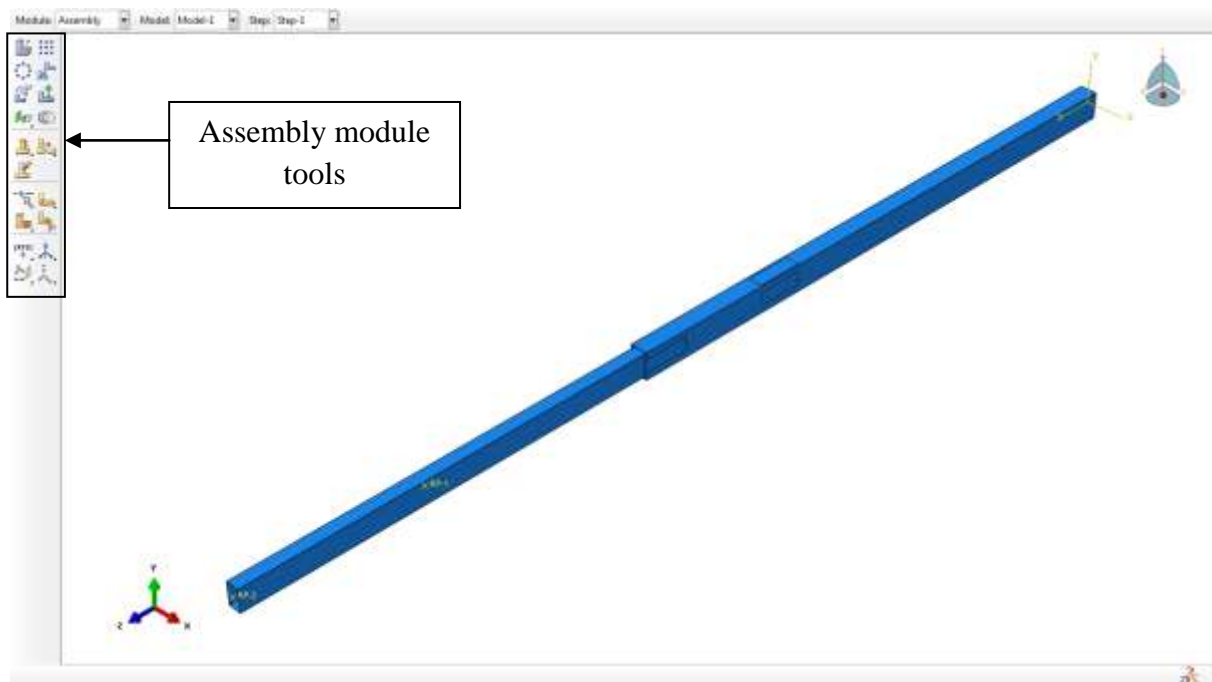


**Figure G.13: Assembly module tools**

An instance maintains its association with the original part. If the geometry of a part changes ABAQUS/CAE automatically updates all instances of the part to reflect these changes. It is not possible to edit the geometry of a part instance directly. A model can contain many parts and a part can be instanced many times in the assembly (as is the case with the wear pad as mentioned earlier) however a model contains only one assembly. Loads, boundary conditions, predefined fields and meshes are all applied to the assembly. Even if the model

consists of only a single part, it is imperative to create an assembly that consists of just a single instance of that part.

A part instance can be thought of as a representation of the original part. It is possible to create either independent or dependent part instances. An independent instance is effectively a copy of the part. A dependent instance is only a pointer to a part, partition or virtual topology; and as a result, it is not possible to mesh a dependent instance. However, the original part from which the instance was derived can be meshed in which case ABAQUS/CAE applies the same mesh to each dependent instance of the part [129].

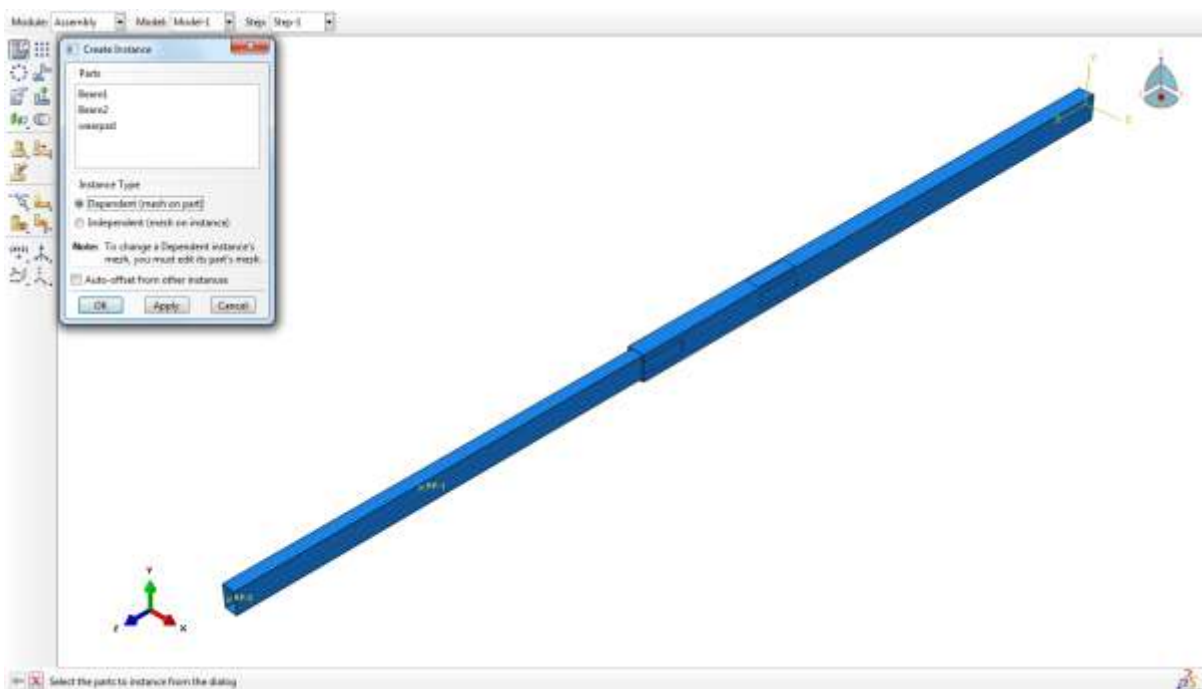


**Figure G.14: Creation of part instances and their assembly to constitute the overall two section telescopic cantilever assembly**

## **G.4 The Step Module**

An ABAQUS/CAE model uses the following two types of steps:

### **The Initial Step**

ABAQUS/CAE creates a special initial step at the beginning of the model's step sequence. ABAQUS/CAE creates only one initial step for the model, and it cannot be renamed, edited, replaced, copied, or deleted.

The initial step allows the definition of boundary conditions, predefined fields, and interactions that are applicable at the very beginning of the analysis. For example, if a boundary condition or interaction is applied throughout the analysis, it is usually convenient to apply such conditions in the initial step. Likewise, when the first analysis step is a linear perturbation step, conditions applied in the initial step form part of the base state for the perturbation.

### **Analysis Steps**

The initial step is followed by one or more analysis steps. Each analysis step is associated with a specific procedure that defines the type of analysis to be performed during the step, such as a static stress analysis or a transient heat transfer analysis. It is possible to change the analysis procedure from step to step in any meaningful way, so as to have greater flexibility in performing analyses. Since the state of the model (stresses, strains, temperatures, etc.) is updated throughout all general analysis steps, the effects of previous history are always included in the response for each new analysis step.

There is no limit to the number of analysis steps that can be defined, but there are restrictions on the step sequence. The Step module is used to perform the following tasks: (1) Create analysis steps, (2) Specify output requests (3) Specify adaptive meshing (4) Specify analysis controls [130].

### **G.4.1 Creation of analysis steps**

Within a model it is possible to define a sequence of one or more analysis steps. The step sequence provides a convenient way to capture changes in the loading and boundary conditions of the model, changes in the way parts of the model interact with each other, the removal or addition of parts, and any other changes that may occur in the model during the course of the analysis. In addition, steps allow for any change to the analysis procedure, the data output, and various controls. Steps can also be used to define linear perturbation analyses about nonlinear base states [130].

#### **Linear Perturbation Procedures in ABAQUS/CAE**

An analysis step during which the response can be either linear or nonlinear is called a general analysis step. An analysis step during which the response can be linear only is called a linear perturbation analysis step. General analysis steps can be included in an ABAQUS/Standard or ABAQUS/Explicit analysis; linear perturbation analysis steps are available only in ABAQUS/Standard.

A clear distinction is made in ABAQUS/Standard between general analysis and linear perturbation analysis procedures. Loading conditions are defined differently for the two cases, time measures are different, and the results should be interpreted differently. These distinctions are defined in this section.

ABAQUS/Standard treats a linear perturbation analysis as a linear perturbation about a preloaded, predeformed state. ABAQUS/Foundation, a subset of ABAQUS/Standard, is limited entirely to linear perturbation analysis but does not allow preloading or predeformed states [130].

#### **Linear Perturbation Analysis Steps**

Linear perturbation analysis steps are available only in ABAQUS/Standard (ABAQUS/Foundation is essentially the linear perturbation functionality in ABAQUS/Standard). The response in a linear analysis step is the linear perturbation response

about the base state. The base state is the current state of the model at the end of the last general analysis step prior to the linear perturbation step. If the first step of an analysis is a perturbation step, the base state is determined from the initial conditions. In ABAQUS/Foundation the base state is always determined from the initial state of the model [130].

Linear perturbation analyses can be performed from time to time during a fully nonlinear analysis by including the linear perturbation steps between the general response steps. The linear perturbation response has no effect as the general analysis is continued. The step time of linear perturbation steps, which is taken arbitrarily to be a very small number, is never accumulated into the total time. A simple example of this method is the determination of the natural frequencies of a violin string under increasing tension. The tension of the string is increased in several geometrically nonlinear analysis steps. After each of these steps, the frequencies can be extracted in a linear perturbation analysis step [130].

If geometric nonlinearity is included in the general analysis upon which a linear perturbation study is based, stress stiffening or softening effects and load stiffness effects (from pressure and other follower forces) are included in the linear perturbation analysis. Load stiffness contributions are also generated for centrifugal and Coriolis loading. In direct steady-state dynamic analysis Coriolis loading generates an imaginary anti symmetric matrix. This contribution is accounted for currently in solid and truss elements only and is activated by using the unsymmetric matrix storage and solution scheme in the step [130].

Eigenvalue buckling analysis:

1. is generally used to estimate the critical (bifurcation) load of “stiff” structures;
2. is a linear perturbation procedure;
3. can be the first step in an analysis of an unloaded structure, or it can be performed after the structure has been preloaded—if the structure has been preloaded, the buckling load from the preloaded state is calculated;
4. can be used in the investigation of the imperfection sensitivity of a structure;
5. works only with symmetric matrices (hence, unsymmetric stiffness contributions such as the load stiffness associated with follower loads are symmetrized); and
6. cannot be used in a model containing substructures.

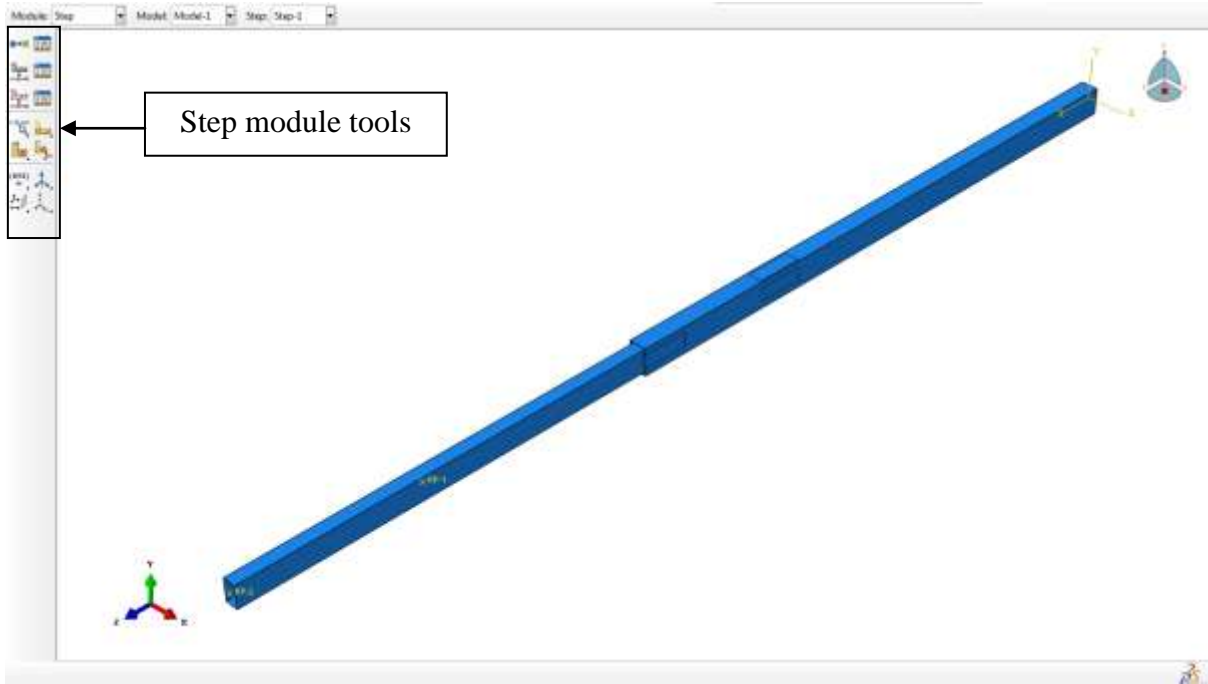


Figure G.15: Step module tools

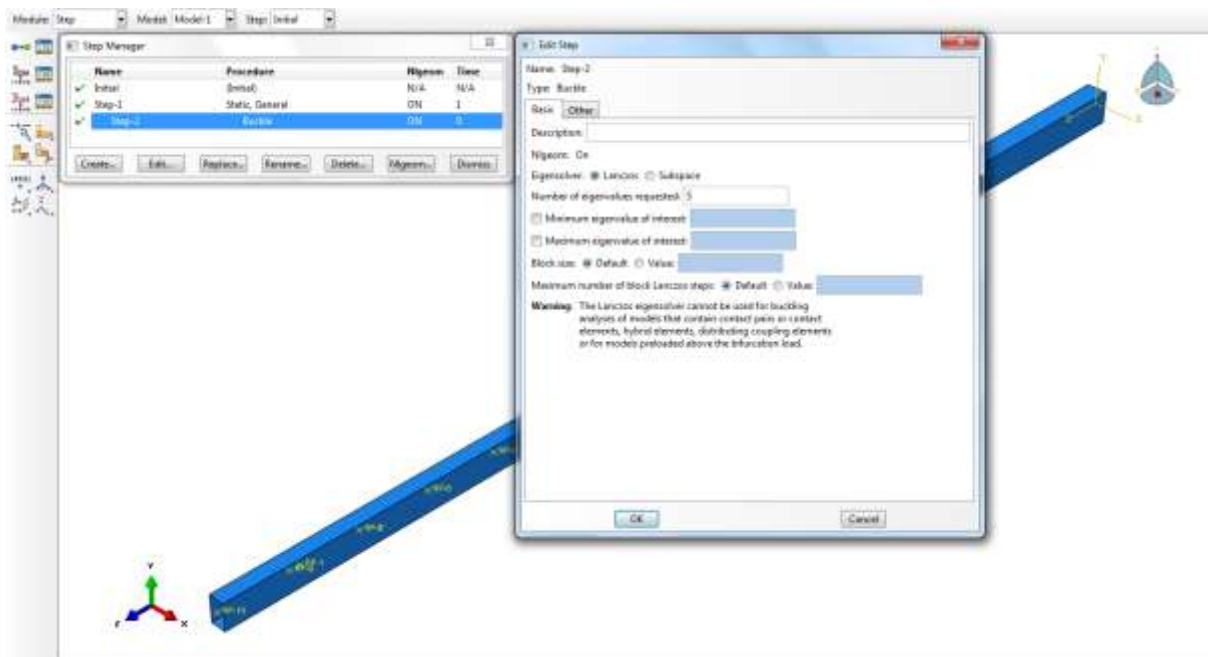


Figure G.16: Creation of buckling step as outlined in [130] and § G.4.1

## G.5 Interaction Definitions

Relation between the piece parts should be established through interactions. Interaction module provides relevant options to identify the piece parts' interfaces. Tie constraint is defined between connected/welded surfaces; whereas the type of interaction defined throughout the analysis is surface-to-surface. This approach optimizes the stress accuracy for a given surface pairing. The improved stress accuracy with respect to the surface-to-surface approach is realised if and only if neither surface of tie pairing is node based.

The surface-to-surface option generally involves more master nodes per constraint than the node-to-surface approach, which in turn results in an additional increase in the solver bandwidth in the ABAQUS/Standard software, thereby increasing the solver cost. The following factors, especially in combination, can lead to the surface-to-surface approach being costly [131]:

1. A large fraction of tied nodes (degrees of freedom) in the model
2. The master surface being more refined than the slave surface
3. Multiple layers of tied shells, such that the master surface of one tie constraint acts as the slave surface of another constraint.

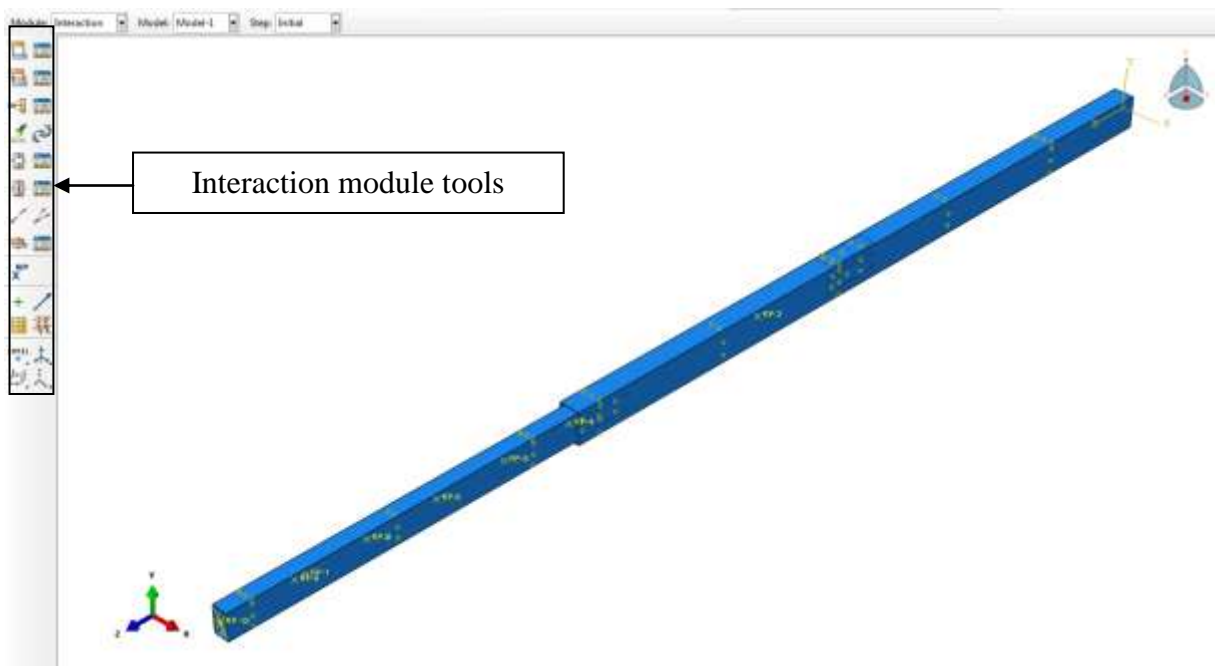


**Figure G.17: Interaction module tools**

In order to set up a *Tie* constraint between two surfaces, the type of interaction should be defined as being either surface-to-surface or node-to-surface by choosing the master surface as being either *Surface* or *Node* region. On choosing the surface option the selected surface becomes the master region and in a similar fashion the slave surface is also defined. In a tie interaction between shell elements ABAQUS allows the user to choose either the inner or outer surfaces with the help of a colour code, with brown representing the outer surface and purple representing the inner surface.

One of the problems that may arise at the time of defining interactions is that of the over constraint. An over constraint can be defined as the application of multiple consistent or inconsistent kinematics constraints. Many models have nodal degrees of freedom that are over constrained. Such over constraints may lead to inaccurate or non-convergent solution generation.

Common examples of situations that may lead to over constraints include [132]:

1. Contact slave nodes that are involved in boundary conditions or multi-point constraints
2. Edges of surfaces involved in a surface-based tie constraint that are included in contact slave surfaces or have symmetry boundary conditions
3. Boundary conditions applied to nodes already involved in coupling or rigid body constraints.

One of the most important steps within the interaction module, is the selection of the *Master* and *Slave* surfaces. Attention is required in selecting slave surfaces as one slave surface cannot have two master surfaces. If such a constraint is present in the model the simulation will exit with over constraint errors. However the converse of this is true i.e. a master surface can have more than one slave surfaces. This conflict usually happens in the selection of slave surfaces which are sharing at least one edge. That edge provides common nodes between two slave surfaces which causes the error at the time of running the simulation.

In addition to the *Tie* constraints, a coupling constraint is also created. A *Coupling* constraint is used to constrain the motion of a surface to the motion of a reference node. This constraint

is created at the free end or the loading end in order to apply loading as is shown in the next section.

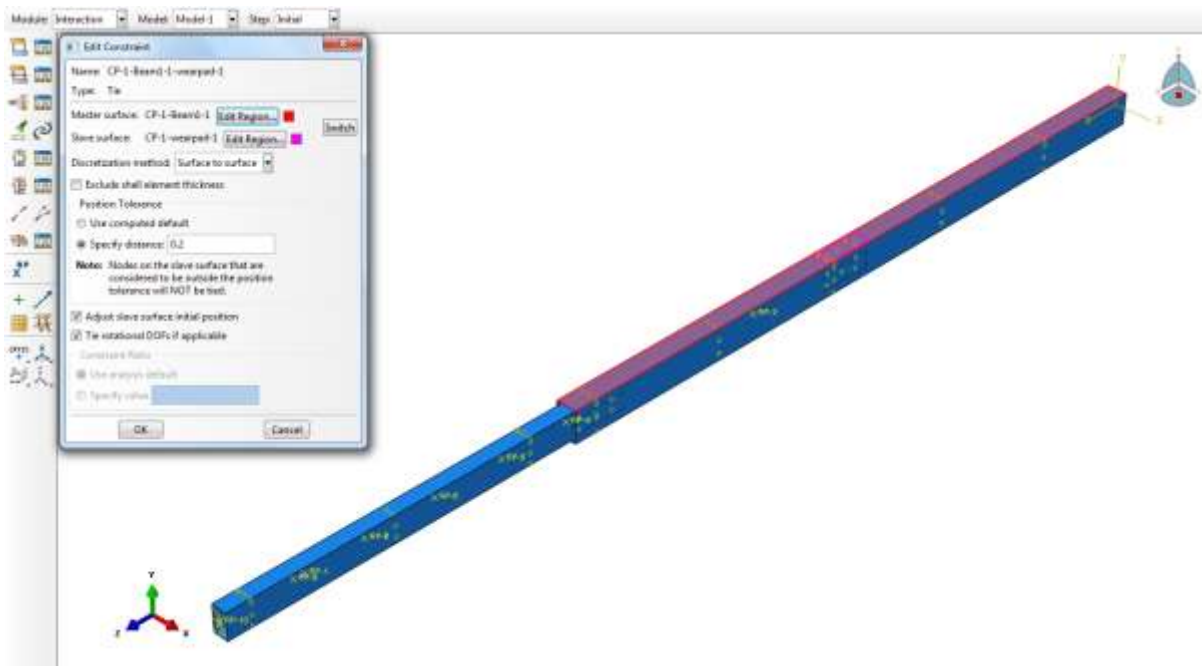


**Figure G.18: Definition of constraints (tie contacts) between surfaces**

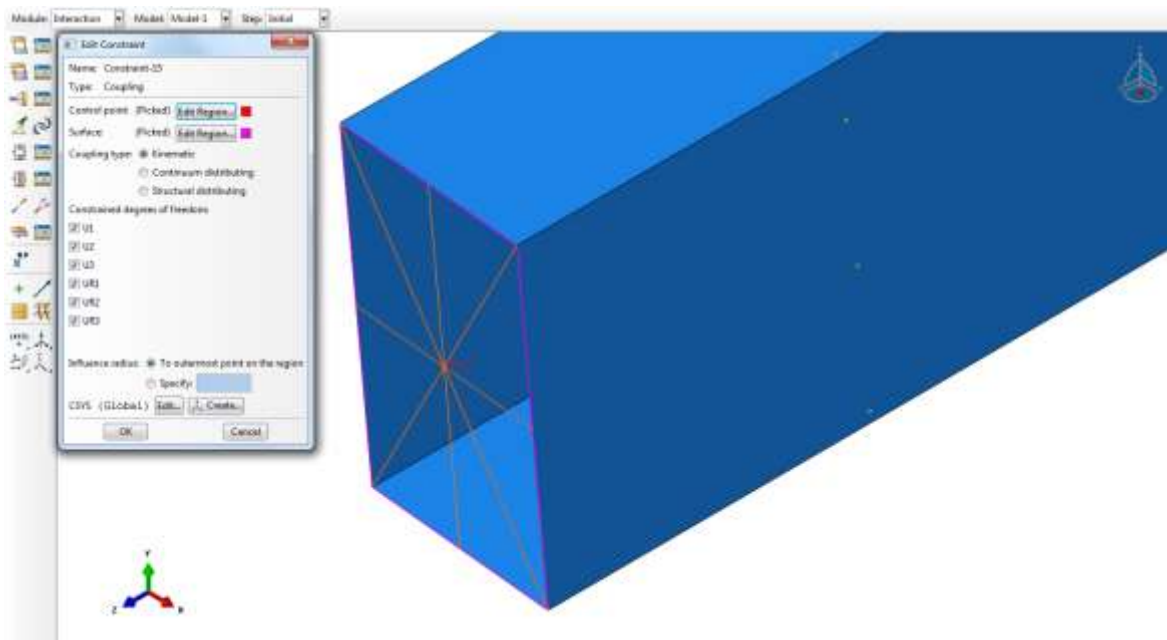


**Figure G.19: Definition of coupling constraint**

The established contacts can be viewed and edited from 'Interaction Manager' tab by selecting the relevant interaction and pressing edit as it is shown in Figure G.20. Also the step

in which each interaction was created whether it be in the initial step or otherwise is also displayed in the ‘*Edit Interaction Manager*’.

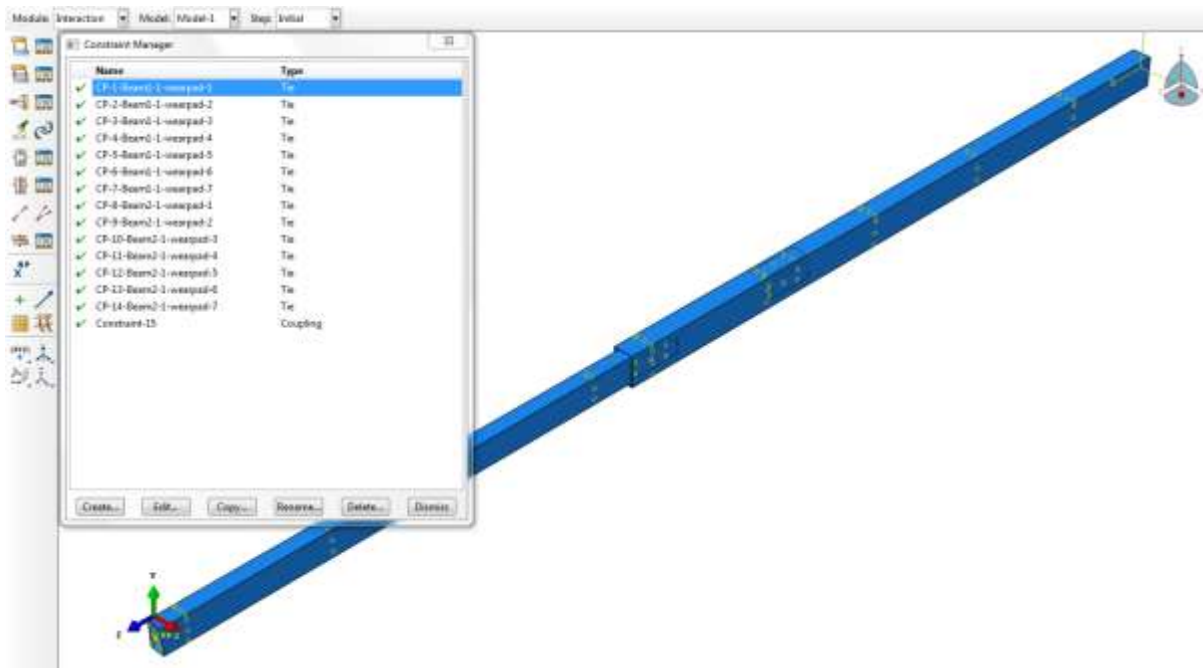


**Figure G.20: Existing tie definitions that can be controlled and edited from the constraint manager tab**

At the end of this process all the interactions between considered parts will be defined and the assembly is ready to be meshed and loaded. Those parts that are not vital to the analysis results are ignored i.e. are not defined with interactions. These parts will no doubt be excluded from the simulation altogether at the time of solving.

## G.6 Loading Conditions

Loads and constraints are applied as per the actual assembly scenario as in the experimental test rig. The effect of self-weight is first applied by entering the gravity specifications. External loads are applied by defining them as concentrated loads, which in turn are applied at the coupling constraint as specified in Figure G.19. Torque is also applied at this constraint point, as a twisting moment. In order to determine the critical buckling load, a separate analysis is conducted and the steps for applying the required load conditions are specified in Figures G.25 and G.26.

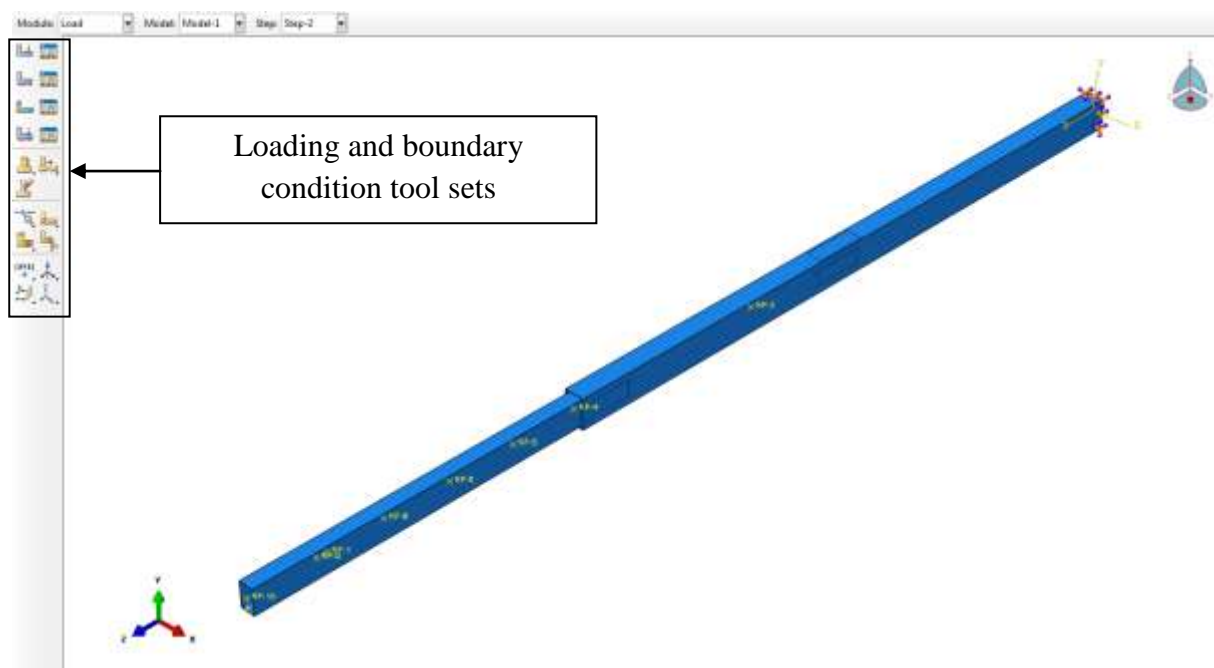


**Figure G.21: Loading and boundary condition tool sets**

First of all the effect of self weight is applied by inputting the gravity. By selecting the 'Create Load' tab from left hand menu and selecting the gravity from the provided list the next window opens to allow for the input of the relevant amount. The magnitude of gravity is entered into the dialog box and the selection is accepted as shown in Figure G.22.

As has been mentioned earlier in this chapter the three outcomes desired from the FEA are: (a) Overall Deflection of the telescopic assembly for increased loading (b) Bending and Shear Stresses at regular intervals of 50mm along the top face and side wall respectively and (c) Determination of the Critical Buckling Load for the telescopic beam assembly.

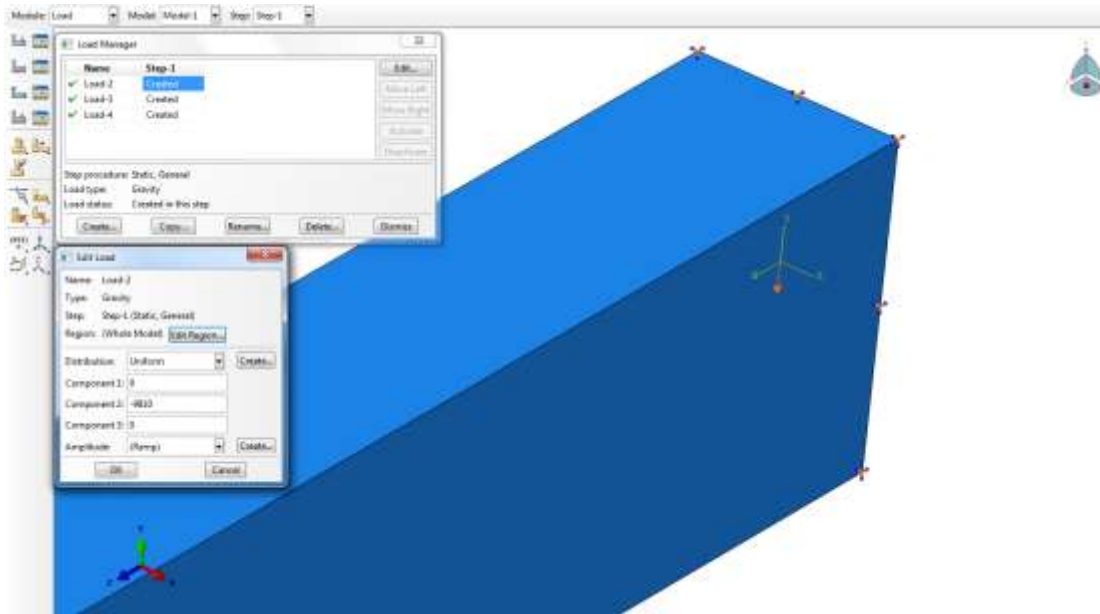


**Figure G.22: Application of self weight or gravity on the assembly**

To this effect in order to achieve the first outcome loading is applied in the form of concentrated force acting at the constraint point shown in Figure G.19. Bending and shear stress values are extracted at regular intervals along the length of the assembly for two types of loading scenarios namely (i) a concentrated end force acting the constraint point (shown in Figure G.19) and (ii) a concentrated end force acting on a torque arm attached to the free end of the telescopic assembly which constitutes both a concentrated end load and a twisting moment. The former and the latter are shown in Figure G.23 and G.24 respectively.

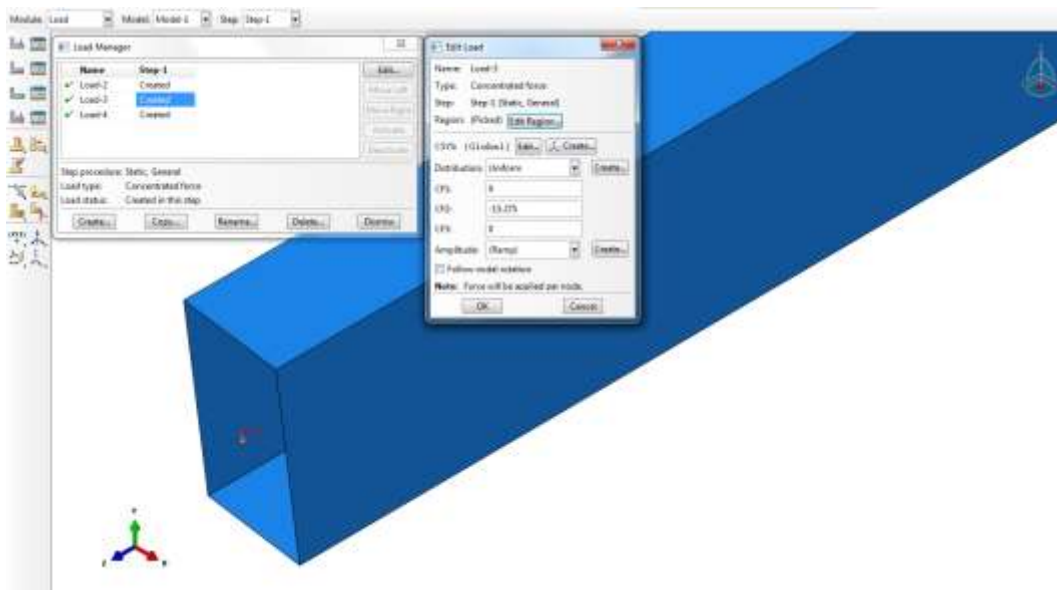


**Figure G.23: Application of the concentrated end force at the free end of the assembly**

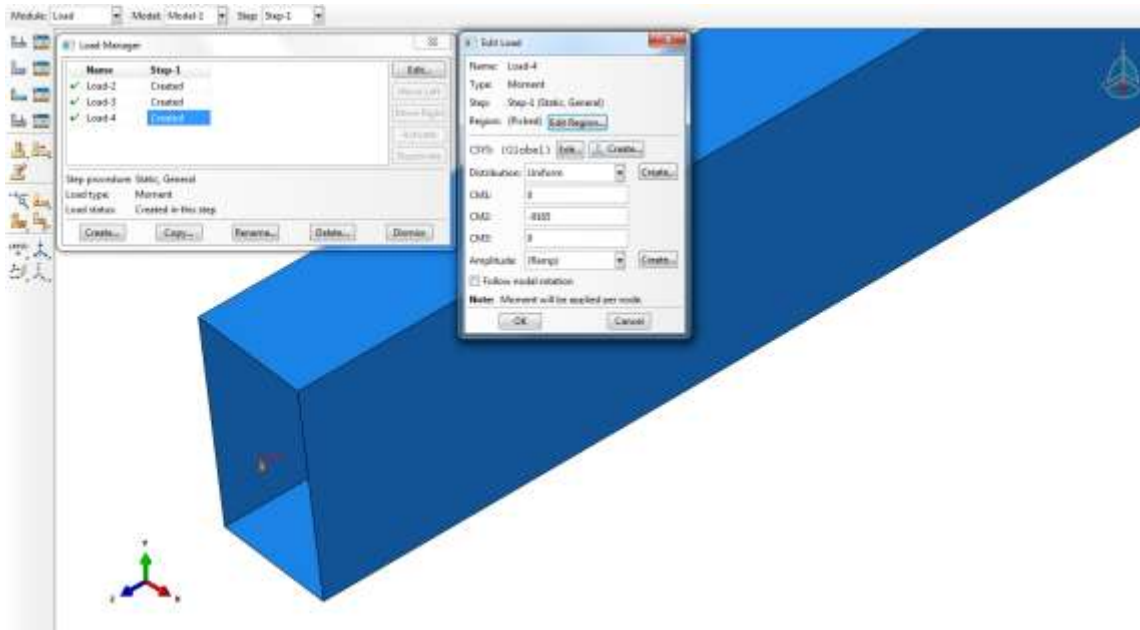


**Figure G.24: Application of the twisting moment at the free end of the assembly**

To determine the critical buckling load of the assembly for different overlap lengths requires a separate analysis to be run for which the values of both dead and live loads are to be entered [107]. The buckling analysis in turn generates the buckling Eigen values which in turn are substituted in the relation shown in Table 7.3, to obtain the critical buckling load. Figures G.25 and G.26 show how the magnitudes of the ‘dead’ and ‘live’ loads, inputted as 5000 N and 500 N respectively.

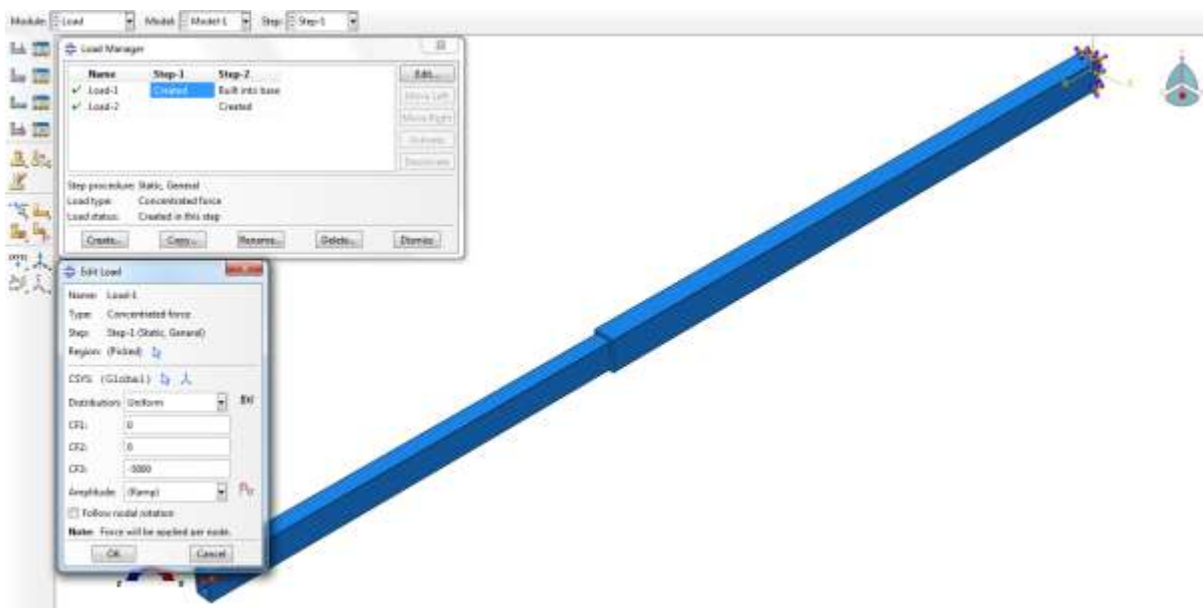


**Figure G.25: Application of *Dead* load on the assembly**

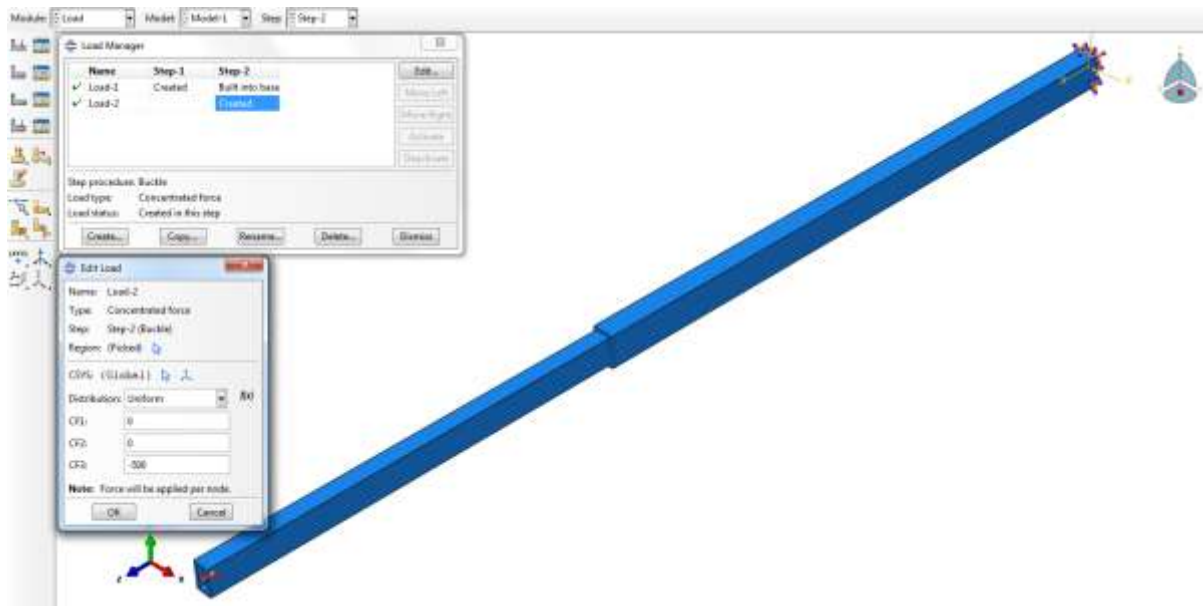


**Figure G.26: Application of *Live* load on the assembly**

For linear buckling analysis - in the elastic state of the structure – *static/general* and *buckling* are the two steps defined in order to determine the critical buckling load of the assembly [107]. The initial Static/General step is used to primarily show the first deformations on the model for buckling, whilst the Buckling step will calculate the Eigen-values from which the *Buckling Load Factor* can be calculated.

Linear-buckling analysis is often associated with the Eigen-value buckling or the Euler buckling analysis because it predicts the theoretical buckling strength. The Eigen-values are values of load at which the buckling takes place, while the Eigenvectors are the corresponding buckling shapes associated with the Eigen-values. The Eigen-value buckling analysis shows that the buckling takes place when the resultant structure stiffness drops to zero [107].

At linear-buckling and modal analysis, FEA provides a large number of buckling modes, but from this analysis, the only buckling mode of practical importance is the first one with a positive Eigen-value, from which the buckling load is determined. The buckling mode shows what shape the structure assumes when it is subject to buckling, in that particular mode.

## G.7 Boundary Conditions

Boundary conditions are conditions that must be placed on a model in order to represent everything about the system that will not be modelled. The boundary conditions are used to constrain the motion of the model at the time of running the simulation. Boundary conditions are conditions around the boundary of the geometry that are known. The locations where the constraints are applied, as well as the degrees of freedom that are restricted, are shown in the Figure G.27 below. Select 'Create Boundary Condition>Symmetry/Antisymmetry/Encastre >Continue ....', as shown in Figure G.27, and select the region where the constraint should be applied (surface, edge, node etc) and confirm accordingly. The resultant window provides the options to set the type of constraints.

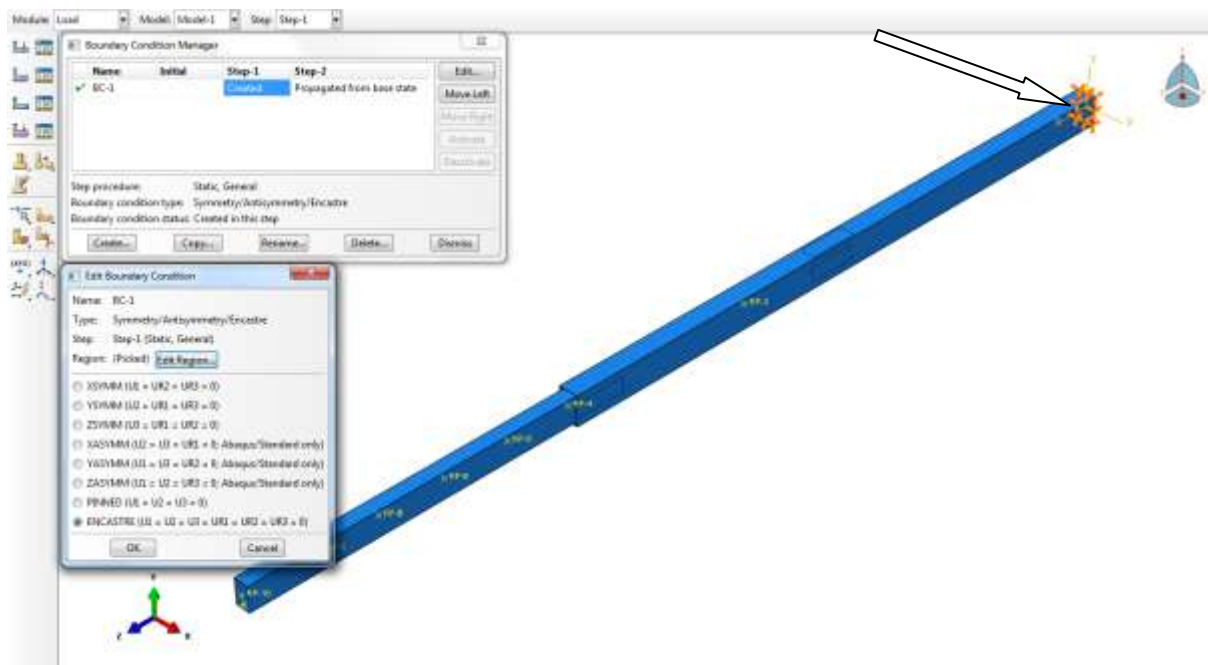


**Figure G.27: Position where the telescopic assembly is constrained as indicated by the arrow, in all degrees of freedom to simulate an encastre type fixing.**

## G.8 Meshing Definitions

The Mesh module allows for the generation of meshes on parts and assemblies created within ABAQUS/CAE. Various levels of automation and control are available so that it is possible to create a mesh that meets the needs of the analysis. As with creating parts and assemblies, the process of assigning mesh attributes to the model—such as seeds, mesh techniques, and element types—is feature based. As a result it is possible to modify the parameters that define a part or an assembly, and the mesh attributes that are specified within the *Mesh module* can be regenerated automatically. Parts are selected individually and meshed according to their size and amount of fine details they contain. Therefore the mesh size is specified exclusively for each part. To ease the process the parts can be appear in the screen individually by switching of the other parts. The mesh size should be defined fine enough to cover the parts feature, however very fine mesh size can result in complicated and time consuming analysis process. Therefore finding the optimum mesh size could reduce the process time and maintain the accuracy.

In ABAQUS, the following element shapes are defined in the *Mesh module*. Depending on whether the region to be meshed was either 2D or 3D, the element shapes were assigned accordingly by default in the *Mesh module*. As mentioned earlier the element shapes that were used in this analysis were the following linear elements namely: quadrilateral, triangular, tetrahedral and wedge shaped elements.

For Shell parts, a mixture of linear quadrilateral elements of type S4R and linear triangular elements of type S3 were used to create the resultant mesh. The S4R element shape is defined as a 4-node doubly curved thin or thick shell, reduced integration, hourglass control, finite membrane strains [133].

For Solid parts, a mixture of linear wedge elements of type C3D6 and linear tetrahedral elements of type C3D4 were used on individual parts. For those solid parts that have hole features or are of a circular or cylindrical disposition, C3D6 type elements were used. The C3D6 element shape is defined as a 6-node linear triangular prism [133]. Those solid parts that have no such features and have no circular cross section are assigned the C3D4 element shape. The C3D4 element shape is defined as a 4-node linear tetrahedron [133].

As far as was possible elements of a linear geometric order were chosen at the time of analysis, as opposed to ideally using elements of a quadratic geometric order. This was because the use of quadratic elements severely affected the analysis run time resulting in the ABAQUS program to hang thereby not providing the required results.

The procedure for the creation of an acceptable mesh is as follows [133]:

#### 1. Assign *Mesh Attributes* and *Set Mesh Controls*

The *Mesh module* provides a variety of tools that allow you to specify different mesh characteristics, such as mesh density, element shape, and element type.

#### 2. Generate the Mesh

The *Mesh module* uses a variety of techniques to generate meshes. The different mesh techniques provide you with different levels of control over the mesh.

#### 3. Refine the Mesh

The *Mesh module* provides a variety of tools that allows the refining of the mesh:

- a. The seeding tools allow you to adjust the mesh density in selected regions.
- b. The *Partition toolset* allows you to partition complex models into simpler sub regions.
- c. The *Virtual Topology* toolset allows you to simplify your model by combining small faces and edges with adjacent faces and edges.
- d. The *Edit Mesh* toolset allows you to make minor adjustments to your mesh.

#### 4. Optimize the Mesh

It is possible to assign re-meshing rules to regions of the model. Re-meshing rules enable successive refinement of the mesh where each refinement is based on the results of an analysis.

## 5. Verify the Mesh

The verification tool provides information concerning the quality of the elements used in a mesh.

### G.8.1 Structured Meshing

The structured meshing technique generates structured meshes using simple predefined mesh topologies. ABAQUS/CAE transforms the mesh of a regularly shaped region, such as a square or a cube, onto the geometry of the region you want to mesh. For example, Figure G.28 illustrates how simple mesh patterns for triangles, squares, and pentagons are applied to more complex shapes.

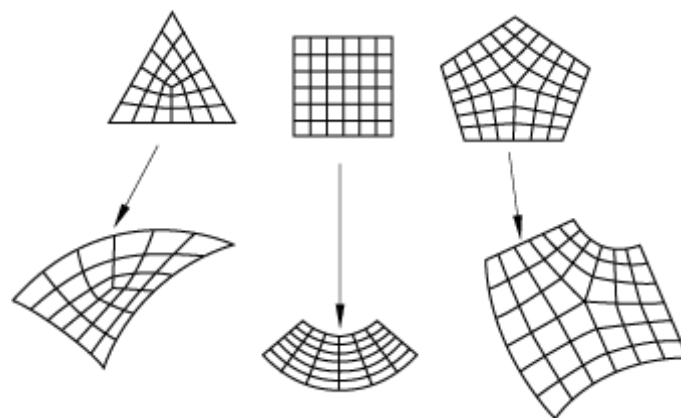


**Figure G.28: Two-dimensional structured mesh patterns [133]**

The structured meshing technique can be applied to simple two-dimensional regions (planar or curved) or to simple three-dimensional regions that have been assigned the *Hex or Hex-dominated element shape option*.

## G.8.2 Swept Meshing

ABAQUS/CAE uses swept meshing to mesh complex solid and surface regions. As per the *The Mesh Module* within the ABAQUS Documentation, the swept meshing technique involves two phases [133]:

1. ABAQUS/CAE creates a mesh on one side of the region, known as the source side.
2. ABAQUS/CAE copies the nodes of that mesh, one element layer at a time, until the final side, known as the target side, is reached. ABAQUS/CAE copies the nodes along an edge, and this edge is called the sweep path. The sweep path can be any type of edge—a straight edge, a circular edge, or a spline. If the sweep path is a straight edge or a spline, the resulting mesh is called an extruded swept mesh. If the sweep path is a circular edge, the resulting mesh is called a revolved swept mesh.

For example Figure G.29 shows an extruded swept mesh. To mesh this model, ABAQUS/CAE first creates a two-dimensional mesh on the source side of the model. Next, each of the nodes in the two-dimensional mesh is copied along a straight edge to every layer until the target side is reached.

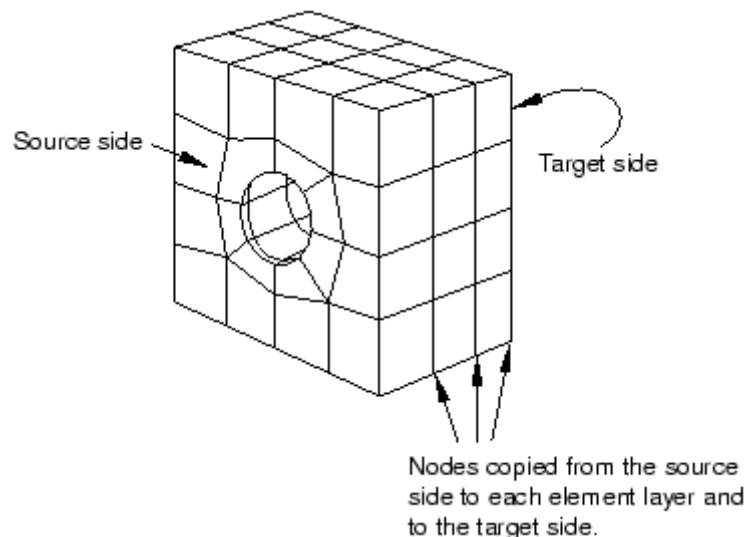


**Figure G.29: The swept meshing technique for an extruded solid [133]**

To determine if a region is swept meshable, ABAQUS/CAE tests if the region can be replicated by sweeping a source side along a sweep path to a target side. In general, ABAQUS/CAE selects the most complex side (for example, the side that has an isolated edge

or vertex) to be the source side. In some cases it is possible to use the mesh controls to select the sweep path. If some regions of a model are too complex to be swept meshed, ABAQUS/CAE asks if these regions should be removed from the selection before it generates a swept mesh on the remaining regions. The free meshing technique can be used to mesh the complex regions, or the regions can be partitioned into simplified geometry that can be structured or swept meshed.

When you assign mesh controls to a region, ABAQUS/CAE indicates the direction of the sweep path and allows you to control the direction. If the region can be swept in more than one direction, ABAQUS/CAE may generate a very different two-dimensional mesh on the faces that it can select as the source side. As a result, the direction of the sweep path can influence the uniformity of the resulting three-dimensional swept mesh, as shown in Figure G.30.

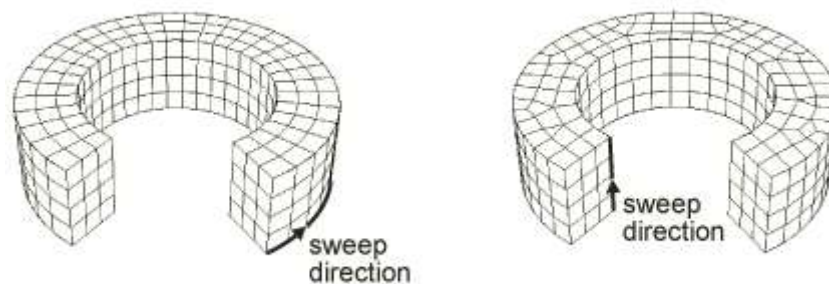


**Figure G.30: The sweep direction can influence the uniformity of the swept mesh [133]**

### G.8.3 Free Meshing

Unlike structured meshing, free meshing uses no pre established mesh patterns. When meshing a region using the structured meshing technique, it is possible to predict the pattern of the mesh based on the region topology. In contrast, it is impossible to predict a free mesh pattern before creating the mesh.

Because it is unstructured, free meshing allows more flexibility than structured meshing. The topology of regions allows for meshing with the free mesh technique can be very complex.

This technique can be used to mesh a region with the Tri, Quad, or Quad-dominated element shape options for two-dimensional regions or the Tet element shape option for three-dimensional regions.

The final meshed assembly is meshed using an amalgamation of the meshing techniques outlined in the [133] and is shown in Figure G.33.

To ease the process of meshing of the individual parts, those parts that are not required within the current view can be individually switched on or off. Select ‘View>Assembly Display option’ from main menu. By selecting the instance tab from the pop up window the required parts can be selected properly. The steps are shown in Figure G.31.

Select ‘Seed Part Instance’ from the left hand tool bar and select the target part and confirm it. The ‘Global Seeds’ window will be opened which provides the option to select the mesh size, displayed in Figure G.32.

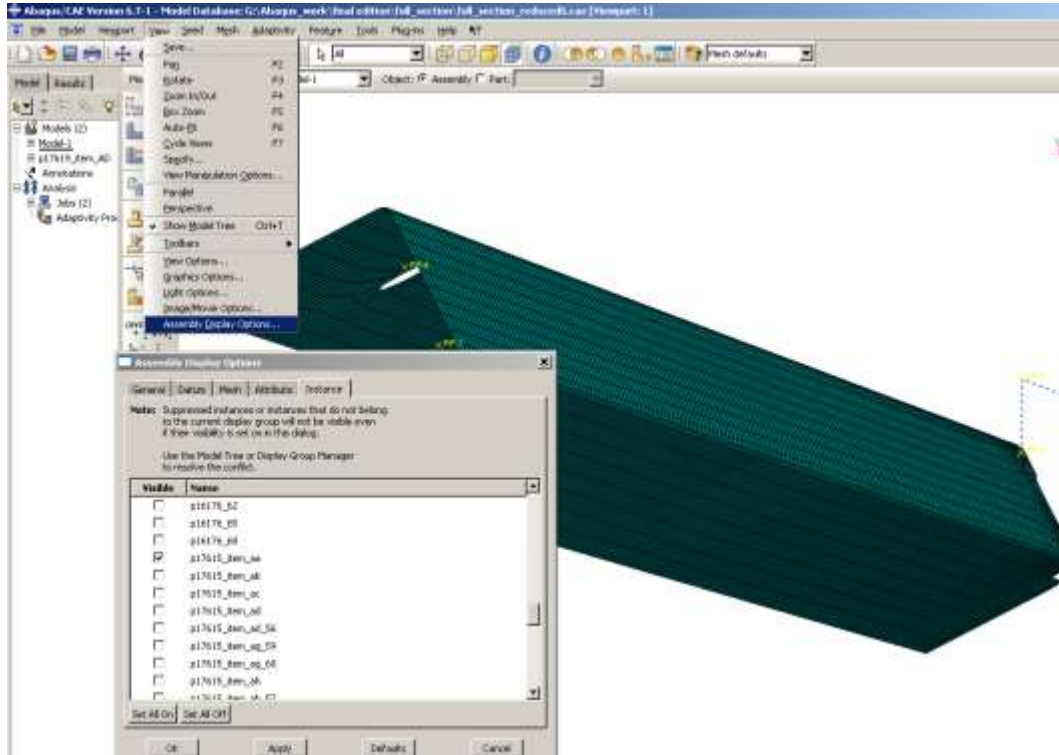


**Figure G.31: Controlling the screen view by switching of the irrelevant parts which provides more control in selecting parts in meshing process**

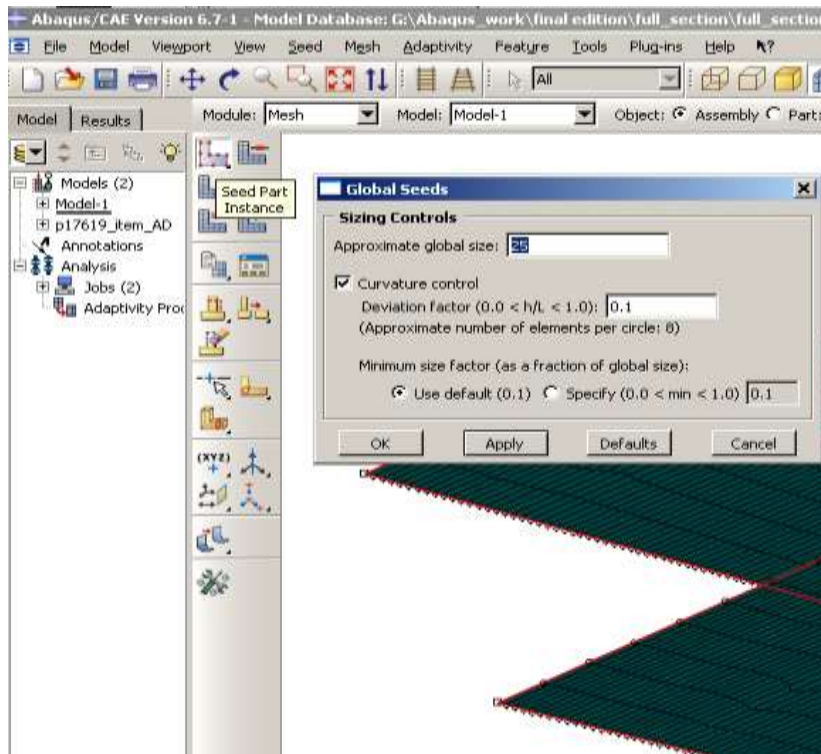


**Figure G.32: Adjustment of mesh size**

The other settings in this window remained untouched in this example. The mesh size will be confirmed and will be assigned to the part by pressing '*Assign Mesh Control*'. The meshing process will be finished by selecting '*Mesh Part Instance*' and selecting the part to be meshed. All the engaged parts have to be meshed in the same manner. The unmeshed parts will not be involved in the analysis hence the parts which need to be temporarily isolated can be remained unmeshed.



Figure G.33: Meshed telescopic beam assembly

## G.9 Generation and Interpretation of results

Once all of the tasks involved in creating a model (such as specifying the geometry of the model, assigning section properties, and defining contact), the *Job module* is entered into to analyse the model. The *Job module* allows for the creation of a job, to submit it to ABAQUS for analysis, and to monitor its progress. It is also possible to create multiple models and jobs and run and monitor these jobs simultaneously. In addition, the option of creating only the analysis input file for a model is available which allows the viewing and editing of the input file before submitting it for analysis.

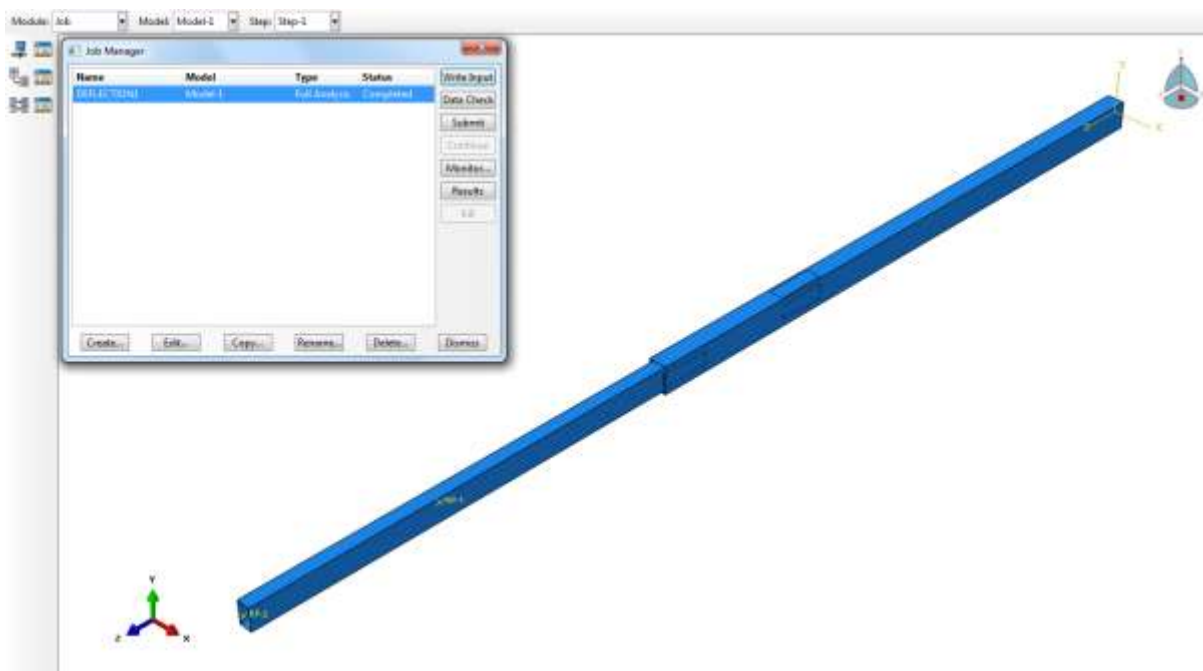
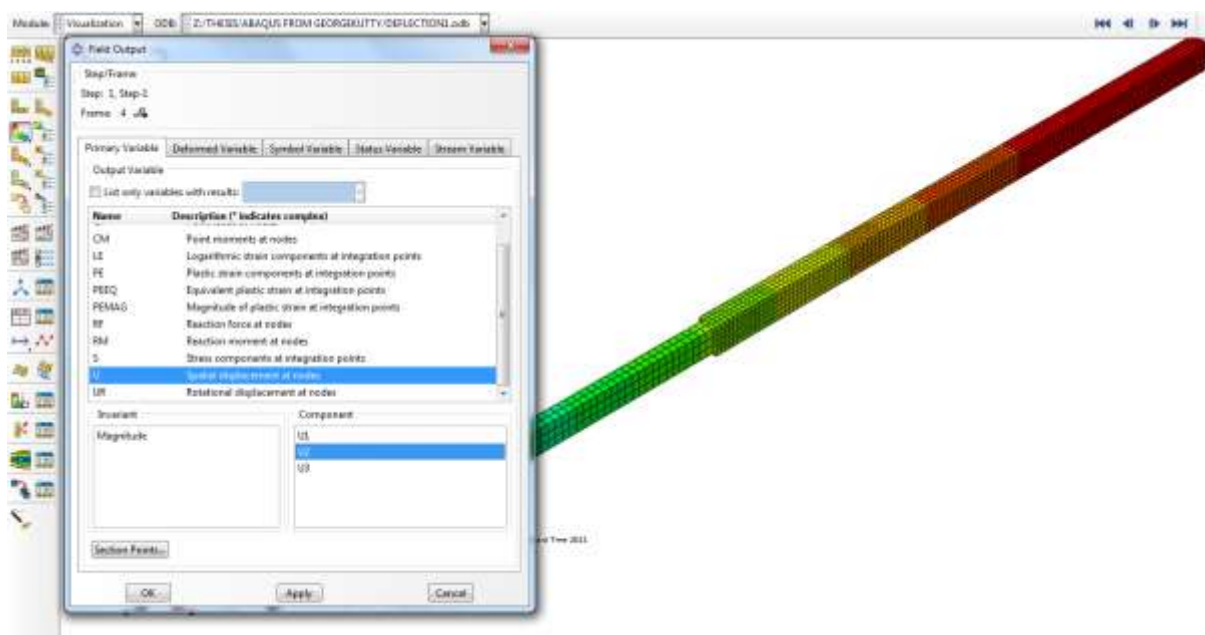


Figure G.34: Submitting a job for analysis

## G.9.1 Tip Deflection Results Extraction

Once the job has been processed and is completed as indicated in the job manager window as shown in Figure G.34, clicking on the ‘Results’ button runs the ‘Visualization Module’ and the assembly will be shown in its meshed format. Selecting ‘Results>Field Output’, the desired quantity to be extracted, whether it be stress or displacement is selected from the main tab window, followed by the component of either, in the appropriate coordinate axes as is required. In Figure G.35, the displacement tab is selected along with the component of displacement required.



**Figure G.35: Selecting the displacement tab and its component in the negative y-direction**

The overall tip deflection induced by any given load upon the assembly can be deduced from the contour plot legend as shown in the top left hand corner in Figure G.36. In order to extract the deflections at individual nodes in the assembly, node numbers or node symbols are generated on the cantilever. This is done by selecting the ‘Options>Common’ tab and within the Common Plot Options dialog box selecting the node labels tab. Once this tab has been selected and accepted by clicking ‘OK’ and the node numbers will appear as shown in the Figure G.38.

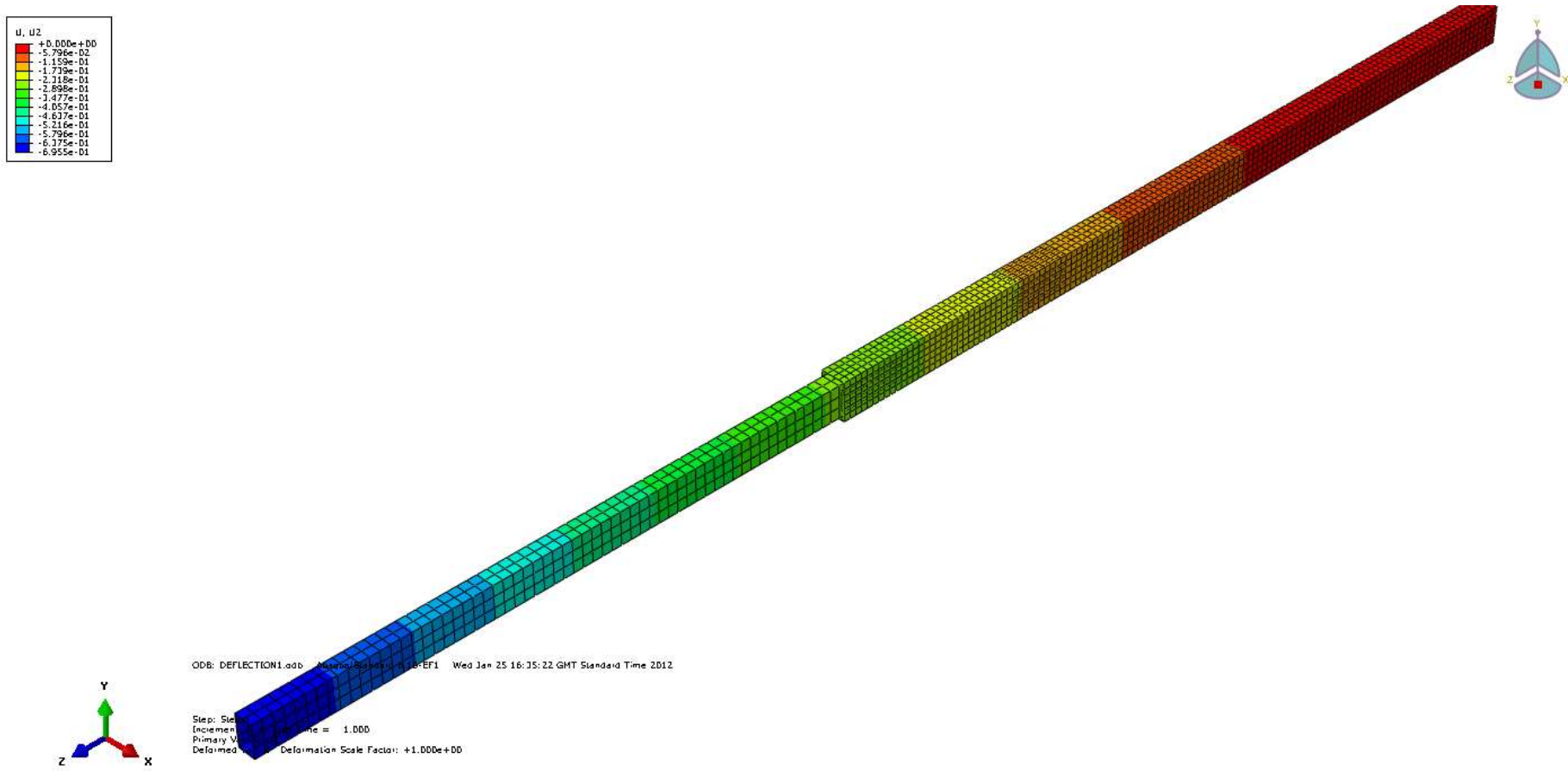


**Figure G.36: The displacement at each of the nodes as is plotted along the assembly**

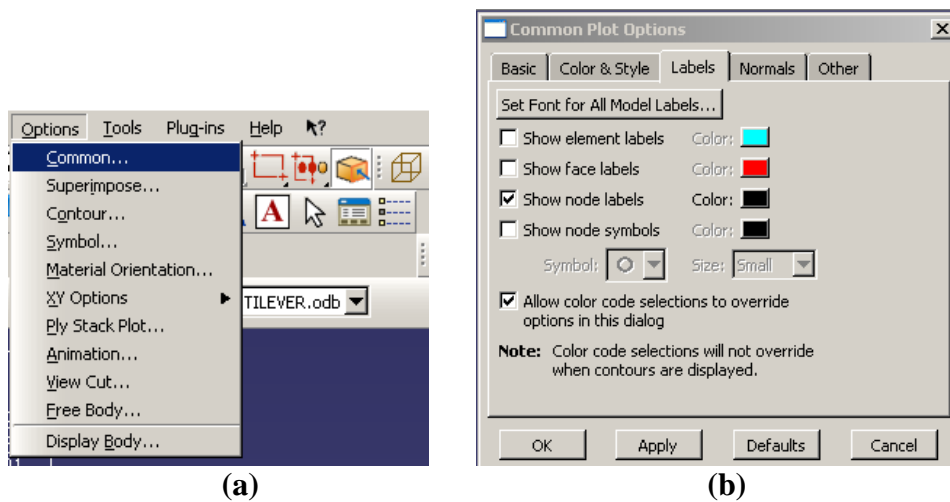


**Figure G.37: Node Label Display Options**

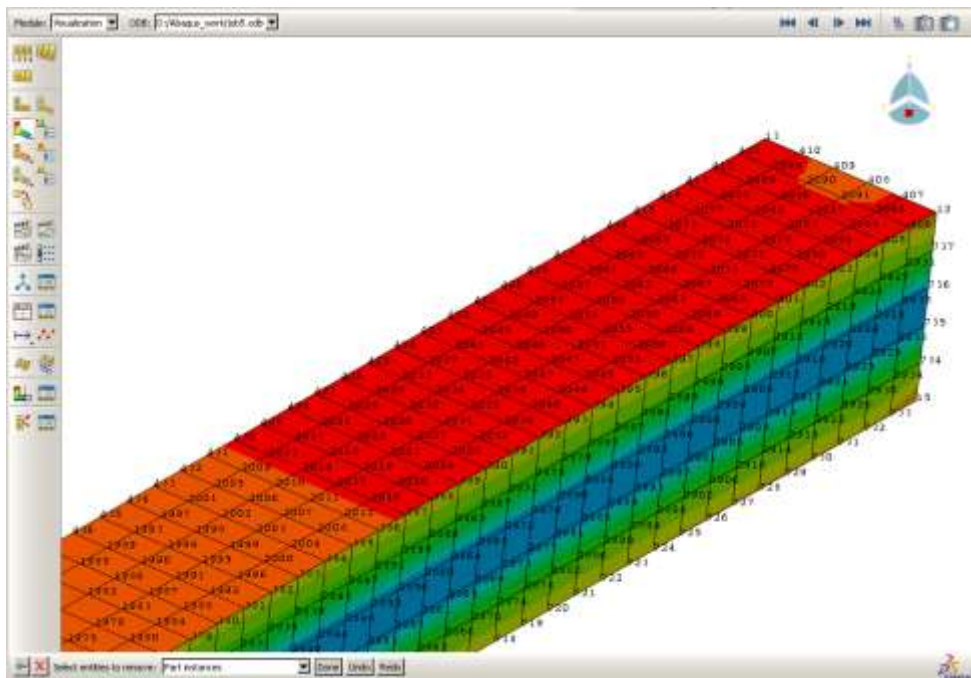


**Figure G.38: Node Labels displayed on Part**

In order to generate reports to determine the deflections at particular sections or points in the cantilever assembly, select '*Report>Field Output*' from the Main Menu bar and in the '*Report Field Output*' dialog box select the options that are needed. In order to obtain results at particular nodes select the '*Unique Nodal*' option within '*Position*', in the '*Variable*' section of the '*Report Field Output*' dialog box. It is also possible to give a unique name to the report file be generated as well as to arrange output according to the node label, element label and so on within the '*Setup*' section of the '*Report Field Output*' dialog box. The report

generation procedure outlined above is illustrated in Figure G.39, and the generated field report in turn is shown in Figure G.40.

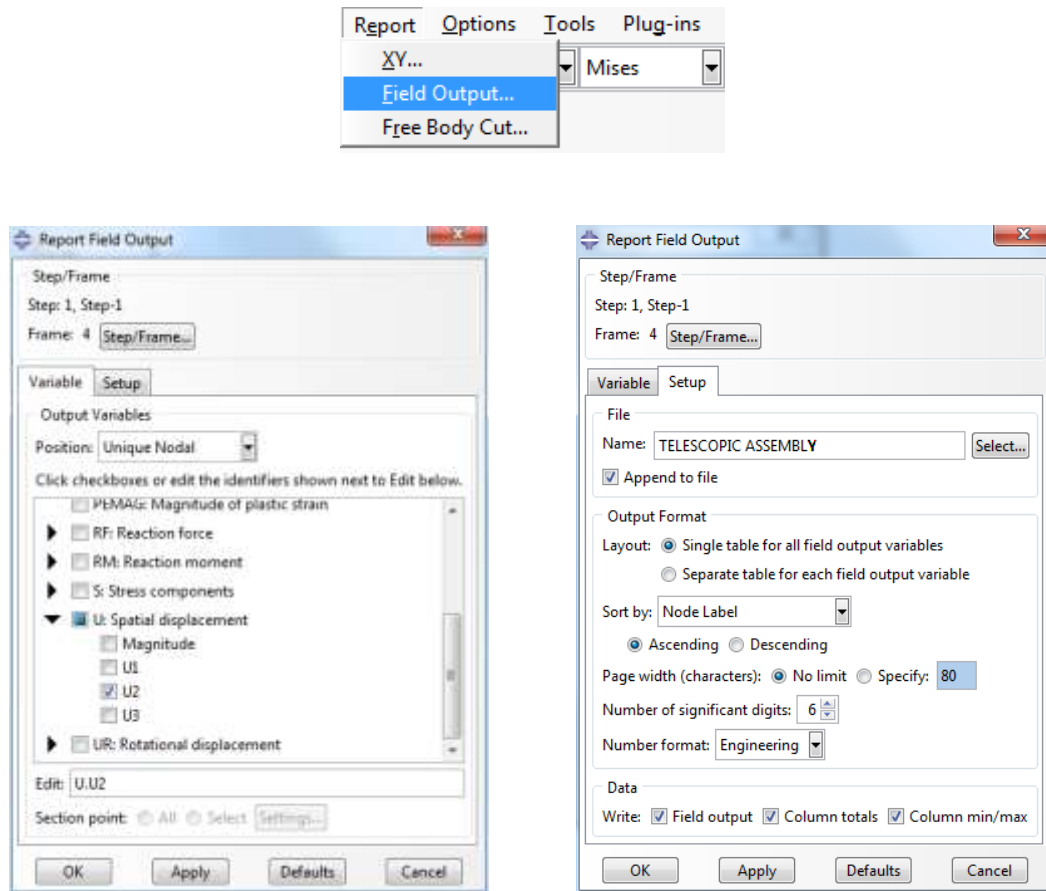


**Figure G.39: Report Generation Procedure for deflection magnitude extraction at individual nodes**

```

ODB: Z:/THESIS/ABAQUS FROM GEORGEKITTY/DEFLECTION1.odb
Step: Step-1
Frame: Increment 4: Step Time = 1.000

Loc 1: Nodal values from source 1
Output sorted by column "Node Label".
Field output reported at nodes for part: BEAM1-1

```

Node Label	U,U2 @Loc 1
1	-279.738E-03
2	-279.809E-03
3	-802.549E-39
4	-803.102E-39
5	-279.809E-03
6	-5.65709E-36
7	-279.738E-03
8	-803.102E-39
9	-279.747E-03
10	-279.781E-03
11	-279.809E-03
12	-279.803E-03
13	-279.797E-03
14	-276.258E-03
15	-272.734E-03
16	-269.170E-03
17	-265.646E-03
18	-262.132E-03
19	-258.634E-03
20	-255.143E-03
21	-251.666E-03
22	-248.202E-03
23	-244.751E-03
24	-241.312E-03
25	-237.885E-03
26	-234.471E-03
27	-231.070E-03
28	-227.682E-03
29	-224.307E-03
30	-220.949E-03
31	-217.597E-03

**Figure G.40: Report arranged according to Node Labels**

Knowing the node numbers and their distance from the fixed end, it is possible to determine the vertical deflection values at said nodes either by means of *Report Generation Procedure* outlined in Figure G.40 as shown above or by using the *Probe function* available in ABAQUS as shown in the Figure G.41 below.

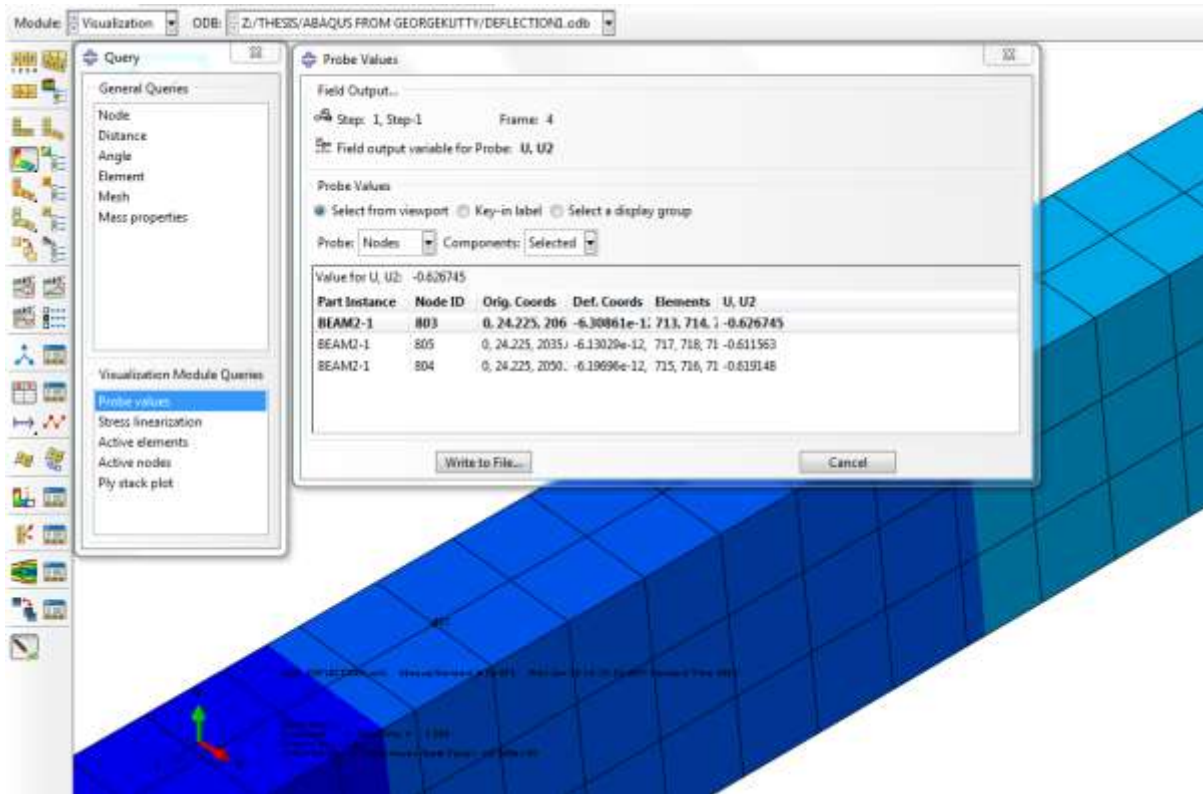


**Figure G.41: Obtaining deflection values directly using the *Probe function* available in ABAQUS**

## G.9.2 Stress Analysis Results Extraction

Once again in order to extract the desired stress values from the assembly the 'Results>Field Output' tab is selected and the desired stress component is selected as shown in Figure G.42. Figure G.43 displays the stress distribution induced by loading the cantilever. As has been outlined in the deflection extraction section in § G.9.1, the stress results can be extracted by either using report generation techniques specific to each node as outlined in Figures G.44 and G.45 or by using the *Probe function* available in ABAQUS as demonstrated in Figure G.46. It must be noted that to extract stress magnitudes using the former method, displaying node labels along the cantilever assembly as shown in Figures G.37 and G.38 is vital.

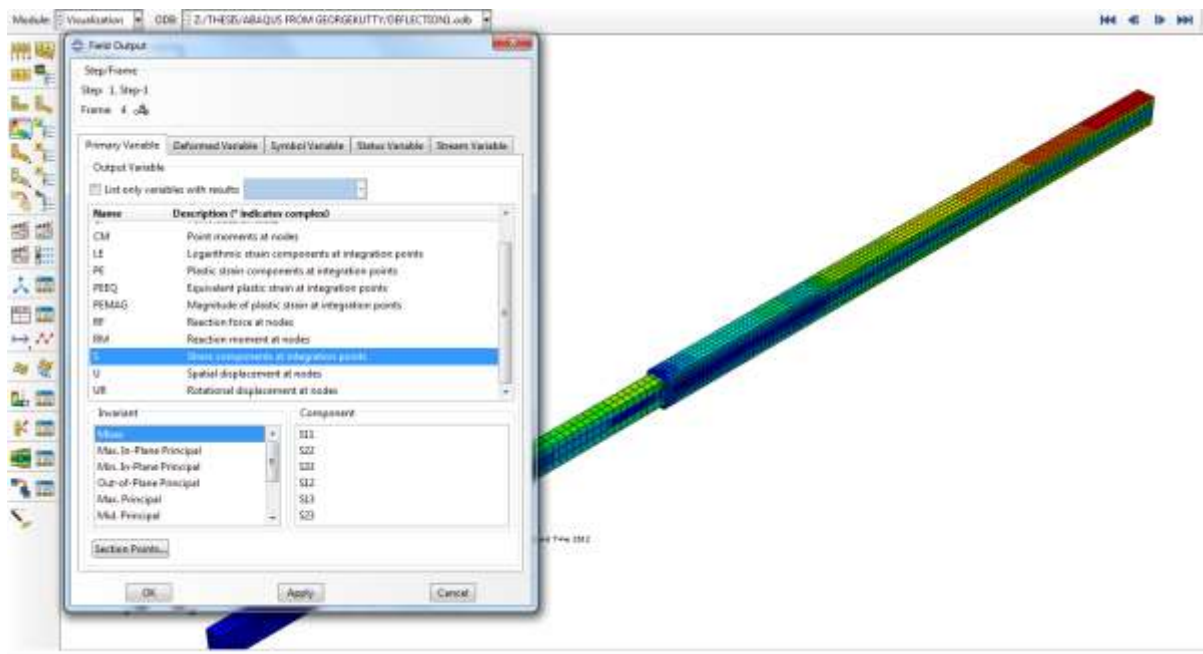


Figure G.42: Selecting the desired stress component tab



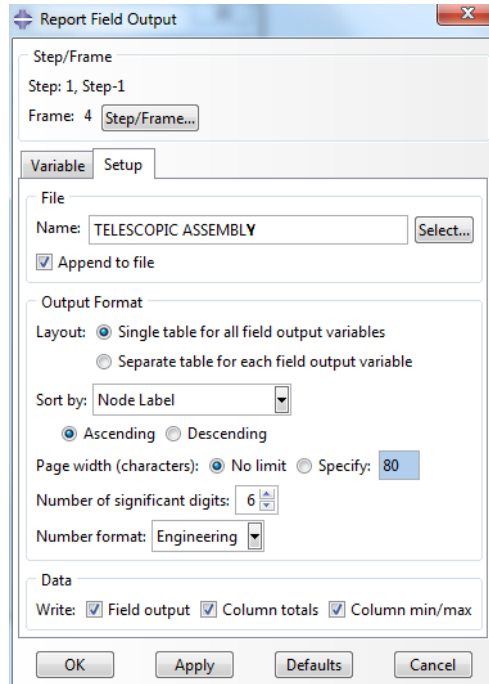
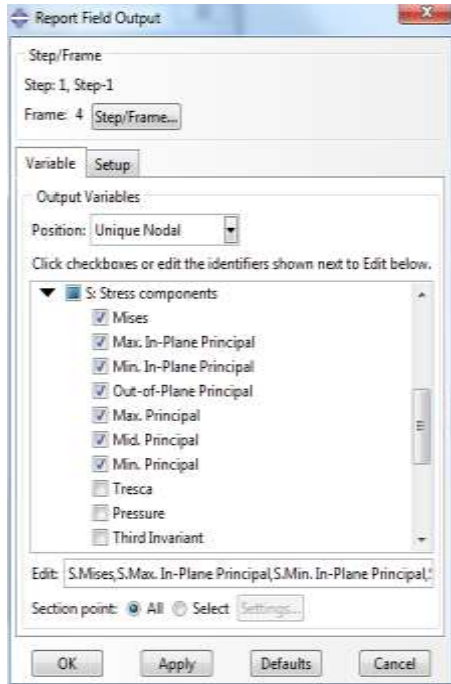
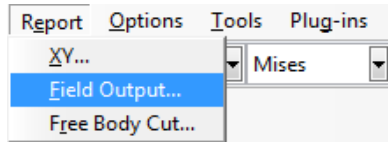


Figure G.44: Report Generation Procedure for stress determination at individual nodes

```

Step: Step-1
Frame: Increment 4: Step Time = 1.000
Loc 1 : Nodal values at shell < STEEL > < 5 section points > from source 1 : SNEG, (fraction = -1.0)
Loc 2 : Nodal values at shell < STEEL > < 5 section points > from source 1 : SPOS, (fraction = 1.0)
Loc 3 : Nodal values from source 1
output sorted by column "Node Label".
Field Output reported at nodes for region: BEAM1-1.Region_1
Computation algorithm: EXTRAPOLATE_COMPUTE_AVERAGE
Averaged at nodes
Averaging regions: ODB_REGIONS

```

Node Label	S.Mises @Loc 1	S.Mises @Loc 2	S.Max. In-P @Loc 1	S.Max. In-P @Loc 2	S.Min. In-P @Loc 1	S.Min. In-P @Loc 2
1	892.138E-03	1.21691	-68.6248E-03	991.034E-03	-924.468E-03	-367.186E-03
4	13.3027	11.7706	14.1155	12.5270	1.81143	1.69691
7	892.138E-03	1.21691	-68.6247E-03	991.034E-03	-924.468E-03	-367.186E-03
8	13.3027	11.7706	14.1155	12.5270	1.81143	1.69691
148	12.9448	12.2792	13.1867	12.7296	588.500E-03	995.443E-03
149	12.8287	12.3944	12.6988	12.4725	-247.251E-03	158.709E-03
150	13.0283	12.2941	13.0495	12.2929	43.0218E-03	-2.39206E-03
151	13.0166	12.4300	12.9923	12.4112	-48.3504E-03	-37.4607E-03
152	12.9857	12.2810	12.9850	12.2726	-1.22284E-03	-16.7937E-03
153	12.9058	12.2516	12.9061	12.2523	786.532E-06	1.31295E-03
154	12.8475	12.1807	12.8425	12.1797	-9.85597E-03	-1.96375E-03
155	12.7841	12.1222	12.7849	12.1239	1.60575E-03	3.33374E-03
156	12.7242	12.0677	12.7213	12.0680	-5.82527E-03	498.208E-06
157	12.6636	12.0078	12.6630	12.0089	-1.22631E-03	2.04075E-03
158	12.6037	11.9520	12.6020	11.9528	-3.54974E-03	1.45321E-03
159	12.5428	11.8944	12.5416	11.8952	-2.40335E-03	1.56168E-03
160	12.4832	11.8371	12.4818	11.8379	-2.91907E-03	1.67735E-03
161	12.4223	11.7804	12.4209	11.7811	-2.62971E-03	1.43274E-03
162	12.3626	11.7226	12.3612	11.7235	-2.79086E-03	1.64971E-03
163	12.3018	11.6660	12.3004	11.6667	-2.62578E-03	1.40429E-03
164	12.2419	11.6084	12.2405	11.6091	-2.74128E-03	1.57286E-03
165	12.1812	11.5515	12.1799	11.5522	-2.60182E-03	1.38864E-03
166	12.1212	11.4941	12.1199	11.4948	-2.69197E-03	1.49694E-03
167	12.0607	11.4371	12.0594	11.4378	-2.58201E-03	1.36587E-03
168	12.0006	11.3798	11.9993	11.3805	-2.64129E-03	1.42964E-03
169	11.9401	11.3228	11.9389	11.3234	-2.56066E-03	1.33560E-03
170	11.8800	11.2655	11.8787	11.2662	-2.59528E-03	1.36902E-03
171	11.8196	11.2084	11.8183	11.2090	-2.53642E-03	1.29981E-03
172	11.7593	11.1511	11.7581	11.1518	-2.52689E-03	1.31362E-03
173	11.6990	11.0940	11.6977	11.0947	-2.50933E-03	1.26046E-03
174	11.6387	11.0368	11.6375	11.0374	-2.51406E-03	1.26148E-03
175	11.5784	10.9797	11.5772	10.9803	-2.47992E-03	1.21899E-03

Figure G.45: Report arranged according to Node Labels

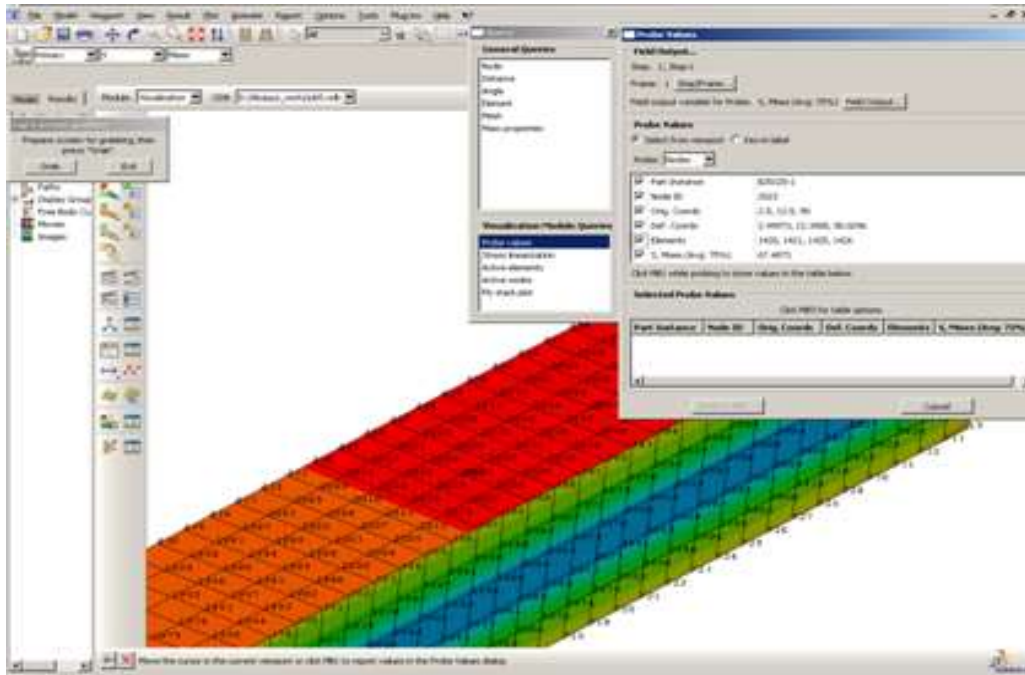


**Figure G.46: Obtaining Stress values directly using the Probe function available in ABAQUS**

### G.9.3 Buckling Analysis Results Extraction

Following completion of the FEA procedure to determine the critical buckling load of the telescoping assembly for varying overlap lengths as detailed in Table 7.3, the results are plotted as shown in Figure 7.10. To avoid duplication, only the determination of the critical buckling load for the telescoping assembly for an overlap ratio of 0.2 is extracted here using the Eigen values generated as is shown in Figure G.47.

From Figure G.47, the first Eigen value of 15.648 is extracted and substituted in the formulae for generating the Critical buckling load [107] as follows:

$$\text{Critical Buckling Load} = \text{Dead Load} + \text{Live Load} \times \text{Eigen Value}$$

As per Figures G.25 and G.26, the dead and live loads are entered as 5000 N and 500 N respectively, and the buckling load is computed as 12,824 N.

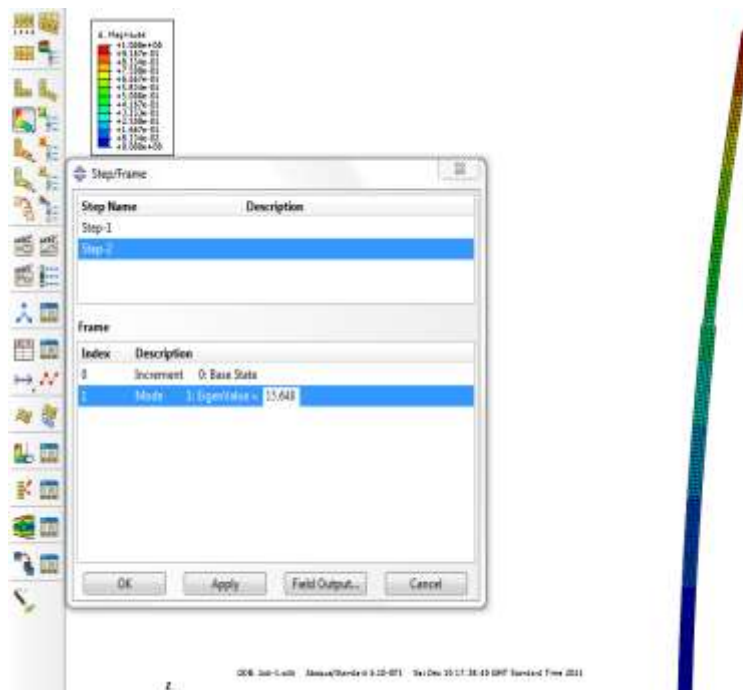


**Figure G.47: Determination of critical buckling load for the telescopic arrangement, for an overlap ratio of 0.2. The single Eigen value generated is highlighted and substituted in the equation above to determine the critical buckling load.**

## **APPENDIX H**

## APPENDIX H – STRAIN GAUGING PRINCIPLES AND PROCEDURES

Strain is a fundamental engineering phenomenon. It exists in all matter at all times, due either to external load or to the weight of the matter itself. Strains vary in magnitude from automatic dimensions to distances easily discernible by the naked eye, depending upon the materials and loads involved. Scientists and engineers have worked for centuries in the attempt to measure strain accurately, but only the last few decades have seen outstanding advancement in the art of strain measurement.

The term strain and linear deformation are synonymous and, as used in engineering, refer to change in any linear dimension of a body, usually due to application of external forces. The strain in a piece of rubber when loaded is ordinarily apparent to the eye but strain in a steel structure or a rigid body may not be. Average unit strain is the total deformation of the body in a given direction divided by the original length in that direction and as such because of its dimensionless character has much greater significance than total strain. Strain gauges are used to determine unit strain.

Keeping in mind the relationship between stress and strain, it becomes apparent that we can determine the average intensity of stress in a body under some given external load by measuring strains and multiplying by the modulus of elasticity. This is one method in which stress can be determined, since stress is not a fundamental physical quantity like strain but only a derived quantity. It is no wonder then that a great deal of effort has been expended towards prefacing a universal strain gauge. In attempting to develop such a strain gauge an ideal might be set up as a goal. This ideal strain gauge would be

1. Extremely small in size
2. Of significance mass
3. Easy to attaché to the member being analyzed
4. Highly sensitive to the strain
5. Unaffected by the temperature, vibration, humidity, or other ambient conditions such as to be encountered in testing machine parts under service load
6. Capable of indicating both static and dynamic strains
7. Capable of remote indication and recording
8. Characterized by the gauge length

External force applied to an elastic material generates stress, which subsequently generates deformation of the material. the length  $L$  of the material extends to  $L+\Delta L$  if applied force is a tensile force. The ratio of  $\Delta L$  to  $L$ , that is  $\Delta L/L$ , is called strain. (Precisely, this is called normal strain or longitudinal strain.) On the other hand, if compressive force is applied, the length  $L$  is reduced to  $L- \Delta L$ . Strain this time is  $(- \Delta L)/L$ . Strain is usually represented as  $\epsilon$ .

Supposing the cross sectional area of the material to be  $A$  and the applied force to be  $P$ , stress  $\sigma$  will be  $P/A$ , since a stress is a force working on a definite cross sectional area. In a simple uniaxial stress field as illustrated below, strain  $\epsilon$  is proportional to stress  $\sigma$ , thus an equation  $\sigma = E \times \epsilon$  is satisfied, provided that the stress  $\sigma$  does not exceed the elastic limit of the material.  $E$  in the equation is the elastic modulus (Young's modulus) of the material.

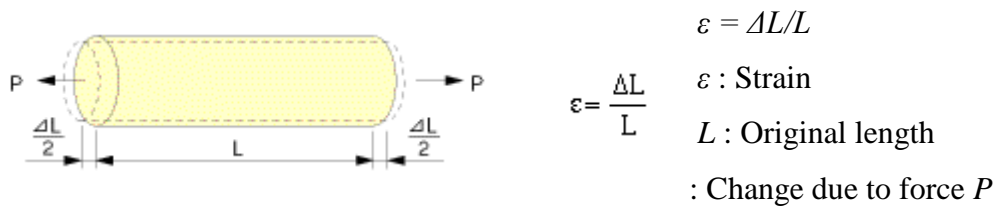


**Figure H.1: Simple illustration for the strain measurement.**

Because longitudinal strain is a ratio between lengths of two wires, it is a quantity having no dimension. Usually it is represented in a unit of  $1 \times 10^{-6}$ , since the ratio of deformation is often very small. Strain may be compressive or tensile and is typically measured by strain gauges. It was Lord Kelvin who first reported in 1856 that metallic conductors subjected to mechanical strain exhibit a change in their electrical resistance. This phenomenon was first put to practical use in the 1930s. Fundamentally, all strain gauges are designed to convert mechanical motion into an electronic signal. A change in capacitance, inductance, or resistance is proportional to the strain experienced by the sensor. If a wire is held under tension, it gets slightly longer and its cross-sectional area is reduced. This changes its resistance ( $R$ ) in proportion to the strain sensitivity ( $S$ ) of the wire's resistance. In a strain gauge  $S$  is the gauge factor defined as

$$\frac{\Delta R}{R} \propto \epsilon$$

$$\frac{\Delta R}{R} = S\varepsilon = S \frac{\Delta L}{L}$$

$$S = \frac{\Delta R/R}{\Delta L/L}$$

## H.1 The Strain Gauge

The electrical resistance of a length of wire varies in direct proportion to the change in any strain applied to it. That's the principle upon which the strain gauge works. The most accurate way to measure this change in resistance is by using the Wheatstone bridge. This is a balanced electrical circuit which displays any resistance change on an indicator or feeds it into a process.

The main component of a strain gauge is a strain sensitive alloy. The most common is constantan at a thickness of 0.0001 inch, which is used in the foil grid. Constantan also has the best combination of properties necessary for many strain gauge applications. The grid consists of a photo-etched pattern mounted on a very thin backing made from a plastic such as polyimide, epoxy or glass-fiber reinforced epoxy-phenolic approximately 0.001 inch thick. This backing allows the strain gauge to be handled during installation. It also provides a ready-to-bond surface for cementing the gauge to the specimen, and electrical insulation between the metal foil and the test piece.

Depending on the particular application, there's a wide range of foils and backings to choose from. There are also many factors to consider when selecting a gauge. These include temperature range, test frequency, elongation, environment and nominal resistance, and so on. Depending on the purpose and accuracy strain gauges can be classified as follows

### 1. General Purpose Gauges

This type of gauges are used in general applications such as measuring strain in a simple cantilever, pressure vessel etc. depending on the orientation of grid pattern it can be classified as follows.

**(a) Uniaxial gauge (Figure H.2)**

Gauge with a single grid for measuring strain in the grid direction. A typical uniaxial strain gage pattern designed to measure strains in the direction of the gridlines. Gauge lengths for *Micro-Measurements* strain gauges range from 0.008 in to 4.000 in (0.20 mm to 101.6 mm).

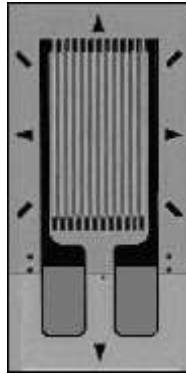


**Figure H.2: Uniaxial strain gauge [112]**

**(b) Biaxial Rosettes (Figure H.3)**

Gauge with two perpendicular grids used to determine principal strains when their directions are known.

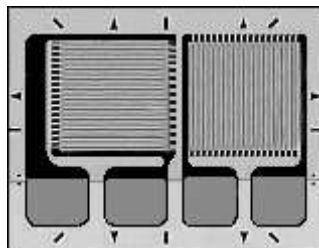


**Figure H.3: Biaxial rosette [112]**

The biaxial ("Tee") rosette pattern has two measuring grids perpendicular to one another. Planar rosettes, like the one shown here, are constructed with all grids on the same plane. Stacked rosettes are also available with separate grids "stacked" on top of one another. At the gauge position two independent measurements are made in perpendicular directions these normally being aligned with strain directions.

**(c) Three-Element Rosettes (Figure H.4)**

Gauge with three independent grids in three different directions are used for ascertaining the principal strains and their directions. The typical "rectangular" rosette pattern shown here has

its three independent grids oriented at 0, 45, and 90 degrees. "Delta" patterns, with grids at 0, 60, and 120 degrees, are also available. Planar rosettes, like the one shown here, are constructed with all grids on the same plane. Stacked rosettes are also available with separate grids "stacked" on top of one another. With three independent strain measurements at the gauge installation, the principal strains and their directions can be calculated.

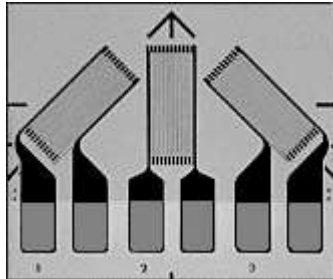


**Figure H.4: Three element rosette [112]**

**(d) Shear Patterns (Figure H.5)**

Gauges having two chevron grids are used in half-bridge circuits for direct indication of shear strain arising under torsion and shear loadings.

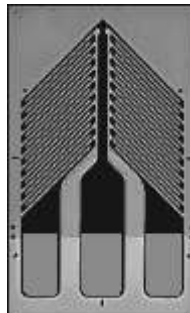


**Figure H.5: Shear patterns [112]**

Shear gauges have two grids in a chevron pattern that sense normal strains in perpendicular directions  $\pm 45^\circ$  to the torque axis. The grids often have a common connection for use in half-bridge circuits which yield the shear strain (difference in normal strains) directly when shear pattern gauges are used.

**2. Transducer-Class Gauges**

Transducer-Class strain gauges are a select group of gauge patterns designed specifically for transducer applications. The main objective is optimum gauge performance at lower cost in high-volume production quantities.

Exclusive features of Transducer-Class gauges include:

1. Optimum backing thickness tolerance - This is particularly important to minimize creep variations between gage installations.
2. Uniform backing trim dimensions - Matrix dimensions listed have a tolerance of  $\pm 0.005$  in ( $\pm 0.13$  mm) on any edge (measured from grid centrelines).
3. Multiple creep compensation choices for most gauge patterns - A close inspection of the gauge pattern will reveal a small letter on the gauge matrix next to the grid.
4. Special pattern refinement for improved gauge-to-gauge reproducibility the creep variation due to operating temperature changes is reduced.

### **3. Special-Purpose Sensors**

This includes variety of products designed to meet special needs and perform special functions in experimental stress analysis. These include:

1. Bondable Temperature Sensors - With nickel-foil grids, these sensors are used for general-purpose temperature measurements over the range of  $-320$  to  $+500^{\circ}$  F ( $-195$  to  $+260^{\circ}$  C).
2. Crack Detection Gauges - Convenient, economical method of detecting cracks or crack growth.
3. Crack Propagation Gauges - Multiple conducting grids on a single backing accurately indicate the rate of crack propagation.
4. Weldable Gauges - Strain gauges and temperature sensors bonded to a metal carrier for spot welding to a test structure when adhesive cannot be used or minimum installation time is required.
5. Shear Modulus Gauges - Special gauges for accurately determining the shear modulus of composite materials within standard obsolete and compact test specimens.
6. Embedment Strain Gauges - Special strain sensors for embedding in concrete.

## H.2 Strain Transformation and Rosette Gauge Theory

It is often desired to measure the full state of strain on the surface of a part, that is to measure not only the two extensional strains,  $\varepsilon_x$  and  $\varepsilon_y$ , but also the shear strain,  $\gamma_{xy}$ , with respect to co-ordinate  $x,y$ . It is clear that a single gauge is capable only of measuring the extensional strain in the direction that the gauge is oriented. Assuming that the  $x$  and  $y$  axes are specified, it would be possible to mount two gauges in the  $x$  and  $y$  directions, respectively to measure the associated extensional strains in these directions. However, there is no direct way to measure the shear strain,  $\gamma_{xy}$ . Nor is it possible to measure the principal strains since the principal directions are not generally known.

The solution to this problem lies in recognizing that the 2D state of strain at a point (on a surface) is defined by three independent quantities which can be taken as either: (a)  $\varepsilon_x$ ,  $\varepsilon_y$ , and  $\gamma_{xy}$ , or (b)  $\varepsilon_1$ ,  $\varepsilon_2$ , and  $\theta$ , case (a) refers to strain components with respect to an arbitrary  $x$ - $y$  axis system, and case (b) refers to the two principal strains and their perpendicular directions. Either case defines the state of 2D strain on the surface and can be used to compute strains with respect to any other co-ordinate system. This situation implies that it should be possible to determine these 3 independent quantities if it is possible to make three independent measurements of strain at a point on the surface. The most obvious approach is to place three strain gauges together in a “rosette” with each gauge oriented in a different direction and with all of them located as close together as possible to approximate to measurements at a point. As will be shown below, if the three strains and the gauge directions are known, it is possible to solve for the principal strains and their directions or equivalently, the state of strain with respect to an arbitrary  $x$ - $y$  coordinate system. The relations needed are the strain transformation equations for which Mohr’s Circle construction provides a good visualization of this process.

### 2D Strain Transformation and Mohr’s Circle

The two dimensional strain transformation equations are very similar to stress transformation equations and are represented below.

$$\begin{aligned}\varepsilon_x' &= \varepsilon_x \cos^2 \phi + \varepsilon_y \sin^2 \phi + \gamma_{xy} \sin \phi \cos \phi \\ \varepsilon_y' &= \varepsilon_x \sin^2 \phi + \varepsilon_y \cos^2 \phi + \gamma_{xy} \sin \phi \cos \phi\end{aligned}\tag{H.1}$$

$$\gamma'_{xy} = 2(\varepsilon_y - \varepsilon_x)\sin\phi\cos\phi + \gamma_{xy}(\cos^2\phi - \sin^2\phi)$$

These transformation equations involve squares and products of sine and cosine functions and these can be replaced with double-angle results to yield the double-angle form of the transformation equations:

$$\varepsilon'_x = \frac{1}{2}(\varepsilon_x + \varepsilon_y) + \frac{1}{2}(\varepsilon_x - \varepsilon_y)\cos 2\phi + \frac{\gamma_{xy}}{2}\sin 2\phi$$

$$\varepsilon'_y = \frac{1}{2}(\varepsilon_x + \varepsilon_y) - \frac{1}{2}(\varepsilon_x - \varepsilon_y)\cos 2\phi - \frac{\gamma_{xy}}{2}\sin 2\phi \quad (\text{H.2})$$

$$\gamma'_{xy} = -(\varepsilon_x - \varepsilon_y)\sin 2\phi + \gamma_{xy}\cos 2\phi$$

Given the ready availability of powerful calculators and spreadsheets, evaluation of these transformation equations is a relatively simple matter today and involves little more than a few seconds to enter the formula in a calculator or a spreadsheet. This was not always so simple a task and the Mohr's Circle graphical representation as in Figure H.6, was developed long ago to aid in this process. Today, Mohr's Circle is not needed for graphical calculation, but it does provide a good visualization of the transformation equations and the geometry can be used to infer the actual form for the equations needed for execution in a calculator or computer.

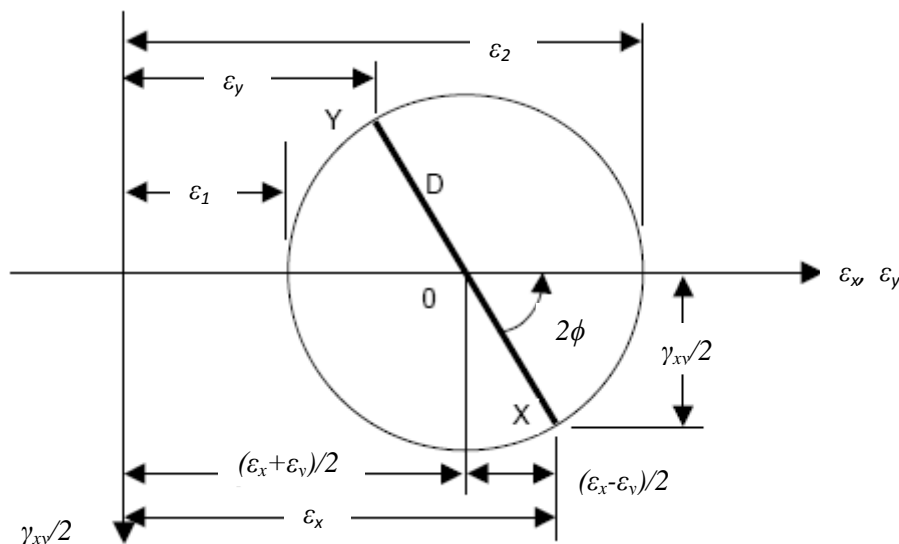


**Figure H.6: Basic Mohr's circle geometry**

The double-angle form of the transformation relations involve simple sine and cosine terms along with a constant that should suggest equations of a circle with centre away from the coordinate origin. The trick here is to identify the appropriate new  $x$  and  $y$  values to plot to construct a circle. This is perhaps easier to do by explaining the Mohr's Circle than it is to actually deduce the form directly. Figure H.6 above shows Mohr's Circle for a state of strain defined by  $xy$  axis. Assume for the moment that the coordinates of the opposite ends (X,Y) of the indicated diameter of the circle define the strain state,  $\varepsilon_x$ ,  $\varepsilon_y$ , and  $\gamma_{xy}$ , in the  $xy$  axis system. Note that both the  $\varepsilon_x$  and  $\varepsilon_y$  extensional strains are plotted on the abscissa ( $x$  axis) while one-half the shear strain,  $\gamma_{xy}/2$ , is plotted along the ordinate. The positive direction for  $\gamma_{xy}$ , is taken to be downward.

One can construct the circle by first plotting the  $(\varepsilon_x, \gamma_{xy}/2)$  pair as point X on the diameter. Next, the pair  $(\varepsilon_y, -\gamma_{xy}/2)$  are plotted as the opposite end Y of the diameter, and the circle can be constructed with X-Y as the diameter. This is the basic Mohr's circle and it always has its centre on the abscissa at a point given by the value  $(\varepsilon_x + \varepsilon_y)/2$ . The circle diameter is easily

computed as: 
$$D = \sqrt{\left(\gamma_{xy}^2 + (\varepsilon_x - \varepsilon_y)^2\right)}$$

So far, there is no clear connection to the double-angle transformation equations above, but this will become evident in a moment. To calculate a new state of strain,  $\varepsilon_x'$ ,  $\varepsilon_y'$  and  $\gamma_{xy}'$  in an  $x',y'$  co-ordinates rotated  $\theta$  counterclockwise from the  $x,y$  axis system, one must construct a new diameter for Mohr's Circle rotated  $2\theta$  counterclockwise from the initial X-Y diameter as shown below in Figure H.7. The coordinates of the new diameter endpoints, X'-Y', represent the new strain state as computed from the double-angle strain transformation equations. This should be clear by inspection of the Mohr's Circle and by evaluation of the circle geometry as shown. Note that rotation in Mohr's Circle is always twice the geometric rotation so that the state of strain defined by opposite ends of a diameter of the circle (e.g.,  $180^\circ$  apart) corresponds to strains that are at  $180^\circ/2=90^\circ$  in geometric axes.

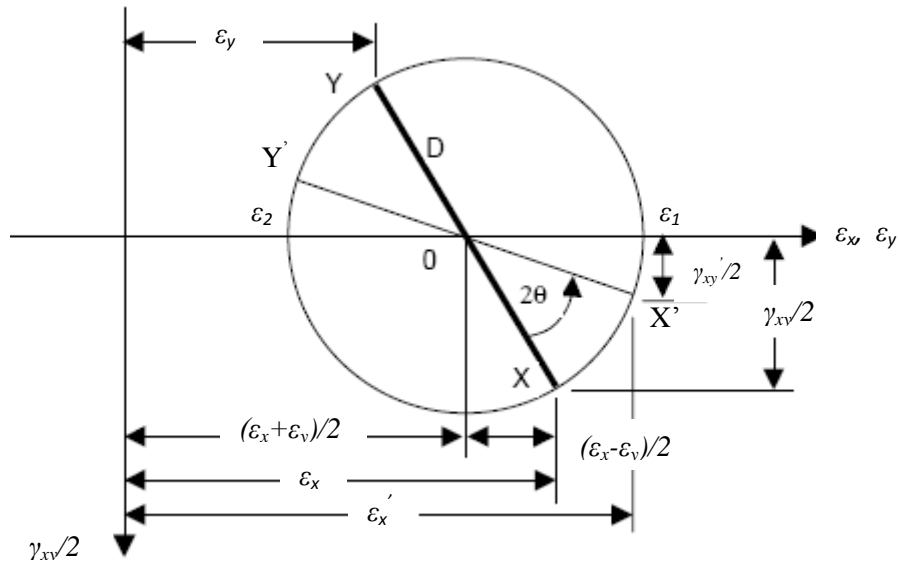


**Figure H.7: Strain transformation of  $\theta$**

It should be pointed out also that this particular form for Mohr's Circle uses an inverted ordinate (y axis) and positive  $\theta$  is counterclockwise. Another popular form for Mohr's Circle uses an upward positive ordinate axis and positive clockwise  $\theta$ . It is strikingly apparent from Figure H.7 that there is a state of strain that does not involve any shear strain and this corresponds to the circle diameter lying along the abscissa and defined by the two points,  $\epsilon_1$  and  $\epsilon_2$  which are the extremities of the diameter as shown. These are called the principal strains and they are associated with an  $x'y'$  axis system rotated,  $\phi$ , counterclockwise from the  $xy$  axis ( $2\phi$  in Mohr's Circle). This defines not only the principal strain magnitudes but also their directions (a,b) torsion and shear, © plane strain and (d) equi-biaxial tension. Figure H.8 shows other useful Mohr's Circle configurations.

### Strain Gauge Rosettes

Strain gauge rosettes consist of two or more co-located strain gauges oriented at a fixed angle with respect to each other. Strict co-location of the gauges requires mounting each individual gauge on top of the others in what is called a stacked rosette, but this leads to a complicated and often inaccurate type of gauge. The more common approach is to place the gauges in a tightly packed pattern as close as possible to the rosette center. Rosettes typically involve 2, 3 or 4 strain gauges with relative orientations of  $30^\circ$ ,  $45^\circ$ ,  $60^\circ$  or  $90^\circ$ . Figure H.9 shows several examples. At least 3 independent strain readings are needed to define the 2D state of strain if no other information is available so the 3-gauge rosettes are the most popular (the  $90^\circ$  2-gauge rosette can be used to measure principal strains when the principal direction is known

and the gage can be oriented accordingly). The rectangular rosette and the delta rosette are the most commonly used 3-gauge rosettes because of their simple geometry.

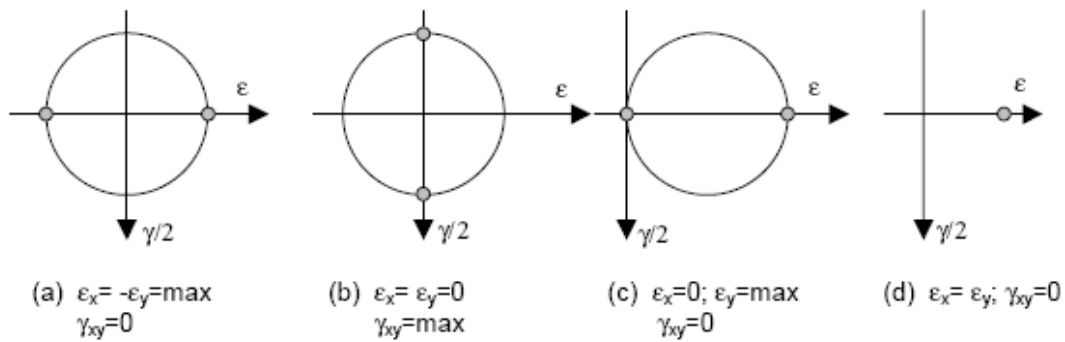


Figure H.8: Some useful Mohr's circle configurations.

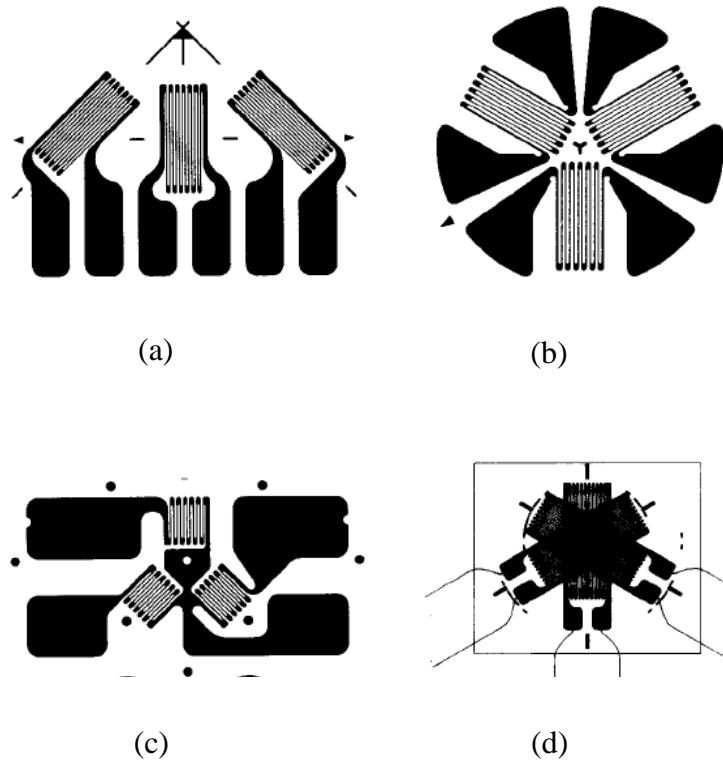
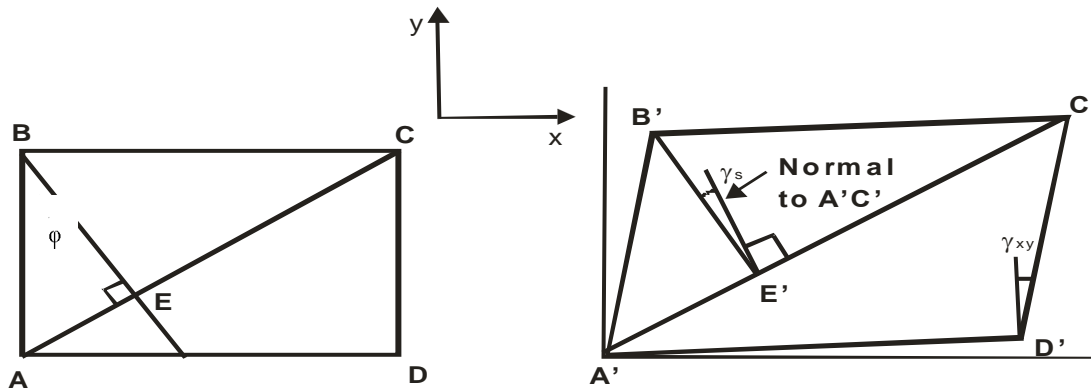


Figure H.9: Typical strain gauge rosettes (a) Rectangular rosette (b) Delta rosette (c) Delta rosette (d) Stacked delta rosette [112]

**Normal Strain  $\epsilon_n$  and Shear Strain  $\gamma_s$  at a plane inclined at  $\phi$**



**Figure H.10: Normal and Shear Strains**

Consider Figure H.10. The objective is to determine the direct strain  $\epsilon_n$  and shear strain  $\gamma_s$  for directions normal and tangential to a plane inclined at  $\theta$  due to  $\epsilon_x, \epsilon_y, \gamma_{xy}$ . The figure shows an unstrained rectangular element ABCD and its strained condition A'B'C'D'. Normal strain  $\epsilon_n$  is obtained by considering the length change along AC. Shear Strain  $\gamma_s$  is obtained by considering the rotation of BE. It can be assumed that  $\Delta A'C'D'$  is formed by AD having an extension  $\delta x$  to become A'D' and DC having an extension  $\delta y$  to become D'C'.

The shear strain  $\gamma_s$  is the rotation angle between the normal to A'C' at E' and B'E'. The shear strain  $\gamma_{xy}$  is the rotation angle between the normal to A'D' at D' and D'C'. Now the following equations can be written

$$A'D' = AD + \delta x = AD \left(1 + \frac{\delta x}{AD}\right) = AD(1 + \epsilon_x)$$

$$C'D' = CD + \delta y = CD \left(1 + \frac{\delta y}{CD}\right) = CD(1 + \epsilon_y)$$

In a similar fashion it can be said that

$$A'C' = AC(1 + \epsilon_n)$$

Now using cosine rule in  $\Delta A'C'D'$  gives

$$(A'C')^2 = (A'D')^2 + (C'D')^2 - 2A'D' \times C'D' \times \cos\left(\frac{\pi}{2} + \gamma_{xy}\right)$$

$$AC^2(1 + \varepsilon_n)^2 = AD^2(1 + \varepsilon_x)^2 + CD^2(1 + \varepsilon_y)^2 + 2AD(1 + \varepsilon_x) \times CD(1 + \varepsilon_y) \times \sin \gamma_{xy}$$

Neglecting higher powers of  $\varepsilon_n, \varepsilon_x$  and  $\varepsilon_y$  and using  $AC^2 = AD^2 + CD^2$  and  $\sin \gamma_{xy} = \gamma_{xy}$  this can be reduced to

$$AC^2(1 + 2\varepsilon_n) = AD^2(1 + 2\varepsilon_x) + CD^2(1 + 2\varepsilon_y) + 2AD \times CD \times \gamma_{xy}$$

$$2\varepsilon_n(AC)^2 = 2\varepsilon_x(AD)^2 + 2\varepsilon_y(CD)^2 + 2AD \times CD \times \gamma_{xy}$$

Dividing both sides by  $2AC^2$  and introducing  $\sin \phi$  and  $\cos \phi$  gives

$$\varepsilon_n = \varepsilon_x \cos^2 \phi + \varepsilon_y \sin^2 \phi + \gamma_{xy} \sin \phi \cos \phi$$

### Rectangular Rosette Gauge Equations

Given the measurement of 3 independent strains from the 3 gauges in a rectangular rosette it is possible to calculate the principal strains and their orientation with respect to the rosette gauge. It is also readily possible to calculate the state of strain at the gauge location with respect to any particular  $xy$  axis system using either the rosette readings or the principal strains and their axis orientation. To illustrate this, consider a situation in which the rosette is oriented with gauges labeled A, B and C at  $45^\circ$  apart as shown in Figure H.11.

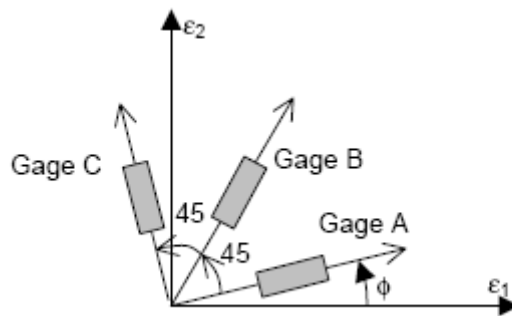


**Figure H.11: Rectangular rosette strain orientation**

Assume also that the principal strains at the rosette are oriented at an angle,  $\phi$ , to the rosette's gauge A. For this case, it is easy to use the strain transformation equations to calculate the strain in each rosette gauge in terms of the principal strains and the angle,  $\phi$ , (simply assume

$\varepsilon_x = \varepsilon_1$ ,  $\varepsilon_y = \varepsilon_2$  and  $\gamma_{xy} = 0$  and compute  $\varepsilon_x' = \varepsilon_A$ ,  $\varepsilon_B$  and  $\varepsilon_C$  for angles of rotation  $\phi$ ,  $\phi + 45^\circ$ , and  $\phi + 90^\circ$  to yield three equations:

$$\varepsilon_A = \frac{\varepsilon_1 + \varepsilon_2}{2} + \frac{\varepsilon_1 - \varepsilon_2}{2} \cos 2\phi \quad (\text{H.3a})$$

$$\varepsilon_B = \frac{\varepsilon_1 + \varepsilon_2}{2} + \frac{\varepsilon_1 - \varepsilon_2}{2} \cos 2(\phi + 45^\circ) \quad (\text{H.3b})$$

$$\varepsilon_C = \frac{\varepsilon_1 + \varepsilon_2}{2} + \frac{\varepsilon_1 - \varepsilon_2}{2} \cos 2(\phi + 90^\circ) \quad (\text{H.3c})$$

In a plane strain situation the full state of strain on the surface of a part can either be defined with three measurements, to including two normal strains,  $\varepsilon_x$  and  $\varepsilon_y$ , and one the shear strain,  $\gamma_{xy}$ , with respect to co-ordinates  $x$ - $y$ ; or two the principal strains  $\varepsilon_1$  and  $\varepsilon_2$ . Gauges however are capable only of measuring the extensional strain in the direction that the gauge is oriented. Therefore a rosette with three gauges is needed for the measurements. In Equations (H.3 (a-c)), these are 3 simultaneous equations relating  $\varepsilon_A, \varepsilon_B, \varepsilon_C$  to  $\varepsilon_1, \varepsilon_2, \phi$ . It is a relatively simple matter to invert these and solve for  $\varepsilon_1, \varepsilon_2, \phi$  in terms of  $\varepsilon_A, \varepsilon_B, \varepsilon_C$  yielding:

$$\varepsilon_1 = \frac{\varepsilon_A + \varepsilon_C}{2} + \frac{1}{\sqrt{2}} \sqrt{[(\varepsilon_A - \varepsilon_B)]^2 + (\varepsilon_B - \varepsilon_C)^2} \quad (\text{H.4a})$$

$$\varepsilon_2 = \frac{\varepsilon_A + \varepsilon_C}{2} - \frac{1}{\sqrt{2}} \sqrt{[(\varepsilon_A - \varepsilon_B)]^2 + (\varepsilon_B - \varepsilon_C)^2} \quad (\text{H.4b})$$

$$\tan 2\phi = \frac{2\varepsilon_B - \varepsilon_A - \varepsilon_C}{\varepsilon_A - \varepsilon_C} \quad (\text{H.4c})$$

The equations obtained above can be used to compute the principal strains and the principal axis orientation directly from the rectangular rosette gauge readings. Note that there are many different possible gauge numbering arrangements besides the particular A, B, C layout here, and they can lead to forms for the final results shown above but with A, B and C interchanged. It should be noted that the above results can also be developed directly from the Mohr's Circle representation with about the same amount of effort and perhaps a bit more visualization of the results alternatively. It is somewhat simpler to arrange the rosette such

that gauge A is along the x axis and gauge C is along the y axis. Here  $x, y$  are not principal directions when from Equation H.3 it follows that:

$$\varepsilon_A = \frac{1}{2}(\varepsilon_x + \varepsilon_y) + (\varepsilon_x - \varepsilon_y)\cos(2 \times 0^\circ) + \frac{1}{2}\gamma_{xy}\sin(2 \times 0^\circ) = \varepsilon_x$$

$$\varepsilon_B = \frac{1}{2}(\varepsilon_x + \varepsilon_y) + (\varepsilon_x - \varepsilon_y)\cos(2 \times 45^\circ) + \frac{1}{2}\gamma_{xy}\sin(2 \times 45^\circ) = \frac{1}{2}(\varepsilon_x + \varepsilon_y) + \frac{1}{2}\gamma_{xy}$$

$$\varepsilon_C = \frac{1}{2}(\varepsilon_x + \varepsilon_y) + (\varepsilon_x - \varepsilon_y)\cos(2 \times 90^\circ) + \frac{1}{2}\gamma_{xy}\sin(2 \times 90^\circ) = \varepsilon_y$$

These equations can readily be solved for the strain in the  $x$ - $y$  co-ordinates:

$$\varepsilon_x = \varepsilon_A \tag{H.5a}$$

$$\varepsilon_y = \varepsilon_C \tag{H.5b}$$

$$\gamma_{xy} = 2\varepsilon_B - \varepsilon_A - \varepsilon_C \tag{H.5c}$$

This defines the strain state at the rosette with respect to co-ordinates  $x$ - $y$ . It is a simple matter to now construct a Mohr's Circle and from this to compute the principal strains and their orientation with respect to the  $x$ - $y$  axis (and therefore the rosette). Figure H.12 summarizes the results and reveals clearly that the maximum shear strain is given by twice the radius of the Mohr's Circle, and in this case it can be computed in terms of principal strains as:  $\gamma_{\max} = |(\varepsilon_1 - \varepsilon_2)|/2$ .

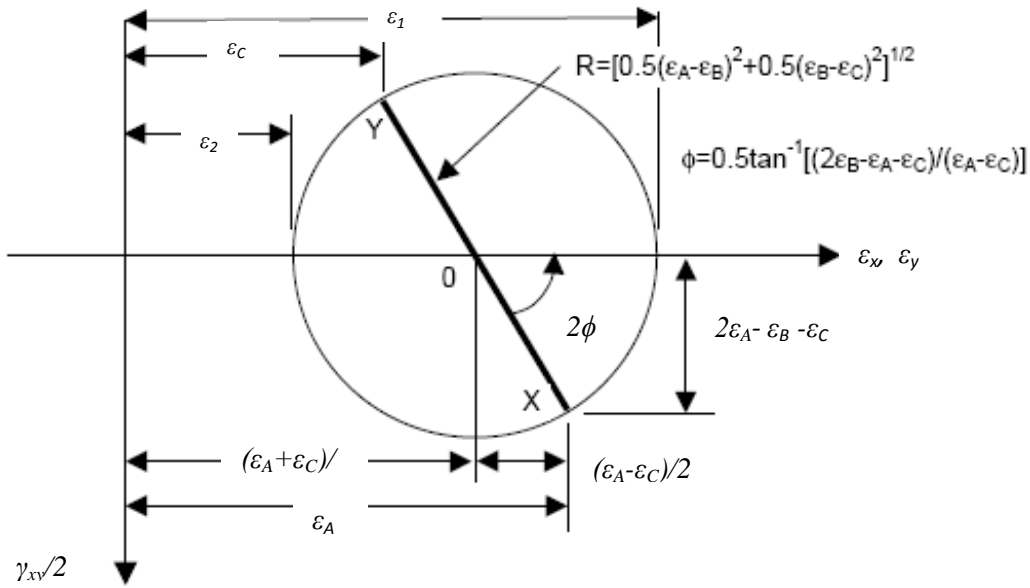


**Figure H.12: Mohr's circle for rectangular rosette**

Alternatively the principal strain equations may be applied to Equations (H.5a-c) to give

$$\varepsilon_1 = \frac{\varepsilon_A + \varepsilon_C}{2} + \frac{1}{\sqrt{2}} \sqrt{[(\varepsilon_A - \varepsilon_B)^2 + (\varepsilon_B - \varepsilon_C)^2]}$$

$$\varepsilon_2 = \frac{\varepsilon_A + \varepsilon_C}{2} - \frac{1}{\sqrt{2}} \sqrt{[(\varepsilon_A - \varepsilon_B)^2 + (\varepsilon_B - \varepsilon_C)^2]}$$

$$\tan 2\phi = \frac{2\varepsilon_B - \varepsilon_A - \varepsilon_C}{\varepsilon_A - \varepsilon_C}$$

### Principal Stresses

It should be pointed out that the above results involve strain only and do not describe the state of stress at the rosette. In order to determine the stress state, it is necessary to use the stress strain relations to express the stress components in terms of the strain components. For linearly elastic (Hookean) behavior, it follows that the principal stresses can be computed from the principal strains (shear strain is zero for principal directions). Principal stresses are obtained using the following equations:

$$\varepsilon_1 = \frac{\sigma_1}{E} - \frac{\nu\sigma_2}{E} \tag{H.6a}$$

$$\varepsilon_2 = \frac{\sigma_2}{E} - \frac{\nu\sigma_1}{E} \tag{H.6b}$$

From Equations (H.6a, b):

$$\sigma_1 = \frac{E}{(1-\nu^2)} [\varepsilon_1 + \nu\varepsilon_2]$$

$$\sigma_2 = \frac{E}{(1-\nu^2)} [\varepsilon_2 + \nu\varepsilon_1]$$

### H.3 Instrumentation and Data Acquisition System

The basic principles for accurate measurement were established many years ago. Modern technology offers better techniques, better resolution, the potential for higher accuracies, but primary much higher speeds for data acquisition and analysis. Almost all strain measurement systems can be broken down into components as shown in below figure.

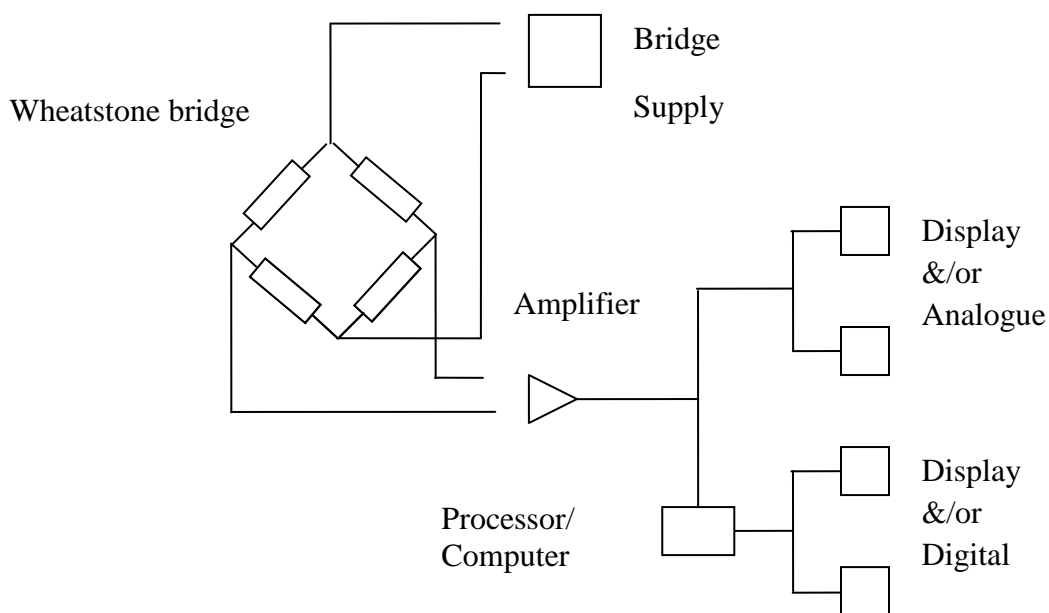


**Figure H.13: Schematic strain measurement system**

The correct choice and the proper installation are very important and it is assumed here that the gauges perform correctly. A gauge can therefore consider as a passive resistor which requires a power source. Changes in resistance caused by mechanical strain are measured in a bridge circuit which produces an out of balance voltage. This voltage needs to be amplified and after processing displayed or stored or both, after processing it to represent the required units. This manipulation may be by means of controls in hardware e.g. gauge factor control.

In a computer based system, all the manipulation may occur in the software (digital) either in the test programming, or in the data reduction and analysis, before or after storage.

For straight forward measurements of static strains from a small number of strain gauges, the commercially available self contained strain indicators are robust, reliable, accurate and almost foolproof. Similarly, for dynamic measurements from a few channels the choice of suitable strain gauge amplifiers and recorders is quite straightforward. For large test programmes, either static or elaborate dynamic systems can be built up from commercially available instrumentation and peripherals or purchased as a build system.

### **Wheatstone bridge circuit and strain gauges**

The strain gauge is connected into a Wheatstone bridge circuit with a combination of four active gauges (full bridge), two gauges (half bridge), or, less commonly, a single gauge (quarter bridge). In the half and quarter circuits, the bridge is completed with precision resistors. The complete Wheatstone bridge is excited with a stabilized DC supply and with additional conditioning electronics, can be zeroed at the null point of measurement. As strain is applied to the bonded strain gauge, a resistive change takes place and unbalances the Wheatstone bridge.

This results in a signal output, related to the strain value. As the signal value is small, (typically a few millivolts) the signal conditioning electronics provides amplification to increase the signal level to 5 to 10 volts, a suitable level for application to external data collection systems such as recorders or PC Data Acquisition and Analysis Systems.

Typical strain gauge resistances range from 30 Ohms to 3 k Ohms (unstressed). This resistance may change only a fraction of a percent for the full force range of the gauge, given the limitations imposed by the elastic limits of the gauge material and of the test specimen. Forces great enough to induce greater resistance changes would permanently deform the test specimen and/or the gauge conductors themselves, thus ruining the gauge as a measurement device. Hence, in order to use the strain gauge as a practical instrument, we must measure extremely small changes in resistance with high accuracy. Such demanding precision calls for a bridge measurement circuit. Using a Wheatstone bridge with a null-balance detector and a human operator to maintain a state of balance, a strain gauge bridge circuit measures strain by the degree of imbalance. A precision voltmeter in the centre of the bridge provides an accurate measurement of that imbalance.

### Quarter bridge strain gauge circuit

Typically, the rheostat arm of the bridge ( $R_2$  in the Figure H.14) is set at a value equal to the strain gauge resistance with no force applied. The two ratio arms of the bridge ( $R_1$  and  $R_3$ ) are set equal to each other. Thus, with no force applied to the strain gauge, the bridge will be symmetrically balanced and the voltmeter will indicate zero volts, representing zero force on the strain gauge.

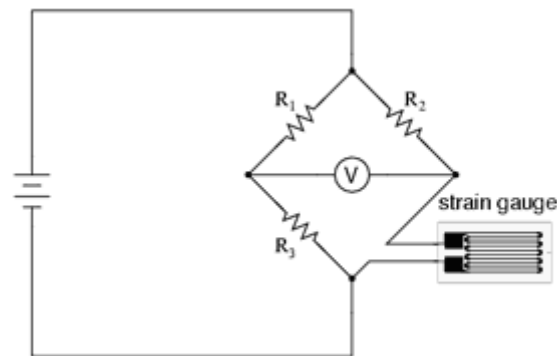


**Figure H.14: Quarter bridge strain gauge circuit [126]**

As the strain gauge is either compressed or tensed, its resistance will decrease or increase, respectively, thus unbalancing the bridge and producing an output at the voltmeter. This arrangement, with a single element of the bridge changing resistance in response to the measured variable (mechanical force), is known as a quarter-bridge circuit. As the distance between the strain gauge and the three other resistances in the bridge circuit may be substantial, wire resistance has a significant impact on the operation of the circuit. To illustrate the effects of wire resistance, the same schematic diagram is shown in Figure H.15 but with the addition of two resistor symbols in series with the strain gauge to represent the wires.

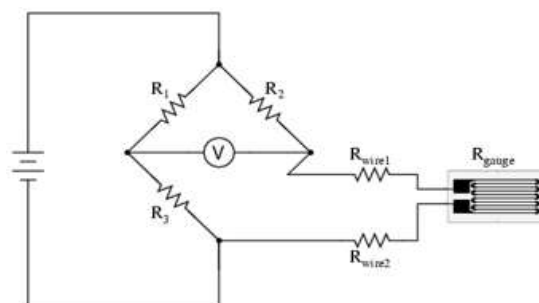


**Figure H.15: Quarter bridge strain gauge circuit with addition of two resistors [126]**

The strain gauge's resistance ( $R_{\text{gauge}}$ ) is not the only resistance being measured: the wire resistances  $R_{\text{wire1}}$  and  $R_{\text{wire2}}$ , being in series with  $R_{\text{gauge}}$ , also contribute to the resistance of the lower half of the rheostat arm of the bridge, and consequently contribute to the voltmeter's indication. This, of course, will be falsely interpreted by the meter as physical strain on the gauge. While this effect cannot be completely eliminated in this configuration, it can be minimized with the addition of a third wire, connecting the right side of the voltmeter directly to the upper wire of the strain gauge:

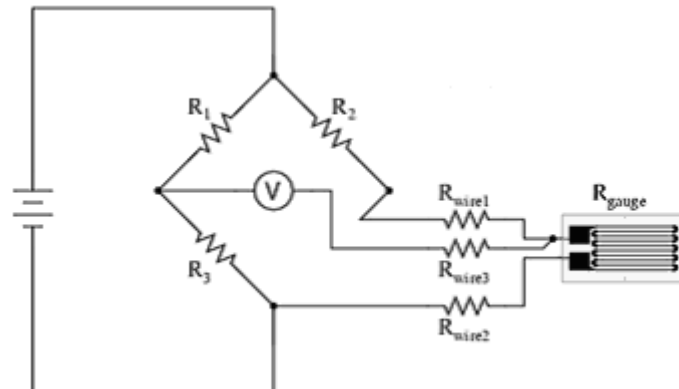


**Figure H.16: Three-wire, quarter-bridge strain gauge circuit [126]**

Because the third wire carries practically no current (due to the voltmeter's extremely high internal resistance), its resistance will not drop any substantial amount of voltage correspondingly. Notice how the resistance of the top wire ( $R_{\text{wire1}}$ ) has been by-passed now that the voltmeter connects directly to the top terminal of the strain gauge, leaving only the lower wire's resistance ( $R_{\text{wire2}}$ ) to contribute any stray resistance in series with the gauge.

There is a way, however, to reduce wire resistance error far beyond the method just described, and also help mitigate another kind of measurement error due to temperature. An unfortunate characteristic of strain gauges is that of resistance change with changes in temperature. This is a property common to all conductors, some more than others. Thus, the quarter-bridge circuit shown (either with two or with three wires connecting the gauge to the bridge) works as a thermometer just as well as it does a strain indicator.

## Factors which affect the choice of an instrumentation system

Selecting a precise acquisition system depend on several factors. Each factor capable of much finer subdivision an infinite number of possible system types can be imagined. Below test conditions stretch the selecting appropriate gauge for the right application.

### (a) Test conditions

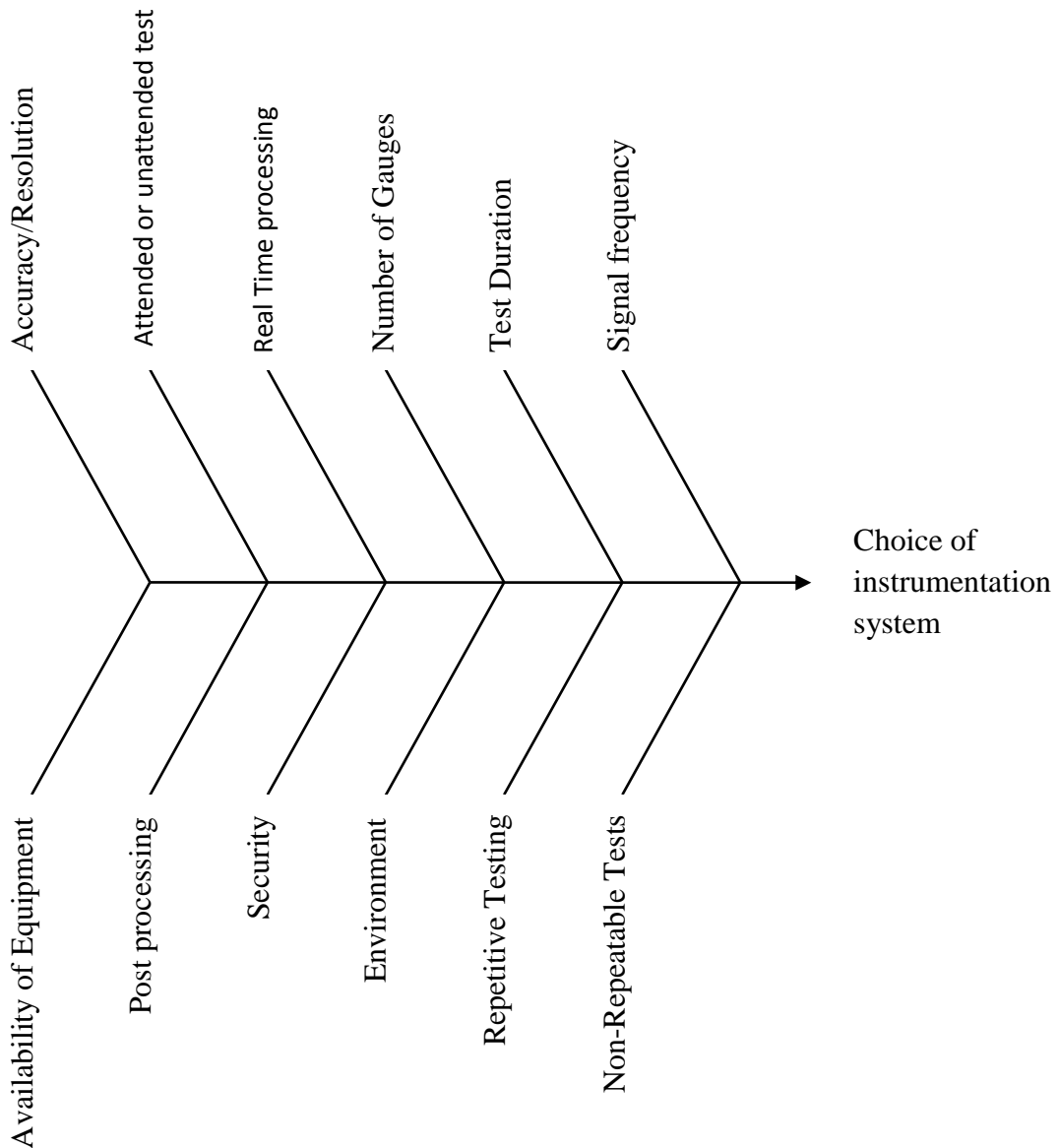


**Figure H.17: Fishbone diagram showing factors which affect the selection of an instrumentation system [112]**

## (b) Typical systems

A static test usually consists of loading a component or structure in increment with the strains being recorded for each increment. The choice of instrumentation depend on the number of channels, the available time or manpower, the time over which each load increment can be held constant for the all the channels to be scanned, and the amount of real time processing required. Testing may be carried out under laboratory, workshop or site conditions.

- (1) The simplest equipment would be a manually operated portable strain indicator as shown in Figure H.18. The equipment is portable and robust and ideal for on-site work. There are channel selectors which can be connected to the indicator so that, typically, one operator can log up to 10 readings per minute on hand written sheets.



**Figure H.18: Strain indicator [112]**

- (2) More elaborate instrumentation systems have much higher scanning speeds and sophisticated computer control of test, real-time processing and storage. The system utilizes a laptop which is only dedicated to the system whilst actually scanning and recording test data. The scanning speed of this system is 25 channels per second with a maximum of 1000 channels. Post processing and test programming can be done with the laptop off site under office or laboratory conditions.
- (3) A Data Logger is a device used mainly in measurement application. Data logging is the measurement of any physical or electrical parameters over a period of time. The data can be in the form of voltage, strain, temperature, current, etc. It acts as an interface between the strain gauge and the LABVIEW software. LabVIEW is a data acquisition software package mainly used with hardware acquisition boards LabVIEW has many features like processing of measured data or simulated signals and used for data acquisition. LABVIEW (short for Laboratory Virtual

Instrumentation Engineering Workbench) is a graphical programming environment used to develop sophisticated measurement, test and control systems using block diagrams that resemble a flowchart. Using Lab VIEW the strain parameters can be measured. The wires of strain gauge are connected to the data logger and measurements will be collected via the LABVIEW given that the LABVIEW is connected to the data logger.

A typical data logger uses a combination of analog and digital filtering to make an accurate representation of in-band signals while giving out-of-band signals. The filters differ between signals based on the frequency range, or bandwidth, of the signal.

Larger centralized computers can be used for post processing either using data recorded on site, or with direct inputs from a remote data acquisition system using a data link, such as a MODEM operating on GPO telephone lines.



**Figure H.19: National Instruments Data acquisition system [112]**

## H.4 Strain Gauge Selection

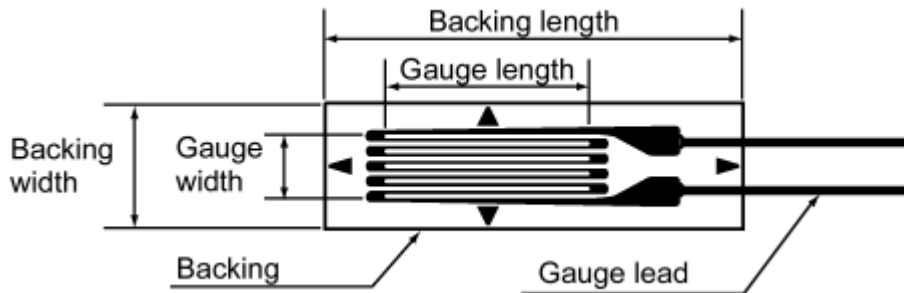


**Figure H.20: Characteristic of a strain gauge [112]**

### 1. Consider the Gauge Pattern

a) Uni-axial strain gauge should be considered if: A single strain is to be measured and the direction is known or low cost is a priority.



**Figure H.21: Uni-axial strain gauge [112]**

b) Bi-axial ( $0^\circ$ ,  $90^\circ$  T-Rosette) should be considered if: Principal strains ( $\epsilon_{1,2}$ ) are to be measured and direction is known (also applicable to torques).

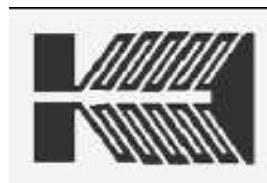


**Figure H.22: Bi-axial strain gauge [112]**

c) Tri-axial/ Three-Element ( $0^\circ$ - $45^\circ$ - $90^\circ$  rectangular rosette,  $0^\circ$ - $120^\circ$ - $240^\circ$  delta rosette) should be considered if: Principal strains ( $\epsilon_{1,2}$ ) are to be measured and direction is unknown.

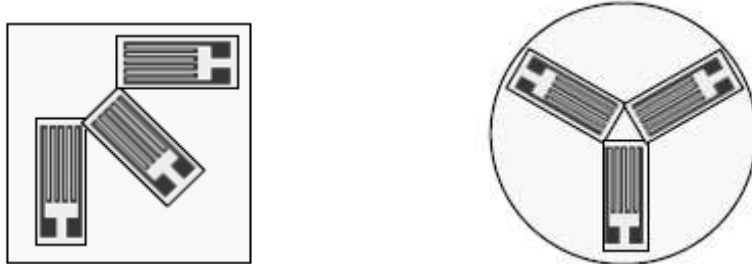


**Figure H.23: 0°-45°-90° Rectangular rosette & 0°-120°-240° Delta Rosette [112]**

d) Stacked rosette gauge configuration should be considered if: There isn't much space available for mounting or if localized strain is to be measured where large strain gradient exists.

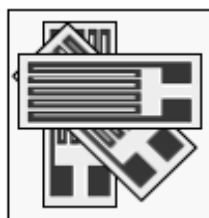


**Figure H.24: Stacked Strain Gauge Configuration [112]**

e) Planar gauge configuration should be considered if: Heat effects are likely to be an issue, where accuracy and stability is critical.

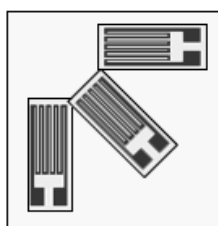


**Figure H.25: Planar gauge configuration [112]**

## 2. Gauge Length

Shorter gauges are used ( $l \leq 3\text{mm}$ ) when

1. There isn't much space available for mounting.
2. Localized strain is to be measured (ex. near a fillet, hole, notch etc.).
3. A large strain gradient exists.

4. Accuracy of the measurement is less critical.

Longer gauges are used ( $l \geq 6\text{mm}$ ) when

1. Easier installation is a priority.
2. Heat effects are likely to be an issue.
3. Accuracy and stability are critical.
4. The surface is non-homogeneous.
5. Low cost is a priority (5-12 mm lengths are usually the cheapest).

### 3. Wire Material

There are a number of different metal alloys that are used in strain gauges. Each one has its own unique properties that make it more suitable for particular applications.

a) Nickel/Copper Alloy (Gauge Factor 2.1)

1. Most common material in gauges, and therefore low cost.
2. Better suited to static strains rather than dynamic.
3. Gauge factor remains nearly constant even through large deformations.
4. Exhibits self-temperature compensation.
5. Temp range  $-30^{\circ}\text{C}$  to  $193^{\circ}\text{C}$  (though can experience a lot of drift above  $65^{\circ}\text{C}$ ).

b) Nickel/Chromium/Iron/Aluminum (Gauge Factor 2.0)

1. Best suited to low temperature environments (as low as  $-265^{\circ}\text{C}$ ).
2. More stable over extended periods of strain.
3. Very difficult to solder.

c) Iso-Elastic: Iron/Nickel/Chromium/Manganese Alloy (Gauge Factor 3.6)

1. High sensitivity.
2. High resistance.
3. Well suited for dynamic strain readings (has a good fatigue life).
4. Does not exhibit temperature compensation.
5. Non-linear response beyond  $-5000\mu\epsilon$ .

d) Platinum Based Alloys, alloyed with Tungsten or Iridium (Gauge Factor - 4.0 to 5.1)

1. High sensitivity.
2. Well suited to high temperature environments (in excess of  $230^{\circ}\text{C}$ ).

e) Semi-Conductor Gauges (Gauge Factor 70 to 135).

1. Very high sensitivity (-50 times that of wire).
2. High resistance.
3. Typically more expensive than wire.
4. Can be made smaller than wire/foil gauges for lower cost.
5. More likely to drift with temperature changes.
6. Resistance doesn't change linearly with strain (making data analysis more difficult).
7. Typically have lower strain limits than a comparable wire gauge.

#### **4. Backing Material**

a) Polyimide

1. Most common backing material and therefore low cost.
2. Better suited to static strains rather than dynamic.
3. Capable of large elongations and is very flexible.
4. Not suitable in extreme temperature conditions.

b) Epoxy

1. Minimizes errors caused by the backing.
2. Brittle and require special skill to install.
3. Maximum elongation is limited.

c) Glass Fibre Enforced Epoxy

1. Performs well over widest temperature range (up to 400°C).
2. Well suited to dynamic strains and fatigue loading.
3. Maximum elongation is limited.

d) Strippable Backing

1. Backing is removed during installation and the adhesive serves as an insulator between the gage and the mounting surface.
2. Best for use in extremely high temperature applications.
3. Installation requires special skill.

## **5. Consider Adhesives**

### a) Cyanoacrylate Cement

1. Very common / Industry standard.
2. Fast bonding -10min.
3. Gentle clamping required for 1-2 minutes.
4. Does not last for extended periods of time (months).

### b) Epoxy

1. Exhibits high bonding strength.
2. Should be used when high strains (e.g. to failure) are to be measured.
3. Required a clamping pressure (-5 to 20psi) during cure.
4. Has a long cure time, can be decreased by applying heat (-120°C).

## H.5 Surface Preparation Steps

For a strain gauge to read properly and reliably it must be installed correctly. This means first preparing the surface to which you will be bonding the gauge later. The procedures for preparing the surface are simple and easy to follow, yet will result in consistent, strong, and stable bonds. The procedures outlined below are generalized for all metals. The sequence of steps that follows is illustrated in Figures H.26-48 [112].

### 1. Surface clean-Degreasing

Use a solvent (such as acetone or alcohol) to remove any grease or oils from the surface to which the strain gauge will be bonded. This is to prevent any contaminants from being driven into the surface while performing subsequent steps. Clean an area significantly larger than the gauge (4 to 6 inches on all sides) to prevent any contaminants from the surrounding area from being introduced into the gauge area.



**Figure H.26: Use a liberal amount of degreaser.**



**Figure H.27: Wipe the specimen surface thoroughly with a gauze sponge.**



**Figure H.28: To avoid recontamination, discard soiled sponges and continue until the sponge comes up clean.**

## **2. Abrade surface**

Remove any oxidation, paint or coating from the surface finishing the abrading with a 400 grit silicone-carbide paper to ensure a proper texture for adhesion. A cross-hatched abrasion pattern is preferable. Be careful not to over-abrade the surface resulting in change of either dimensions or mechanical properties.



**Figure H.29: Flood the gagging area with conditioner.**

Wet lap with the 320-grit silicon carbide paper . Do not allow conditioner to dry on the surface.



**Figure H.30: A dozen strokes are usually adequate.**



**Figure H.31: Wipe dry with a gauze sponge . Use only once through the gauging area.  
With a refolded or fresh sponge, wipe away from the gauging area.**



**Figure H.32: Remove any excess chemicals from the work surface.**

### **3. Mark layout lines-Burnishing**

Use a clean rule and a hard pencil or pen to mark the desired position of the gage. Perpendicular lines crossing at the center of the gage area is standard, so that they can be lined up with reference marks on the gage.



**Figure H.33: With a clean straight edge, and a 4H pencil firmly burnish a layout line.  
Hold the pencil perpendicular to the surface.**

### **4. Cleaning**

Scrub the area with a solvent or marketed acid conditioner with a cotton-tipped applicator until the tip no longer comes up discolored. Do not allow the conditioner to dry on the surface, use a gauze sponge to wipe it off in a single slow stroke, then again with a clean sponge in the opposite direction. This prevents dragging any of the contaminates back into the gage area.



**Figure H.34: Use a liberal amount of acid conditioner to remove all graphite from the burnished layout line by scrubbing along the line with a cotton-tipped applicator.**



**Figure H.35: Keep scrubbing, but check the applicator tip for soiled appearance. Continue until the tip comes up clean.**



**Figure H.36: Now, flood and re-clean the entire gagging area.**



**Figure H.37: Replace the applicators when they become soiled. As before, continue scrubbing until the tip comes up clean.**



**Figure H.38: Refold, and dry the remaining area.**

## **H.6 Bonding Procedure**

1. Using tweezers to remove the gage from the transparent envelope, place the gage (bonding side down) on a chemically clean glass plate or gauge box surface. If a solder terminal will be used, position it on the plate adjacent to the gage as shown. Place a gage installation tape over the gage and terminal. Take care to center the gage on the tape. Carefully lift the tape at a shallow angle (about 45 degrees to specimen surface), bringing the gage up with the tape as illustrated above.

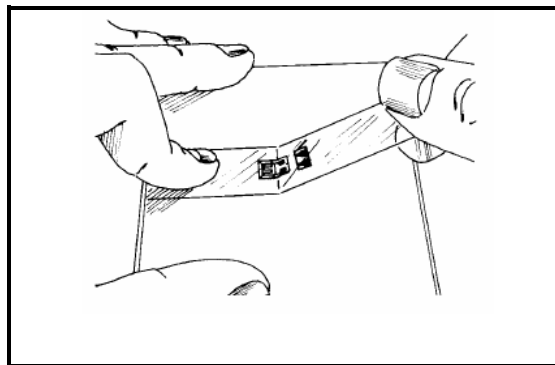


**Figure H.39: Removing the gauge from transparent envelope.**

2. Position the gauge/tape assembly so that the triangle alignment marks on the gauge are over the layout lines on the specimen. If the assembly appears to be misaligned, lift one end of the tape at a shallow angle until the assembly is free of the specimen. Realign properly, and firmly anchor at least one end of the tape to the specimen.

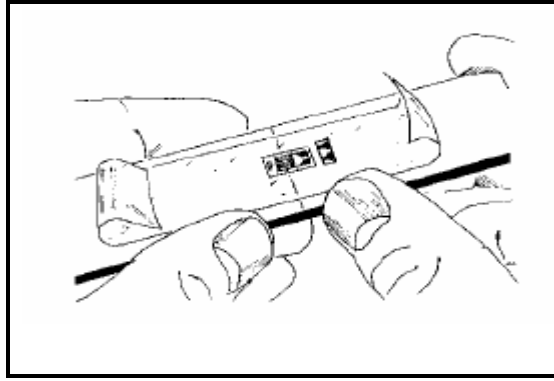


**Figure H.40: Positioning the gauge on the layout line.**

3. Lift the gauge end of the tape assembly at a shallow angle to the specimen surface (about 45 degrees) until the gage and terminal are free of the specimen surface. Continue lifting the tape until it is free from the specimen approximately 1/2 in [10 mm] beyond the terminal. Tuck the loose end of the tape under and press to the specimen surface so that the gauge and terminal lie flat, with the bonding surface exposed.

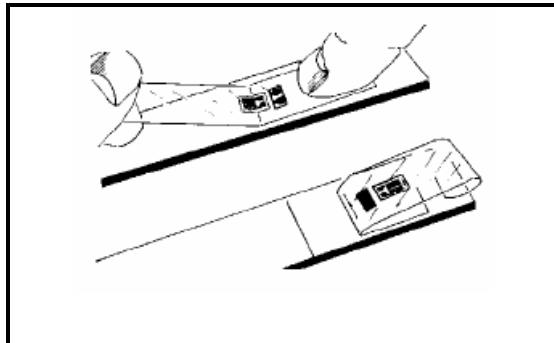


**Figure H.41: Lift the tape to allow applying catalyst.**

4. A cyano acrylate can now be applied to the bonding surface of the gage and terminal. Very little of this catalyst is needed, and it should be applied in a thin, uniform coat. Wipe the brush approximately 10 strokes against the inside of the neck of the bottle to wring out most of the catalyst. Move the brush to the adjacent tape area prior to lifting from the surface. Allow the catalyst to dry at least one minute under normal ambient conditions of +75°F [+24°C] and 30% to 65% relative humidity before proceeding.

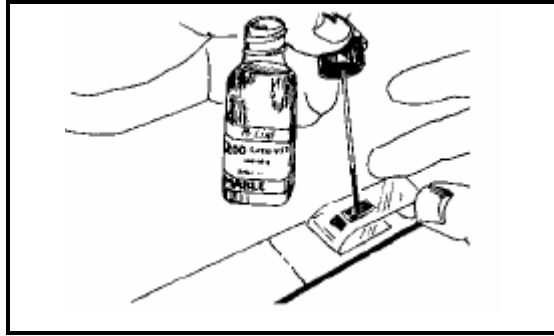


**Figure H.42: Applying cyano acrylate.**

5. Lift the tucked-under tape end of the assembly, and, holding in the same position, apply one or two drops of adhesive at the fold formed by the junction of the tape and specimen surface. This adhesive application should be approximately 1/2 in [13 mm] outside the actual gauge installation area. This will insure that local polymerization that takes place when the adhesive comes in contact with the specimen surface will not cause unevenness in the gauge glue line.

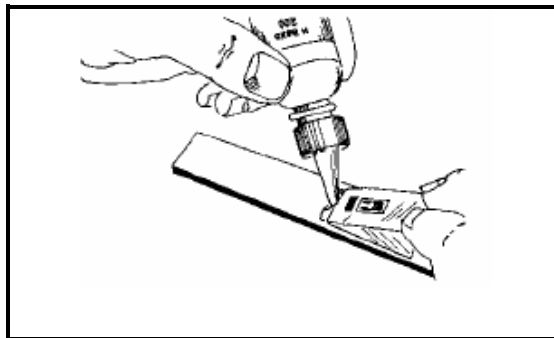


**Figure H.43: Applying adhesive.**

6. Immediately rotate the tape to approximately a 30-degree angle so that the gage is bridged over the installation area. While holding the tape slightly taut, slowly and firmly make a single wiping stroke over the gage/tape assembly with a piece of gauze bringing the gauge back down over the alignment marks on the specimen. Use a firm pressure with your fingers when wiping over the gage. A very thin, uniform layer of adhesive is desired for optimum bond performance.

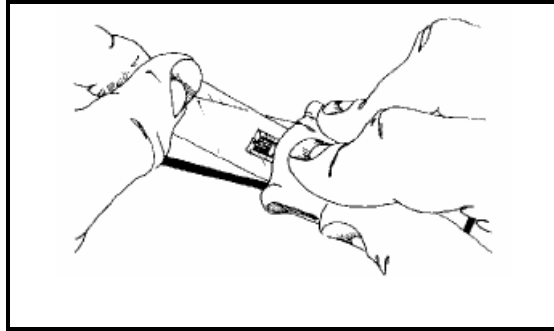


**Figure H.44: Applying gauge on the test specimen.**

7. Immediately upon completion of wipe-out of the adhesive, firm thumb pressure must be applied to the gage and terminal area. This pressure should be held for at least one minute. In low-humidity conditions (below 30%), or if the ambient temperature is below +70°F [+20°C], this pressure application time may have to be extended to several minutes.

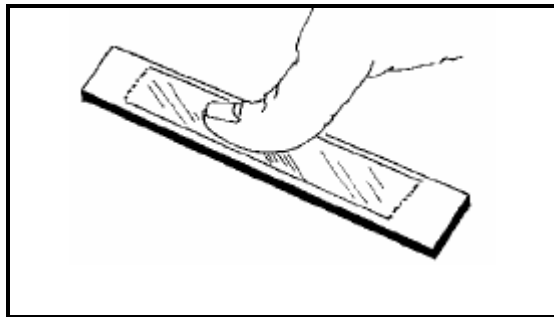


**Figure H.45: Applying uniform pressure.**

8. The gage and terminal strip are now solidly bonded in place. It is not necessary to remove the tape immediately after gage installation. The tape will offer mechanical protection for the grid surface and may be left in place until it is removed for gage wiring. To remove the tape, pull it back directly over itself, peeling it slowly and steadily off the surface. This technique will prevent possible lifting of the foil on open-faced gauges or other damage to the installation.

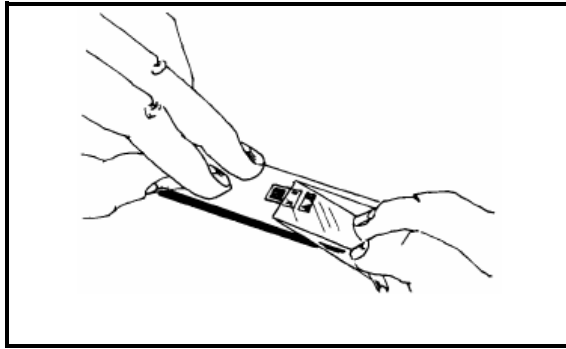


**Figure H.46: Remove the tape.**

### **H.7 Lead Wire Attachment**

When attaching lead wire, the most important factor is to prevent overheating of the gauge. This can melt the gauge and render it useless.

1. Mask the strain gauge with drafting tape leaving only the solder tabs exposed.
2. Clean the tip of the soldering iron on the wet sponge pad.
3. Tin the soldering tip with some rosin core solder.
4. Lay the end of the solder across the solder pad and apply the iron tip onto the solder. Apply firm pressure for no more than one second and remove both the solder and the iron simultaneously.
5. You should now have a bright even mound of solder on the pad. Repeat the above procedure until you have a nice even mound of solder on each solder pad and each strain relief terminal.
6. Strip and tin the wires. Bend the ends of the wire such that there will be a small bend between the strain relief and the gauge when the wire is soldered to the gauge.
7. Tape the wire assembly in place using the provided drafting tape. Make sure the wires are in the exact place they will be once they are installed. If you are installing a rosette or multiple gauges, labeling the wires at this point will allow you to identify them once they are soldered into place.
8. Press the soldering iron onto the wire over a pad while feeding a small amount of solder between the iron and the wire. The wire should slide into the melting solder. Allow the connection to cool thoroughly before handling.
9. Repeat for each solder tab and the strain relief terminals.

10. Remove any leftover flux from the solder with a gauze sponge soaked in rosin solvent. Use a dabbing action to prevent damage to the gauge.
11. Check the connections and their resistances. If there are any unexpected resistances or the wires are not solidly attached, re-solder the connections.